UGC Approved Journal No. 63628
ICV 2016 : 55.77
SJIF Impact Factor 4.11

ISSN: 2322-0015

International Research Journal of

SCIENCE & ENGINEERING

An International Peer Reviewed Open Access Refereed Journal

Special Issue A2 January 2018

State level Seminar on

Advanced Methods for Material Characterization" (SCAMMC- 2018)

5th and 6th January, 2018

STATUTORY WARNING

Articles, data, figures, scientific contents and its interpretation and authenticity reported by author(s) and published in IJLSCI are the exclusive views of author(s). The editorial board, IJLSCI is not responsible for any controversies arising out of them.
In case of any plagiarism found, author(s) will have to face its consequences.

Organised by
Department of Physics
Dnyaneshwar Gramonnati Mandal's
Hon. Balasaheb Jadhav
ARTS, COMMERCE AND SCIENCE COLLEGE
Ale, Tal. Junnar, Dist. Pune -412411

ABOUT IRJSE

IRJSE is a peer-reviewed journal, which aims to provide the most complete and reliable source of information on current developments in the field. The emphasis will be on publishing quality research papers rapidly and freely available to researchers worldwide. IRJSE serves an important role by encouraging, fostering and promoting developments in Science & Engineering areas. It is an open access journal, which publishes original research articles, reviews and short communication in all areas of Sciences and Engineering and Technology at the interface of related disciplines.

Science Discipline Viz. Mathematics, Statistics, Physics, Chemistry, Geology & Earth Science, Environmental Science, Life Sciences, etc.

Engineering sciences and technology discipline Viz. Mechanical Engineering, Civil Engineering, Electrical Engineering, Electronics & Telecommunication Engineering, Computer Engineering, Chemical Engineering, Biotechnology, Information Technology, Architecture Engineering, Artificial Intelligence, Computer Software and Application, Computing, Data Mining, Design. Energy, Image Processing, Internet and World wide web, manufacturing, military, mining, Nanotechnology and smart materials, Networking, Polymers and Plastics, Renewable Energy, Robotics, Space environment and Aviation Technology, Systems Engineering transport, etc. RJET publishes Original research Articles, Short Communications, Review Articles in all areas of Engineering and Technology. The subject covered is Engineering Mechanics, Construction Materials, Surveying, Fluid Mechanics and Hydraulics, Modeling and Simulations, Thermodynamics, Refrigeration & Air-conditioning, Metallurgy, Electronic Communication Systems, Agricultural Machinery & Equipment, Applied Sciences, Chemical Engineering, etc.

TYPES OF RESEARCH PAPER

Original Articles:
These should describe new and carefully confirmed findings, and experimental methods should be given in sufficient detail for others to verify the work. The length of an original article is the minimum required to describe and interpret the work clearly.

Short Communications:
Short communication also contain abstract. The list of references should not exceed 15. The presentation of Short Communications should contain headings such as Introduction, Materials and Methods, Results and Discussion, etc.

Reviews Articles:
Submissions of review articles and perspectives covering topics of current interest are welcome and encouraged.

The journal is published in online version only which is free access and downloads.

This Journal is circulated / Distributed Through Subscription only

Submission of Paper: Submission of paper is encouraged by e-mail to editorirjse@gmail.com OR editor@irjse.in
Subscription Plan: Rs. 3500 /- or 250 US$ (Individual Annual); Rs. 4500/- or 350 US$ (Institutional)
Life Membership: Rs. 15000/- or 550 US$ (Individual) Rs. 25000/- or 850 US$ (Institutional)
Fellow Membership: Rs. 25000/- or 850 US$ (Individual) Rs. 35000/- or 1700 US$ (Institutional)

Publisher and Owner: Dr. Arvind Chavhan, Published from IRJSE, 46, Guruwandan, Jawahar Nagar VMV Road, Amravati- 444604. India

Publisher, Editorial Board and Editor in Chief take no responsibilities for the inaccurate, misleading data, opinion and statement appeared in the articles published in this journal. All responsibilities of the contents rest upon the authors (especially upon the corresponding author).

?

Indexing:
INNOSPACE (SJIF), ROAD, OAJI, Academic Keys, J-index.net, Scholar Steer, Research Bible, Google Scholar, DAIJ, DRIJ, DIIF, SIS, ISI, ASI.

All the Articles are freely accessible on the website of the International Research Journal of Science & Engineering http://www.irjse.in, As well as some of the Indexing agencies website via., oaji.net, research bible, Cite factors, ISI, etc.

IRJSE International Research Journal of Science & Engineering
ISSN:2322-0015
An International Peer Reviewed Open Access Referred Journal

Editorial Board

IRJSE INSTRUCTION FOR PREPARING THE MANUSCRIPT:

International Research Journal of Sciences & Engineering (IRJSE) publish research papers, case studies and short communications containing original research work of good standard and review papers of contemporary relevance from all over the world. Following types of contributions are considered for publication:

RESEARCH PAPERS (Full Length - Maximum of 12 pages-A/4 size). CASE STUDIES, SHORT COMMUNICATIONS, REVIEW PAPERS including Mini Reviews

AUTHORISATION AND DECLARATION

Authors must accept full responsibility for the content of their articles. The Members of the Editorial Board and the Publisher of the journal are not responsible for the statements and opinions expressed by the authors in their articles/write-up published in the journal. To use the copyrighted material (for example table, figure etc.), the author/s must seek the permission from the Author/s and Publisher of the material and send the copy of the permission letters via e-mail to the Administrative Editor for records. In case, if it is not possible than do not use that material.

While submitting the paper the author (s) must give a declaration that "the article has not been published or sent for publication elsewhere".

Article Preparation Guidelines

Manuscript title: The title should be limited to 25 words or less and should not contain abbreviations. The title should be a brief phrase describing the contents of the paper.

Author Information: Complete names and affiliation of all authors, including contact details of corresponding author (Telephone, Fax and E-mail address).

Abstract: The abstract should be informative and completely self-explanatory, briefly present the topic, state the scope of the experiments, indicate significant data, and point out major findings and conclusions. The abstract should summarize the manuscript content in 300 words or less. Standard nomenclature should be used and abbreviations should be avoided. The preferable format should accommodate a description of the study background, methods, results and conclusion. Following the abstract, a list of keywords (3-10) and abbreviations should be included.

Text:

Introduction: The introduction should set the tone of the paper by providing a clear statement of the study, the relevant literature on the study subject and the proposed approach or solution. The introduction should be general enough to attract a reader's attention from a broad range of scientific disciplines.

Materials and Methods: This section should provide a complete overview of the design of the study. Detailed descriptions of materials or participants, comparisons, interventions and types of analysis should be mentioned. However, only new procedures should be described in detail; previously published procedures should be cited and important modifications of published procedures should be mentioned briefly. Capitalize trade names and include the manufacturer's name and address.

Results: The results section should provide complete details of the experiment that are required to support the conclusion of the study. The results should be written in the past tense when describing findings in the authors'experiments. Previously published findings should be written in the present tense. Results and discussion may be combined or in a separate section. Speculation and detailed interpretation of data should not be included in the results but should be put into the discussion section.

Acknowledgment: This section includes acknowledgment of people, grant details, funds, etc.

Note: If an author fails to submit his/her work as per the above instructions, they are pleased to maintain clear titles namely headings, subheading.

References:

Only published or accepted manuscripts should be included in the reference list. Meetings abstracts, conference talks, or papers that have been submitted but not yet accepted should not be cited. All personal communications should be supported by a letter from the relevant authors.

IRJSE uses the numbered citation (citation-sequence) method. References are listed and numbered in the order that they appear in the text. In the text, citations should be indicated by the reference number in brackets. Multiple citations within a single set of brackets should be separated by commas. When there are three or more sequential citations, they should be given as a range. Example: "... now enable biologists to simultaneously monitor the expression of thousands of genes in a single experiment [1,5-7,28]". Make sure the parts of the manuscript are in the correct order for the relevant journal before ordering the citations. Figure captions and tables should be at the end of the manuscript.

Authors are requested to provide at least one online link for each reference as following (preferably PubMed).

Because all references will be linked electronically as much as possible to the papers they cite, proper formatting of the references is crucial. Please use the following style for the reference list:

Examples:

Published Papers:

1.Laemmli UK. Cleavage of structural proteins during the assembly of the head of bacteriophage T4. Nature, 1970 227: 680-685.

2. Brusic V, Rudy G, Honeyman G, Hammer J, Harrison L. Prediction of MHC class II- binding peptides using an evolutionary algorithm and artificial neural network. Bioinformatics, 1998; 14: 121-130.

Note: Please list the first five authors and then add "et al." if there are additional authors.

Electronic Journal Articles Entrez Programming Utilities

1.Https://www.ncbi.nlm.nih.gov/books/NBK25500/

Books:

1.Baggot JD. Principles of drug disposition in domestic animals: The basis of Veterinary Clinical Pharmacology. (1stedn), W.B. Saunders Company, Philadelphia, London, Toranto, 1999.

2.Zhang Z. Bioinformatics tools for differential analysis of proteomic expression profiling data from clinical samples. Taylor & Francis CRC Press. 2006.

Conferences:

1.Hofmann T. The Cluster-Abstraction Model: unsupervised learning of topic hierarchies from text data. Proceedings of the International Joint Conference on Artificial Intelligence. 1999.

Tables:

These should be used at a minimum and designed as simple as possible. We strongly encourage authors to submit tables as .doc format. Tables are to be typed double-spaced throughout, including headings and footnotes. Each table should be on a separate page, numbered consecutively in Arabic numerals and supplied with a heading and a legend. Tables should be self-explanatory without reference to the text. Preferably, the details of the methods used in the experiments should be described in the legend instead of in the text. The same data should not be presented in both table and graph form or repeated in the text. Cells can be copied from an Excel spreadsheet and pasted into a word document, but Excel files should not be embedded as objects.

Note: If the submission is in PDF format, the author is requested to retain the same in .doc format in order to aid in completion of process successfully.

Figures:

The preferred file formats for photographic images are .doc, TIFF and JPEG. If you have created images with separate components on different layers, please send us the Photoshop files.

All images must be at or above intended display size, with the following image resolutions: Line Art 800 dpi, Combination (Line Art + Halftone) 600 dpi, Halftone 300 dpi. See the Image quality specifications chart for details. Image files also must be cropped as close to the actual image as possible.

International Research Journal of
Science & Engineering
An International Peer Reviewed Open Access Refereed Journal

Special Issue A 2 January, 2018
on
Advanced Methods for Material Characterization

ORIGINAL ARTICLES

ISSN 2322-0015

IRJSE *Int. Res. J. of Science & Engineering,* 2018; Special Issue A2: 1-5
ISSN: 2322-0015
SJIF Impact Factor 4.11
UGC Approved Journal No. 63628
RESEARCH ARTICLE **OPEN ACCESS**

The Effect of over Doses in Gibberellic acid in Grape Vineyards (*Vitis Vinifera* L) Leaves using Biophysical Techniques in Agriculture

Dhakane SF[1] and Pandit Vidyasagar[2]

[1]Department of Physics, A. W. College, Otur, Tal-Junnar, Dist-Pune, 412409
[2]Vice-Chancellor, SRTM University, Nanded, MS, India
E-mail: dhakanesf@gmail.com

Manuscript Details
Available online on http://www.irjse.in
ISSN: 2322-0015

Editor: Dr. Arvind Chavhan

Cite this article as:
Dhakane SF and Pandit Vidyasagar. The Effect of over Doses in Gibberellic acid in Grape Vineyards (*Vitis Vinifera* L) Leaves using Biophysical Techniques in Agriculture. *Int. Res. Journal of Science & Engineering,* 2018; Special Issue A2 : 1-5.

ABSTRACT

Grape vineyards have been facing problem of disease like pink berry. The causes of which are still unknown. Earliear researchers had studied possible causes of such disease by studying effects of overdoses of pesticides, antibiotics and growth regulators. This study is based on biophysical techniques such as absorption, fluorescence and thermo luminescence. Though the cause of this disease is unknown it has been observed that the occurrence of the disease is more where application of fertilizers, pesticides, antibiotics and growth regulator is un scientific and heavy. Under such circumstances the study of biophysical applications in using PMT cryostatic method of grape vine yards becomes necessary. Steady state Florescence (FL) spectra and Thermo luminescence (TL) glow curves we are recorded from grape leaves treated with Gibberellic acid individually as well as in combination with endosulfan and Benomyl. The TL peaks were analyzed using a computer assisted model based on the general order kinetics theory, various thermodynamical parameters, such as activation energy (E), entropy (ΔS), frequency factor (So) and free energy (FE), associated with TL peaks were calculated. The TL study shows that GA at a lower concentration improves photosynthetic efficiency of plant by shifting redox potential of Q_b towards Q_a, the thermodynamical parameters also showed increase due to pesticide.

Keywords: Vineyards, Pesticides, Biophysical technique, Florescence spectra and Thermoluminescence, etc

INTRODUCTION

The term biophysical thereby emphasizes that photons are neither particles nor the waves; they are different in that they have both particle and wave nature. It covers all technical applications of light over the whole spectrum from ultraviolet over the visible to the near, mid and far-infrared. Most applications, however, are in the range of the visible and near infrared light. The term photonics developed as an outgrowth of the first practical semiconductor light emitters invented in the early Photonics also relates to the emerging science of quantum information in those cases where it employs photonic methods. Applications of photonics are ubiquitous. Included are all areas from everyday life to the most advanced science, e.g. light detection, telecommunication, information processing spectroscopy, medicine (surgery, vision correction, endoscopy, health monitoring), military technology, laser material processing, visual art, biophotonics, agriculture, and robotics. Thompson seedless, a *vitis vinifera* and its successor varieties are being cultivated widely in India. However, it has been observed that these varieties are more prone to different type of diseases. Hence in order to save the crop and to increase the yield, indiscriminate application of pesticides had become a routine practice, since the biochemical processes of cellular and sub cellular levels of the target organism and the host plant are often quite similar. The possibility of direct effects of the protective chemicals on the host plant cannot be overload.

In the present work the effects of Gibberellic acid when applied individually and also in combination with an insecticide endosulfan and fungicide benomyl on grape leaves have been investigated. The photonic technique such as fluorescence (FL) Thermolumine-scence (TL) has been adopted. Also, the modified TL set- up was developed using PMT.

MATERIALS AND METHODS:

The Commonly cultivated grape varieties in south west India Thompson seedless (*Vitis vinifera* L) were taken. The samples were collected from Narayangaon area in Pune district. TL was recorded from mature leaves at around the sixth nodal position of the shoot for different concentrations of pesticides, viz growth regulator (GA), Insecticide (Endosulfan) and fungicide (Benomyl) were selected. Different concentrations of these pesticides were prepared ranging from normal to heavy dose. Steady state fluorescence was measured from control and treated leaf discs of diameter 1.5 cm. Using Perkin Elmer LS 50 spectroflurometer, fluorescence emission spectra were measured between 650-770 nm by keeping the excitation wavelength fixed at 440nm. The biophysical technique such as thermo luminescence (TL) has been adopted the experimental set-up can be divided in to three parts (Figure) cryostat arrangement to cool the system, the heating system and PMT sliding recording system. Cryostat consists of stainless steel cylindrical container having capacity 5 liters. A copper rod along with copper plate arrangement is dipped in to this container and it acts as a cold finger. When liquid nitrogen is filled in the container the copper rod and copper plate get cooled and sample holder attains low temperature. The sample for the study of TL method needs an adjustable variable temperature in the range between 77K to room temperature (-80°C to +50°C) and this is done by heater. The heating block "K" made up of copper used in the system is circular in shape having 4 cm diameter and 30 cm thickness. In the centre of this block to hold the sample holder cavity 'S' with 2 cm diameter and 25 mm depth has been made sample holder is soldered over the heater. A hole from the surface of the sample holder cavity up to the outer side of the 'K' block has been drilled to hold the thermocouple (TC) so that its one junction is kept in such a position that it permitted a good contact

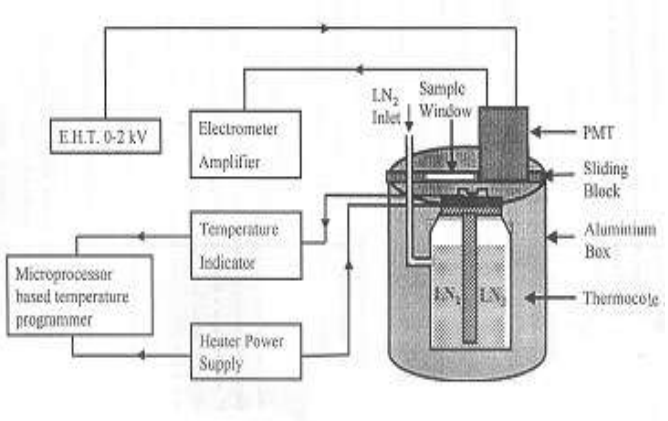

Fig. 1 Block diagram of new TL setup

with the sample holder. At the bottom of this the heater element is of nicrome wire with 26 ohms resistance and of wattage is 200W at 230V A.C. The wire is wound around a Mica sheet and its terminals are taken out for connection. The heater is fitted on the top of copper rod. It is dipped in to LN_2 for cooling purpose. Photomultiplier tube (PMT) is used here to measure the luminescence and it is the heart of recording system, PMT should have large area for light detection, high gain and ability to detect a single photon. The 9798B has a S20 type response which is sensitive from 200 nm to 900 nm. This TL set up requires less LN_2 and less time to cool the system for next observation.

RESULT AND DISCUSSION:

(A) Thermoluminescence: In Thermoluminescence, the fitted TL glow curve from the control untreated grape (*Vitis vinifera* L) leaf disc. It shows the presence of only one peak at about -6^0C. As per standard TL nomencla-ture this peak can be assigned as peak II attributed to S_2/S_3 Q_a recombination 3. The fitted TL spectra recoded from grape leaf disc treated with GA. It shows the presence of the entire peaks viz. peak I, II, III, IV, and V at around -21^0C, -4^0C, 11^0C, 29 ^{0}C and 51 ^{0}C, respectively the intensities of the peak shows increase. Except for peak II all the peaks are broad Table shows the calcula-ted values of all the Thremodynamical parameters.

The present study was planned to check the effect of growth regulator when applied individually as well as in combination with other pesticides on the photosynthetic electron transport chain of grape (*Vitis vinifera* L) leaves. This result confirm that lower concentration of GA improves photosynthetic efficiency of plant by shifting redox potential of Q_b towards Q_a, but when GA was applied with other pesticides damage to the photo-synthetic apparatus started right from lower concentration. Though GA tries to improve photosynthetic efficiency the presence of other pesticides creates stress on the plant. The increase in thermo dynamical parameters also indicates damage to the photosynthetic apparatus due to the pesticides. The studies have indicated that the TL techniques can be used to monitor the effect of pesticides on the photo-synthetic electron transport chain and can detect minute alternation in the photo-synthetic apparatus of plants. Such an alternation is otherwise undetectable and hence may go unobserved till the fruiting period.

Table 1: Thremodynamical parameters of thermo luminescence glow curves recorded from *Vitis vinifera* L. leaves using the general order kinetics theory.

Control (untreated)

Peak	Activation Energy E(eV)	Entropy ($\Delta S/k_B$)	Free Energy F.E.(eV)	Frequency Factor S^{-1}
I	0.677	-1.58	0.712	4.28 $X10^{14}$
II	1.55	35.34	0.739	4.66 $X10^{25}$
Effect of GA				
I	0.572	-4.07	0.654	3.52 x 10^8
II	0.774	-1.45	0.715	4.85 x 10^9
III	0.964	0.546	0.61	3.59 $x10^{10}$
IV	0.993	6.59	0.802	1.52 x 10^{13}
V	1.192	4.93	0.863	2.89 x 10^{12}
Effect of Benomyl with GA				
I	0.861	6.918	0.71	2.1 $x10^{13}$
II	1.541	35.909	0.736	3.6 $x10^{23}$
III	1.49	30.803	0.761	5.22 $x10^{22}$
IV	1.784	40.159	0.793	5.75 x 10^{27}
V	1.257	4.65	0.868	2.97 x 10^{30}

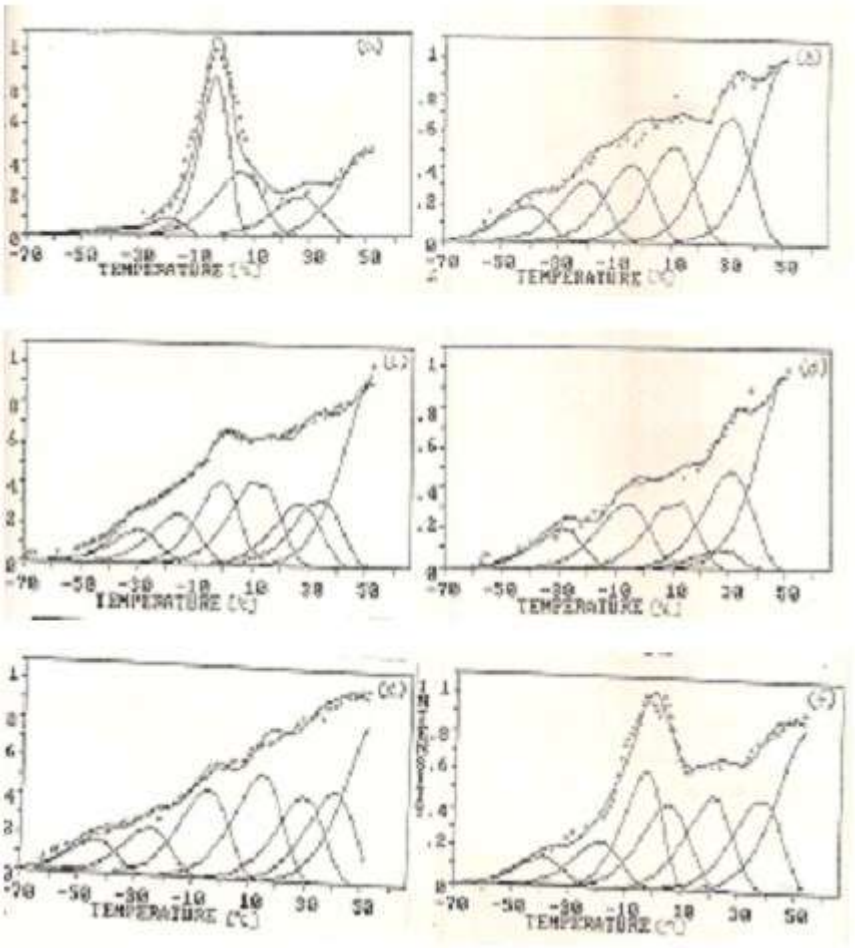

Fig 2 Thermoluminescence glow curve

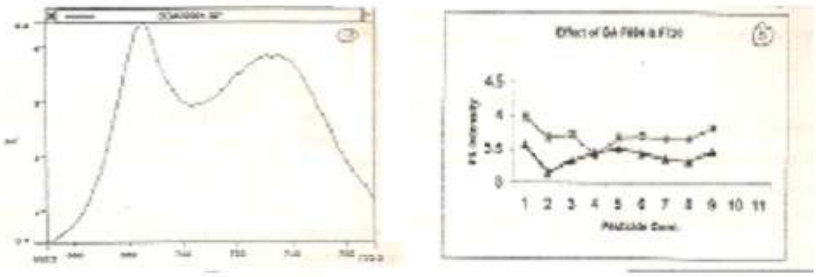

Fig. 3: Fluorescence

(B) Fluorescence: As reported earlier Benomyl treatment results in increasing fluorescence intensity. Hence Benomyl and Gibberellic acid when applied together no variation in fluorescence intensity was observed. The more or less intensity level of FL, at 684 nm as observed for lower concentration of pesticides is indicative of the compensating effects of Gibberellic acid and Benomyl. The heaviest concentration though results in degenerative effects due to application of both the pesticides and the subsequent increase in fluorescence intensity.

Figure 3 (a) shows steady states fluorescence spectra recorded from control (unsaturated) grape leaf disc. It shows one major peak at around 684 nm attributed to PS-II and a shoulder at 730 nm, from PS-I. Figure 3(b) shows variation in florescence intensity for 684 nm as well as 730 nm. Peak recorded from grape leaves

treated with different concentration of GA. For the lower concentration of GA decrease in fluorescence intensity is observed, while for higher concentration the fluorescence intensity is almost constant. This indicates that lower concentration of GA favors forward flow of electron and improves photosynthetic efficiency of grape leaf. Earlier studies have reported that individual application of endosulfan increases fluorescence Intensity, while as mentioned above Gibberellic acid treatment decreases fluorescence intensity. Hence the observed oscillatory pattern indicates that endosulfan and Gibberellic acid when applied in combination compete to demonstrate their individual effects, though Gibberellic acid seems to have an upper hand.

CONCLUSION

The present study was planned to check the effect of growth regulator when applied individually as well as in combination with other pesticides on the photosynthetic electron transport chain of grape (*Vitis vinifera* L) leaves. The FL results have indicated that growth regulator Gibberellic acid for lower concentration improves the photosynthetic efficiency of plants. But when its concentration is increased or when it is applied with other pesticides it affects PS-II adversely. In fact, PS-II is more damaged as compared to PS-I.due to the application of Gibberellic acid and also with pesticides. The TL results confirm that lower concentration of GA improves photosynthetic efficiency of plant by shifting redox potential of Q_b towards Q_a, The increase in thermo dynamical parameters also indicates damage to the photosynthetic apparatus due to the pesticides. This is not the only cause of pesticides but other factors also take part in that like soil nutrients, temperature, and humidity. There for further study will be necessary.

REFERENCES

1. Winkler AJ. General Viticulture, University of California press, 1962
2. Sane PV, Rutherford AW. Light Emission by Plant and Bacteria", Academic Press, New York, 1986, pp: 329-361.
3. Inoue Y. Photosynthetic Thermoluminesceance as a simple probe of Photosystem-II electron transport in Biophysical Techniques using Photosynthesis", Kluwar Academic Publication, 1996, pp: 93-107.
4. Vidyasagar PB, Thomas S, Banerjee M, Hegade U, Shaligram A.D., *Journal of Science Technology*, 1993, pp: 125-128.
5. Jyoti Gaikawad, Sarah Thomas, Vidyasagar PB, Aghav SD, Banerjee M, Hedge U, Shaligram AD. Mathematical model based on general order kinetics, *Journal of Photobiology, B. Biology*, 19, 1993, pp: 25-128.
6. Gaikwad J, Thomas S, Aghav SD, Vidyasagar PB, *Vitis*.37(1), 1998, pp: 11-14.
7. Sarah Thomas, Jyoti Gaikwad, Vidyasagar PB. *Indian Journal of Biochemistry and Biophysics*, 36, 1999, pp: 189-195.

IRJSE International Research Journal of Science & Engineering
Int. Res. J. of Science & Engineering, 2018; Special Issue A2: pp 6-9
ISSN: 2322-0015
SJIF Impact Factor 4.23
UGC Approved Journal No. 63628
RESEARCH ARTICLE **OPEN ACCESS**

Study of Dielectric and Electric properties of La^{3+} Doped Ni-Zn Nanoferrite

Kulkarni VD[1] and Rathod SM[2]

[1]Department of Physics, Hutatma Rajguru Mahavidyalaya, Rajgurunagar, Pune, 410505, MS, India
*Research Student, Science College, SRTM University, Nanded
[2]Nanomaterials & Lasers Research Lab, Abasaheb Garware College, Pune, 411004, MS, India
E-mail: kulkarni_vd55@yahoo.co.in | smragc@rediffmail.com

Manuscript Details
Available online on http://www.irjse.in
ISSN: 2322-0015

Editor: Dr. Arvind Chavhan

Cite this article as:
Kulkarni VD and Rathod SM. Study of Dielectric and Electric properties of La^{3+} Doped Ni-Zn Nanoferrite, *Int. Res. Journal of Science & Engineering,* January 2018 | Special Issue A2 : 6-9 .

ABSTRACT

The rare earth La^{3+} material substituted in Nickel-Zinc nano ferrite was synthesized by sol-gel auto combustion method. The dielectric and electric properties of the $Ni_{0.5}Zn_{0.5}$ $La_xFe_{2-x}O_4$nanoferrite where (x=0.025, 0.050, 0.075, 0.100, 0.125) were studied. The dielectric constant and dielectric loss was observed with the variation in frequencies. The a. c. resistivity was observed with the increase in Lanthanum concentration. The dc resistivity of $Ni_{0.5}Zn_{0.5}$ $La_xFe_{2-x}O_4$ nanoferrite with increase in frequency was investigated at constant temperature 200^0C using Two Probe method. The dc conductivity of $Ni_{0.5}Zn_{0.5}$ $La_xFe_{2-x}O_4$ nanoferrite was observed with increase in Lanthanum concentration.

Keywords: - Sol-gel method, Ni-Zn nano ferrite, dielectric constant, dielectric loss, dc resistivity, a. c. resistivity.

INTRODUCTION

The Al^{3+} and Cr^{3+} doped Co-Ni spinel ferrites was successfully synthesized by the sol gel auto combustion method. The dielectric parameters decrease due to the doping of the nickel, aluminum and chromium ions in the cobalt ferrites. Such ferrite has the applications in the high frequency and electromagnetic wave absorbing devices due to the high dc resistivity [1]. The sol gel auto combustion method has the excellent mixture of the combustion and chemical gelation route. The sol gel auto

combustion method has the good stoichiometric ratio and gives the ultrafine nanoparticles. The Lanthanum substituted in Nickel ferrite [2]. The cadmium substituted nickel- cobalt nanoferrite was synthesized by standard double sintering ceramic method. The resistivity was decreases with increase in cadmium content. The dielectric constant decreases as frequency increases. The AC conductivity increases as increase in frequency [3]. The Ni-Zn ferrite was prepared using the solid state reaction method. As temperature increases then the DC resistivity also decreases and DC resistivity was obtained by Two Probe Method [4]. The Zinc doped cobalt ferrite was successfully prepared by the solution combustion method. The electric and dielectric properties of Zinc doped cobalt ferrite were studied and it was found that dielectric constant and dielectric loss decreases as frequency increases [5]. The Cu^{+2}doped Ni-Zn ferrite was synthesized by auto combustion method. It was reported that that dielectric constant and dielectric loss are depends on the frequency. The dielectric constant increases as copper content increases [6]. The $Ni_{1-x}Cd_xFe_2O_4$ ferrite was obtained by the sol gel auto combustion method. It was noted that dc resistivity is the temperature dependent. The dc resistivity decreases as temperature increases and hence Ni-Cd ferrite shows that the semiconducting behavior [7]. The $Cu_{1+x}Ti_xFe_{2-2x}O_4$ (x= 0.0, 0.05, 0.1, 0.15, 0.2 and 0.3) was synthesized by ceramic method. It was noted that dielectric constant and dielectric loss decreases as frequency increases and concluded that normal behavior of the dielectric [8]. The Ni–Cu–Zn ferrites were prepared by the oxalate based precursor method. The dielectric constant and dielectric loss decreases as increase in frequency [9].

The ferrites have large number of applications in various fields. Therefore, rare earth La^{3+} material doped in Nickel- Zinc ferrite was prepared by sol-gel auto combustion method. The dielectric and electric properties was studied.

MATERIALS AND METHODS:

All chemicals such as Ferric nitrate ($Fe(NO_3)_3.9H_2O$), Nickel nitrate ($Ni(NO_3)_2 \cdot 6H_2O$), Zinc nitrate ($Zn(NO3)_2 \cdot 6H_2O$), Citric acid ($C_6H_8O_7$), Ammonium hydroxide (NH_4OH) was used in high purity AR grade. The stoichiometric ratio proportion of all nitrates and citric acid was used. All nitrates were added in distilled water and stirred till to obtain the homogeneous solution. To maintain pH= 7, the ammonium hydroxide solution was added drop by drop during the stirring process. The Citric acid was used as a Fuel. This solution was stirred constantly for 3 to 4 hours to obtain sol at temperature 100˚C. When a viscous brown gel was formed, then the auto-combustion takes place. The fine powder of $Ni_{0.5}Zn_{0.5}La_xFe_{2-x}O_4$ nanoferrite was obtained. The $Ni_{0.5}Zn_{0.5}La_xFe_{2-x}O_4$ nanoferrite powder was sintered at 600 ˚C for 4 hours. The $Ni_{0.5}Zn_{0.5}La_xFe_{2-x}O_4$ (Where x=0.025, 0.050, 0.075, 0.1, 0.125) nanoparticles were synthesized by sol-gel auto combustion synthesis Method.

RESULT AND DISCUSSION:

Dielectric Properties:

The dielectric constant **(ε)** was calculated using the formula

$$\varepsilon = \frac{C^* t}{Eo * S}$$

Where

C=capacitance in farad,
t =thickness in meters,
C=cross sectional area of pellet and
εo = permittivity of free space.

The dielectric constants (ε) of the $Ni_{0.5}Zn_{0.5}La_xFe_{2-x}O_4$ where (x=0.025, 0.050, 0.075, 0.100, 0.125) nanoferrite was observed from 100Hz to 5 MHz and it is shown in Fig.1. It was found that the dielectric constant decreases as increase in the frequency, this shows that normal behavior of magnetic material. The dielectric loss (Tan δ) of the $Ni_{0.5}Zn_{0.5}La_xFe_{2-x}O_4$ where (x=0.025, 0.050, 0.075, 0.100, 0.125) nanoferrite was observed from 100Hz to 5 MHz and it is shown in Fig.2.The peaks was observed initially at lower frequencies. It was noted that the dielectric loss decreases with increase in frequencies at higher frequencies. Hence it gives the abnormal behavior of the dielectric loss at certain frequencies. The AC resistivity versus concentration of the Lanthanum graph is shown in Fig.3.

The AC resistivity is maximum at x=0.075. The AC resistivity is varying with the increase in Lanthanum concentration.

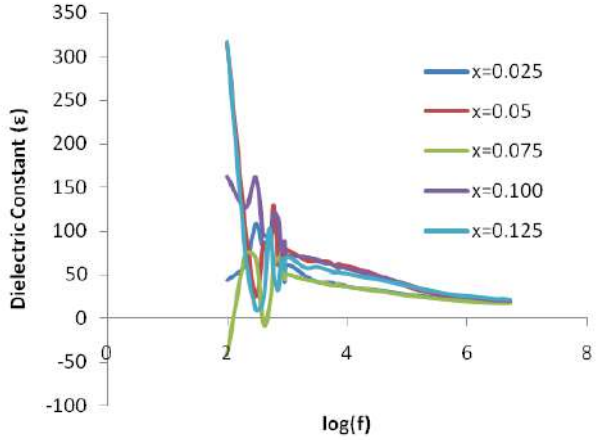

Fig.1: Graph of Dielectric Constant (ε) with log(f)

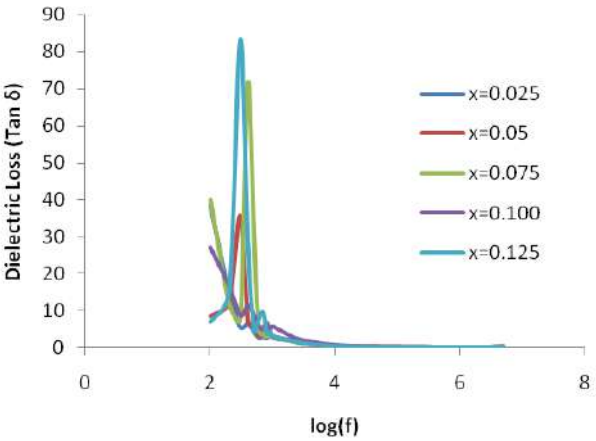

Fig.2: Graph of Dielectric Loss (Tan δ) with log(f)

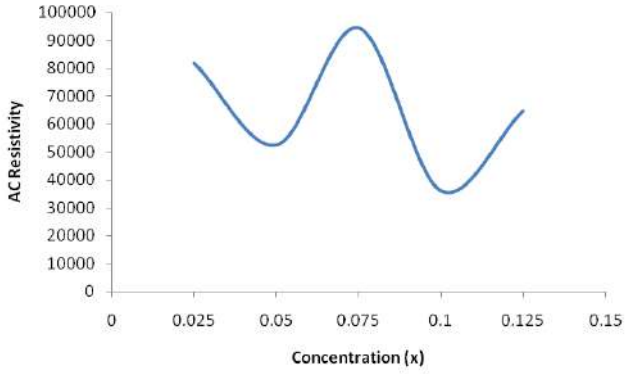

Fig.3: Graph of Concentration (x) with AC Resistivity

Electric Properties:

The dc resistivity (ρ) of the $Ni_{0.5}Zn_{0.5}La_xFe_{2-x}O_4$(where x = 0.025, 0.050, 0.075, 0.100 and 0.125) nanoferrite was obtained by Two Probe method. The dc resistivity was calculated by the formula

$$\text{DC Resistivity } (\rho) = \frac{AP * R}{L}$$

Where,

Ap= Surface area of the pellet,

R= Resistance of the sample,

L= Length of the pellet

It was found that the DC resistivity of the $Ni_{0.5}Zn_{0.5}La_xFe_{2-x}O_4$ nanoferrite at 200^{0}C increases as Voltage increases and shown in Fig.4. The electric properties of the nanoferrite were decided by the cation distribution. The DC conductivity increases up to x=0.05 and decreases after x=0.05 at 200^{0}C, which is shown in Fig.5.

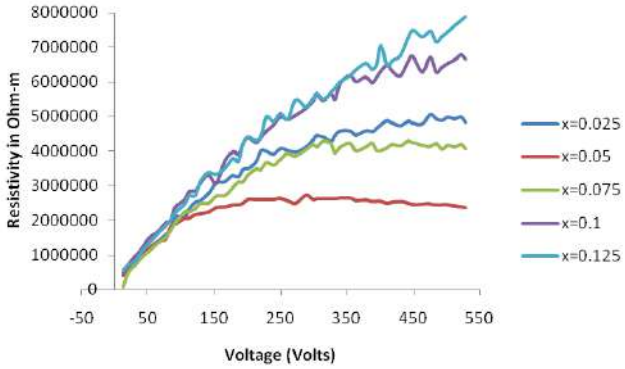

Fig.4: Graph of dc Resistivity with Voltage at 200^{0}C

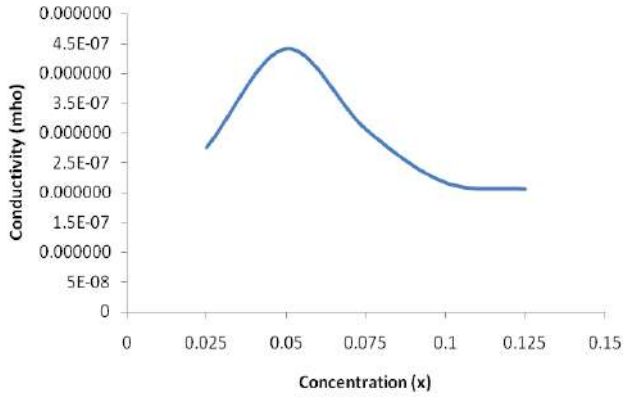

Fig.5: Graph of dc conductivity with concentration (x) at 200^{0}C

CONCLUSION

The $Ni_{0.5}Zn_{0.5}$ $La_xFe_{2-x}O_4$nanoferrite where (x=0.025, 0.050, 0.075, 0.100, 0.125) were synthesized successfully by the sol gel auto combustion method. The dielectric constant of all samples decreases as increase in the frequency; this indicates the normal behavior of magnetic material. The dielectric loss of all samples decreases with increase in frequencies after some initial peaks. It shows that the abnormal behavior of the dielectric loss at specific frequencies. The AC resistivity is fluctuating with the increase in Lanthanum concentration. The DC resistivity of all nanoferrite samples at 200^0C increases with increase in Voltage. The DC conductivity decreases after x=0.05 at 200 ^{0} C.

Acknowledgement

We are thankful to Science College, Nanded, SAIF, IIT, Powai, Mumbai, Modern College, Ganeshkhind, Pune and Abasaheb Garware College, Pune.

REFERENCES

1. Pervaiz E, Gul IH. Low temperature synthesis and enhanced electrical properties by substitution of Al^{3+} and Cr^{3+} in Co–Ni nanoferrites", *Journal of Magnetism and Magnetic Materials*, 343, 194-202(2013).
2. Maria Lumina Sonia M, Blessi S, Pauline S. Role of Lanthanum substitution on the Structural and Magnetic properties of nanocrystalline Nickel ferrites" IJARSE, 2014; 3(7): 360-367.
3. Aldar BA, Pinjari RK, Burange NM. Electric and Dielectric Behavior of Ni-Co-Cd Ferrite, *IOSR Journal of Applied Physics*, 2014; 6(4) Ver.II : 23-26.
4. Abdul Samee Fawzi, Sheikh AD, Mathe VL, Structural, dielectric properties and AC conductivity of $Ni_{(1-x)}$ $ZnxFe_2O_4$ spinel ferrites, *Journal of Alloys and Compounds*, 2010; 502:231–37.
5. Rani R, Gagan Kumar, Batoo Khalid Mujasam, Singh M. "Electric and Dielectric Study of ZincSubstituted Cobalt Nanoferrites Prepared by Solution Combustion Method", *American Journal of Nanomaterials,* 2013; 1(1): 9-12.
6. Awati VV, Bobade DH, Kulkarni SD, Rathod SM. Structural, Dielectric and Magnetic Behavior of Cu+2 substituted Ni-Znferrite by Auto-combustion Technique", *International Journal of Engineering Research and Applications*, 2012; 2(6): 482-489.
7. Devmunde BH, Raut AV, Birajdar SD, Shukla SJ, Shengule DR and Jadhav KM. Structural, Electrical, Dielectric, and Magnetic Properties of Cd^{2+} Substituted Nickel Ferrite Nanoparticles", *Journal of Nanoparticles*, 2016, Article ID 4709687, 8pp.
8. Chaudhari SC and Patil RN. Dielectric behavior and A. C. Conductivity in Cu-Ti Ferrites", *Adv. Appl. Sci. Res.*, 2012; 3(6): 3848-3854.
9. Raghavender AT, Shirsath SE, Vijaya Kumar K, "Synthesis and study of nanocrystalline Ni–Cu–Zn ferrites prepared by oxalate based precursor method", *Journal of Alloys and Compounds*, 2011; 509: 7004-7008.

IRJSE *Int. Res. J. of Science & Engineering,* 2018; Special Issue A2: 10-12 SJIF Impact Factor 4.11
ISSN: 2322-0015 UGC Approved Journal No. 63628
RESEARCH ARTICLE **OPEN ACCESS**

Synthesis and Characterization of Bismuth Ferrite by Chemical Route

Sherkar VB and Mancharkar AV (*Ph.D.)*

New Arts, Commerce and Science College, Parner, MS, India
Email: sherkarvishal@gmail.com

Manuscript Details
Available online on http://www.irjse.in
ISSN: 2322-0015

Editor: Dr. Arvind Chavhan

Cite this article as:
Sherkar VB and Mancharkar AV. Synthesis and Characterization of Bismuth Ferrite by Chemical Route. *Int. Res. Journal of Science & Engineering,* 2018; Special Issue A2: 10-12.

ABSTRACT

In the present work of bismuth ferrite ($BiFeO_{3)}$ multiferroic Nanoparticles synthesized by Chemical Route followed by thermal treatment at annealed at 300°C, 400°C and 500°C. It is found that $BiFeO_3$ nanoparticles crystallized at annealed 300°C. $BiFeO_3$ nanoparticles with different sizes distributions show obvious ferromagnetic properties, and the magnetization is increased with reducing the particle size. The prepared samples were characterized by X-ray diffraction of powder (XRD), scanning electron microscope (SEM) or extracting their surface morphology and their crystallographic structure and revealed a homogenous size distribution of nanometric Bismuth Ferrite perovskite powders with a grain size of 200 nm which is in well agreement.

Keywords: Bismuth ferrite, Nanoparticles, X-ray diffraction, SEM

INTRODUCTION

Bismuth Ferrite $BiFeO_3$ is also commonly referred to as BFO in materials science. It is an inorganic chemical compound with perovskite structure and one of the most promising multiferroic materials. Bismuth ferrite BiFeO3 (BFO) is one of the most popular research materials in condensed matter physics at present. The room temperature phase of $BiFeO_3$ is classed as rhombohedral belonging to the space group R3C. It is synthesized in bulk and thin film form and both its antiferromagnetic (G type Ordering) Neel Temperature and ferroelectric Curie

temperature are well above room temperature. BFO is much important for novel applications as sensors as well as actuators due to the coupling between magnetic and electric domains above room temperature and accepted high polarization in single crystal.

METHODOLOGY

(i) Chemicals Used: Bismuth nitrate, Ferric nitrate, Citric Acid

(ii) Preparation of BiFeO3 materials by chemical route. A stock solution of 0.2 M Bismuth nitrate in aqueous medium was prepared. The 0.2 M Ferric nitrate solution and 0.2 M

Bismuth nitrate solutions were mixed in a 500 mL beaker under stirring condition. Citric acid was added cautiously. The ammonia solution was then added drop-wise into the mixed solution under continuous stirring condition and a light brownish gel was obtained. The powders obtained from the above procedures were annealed at 300°C, 400°C and 500 °C so that the volatile matters like moisture and other unwanted components were removed. After the complete chemical synthesis and heat treatment of the synthesized products, the sample were characterized using X-ray diffraction (XRD) with a X-ray diffra-ctometer with CuKα radiation (λ=0.154178 nm) and Scanning Electron Microscope (SEM) for extracting their surface morphology and their crystallographic structure.

.

RESULT AND DISCUSSION:

The synthesized bismuth ferrite nanoparticles were characterized by using the room temperature powder X-ray diffraction with filtered 0.154 nm CuKα radiation for their phase analysis studies at different annealed temperatures of annealed 300 ℃, 400 ℃ and 500 ℃. The prominent peaks in XRD plot are indexed to various hkl planes of BFO, indicating formation of BFO. Besides these prominent peaks, some other peaks of low intensity are also observed, which do not belong to BFO. The sample annealed at 500 ℃ is having many extra peaks other than BFO whereas that prepared at 300 ℃ is less impurity peaks. The literature survey of BFO synthesis relates these impurity peaks to be that of BFO. The appearance of these extra phases at 500 ℃ could be due to large bismuth loss at higher temperature. Powder annealed at 400 ℃ is having less impurity phase of BFO, as is evident from the lesser peak height than 500 ℃. The synthesized bismuth ferrite nanoparticles were characterized by using the SEM for revealing their

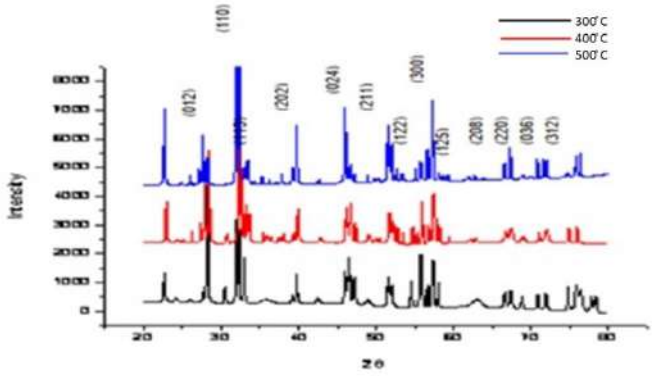

The proportional increase in particle size is also confirmed by their surface morphology studies

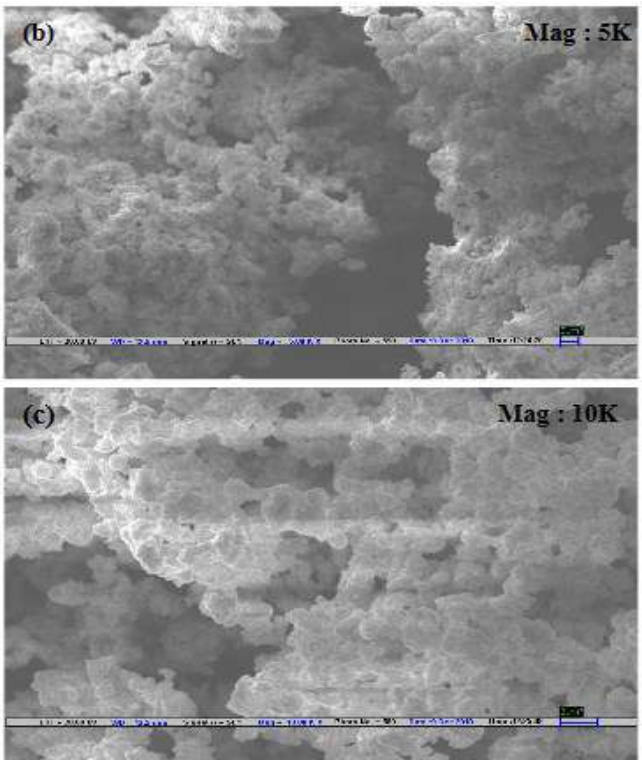

Figure: SEM image of BFO of nanoparticle size of 200nm

surface morphology at different annealed temperatures of 300 ℃, 400 ℃ and 500 ℃. The particle size estimated from SEM images for the BFO sample is about 200 nm for the annealed temperature 300 ℃, 400nm for the annealed temperature of 400 ℃ and 500 nm for the annealed temperature of 500 ℃.

In the reported experiment, bismuth ferrite nanoparticles are successfully synthesized by chemical route method using citric acid. The synthesized bismuth ferrite nanoparticles were characterized by X-Ray Diffraction (XRD) and Scanning Electron Microscope (SEM). The XRD characterization results indicates the rhombo centered structure of bismuth ferrite nanoparticles and the SEM analysis reveals that the diameter of bismuth ferrite nanoparticles changes with thermal treatment and varies from 200 to 500 nm by increasing the annealed temperature from 300 ℃ to 500 ℃. This method avoids using traditional high temperature and therefore could be easily extended to other systems.

REFERENCES

1. Glenda Biasotto,A.Z.Simoes, C.R. Foschini, S.G. Antonio, Maria A.Zaghete, Jose A. Varela , "A novel synthesis of perovskite bismuth ferrite nanoparticles", Processing and Application of Ceramics 5(3)(2011)171-179.
2. K.Y Yun, M.Noda. M. Okuyama, H.Saeki, H.Tabata, K. Saito, "Structural and multiferroic properties of BiFeO3 thin films at room temperature",J.Appl. Phys.96(2004)3399 -3403.
3. Y.P. Wang, L.Zhou,M.F. Zhang, X.Y. Chen, J.M. Liu, Z.G. Liu,"Room temperature saturated ferroelectric olarization in BiFeO3 ceramics synthesized by rapid liquid phase sintering",Appl.Phys. Lett.,84(2004)1731-1734.
4. S.Ghosh, S. Dasgupta, A. Sen, H. Shekhar, "Low temperature synthesis of nano sized bismuth ferrite by soft chemical route",J.Am.Ceram.Soc.,88(2005)1349-1352.
5. C.Chen, J. Cheng, S.Yu, L.Che, Z. Meng, "Hydrothermal synthesis of perovskites bismuth ferrites crystallites", J.Crystal Growth, 291(2006)135-139.
6. J.T. Han,Y.H Huang, X.J.Wu, C.L. Wu, W.Wei, B.Peng, W. Huang, J.B. Goodenough, " Tunable synthesis of bismuth ferrites with various morphologies". Adv.Mater.18(2006)2145-2148.
7. X.Qi, M. Wei, et.al., "High Resolution X-Ray diffraction and transmission electrons microscopy of multiferroic BiFeO3 films,Appl.Phys.Lett.,87(2005)71913-71915.
8. Yongming Hu, Lingfeng Fei,Yiling Zhang, Jikang Yuan,YU Wang, and Haoshuang Gu, " Synthesis of Bismuth Ferrite Nanoparticles via a Wet Chemical route at low temperature. "Journal of Nanomaterials, 2011(2011),Article I.D.797639, 6 pages.
9. S.M. Selbach, T.Tybell, M.A Einarsud and T. Grande, " Size dependent properties of multiferroic BiFeO3 Nanoparticles", Chem. Mater., 19(26) 6478-84(2007).

IRJSE *Int. Res. J. of Science & Engineering,* 2018; Special Issue A2: 13-19 SJIF Impact Factor 4.11
ISSN: 2322-0015 UGC Approved Journal No. 63628
RESEARCH ARTICLE **OPEN ACCESS**

Density Functional Study of Adsorption of Nickel Atom on Carbon Nanotube

Nirmal Sangeeta A[1], Sonawane MR[2] and Atram RG[2]

1 Institute of Science, Mumbai,
2 Institute of Science, Nagpur
E-mail: sangeetakanojia@gmail.com | smahadev123@gmail.com | ramdasatram@yahoo.co.in

Manuscript Details

Available online on http://www.irjse.in
ISSN: 2322-0015

Editor: Dr. Arvind Chavhan

Cite this article as:
Nirmal Sangeeta A, M. R. Sonawane and Atram RG. Density Functional Study of Adsorption of Nickel Atom on Carbon Nanotube. *Int. Res. Journal of Science & Engineering,* January 2018; Special Issue A2: 13-19.

ABSTRACT

The adsorption of individual atoms on the semiconducting carbon nanotubes (CNT) has been investigated by using the first principles method within density functional theory. The stable adsorption geometries and binding energies have been determined for a Nickel (Ni) Transition Metal (TM) atom. We have found that the character of the bonding and associated physical properties strongly depends on the type of adsorbed atoms, in particular on their valence electron structure. Our results indicate that the properties of CNTs can be modified by the adsorbed Ni adatom. Owing to the curvature effect, these binding energies are larger for different sites of adsorption that we have used. We have showed that the Ni adatom can form strong and directional bonds with carbon atom of CNT. We have calculated Band Structure (BS), density of state (DOS) and charge transfer to find out the conducting nature of CNT. We have also calculated the HOMO and LUMO energy from which we can say HOMO shows the ability to donate electron and LUMO shows ability to accept the electron.

Keywords: DFT, Ni Atom, adsorption, CNT.

INTRODUCTION

Carbon nanotubes (CNT) have been remarkable objects that look to revolutionize the technological landscape in the future. Tomorrow's society will be shaped by nanotube applications, just as silicon-based technologies dominate society today. [1, 2] The mechanical properties of carbon nanotubes have prominent application as they are flexible and can sustain large elastic deformations radially. At the same time CNT are very strong with high yield strength i.e. it is easy to apply elliptical de- formations but it becomes very difficult to elongate the system. Their strength exceeds far from any other fiber [3, 7]. Even more striking properties of CNT are the response of electronic structure to the radial deformation leading dramatic changes. As it has been predicted theoretically and confirmed experimentally, a semiconducting zigzag tube becomes metallic with finite state density at the Fermi level as a result of radial deformation, transforming the circular cross section into an ellipse. At the same time chemical activity of the surface of the tube undergoes into change; the interaction of adatoms with the CNT occurs differently at high and low-curvature sites. Metal-semiconductor transition induced by an elastic deformation has important implications.

The Physical properties of a CNT can also be modified by the adsorption of foreign atoms or molecules. This process is usually named as functionalization, and carries a great potential in constructing new nanostructures and to engineer them according to a desired application. For example, depending on the pattern of hydrogen atom coverage, while a metallic armchair CNT is transformed to wide-band gap semiconductor, a semiconducting zigzag tube becomes a metal with very high state density [8]. A free CNT, which is normally non-magnetic, becomes magnetic with unpaired spins upon the adsorption of oxygen molecule or specific transition metal atoms [9]. A recent study demonstrates that a semiconducting zigzag tube becomes both magnetic and high-conducting wire as a result of Ti coating. The increasing interest in the interactions between metal atoms and carbon nanotubes surface arises from the important role of CNT-metal junctions such as electronic devices, nanocomposites materials and catalysts systems. The Binding Energy between CNTs and Metals can be efficiently tuned by reactive chemical groups at the CNT surface.

The Binding between transition metals and the sidewall of carbon nanotubes plays very important role in the performance CNT-based nano devices. The Binding nature of TM can be identified by the magnitude of the binding energy and formation of bonds. The chemisorbed TM atoms can modify the electronic structure of Carbon nanotubes here have chosen Ni atom to test its interaction on side wall of CNT, and found nature of its adsorption on CNT.

METHODOLOGY

The computing calculations were carried out using Doml3 code of Accelrys [10] based on density functional theory (DFT). Structural and electronic properties of CNT were derived to investigate the interaction of adatom Nickel on CNT. The Geometry optimizations of CNT along with Ni were performed using GGA and PBE functional [11, 14]. For Supercell geometries, spin unrestricted calculations were carried out with a double numeric polarized (DNP) basis set available and orbital cut-off was set to 4.4 Å. Scalar relativistic effects were included via a pseudo potential for all-electron calculations. 1 x 1 x 2 k-points were used for the Brillioun zone. All the calculations were performed using boundary conditions with 64 atoms within the Supercell. The tetragonal unit cell of 20 x 20 x 8.4 Å dimensions and sufficient separation between tubes is used to avoid interaction between the atoms. The chosen cut off value leads to atomic energies with an accuracy of 0.1 eV/atom, allowing calculations without sufficient loss of accuracy. Mulliken population analysis was carried out to predict the charge transfer and spin between Ni-adatom and nanotubes.

The (8, 0) zigzag CNT of diameter 6.26 Å and the length of tube is 8.52 Å as a model to study the adsorption of Nickel atom. We have examined different site for adsorption of Nickel atom as shown in figure (1). The Sites were (1) Carbon Atom (Site A), (2) Carbon-Carbon Axial Bond (site C), (3) Carbon-Carbon Chiral bond (site B) and (4) Hexagon (site D).

In all calculations, the carbon nanotubes along with Nickel atom were first optimized to occupy their ground state energy.

For each site Ni adatom has kept at a finite distance of 3.0 Å and then system is optimized to get stable structure. The binding energy (E_b) of adsorption of Ni atom on nanotube for all ground state structures were calculated by

$$E_b = -[E_{T\,(adsorbent + adsorbate)} - E_{T\,(adsorbent)} - E_{T\,(adsorbate)}].$$

Where $E_{T\,(adsorbent + adsorbate)}$ is the total energy of atom and CNT system, $E_{T\,(adsorbent)}$ is total energy of CNT and $E_{T\,(absorbate)}$ is the total energy of atom. To verify the computational accuracy of the structure we have calculated the binding energy of CNTs, density of state, band gap Charge Density, HOMO-LUMO, Milliken Charge and spin [15].

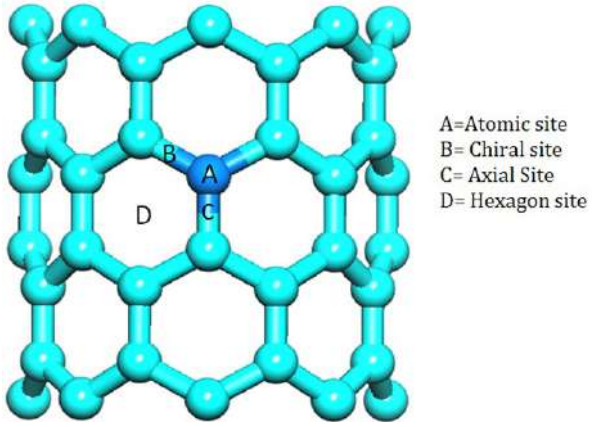

(a)

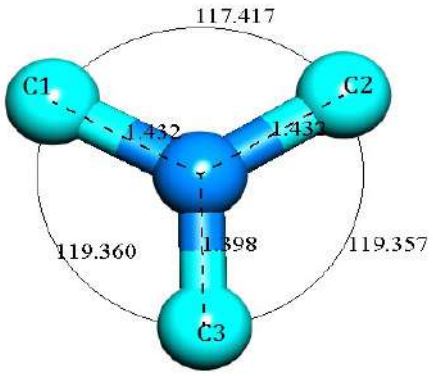

(b)

Figure 1: (a) Structural model of CNT (8, 0) (b) structural parameter at target atom

RESULT AND DISCUSSION:

1. Geometrical properties

In order to get the accuracy of the first principles approach to the geometrical and electronic structure of the CNT, we have optimized the structure of (8, 0) CNT and then CNT along with Ni adatom. The optimized structure of (8, 0) CNT has a C - C axial bond of length 1.382 Å and C - C Chiral bond of length 1.44 Å. After performing geometry optimization CNT along with Ni adatom the bond length of C - C axial bond and C - C chiral bonds are slightly changed to 1.44 Å and 1.46 Å respectively as shown in Figure 1(a-b). The variation in bond length of C – C atom at all adsorption site is negligible therefore the change in bond angle between carbon atom of CNT is very less, this shows the SP2 hybridization of carbon atom of CNT is not changed due to interaction of Ni adatom. For all four sites the Ni atom is chemisorbed on carbon nanotube with minimum binding distance of 1.9 Å. The Ni adatom is chemisorbed on all four sites forming covalent bonds. The Bond length for C – Ni adatom for Site - A, Site - C, Site – B and Site – D is 1.9 Å as shown in figure in figure 2(a-d).

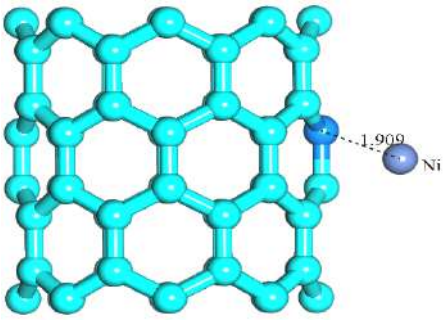

Figure 2: (a) Geometrically optimized structure for Ni-CNT at atom, site (A)

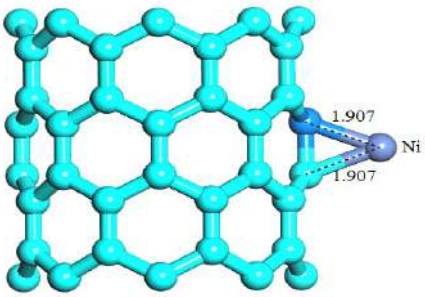

Figure 2: (b) Geometrically optimized structure for Ni- CNT at Axial bond position, site B

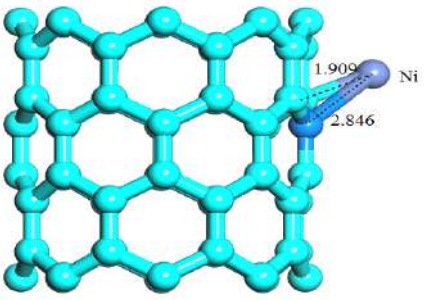

Figure 2: (c) Geometrically optimized structure for Ni-CNT at Chiral bond position, site C

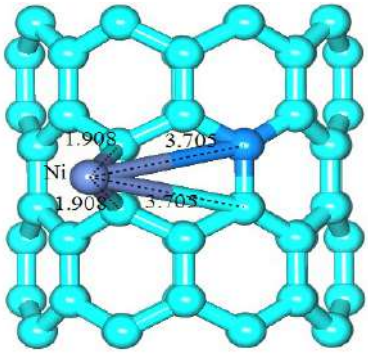

Figure 2: (d) Geometrically optimized structure for Ni- CNT at Hexagon position, site D

2. Electronic properties

The binding energies of CNT with Ni adatom were calculated for different adsorption sites. The value of binding energy determines the stability of system. The lower the binding energy is higher the stability of the system. The table 2 summarizes the calculated binding energies to the four different adsorption sites as mentioned. The binding energy of Ni adatom on CNT is - 1.8 eV. The larger value of B.E. indicates the Ni adatom is chemisorbed on CNT clearly seen in figure 2 (a – d). The band Structure and DOS Shown in figure 3 (a - d) shows that two states in valence band near fermi level merges into single highly occupied energy state at - 0.64 eV which is very close to Fermi energy. Due to adsorption of Nickel atom, highly occupied state in valance band and unoccupied states in conduction band near the Fermi energy level get closer and they reduce the bang gap of CNT from 0.701 eV to 0.46 eV for all four adsorption sites. The creation of highly occupied state at Fermi energy changes the semiconducting nature of CNT into almost metallic. We also performed Milliken population analysis to find the charge transfer between CNT and Ni adatom as shown in table 2. The Ni atom acquires positive charge of magnitude 0.364 e by donating charge to carbon atom. The isosurface electron density shows the formation of covalent bond between Nickel atom and neighboring carbon atoms as shown in figure 4.

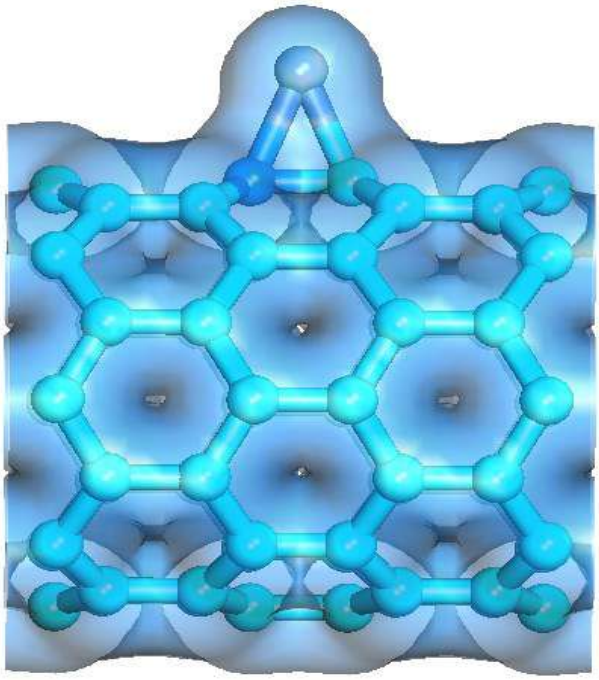

Figure 4 : Isosurface of Ni-CNT at Axial bond site

Figure 5(a) and (b) Shows HOMO and LUMO structure in which HOMO shows the ability to donate electron and LUMO shows ability to accept the electron. HOMO has energy - 3.804 eV and LUMO has energy - 3.510 eV.

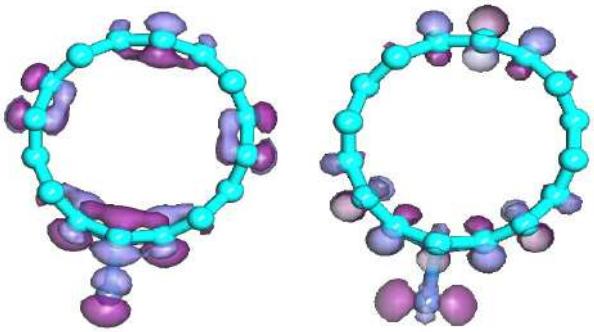

(a)HOMO (b) LUMO

Figure 5: Stable structure of HOMO and LUMO

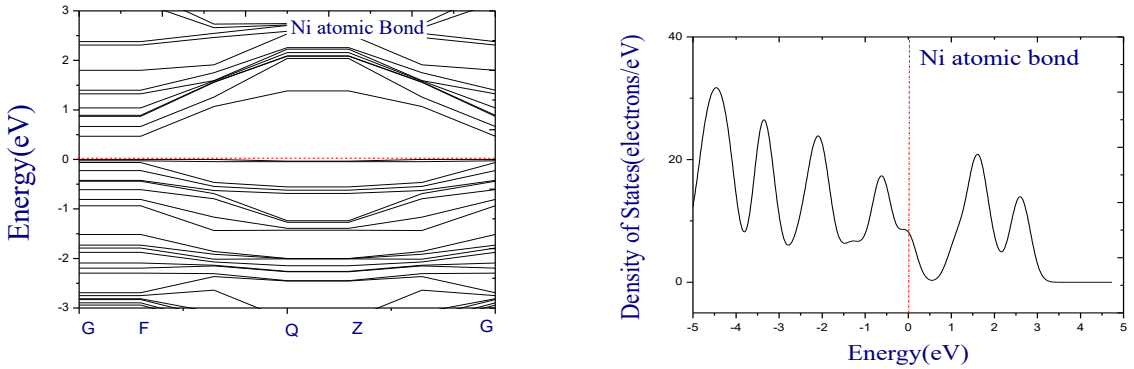

(a) Band structure and DOS of atomic (site A)

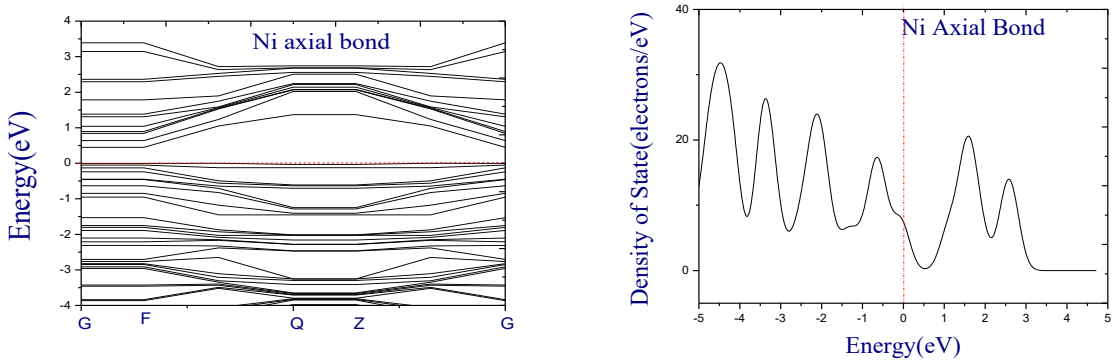

(b) Band structure and DOS of Axial Bond (site c)

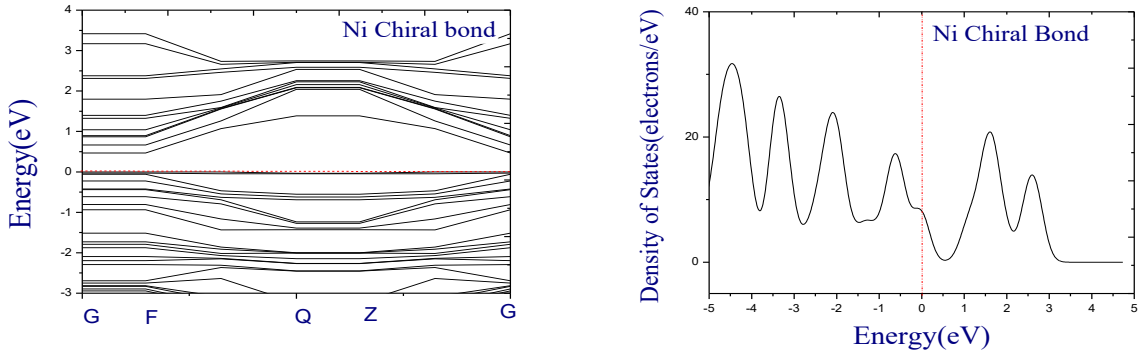

(c) Band structure and DOS of Chiral Bond (site B)

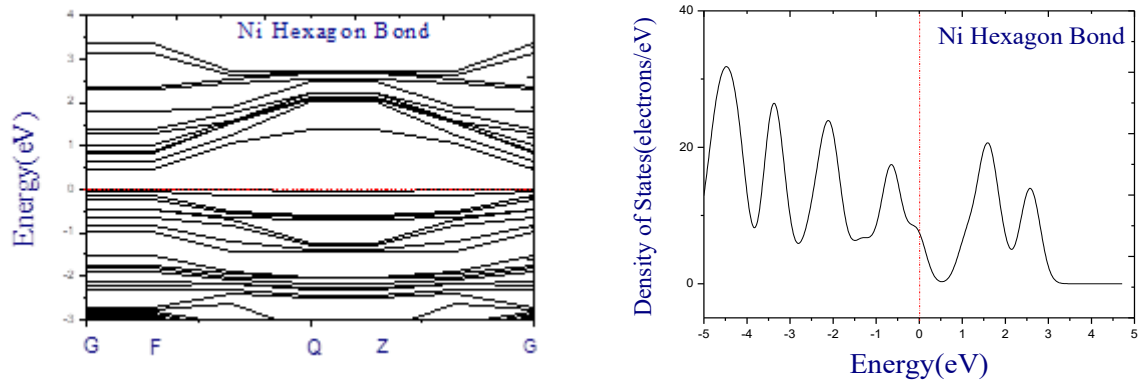

(d) Band structure and DOS of Hexagon (site D)

Table 1: shows structural properties i.e. binding distance and bond angles.

Site	Binding distance in Å	Angle of CNT with Ni in degree
Pure (8,0) CNT		
3.0 Ni Atomic	l(C-Ni)=1.909 Å	
3.0 Ni Axial Bond	l(C-Ni)=1.907 Å	<(C-Ni-C)=44.498^0
3.0 Ni Chiral Bond	l(C-Ni)=1.909, Å -2.846 Å	<(C-Ni-C)=28.002^0
3.0 Ni Hexagon	l(C-Ni)=1.909, Å -3.705 Å	<(C-Ni-C)=37.855^0
		<(C-Ni-C)=44.459^0

Table 2: Electronic properties of Ni-CNT

	B.E (eV)	Band gap (eV)	Charge (Qt)	HOMO energy (eV)	LUMO energy (eV)
CNT (8,0)		0.701			
CNT - 3.0 Cr Atomic	- 1.815	0.467	0.467	- 3.806	- 3.502
CNT - 3.0 Cr Axial Bond	- 1.8205	0.449	0.449	- 3.804	- 3.510
CNT - 3.0Cr Chiral Bond	- 1.815	0.45	0.45	- 3.804	- 3.502
CNT - 3.0 Cr Hexagon	- 1.8232	0.468	0.468	- 3.806	- 3.510

CONCLUSION

The interaction (8, 0) CNT with Nickel was investigated using DFT method. Transition metal interaction caused in the change in electronic structure of CNT and stability of the system is increased. Even though, the geometrical structure of CNT is not changed due to adsorption of Ni adatom. The Ni adatom is chemisorbed on CNT and forms covalent bonds. The band gap for CNT – Ni system is reduced and conductivity of CNT almost reached metallic. Improved conductivity of CNT can be used as fundamental tool to investigate nano electronic and sensing devisees.

Conflicts of interest: The authors stated that no conflicts of interest.

REFERENCES

1. Dresselhaus MS, Dresselhaus G and Eklund PC. Science of Fullerenes and Carbon Nanotubes (Academic Press, San Diego, 1966).
2. Saito R, Dresselhaus G and Dresselhaus MS. Physical Properties ofCarbon Nanotubes;Imperial College Press, London (1998).
3. Salvetat JP et al., Mechanical properties of carbon Nanotubes Appl. Phys. A 69, 255 (1999).
4. Iijima S. Helical microtubules of graphitic carbon,1991,p.56-58.
5. Chen XQ and Saito T. Aligning single-wall carbon nanotubes with an alternating-current electric field 2001, Appl. Phys. Lett. 78, 3714.
6. Gao B, Kleinhammes A, Tang XP, Bower C, Fleming L, Wu Y and Zhou O. ,Electrochemical intercalation of single-walled carbon nanotubes with lithium , 1999, 153-157.
7. Yahachi Saito, SashiroUemura, Field emission from carbon nanotubes and its application to electron sources ,2000, p. 169-182.
8. Durgun E, S. Dag, V.M.K. Bagci, O. Gu¨lseren, T. Yildirim S. Ciraci, Systematic study of adsorption of

singleatoms on a carbon nanotube, Phys. Ver. 67, R201401 (2003).

9. Dag S, Gu¨lseren O, Yildirim T, and S. Ciraci,Atomic structure, energetics, and electronic structure Oxygenation of carbon nanotubes,Phys. Rev. B 67, 165424 (2003).
10. Xiaoxing Zhang,Ziqiang Dai, Li-Wei,Naifeng Liang and Xiaoqing Wu,Theoretical calculation of the gas – sensing properties of Pt- Decorated Carbon Nanotubes, p.15159-15171(2013).
11. Hyun-Hee Cho, Billy A. Smith, Joshua D, Wnuk D, Howard Fairbrother and William P. Ball Influence of Surface Oxides on the Adsorption of Naphthalene onto Multiwalled Carbon Nanotubes", 2008,p. 2899–2905).
12. Xiangke Wang,Changlun Chen,Jinzhou Du,Xiaoli Tan,Di Xu, and Shaoming Yu ,Effect of pH and Aging Time on the Kinetic Dissociation of 243Am(III) from Humic Acid-Coated γ-Al2O3: A Chelating Resin Exchange Study,(2005),p. 7084–7088.
13. Segall MD, Lindan PJD, Probert MJ, Pickard, Christopher James, Hasnip PJ, Clark SJ, Payne MC. First-principles simulation: ideas, illustrations and the CASTEP code(2002), p. 2717-2744.
14. Stewart J. Clark, Matthew D. Segall, Chris J. Pickard, Phil J. Hasnip, Matt IJ, Probert Keith Refson and Mike C Payne, First principles methods using CASTEP(2005), 567–570.
15. Emmanuel Silva Marinho, Márcia Machado Marinho A DFT study of synthetic drug topiroxostat: MEP, HOMO, LUMO,p. 2229-5518 ,(2016).

IRJSE *Int. Res. J. of Science & Engineering,* 2018; Special Issue A2: 20-22 SJIF Impact Factor 4.11
ISSN: 2322-0015 UGC Approved Journal No. 63628
RESEARCH ARTICLE **OPEN ACCESS**

Optical and Structural Properties of CuSe Thin Films Deposited by Chemical Bath Deposition (CBD) Technique

Sadekar Harishchandra K

Department of Physics, Arts, Commerce and Science College, Sonai (MS), India-414105
Email: sadekarhk@gmail.com

Manuscript Details

Available online on http://www.irjse.in
ISSN: 2322-0015

Editor: Dr. Arvind Chavhan

Cite this article as:
Sadekar Harishchandra K. Optical and Structural Properties of CuSe Thin Films Deposited by Chemical Bath Deposition (CBD) Technique. *Int. Res. Journal of Science & Engineering,* January 2018; Special Issue A2 : 20-22.

ABSTRACT

Copper selenide (CuSe) thin films have been deposited on to glass slide substrates by using chemical bath deposition (CBD) technique at room temperature. Growth parameters were investigated to obtain good quality thin films. Structural and optical properties of the thin films were studied by X-ray diffraction, Scanning electron microscopy (SEM) and spectrophotometer, respectively. XRD and SEM study revealed that the as-deposited CuSe films were amorphous in nature and the deposition was uniform. Optical study revealed that the direct band gap value is 2.3 eV.

Keywords: thin films; CBD; structural; optical.

1. INTRODUCTION

Copper selenide (CuSe) is a metal chalcogenide p-type semiconducting material, which has electrical and optical properties suitable for opto electronic device applications [1]. CuSe has many applications in fabrication of solar cell [2], photo detectors, thermo electric converter, photo electro chemical cells etc. Copper selenide comes in different stoichometric form such as CuSe, Cu_2Se, Cu_3Se_2, Cu_5Se_4 and non stoichometric form $Cu_{2-x}Se$. This material is synthesized in thin film form by various methods such as Chemical Bath Deposition (CBD) [1], Spray pyrolysis [3], Vacuum evaporation [4], electro deposition [5], etc. Researchers are continuously in search of more applications of CuSe due to its promising properties. In the present investigation CuSe thin films have been deposited by chemical bath deposition (CBD) technique.

2. METHODOLOGY

The substrates used for the deposition of CuSe thin film were commercial microscope glass slides (Blue Star).. Before deposition, the substrates were cleaned by commercial detergent and finally rinsed with de-ionized water and dried in air. This process is to ensure clean surface, which is essential for formation of nucleation centers, required for thin film deposition. Thin films of CuSe have been deposited by chemical bath deposition technique using selenium powder, sodium sulphite, cupric chloride and ammonia. All chemicals used in the present investigation were AR grade. A solution of sodium selenosulphate (Na_2SeSO_3) was prepared by refluxing method [6]. Typically, 10 mL 0.25M $CuCl_2 \cdot 2H2O$ solution was taken in a 100 mL glass beaker. Under continuous stirring 1 mL of 30% ammonia solution was added drop by drop. Then 10 mL freshly obtained sodium selenosulphate solutions were added slowly with constant stirring and the pH of the final mixture was adjusted to ~ 10. The rest distilled water is added to make the volume 50mL.

Pre-cleaned glass substrates were inserted into the reaction mixture in the beaker standing parallel with the walls of the beaker, which was kept in room temperature bath for 4 h. After deposition, the glass slides were taken out from the bath, washed with de-ionized water and was dried in air. It was observed that the films were uniform and well adhered.

3. CHARACTERIZATION TECHNIQUES

The as-deposited thin films of CuSe were characterized for structural and optical properties. The CuSe film thickness was measured by weight difference method. Glancing incidence angle X-ray diffraction (GIXRD) pattern of the film was recorded on a Bruker AXS, Germany (D8 Advanced) diffractometer in the scanning range 20–70° (2θ) using Cu-Kα1 radiations with wavelength 1.5405 Å at 0.5° glancing angle. The surface morphology was studied by scanning electron microscopy (SEM, JOEL-JSM-5600). Transmittance and absorbance spectra were recorded in the range 300–1100 nm by means of Jasco V630 spectrophotometer

4. RESULT AND DISCUSSION

4.1 Structural Characterization

Fig. 1 shows the XRD pattern of CuSe thin film. It shows from the pattern that no well-defined peak was found and no well-defined plane was obtained in the case of as-deposited films, which suggests that the as-deposited films were amorphous in nature [7].

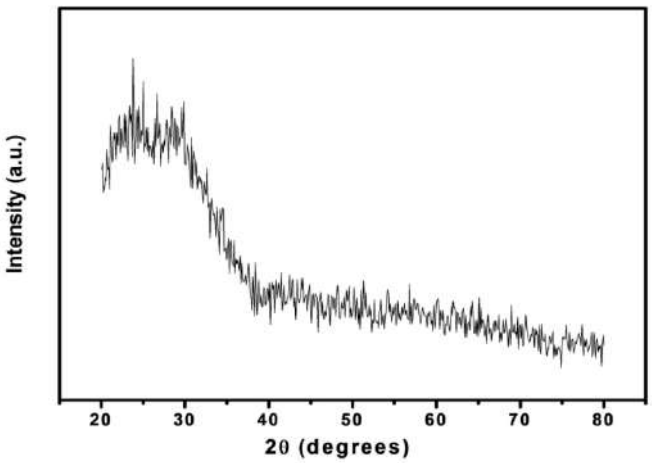

Figure 1. XRD pattern of as-deposited CuSe thin film

4.2 Surface morphological and topographical Characterization

Fig. 2 shows the scanning electron microscopy (SEM) image of as-deposited CuSe films. It is observed that the CuSe thin films are uniform and cover the substrate well. From the image, it is clear that the films were composed of a compact structure single type of small densely packed crystals. The grains are well defined, spherical and almost similar in size, that may correspond to the amorphous phase of CuSe film [8].

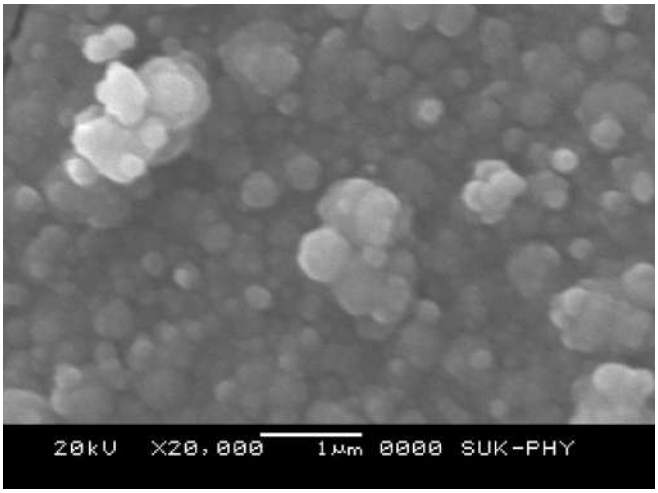

Figure 2. SEM image of as-deposited CuSe thin film

4.3 Optical Characterization

Absorbance spectra obtained from as-deposited CuSe thin film is used to obtain optical band gap. The relation between the absorption coefficient α and the incident photon energy (hν) can be written as [6],

Figure 2: (d) Geometrically optimized structure for Ni- CNT at Hexagon position, site D

$$\alpha h\nu = A(h\nu - E_g)^n \qquad (1)$$

where 'A' is constant, n= ½ for direct allowed transition, 'E_g' is optical band gap of the material. Fig. 3 shows the plot of $(\alpha h\nu)^2$ against (hν) for CuSe thin film derived from the optical spectra. Extrapolating the straight-line portion of the plot of $(\alpha h\nu)^2$ vs (hν) [40] for zero absorption coefficient value gives the band gap, which is found to be 2.3 eV at room temperature.

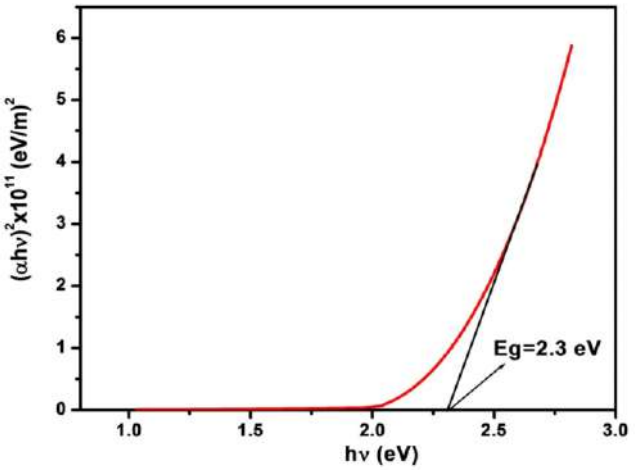

Figure 3. Plot of $(\alpha h\nu)^2$ vs. hν for CuSe thin films

CONCLUSION

Thin films of CuSe have been successfully deposited by Chemical Bath technique. Amorphous nature was confirmed by X-ray diffraction studies. Scanning electron microscopy study revealed uniform deposition. The optical band gap was found to be 2.3 eV.

Acknowledgements

The author is thankful to Principal, Arts, Commerce and Science College, Sonai for providing the laboratory facilities.

REFERENCES

1. Gosavi SR, Deshpande NG, Gudage YG and Sharma R, Physical, optical and electrical properties of copper selenide (CuSe) thin films deposited by solution growth technique at room temperature, *J. Alloys Compd.*, 2008; 448:344-348.
2. Zhu XL, Wang YM, et al, 13.6%-efficient Cu(In,Ga)Se_2 solar cell with absorber fabricated by RF sputtering of (In,Ga)2Se3 and CuSe targets, Sol. *Energy Mater. Sol. Cells*, 2013; 113:140-143.
3. Yadav AA, Nanocrystalline copper selenide thin films by chemical spray pyrolysis, *Journal of Materials Science: Materials in Electronics*, 2014, 25(3):1251-1257.
4. Muthukannan A, Henry J, Sivkumar G, Fabrication and characterization of vacuum evaporated Al:$CuSe_2$ thin films, Superlattices *Microstruct.*, 2016; 89:83-88.
5. Ramesh K, Thanikaikarasan S and Bharathi B., Structural, Morphological and Optical Properties of Copper Selenide Thin Films, *International Journal of ChemTech Research*, 2014; 6(13):0974-4290.
6. Sadekar HK, Ghule AV, Sharma R, Nanocrystalline ZnSe thin films prepared by solution growth technique for photosensor application, Composites Part B, 2013; 44(1):553-557.
7. Yakuphanoglu IF, Vishwanathan C, Electrical conductivity and single oscillator model properties of amorphous CuSe semiconductor thin film, *J. Non-Cryst. Solids*, 2007; 353(30-31):2934-2937.
8. Ya-dan Li, Ping Fan et al, The influence of heat treatments on the thermoelectric properties of copper selenide thin films prepared by ion beam sputtering deposition, *J. Alloys Compd.*, 2016; 658:880-884.

.

IRJSE *Int. Res. J. of Science & Engineering,* 2018; Special Issue A2: 23-26 SJIF Impact Factor 4.11
ISSN: 2322-0015 UGC Approved Journal No. 63628
RESEARCH ARTICLE **OPEN ACCESS**

Synthesis of Silver Nanoparticles from *Fargesia Sp*. Jiuzhaigou leaf and investigating it's effects on plant growth

Alaa Fadel Jassem, Shinde Rachana, Yande Jyoti and Aghav Sakharam D

Department of Physics, P.D.E.A's Baburaoji Gholap College, Sangvi, Pune 27(SPPU)
E-mail- sdaghav@gmail.com

Manuscript Details

Available online on http://www.irjse.in
ISSN: 2322-0015

Editor: Dr. Arvind Chavhan

Cite this article as:
Alaa Fadel Jassem, Shinde Rachana, Yande Jyoti and Aghav Sakharam D. Synthesis of Silver Nanoparticles from *Fargesia Sp*. Jiuzhaigou leaf and investigating it's effects on plant growth. *Int. Res. Journal of Science & Engineering,* January 2018; Special Issue A2: 23-26.

ABSTRACT

Silver nanoparticles are assumed to enhance nutrients efficiency in plants. Silver nanoparticles are one of the most widely used and expected to enter natural ecosystem. Nanoparticles have potential to improve growth and yield of wheat plant. They interact with plant causing many morphological and physiological changes. The present work highlights the role of nanoparticles on plant development. The study focuses the impact of silver nanoparticles on root length, shoot length, seed germination rate. The green synthesis was done by using the aqueous solution of Fargesia sp. Jiuzhaigou (Bamboo) leaf extract and AgNO3. A fixed ratio of plant extract added into $AgNO_3$. The solution was prepared and the colour change was observed which proved formation of nanoparticles. The nanoparticles were characterized by XRD. The size of nanoparticles is observed in the range from10-30 nm. The study indicates that the silver nanoparticles synthesized have positive growth promontory effects on growth of wheat seedlings.

Keywords: Silver Nanoparticles, root length, shoot length, plant growth.

1. INTRODUCTION

Use of nanoparticles in agriculture is consistently increasing. Silver nanoparticles have remarkable uses in crop production [1]. Application of nanoparticles has been found to improve germination, enhance growth and physiological activities, fertilizers use efficiency [2]. Plants provide a better platform for nanoparticles synthesis. They are free from toxic chemicals and provide natural capping agents. Moreover, use of plant extracts also reduces the cost of microorganisms isolation and culture media enhancing the cost competitive feasibility over nanoparticles synthesis by microorganisms. Nanoparticles interact with plants causing many morphological and physiological changes [3]. Efficacy of nanoparticles is determined by their chemical composition, size, surface covering, reactivity, and most importantly the dose at which they are effective.

2. METHODOLOGY

a. Preparation of agar:

Take about 0.8%agar (8gm in 1000ml) in distilled water. With continues stirring boil the mixture (Fig.1). Now pour the boiled mixture in beaker and cool-down the mixture naturally.

Fig.1: Agar preparation

b. Preparation of the nanoparticle solution:

The major advantage of using plant extracts for silver nanoparticle synthesis is that they are easily available, safe, and nontoxic. Fresh and green leaves of bamboo (*Fargesia sp. Jiuzhaigou*) were collected from the garden. They were washed several times with distilled water to remove dust particles on leaves. The leaves were obliterated by cotton and cut by plastic knife into small pieces. The leaves were boiled in the distilled water for 20 minutes. The extract is filtered by simple filter paper. Filtrate solution is kept in cold storage. 10 ml of filtrate is taken for further experiments and 2 mm concentration of $AgNO_3$ and 100 ml double distilled water is added in it. Resulting mixture is heated for 20 minutes. The colour change is noted (from faint white to dark brown) indicating confirmation of silver nanoparticles [4].

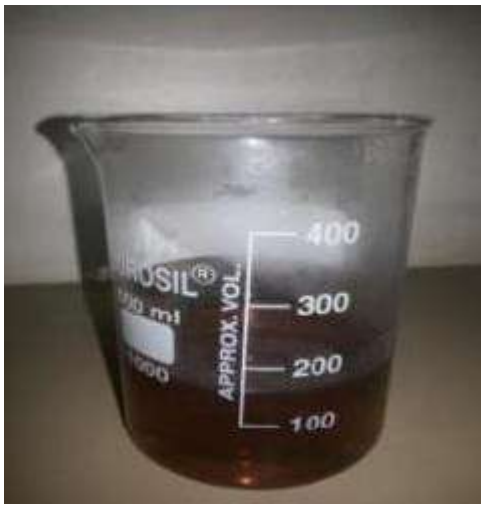

Fig.2: Nanoparticle solution

c. Germination of seed:

Wheat seeds were soaked in distilled water for controlled observations. Similarly wheat seeds were soaked in silver nanoparticle solution for 1hour, 1.5 hour and 2 hours respectively. After treatment seeds were sown in 0.8% agar gel at room temperature along with control. Observations were taken after 10 th day.

3. RESULT AND DISCUSSION

The seed germination rate, root length, shoot length were measured for 10 days. Photoshots on 5th day,7 th day,9 th day and 10th day are shown in Fig3, Fig.4, Fig 5, and Fig 6 respectively.

Fig.3: Photoshot on 5th day (Controlled, 1 hr, 1.5 hr, and 2 hr soaked)

Fig.4: Photoshot on 7th day (Controlled, 1 hr, 1.5 hr, and 2 hr soaked)

Fig. 5: Photoshot on 9th day (Controlled, 1 hr, 1.5 hr, and 2 hr soaked)

Fig. 6: Photoshot after 10 day(Controlled, 1 hr, 1.5 hr, and 2 hr soaked)

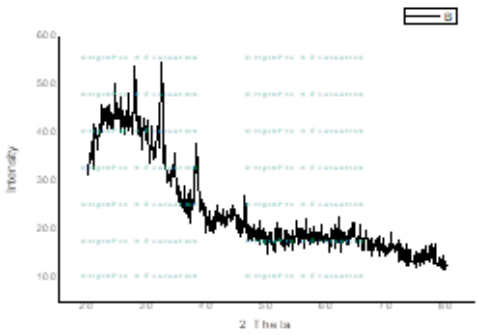

Fig.7: XRD of silver nanoparticles

A typical XRD spectrum of silver nanoparticle is shown in Fig7 and particle sizes are shown in Table1.

Table 1: A typical XRD spectrum of silver nanoparticle

Peak	2θ	β	D nm
111	0.59	0.0051	28.45
200	0.45	0.00392	35.35
220	0.15	0.002616	45
110	0.4	0.0035	39.63

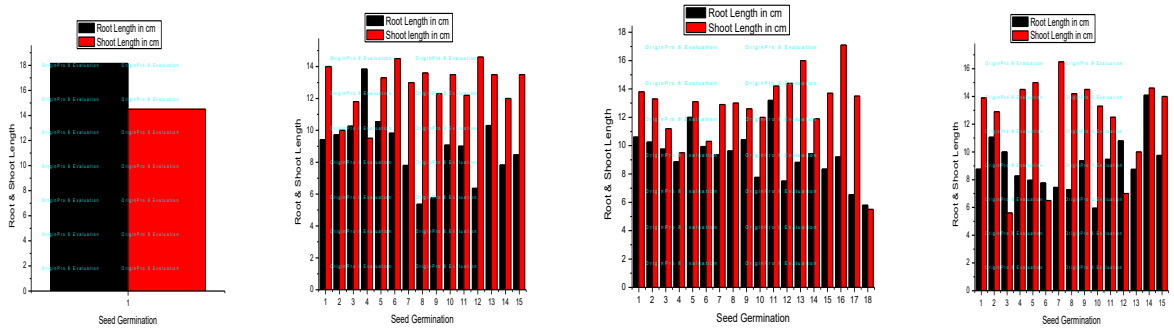

Fig.8: **Normal Wheat** **1 Hour Soaked** **1.30 Hour Soaked** **2.00 Hour Soaked**

Variation in Root Length & Shoot Length:

The changes in root length and shoot length when seeds are soaked in nanoparticles for 1 hour, 1.30 hours and 2 hours are shown in Fig.8.

CONCLUSION

The synthesized nanoparticles under laboratory conditions It is observed that nanoparticles they play an important role in seed germination and seedling growth of wheat. When seed were soaked in silver nanoparticles there was a significant enhancement in germination percentage as compared to control conditions. The number of seeds germinated increased in the case where wheat seeds were soaked in nanoparticles for 1 and half hour. A significant positive influence on root length and shoot length was observed for all seeds in compared to those of unexposed control germination. Present study indicated that shoot length after treatments has considerably increased in place of root length. Nanoparticles can promote Plant germination in earlier stages, significant enhancement in germination percentage as compared to control. The number of seeds germinated increased when soaked in nanoparticless for 1 and half hour and there is significant increase in root length and shoot length.

Acknowledgement

Authors are grateful to Principal Dr. M.G. Chaskar of Baburaoji Gholap College and office beares of P.D.E.A. Pune for allowing us to use the facility in labortory. Alaa Fadel Jassem acknowledge Republic of Iraq for felloship offered by government for his study.

REFERENCES

1. Hanan M Abou-Zeid & Yehia Moustafa. Physiological & cytogenetic responses of wheat & barley to silver Nanopriming treatment. *International Journal of applied Biology & pharmaceutical technology*,2014; 5(3): 265-278.
2. Hafiz Muhammad Jhanzab, Abdul Razzaq, Ghulam Jilani, Ammara Rehman, Abdul Hafeez, Farhat Yasmeen. Silver nano-particle enhance the growth, yield and nutrient use efficiency of wheat. *International Journal of Agronomy and Agricultural Research*, 2015; 7(1): 15-22.
3. Zainab M. Almutairi, Amjad Alharbi. Effect of Silver nanoparticles on seed germination of crop plant. *International Journal of biological, Biomolecular, Agriculture, food & biotechnological engineering*, 1999: 9(6): 1-5.
4. Packia Lakshmi N & Fazila Beevi. H. Green synthesis of silver nanoparticles using Argyreia cymosa leaf extract and Antibacterial activity. *American journal of Ethnomedicine*, 2014; 1(4): 216-225

IRJSE *Int. Res. J. of Science & Engineering,* 2018; Special Issue A2: 27-29 SJIF Impact Factor 4.11
ISSN: 2322-0015 UGC Approved Journal No. 63628
RESEARCH ARTICLE **OPEN ACCESS**

Electrode surface-gas interface as seat of light-effect under silent electric discharge

Pimple Sushama Sitaram

Department of Physics, S S & L S Patkar College of Arts and Science, S.V. Road, Goregaon(west), Mumbai - 400 062.
Email: sushamapimpale04@gmail.com

Manuscript Details
Available online on http://www.irjse.in
ISSN: 2322-0015

Editor: Dr. Arvind Chavhan

Cite this article as:
Pimple Sushama Sitaram. Electrode surface-gas interface as seat of light-effect under silent electric discharge, *Int. Res. Journal of Science & Engineering,* January 2018; Special Issue A2 : 27-29.

ABSTRACT

A negative and positive hysteresis effects have been observed in the variation of electrical conductivity with applied V during silent discharges through air and H_2 in ozonizers. The ratio (i_5/i_{50}) of the discharge pulses at a counting time for the biases of 5V and 50V have been measured in dark and under light. These measurements are then used for determination of its associated light-effects, like net and relative light- effects, net average current in increasing and decreasing fields. The present series of experiments are to study the relative effect % Δ (i_5/i_{50}) in the ratio of discharge currents measured with different detectors in pure gases and to understand the mechanism responsible for its occurrence.

Keywords: Anti-hysteresis, Light-effect, Ozonizer discharge, etc.

INTRODUCTION

The phenomenon of hysteresis has recently been reported by several researchers [1-3]. The effect has been caused by injection of thermo-electrons [4] in an annular space of tube excited by corona discharge [5-7]. Salvi and Pimpale [8] have shown that the positive hysteresis was caused due to the photo-enhancement of the discharge current with the decrease in voltage being larger than the discharge current with increase in voltage. These studies have further revealed the dependence of discharge current on the applied potential in rising and falling fields, the discriminator bias, the capacitor formed by gas and salt solution, the nature of gas, the nature of current detector, the size of the tube the electrical and optical factors etc.

The present work reports the ratio (i_x/i_y) i.e. the pulse height distribution as a function of the applied potential in both dark and under light by using different detectors.

METHODOLOGY

A Siemen's type ozonizer formed by sealing together two cylindrical glass tube coaxially. The experimental procedure used in the present work is to compare the discharge current in dark and under light produced in hydrogen and air. In each system the measurements are taken for a biases of x = 5 and y = 50 volts at temperature 27^0 C with a sensitive reflection galvanometer actuated by crystal rectifier. Also, a side by side measured discharge current in terms of counts with a scaler connected across a series resistance included in the low-tension circuit. The experimental arrangement was exactly the same as that described earlier [8].

RESULT

Two ozonizers one filled with air and the other with H_2 at 4 torr, were used in this work. Using these tubes, the potential-variation (50Hz) of the discharge current (i.e. scaler counts) with and without irradiation is taken for different values of d.c. bias, viz, 5V and 50 V. For different voltages, the ratio of discharge currents at the two biases is then determined in dark $(i_5/i_{50})_D$ and under light $(i_5/i_{50})_L$. The difference between the two ratios i.e. $\% \Delta (i_5/i_{50}) = (i_5/i_{50})_L - (i_5/i_{50})_D$, and the percentage value of light – effect i.e. $100 \times \Delta (i_5/i_{50}) / (i_5/i_{50})_D$, represents the net and relative effects of light at a given potential. The measurements are repeated at different potentials and its associated net effects are also determined in their increasing and decreasing fields. The non-identity of the discharge current ratios and of the corresponding effects in the two fields refers to the hysteresis or anti-hysteresis. In the case of hydrogen, the values of (i_5/i_{50}) with decrease in kV are found to be greater than those observed during its progressive increase. This incongruity of the discharge current ratio in the two fields clearly indicates the phenomenon of anti-hysteresis, and the hysteresis is observed in air. In air, the magnitude of both the net and relative effects of the current ratio is comparatively more pronounced than those observed in hydrogen.

It is seen from Table 1 that for suitable operational conditions $+\% \Delta (i_5/i_{50})$ inverts to $-\% \Delta (i_5/i_{50})$ as the voltage is increased progressively above the threshold value. This potential –reversal of a positive into negative or / and a negative in to positive light- effect is observed. Such an inversion as well as enhancement in $+\% \Delta (i_5/i_{50})$ with kV is non-linear, the threshold voltage decreases with electro-conditioning. The inversion with the different detectors occurs in the different potential ranges.

DISCUSSION

Since the discharge current contains high frequency (h.f.) component, it is evident that the intensity of detected current would depend on the type of the detector used. The detecting instrument for recording the voltage is generally placed across a high resistance R put in series with discharge circuit. The counter scaler in series with the discharge circuit has been used to measure the discharge pulses directly. Now,

Table 1: Inversion of net effect of light in the discharge current ratio in pre-aged hydrogen (at 4 torr) with potential of 50 Hz.

Applied kV (r.m.s.)	Ratio of count rate $(i_5/i_{50})_D$ in dark	$(i_5/i_{50})_L$ in light	$\Delta (i_5/i_{50})$	$\% \Delta (i_5/i_{50})$
0.28	00.00	00.00	0.00	00.00
0.70	48.29	00	- 48.29	- 100.00
1.05	09.120	11.160	+ 2. 08	+ 22.81
1.40	03.520	03.434	- 0.086	- 02.44
2.10	03.595	03.454	-0.141	-03.91
2.45	03.398	02.813	-0.58	-176.07

since the discharge current has a h.f. component, it is obvious that the current value as obtained from the instrument is less if the detecting instrument has appreciable self-capacity through which the h.f. is by-passed. The authors in their experiments noticed the difference between the readings of a scaler, a galvanometer actuated by crystal rectifier coupled resistively through a bell type transformer and hence concluded that there was a h.f. component of the discharge current. In recent years, unfortunately this simple fact has not been recognized and there has been much confusion in the interpretation of the experimental results. The result obtained by the authors can all be explained if the capacities, inherent or stray, of the indicating instrument and the associated apparatus are taken into account. For example, the scaler indicates a higher discharge current as also higher relative light-effect while the galvanometer actuated by a crystal rectifier not coupled or coupled resistivity though a step-down transformer shows a smaller effect. The result is as expected. The galvanometer actuated by a crystal rectifier coupled resistively has much larger associated capacity than the other two detectors which by-pass a large proportion of the h.f. current. Again, it has been found that the other conditions remaining the same, the +% Δ (i_5/i_{50}) obtained by using galvanometer actuated by a crystal rectifier coupled resistively, galvanometer actuated by a crystal diode and scaler as detectors, were 40%, 80% and 97% respectively. Here also the input capacities of three detectors for both the ozonizers decrease in the order mentioned.

On the basis of Joshi's theory reported by Ramaiah [9] it may be seen that the effect +% Δ (i_5/i_{50}) contemplates three stages, viz (1) at and above the characteristic threshold, an ionic + molecular adsorption like boundary layer is formed on the surfaces of electrode under field, (2) photo-electric emission occurs from this layer due to visible radiation and (3) these photo-electrons are captured by the excited atoms and molecules to form slow moving negative ions and produce the observed photo-diminution in the current ratio, i.e. – Δ (i_5/i_{50}) , as a space charge effect. Conditions disfavoring (3) give rise to the + Δ (i_5/i_{50}). Since stages (2) and (3) are instantaneous and fully reversible, the development with time in magnitude of the current ratio is attributable to that of adsorption in stage (1) of this theory.

CONCLUSION

All the above observations confirm that the localization of % Δ (i_5/i_{50}) is the dielectric, specially in the charged layer at the glass-gas interface. Further studies are in progress to study the mechanism of the formation and light modulation of this interface layer.

Conflicts of interest: The authors stated that no conflicts of interest.

REFERENCES

1. Chang JS, Pontiga F, Atten P and Castellanos A. Hysteresis effect of corona discharge in a narrow coaxial wire -pipe discharge tube. *IEEE Trans. Ind. Appl.* (U.S.A.), 1996, 32 (6), pp 1250
2. Stefanovic I and Petrovic ZL. Volt ampere characteristics of low current DC discharges in Ar, H_2, CH_4 and SF_6 *J. Appl. Phys. Regul. Pap*. Short Notes Rex, Pap (Japan),1997,36(B), pp 4728
3. Kirichenko NA and Nokolaeva EG. Hysteresis of laser deposition of matter from the gaseaous phase. *Quantum Elctron* (U K), 1997, 27 (4),pp 322
4. Shany NJ and Hadj-Ziane S. Czechoslovak, *J. Phys*., 2002, 52(1), pp 85
5. Ohm H. S. and Lee W.M. An analytical theory of corona discharge plasma. *Phys Plasma* (U.S.A.). 1997; 4 (9), pp311
6. Bonifaci N, Denat A and Atrazhev VM. Onset voltage for carona pulses in gaseous Ar under high pressure and in liquid Ar. IEEE Trans. *Dielectric Electr. Insul*. (U.S.A.). 1995; 2(1), pp137
7. Kochetov JV, Napartovich AP and Trushkin NI. The generation –zone structrure in negative –polarity carona discharges. *Plasma Phys. Rep*. 1995; 21(2),pp179
8. Salvi SV and Pimpale SS. Positive hysteresis of electrodeless discharge in Hydrogen in a co-axial cylindrical configuration. *Ind. J of pure and applied Phys*. 2005 ,43. pp386-389
9. Ramaiah R. Ph.D. Thesis, Dept. of Chem, B.H.U., 1964, Section 6, pp 67.

IRJSE *Int. Res. J. of Science & Engineering,* 2018; Special Issue A2: 30-34 SJIF Impact Factor 4.11
ISSN: 2322-0015 UGC Approved Journal No. 63628
RESEARCH ARTICLE **OPEN ACCESS**

Comparative Study of Influence of pH on Structural and Magnetic Properties of Ni-Zn Spinel Ferrite by Wet Chemical Method

Kakade GN and Gunjal RP

Department of Physics, R.B. Narayanrao Borawake, College, Shrirampur, 413709 (M.S.) India
Email: genudaskakade@gmail.com

Manuscript Details
Available online on http://www.irjse.in
ISSN: 2322-0015

Editor: Dr. Arvind Chavhan

Cite this article as:
Kakade GN and Gunjal RP. Comparative Study of Influence of pH on Structural and Magnetic Properties of Ni-Zn Spinel Ferrite by Wet Chemical Method, *Int. Res. Journal of Science & Engineering,* January 2018; Special Issue A2: 30-34.

ABSTRACT

In this work we have synthesis the Ni-Zn ferrite nanoparticles having composition $Ni_{0.65}$ Zn $_{0.35}Fe_2O_4$ at two p^H values 7 and 8, synthesized by wet chemical sol-gel autocombution method using L-Ascorbic acid as chelating agent. The single phase cubic spinel structure was confirmed by X-ray diffraction studies. The surface morphological studies were carried out using scanning electron microscopy using JEOL JSM-6360 scanning electron microscopy (SEM). The effect of p^H values on structural properties of synthesized nanoparticles has been investigated. Lattice parameter (a) increases, X-ray density (d_x) decreases, Unit cell volume (V) increases and Crystallite size (t) increases with increase in p^H value from 7 to 8. The grain size obtained from SEM images show decreasing trend with increasing pH Value.

Keyword: Ni-Zn spinel ferrite, sol-gel auto combustion technique, XRD, SEM.

INTRODUCTION

Nano sized spinel ferrite particles, a kind of soft magnetic material with structural formula M-Fe_2O_4 are one of the most attracting a novel class of magnetic material due to their interesting and most important properties, such as low melting point, high specific heating, low saturation magnetic moment and low magnetic transition temperature [1, 2]. Ferrites with electrical, dielectric, magnetic, optical, gas sensing etc. properties find numerous applications in variety of fields [3].

The important electrical as well as magnetic properties of spinel ferrite are sensitive to various factors viz. synthesis technique, variation in synthesis parameters in corporation with dopants at interstitial sites and nature and amount of dopant [4]. The most influencing synthesis parameter is p^H of solution. Many of the applications of spinel ferrites depend upon synthesis parameters such as pH, fuel, sintering temperature, sintering time etc. ultimately the size of nanoparticle. The properties of spinel ferrites can also be improve by suitable dopants or cautions and by optimizing the various synthesis parameters like pH, sintering temperature, sintering time, sintering atmosphere [5-7].

METHODOLOGY

In the synthesis of Nickel -Zinc spinel ferrite AR grade with high purity (99.99 %) nitrates of metal ions (Nickel, Zinc and ferric) were used and L-Ascorbic acid was used as fuel. All as nitrates and L-Ascorbic acid as per calculation was taken and dissolved in minimum amount of double distilled water in separate beaker. The metal nitrate to fuel ratio was taken 1:3. All these solutions are mixed homogenously in single beaker by continuous stirring. Ammonia was added to adjust the p^H of value 7 and8 of initial solution. This solution was evaporated at 75^0c to get a dense sticky gel, then temperature was increased to 110^0c for the dehydration process. The temperature was then increased rapidly and when it reached approximately 120^0c large of gases (CO_2, H_2O, and N_2) were liberated and dark brown power was produced through combustion process. The prepared power of Ni-Zn spinel ferrite is sintered at 500^0c for 6 h and various properties of Ni-Zn ferrite were studied.

RESULT AND DISCUSSION

Structural characterization:

Phase formation of the cubic spinel structure samples was examined by X-ray diffraction XRD) pattern obtained using Rigaku Corporation, Japan diffractometer at room temperature. The pattern was recorded using Cu-Kα radiation (λ=1.54182 Å) in the 2θrange 20° – 80° with step size 0.02° and time/step 2 s. Structural information such as the present phases, lattice parameter and crystalline size can be extracted from the samples diffraction pattern

X-ray diffraction study:

Fig.1 (a) and (b) shows the x-ray diffraction pattern of Ni-Zn samples synthesized at pH-7 and pH -8.X-ray diffraction analysis revealed that all the diffraction peaks seen in the XRD pattern well match with the standard pattern of pure nickel ferrite. The analysis of XRD pattern revealed the formation of single phase cubic spinel structure. The peaks of the XRD pattern corresponds to (220), (311), (222), (400), (422), (511) and (440) planes. The width of diffraction maxima peaks of planes (311) reduced and intensity of peaks increased as the p^H value increases.

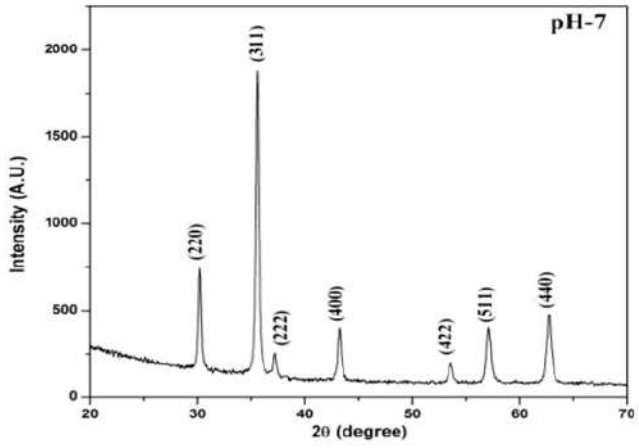

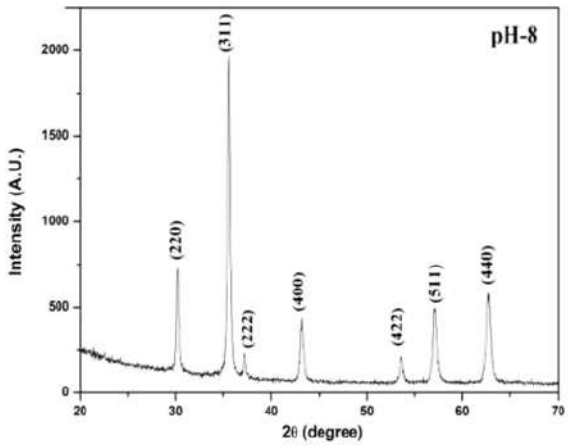

Fig .1 (a) x-ray diffraction pattern of $Ni_{0,65}Zn_{0.35}Fe_2O_4$ nanoparticles for pH -7

(b) x-ray diffraction pattern of $Ni_{0,65}Zn_{0.35}Fe_2O_4$ nanoparticles for pH -8

Table 3. 1 (a): Miller indices (h k l), Bragg's angle (θ), Interplanar spacing (d), Intensity (I) and Relative intensity ratio (I/Io) of $Ni_{0.65}Zn_{0.35}Fe_2O_4$ nanoparticles (pH- 7)

(h k l)	2θ (degree)	θ (degree)	Sin (θ)	Sin (θ)/λ	d (Å)	I (a.u)	I/I_O
(220)	30.191	15.0955	0.2604	0.1690	2.9571	782.7	40
(311)	35.587	17.7935	0.3056	0.1984	2.5201	1933.4	100
(222)	37.257	18.6285	0.3194	0.2073	2.4109	277.5	14
(400)	43.227	21.6135	0.3683	0.2391	2.0907	425.0	22
(422)	53.601	26.8005	0.4509	0.2927	1.7080	222.8	12
(511)	57.116	28.5580	0.4780	0.3103	1.6109	434.3	22
(440)	62.699	31.3495	0.5203	0.3377	1.4802	512.5	27

Table 3.1 (b): Miller indices (h k l), Bragg's angle (θ), Interplanar spacing (d), Intensity(I) and Relative intensity ratio (I/Io) of $Ni_{0.65}Zn_{0.35}Fe_2O_4$ nanoparticles (pH-8).

(h k l)	2θ (degree)	θ (degree)	Sin (θ)	Sin (θ)/λ	d (Å)	I (a.u)	I/I_O
(220)	30.186	15.0930	0.2604	0.1690	2.95830	738.0	37
(311)	35.576	17.7880	0.3055	0.1983	2.52145	1977.3	100
(222)	37.175	18.5875	0.3188	0.2069	2.41658	253.8	13
(400)	43.214	21.6070	0.3682	0.2390	2.09183	450.6	23
(422)	53.559	26.7795	0.4506	0.2925	1.70964	210.2	11
(511)	57.084	28.5420	0.4778	0.3101	1.61216	520.6	26
(440)	62.764	31.3820	0.5207	0.3380	1.47923	608.5	31

Table 3.2: Lattice parameter (a), X-ray density (d_x), Unit cell volume (V) and Crystallitesize (t) of $Ni_{0.65}Zn_{0.35}Fe_2O_4$ nanoparticles (pH-7, 8)

'pH' maintain at	a (Å)	d_x (gm/cm^3)	V ($Å^3$)	Crystallite size (t)
pH-7	8.3640	5.3748	585.557	22
pH-8	8.3678	5.3671	586.334	24

Table 3.3: Hopping length (L_A, L_B), Tetrahedral bond (d_{AX}), Octahedral bond (d_{BX}), Tetraedge (d_{AXE}) and Octa edge (d_{BXE}) of $Ni_{0.65}Zn_{0.35}Fe_2O_4$ nanoparticles (pH-7, 8).

'pH' Maintain at	L_A (Å)	L_B (Å)	dAX (Å)	dBX (Å)	dAXE (Å)	dBXE (Å)	
						Shared	Unshared
pH-7	3.6217	2.9571	1.8978	2.0420	3.0911	2.8152	2.9588
pH-8	3.6235	2.9585	1.8987	2.0430	3.1005	2.8165	2.9602

Table 3.1(a) and (b) gives the miller indices (hkl), Bragg's angle (2θ) along with their corresponding interplanar spacing (d) values, intensity and relative intensity ratio of the Ni-Zn ferrite with varying p^H values. It is seen that the interplanar spacing (d) values shows gradual decrease with increasing Bragg's angle. The intensity of (311) plane is more as compared to other planes. The lattice constant value 'a' (Å) of $Ni_{0.65}Zn_{0.35}Fe_2O_4$ nanoparticles synthesized at different pH was determined by using the relation [9]. The obtained values of the lattice constant (a) are tabulated in Table 3.2. There is slight changes were observed for lattice constant '*a*' which could be associated with the pH solution. The results presented in Table 4.2 show that the lattice parameters a, b and c agree with the equation a = b = c, indicating that the prepared sample belongs to cubic lattice. The average

crystallite size of $Ni_{0.65}Zn_{0.35}Fe_2O_4$ nanoparticles synthesized at two pH value (pH-7,8) was determined using the relation [10].

The obtained values of the crystallite size are tabulated in Table 3.2. Using the Scherer's formula, the variations of full-width at half maximum (FWHM) at different XRD peaks indicated that the average crystallite size of the nanoparticles were about 22, 24 nm corresponding to the pH of 7, 8 respectively. The average crystallite size is increased as the pH increases. Due to the rapid combustion rate and high flame temperature with increasing pH, higher pH produces larger crystallite size and good crystallinity. It has been experimentally observed by some researchers that nanocrystalline powders are quite susceptible to the formation of inter-particle London–van der Waals bonds either in the wet or in the dry state due to their very fine particle size [11]. The X-ray density (dx) of $Ni_{0.65}Zn_{0.35}Fe_2O_4$ nanoparticles synthesized at two pH value (pH -7, 8) was calculated by using the relation [8, 12].

The X-ray density depends on the molecular weights of the samples and lattice constants. The X-ray density values are tabulated in Table 4.2; the obtained values of X-ray density are in reported range, which are depends on lattice constant, therefore same nature of lattice constant observed in the X-ray density value with increase pH of sample. The value of volume of unit cell value determined from cube of lattice constant, which indicate that the volume of the unit cell depends on the lattice constant, therefore same nature of lattice constant observed in the volume of unit cell values with increase pH of sample.

Various other structural parameters like hopping lengths (L_A, L_B), tetrahedral bond length (d_{AX}), octahedral bond length (d_{BX}), tetra edge (d_{AXE}) and octa edge (d_{BXE}) were evaluated from relation for two pH value [13, 14]. Using the values of the lattice constant (a), the various other structural parameters like hopping lengths (L_A, L_B), tetrahedral bond length (d_{AX}), octahedral bond length (d_{BX}), tetra edge (d_{AXE}) and octa edge (d_{BXE}) were evaluated from XRD data for different pH value and indexed in Table 3.3.

The obtained structural parameters are depends on lattice constant values, there were no increasing or decreasing trend observed in the hopping lengths (L_A, L_B), tetrahedral bond length (d_{AX}), octahedral bond length (d_{BX}), tetra edge (d_{AXE}) and octa edge (d_{BXE}) values with increasing pH value of Ni-Zn sample.

The tetrahedral A-site ionic radii can be calculated using the value of lattice constant 'a' and oxygen positional parameter 'u' (u = 0.381Å) as:

$$r_A = \left(u - \frac{1}{4}\right) a\sqrt{3} - r\left(\frac{2}{o}\right)\overset{0}{A}$$

where, '$r_{A'}$ represents radius of tetrahedral (A) site cation,'u' oxygen positional parameter, 'O' represents radius of oxygen anions. The octahedral B-site ionic radii can be calculated using the equation:

$$r_B = \left(\frac{5}{8} - u\right) a - r\left(\frac{2}{o}\right)\overset{0}{A}.$$

Where, r_B represents radius of octahedral [B] site cation.

Table 3.4: Ionic radii (r_A, r_B) of $Ni_{0.65}Zn_{0.35}Fe_2O_4$ nanoparticles (pH-7, 8).

'pH' Maintain at	**r_A(Å)**	**r_B(Å)**
pH-7	0.5778	0.7208
pH-8	0.5787	0.7218

The values of tetrahedral (A-site) and octahedral [B-site] of ionic radius are given in Table 4.4. The values of tetrahedral (A-site) and octahedral [B-site] value depends on the values of lattice constant, therefore, it is found that obtained values tetrahedral (A-site) and octahedral [B-site] are in reported range. There are no more changes observed in tetrahedral and octahedral ionic radii values with increasing pH of sample [15, 16].

CONCLUSION

Nanocrystalline Ni-Zn ferrite has been synthesized at different pH via Sol-gel auto combustion method, which is characterized on nanosized shape etc by X-Ray diffraction. The particle size is in the range of 22-24nm. The particle size increases with increase in p^H value. The prepared Ni-Zn samples annealed at

temperature 500 °C for 2 hr is formed a good crystalline cubic phase spinel structure. The grain size is in the range of 78-89 nm for two pH values. With increase in pH from 7 to 8 the grain size decreases. The surface morphology of the prepared samples is strongly influenced by pH. The grain size obtained from SEM images show decreasing trend with increasing pH.

Acknowledgement
The authors are very much thankful to Dr.K.M. Jadhav, Professor, Department of Physics Dr. Babasaheb Ambedkar Marahtwada University, Aurangabad (M.S.),India for their fruitful guidance and for providing laboratory facilities.

Conflicts of interest: The authors stated that no conflicts of interest.

REFERENCES

1. Lu AH, Salabas EeL, Schüth F. Magnetic nanoparticles: synthesis, protection, functionalization, and application, Angewandte Chemie International Edition, 2007; 46; 1222-1244.
2. Richerson DW. Modern ceramic engineering: properties, processing, and use in design, CRC press, 2005.
3. Mathew DS, Juang RS. An overview of the structure and magnetism of spinel ferrite nanoparticles and their synthesis in microemulsions, *Chemical Engineering Journal*, 129 (2007) 51-65.
4. Goldman A. Modern ferrite technology, Springer Science & Business Media, 2006.
5. Teja AS, Koh PY. Synthesis, properties, and applications of magnetic iron oxide nanoparticles, Progress in crystal growth and characterization of materials, 55 (2009) 22-45.
6. Rath C, Anand S, Das R, Sahu K, Kulkarni S, Date S, Mishra N. Dependence on cation distribution of particle size, lattice parameter, and magnetic properties in nanosizeMn–Zn ferrite, *Journal of Applied Physics*, 91 (2002) 2211-2215.
7. Upadhyay C, Mishra D, Verma H, Anand S, Das R. Effect of preparation conitions on formation of nanophase Ni–Zn ferrites through hydrothermal technique, *Journal of Magnetism and Magnetic Materials*, 260 (2003) 188-194.
8. Gul I, Ahmed W, Maqsood A. Electrical and magnetic characterization of nanocrystalline Ni–Zn ferrite synthesis by co-precipitation route, *Journal of Magnetism and Magnetic Materials*, 320 (2008) 270-275.
9. Khirade PP, Birajdar SD, Humbe AV, Jadhav K. Structural, electrical and dielectrical property investigations of Fe-doped BaZrO3 nanoceramics, *Journal of Electronic Materials*, 45 (2016) 3227-3235.
10. Rajendran M, Pullar R, Bhattacharya A, Das D, Chintalapudi S, Majumdar C. Magnetic properties of nanocrystallineCoFe 2 O 4 powders prepared at room temperature: variation with crystallite size, *Journal of Magnetism and Magnetic Materials*, 232 (2001) 71-83.
11. Hamaker H. The London—van der Waals attraction between spherical particles, physica, 4 (1937) 1058-1072.
12. Kambale R, Shaikh P, Kamble S, Kolekar Y. Effect of cobalt substitution on structural, magnetic and electric properties of nickel ferrite, Journal of Alloys and Compounds, 478 (2009) 599-603. Vinayak V, Khirade PP, Birajdar SD, Gaikwad P, Shinde N, Jadhav K. Low temperature synthesis of magnesium doped cobalt ferrite nanoparticles and their structural properties, *Int. Adv. Res. J. Sci. Eng. Technol*., 2 (2015) 55-58.
13. Sindhu S, Birajdar D. Structural and magnetic characterization of Co2+ substituted nano structured Copper-Zinc spinel ferrite, *IOSR Journal of Applied Physics*, 3 (2013) 33-41.
14. El-Sayed A. Influence of zinc content on some properties of Ni–Zn ferrites, *Ceramics International*, 28 (2002) 363-367.
15. Priyadharsini P, Pradeep A, Rao PS, Chandrasekaran G. Structural, spectroscopic and magnetic study of nanocrystalline Ni–Zn ferrites, *Materials Chemistry and Physics*, 116 (2009) 207-213.
16. Janghorban K, Shokrollahi H. Influence of V 2 O 5 addition on the grain growth and magnetic properties of Mn–Zn high permeability ferrites, *Journal of magnetism and magnetic materials*, 308 (2007) 238-242.
17. Thorvaldsen A. The intercept method—2.Determination of spatial grain size, Actamaterialia, 45 (1997) 595-600.

IRJSE *Int. Res. J. of Science & Engineering,* 2018; Special Issue A2: 35-40 SJIF Impact Factor 4.11
ISSN: 2322-0015 UGC Approved Journal No. 63628
RESEARCH ARTICLE **OPEN ACCESS**

Synthesis, Characterization and Biological activity of Schiff base 2-{[2-(2-Methoxy-phenoxy)-ethylimino]-methyl} - phenol and its transition metal complexes

Palande Sheetal V[1*] and Swamy Deelip K[2]

[1*]NES Science College Nanded, Maharashtra, India,
[2]Head, Department of Chemistry, Pratibha Niketan College, Nanded, MS, India.
[1*]Postal Address: 604, Alkapuri CHS Ltd, 3rd Akurli Cross Road, Kandivli East, Mumbai 400101,
Email: palandesheetal@gmail.com

Manuscript Details
Available online on http://www.irjse.in
ISSN: 2322-0015

Editor: Dr. Arvind Chavhan

Cite this article as:
Palande Sheetal V and Swamy Deelip K. Synthesis, Characterization and Biological activity of Schiff base 2-{[2-(2-Methoxy-phenoxy)-ethylimino]-methyl} - phenol and its transition metal complexes, *Int. Res. Journal of Science & Engineering,* January 2018; Special Issue A2 : 35-40.

ABSTRACT

Coordination complexes of transition metals with Schiff base ligand were synthesized. The characterization of these complexes was elucidated by physical parameters and spectral analysis namely colour, melting point, IR, NMR, UV, Magnetic measurements, TGA and ESR studies. Plant growth regulating activity on seeds of *Trigonella foenum-graecum* (Methi), *Triticum aestivum* (wheat) and Brassica nigra (black mustard) has been studied using standard Blotter method for evaluation of inhibitory or stimulatory effects of the synthesized compounds. The plant growth analysis was decided by measurement of parameters like percentage of germination, seedling height, shoot length, root length, root/shoot ratio and vigor index. The values of these parameters have been used to make a conclusion about plant growth regulating activity of ligand and its complexes

Keywords: Schiff bases, Metal Complexes, Plant growth studies, Standard Blotter method.

INTRODUCTION

Research in agriculture involves production of new and better varieties of crop plants, plant protection against insects and weeds, manage soil fertility. Many substances are capable of inducing same plant responses. In this context role of coordination chemistry is significant. Many transition metal complexes are been used to produce new varieties of crops, control soil fertility, protect the plants from insects, diseases and weeds. It has been observed that on comlexetion, the biological activity of metal chelate changes compared to that of free metal and ligand alone [1,2,3]. The microbial activity like antifungal and antibacterial of metal complexes showing an enhanced activity as compared to free metal and ligand has been reported [4]. Transition metal complexes of substituted pyrazoles were tested for their plant growth regulating activity [5]. Piperidene-2-carboxylic acid complexes of bivalent metal ions have been found to be useful in agriculture as plant growth regulating [6]. Plant growth regulating activity of (2-chlorophenyl) (5-(2- hydroxyphenyl)-3-(pyridin-3-yl)-1H-pyrazol-4-yl) methanone and its Fe (III) and Cu (II) complexes on Trigonella foenum-graecum were studied7. Piperidene-2-carboxylic acid complexes with some bivalent metal ions have been reported to be useful in agriculture as plant growth regulating [8]. Many workers have studied the plant growth regulating activities of various organic ligands and their transition metal ion complexes for various plants [9-14].

METHODOLOGY

Chemicals and reagents:

The chemicals used are 1-Naphthalen-1-yl-ethylamine (Merck, AR grade) and Salicydehyde (2-Hydroxy benzaldehyde) (Merck, AR grade), Ethyl alcohol (Merck, AR grade), Cobalt (II) chloride dihydrate (Sigma Aldrich), Nickel(II) chloride hexahydrate (Sigma Aldrich), Copper(II) chloride dihydrate (Sigma Aldrich), Zinc (II) chloride (Sigma Aldrich), Manganese (II) chloride tetrahydrate (Sigma Aldrich).

Synthesis of Ligand (MPEMP-MPEMP):

The Schiff Base ligand 2-{[2-(2-Methoxy-phenoxy)-ethylimino]-methyl}- phenol (Fig 1) was synthesized by condensing amine 2-(2-Methoxy-phenoxy)-ethylamine with Salicydehyde in equimolar proportions. To an ethanolic solution (10 ml) of the amine (0.01 mole) was added Salicydehyde (0.01 mole) in ethanol (10 mL) with stirring. The mixture was then refluxed for 30 mins. The reaction mixture was then cooled which immediately gave a precipitated product. The product then obtained was filtered, washed with ethanol and then dried. The crude product was then crystallized from aqueous ethanol to give a yield of 89%.

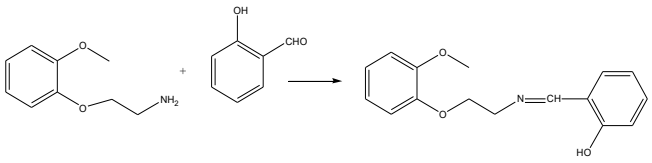

2-(2-Methoxy-phenoxy) - ethylamine | Salicydehyde | 2-{[2-(2-Methoxy-phenoxy)-ethylimino]-methyl}-phenol

Fig 1: Formation of Schiff base MPEMP-MPEMP

Synthesis of metal complexes:

The ligand and metal salt in the molar ratio of 2:1 was dissolved in a ethanol and the reaction mixture was heated on water bath for about one hour. It was then cooled when colored solid separated out which was washed with ethanol and dried. This is the general method employed for the synthesis of metal complexes of ligand with metal chlorides viz Ni(II), Cu(II), Co(II), Mn(II) and Zn(II).

Plant Growth Activity study:

The plant growth activity studies were carried out on the seeds of three plants *Trigonella foenum-graecum (Methi), Triticum aestivum* (wheat) and Brassica nigra (black mustard) by standard blotter method. Metal complex solutions (5 ppm) and ligand solution (5ppm) were prepared using 20% DMSO solution in doubly distilled water. The seeds were soaked in water overnight. Healthy seeds of equal size were chosen, and then immersed in distilled water, 20 % DMSO solution, ligand solution and complex solutions for 6 hours. The seeds soaked were taken out of each solution and washed thoroughly with distilled water. The seeds were then placed on Petri plate with 20

seeds per plate containing moistened blotters. The plates were observed for germination, root-shoot length for 10 days.

RESULT AND DISCUSSION

Formation of the complex was indicated by color change and melting point. Physical characteristics and yield of Schiff base and metal complexes are given in Table 1.

NMR and IR spectra:

In NMR spectra formation of ligand was confirmed by presence of CH=N peak at 8.7 δ and OH at 5.7 δ. In the present investigation the Infra red values for major peaks are assigned. The IR spectrum of ligand gave a strong band at 1634.77 cm-1 and 2904.61cm^{-1} which are attributed to the stretching frequencies of HC=N (azomethine) and OH respectively. Complexes showed a lower shift of wave numbers for HC=N. Also IR bands were observed for M-O and M-N. All complexes showed bands 3300 cm^{-1} to 3400 cm^{-1} indicating co-ordinated H_2O moiety in the complexes. Complex of SB1-Ni showed IR bands at 1617.28 cm^{-1} and 3347.77 cm^{-1} corresponding to HC=N and H_2O , IR values of 490.7cm^{-1} and 604.67 cm^{-1} were assigned to M-O and M-N respectively. Similarly complex of SB1-Zn complex showed bands at υ(HC=N) 1629.24 cm^{-1}, υ(H_2O) 3260.38 cm^{-1} , υ (M-O) 485.87 cm^{-1} and υ (M-N) 575.59 cm^{-1}. Similarly bands were observed for Cu complex at υ(HC=N) 1598.23 cm^{-1}, υ(H_2O) 3339.22 cm^{-1} ,υ (M-O) 475.58 cm^{-1} and υ (M-N) 559.66 cm^{-1}. Co complex υ(HC=N) 1616.33 cm^{-1}, υ(H_2O) 3361.73 cm^{-1} ,υ (M-O) 461.73 cm^{-1} and υ (M-N) 607.77 cm^{-1}. Mn complex υ(HC=N) 1615.28 cm^{-1}, υ(H_2O) 3446.57 cm^{-1}, υ (M-O) 471.59 cm^{-1} and υ (M-N) 580.65 cm^{-1}.

Electronic absorption spectra:

In the electronic spectra the ligand exhibited energy peaks at 25000 cm^{-1} and 27392 cm^{-1}. The Co(II) complexes exhibited two energy peak at 27247 cm^{-1} and 23866 cm^{-1}, which can be assigned[5] to the transitions 4T1g(F) → 4T2g(F), 4T1g(F) → 4A2g(F) and 4T1g (F) → 4T2g (P) for a high spin octahedral geometry respectively. The electronic spectra of the Ni(II) complexes showed d–d transition at 27248 cm^{-1} and 30487 cm^{-1} [15] while Mn complexes showed peaks at 25000 cm^{-1}, 27173 cm^{-1} and 24630 cm^{-1}. These are assigned to 3A2g(F) → 3T2g(F), 3A2g(F) → 3T1g(F) and 3A2g (F) → 3T2g(P) transitions, respectively. These are consistent with a well- -defined octahedral geometry. The Zn(II) complexes exhibited only a high intensity band at 27777 cm^{-1} and 33444 cm^{-1}, which is assigned to ligand–metal charge transfer. In case of the Cu(II) complexes, a broad band at 23809 cm^{-1} and 30487 cm^{-1} [15] was observed that is assigned to the 2Eg → 2T2g transition, which confirms its octahedral geometry.

Thermo Gravimetric Analysis:

TGA analysis is carried out to explain the thermal stability of complexes. TGA study (Table 2) of complex showed weight loss in the temperature range of 110^{o}C-200 ^{o}C is due to elimination of coordinated water molecule. Also gradual decrease in mass is seen up to 300 ^{o}C due to loss of volatile matter. And a plateau observed above 350 ^{o}C respectively which corresponds to the formation of stable metal oxide.

ESR:

The gll and g⊥ value for Copper complex is reported in the following Table 2. The spectrum showed asymmetric bands with two g values. The trend gll> g⊥> 2.00277, indicating that the unpaired electron lay predominately in the dx^2-y^2 orbital with possibly mixing of dz^2 orbital because of the low symmetry. The axial symmetry parameter 'G' is determined as $G = \frac{(gll - 2.00277)}{(g\perp - 2.00277)}$. G values found to be more than 4 suggesting very weak or no interaction in the solid state.

Magnetic susceptibility measurements:

The effective magnetic moment values for the complexes were determined. The magnetic moment value 4.12 B.M for Co(II) complex suggests an octahedral environment [16,17]. The magnetic moment value of the Cu (II) complexes of 1.63 B.M suggests distorted octahedral geometry [18,19]. The magnetic moment value of the Ni(II) complexes 3.12 B.M suggests an octahedral geometry. Mn (II) complexes with the value of 5.56 B.M indicate octahedral geometry [20]. The Zn(II) complexes were found to be diamagnetic, as expected for d10 configuration.

Conductivity measurements:

Solid complexes were dissolved in DMSO to perform conductivity experiments. Solutions of 10^{-1} M concentration were prepared and the molar conductivity of these solutions was measured at room temperature. The Molar conductance values for all the newly synthesized complexes were in the range 23 to 94 mhos cm^2 mol^{-1}, indicating very low conductance. These values indicate that the complexes are non-electrolytic nature. The conductance values of the metal complexes were given in Table3.

From the discussion of the results of various physico-chemical studies presented above, it may be concluded that the most probable geometry for the transition metal complexes with general formula $ML_2.2H_2O$ is octahedral and the bonding in the complexes can be represented in Fig 2.

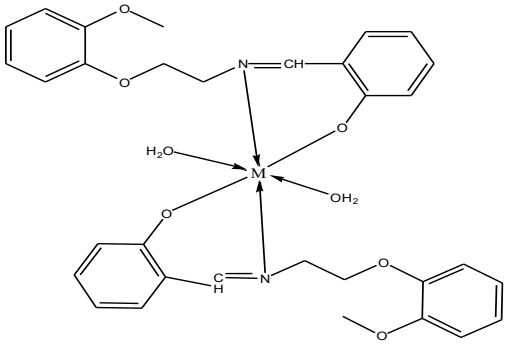

Fig: 2 Structure of complex (M= Ni, Cu, Co, Mn, Zn)

Table 1: Physical characteristics and Yield

Compound	Color	Yield %	M.P (°C)
Ligand (MPEMP)	MPEMP	Fluoroscent light yellow	89
MPEMP-Ni complex	MPEMP Ni	Light green	78
MPEMP-Cu complex	MPEMP Cu	Brown	57
MPEMP-Co complex	MPEMP Co	Orangish brown	55
MPEMP-Mn complex	MPEMP Mn	Dirty green	70
MPEMP-Zn complex	MPEMP Zn	Light yellow	78

Table 2: Thermogravimetric Data of the Metal Complexes of MPEMP

Complexes	Temperature(°C)	Calc (%)	Obs (%)	Mass loss
MPEMP Ni	110 - 200	5.67	6.0	Mass loss due to H_2O molecules
	250 - 320	14.60	18.0	Mass loss due to volatile matter
	Above 350	11.76	12.0	Mass of the metal oxide
MPEMP Cu	110 - 200	5.62	5.0	Mass loss due toH_2O molecules
	250 - 320	15.33	17.0	Mass loss due to volatile matter
	Above 350	9.92	10.0	Mass of the metal oxide
MPEMP Co	110 - 200	5.6	5.0	Mass loss due toH_2O molecules
	275 - 320	14.69	17.0	Mass loss due to volatile matter
	Above 350	11.79	11.0	Mass of the metal oxide
MPEMP Mn	110 - 200	5.70	6.0	Mass loss due toH_2O molecules
	220 - 330	14.18	16.0	Mass loss due to volatile matter
	Above 350	11.23	11.0	Mass of the metal oxide
MPEMP Zn	110 - 200	5.6	6.0	Mass loss due toH_2O molecules
	225 - 275	15.58	16.0	Mass loss due to volatile matter
	Above 350	12.67	11.0	Mass of the metal oxide

Table 3: ESR values for Copper complex

Complex	gll value	g⊥ value	g_{avg}	G
MPEMP Cu complex	2.372	2.080	2.274	4.779

Table 4: Effects of MPEMP and its complexes on growth parameters for *Trigonella foenum-graecum* (Methi) plant.

Parameters	Effect of		Effect of complexes				
	Water	Ligand	Ni (II)	Cu (II)	Mn (II)	Co (II)	Zn (II)
Germination seed number	20	20	20	20	20	20	20
% Germination after 7 days	100	85	70	70	75	85	80
% Survival after 10 days	100	94.11	85.71	85.71	86.66	94.11	93.75
Root length (cm)	2.8	2.2	1.9	1.4	1.3	1.0	0.9
Shoot length (cm)	4.0	3.4	3.0	2.8	2.1	2.2	2.7
Vigor index	680	476	343	294	255	272	288
Root-shoot ratio	0.657	0.60	0.52	0.47	0.47	0.47	0.38

Table 5: Effect of MPEMP and its Ni(II), Cu(II), Co(II), Mn(II) and Zn(II) complexes on growth parameters for *Triticum aestivum* (wheat)) plant.

Parameters	Effect of		Effect of complexes				
	Water	Ligand	Ni (II)	Cu (II)	Mn (II)	Co (II)	Zn (II)
Germination seed number	20	20	20	20	20	20	20
% Germination after 7days	100	80	65	60	60	65	65
% Survival after 10 days	95	93.75	84.61	91.66	91.66	84.61	84.61
Root length (cm)	2.4	2.1	1.4	1.2	1.4	1.0	0.5
Shoot length (cm)	3.8	3.5	1.9	2.0	2.1	1.5	0.9
Vigor index	620	448	214.5	192	210	162.5	91
Root-shoot ratio	0.65	0.63	0.73	0.56	0.66	0.72	0.75

Table 6: Effect of 2-[(1-Naphthalen-1-yl-ethylimino)-methyl]-phenol and its Ni(II), Cu(II), Co(II), Mn(II) and Zn(II) complexes on growth parameters for *Brassica nigra* (black mustard) plant

Parameters	Effect of		Effect of complexes				
	Water	Ligand	Ni (II)	Cu (II)	Mn (II)	Co (II)	Zn (II)
Germination seed number	20	20	20	20	20	20	20
% Germination after 7 days	95	70	60	60	65	60	70
% Survival after 10 days	100	92.85	83.33	83.33	84.61	91.66	92.85
Root length (cm)	2.2	2.0	1.1	1.0	1.0	0.8	0.4
Shoot length (cm)	3.6	3.2	3.4	3.3	3.1	3.0	2.6
Vigor index	551	364	270	279.5	266.5	228	210
Root-shoot ratio	0.58	0.62	0.28	0.27	0.28	0.24	0.13

Plant growth activity:

The values plant growth parameters such as percentage of germination, survival, shoot length, root length, root/shoot ratio, vigor index for *Trigonella foenum-graecum* (Methi) are reported in Table (4), similar parameters for *Triticum aestivum* (wheat) are reported in table (5) and for Brassica nigra (black mustard) in table 6. Vigor index was determined using equation

Vigour index = % germination x (root length + shoot length)

The root:

shoot ratio is one of the measures of overall health of the plants. Change in the root: shoot ratio over control (water) indicates change in overall health of the plant.

The root/shoot ratio was determined by using equation

root/shoot ratio = dry weight for roots/dry weight for top of plant

The general order of plant growth activity of ligand and its complexes compared to water are shown in Table (4), Table (5) and Table (6).

CONCLUSION

In present investigation it was observed that the root: shoot ratio has decreased for the complexes compared to ligand and water. Hence it was concluded that the synthesized complexes have plant inhibitory activity rather than plant growth activity. The activity can be summarized in a decreasing order as follows: Water > Ligand > Metal complexes.

Conflicts of interest: The authors stated that no conflicts of interest.

REFERENCES

1. Gershon H, Parmegiani R, Nicerson WJ. *Appl. Microbiol*., 1962, 10(6), 556-560.
2. Gershon H, Parmegiani R. *Appl. Microbiol*., 1963, 11(1), 62-65.
3. Anant Prakash, Devjani Adhikari, *International Journal of ChemTech Research; 2011;* 3(4):1891-1896.
4. Mangamamba T, Ganorkar MC and Swarnabala G, *International Journal of Inorganic Chemistry,* 2014, Article ID 736538, 22 pages.
5. Deosarkar SD, Chavan SA and Avinash L. *Puyad, J. Chem. Pharm. Res*., 2011, 3(4):703-706.
6. Sharma RC, Tripathi SP, Khanna S, Sharma RS. *Curr. Sci*., 1981, 50, 748-750.
7. Deosarkar, SA Chavan and AL Puyad, J. Chem. Pharm. Res., 2011, 3 (4), 703-706.
8. Adams CM and Bernays EA, Entamol. Exp. Appl., 1978, 23, 101-109.
9. Patil AB, *Orient. J. Chem*., 2009, 25 (2), 459-460.
10. Thakare VJ, Ph. D. Thesis, Chemistry, S. G. B. Amravati University, INDIA, 2007.
11. Adams CM, EA Bernays, Entomol. Exp. Appl., 1978, 23, 101-109.
12. Meshram UP, Khobragade BG, ML Narwade, VB Khobragade, Der Pharma Chemica, 2011, 3 (2), 376-382.
13. Singh VP, Yashovardhan, SK Bhati, Int. J. ChemTech Res., 2011, 3 (2), 892-900.
14. Kumar S, Kumar Singh A, *J. Chem. Pharm. Res*., 2010, 2(6), 118-124.
15. Zahid H. Chohan et al. Metal based drugs, 2001, 8 (3).

IRJSE *Int. Res. J. of Science & Engineering,* 2018; Special Issue A2: 41-45 SJIF Impact Factor 4.11
ISSN: 2322-0015 UGC Approved Journal No. 63628
RESEARCH ARTICLE **OPEN ACCESS**

Dielectric Study of Binary Liquid Mixtures of 1,2 di-amino-propane (1,2-Dap) With Methanol At 9.85 Ghz Microwave Frequency

Meshram SS[1], Tumberphale UB[2], Gawali PG[3]

[1,2]Microwave Research Laboratory. N. E. S. Science College, Nanded-431605, Maharashtra, India
[3]Department of Physics B.S. College, Basmatnagar, Hingoli-431512 India
Email: sangita.meshram@rediffmail.com

Manuscript Details
Available online on http://www.irjse.in
ISSN: 2322-0015

Editor: Dr. Arvind Chavhan

Cite this article as:
Meshram SS, Tumberphale UB, Gawali PG. Dielectric Study of Binary Liquid Mixtures of 1,2diaminopropane (1,2-Dap) With Methanol At 9.85 Ghz Microwave Frequency, *Int. Res. Journal of Science & Engineering,* January 2018; Special Issue A2: 41-45.

ABSTRACT

Using Surber's technique of measuring reflection coefficient from the air-dielectric boundary of liquid the dielectric constant (ε′), dielectric loss(ε″) of 1,2-Diaminopropane (1,2-DAP) with methanol and their binary mixtures for different mole fractions of 1,2-Diaminopropane (1,2-DAP) have been measured at 9.85 GHz microwave frequency at 30 ^{0}C.The values of density (ρ), viscosity (η), Square refractive index (n_D^2) of pure liquids as well as those of binary mixtures are reported. The observed data have been utilized to calculate various parameters such as the molar polarization (P_{12}), loss tangent (tanδ), activation energy (E_a). The excess Square of refractive index (Δn_D^2), viscosity ($\Delta\eta$), and activation energy (ΔE_a) of the viscous flow have been estimated.These parameters have been used to explain the formation of complexes in the system. The results were discussed in terms of the existence of intermolecular interactions between the components in the liquid mixtures.

Keywords: 1,2-Diaminopropane (1,2-DAP), methanol, binary mixture, excess parameters.

INTRODUCTION

Dielectric studies of the binary mixtures of both polar and polar-non polar are important for understanding the intermolecular and intra molecular interactions due to the dipole interactions and hydrogen bonding. The dielectric investigations of binary polar liquid mixtures provide valuable information regarding intermolecular interactions and the consequent structural rearrangement of molecules in solution. The heterogeneous and homogeneous interactions in binary mixtures using dielectric measurements have been studied and reported by several investigators. The refractive index measurements in combination with density and other analytical data have wide application in chemical analysis and industry. Measurement of relative permittivity has been shown to be a useful technique in characterizing the molecular structure, solute – solute and solute - solvent interactions in solutions. [1,5]. 1,2-Diaminopropane (1,2-propanediamine) is organic compound with the formula $CH_3CH(NH_2)CH_2NH_2$. It is the simplest chiral diamine commonly used as a bidentate ligand in coordination chemistry. 1,2-Diaminopropane can be converted to *N,N'*-disalicylidene-1,2-propanediamine, a useful salen-type ligand that is abbreviated salpn. Salpn is used as a fuel additive as a metal deactivator in motor oils. Trace metals degrade the fuels by catalyzing oxidation processes that lead to gums and solids. Metal deactivators like salpn form stable complexes with the metals, suppressing their catalytic activity [2]. Methanol is a polar liquid at room temperature. It is used as antifreeze, solvent, fuel, and as a denaturant for ethanol Methanol is essential in our lives every day. It is also used in automotive antifreezes, in rocket fuels, and as a general solvent. Methanol is also a high-octane, clean-burning fuel that is a potentially important substitute for gasoline in automotive vehicles. The methanol derived from wood is used chiefly for rendering ethyl alcohol unfit to drink. Literature survey shows that intermolecular interaction among the components of binary mixtures lead to dipole – dipole or polarization interaction between molecules confirm the interaction.[6]

METHODOLOGY

The chemicals used were of AR grades and purified.The densities were measured using Picnometer.The viscosities were measured with the help of Ostwalds viscometer.The refractive indices were measured by an Abbes refractometer.The mesurement of dielecric constant and dielecric loss at an angular frequency were carried out in the X-band microwave frequency of 9.85 GHz

Dielectric Parameters:

The dielectric constant (ε') and dielectric loss (ε″) have been calculated from the following equations. [12], [10], [11].

$$\varepsilon' = \left(\frac{\lambda_o}{\lambda_c}\right)^2 + \left(\frac{\lambda_o}{\lambda_d}\right)^2 \qquad (1)$$

$$\varepsilon'' = \frac{2}{\pi}\left(\frac{\lambda_o}{\lambda_c}\right)^2 \left(\frac{\lambda_g}{\lambda_d}\right)\frac{d\rho}{dn} \qquad (2)$$

Where, λ_o is free space wavelength, λ_c is cut off wavelength for the wave guide and λ_d is the wavelength in the wave guide filled with the solution. ρ is the inverse of the voltage standing wave ratio (VSWR) and $\frac{d\rho}{dn}$ is the slope of ρ versus n where, n = (1, 2, 3 ……) such that $\frac{n\lambda_d}{2}$ represents the length of the dielectric filled with waveguide.

The free energy of activation E_a of the viscous flow for the pure liquids and their binary mixtures is obtained by using the following equation

$$\eta = \left(\frac{hN}{V}\right)\exp\left[\frac{E_a}{RT}\right] \qquad (3)$$

Where, η is the viscosity and V is molar volume of the liquid.

The values of molar polarization of the mixtures were obtained by using the formula

$$P_{12} = \left(\frac{\varepsilon'-1}{\varepsilon'+2}\right)\left[\frac{M1X1+M2X2}{\rho}\right] \qquad (4)$$

Where, M_1 and M_2 are the molecular weight, $X_1$and X_2 are the mole fraction of the constituents of the mixture. The excess dielectric properties such as excess permittivity(Δὲ), excess loss factor (Δε''),excess

activation energy a (ΔE_a) and excess viscosity ($\Delta\eta$) etc. can be obtained by using the relations of the form.

$$\Delta Y = Y_m - [X_1Y_1 + X_2Y_2] \quad (5)$$

Where, ΔY any excess parameter and Y is refers to the above mentioned quantities, that is, permittivity ($\acute{\varepsilon}$), loss factor (ε'') activation energy(E_a)etc. The subscripts, 1 and 2 used in the above equation are respectively for the mixture, liquid (1) and liquid (2). X_1andX_2 are the mole fractions of the two components in the liquid mixtures.

RESULT AND DISCUSSION

The variation of dielectric constant (ε') with the mole fraction (X) of 1,2-DAP in the mixture is shown in Figure-1 According to Narwade et al [7], if relationship observed between dielectric constant (ε') and mole fraction for the binary mixture is non linear then thereis complex formation and curve show the maximum deviation from linearity at mole fraction X= 0.22 of DAP.

The variation of viscosity (η) with the mole fraction (X) 1,2 DAP in the mixture is shown in Figure-2 The graph indicates that the solute- solute interactions between metanol and 1,2 DAP the value of viscosity (η) increases around 0.3204 mole fraction of. 1,2 DAP. Therefore it is seems reasonable to assume that the formation of associates composed of metanol and 1,2 DAP in this composition range is held together by comparatively stronger intermolecular dipole-dipole interactions. The increase in viscosity (η) may also be attributed to the mutual viscosity of alcohol-amine molecules as per Andrade's theory [4]. The variation of molar polarization (P_{12}) with mole fraction of DAP shown in Figure-3 shows the nonlinear and maximum slope occurs at X = 0.22 mole fraction of DAP which supports to our earlier conclusion that complexion is at X = 0.22 mole fraction of DAP.

The values of excess viscosity ($\Delta\eta$) shown in Figure-4 are positive for the entire range of mole fraction of DAP. It indicates that there is a strong interaction between unlike molecules of the system[3]. The values of excess dielectric loss ($\Delta\varepsilon''$) with the molar concentration (X) of ethylene diamine DAP in the

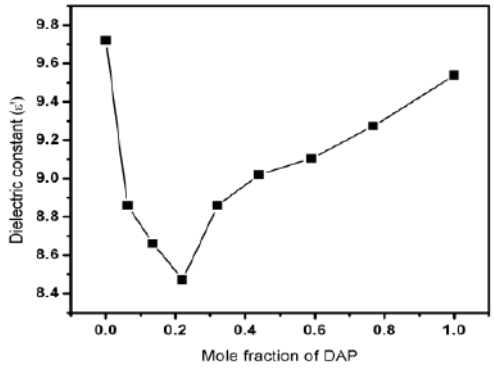

Figure-1

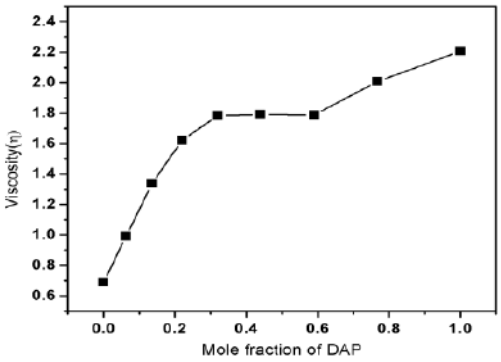

Figure-2

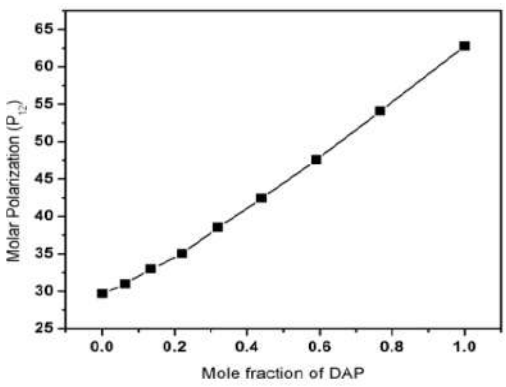

Figure-3

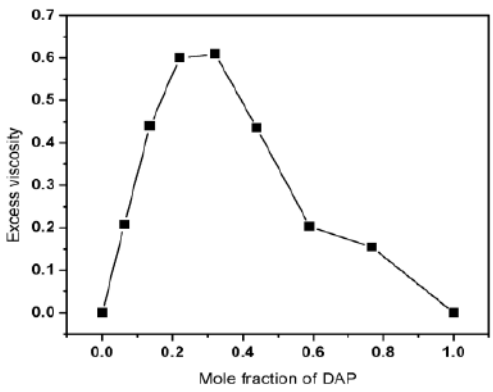

Figure-4

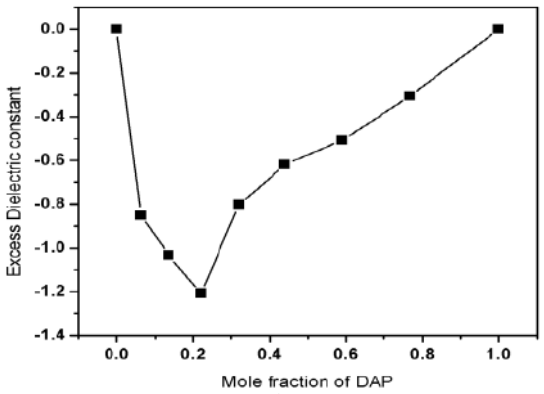

Figure-5

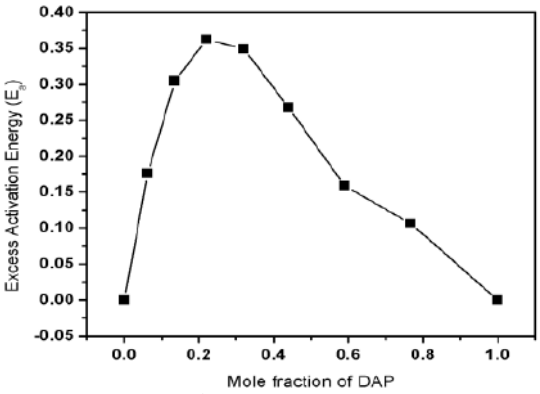

Figure-6

Table-1 The values of viscosity (η), square of refractive index (n_D^2), dielectric constant (ε'), loss factor (ε″), loss tangent (tanδ), activation energy (E_a), and the molar polarization (P_{12}) with increasing mole fraction (*X*) of DAP with Methanol.

Mole fraction (X) of 1,2-DAP	Density gm/cm^3 ρ	Viscosity (η) cp	Refractive index n^2_D	Dielectrc constant ε′	Dielectrc loss ε″	Loss tangent tanδ	Activation energy *Ea* (Kcal/mol)	Molar polarization P12
0.0000	0.8039	0.6883	1.7828	9.7199	2.4035	0.2472	3.0093	29.6537
0.0631	0.8111	0.9916	1.8832	8.8575	2.1474	0.2424	3.2292	30.9541
0.1358	0.8228	1.3370	2.0868	8.6607	2.1675	0.2502	3.4091	32.9713
0.2205	0.8421	1.6227	2.0695	8.4707	2.7351	0.3228	3.5258	35.0072
0.3204	0.8551	1.7838	2.0378	8.8575	2.2431	0.2532	3.5828	38.5268
0.4400	0.8675	1.7913	2.0349	9.0201	2.4224	0.2685	3.5853	42.4132
0.5903	0.8728	1.7870	2.0637	9.1032	2.4403	0.2680	3.5815	47.5633
0.7674	0.8733	2.0074	2.0906	9.2729	2.7300	0.2944	3.6539	54.0652
1.0000	0.8740	2.206	2.0927	9.5371	2.5455	0.2669	3.7107	62.7621

Table-2 The values of excess viscosity (η), excess dielectric constant (ε'), excess loss factor (ε″), excess activation energy (E_a), and the excess molar polarization (P_{12}) with increasing mole fraction (*X*) of DAP with Methanol

Mole fraction of DAP(X)	(Δη)	Δε′	Δε″	Δ*Ea*	ΔP12
0.0000	0.0000	0.0000	0.0000	0.0000	0.0000
0.0631	0.2076	-0.8498	-0.2648	0.1759	-0.7858
0.1358	0.4397	-1.0334	-0.2550	0.3048	-1.1755
0.2205	0.5998	-1.2079	0.3005	0.3621	-1.9439
0.3204	0.6092	-0.8028	-0.2056	0.3491	-1.7318
0.4400	0.4352	-0.6183	-0.0433	0.2677	-1.8052
0.5903	0.2028	-0.5078	-0.0467	0.1585	-1.6313
0.7674	0.1544	-0.3057	0.2177	0.1067	-0.9929
1.0000	0.0000	0.0000	0.0000	0.0000	0.0000

mixture are occurs negative up to mole fraction X= 0.1358 and it becomes positive at X=0.2205. As the molar concentration DAP increases, excess dielectric loss becomes negative up to mole fraction X= 0.5903.

The excess dielectric permittivity is associated with the polarization and excess loss is regarded due to molecular motions which are governed by the complex forces of the molecular interaction. [9] The

variation of excess dielectric constant (Δε′) shown in Figure-5 with the mole fraction (*X*) of 1,2 DAP in the mixture is shown in fig.3. The excess dielectric constant (Δε′) is negative over entire range of mole fraction of DAP indicating the solute-solute interactions such that the total effective dipoles gets reduced [13][14][8].

The values of excess activation energy (ΔE_a) shown in Figure-6 are positive for the entire range of mole fraction of DAP .It indicates that there is a strong interaction between the solute-solvent[7], which supports to our earlier conclusion. The values of viscosity (η), square of refractive index (n_D^2), dielectric constant (ε'), loss factor (ε″), loss tangent (tanδ), activation energy (E_a), and the molar polarization (P_{12}) with increasing mole fraction (*X*) of DAP with Methanol are listed in table (1).

The values of excess viscosity (η), excess dielectric constant (ε'), excess loss factor (ε″), excess activation energy (E_a), and the excess molar polarization (P_{12}) with increasing mole fraction (*X*) of DAP with Methanol are listed in table (2).

CONCLUSION

This study suggests the strong interaction between 1,2- Diaminopropaneand Methanol molecules. Also from the dielectric constant viscosity curve suggest formation of 1:1 complex in the binary mixture.

Acknowledgement
The authors thank to Prof. N.P. Pawar, Head of Department of Physics, Science College, Nanded for the provision of laboratory facilities at Microwave Research Laboratory, Department of Physics, Science College, Nanded. 431605.

Conflicts of interest: The authors stated that no conflicts of interest.

REFERENCES

1. Ghanadzadeh A, Ghanadzadeh H, Alinejad M. Dielectric Study on Polar Binary Mixtures of (Ester-Alcohol) at 298.2] K, Iranian Journal of Chemical Engineering Vol. 9, No. 3 (Summer), 2012,
2. Dabelstein W, Reglitzky A, Schutze A, Reders K. Automotive Fuels", *Ullmann's Encyclopedia of Industrial Chemistry*, Weinheim: Wiley-VCH, 2005
3. Das D, Das B, Hazra DK. Electrical conductance of some symmetrical tetraalkylamonium and alkali salts in N,N-dimethylactamide at 25^0C
4. Hill NE, Vaughan WE, Price AH and Device M. *Dielectric properties and molecular behavior"* Van Nostrand, London.(1968)
5. Meenachi M and Krishnamurthi P. Dielectric characteristics of binary mixtures of esters with hydrocarbons at 303k, *Rasayan J. Chem*.2015;8(1):98-104.
6. Meshram SS, Tumberphale UB, Gawali PG. Molecular Interaction Studies of Ethylene Diamine with 2-Methoxyethonol at 9.85 GHz Microwave Frequency, *Bionano frontier*, 2016; 9 (1),pg.7-10.
7. Narwade BS, Gawali PG, Pande R, Kalmase GM. "*Dielectric studies of binary mixtures of n-propyl alcoholandethylenediamine. J. of chemical sciences.2005;* 117 (6): 673-676.
8. Pawar VP and Mehrotra SC. Dielectric relaxation study of dimethylene chloride with ethanol using time domain reflectometry. *J. of molecular liquids, 2003*; 108/1-3pp: 95-105.
9. Singh PJ and Sharma KS. Dielectric Behavior of Ketone-Amine Binary mixtures at Microwave Frequencies. *Pramana J. Phys.*, 1996; 46 (4): 259-270.
10. Sisodia ML, and Raghuvanshi GS. Basic microwave Techniques and Lab manual .Wiley Eastern Ltd,New Delhi: Chapter 6,1990.
11. Surber WH. Universal Curves for Dielectric-Filled Wave Guides and Microwave Dielectric Measurement Methods for Liquids. 1948, *J Appl. Phys*; 19: 514-20.
12. Tumberphale UB, Kawale RS, Kalmase VG, Kalmase GM. Dielectric behavior of aniline and propane diol binary mixtures at 9.85 GHz microwave frequency. *Bionano Frontier*, 2013; 6(2):211-214.
13. Tumberphale UB. Molecular Interaction studies in binary liquid mixtures from dielectric data at microwave frequency. *Ph.D.Thesis* .SRTMU Nanded, Maharashtra, India, June 2013,p:26.
14. Undre P, Helambe SN, Kathare RV et.al. *Microwave and optoelectronics*, Amaliya publication Delhi, pp:168.

IRJSE *Int. Res. J. of Science & Engineering,* 2018; Special Issue A2: 46-48 SJIF Impact Factor 4.11
ISSN: 2322-0015 UGC Approved Journal No. 63628
RESEARCH ARTICLE **OPEN ACCESS**

Study of Chemically Deposited Nanocrystalline $Cd_{1-X}ni_xs$ Thin Films

Sanap VB[1]*, Suryawanshi AD[2] and Pawar BH

[1]Department of Physics, Yeshwantrao Chavan College, Sillod, Aurangabad- 431112,(M.S.) India.
[2]Department of Physics, B. J. College, Ale, Dist. Pune-412411(M.S.) India.
Email: vbsanap@rediffmail.com

Manuscript Details
Available online on http://www.irjse.in
ISSN: 2322-0015

Editor: Dr. Arvind Chavhan

Cite this article as:
Sanap VB, Suryawanshi AD and Pawar BH. Study of Chemically Deposited Nanocrystalline $Cd_{1-X}ni_xs$ Thin Films, *Int. Res. Journal of Science & Engineering,* January 2018; Special Issue A2: 46-48.

ABSTRACT

Nickel doped cadmium sulfide ($Cd_{1-x}Ni_xS$) thin films were prepared by a simple and inexpensive chemical bath deposition (CBD) technique. $Cd_{1-x}Ni_xS$ thin films have been deposited on commercial glass substrate for various nickel concentration (x= 0, 0.3, 0.5. 0.7, 1) at 70±2^oC. The effect of nickel content (x value) on structural, morphological and optical properties have been studied. The as-deposited $Cd_{1-x}Ni_xS$ thin films were characterized using X-ray diffractometer (X-PERT PRO), SEM and UV-VIS spectrophotometer. The obtained film shows good crystallinity with hexagonal structure. The average grain size estimated is 4.22nm. The values of energy bandgap obtained are between 2.48 eV and 2.82 eV for varying Ni content between x= 0 to 1 respectively. The other optical properties were under consideration.

Keywords: CdNiS, chemical bath deposition, thin films.

INTRODUCTION

Cadmium nickel sulfides $Cd_{1-x}Ni_xS$ have properties in between CdS and NiS. Addition of Ni to the most widely used CdS buffer layer material enhances the electronic and optical properties of optoelectronic devices. The CdNiS thin film band structure has energy gap between CdS and NiS. From the analysis, due to its high bandgap these films were found to possess favorable properties for solar and industrial applications such as antireflection

coating in the solar collectors [1-2], solar control coatings, warming coatings as well as solar absorber layer of a solar cell[3]. Keeping these aspects in view, more attention is being given in producing good quality CdNiS thin films for comprehensive structural, optical studies and their various applications. A number of film deposition methods such as spray pyrolysis, sputtering, electro deposition, vacuum evaporation, chemical vapour deposition and chemical bath deposition (CBD) have been used for preparing II-VI compounds.[4-6]. In this study, we were prepared the $Cd_{1-x}Ni_xS$ thin films for varying Ni content by simple CBD technique. The effects of Ni content on structural, morphological and some optical properties have been investigated.

METHODOLOGY

The $Cd_{1-x}Ni_xS$ thin films were prepared by CBD technique on commercial glass slide for various nickel concentration (x= 0, 0.3, 0.5, 0.7, 1). The starting materials used were $CdCl_2$ (1M) as a Cd^{2+} ion source, $NiCl_2$ (x= 0, 0.3, 0.5, 0.7, 1M) as Ni^{2+} ion source, thiourea (1M) as an S^{2-} ion source. An alkaline solution of ammonia was used to adjust pH of the reaction mixture. All the chemicals used were of Analytical Reagent grade. The process involving a controllable chemical reaction at a low rate, by adjusting the pH value and temperature of the working solution allows maintaining the stoichiometry constant for any ratio of anions and cations. The experimental arrangement consists of a special substrate holder which is attached to a motor having a constant speed of 60 r.p.m. The temperature of chemical bath was adjusted with a hot plate and temperature controller (72±2°C), while magnetic stirrer is applied to promote ion-by-ion heterogeneous growth on the substrate. The $Cd_{1-x}Ni_xS$ samples were prepared on carefully cleaned glass substrates. Cleaning of substrate is important in deposition of thin films, cleaning steps and growth procedure is reported elsewhere [7]. As-deposited thin films were rinsed with distilled water and allowed to dry in air.

The grown films were characterized by (XPERT-PRO) X-ray diffractometer using Cu-Kα radiation with wavelength, 1.5418Å for the study of crystallographic structure. The thickness of thin film was measured by the weight difference method at room temperature. The average grain size in the deposited films was obtained from a Debye-Scherrer formula. Surface morphology was examined by JEOL model JSM-6400 scanning electron microscope (SEM). Optical properties were measured at room temperature by using Perklin-Elmer UV-VIS lambda-35 spectrometer in the wavelength range 300-1100nm.

RESULT AND DISCUSSION

Structural & Morphological properties:

Fig. 1 shows the XRD pattern of $Cd_{1-x}Ni_xS$ films for Ni content x=0.5, A comparison of the peak position (2θ values) of the JCPDS XRD spectra data suggests that the as-deposited films have hexagonal structure. The 2θ value of 24.54° (d = 3.6179 Å) and 28.72° (d = 3.0998 Å) correspond to the diffraction lines produced by (100) and (101) planes respectively.[9] The grain sizes (g) has been estimated from the XRD pattern using Debye-Scherrer's relation, [7-11]

$$g = K\lambda / \beta \cos\theta \quad \ldots (1)$$

Where, K = constant taken to be 0.94, λ = wavelength of X-ray used (1.542Å), β = FWHM of the peak and θ = Bragg's angle. The calculated average grain size of the film is about 4.22 nm.

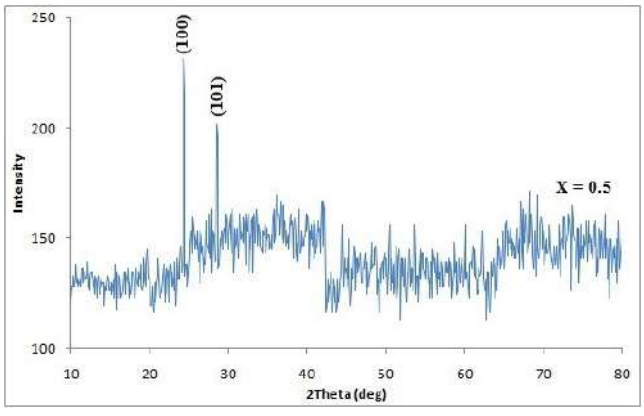

Fig. 1. XRD pattern of $Cd_{1-x}Ni_xS$ films for x= 0.5

The SEM micrograph shows smoother and more uniform films (as shown in fig. 2). It is observed that the grain size obtained from XRD and SEM matches

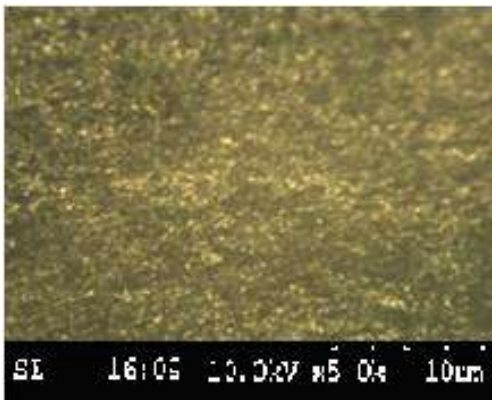

Fig. 2. SEM of $Cd_{1-x}Ni_xS$ films at x=0.5

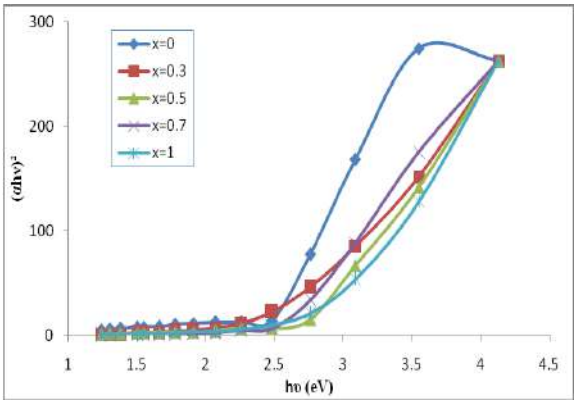

Fig. 3. Plot of $(\alpha h\nu)^2$ vs $h\nu$ for all $Cd_{1-x}Ni_xS$ thin films.

well. The band gap energy was determined from absorbance data by plotting $(\alpha h\nu)^2$ versus $h\nu$ and then extrapolating the straight line portion to the energy axis at $\alpha = 0$ (as shown in fig. 3). The band gap energy Eg obtained for each Ni content is different. For higher Ni content (x=1) the band gap is 2.75 eV and for lower Ni content (x=0) it is 2.48 eV. The band gap of other films is intermediate.

CONCLUSION

$Cd_{1-x}Ni_xS$ nano-crystalline thin films have been grown successfully onto glass substrates using modified CBD technique. The structural, morphological and optical energy bandgap characteristics have been studied. The structural analysis indicates that the grown film has hexagonal crystalline structure with the average grain size of 4.22nm. The band gap energy obtained is in between 2.48eV and 2.72eV. The wider bandgap makes the films suitable for optoelectronic devices, for instance window layers in solar cells as well as suitable for coating in solar collector plates as an anti reflection films.

Acknowledgement

The authors are grateful to Head, School of Physical sciences, NMU, Jalgaon, for providing XRD facilities, IICT, Hyderabad for SEM. We would also like to acknowledge Head and staff of Bio-Tech dept. Y.C.C. Sillod, for UV-VIS-Near IR facilities.

Conflicts of interest: The authors stated that no conflicts of interest.

REFERENCES

1. Chopra KL and Malhotra LK. Thin Film Technology and Applications. Tata McGraw Hill: New Delhi, India, 1985, 3, 237-249.
2. Ezema FI. Optoelectronics and Advanced Material Rapid Communications, 2009, 3(2), 141
3. Dona JM, J. Herrero, Thin Solid Films, 1995, 268, 5-12.
4. Saliha Ilican, Muhsin Zor et al, Optica Applicata, 2006, XXXVI, 1.
5. Okoli DN, Ekpunobi AJ and Okeke CE, Academic Open Internet Journal, 2006, 18.
6. Nair PK, Nair MTS et al., *J. Phys*, 1989, D**22**, 829.
7. Sanap VB, Pawar BH, *Chalcogenide Letters*, 2010; **7** (3): 227-231.
8. Ates A, Yildirim MA, Kundaki M, Yildirim M. *Chinese J. of Phys*., 2010, 45, 2.
9. Jiyon Song, Sheng S Li et al, IEEE, 2005, 449-452.
10. Ezugwu SC, Ezema FI et al., *Optoelectronics and Advanced Materials–Rapid Communications*, 2009, 3(2): 141 –144.
11. Ottih IE. and Ekpunobi AJ. *Pacific Journal of Science and Technology*, 2011, 12(1), 351
12. Ottih IE. *Adv. Appl. Sci. Res*., 2013, 4(5), 5-9.

IRJSE *Int. Res. J. of Science & Engineering,* 2018; Special Issue A2: 49-54
ISSN: 2322-0015
SJIF Impact Factor 4.11
UGC Approved Journal No. 63628
RESEARCH ARTICLE **OPEN ACCESS**

Dielectric and Thermal Behaviour of Yttrium Substituted Magnesium-Cadmium Ferrites ($Mg_{1-X}Cd_xY_yFe_{2-Y}O_4$, x = 0.2, 0.4, 0.6 and y = 0, 0.075) Synthesized Using Sol-gel Autocombustion Method

Bhise RB[1*] and **Rathod SM[2]**

[1]Department of Physics, B. J. College, Ale, Tal: Junnar, Dist: Pune, 412411, India
[2]Nanomaterials and Laser Research Laboratory, Abasaheb Garware College, Pune, 411004, India
Email: bhiseramesh@gmail.com

Manuscript Details
Available online on http://www.irjse.in
ISSN: 2322-0015

Editor: Dr. Arvind Chavhan

Cite this article as:
Bhise RB and Rathod SM. Dielectric and Thermal Behaviour of Yttrium Substituted Magnesium-Cadmium Ferrites ($Mg_{1-X}Cd_xY_yFe_{2-Y}O_4$, x = 0.2, 0.4, 0.6 and y = 0, 0.075) Synthesized Using Sol-gel Autocombustion Method, *Int. Res. Journal of Science & Engineering,* January 2018; Special Issue A2 :49-54.

ABSTRACT

Fine powders of Y^{3+} doped $Mg_{1-X}Cd_xY_yFe_{2-Y}O_4$ (where x = 0.2, 0.4, 0.6 and y = 0, 0.075) spinel nanoferrite were prepared using a sol-gel autocombustion techniques and sintered at 400 ^oC for duration of 2 hrs. The analysis of XRD patterns revealed the formation of single phase cubic spinel structure. The lattice parameter and crystallite size decreases with increase in Y^{3+} concentration and average grain size was found to be between 17.79 to 24.2 nm. The dielectric properties have been studied as a function of frequency (100 Hz to 5 MHz) at room temperature using LCR meter and shown the normal dielectric behaviour. The value of ac conductivity increases with increase in frequency for all the compositions. TG-DTA analysis of the auto combusted ferrites was carried out with a heating rate of 10 °C/min in air. These results may be applicable for promising area such as high frequency electrical devices.

Keywords: Nanoferrite; Sol-gel autocombustion method; Optical properties; Dielectric constant; Thermal properties;

INTRODUCTION

Ferrites are very good dielectric materials which have numerous applications at microwave to radio frequencies and plays a vital role in the technological applications (Chand *et al,* 2011). The study of dielectric properties gives valuable information and can explain the phenomenon of dielectric in the material. Several methods have been used in the preparation of nanoparticles, like the co-precipitation method, sol-gel technique, hydrothermal method, microwave sintering method, spray-spin-heating-coating method and autocombustion method. The ac conductivity increases with increasing in frequency and Cr concentration. The incorporation of Cr^{3+} for Fe^{3+} ions results in a significant impact on the dielectric behavior of the Cr-Zn ferrite system (Lakshmi *et al,* 2016). Out of all these, sol-gel autocombustion method is most convenient and promising technique to synthesize nanoparticles because of its simplicity, inexpensive precursors, short preparation time, better control over crystallite size and other properties of the materials (Srivastava *et al,* 2009). The dielectric properties of ferrites are dependent on several factors, such as the method of preparation, heat treatment, sintering conditions, chemical composition, cation distribution, pH, nature and type of substituent, the ratio of Fe^{3+}/Fe^{2+} ions, frequency and crystallite size (Kharabe *et al,* 2006; Nadeem *et al,* 2014; Huili *et al,* 2014). Y^{3+} substituted in Ni-Cd ferrite powders were synthesized by sol-gel autocombustion technique at low temperatures for different compositions and studied phase crystal structure with magnetic properties (Bhise *et al,* 2015). Ferrites are extremely important magnetic ceramics in the production of electronic components, electrical insulators, torsion sensors and energy storage applications such as anode materials in lithium batteries, fuel cells and solar cells. Yttrium doped cobalt ferrite was prepared using a sol-gel combustion technique and reported the resistivity of the prepared samples increased with increasing yttrium, so that conductivity should decrease with increasing yttrium addition (Shobana *et al,* 2013). The effects of heat treatment on nanocrystalline MnZn ferrite powders could be attributed to an increase in phase formation, crystallinity, microstructure and crystalline sizes (Ping *et al,* 2010). The presence of Zn ions causes appreciable changes in the electrical and dielectric properties of $CoFe_2O_4$ (Rani *et al,* 2013).

The present work investigation on the synthesis of nano-sized Y^{3+} material substituted in Ni-Cd nanocrystalline ferrites by sol-gel autocombustion techniques and characterized by XRD and two probe methods. It reports the consequent changes on their structural, dielectric and thermal properties.

MATERIAL AND METHOD

The Y^{3+} doped in Mg-Cd ferrite powders were synthesized by sol-gel autocombustion method at low temperatures for different compositions of $Mg_{1-x}\ Cd_x\ Y_y\ Fe_{2-y}\ O_4$ (Where x = 0.2, 0.4, 0.6, and y = 0.0 and 0.075). The AR grade nitrate of Merck company (purity of 99%) are used in the experiments such as Yttrium nitrate ($Y(NO_3).6H_2O$), Magnesium nitrate ($Mg(NO_3)\cdot 6H_2O$), Cadmium nitrate ($Cd(NO_3)\cdot 6H_2O$), Ferric nitrate ($Fe(NO_3)_3.9H_2O$). These nitrates and citric acid are using stoichiometric ratio proportion to obtain the final product and the citric acid ($C_6H_8O_7$) is used as a fuel in the ratio 1:3. The proportion of each reagent was defined according to its respective molar amounts. All chemicals are dissolved in distilled water and were stirred till to obtain the homogeneous solution. To maintain pH equal to 7 by adding drop by drop ammonium hydroxide (NH_4OH) during the stirring process. This solution was stirred continuously with 80 ˚C for about 4-5 hours to obtain sol. After 4-5 hours, gel converts into ash and finally ash convert into fine powder of $Mg_{1-x}\ Cd_x\ Y_y\ Fe_{2-y}\ O_4$ ferrite nanoparticles after autocombustion. The powder was sintered at 400 ˚C for 2 hours.

The general chemical reaction of the synthesis sample is as follows;

$$(1-x)\ Mg(NO_3)_2 + x\ Cd(NO_3)_2 + y\ Y(NO_3)_3 + (2-y)\ Fe(NO_3)_3 + 3\ C_6H_8O_7 + NH_4OH \rightarrow Mg_{(1-x)}\ Cd_x\ Y_y\ Fe_{2-y}O_4 + CO_2 + H_2O + 4N_2$$

The structural characterization was done by using XRD analysis. The X-ray diffractometer with Cu-Kα radiation of wavelength 1.5405 A^0 at 40 kV performed

a scanning from 20 to 80 degree at a step size of 0.02 degree per second for each prepared sample and determined crystal structure, lattice parameter and crystallite size. The capacitance (Cp) and loss tangent (tan δ) were measured by two probe method in the frequency range 100 Hz to 5MHz at room temperature using precision LCR meter (HIOKI Model L2000). The variation of dielectric constant, dielectric loss and loss tangent with frequency were studied. The frequency dependent AC conductivity was calculated from dielectric constant and loss tangent data. The DC resistivity measurements of the samples were performed by means of a four probe method. Thermo gravimetric and differential thermal analysis (TG-DTA) of the auto combusted ferrites was carried out with a heating rate of 10 °C/min in air.

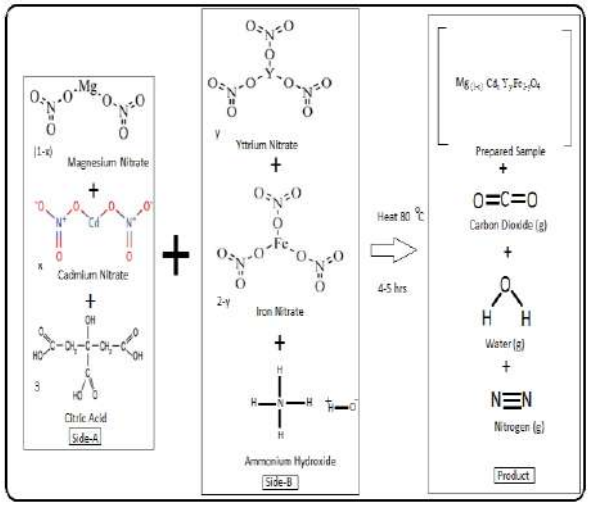

Figure 1: General chemical reaction of $Mg_{(1-x)}$ Cd_x Y_y $Fe_{2-y}O_4$ for different concentration of Yttrium

RESULT AND DISCUSSION

Structural Studies: The resulting powder $Mg_{1-x}Cd_xY_yFe_{2-y}O_4$ (Where x = 0.2, 0.4, 0.6, and y = 0.0 and 0.075) nano crystals were characterized by XRD pattern. The XRD pattern of sintered Y^{3+} doped the nickel-cadmium ferrite as shown in figure-2. Obtained XRD pattern and crystalline phases were identified and it conform the formation of a homogeneous well-defined spinal cubic structure. The broad peaks in the XRD pattern indicate a fine particle nature of the particles. The particle size was determined using Scherer's formula,

$$t = \frac{0.9\,\lambda}{\beta\,Cos\,\theta} \qquad \ldots\ldots. (1)$$

Where, λ = Wavelength of X-ray, θ = Peak position and β = FWHM of the peak θ and it is corrected for instrumental broadening. The average particle sizes of nanoparticles are given in Table-1. The particle size decreases as the concentration of Y^{3+} increases. Lattice parameter obtained for prepared sample is ranging between 8.3399 to 8.3665 A^0. The deviation in lattice parameter can be attributed to the cations rearrangement in the nano sized prepared ferrites. The value of lattice constant for Mg-Cd doped yttrium ferrite shows the expansion of unit cell with rare earth doping when compared with pure yttrium ferrite. This is expected due to substitution of large ionic radius of Y^{3+} ions (0.9 A^0) with small ionic radius Fe^{3+} ions (0.645 A^0). This result in Y^{3+} substituted ferrites to have higher thermal stability relative to Mg-Cd ferrite. Yttrium doped Mg-Cd nanoferrites were synthesized with average grain size ranging between 8.3562 to 8.3667 nm which will give great effect on its dielectric and thermal properties.

Table-1: The particle size of Mg_{1-x} Cd_x Y_y Fe_{2-y} O_4 by XRD/

Composition	Average grain size (t) nm	Lattice constant (a) A^o
$Mg_{0.8}Cd_{0.2}Fe_2O_4$	24.2	8.3601
$Mg_{0.8}Cd_{0.2}Y_{0.075}Fe_{1.925}O_4$	23.24	8.3562
$Mg_{0.6}Cd_{0.4}Y_{0.075}Fe_{1.925}O_4$	18.53	8.3667
$Mg_{0.4}Cd_{0.6}Y_{0.075}Fe_{1.925}O_4$	17.79	8.3658

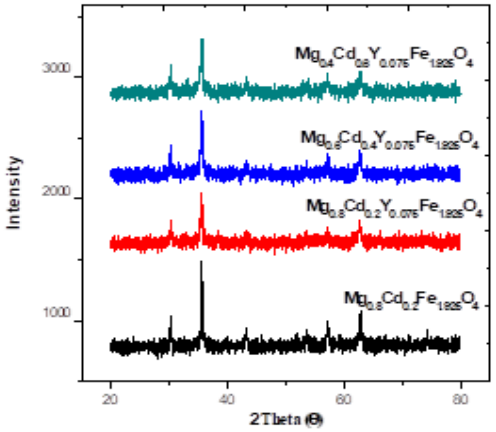

Figure 2: Structural properties of Mg_{1-x} Cd_x Y_y Fe_{2-y} O_4 by XRD

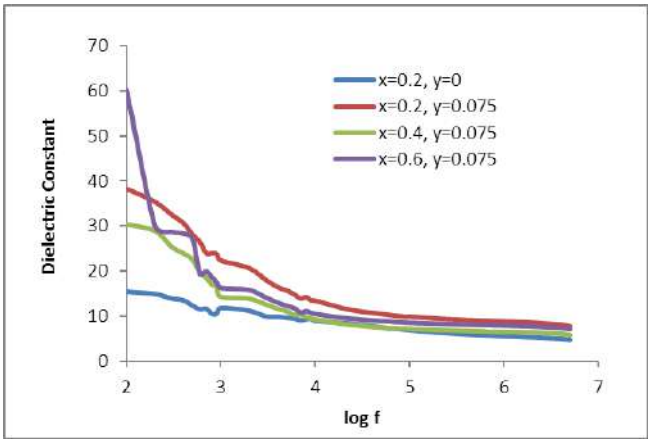

Figure 3: Variations of dielectric constant with frequency of $Mg_{1-x}Cd_xY_yFe_{2-y}O_4$ nanoferrites

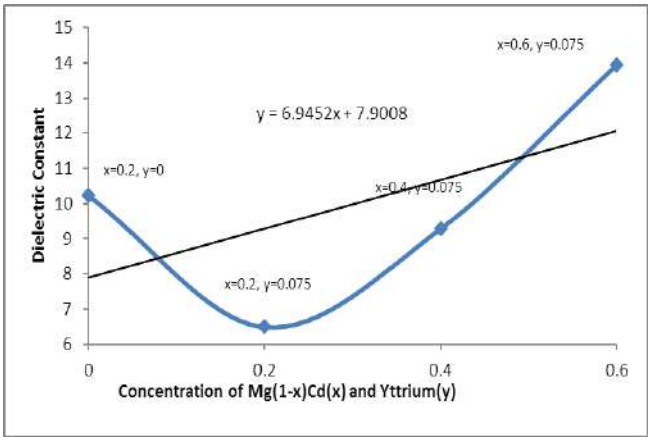

Figure 4: Variation of Dielectric Constantwith Y^{3+} content of $Mg_{1-x}Cd_xY_yFe_{2-y}O_4$

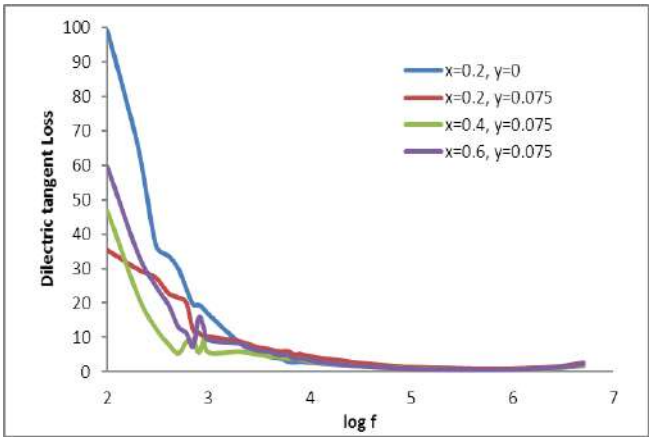

Figure 5: Variations of dielectric loss with frequency of $Mg_{1-x}Cd_xY_yFe_{2-y}O_4$ nanoferrites

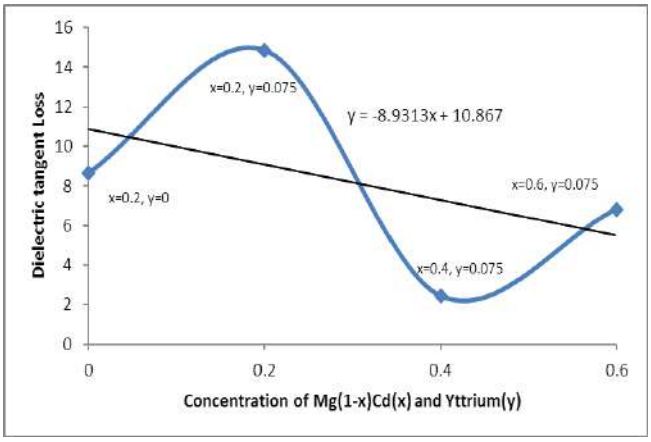

Figure 6: Variation of Dielectric tangent loss with Y^{3+} content of $Mg_{1-x}Cd_xY_yFe_{2-y}O_4$

Dielectric Studies: Dielectric measurements were carried out at room temperature over a wide frequency range from 100 Hz up to 5 MHz. The value of dielectric constant is calculated by using the following relation:

$$\dot{\epsilon} = \frac{Cp\ d}{\varepsilon 0\ A} \qquad \text{..... (2)}$$

Where, ε_0 is the permittivity of free space, d is the thickness of the pellets, A is the area of cross-section of the pellet and Cp is the measured value of the capacitance of the pellet.

The variation of dielectric constant and dielectric loss tangent with frequency for the as-prepared ferrites doped with different amounts of yttrium ions are shown in figure-3 and figure-4 respectively.

Figure-3 shows the variation of dielectric constant as a function of frequency at room temperature from 1 kHz to 5MHz. It is observed that for each sample the dielectric constant decreases with an increase of frequency and a normal dielectric behaviour of spinel ferrites. This can be explained on the basis of mechanism of polarization process which is similar to that of conduction process. The whole polarization in ferrites is mainly contributed by space charge polarization, the conductivity in materials and hopping exchange of the charges between two localized states. The value of dielectric loss tangent is calculated by using the following relation:

$$\epsilon'' = \dot{\epsilon} \tan \delta \qquad \text{..... (3)}$$

From figure-3 it is observed that the small variation of dielectric constant occurs up to 1000 Hz frequency and from the frequency 5000 Hz, it becomes stable.

Figure-5 shows the frequency dependence of dielectric loss in $Mg_{1-x}\,Cd_x\,Y_y\,Fe_{2-y}\,O_4$ nanoferrites. The value of dielectric loss tangent is very low in the present work indicating that the samples are structurally prefect. From figure-5 we conclude that the dielectric loss tangent is very low and varies up to 1000 Hz and above that it becomes stable. The AC conductivity of the sample can be evaluated from the dielectric permittivity (ϵ_0) and the loss factor (tan δ) using the equation

$$\sigma_{AC} = 2\pi\epsilon_0 f \tan\delta \qquad \ldots\ldots\ldots\ldots (4)$$

Where, *f* is the frequency.

The variation of dielectric constant, dielectric loss tangent and AC conductivity with frequency for the as-prepared ferrites doped with different amounts of yttrium ions are noted in following table.

Table 2: The Value of dielectric constant, dielectric loss tangent and AC conductivity with frequency

Concentration	Q	ἐ x 10^{-5}	ϵ″	σ_{AC}
x=0.2, y=0	10.2277	3.68	8.6501	3.5227
x=0.2, y=0.075	6.4976	5.04	14.8305	4.6909
x=0.4, y=0.075	9.2828	3.63	2.4459	5.3534
x=0.6, y=0.075	13.9294	4.29	6.8241	5.4791

The AC conductivity increases with increasing frequency at low temperatures. Figure-7 shows AC conductivity increases linearly with the frequency.

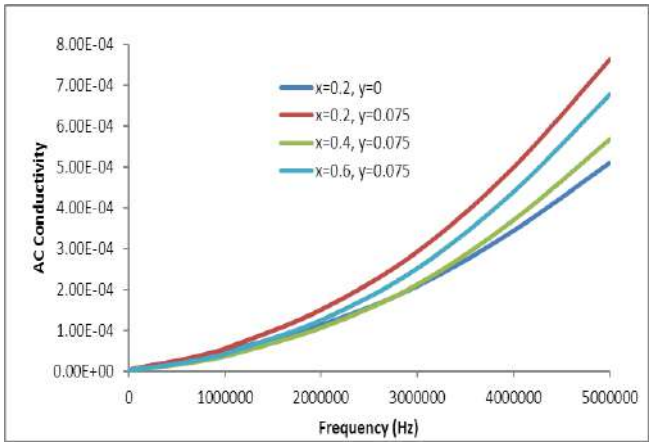

Figure 7: Variations of AC Conductivity with frequency of $Mg_{1-x}\,Cd_x\,Y_y\,Fe_{2-y}\,O_4$ nanoferrites

Thermal Studies:

In order to investigate the mechanism of the Y^{3+} doped Mg-Cd ferrites autocombustion, Thermo gravimetric analysis (TGA) and differential thermal analysis (DTA) was carried out with a heating rate of 10 °C/min in air and the results are shown in Figure-8 and Figure-9 respectively.

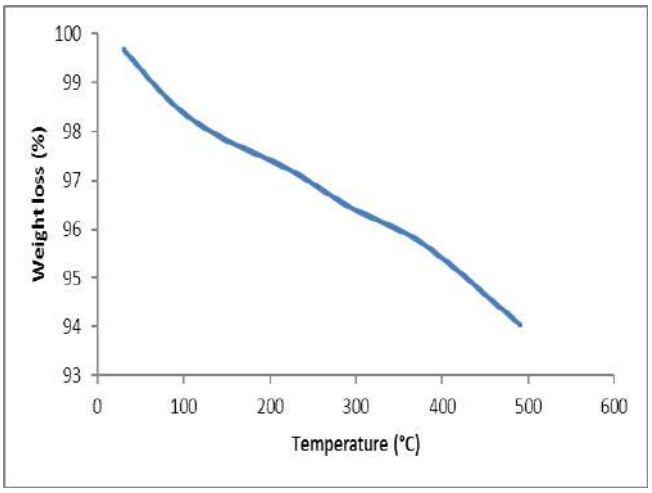

Figure 8: TGA curve

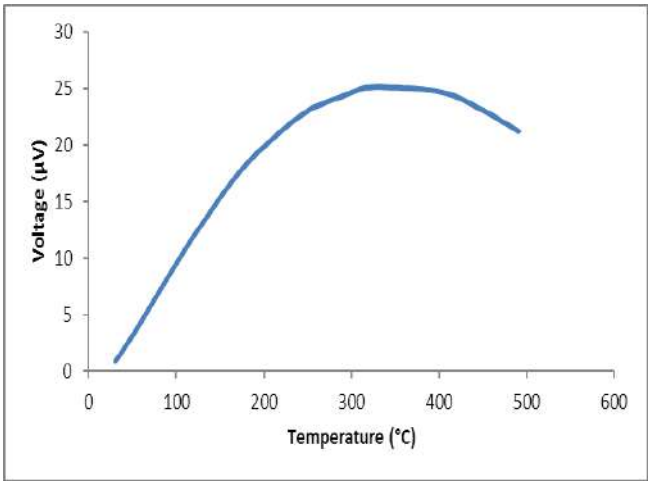

Figure 9: DTA curve for $Mg_{0.8}\,Cd_{0.2}\,Y_{0.075}\,Fe_{1.925}\,O_4$ nanoferrites

From TGA analysis it is observed that as the temperature increase the percentage weight loss decreases. From DTA analysis we observe that with increase in the temperature the voltage increases up to 316 °C and it decreases with the increase in temperature.

CONCLUSION

Nanostructured Mg_{1-x} Cd_x Y_y Fe_{2-y} O_4 (Where x = 0.2, 0.4, 0.6, and y = 0.0 and 0.075) powder were successfully prepared by sol-gel autocombustion method and the conclusions can be summarized as followings;

1) The XRD pattern shows that nanoparticles decreases with the increase in Y^{3+} content.
2) A dielectric study indicates that for each sample the dielectric constant decreases with an increase of frequency and a normal dielectric behaviour of spinel ferrites. The value of dielectric loss tangent is very low in the present work indicating that the samples are structurally prefect. The AC conductivity increases with increasing frequency at low temperatures.
3) From TGA analysis it is observed that as the temperature increase the percentage weight loss decreases and from DTA analysis we observe that with increase in the temperature the voltage increases up to 316^0C and it decreases with the increase in temperature.

Acknowledgement

The authors are thankful to SAIF, IIT, Powai (Mumbai) and SRTM University, Science College, Nanded, India for providing the sample characterization facilities.

Conflicts of interest: The authors stated that no conflicts of interest.

REFERENCES

1. Chand J, Kumar Gagan, Kumar P, Sharma SK, Knobel M and Singh M. Effect of Gd^{3+} doping on magnetic, electric and dielectric properties of $MgGd_xFe_{2-x}O_4$ ferrites processed by solid state reaction technique. *J. Alloys and Compds.*, 2011; **509**: 9638-9644.
2. Lakshmi M, Vijaya Kumar K and Thyagarajan K. Study of the Dielectric Behaviour of Cr-Doped Zinc Nano Ferrites Synthesized by Sol-Gel Method. *Advances in Materials Physics and Chemistry*, 2016; **6**: 141-148.
3. Srivastava M, Chaubey S and Ojha AK. Investigation on Size Dependent Structural and Magnetic Behavior of Nickel Ferrite Nanoparticles Prepared by Sol-Gel and Hydrothermal Methods. *Materials Chemistry and Physics*, 2009; **118**: 174-180.
4. Kharabe RG, Devan RS, Kanamadi CM and Chougule BK. Dielectric Properties of Mixed Li-Ni-Cd Ferrites. *Smart Materials and Structures*, 2006; **15**: 36-39.
5. Nadeem K, Zeb F, Azeem Abid M, Mumtaz M and Anis ur Rehman M. Effect of Amorphous Silica Matrix on Structural, Magnetic, and Dielectric Properties of Cobalt Ferrite/Silica Nanocomposites. *Journal of Non-Crystalline Solids*, 2014; **400**: 45-50.
6. Huili H, Grindi B, Viau G and Tahar LB. Effect of Cobalt Substitution on the Structure, Electrical, and Magnetic Properties of Nanorcrystalline $Ni_{0.5}Zn_{0.5}Fe_2O_4$ Prepared by the Polyol Process. *Ceramics International*, 2014; **40**: 16235-16244.
7. Bhise RB, Bhong V and Rathod SM. Influence of Structure and Magnetic properties of Y3+ doped Ni-Cd nanoferrite by Sol-gel Autocombustion Method. *BIONANO FRONTIER*, **8(3)**: 107-109.
8. Shobana M.K., Nam Wonjong, and Choe Heeman. (2013). Yttrium-Doped Cobalt Nanoferrites Prepared by Sol-gel Combustion Method and Its Characterization. *Journal of Nanoscience and Nanotechnology*, 2015; 13: 3535-3538.

IRJSE International Research Journal of Science & Engineering
Int. Res. J. of Science & Engineering, 2018; Special Issue A2: 55-57
ISSN: 2322-0015
SJIF Impact Factor 4.11
UGC Approved Journal No. 63628
RESEARCH ARTICLE **OPEN ACCESS**

Synthesis and Characterisation of Genuine Bhasma by EDAX Analysis

Gulalkari Rupali A

Department of Chemistry, BJS College Wagholi, Pune, India
Email: rupalilad.2009@rediffmail.com

Manuscript Details
Available online on http://www.irjse.in
ISSN: 2322-0015

Editor: Dr. Arvind Chavhan

Cite this article as:
Gulalkari Rupali A. Synthesis and Characterisation of Genuine Bhasma by EDAX Analysis, *Int. Res. Journal of Science & Engineering*, January 2018; Special Issue A2 : 55-57.

ABSTRACT

The supreme role of the plant kingdom as a whole and of medicinal plants in particular in the human welfare was properly realized in India since the time of Vedas, and ayurvedicians have made maximum utilization of plant kingdom in the field of pharmacy. In the subsequent periods also most of the research and interest has been centered on the detailed studies of medicinal plants. For the safer use of bhasma characterization of genuine mettali bhasmas and confirmation of their identity is important to lose all metallic characteristics. Complete conversion of metallic powder to the Bhasma is essential for this purpose. Using plant extract we synthesized Bhasmas and then characterization of it is done by E-DAX analysis.

Keywords- Lohabhasma, Marana, Gajputa etc.

INTRODUCTION

Iron has been one of the most important metal which has played significant role in ancient Indian civilization and Indian system of medicine. The chemistry and metallurgy of iron was highly developed in India from ancient times. The *ayurvedic* principles and method of treatment involving ayurvedic medicine are quite different as compared to those of other pathies, especially modern allopathy.

This must be taken into account while undertaking any research programme related to *ayurvedic* drug. Thus, most of the modern allopathic drugs are designed for specific purpose and they work effectively for that purpose only. On the other hand, an *ayurvedic* drug specially one belonging to drug of mineral origin, is designed according to class and condition of patients and it may not be useful for other patients. Because the origin of the disease or complaint may be quite different in two cases. Second differential aspect which is more important for research investigation of a *ayurvedic* drugs is that it is possible to induce desired medicinal properties in metallic *bhasmas* by modifying the method of synthesis. In the case of *bhasma* therapy, there is one more parameter- *anupana* (medium of drug administration) through which the same drug can be used for different aliments. Therefore, these *bhasmas* can work as versatile drugs if used according to *ayurvedic* pharmacology. Now, we are concerned here with the first aspect in which the medicinal properties can be changed by modifying synthetic procedure. This modification is developed by Nagarjun, a reputed authority in *rasashastra* according to which specific medicinal property can be induced on an *ayurvedic bhasma* with the help of an appropriate medicinal plant. The use of medicinal plant for this purpose is done as follows.

MATERIAL AND METHOD

Using *Trifala* Extract:

In this method firstly the iron powder (500g) was subjected to general method of purification in which the powder was heated to red heat and then dipped successively in *til* oil, butter milk, cow urine and aqueous extract of dolichos (*kulith*) and rice (*kanji*). Then special purification was done in *trifala* extract (aqueous extract of the powder of *Terminalia chebula* (*hirada*) + *Terminalia bellirica* (*behada*) + *Phyllanthus emblica* (*awla*) all taken in equal parts). The destruction of metallic character (*marana*) was done by triturating the purified iron powder in *trifala* extract for about six hours. The process of *bhasmikarana* was also done using concentrated extract of *trifala* for which above processed powder was triturated in a mortar with *trifala* extract till a homogeneous paste is formed. This was then subjected to *gaja-puta* in a closed crucible system. This entire process of *bhasmikarana* was repeated seven times to get the desired *lohabhasma.*

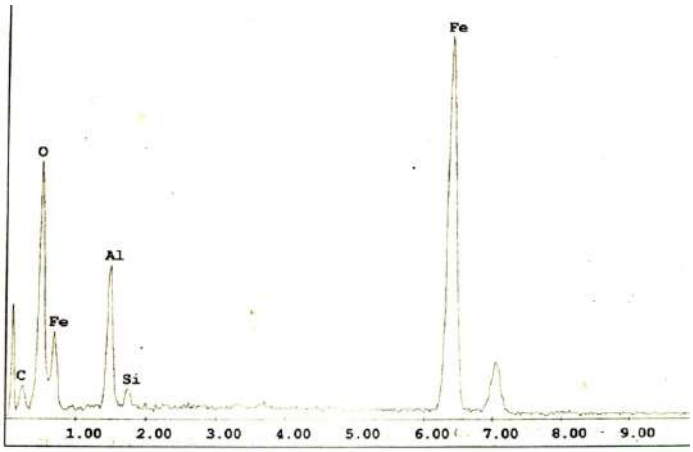

Figure: EDAX of Loha-01 Bhasma

Chemical constituents of synthetic loha-01 bhasma samples

Element	CK	OK	AIL	SiK	FeK
Wt %	12.95	24.66	9.86	1.01	51.52

Sample	**Major constituent**			**Minor / Trace constituents**								
	Iron	**O**	**C**	**Si**	**S**	**Na**	**K**	**Ca**	**Al**	**P**	**Cr**	**Mg**
Loha-01	51.52	24.66	12.95	1.01	0.65	-	1.02	-	9.86	-	-	-

RESULTS

The significant percentage of carbon identified by E-DAX and the nature of the IR spectra of loha bhasma (as well as for metallic bhasmas obtained from other metals) give some indications in favour of the presence of organic components associated with loha bhasma particles.

CONCLUSION

It is hoped that the results and conclusions from this attempt, will provide some appreciable base and guidelines for more extensive and intensive work in future. The significant results and conclusions of this work are as follows.

a. The major constituent of all five samples is Fe_2O_3 irrespective of their preparation, its percentage being in the range 58-76 Carbon is found another major constituent of fundamental importance. Its percentage varies from 6.9 to 36.9. The exact form in which this carbon is present is not yet known.

b. Other minor constituent include SiO_2, Na, K, Ca, P and S whose percentage show slight variation depending on the methods of preparation.

c. As referred above, presence of carbon in substantial amount is an encouraging observation. It is consistent with the previously observed and confirmed work on synthesis and characterization of tamra *bhasma* and swarna *bhasma*.

Where also percentage of carbon was found to be high to the extent of 10-30 percent. This percentage of carbon depends on correctly followed technique and skill of the process of *bhasmikarana*. Introduction of carbon in these *bhasmas* is expected to take place during purification and trituration with plant juices where the metal in its finely divided juices interacts strongly with vegetable or organic matter. Identification of such carbon supports the *ayurvedic* concept of imparting organic component to *bhasma* particles so that they are easily assimlable to human system. This also may be major factor behind differential medicinal properties of metallic *bhasma* and their pure oxides.

Conflicts of interest: The authors stated that no conflicts of interest.

REFERENCES

1. Kulkarni SB, Dudhgaonkar, Rasarattna Sammuchhaya (Marathi), Shivaji University (Kolhapur) pub (1970)
2. Kulkarni SB, Dudhgaonkar, Rasarattna Sammuchhaya (Marathi), Shivaji University (Kolhapur) pub. (1970)
3. Pandit Kashinath Shastri, Rasatarangini (Hindi), Motilal Banarasidas Delhi (2004)
4. Borkar DB, Rasarathnakar (Marathi translation), Shri. Gajanan Book Depo Pune(1986)
5. Vaidya PV, Dhamankar, Ayurvedic Aushadhikaran, Dhoot papeshwar Publication
6. Vaidya Chhaganlal Samadarshi (Chief Editor), Dhanwantari. Sp. issue on Ayurvedic Drugs of animal, And mineral origin, Jwala Ayurvedic, havan. Aligarh. (1973)
7. Takele ST, Kanase DG, Rupali Lad, Kankaria RD, Mrudula Wadekar and Ashmita Prabhune, Comparative study of loha bhasma and iron oxides, Indian Science congress, Chidambaram.Tamil Nadu (2007)
8. Mrudula Wadekar,Shivaji Takale,Rupali Lad,Pratibha Jadhav and B.A. Kulkarni, Validity of the traditional test for lohabhasma involving use of Phyllanthus emblica and its practical utility, 2nd International conference on drug discovery and process, Belgaon (India) P. 133 (2006).

IRJSE *Int. Res. J. of Science & Engineering,* 2018; Special Issue A2: 58-60 SJIF Impact Factor 4.11
ISSN: 2322-0015 UGC Approved Journal No. 63628
RESEARCH ARTICLE **OPEN ACCESS**

Dielectric Behavior, Resistivity and Thermoelectric Power of Multiferroic Composite

Kadam SL *M. Sc. M. Phil. Ph. D.*

Post Graduate Department of Physics, New Arts, Commerce and Science College, Parner, Tq. Parner Dist. Ahmednagar, MS, India

Manuscript Details
Available online on http://www.irjse.in
ISSN: 2322-0015

Editor: Dr. Arvind Chavhan

Cite this article as:
Kadam SL. Dielectric Behavior, Resistivity and Thermoelectric Power of Multiferroic Composite, *Int. Res. Journal of Science & Engineering,* January 2018 | Special Issue A2 |: 58-60.

ABSTRACT

Composite materials were prepared by ceramic method. Initially Ferrite and ferroelectric phases were prepared separately by solid state reaction. By thoroughly mixing required mole percent of sintered phases composites were prepared. Composites were pressed into pellets. The XRD patterns of all the samples were taken by using CuKœ radiation (λ=1.5418 A^0) on Philips PW 1710 diffractometer. XRD patterns shows well defined peaks. The occurrence of the peaks with specific indices characteristic of spinel and perovskite structure confirms the formation of cubic spinel structure in ferrite and tetragonal perovskite structure in ferroelectrics. The well defined XRD peaks show crystalline nature of the samples.

Keywords: ME output, Dielectric properties, XRD, Composite.

INTRODUCTION

The existence of the magnetoelectric effect in some materials was given by Pierre Curie [1]. The magnetoelectric effect is a coupled, two –field effect in which the application of an electric field induces magnetization and a magnetic field induces electric polarization [2]. Such magnetoelectric composites are prepared by sintering together powders of piezoelectric and piezomagnetic phases. These particulate and in situ grown composites have been developed to overcome the problem of single phase magnetoelectric materials, which

have complicated crystal structures and show low outputs at low temperatures [3, 4]. In 1978, Boomgard *et. al* [3] outlined the requirements for a good ME effect in composites, which can be summarized as: **i-** the two phases should be in equilibrium; **ii-** no chemical reaction should occur between the constituent phases; **iii**- the resistivity of magneto-strictive phase should be as high as possible to avoid the leakage of current during electric poling; **iv**- a proper poling strategy should be adopted to get a large ME effect in a composite. These ME materials are used as transducers, actuators, magnetic sensors for dc and ac magnetic field measurements [5,6]. In the present work cobalt ferrite is used as it is highly magnetostrictive and resistive [7-9]. Also BaTiO3 ferroelectric has high permittivity.

PREPARATION

Piezomagnetic phase (ferrite) was prepared by solid state reaction by using CoO & Fe_2O_3 in molar proportions as starting materials. Piezoelectric phase (ferroelectric) was prepared by using BaO, PbO & TiO_2 oxides in molar proportions. The constituent phases were presintered at 900^0C. for 12 hrs. separately. After presintering, the constituent phases were ground to fine powder. ME composites were prepared by thoroughly mixing 85, 70 & 55 mole % of ferroelectric material with 15, 30 & 45 mole % of ferrite material respectively. The mixture was presintered again at 1100^0C for 24 hrs .in programmable furnace. The composites were again ground for 3hrs. to mix them thoroughly. The powder was then pressed into pellets and final sintering was carried at 1100^0C for 24hrs.

CHARACTERIZATION

The samples were characterized by X-ray Diffractometer (Philips Model PW 1710). The XRD patterns show the presence of constituent phases. The patterns do not indicate any chemical reaction between the components during sintering. The dc resistivity measurements were performed by means of a two probe method. A low value of constant voltage was applied across the sample and current through the sample was measured as a function of temperature in the range from room temperature to 600^0C. Flat surfaces of the pellets were silver pasted for good ohmic contacts. The seebeck coefficient was measured at different temperature by maintaining the thermal gradient of 25^0C across the sample surface. The frequency dependent measurements of parameters such as capacitance and dissipation factor (tan δ) were carried out using LCR meter bridge (Model HP 4248 A) in the frequency range 20 Hz to 1MHz at room temperature. To realize the magnetoelectric voltage coefficient, the electric poling was carried out by heating the samples at about 30-40^0C above the ferroelectric Curie temperature in an external electric field of 2-2.5 kV/cm. The ME output $(dE/dH)_H$ was determined by measuring the electric field generated across the sample using the Keithley electrometer (Model 2000) when dc magnetic field up to 5.0 K Oe was applied to it. The variation of ME output voltage as a function of dc magnetic field was used to measure the magnetoelectric coefficient.

RESULTS AND DISCUSSION

The XRD pattern of one of the representive composite is shown in **Fig.1**. It reveals that the composites consist of ferrite and ferroelectric as predominant phases with no unidentified peaks observed. The intensity of ferrite peaks increases with its content in the composites. The indexing of patterns confirms that ferrite has cubic spinel structure and ferroelectric has tetragonal perovskite structure [10, 11]. The lattice parameters of both the phases in these composites do not vary much with the composition.

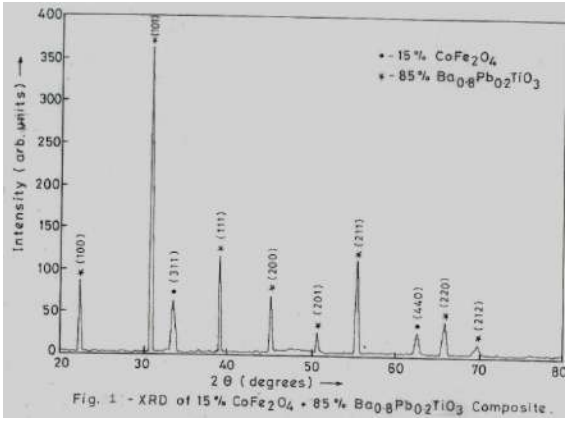

Fig. 1: The XRD pattern of one of the representive composite

The variation of dielectric constant with frequency is shown in **Fig.2**. The dielectric constant decreases with increase in frequency showing dispersion in a certain lower frequency range. It attains a constant value independent of frequency thereafter. All the samples reveal dispersion due to Maxwell-Wagner type interfacial polarization in agreement with Koop's Phenomenological theory [12].

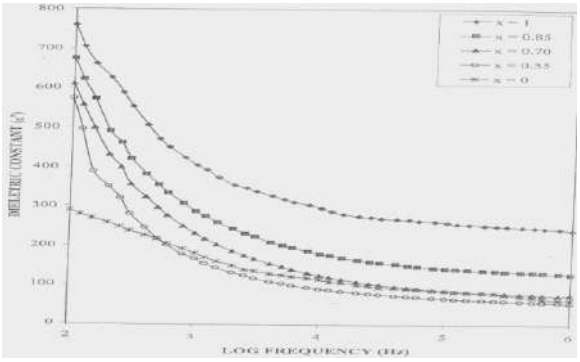

Fig.2: variation of dielectric constant with frequency for $xBa_{0.8}Pb_{0.2}TiO_3 + (1-x)\ CoFe_2O_4$ composites

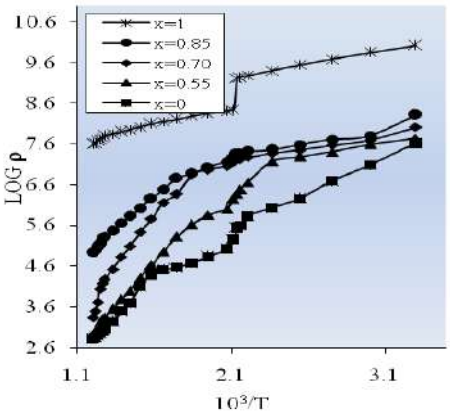

Fig.3-variation of log resistivity (ρ) with temperature for $xBa_{0.8}Pb_{0.2}TiO_3$+ $(1-x)CoFe_2O_4$ composites

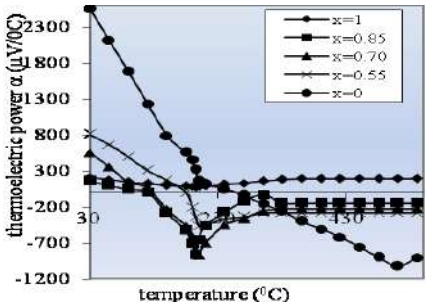

Fig.4- variation of thermoelectric power with temperature for$xBa_{0.8}Pb_{0.2}TiO_3$+ $(1-x)CoFe_2O_4$ composites

The variation of resistivity with temperature is shown in **Fig.3**. There are two regions in the resistivity plots. The first region at low temperature is attributed to the ordered state of the ferroelectric phase in the composite while the second region is for the paraelectric state of the composite. The first region indicating insulating behavior while second region indicating the conduction due to hopping mechanism. The change in activation energy is observed when transition from ferroelectric to paraelectric state takes place [13].

The variation of Seebeck coefficient (α) with temperature is shown in **Fig. 4.** At lower temperature all the samples show positive values of Seebeck coefficient, which indicates that the charge carriers are of p-type. A p-n transition is observed in all the composites and pure ferrite. It is well known that the evidence for polaron hopping conduction of p-n transition and the temperature independence of Seebeck coefficient [14].

Conflicts of interest: The authors stated that no conflicts of interest.

REFERENCES

1. Suchetelene JV. *Philips Res. Rep*., (1972) , 27-28.
2. Zing M, Wan JG, Yu H, Lin JM, Jiang XP and Nan CW. *J. Appl. Phys*., (2004) ,95, 8069-73.
3. Ryu J, Priya S, Carazo AV and Uchino K, *J. A. M. Zool Ceram. Soc*., 1995, 84, 2905-8
4. Zhai J, Cai N, Shi Z, Lin Y and Nan CW *J. Phys, D. Appl. Phys*. (2004) ,37, 823-7.
5. Wood E and Austin AE, *Int. J. Magnet*, 1974: 5, 303.
6. Bracke CMP, Van Vliet RG, *J. Electro*., 1981: 51,255.
7. Kanamadi CM, Pujari LB, Chougule BK, *J. Magn. and Magn. Mater*., 2005, 295, 139-144.
8. Zeng M, Wan JG, Wang Y, Yu H, Liu JM, Jiang XP, Nan CW, *J. Appl. Phys*., 2004, 95(12), 8069-8073.
9. Shrinivas G, Rasmussen ET. *Appl. Phys. A*, 2004, 721.
10. Boomgaard JV, Born RAJ. *J. Mater. Sci*.,(1978),13,1538.
11. Kadam SL, Patankar KK, Mathe VL, Kothale MB, Kale RB, Chougule BK. *Mater. Chem. Phys*.,(2000),78, 178.
12. Koop CG. *Phys. Rev*.,(1951), 83, 121.
13. Keer HV 2000,4,13,178.
14. Deshmukh LS, Krishnakumar K, Balakshan S, RamKrishan A and Sasathaiah G. *Bull. Mat. Sci*.,(1998), 21(5), 219.

IRJSE *Int. Res. J. of Science & Engineering,* 2018; Special Issue A2: 61-63 SJIF Impact Factor 4.11
ISSN: 2322-0015 UGC Approved Journal No. 63628
RESEARCH ARTICLE **OPEN ACCESS**

Transport Properties of PbS Thin Films

Sonavane DK*[1], Jare SK[1], Suryawanshi RV[2], Kathare RV[3] and Bulakhe RN[4]

[1]P.G. Department of Electronic Science, New Arts, Commerce and Science College, Ahmednagar – 414001, India.
[2]Department of Electronic Science, Azad mahavidyalaya, Ausa, Latur-413520, India.
[3]Karmaveer Mamasaheb Jagdale Mahavidyalaya, Washi, Osmanabad, 413503, India.
[4]School of Chemical Engineering, Yeungnam University, Gyeongsan, Gyeongbuk, 712-749, Republic of Korea

Manuscript Details
Available online on http://www.irjse.in
ISSN: 2322-0015

Editor: Dr. Arvind Chavhan

Cite this article as:
Sonavane DK, Jare SK, Suryawanshi RV, Kathare RV and Bulakhe RN. Transport Properties of PbS Thin Films, *Int. Res. Journal of Science & Engineering,* January 2018; Special Issue A2: 61-63.

ABSTRACT

Thin films of PbS were obtained by chemical bath deposition method onto the glass substrates. To obtain the PbS thin films the reactive substances lead acetate, thiourea, sodium hydroxide, ammonia, triethanolamine and distilled water were used. The effect of pH of reactive mixtures on the film growth and quality has been studied. The temperature dependence of dark electrical conductivity was studied using two-probe method. The transport characteristic such as thermo-electric power shows that deposited films were p-type in nature.

Keywords: PbS thin film, Chemical bath deposition, Electrical conductivity, TEP.

INTRODUCTION

Lead sulphide is a unique direct bad gap material which has developed a lot research interest, especially in the fabrication of infrared detection and solar cell applications [1], Semiconductor materials are always in focus due to their outstanding electronic and optical properties. Due to the non-linear optical properties PbS nanoparticles has found an extensive application in optical devices such as optical switch [2]. These properties have been correlated with the growth conditions and the nature of the substrate. In addition, PbS has been utilized as photo resistance, diode lasers, humidity and temperature sensors, decorative and solar control coating [3]. The preparation of the thin film of.

PbS explored by a number of methods such as electro deposition [4], spray paralysis [5], photo accelerated chemical deposition [6], microwave heating [7] and chemical bath deposition [8]. CBD is relatively inexpensive, simple and convenient method for large area deposition and a variety of substrates can be used to grow thin films. It does not require complicated instrumentation [9]. We have selected chemical bath deposition method owing to its many advantages.

MATERIAL AND METHOD

The deposition was carried out using commercial glass slides of dimensions 25 mm X 30mm X 1.2mm. All the chemicals used for the deposition were analytical grade reagents. It includes lead acetate, thiourea, sodium hydroxide, ammonia, triethanol-amine (TEA). The deposition was done in a reactive solution prepared in a 250 ml beaker containing equimolar solutions of lead acetate and thiourea. TEA was used as a complexing agent and pH of the reaction mixture was adjusted to about 10.5 with the help of sodium hydroxide and ammonia solution. The bath temperature was fixed at an appropriate temperature, pre-treated substrates were inserted vertically into the beaker. After deposition for 2 hours, the substrates were taken out, washed with distilled water and dried in air.

RESULTS

The deposition rate process was studied by monitoring the variations of film thickness with pH. The growth rate and quality of the film was found to be a stringent function of the pH of the reaction mixture. Fig.1 shows the variation of film thickness with a pH of reaction mixture. pH below 10.5 was found to consist of non-adherent powder like precipitates indicating poor quality of deposition. The reaction mixture also tends to lose stability for pH<10.5. However, above pH value of 10.5, the growth rate decreases abruptly. The film thickness increased with increase in pH up to 10.5 and then it decreases for further increase in pH of the reaction mixture so the optimized pH value of the reaction mixture is 10.5. The dark electrical conductivity of the PbS thin film was studied in the temperature range 383 to 498°K using dc two- point probe method.

Conductivity is an important factor, which reveals important information about the transport phenomenon of the material. The dc electrical conductivity of a semiconductor at temperature T is given by,

$$\sigma_{DC} = \sigma_0 \exp(-\Delta E / KT) \qquad (1)$$

Where ΔE is activation energy and K is the Boltzmann constant. When we plot a graph between lnσ and 1000/ T a straight line is obtained having slope ΔE/1000k, we may calculate the activation energy as follows.

$$\Delta E = 1000k \times \text{slope of straight line} \qquad (2)$$

The variation of lnσ with reciprocal temperature ((1/T) X10^3) is shown in Fig.2. It can be observed that electrical conductivity has two linear portions. First in the lower temperature range (383-473°K) has activation energy 0.143 eV and second in the higher temperature range (473-498°K) having activation energy 0.794 eV. The increase in conductivity with increase in temperature indicating the semiconducting nature of films The thermally generated voltage at the cold end is positive, indicating the films are p-type. Fig.3 shows variation of thermo-emf with temperature, which shows that thermo-emf increases with increase in temperature. The carrier concentration of semiconductor at temperature T is given by

$$\text{Log}(n) = 3/2 \log(T) - 0.005p + 15.7198 \qquad (3)$$

Where T is the temperature and P is T.E.P.

The variation of log (n) with 1000/T is shown in Fig.4. The mobility is given by $\mu = \sigma / ne$ where σ is conductivity, n is carrier concentration and e is electron charge (1.6 X 10^{-19}C). A graph between ln (μT) $^{1\backslash 2}$ and 1000/T is as shown in Fig.5. From which we can calculate barrier height in the lower temperature range (383-473°K) is 0.17 eV and in the higher temperature range (473-498 °K) is 0.99 eV.

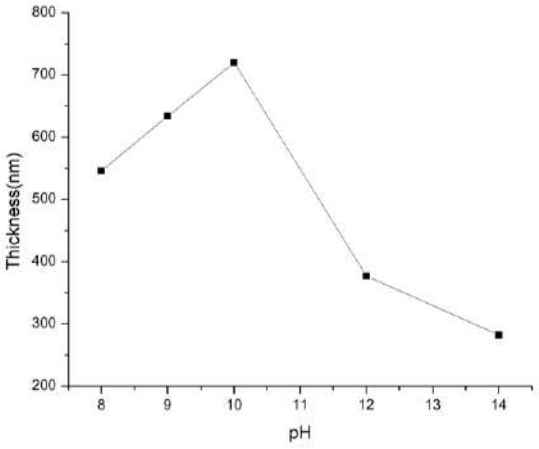

Fig.1. Thickness variation with pH

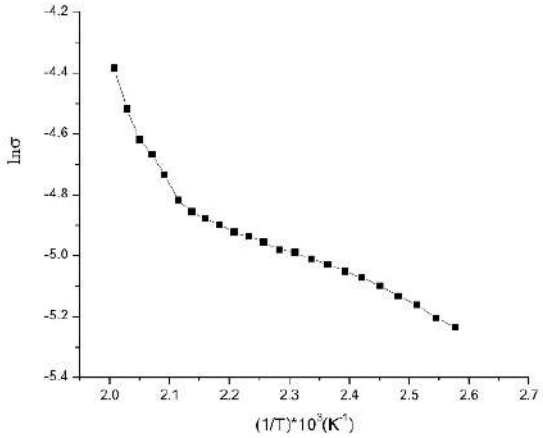

Fig.2.Variation of lnσ with function of temperature

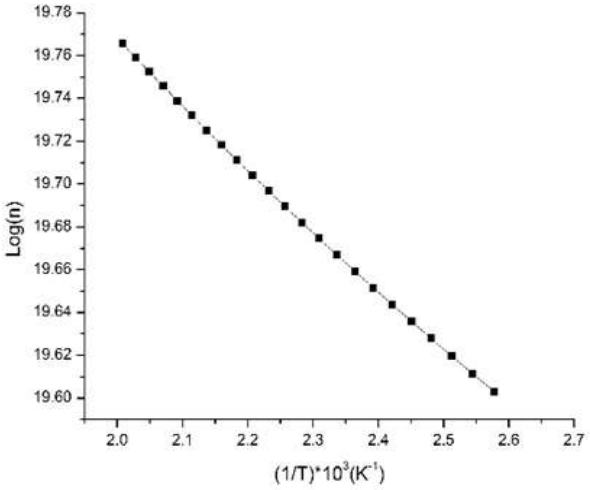

Fig.4. Carrier concentration variation with 1/T

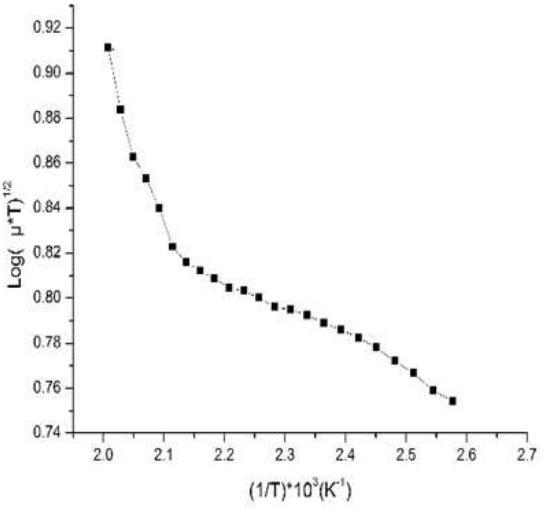

Fig.5. Variation of mobility with 1/T

CONCLUSION

We have deposited PbS thin film on glass substrate. The dc electrical conductivity indicating the semiconducting nature of thin film and thermo-emf measurements confirms the p-type nature of PbS thin films.

Conflicts of interest: The authors stated that no conflicts of interest.

REFERENCES

1. Mosiori, Cliff O, Njoroge, Walter N, Okumu J. International Journal of Advanced Research in Physical Science, 2014; 1 (1): 25-32.
2. Borote MA, Yadav AA, Chavan TV, Mmasumder EU. Optoelectronics and Advanced Materials- Rapid Communications. 2011; 4(1.5):387-392.
3. Seghaier S, Kamoun N, Brini R, Amara AB, Material Chemistry and Physics. 2006; 71-80.
4. Maheshwar S, Ramaiah KS, Kumar M, Spallart M, Neumann, Levey-Clement C. Electroanal. Chem. 1997; 436: 49-52.
5. Thangaraju B, Kaliannam P.Semicond. Sci. Technol. 2000; 15:849-853.
6. Nair PK, Garcia VM, Hemande AB, Nair M-TS.J. Physics D. Appl. Phys. 1991; 24: 1466-1472.
7. Zhao Y, Xue-tlong L, Jion-Min T, Jun-Jie Z.Mater. Chem. Phys. 2004; 87: 149-153.
8. Gumus C, Ulutas C, Esen R, Ozkendir OM, Ufuktepe Y. Thin solid Films; 2005; 492: 1-5.

IRJSE *Int. Res. J. of Science & Engineering,* 2018; Special Issue A2: 64-68
ISSN: 2322-0015
SJIF Impact Factor 4.11
UGC Approved Journal No. 63628
RESEARCH ARTICLE **OPEN ACCESS**

Ultrasonic Study of Molecular Interactions in Binary Liquid Mixtures and Acoustic Parameters of Dimethylsulphoxide with Ethanol at 303K

Kolhe RK[1] and Bhosale BB[2]

Research Scholar, JJT University, Jhunjhunu, Rajasthan, India
Department of Physics, K.J. Somaiya College, Kopargaon, Maharashtra, India
E-mail: rangnath_kolhe@rediffmail.com

Manuscript Details
Available online on http://www.irjse.in
ISSN: 2322-0015

Editor: Dr. Arvind Chavhan

Cite this article as:
Kolhe RK and Bhosale BB. Ultrasonic Study of Molecular Interactions in Binary Liquid Mixtures and Acoustic Parameters of Dimethylsulphoxide with Ethanol at 303K, *Int. Res. Journal of Science & Engineering,* January 2018; Special Issue A2: 64-68.

ABSTRACT

The Ultrasonic velocity (U), density (ρ) and viscosity (η) of binary liquid mixtures of Dimethylsulphoxide and ethanol have been measured using Ultrasonic Interferometer at frequency 2MHz and at constant temperature 303K for entire composition. From the measured data of ultrasonic velocity, density and viscosity, acoustical parameters such as adiabatic compressibility (β), intermolecular free length (L_f), free volume (V_f), acoustic impedance (Z), internal pressure (πi), Gibb's free energy (ΔG) and Rao's constant (R) have been calculated using standard relations. The variation of adiabatic compressibility (β), intermolecular free length (Lf), free volume (Vf), acoustic impedance (Z), internal pressure (πi), Gibb's free energy (ΔG), Rao's constant with mole fraction at constant temperature have been studied. Acoustic parameters provide valuable information in understanding the molecular interaction in binary liquid mixtures.

Keywords: ultrasonic velocity, acoustical parameters, Hydrogen bonding;

INTRODUCTION

The ultrasonic study of liquid and liquid mixture is important in understanding the nature of molecular interactions. The biological activity of drug molecules and the activation energy of the metabolic process basically depend on the type and strength of the intermolecular interactions. The thermo-acoustic properties of liquid mixtures have been extensively used to study the departure of a real liquid mixture behavior from ideality. The nature and degree of molecular interactions in different solutions depends upon the nature of solvent, the structure of solute molecule and extent of solutes taking place in the solution [1]. Ultrasonic investigation of liquid mixture is of considerable importance in understanding intermolecular interaction between the molecules which finds application in industrial and technological processes. Ultrasonic velocity and the derived acoustical parameters provide valuable information about the molecular interactions. This has been studied for various binary mixtures with respect to variation in concentration of the liquids [2-3]. The acoustical and thermodynamic parameter have been used to study different kinds of association, molecular motion and various types of interaction and their strength influenced by the size of pure component and the mixtures [4]. The accurate thermodynamic and acoustic properties of alcohols, in particularly 1-propanol are of interest for different branches of science and engineering.1-propanol is an important industrial chemical fluid. 1-propanol is used as a solvent in the pharmaceutical industry. Hydrogen bonding is one of the most important types of intermolecular interactions play an important role in various physicochemical, biological and industrial processes [5-6].

In the present paper, variations of some acoustic parameters of binary mixture of DMSO and 1-propanol with different concentration have been studied for a constant temperature at 303K..

METHODOLOGY

The ultrasonic velocities were measured by using a single crystal Ultrasonic Interferometer (Mittal Enterprises, Model No. M-81S). The measurement of velocities was made at a fixed frequency of 2MHz. The temperature was controlled by circulating water around the cell from thermostatically controlled constant temperature water bath. The densities of pure liquid and liquid mixtures were measured by using 25ml specific gravity bottle with an accuracy of ± 0.5% and weight was measured with an electronic balance (Citizen, Model- CY-220, India) capable of measuring up to 1mg. The viscosity of liquid mixtures was measured by Ostwald's viscometer and distilled water has been used as a standard liquid. The liquid mixtures of various concentrations in mole fraction were prepared by taking AR grade chemicals (Merck, Germany- 99%) DMSO and 1- Propanol. From experimental data, various acoustic parameters were calculated [7].

Adiabatic Compressibility $\beta = 1/ (U^2 \times \rho)$ (1)

Intermolecular free Length

$L_f = K_T \times \beta^{1/2}$ where K_T is Jacobson constant (2)

Free Volume $V_f = [M_{eff}\, U/ K\eta]^{3/2}$ (3)

Acoustic Impedance $Z = \rho \times U$ (4)

Internal Pressure $\pi_i = bRT\, [(k\eta / U)^{1/2} (\rho^{2/3} / M^{7/6})]$ (5)

Gibbs Free Energy $\Delta G = K_B T \ln (K_B T \tau / h)$ (6)

Rao's constant $R = U^{1/3} M_{eff} / \rho$ (7)

RESULT AND DISCUSSION

The Experimentally measured value of ultrasonic velocity, density and viscosity for the binary mixtures of DMSO and 1-Propanol in different mole fractions at temperature 303K is given in **table 1.** The values of acoustical parameters such as adiabatic compressibility, free length, free volume, available volume, acoustic impedance, relaxation time, internal pressure, Gibb's free energy, Rao's constant and absorption coefficient at constant temperature 303K has been given in **table 2.**

Figure 1 shows that the ultrasonic velocity increases with increase in mole fraction of DMSO, which indicates the presence of molecular association between solute and solvent. The variation of ultrasonic velocity in a mixture depends upon the increase or decrease of intermolecular free length, on the basis of a model for propagation proposed by Eyring and Kincaid [8]. The increase in velocity may be due to the structural changes of molecules in the mixture take place due to

the existence of electrostatic field between the interacting molecules. From **Figure 2** it can be seen that the density of mixture increases with concentration due to the presence of large number of molecules in the mixture, while viscosity (**Figure 3**) decreases with increase in concentration. The decrease in viscosity indicates the weak intermolecular forces between the molecules.

Table -1 Values of Ultrasonic Velocity (U), Density (ρ) and Viscosity (η) of DMSO + ethanol at 303^{0}K

Mole Fraction of DMSO	Mole Fraction of 1-Propanol	Ultrasonic Velocity U(ms^{-1})	Density (kg m^{-3})	Viscosity x10^{-3} ($Nm^{-2}s$)
0.0000	1.0000	1175.16	789.02	0.1398
0.0756	0.9399	1180.21	808.90	0.1362
0.1554	0.8711	1181.37	818.30	0.1297
0.2398	0.7930	1191.47	873.20	0.1262
0.3292	0.7053	1192.80	910.20	0.1088
0.4240	0.6075	1195.3	933.70	0.0836
0.5248	0.5002	1197	963.40	0.0788
0.6320	0.3839	1203.57	993.50	0.0744
0.7465	0.2602	1208.84	1017.90	0.0684
0.8689	0.1313	1214.4	1030.50	0.0652
1.0000	0.0000	1229.26	1087.80	0.0631

Table -2 Values of adiabatic compressibility (β), acoustic impedance (Z), free length (L_f), (free volume (V_f), (internal pressure (π_i), Gibbs free energy (ΔG), Rao's constant (R) of DMSO +ethanol at 303^{0}K

×10^{-10} ms^2 kg^{-1}	Z×10^6 kg $m^{-2}s^{-1}$	L_f ×10^{-9}m	V_f ×10^{-6} (ml)	π_i (×10^3 Nm^{-2})	G ×10^{-21} $Jmol^{-1}$	Rao's Const. 'R'
9.177	0.927	0.634	5.5523	6.500	8.843	991.32
8.875	0.955	0.624	5.9717	6.372	8.828	986.10
8.756	0.967	0.620	6.6199	6.127	8.812	993.61
8.067	1.040	0.595	7.1723	6.157	8.784	950.33
7.722	1.086	0.582	9.1791	5.772	8.735	925.82
7.496	1.116	0.573	13.9066	5.073	8.660	913.50
7.244	1.153	0.564	15.3880	4.985	8.636	891.92
6.948	1.196	0.552	16.9530	4.921	8.610	867.90
6.723	1.230	0.543	19.2268	4.811	8.580	844.48
6.580	1.251	0.537	20.4369	4.790	8.563	825.62
6.084	1.337	0.517	21.1997	4.973	8.534	769.40

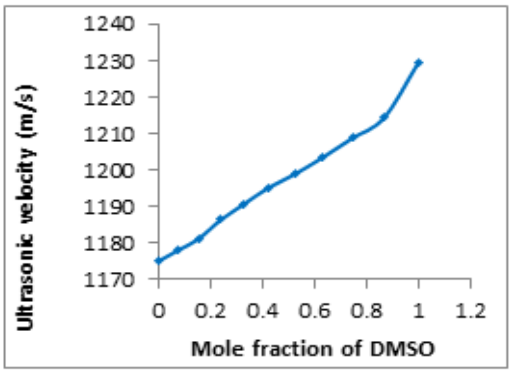

Figure 1: Variation of Ultrasonic velocity

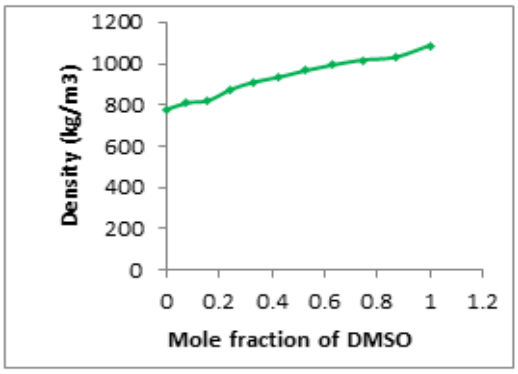

Figure 2: Variation of density versus mole fraction at temperature 303K versus mole fraction at temperature 303K

Figure 1

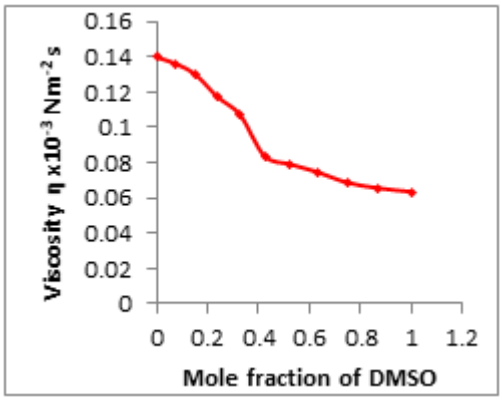

Figure 3:

Figure 2

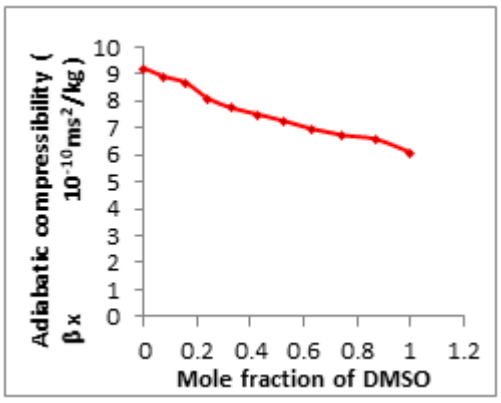

Figure 4:

Figure 3: Variation of viscosity versus mole fraction at temperature 303K

Figure 4: Variation of adiabatic compressibility versus mole fraction at temperature 303K

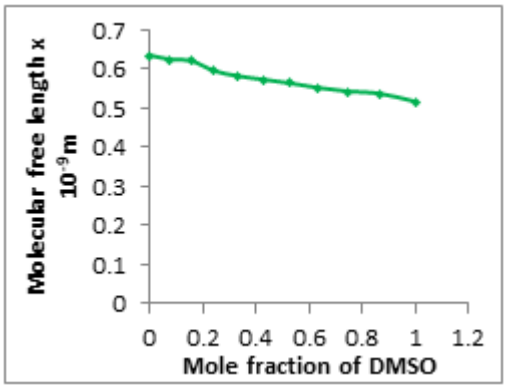

Figure 5:

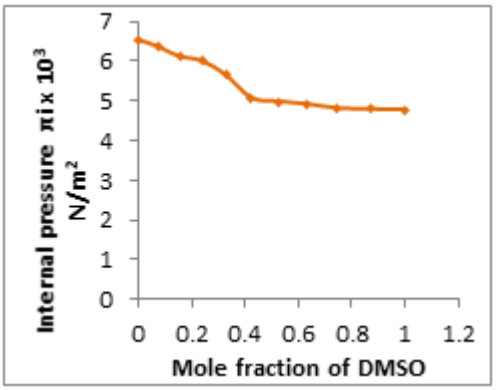

Figure 6:

Figure 5: Variation of molecular free length versus mole fraction at temperature 303K

Figure 6: Variation of internal pressure versus mole fraction at temperature 303K

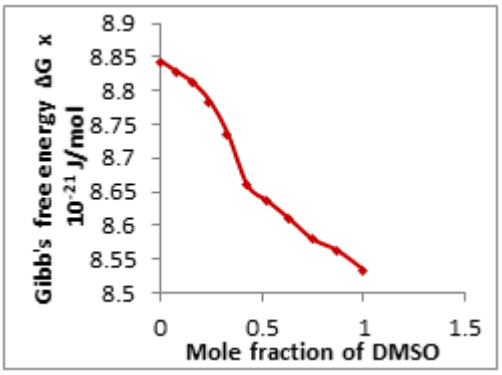

Figure 7:

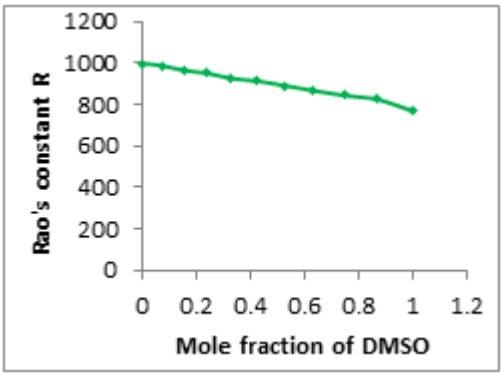

Figure 8:

Figure 7: Variation of Gibb's free energy versus mole fraction at temperature 303K

Figure 8: Variation of Rao's constant versus mole fraction at temperature 303K

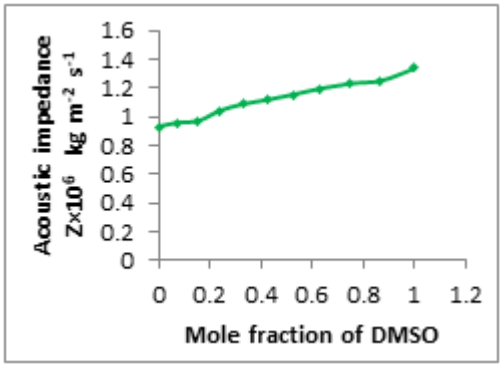

Figure 9:

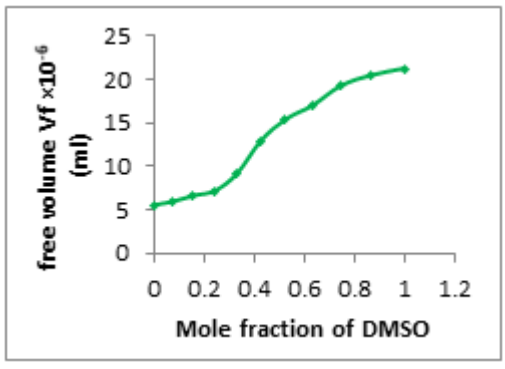

Figure 10:

Figure 9: Variation of acoustic impedance versus mole fraction at temperature 303K

Figure 10: Variation of free volume versus mole fraction at temperature 303K

The adiabatic compressibility decreases with increasing concentration which shows that there is strong interaction between the molecules of liquid mixture shown in **Figure 4**. **Figure 5** depicts the variation in intermolecular free length with mole fraction. This decrease in free length is due to the decreased adiabatic compressibility which brings the molecules to a closer packing.

Figure 6 gives variation in internal pressure with concentration of DMSO. Due to decrease in internal pressure of the mixture there is an increase in the values of free volume which indicates that the strength of interaction between the molecules decreases gradually with increase in concentration and hence weak interaction between the molecules is found.

Figure 7 shows variation in Gibb's free energy with concentration of DMSO. Gibb's free energy decreases with increase in concentration which confirms the hydrogen bonding formation in binary liquid mixtures [9]. Rao's constant decreases with increase in concentration as shown in **Figure 8,** which predicts that there is presence of small complex formation in the mixture.

Acoustic impedance increases with increase in concentration of DMSO (**Figure 9**). Acoustic impedance shows opposite behavior as that of adiabatic compressibility and intermolecular free length. **Figure 10** shows that free volume increases with increase in concentration which suggests that there is weak interaction among the solute and solvent molecules.

CONCLUSION

In the present investigation, the various acoustical parameters such as adiabatic compressibility, intermolecular free length, internal pressure, Gibb's free energy, Rao's constant, acoustic impedance and free volume have been evaluated from ultrasonic velocity, density and viscosity for the binary liquid mixtures of DMSO with ethanol at 303K. From the above studies it is concluded that ultrasonic velocity increases as intermolecular free length decreases. The decrease in viscosity indicates the weak intermolecular forces between the molecules. The decrease in adiabatic compressibility shows that there is strong interaction between the molecules of liquid mixture. Decrease in Gibb's free energy confirms formation of hydrogen bonding in the liquid mixtures.

Conflicts of interest: The authors stated that no conflicts of interest.

REFERENCES

1. Bedare GR, Suryavanshi BM and Vandakkar VD, *International Journal of Advanced Research in Physical Sciences*, 2014; 1(5): 1-5.
2. Praharaj M, Satapathy A et al, *Journal of Theoretical and Applied Physics*, 2013; 7: 23.
3. Vasantharani P, Kalaimagal P and Kannappan A.N., *Asian J Applied Sci*, 2009; 2: 96-100.
4. Dange SP and Chimankar OP, *Global Research Analysis*, 2013; 2(7): 167-168.
5. Vasantharani P Pandiyan V and Kannappan AN, *Asian J Applied Sci*, 2009; 2: 169-176.
6. Furniss BS, Hannford AJ, et al, Vogel's Textbook of Practical Organic Chemistry, 5th Edn,
7. Harlow, Longman, 1989, ISBN: 0-582-46236-3.
8. Kaur K and Juglan KC, *Der Pharma Chemica*, 2015; 7(2): 160-167.
9. Eyring H and Kincaid JF, *Ind. J. Phys*., 1938; 6: 620.

IRJSE *Int. Res. J. of Science & Engineering,* 2018; Special Issue A2: 69-72 SJIF Impact Factor 4.11
ISSN: 2322-0015 UGC Approved Journal No. 63628
RESEARCH ARTICLE **OPEN ACCESS**

Preparation of Nickel Sulphide Nano Films

Pingale Shirish S

Department of Chemistry, ACS College, Narayangaon, Pune410504, MS, India.
E-mail: drshirishpingale@rediffmail.com

Manuscript Details
Available online on http://www.irjse.in
ISSN: 2322-0015

Editor: Dr. Arvind Chavhan

Cite this article as:
Pingale Shirish. Preparation of Nickel Sulphide Nano Films, *Int. Res. Journal of Science & Engineering,* January 2018; Special Issue A2 : 69-72.

ABSTRACT

In present work Ni-S films were prepared by electro deposition method. Sprayed SnO_2:F Films on glass to be used as electrodes. Characterization was done by 'XRD' analysis and TGA analysis. The observed 'd' values were compared with standard ASTM data. Good matching was observed in data and observed values. The bulk X-Ray diffractogram was used to calculate grain size. The thermo gravimetric studies of sample gave us the information regarding the thermal properties of a material. TGA & DTG data also supports to the formation of Nickel sulphide with Nickel having plus two (II) Oxidation state (Ni_7S_6).

Keywords: Electroplating, Electrodes, XRD, TGA, Ni-S, etc.

INTRODUCTION

The preparation method for obtaining the amorphous alloys by the plating techniques has some merits which are different from those of other techniques. For example rapid quenching, sputtering and evaporation. It is possible to prepare wide or bulky amorphous materials as well as covering a material with complicated shape by an amorphous material. There is no need of vacuum equipments or furnaces for electroplating. The composition and microstructure of the alloy can be varied by changing the composition of electrolyte. It has been reported that electrodeposited Ni-P, Ni-S glasses are most stable.

The mass production of electroplating by continuous operation is possible. It has been thought that the amorphous materials prepared by the electroplating technique have high probability as new technologically viable materials.

METHODOLOGY

Preparation of Sprayed SnO_2: F Films on Glass to be used as electrodes:

SnO_2:F Films were deposited on Corning 7059 glass substrates using spray pyrolysis technique. Details of the experimental setup are given in paper (25). The F/Sn atomic ratio in the solution was kept constant and methanol to water volume ratio was maintained to 9:1. All the films were grown at 450^0C (+ 5^0C) using a solution flow rate of 4 ml per minute. The films of about 15 - 20 $ohm^{-1}cm^{-1}$ conductivities were prepared by spraying 10 ml of solution which was prepared by taking 7 g of $SnCl_4$ $5H_2O$ (Stannic chloride) + 1.5g of Nh_4F (Ammonium fluoride) + 90 ml (Methanol) CH_3OH A.R. Grade +10ml H_2O. These Sno_2:F film deposited substrates were used as cathode in the present experiment.

Electrochemical Deposition of Ni-S films:

Ni-S films were prepared by electrode position method. Experimental setup is arranged properly for the deposition of Ni-S films. The electrolyte solution was prepared by mixing 20 g of Nickel Ammonium Sulfate, 2.00 g of Sodium Thiosulfate and 3.0 g of Sodium Citrate ($Na_3C_6H_5O_7$. $5H_2O$) as a buffer in a fixed volume of double distilled water (200ml). The above prepared solution was transferred to a five necked flask (electrolytic bath). The pH of the solution was maintained constant by using sodium citrate and was maintained between 6.2 to 6.5 by adding Ammonical water or dilute H_2SO_4 solution. From the central neck, the SnO_2:F film as a cathode was inserted. It was previously checked for proper contact with the help of a multimeter by checking the resistance of the SnO_2: F film. From the second neck of electrolytic bath the platinum electrode was inserted which was previously washed with distilled water. The distance between platinum anode and (SnO_2: F coated on glass) cathode was kept constant throughout the deposition. The cathode area was also maintained constant for successive deposition. The third neck of electrolytic bath was utilized for bubbling nitrogen gas with the help of bubbler during deposition process to prevent oxidation of electrolyte by dissolved oxygen in electrolyte. The fourth neck was used for temperature measurements during deposition and was maintained constant throughout the deposition with help of heater and magnetic stirrer. A regulated D.C. Power Supply was used for deposition purpose, supplied by 'CONEL', whereas the micro ammeter was supplied by 'Simpson'. The Ni-S films were deposited for different time intervals between one hour to three hours. The cathodically electrodeposited films of Ni-S shows brownish (thin) or Black (thick) colour. The films are then analysed by using XRD analysis and TGA analysis.

RESULT AND DISCUSSION

The nickel sulphide is an attractive material from physical as well as application point of view. In the hexagonal form it exhibits a transition at 295^0K. The band gap of the order of 0.4 eV opens up at low temperature while the hexagonal lattice remains undistorted. The semiconductor to metal transition has been described by Mott-Hubbard Model. Nickel sulphide is however not a Mott insulator. The semiconductor to metal transition has been studied by various researchers and the query still remains unresolved. Small stoichiometric changes in nickel sulphide are expected to influence the semiconductor-metal transition. Electroplating can be conveniently used to obtain nonstoichiometric Ni-S films by simply varying the current density, molarity, composition and pH of electrolyte. We have prepared Ni-S films by cathodic reduction of metal ion containing suphide in electrolyte solution or they can also be deposited from aqueous solutions containing soluble metal and chalcogen compounds.

$$M^{++} + S^{-} \longrightarrow MS$$

The nickel sulphide coating in aqueous medium has been obtained first by "Sawada" et. al. However, they report crystalline film formation only after annealing at 100^0C. We were successful in obtaining crystalline Ni-S films on chemically inert SnO_2: F films with

slightly higher nickel content by electroplating method for various time intervals. Ni-S can be used as an anti-corrosive layer in catalysis and in photochemical solar energy conversion. The band gap of Ni-S is 0.4 eV; it absorbs all the photons in visible and U.V. range. Hence it can be used in photo thermal energy conversion.

The typical diffractogram for the thickest Ni-S sample was shown in above Figure 1. The diffractogram exhibits highly oriented crystallites, (0 2 2) peak which is dominant. While for all other planes epitaxial intensity is less than 30%. The grain size cannot be obtained correctly from glancing incidence X-ray diffractogram. We have used the glancing incidence X-ray diffractogram for determining crystal structure or phase of Ni-S. The bulk X-ray diffraction pattern was used to calculate the grain size Figure.

Interplanar spacing is obtained by using well known Bragg's relation. The observed 'd' values are compared with standard ASTM data (Card 22-1193). Good matching was observed in data and observed values. The standard deviation is given in Table 1, Card 22-1193 Ni_7S_6 Orthorhombic a_o = 9.180, b_o=11.283, c_o =9.457.

Nickel rich Ni_7S_6 phase was obtained. The bulk X-ray diffractogram for the sample deposited for highest time interval is shown in Figure 2. This was used to calculate the grain size. Although the complications due to diffraction pattern from the substrate SnO_2: F is unavailable. This method is useful in estimating grain size. Note that the X-ray diffraction is inferior to microscopic examination in the accurate measurement of grain size. Diffractogram can yield semi quantitative information about the grain size together with the information about crystal perfection and orientation.

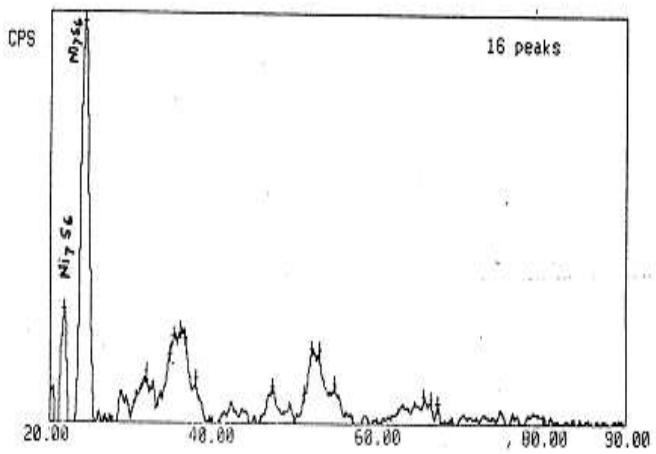

Fig 1: Typical diffractogram of the thickest Ni-S film

Table 1: X-ray diffractogram data

Obs. No.	d(Calculated)	D (Standard)	SD	(h k l)
01.	4.077	4.14	0.063	2 0 1
02.	3.672	3.93	0.258	1 1 2
03.	2.815	3.02	0.205	0 2 2
04.	2.379	2.33	0.049	2 4 1
05.	1.787	1.795	0.008	0 2 5

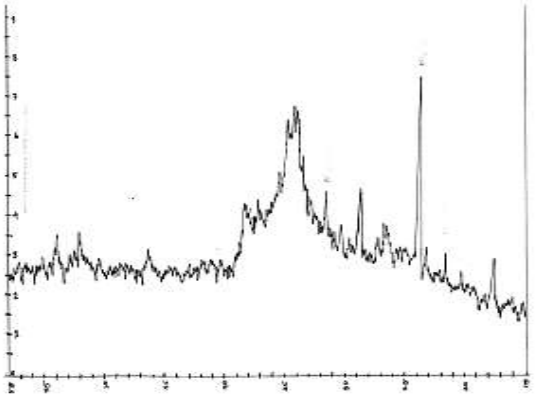

Fig 2: X-ray Diffractogram of Ni-S film

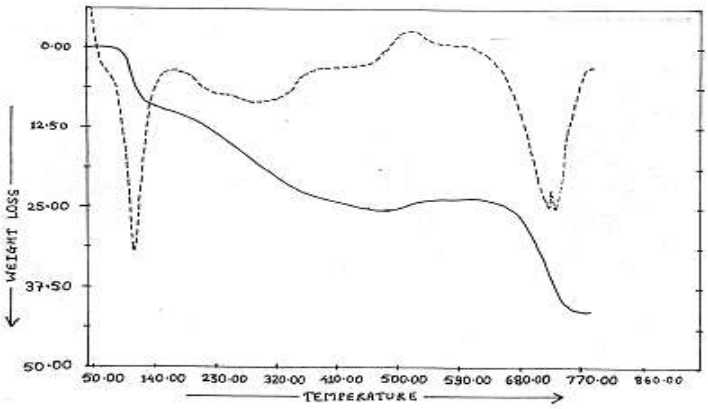

Fig 3: TGA for Typical Ni-S Film

The governing effect is due to the number of grains which take part in diffraction. This number in turn related to cross-Sectional area of the incident beam and its depth of penetration and also the sample thickness. When the grain size is coarse only few crystals diffract and diffraction consists of superimposed lines, one from each crystal due to white radiation present. For finer grains the pattern exhibits broad lines.

Additional broadening due to finite temperature is present. We estimated the grain size from the diffractogram as shown in Figure. A typical grain size was about 500^0A.

The TGA of Ni-S film is shown in Figure 3. The initial small loss of weight must be due to trapped solvent molecules in the film not maintained in vacuum. The loss of weight about 30 % corresponds to the loss of sulphide from the matrix. However, it extends over a large temperature range from 140^{o}C to 770^{o}C indicating that the sulphide matrix has strong bonding. This data also indicates that the film must be corresponding to the formation of nickel suphide with Ni having plus two oxidation state. However, the emphasis was laid on aqueous electrolyte; cathodic deposition of Ni-S films, X-ray diffraction, and this technique is used in solid state physics and Chemistry and is employed for phase and particle size determination.

Conflicts of interest: The authors stated that no conflicts of interest.

REFERENCES

1. Hasegawa R and Issue CC, *Phys. Rev*.B2 1632
2. Pampillo A, *J.Mater.Sci*.10,1194 (1975)
3. Berry BS, Gilman JJ & Leamy HJ, *Amm. Society for metals*, Leveland (1977)
4. Harris R, Plischte M, Zuckermann MJ, *Phys.Rev.Lett*. 31,160 (1973)
5. Chandhary P, Cuomo JJ, Gambino RJ. *IBM J. Res. Dev*. 17,66 (1973).
6. Rhyne JJ, Picort SJ, Alperine HA, *Phys.Rev.Lett*.,1972; 29,1568.
7. Paul DI. In proceedings of the 2nd international conference on amorphous magnetism, R.A. Lavy & R. Hasegawa, Edj. (Plenum, New York 1977) P.403.
8. Weaire D, Ashby MF, Logan J, Weans MJ. *Acta.Metall*, 1971; 19, 779(1971)
9. Dingle RB and Slater JE, *Corrosion*, 1976; 32, 155.
10. Hashimoto K and Masumoto J. *Mater, Sci. Epg*. 1976; 23,285.
11. Polk DE and Glessen BC. In Metallic Glasses Edg, J.J.Gilman and H.J. Leamy
12. Pond RB, Maringer RE, Mobley CE, In New trends in material Processing, American Society for Metals, New York (1979) P.128.
13. Goldstein AW, Rostoker W and Schossfergere F, *J. Electrochemical Soc*.1957; 104.
14. Sead Satal and Herbert Herman in Trestise on Material Science and Technology, Vol. 20 ed. Herbert Herman Academic Press, New York (1981)
15. Chaudhary P, GuomoJJ, Gambino RJ, Appl.Phys.Lett., 1973. 27, 337.
16. Surago K., Matsushita S, SakuraiY, IEEE Trans., Magn. MAG 12,776 (1976)
17. Minumura Y, Manura NI, Kobyasni T, Ibid P. 779
18. Hans-Werner Schroeder in Rapidly quenched metals, Vol.II, ed.S. Steeb.
19. Warlimont H, Elsevier Science, Publishers, B.V. (1985), P.1027
20. Narita A, Watnable J and Tanade Y. In rapidly Quenched Metals Vol. I ed. S. Steels, H.Warlimont, Elsevier Science Publishers, B.V. (1985) P. 133
21. Bestegen H. In Rapidly Quenched Metals, Vol. I ed. S. Steels, H. Warlimant Elsevier Science Publishers, B.V.(1985) P. 445.
22. Asami K, Kawashima A, SatoT, Hashimoto K, Lizawa KL and Plaito K . In Rapidly Quenched Metals, Vol. II ed.S. Steels, H. Warlimont, Elsevier Science Publishers, B.V.(1985) P. 1027.
23. Hashimoto K and Masumoto T. In Proc. Second International Conference on Repidly Quenched Metals Section II .

IRJSE *Int. Res. J. of Science & Engineering,* 2018; Special Issue A2: 73-75 SJIF Impact Factor 4.11
ISSN: 2322-0015 UGC Approved Journal No. 63628
RESEARCH ARTICLE **OPEN ACCESS**

Biosynthesis of silver nanoparticles using the *Agaricus bisporus* (Button Mushroom) extract

Kulkarni Vasudeo D*, Kute Nilam S and Tanpure Priya D

Department of Physics, Hutatma Rajguru Mahavidyalaya, Rajgurunagar. Pune(MS),410505(INDIA)
Email: kulkarni_vd55@yahoo.co.in

Manuscript Details
Available online on http://www.irjse.in
ISSN: 2322-0015

Editor: Dr. Arvind Chavhan

Cite this article as:
Kulkarni Vasudeo D, Kute Nilam S and Tanpure Priya D. Biosynthesis of silver nanoparticles using the *Agaricus bisporus* (Button Mushroom) extract, *Int. Res. Journal of Science & Engineering,* January 2018 | Special Issue A2 |: 73-75.

ABSTRACT

Biosynthesis of silver nanoparticles using ***Agaricus bisporus*** was carried out. The large-scale application of silver nanoparticles (AgNPs) in areas such as chemical sensing, nanomedicine, and electronics has led to their increased demand. The Silver nanoparticles were characterized with the help of X-Ray Diffraction and FTIR (Fourier Transform Infrared Spectroscopy). The XRD confirms the formation of nanoparticles and size of nanoparticles was found to be 27.33 nm. The FTIR gives the prominent bands of absorbance at 1627 cm^{-1}, 2923.45 cm^{-1} , 3442.44 cm^{-1} .The observed peak 3442.44cm^{-1} denote the occurrence of O-H stretching bond of alcohol functional groups. These groups may responsible for efficient capping and stabilization of silver nanoparticles.

Keywords: Silver nanoparticles, *Agaricus bisporus* extract, biosynthesis, XRD, FTIR.

INTRODUCTION

The medicinal plants are easily accessible in every part of India. Such medicinal plants have large applications in nanotechnology. These plants have great significance in Ayurveda [1]. The silver nanoparticles were synthesized using Ocimum sanctum (Tulsi) leaf extract. The prepared nanoparticles were characterized by XRD, UV, TEM, and FTIR [2]. The gold nanoparticles using *Mentha arvensis* leaf extract was prepared. The gold nanoparticles were found in spherical and hexagonal shape from TEM [3].

The silver nanoparticles were prepared from medicinal plants. The silver nanoparticles were synthesized using the leaves of *Svensonia hyderobadensis* and the stem barks of *Boswellia, Shorea* species. These nanoparticles showed the best antimicrobial activity against various microorganisms [4]. The biological synthesis of nanoparticles is ecofriendly and cost effective [5]. The silver nanoparticles was synthesized using mangrove plant extract [6].

METHODOLOGY

The *Agaricus bisporus* was collected for biosynthesis of silver nanoparticles. The *Agaricus bisporus* was cut into small pieces and 10 gm of pieces was added into 100 ml deionised water and extract was prepared for further study. The silver nitrate solution of 1mMole was prepared and 20 ml extract was added in 1mMole $AgNO_3$ solution and the solution was heated up to 80^o C. This solution was stirred up to three hours. The colour of solution was changes from pale yellow to light brown to dark brown. It was indicated that the formation of silver nanoparticles. Kept this flask at room temperature for overnight and silver nanoparticles settled at the bottom of this solution. The silver nanoparticle was obtained by centrifugation method at 15000 RPM for 30 minutes and this process is repeated. Then the silver nanoparticles were dried in oven at 80^{0}C.

RESULT AND DISCUSSION

The Button Mushroom is shown in Fig.1. The 1m Mole $AgNO_3$ solution and extract of the Button Mushroom is shown in Fig. 2. The extract of the Button Mushroom is added in 1mMole $AgNO_3$ solution which showed the color change of the solution and shown in Fig. 3.

Fig.1: Button Mushroom (*Agaricus bisporus*)

Fig. 2: 1mMole $AgNO_3$ solution and Extract

Fig. 3: 1mMole $AgNO_3$ + Extract

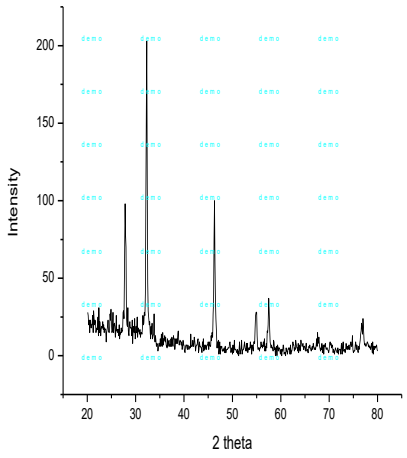

Fig.4: XRD of Silver nanoparticles

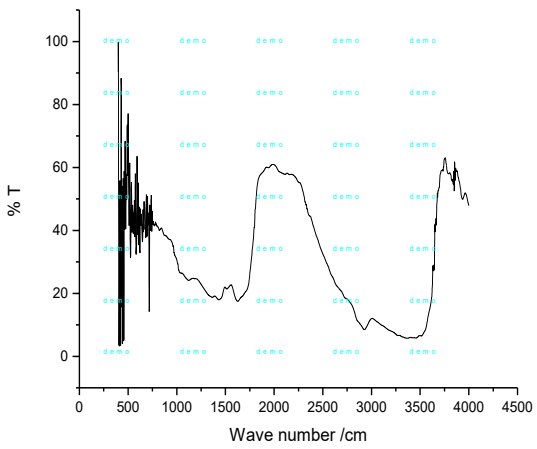

Fig.5: FTIR of Silver nanoparticles

X-Ray Diffraction:

The XRD pattern of synthesized AgNPs using extract is as shown in Fig.4. The sample demonstrated a high crystallinity level with diffraction angles (2θ) of 26.18^0, 32.3^0, 46.3^0, 54.1^0, and 57.5^0. The size of nanoparticles determined using debye-scherrer equation.

$$D = \frac{0.9 * \lambda}{\beta * Cos(\theta)}$$

Where, D= grain size, β= Full Width at Half Maxima (FWHM), θ = Corresponds to angles of diffraction peaks.

The average size of nanoparticles was found to be 27.33 nm.

Study of FTIR Spectrum:

FTIR spectra of biosynthesized AgNPs using *Agaricus bisporus* (Button Mushroom) were shown in Fig.5. The FTIR Spectra were used to identify the capping reagent and stability of the metal nanoparticles present in *Agaricus bisporus*. The FTIR gives the prominent bands of absorbance at $1627cm^{-1}$, $2923.45cm^{-1}$, $3442.44\ cm^{-1}$. The observed peak $3442.44cm^{-1}$ denote the existence of O-H stretching bond of alcohol functional groups.

CONCLUSION

The Silver nanoparticles using Button Mushroom extract was successfully prepared. The biosynthesis method is ecofriendly and easily developed in laboratory. The size of Silver nanoparticles was recorded 27.33 nm from XRD. The peaks were recorded at $1627\ cm^{-1}$, $2923.45\ cm^{-1}$, $3442.44\ cm^{-1}$ from FTIR. The observed peak $3442.44cm^{-1}$ denotes the presence of O-H stretching bond of alcohol functional groups.

Acknowledgement:

The authors are thankful to University Grant Commission (UGC), New Delhi for the fund provided of this research work.

Conflicts of interest: The authors stated that no conflicts of interest.

REFERENCES

1. Banerjee P, Satapathy M, Mukhopahayay A and Das P. Leaf extract mediated green synthesis of silver nanoparticles from widely available Indian plants: synthesis, characterization, antimicrobial property and toxicity analysis, *Bioresources and Bioprocessing*, 2014 1(3): 1-10.
2. Garima Singhal, Riju Bhavesh, Kunal Kasariya, Ashish Ranjan Sharma, Rajendra Pal Singh. Biosynthesis of silver nanoparticles using Ocimum sanctum(Tulsi) leaf extract and screening its antimicrobial activity, *J Nanopart Res*., 2011; 13: 2981–2988.
3. Punuri Jayasekhar Babu, Pragya Sharma, Bibhuti Bhusan Borthakur, Ratul Kumar Das, Pradip Nahar, Utpal Bora. Synthesis of Gold Nanoparticles Using Mentha arvensis Leaf Extract", *International Journal of Green Nanotechnology: Physics and Chemistry*, 2:, (2010), 62–68.
4. Savithramma N, Linga Rao M, Rukmini K, Suvarnalatha devi P. Antimicrobial activity of Silver Nanoparticles synthesized by using Medicinal Plants" *International Journal of ChemTech Research*, 2011; 3(3): 1394-1402.
5. Thirumurugan A, Neethu Anns Tomy, Jai ganesh R, Gobikrishnan S. Biological reduction of silver nanoparticles using plant leaf extracts and its effect on increased antimicrobial activity against clinically isolated organism", *Der Pharma Chemica*, 2010; 2(6): 279-284.
6. Gnanadesigan M, Anand M, Ravikumar S, Maruthupandy M, Vijayakumar V, Selvam S, Dhineshkumar M, Kumaraguru AK. Biosynthesis of silver nanoparticles by using mangrove plant extract and their potential mosquito larvicidal property, *Asian Pacific Journal of Tropical Medicine*, 2011: 799-803.

IRJSE International Research Journal of Science & Engineering
Int. Res. J. of Science & Engineering, 2018; Special Issue A2: 76-82
ISSN: 2322-0015
SJIF Impact Factor 4.11
UGC Approved Journal No. 63628
RESEARCH ARTICLE **OPEN ACCESS**

Relationship between Dielectric Constant and Water Content of Soil from Western Ghat of Maharashtra, India

Dhiware MD[1], Nahire SB[2], Deshmukh Sushant[3]

[1]G.M.D. Arts, B.W. Commerce and Science College, Sinnar, Nasik, Maharashtra, India 422 103
[2]Arts, Science & Commerce College, Ozar (Mig) Dist- Nashik. 422 206 INDIA
[3]J.E.S. College, Jalana, Maharashtra, India 431 203
E-mail:- sushant.d59@gmail.com

Manuscript Details
Available online on http://www.irjse.in
ISSN: 2322-0015

Editor: Dr. Arvind Chavhan

Cite this article as:
Dhiware MD, Nahire SB, Deshmukh Sushant. Relationship between Dielectric Constant and Water Content of Soil from Western Ghat of Maharashtra, India, *Int. Res. Journal of Science & Engineering,* January 2018; Special Issue A2 : 76-82.

ABSTRACT

Microwaves play important role in the moisture detection in soil, plants and other agricultural products. Electrical properties such as dielectric loss, dielectric constant of soils has been measured at an automated x band microwave setup in TE_{10} mode operating at 9.56 GHz. It is measured for different moisture content. Soil samples are collected from agricultural land of Western Ghat of Maharashtra. Soil samples were analyzed for physical and chemical properties for the status of available micro nutrients. The measurement is very sensitive to volumetric water content. It is observed that there is slow increase in dielectric constant at lower per cent of water content, whereas it increases sharply at higher water content and becomes constant at certain value of water content in soil. It is observed that dielectric constant increases with increase in moisture content slowly up to transition moisture then it increases rapidly with increase in moisture content. The result shows the change in the electrical properties of soil before and after the addition of water. Also dielectric loss is directly proportional to the ac microwave conductivity and transition temperature. It has been found that emissivity decreases with increase in moisture content. In the field of remote sensing and agriculture, results obtained are useful.

Keywords: Moisture content, Dielectric constant, Dielectric loss, Micronutrients, Microwave frequency

INTRODUCTION

Soil is the loose collection of broken and chemically weathered rock mixed with organic and living matter on the earth's surface capable of supporting plants. Contrasts in texture are common in soils formed from alluvium where watercourses have deposited layers of sand and silt. Varying texture with depth usually indicates a soil may have formed one or more materials. With mineral soils the top soil is often dark in color, due to partially decomposed organic matter from plant and animal remains known as humus. Below the top soil is subsoil which may be various colors such as red, yellow, white, brown, orange or even blue. The upper half of the subsoil often differs in color from that of the lower half. Subsoil may also have mottles or blotches of another color through it. The arrangement and organization of soil particles in the soil, and the tendency of individual soil particles to bind together in aggregates. Soil moisture and roughness parameters play a key role in hydrological and climate studies. All essential elements are by definition required for plant growth and completion of the plant life cycle from seed to seed. Some essential elements are needed in large quantities and others in much smaller quantities. However, from a practical standpoint, three of the six essential macronutrients are most often "managed" by the addition of fertilizers to soils, while the others are most often found in sufficient quantities in most soils and no soil amendments are required to supply adequate supplies. From a management perspective only, the **primary nutrients** are N, P, and K, because they are most often limiting from a crop production standpoint. All of the other essential macronutrient elements are **secondary nutrients** because they are rarely limiting, and more rarely added to soils as fertilizers. Whether a macronutrient or micronutrient, or whether a primary or secondary nutrient, the most growth-limiting nutrient will limit growth, no matter how favorable the nutrient supply of other elements. For example, a deficiency of Fe or Mn (most common in soils containing calcium carbonate) can severely limit plant growth in spite of adequate N, P, and K. The ability of soils to supply secondary nutrients to plants indefinitely is subject to the law of conservation of matter and is therefore dependent upon nutrient cycling. Continued crop removal of Ca, Mg, and S requires replenishment just as surely as primary nutrients, but most likely less frequently. Calcium and magnesium are often supplied by mineral weathering, either of natural soil materials or of **aglime**, ground limestone added to correct soil acidity. Sulfur is often added to soil as either atmospheric deposition (associated with air pollution) or as impurities in fertilizers, particularly common P fertilizers.

Soil colour gives an indication of the various processes going-on in the soil as well as the type of minerals in the soil. For example the red colour in the soil is due to the abundance of iron oxide under oxidised conditions (well-drainage) in the soil; dark colour is generally due to the accumulation of highly decayed organic matter; yellow colour is due to hydrated iron oxides and hydroxide; black nodules are due to manganese oxides; mottling and gleying are associated with poor drainage and/or high water table. Abundant pale yellow mottles coupled with very low pH are indicative of possible acid sulphate soils. Colours of soil matrix and mottles are indicative of the water and drainage conditions in the soil and hence suitability of the soil for aquaculture.

Soil colour is described by the parameters called hue, value and chroma. Hue represents the dominant wave length or colour of the light; value, refers to the lightness of the colour; chroma, relative purity or strength of the colour. The colour of the soil in terms of the above parameters could be quickly determined by comparison of the sample with a standard set of colour chips mounted in a note-book called MUNSELL SOIL COLOUR CHARTS (Munsell Soil Colour Charts, 1973). In these charts, the right hand top corner represents the Hue; the vertical axis, the value; and the horizontal axis, the chroma. Different percentage of fertilizer content in soil gives large variation dielectric constant which is important for efficient use of soil [1]. Calla O. P. N. et. al. (2007) have carried out dielectric study, emissivity, scattering coefficient of dry and wet soils of Rajasthan with different moisture content using Waveguide Cell Method [2]. Microwave remote sensing of natural earth materials such as soil, water and plants has a very close dependence on their electrical parameters. This thesis discusses the use of microwaves and its response to red soils and associated moisture content.

Remote sensing of soil moisture depends on measurement of electromagnetic energy that has been reflected or emitted from soil surface. Bapna and Joshi. [3] studied the dielectric constant at different moisture that whatever be the moisture condition and type of soils, the dielectric constant decreases with increase in frequency. Gadani [4] have studied the effect of saline water on the emissivity of different soils with C band microwave frequency. Chaudhri from his paper [5] explains that a comprehensive study of complex permittivity of soils of Maharashtra and Karnataka state has been undertaken. The dielectric properties of urea and diammonium phosphate fertilizers in aqueous solution at different temperatures in microwave frequency are reported [6]. The characteristics of the soil of Chhattisgarh at X-band frequency are studied using Infinite sample method [7]. Microwave emission depends upon the dielectric constant of the soil [8]. Mohan et al. [9] explores the relevance of usage of microwave frequencies for the dielectric-property extraction of soil. Many important soil processes take place in soil pores (the air or water-filled spaces between particles). As the dielectric permittivity of water is an order of magnitude grater than the corresponding values of soil constituents, changes in dielectric constant can be attributed to change in water content in nonexpanding soils [10]. Due to this increase in soil moisture there is small increase in dielectric constant. The variation in dielectric constant and soil water content with increasing volumetric water for the three samples is very similar to the work of Behari [11], Vyas and Gadani [12], and Srivastava and Mishra [13]. Soil texture and structure influence porosity by determining the size, number and interconnection of pores. Coarse textured soils have many large (macro) pores because of the loose arrangement of larger particles with one another. Fine-textured soils are more tightly arranged and have more small (micro) pores. Macro pores in fine-textured soils exist between aggregates. Because fine-textured soils have both macro- and micropores, they generally have a greater total porosity, or sum of all pores, than coarse-textured soils. In the frequency range from 2 GHz to 20 GHz, Calla et al. [17] measured the complex dielectric constant of loamy sand for various moisture contents by weight. The measurements were carried out using HP network analyzer and an HP dielectric probe employing coaxial probe method. It is observed that the dielectric constant increases slowly up to certain moisture contents after which it increases rapidly. It has been observed that the change in loss factor is more at higher frequencies than that at lower frequency.

METHODOLOGY

The soil samples are collected from Western Ghat of Maharashtra state. Soil samples are collected from different locations of agricultural land at the depth of ranging between 0-20 cm. in zigzag pattern across the one site areas. Five pits were dug for each sample. A composite sample of about 3 to 4 Kg representing one site was taken after thorough mixing of all above soil samples. This procedure was repeated while preparing composite samples representing all ten sites covering Western Ghat of Maharashtra. These topsoil samples are first sieved by gyrator sieve shaker (size 425 µm) to remove the coarser particles. The sieved out fine particles are then dried in the hot air oven to a temperature around 110oC for about 24 hours in order to completely remove any trace of moisture. Such dry sample is then called as oven dry or dry base sample when compared with wet samples. The Physical and chemical properties of the soil are measured at soil analysis laboratory.

A study of soil profile supplemented by physical and chemical properties of the soil will give full picture of soil fertility and productivity. Every soil has its natural fertility, which differs from soil-to-soil. In the world, cropping pattern is not same; it changes from one place to another place with response to types of their soil and its characteristics.

Number of soil samples of different physical and chemical properties are used for study. The field capacity (FC) can be approximated by the empirical formula on soil composition [14].

FC= 25.1 - 0.21 (% Sand) + 0.22 (% Clay)

Wilting coefficient (Wp) is calculated by using the Wang and Schmugge model [15].
Wp=0.06774 –0.00064 (% Sand) +0.00478 (%Clay)

The details of the land are given in the table below:

Name of the farmer	Survey No.	Area	Latitude	Longitude
Kondaji Khandu Tokade	35	Deole	19°72"39'	73°65"11'
Dinanath Pandurang Bhagat	53	Take(Ghoti)	19°70"42'	73°61"09'
Gopal Dharma Jagtap	7477	Talegaon	19°68"73'	73°55"92'
Arun Haribhau Jadhav	350/3	Alwand	19°71"59'	73°60"86'
Nivrutti Namdeo Chaudhari	572	Khambale	19°74"06'	73°63"78'
Shravan Savliram Potkule	118	Senvad	19°77"82'	73°67"31'
Dashrath Muralidhar Malunjkar	54	Wadiwarhe	19°86"13'	73°67"87'
Kailas Thakaji Mate	375	Morambi	19°85"10'	73°65"52'
Santu Rama Sarai	316/B	Kushegaon	19°86"42'	73°57"87'
Trimbak Kishan Mahale	29	Wanjole	19°83"60'	73°56"66'

The complex dielectric constant is calculated using the relation

$\varepsilon^* = \varepsilon' - j\varepsilon''$

The two point method described by Altschuler [16] is used for the measurement of dielectric constant (ε′) and dielectric loss (ε′′).

Theory:

The interaction of electromagnetic energy with matter is affected by the characteristics of the material and by the frequency of the electromagnetic energy. Frequency dependent dielectric properties can be characterized in terms of losses of energy due to relaxation mechanisms that operate at different frequencies. The relaxations are caused by different forms of atomic- or molecular-scale resonance [18]. In a soil mixture the relaxation mechanisms may be attributed to the solid material and the pore water as well as to interfacial phenomena.It summarizes some of the different types of relaxation mechanisms that play a role in wet soils. Many geophysical tools for detection of subsurface objects operate in frequency ranges between 0.1 and 10 GHz, which makes bound water relaxation the major resonance mechanism of interest.

Measurement of Dielectric Constant of dry Soil Samples:

The waveguide cell method is used to determine the dielectric properties of the dry soil samples. X-band microwave bench set-up for measurement of dielectric constant of soil samples is used. An automated X-band microwave set-up in the TE10 mode with Reflex Klystron source operating at frequency 9 .56 GHz is used for measuring dielectric constants .PC-based slotted line control and data acquisition system is used for this purpose. The solid dielectric cell with soil sample is connected to the opposite end of the source. The signal generated from the microwave source is allowed to incident on the soil sample. The sample reflects part of the incident signal from its front surface. The reflected wave combined with incident wave to give a standing wave pattern. These standing wave patterns are then used in determining the values of shift in minima resulted due to before and after inserting the sample. Experiments were performed at room temperatures ranged between 25° -35° C. The dielectric constant ε' of the soils is then determined from the following relation:

$$\varepsilon' = \frac{g_\varepsilon + \left(\lambda_{gs}/2a\right)^2}{1 + \left(\lambda_{gs}/2a\right)^2}$$

and

$$\varepsilon'' = \frac{\beta_\varepsilon}{1 + \left(\lambda_{gs}/2a\right)^2}$$

Where, a = Inner width of rectangular waveguide. λ_{gs} = wavelength in the air-filled guide. g_ε = real part of the admittance, β_ϵ = imaginary part of the admittance

The sample holder for X band measurements was fabricated from the standard waveguides available. At the one end of the sample holder a metallic flange was connected, so that it can be connected to the main line and the other end was shorted. Length of X band is 3 cm. Initially, with no dielectric in short circuited line the position of the first minimum D_R in the slotted line

was measured. Now the soil sample of certain length ($l\epsilon$) having certain moisture content was placed in the sample holder, such that the sample touches the short circuited end. Now the position of the first minimum D on the slotted line and the corresponding VSWR, r were measured. This procedure was repeated for another soil sample of same moisture content for another soil sample length ($l\epsilon'$).Now the propagation constant (in the empty waveguide) is calculated as

$$k = \frac{2\Pi}{\lambda g}$$

where λg = 2x (distance between successive minima

with empty short circuited waveguide sample holder). Then, from impedance matching at the air –powder boundary, we obtain

$$\frac{tan\beta\,(DR - D + l\varepsilon)}{\beta l\varepsilon} = \frac{tan\,\beta\varepsilon l\varepsilon}{\beta\varepsilon l\varepsilon}$$

Where Phase factor $\beta = (2\pi / \lambda_g)$, λ_g being the guide wavelength for the waveguide containing air.
The phase factor β_ε for the waveguide filled with the dielectric is given by

$$\beta_\varepsilon = (2\pi / \lambda_0)\{\varepsilon_r \mu_r - (\lambda_0 / \lambda_c)^2\}^{1/2}$$

Here λ_0 represents free space wavelength, λ_c is the cut off wavelength of the waveguide and for the non-magnetic materials μ_r =1. The phase difference φ in the waves travelling in the guide with and without dielectric material in the cell is given by

$$\varphi = 2\beta(" x - l\varepsilon)$$

where x is the shift in minimum.

Voltage standing wave ratio(S) is determined for the load and then magnitude of the reflection coefficient is computed by employing the relation

$$\tau = \frac{s-1}{s+1}$$

In the two point method, the complex dielectric constant is given by

$$C\angle -\psi = \frac{1}{j\,\beta\, l\varepsilon}\,\frac{1-|\tau|e^{j\varphi}}{1+|\tau|e^{j\varphi}} = \frac{tanX\angle\theta}{X\angle\theta} \quad \text{.....(A)}$$

Where, C and Ψ represent respectively the magnitude and phase of the complex quantity in θ represents the∠the middle of Eq. (A) and X solution of this transcendental equation .

This equation provides several solutions for X_θ, which can be found by employing graphs and tables provided for solution of such equations by Hippel [1953] or alternatively the problem can be solved by using a computer based mathematical tool like MATLAB/ M+athematica.

Graphical Representation:

For moisture content below transition moisture in the soil, most water molecules are tightly bound to the soil particles. It is difficult to polarize these bound water molecules and the bulk of water shows a smaller dielectric constant ' ∈ than that of free water [15]. The present values of dielectric constant are in good agreement with the values reported by other authors. It is observed that dielectric constant increases with increase in moisture content slowly up to transition moisture then it increases rapidly with increase in moisture content. The result shows the change in the electrical properties of soil before and after the addition of water.

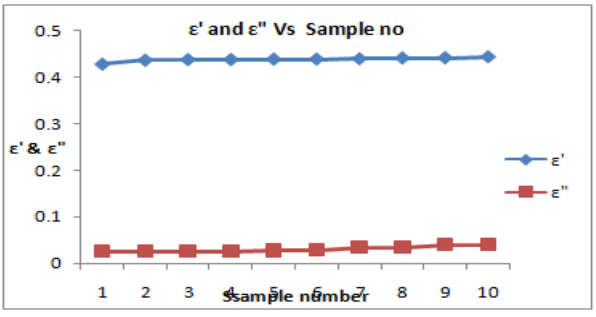

Dry soil

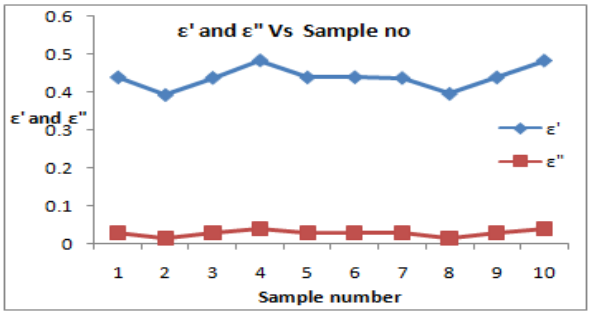

10% moisture content soil

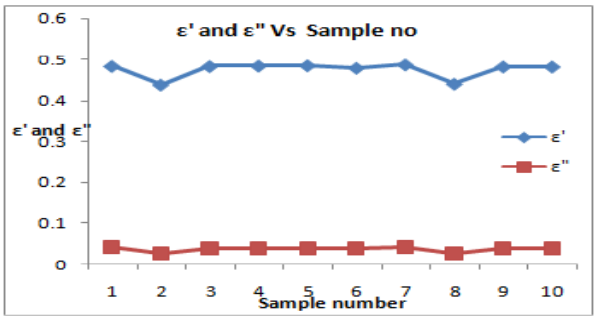

20% moisture content soil

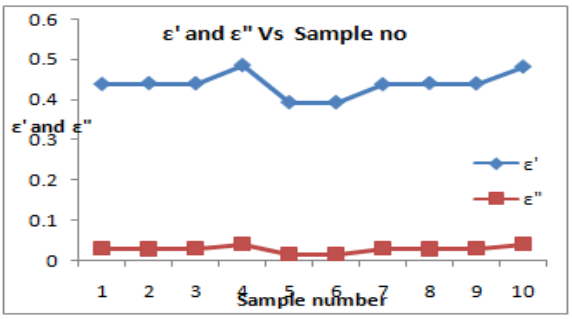

30% moisture content soil

RESULT AND DISCUSSION

Correlation coefficient (r) between soil parameters and regression equations			
Relation of Soil parameters with DC	Correlation Coefficient (r)	Level of significance	Regression Equations
DC(x)-Sand %(y)	0.5123	Positive	y= 31.26x-29.86
DC(x)-Silt %(y)	-0.4682	Negative	y= -21.02+79.66
DC(x)-clay %(y)	-0.4389	Negative	y= -12.18x+50.03
DC(x)-BD (y)	0.3819	Positive	y= 0.132x+1.001
DC(x)-Porosity(y)	-0.4429	Negative	y= -5.963x+63.35

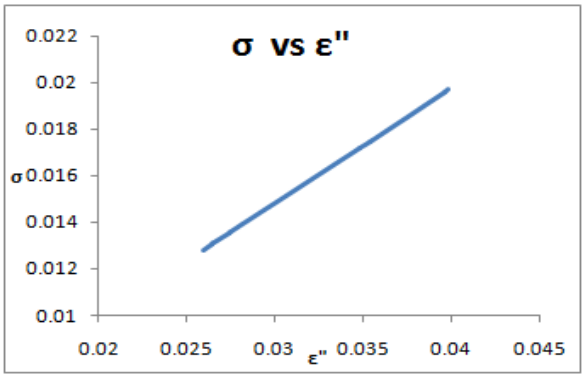

Fig. 2 (a):dielectric loss vs microwave conductivity

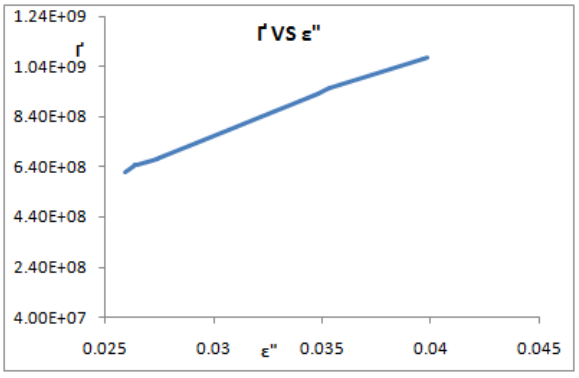

Fig.2 (b) : dielectric loss vs transition temperature

Relation between dielectric constant and percentage of sand, silt, clay in soil :

As per our data, it is observed that dielectric constant of soil has significant positive correlation (r = 0.5123) with percentage of sand and significant negative correlation of dielectric constant with percentage of silt (- 0.4682) and clay (- 0.4389). Also significant negative correlation (-0.4429) with porosity of soil. The graphical of representation shows that, dielectric loss is directly proportional to the ac microwave conductivity and transition temperature.

CONCLUSION

It is observed that there is slow increase in dielectric constant at lower per cent of water content, whereas it increases sharply at higher water content and becomes constant at certain value of water content in soil. The

measurement is very sensitive to volumetric water content. The dielectric constant of Western Ghat of Maharashtra soil is dependent on the texture of soil i.e. the percent content of sand, slit and clay. It is observed that the dielectric constant has significant positive correlation with sand content of soil and negative correlation with clay and silt content of soil. The dielectric constant of Western Ghat of Maharashtra soil depend on the bulk density of soil and hence on porosity and wilting point of soil. Dielectric constant has positive correlation with bulk density of Western Ghat of Maharashtra and negative correlation with their porosity and wilting point.

Conflicts of interest: The authors stated that no conflicts of interest.

REFERENCES

1. Yadav Vivek, Kumar Anil, Sharan Sudeep and Sinha AK. Measurement of Dielectric Behavier of Fertilized soil at Microwave frequency", *Journal of Agricultural Science*, 2009; 1(2).
2. Calla OPN, Applications of Microwave in Remote Sensing", A special Issue from IJCA
3. Bapna PC and Joshi S. Measurement of Dielectric Constant of Soils of Marble Mining Areas of Mewar Region, Rajasthan State at X-band. IJETEE3, 66-69 (May-2013.).
4. Gadan DH, A. DV. Measurement of complex dielectric constant of soils of Gujarat at Xand C-band microwave frequencies. *Indian J. Radio Space Phys*., 2008; 7, 221-229.
5. Chaudhri HC. Dielectric Properties of Soils with Inorganic Matter at S-Band Microwave Frequency. IJCPSl 2014 3, 59-66.
6. Vivek Yadav, Anil Kumar, Sudeep Sharan, A.K.Sinha, "Analysis of Dielectric Properties of Fertilizers (urea and diammonium phosphate) in Aqueous Solution at Different Temperatures in Microwave Frequency", *International journal of the physical sciences*, 2010; 5(16), pp. 2466-2470.
7. Srivastava SK and. Mishra GP. Study of the Characteristics of the Soil of Chhattisgarh at Xband Frequency", *Sadhana*, 2004; 29(4), pp. 343-347.
8. Calla OPN, Vivek Ranjan, Chetan Bohra, Naik GL. Estimation of Dielectric constant of soil from the given texture at microwave frequency", *Indian Journal of Radio and Space Physics*, 2004; 33, pp. 196-202.
9. Rajesh. Mohan. R, SM., Mohanan P. Study and Analysis of Dielectric Behavior of Fertilized Soil at Microwave Frequency. *Euro. J. Adv. Engg. Tech*., 2015; 2, 73-79.
10. Bilskie J. Using dielectric properties to measure soil water content, *Sensors Mag*., 1980l 14, 26–32.
11. Behari J. Frequency dependent variation of dielectric parameters of wet soil, Microwave measurement techniques and applications, pp. 71–79, *Anamaya Publishers*, New Delhi (2003).

IRJSE *Int. Res. J. of Science & Engineering,* 2018; Special Issue A2: 83-88
ISSN: 2322-0015
SJIF Impact Factor 4.11
UGC Approved Journal No. 63628
RESEARCH ARTICLE OPEN ACCESS

Effects of Short-term Magnetic Field on Germination and Growth of Plants

Ashutosh Khade and Mancharkar Avinash

P.G. Department of Physics, New Arts, Commerce & Science College, Parner, 414302, India
Email: ask16590@gmail.com

Manuscript Details
Available online on http://www.irjse.in
ISSN: 2322-0015

Editor: Dr. Arvind Chavhan

Cite this article as:
Ashutosh Khade and Mancharkar Avinash. Effects of Short-term Magnetic Field on Germination and Growth of Plants, *Int. Res. Journal of Science & Engineering,* January 2018; Special Issue A2: 83-88.

ABSTRACT

The Numerous studies have been carried out to investigate the effect of short-term magnetic field exposure on plants, where seedlings (4–5 days old) were continuously exposed and grown under short exposure condition. Here, we have used a novel 'short-term magnetic field exposure experimental method' where imbibed seedlings were exposed to higher gauss values ranging from 300 gauss to 0.2 Tesla for a short interval time of 10 minutes. Changing patterns in peas and chick-peas germination and growth, along with various photo-synthetic and biochemical parameters were studied. Results revealed the significant inhibition of germination and growth in short-term magnetic field exposure treated seeds over control. Photosynthesis parameters such as chlorophyll content were found to be affected significantly in 5 days old seedlings exposed to short-term magnetic field exposure treatment. In order to investigate the cause of observed inhibition, we examined the α-amylase activity and antioxidative enzyme activities. α-amylase activity was found to be inhibited, along with the reduction of sugars necessary for germination and earlier growth in shortterm magnetic field exposure. In addition, the health status was measured by leaf color, spots and the stem curvature and the death rate. The result showed the magnetism had a significant positive effect on plant growth. Plant seeds under the influence of magnetic field had higher germination rate and these plants grew taller, larger and healthier.

Keywords: Hall-probe Instrument, Pisum-sativum, Cicer-arietinum, Chlorophyll content, Photosynthesis, Short-term magnetic field

INTRODUCTION

Plants have adapted themselves to the ever existing force of gravity (1 *g*) on earth for eons of years. Any change in the magnitude of gravity as result in magnetism therefore affects the plant growth and development. In recent years, gravity as well as magnetism driven changes in plant productivity has remained an exciting research area in the mainstream of plant physiology research. To understand the role of changing magnetism on plant behavior various systems have been developed. In most of the earlier reports, three to five days old seedlings were exposed to higher *gauss* values up to 3000 *gauss* for longer durations and effects were studied. For instance, suppression in elongation of both epicotyls and roots as well as inhibition in lateral root growth was observed in peas centrifuged at 140 *gauss*, 370 *gauss* and 1050 *gauss* for five days continuously. The decrease in percentage germination and growth was observed in wheat exposed to basipetal magnetic field for three days at 25 ^{o}C in the dark. Stem elongation in 5 mm *Arabidopsis thaliana* inflorescence stems was suppressed, while dry weight of the inflorescence stems increased, when exposed to 300 *gauss* for 24 hrs in dark at 25 $^{\circ}$ C. Such approach does not provide any information about the magnetic field effect on germination. Moreover, the duration of field exposure were considerably high ranging from 12 hrs to 21 days. Many studies have reported a reduction in percentage germination under field exposure environment, which has been maintained for a longer duration, but none have explained the possible cause for such reduction. Also, the influence of higher *gauss* values on important aspects of photosynthesis process such as chlorophyll pigment content, net photosynthetic rate, efficiency of photosystem PSII etc. have not been reported.

This showed that the growth and yield of lettuce could be improved by treatment of its seeds before they were grown, using rectified sinusoidal non-uniform electromagnetic fields. It was observed that magnetism has effects on lettuce at the nursery, vegetative, and maturity stages, including a significant increase in root length and shoot height, a greater growth rate, and a significant increase in plant height, leaf area, and fresh mass. Positive biological effects of magnetism on sunflower and wheat seedlings weights were reported. Further data show that the magnetic field induced by the voltage of a specific waveform enhanced or inhibited mung bean growth, depending on the frequencies, which suggests that the magnetic field on plant growth may be sensitive to the waveform and frequency of the source electrical voltage. The effect of static magnetic field on plant growth has also been studied. We have found that static magnetic field accelerated germination and early growth of wheat and bean seeds, obtained similar results with chickpeas; furthermore, they found that the responses of the plant to static magnetic field varied with field strength and duration of exposure with no particular trend. However, as indicated by a literature review, weak magnetic field exhibited negative effects on plant growth, such as inhibition of primary root growth, in some cases. For instance, exposure to magnetic field inhibited early growth of radish seedlings with decrease in the weight and leaf area. An interesting result is that the biological effect of a magnetic field is different between the south and north poles, as illustrated by a study, which showed that radish seedlings had a significant tropic response to the south pole of the magnet, but insignificant response to the North Pole. It is theorized that the south pole of the magnet enhances plant and bacterial growth by conferring energy, whereas the north pole retards their growth. Thus, it is possible to utilize the magnetic north pole against infections or tumor growths. Morphological anomalies in pollen tubes of a particular plant exposed to magnetism were observed, which raises an important question of whether magnetism can cause gene mutation and cancer. This issue is still controversial and demands more research evidence before any conclusion can be drawn.

Therefore, the aim of the present study was to analyze the effect on the germination and various physiological parameters, when seeds were exposed to short-term magnetic field. Various physiological and biochemical parameters such as germination, growth, chlorophyll content, photosynthesis, chlorophyll fluorescence as well as antioxidative response were studied. As per our knowledge such kind of work has not been carried so far.

METHODOLOGY

Seeds Selection and Short-term magnetic field exposure Treatment Pea seeds ***(Pisum sativum)*** and chick peas ***(Cicer arietinum)*** were procured from the local market of Parner city (MH). They were treated with 0.5 % systemic fungicide (Uthane M-45, United Phosphorus Limited), washed thoroughly and imbibed in distilled water (D.W) for 24 hours. After imbi-bition these seeds were subjected to short-term magnetic field treatment viz.1000 gauss 1500 gauss, 2000 gauss for 10 min each at 25 ◦ C, using a Hall probe Method. Light intensity was maintained as 15 µE $m^{-2}s^{-1}$. All the measurements were carried out on 5th day post sowing with emerged out shoots.

Estimation of Embryo Viability

Immediately after 10 min of short-term field treatment, control and treated seeds were stained with 1 % tetrazolium solution to check the embryo viability.

Seed Germination, Growth and Vigor Index Measurement:

Percentage germination, root length, shoot length, fresh weight of shoot and root were measured for both control and short-term magnetic field treated samples on fifth day from sowing. Vigor index of the seedlings was calculated by using the relation,

Vigor Index = Average total height of seedlings x % seed germination

Enzyme Extraction and Assays

Five days post short-term magnetic field exposure, control and short-term field treated seeds without leaf blades were homogenized in ice cold 0.05 M phosphate buffer (pH 6.8) containing EDTA (0.5 mM). Each homogenate was centrifuged at 10,000 x *g* for 10 min at 4 ◦C. The supernatant was used for enzyme assays.

a-Amylase activity, catalase activity (CAT) and guaiacol peroxidase (GPX) activity were determined as described by Sadasivam and Manickam with some minor modifications. One unit of Amylase activity was defined as the amount of enzyme required for liberating 1 mg of maltose per min at 37 ◦ C. Catalase activity was measured by the decrease in H_2O_2 concentration in a reaction mixture containing 0.05 M phosphate buffer (pH 7.0), enzyme extract & H_2O_2 at 430 nm. Guaiacol Peroxidase activity was determined as the rate of oxidation of guaiacol to tetraguaiacol that is being monitored by recording the absorbance change at 436 nm for one min. Protein concentration was determined according to using bovine serum albumin standard.

Biochemical Quantification of Non Structural Carbohydrate Reserve:

Starch content and total reducing sugars were estimated from caryopses of five-days old seedlings raised from short-term magnetic field and control as described by Sadasivam and Manickam

Estimation of Chlorophyll Content

Chlorophyll was extracted from shoots of five days old seedlings raised from control and short-term magnetic field exposed seeds according to the method of Absorption spectra of total chlorophyll were recorded by using UV-Visible spectrometer. Chlorophyll a, b and total chlorophyll contents were calculated using Arnon's formula.

Photosynthesis and Chlorophyll Fluorescence Parameter

Photosynthesis parameters were recorded with the help of TPS-2, a portable photosynthesis system (PP systems, USA). Shoots of five days old peas seedlings were placed in the leaf cuvette (PLC4-B type, area 2.5 cm^2) and pho-tosynthesis rate (P_N), transpiration rate (Evap), stomatal conductance (G_S) and intracellular CO_2 concentration (C_{int}) were measured at PAR intensity of 600 µmol $m^{-2}s^{-1}$.

Before recording chlorophyll fluorescence, shoots were dark adapted for 15 minutes. The chlorophyll fluorescence transient was induced by applying a pulse of saturating red light (peak at 650 nm, maximum intensity > 3000 µmol m^{-2} s^{-1}) at the sample surface. The LEDs are focused via lenses onto the leaf surface to provide even illumination over the area of leaf exposed by the leaf clip (4 mm diameter). Fluorescence parameters defining the photochemistry of PSII such as maximum quantum efficiency of PSII photochemistry (Fv/Fm), performance index on the basis of absorption (PI) and maximal photochemical

efficiency of PSII (Fv/Fo) were measured using Handy PEA (Hansatech Instruments Ltd, England).

Statistical Analysis

Each experiment was done in triplicates. For each measurement, the mean values and the standard error of the means (SE) were calculated. The significance of differences between control and treatment was analyzed by the Student's t-test.

RESULT AND DISCUSSION

In the present study we have analyzed the post effects of short-term magnetic field exposure on peas and chick peas germination and growth parameters. The results provide physiological and biochemical evidences suggesting that seeds are able to perceive magnetic field stress within short duration interval of 10 min, can memorize and respond to it upto five days.

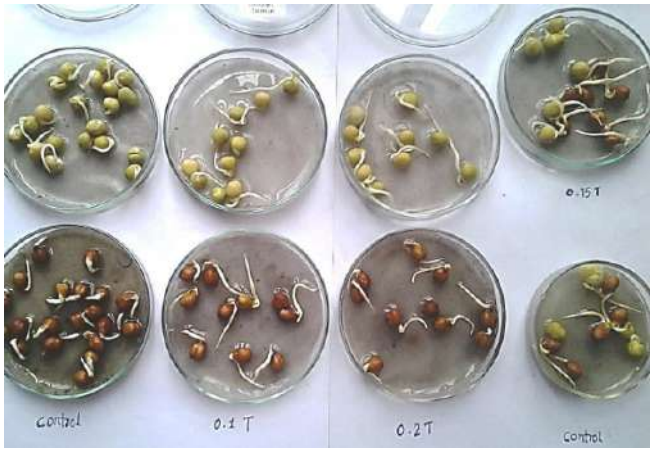

Fig 1: The unhealthy changes in control and experimental groups at the end of the fourth week. *Embryo Viability, Caryopses Germination, Growth and Vigour Index.*

Embryo viability test was performed to rule out the pos-sibility of physical damage to the seeds exposed to field values.Result showed that seeds were 100 % viable even after exposure to field value and have ability to grow. Fig.1 shows the growth of five days seedlings raised from control and short-term magnetic field exposed seeds. No germination was observed in 2500 gauss.Any change in the magnitude of field is thus expected to affect seed physiology. In the preliminary experiments it was found that germination and growth was resistant to the inhibitory effect of short-term magnetic field up to 400 *gauss*. This could be due to the relatively harder seed coat which might be shielding the effective magnetic force experienced by the embryo. It is only after 500 *gauss*, that the inhibitory effects on germination and growth related parameters were observed.

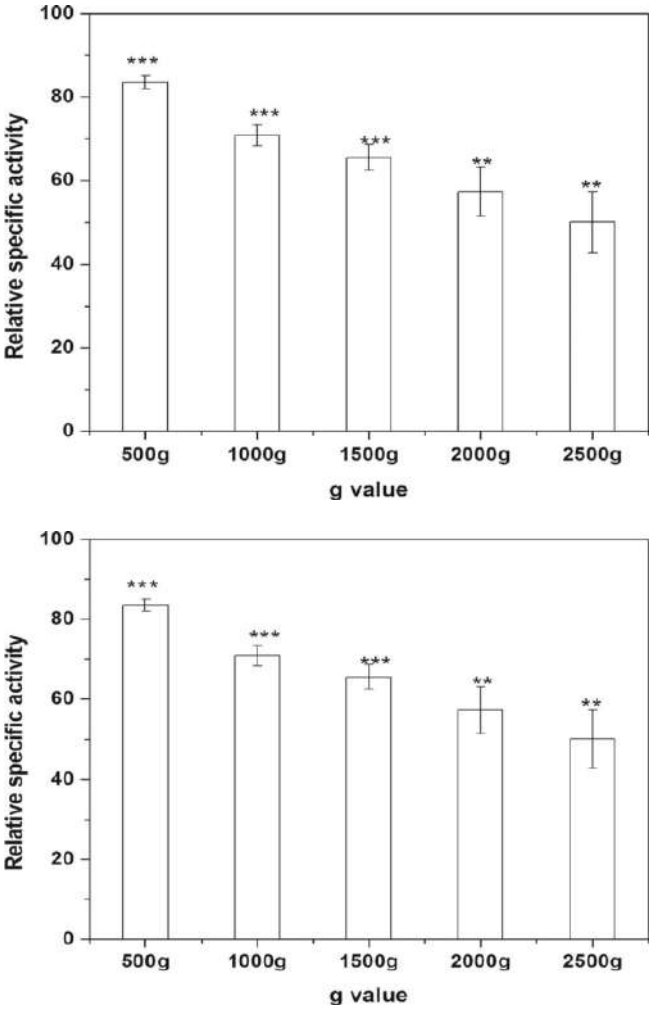

Fig 2: Effect of short-term magnetic field on relative *a*-amylase activity in seeds (U g^{-1} of seed). Percent relative activity was calculated with respect to control Chlorophyll Content.

After germination, degreening, a major event occurs in seedlings, where etioplasts get converted to chloroplast. At this stage, chlorophyll is synthesized with a greater rate.

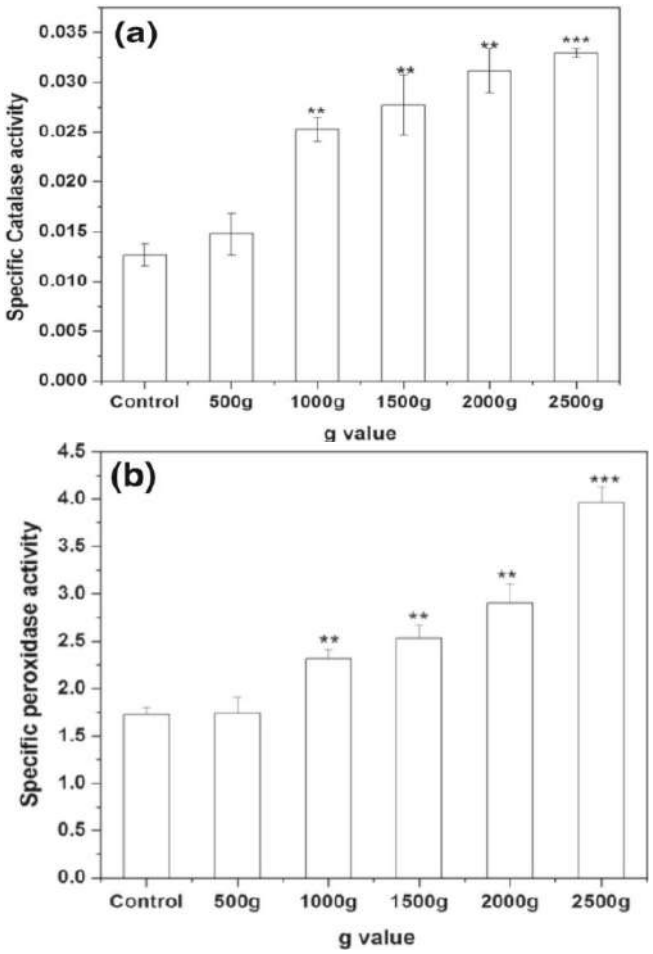

Fig. 3 **a**. Effect of short-term magnetic field exposure on Catalase specific activity (U g^{-1} of seed) in pea seeds. **b** Effect of short-term magnetic exposure on Guaiacol peroxidase specific activity (U g^{-1} of seed) in chick pea seeds.

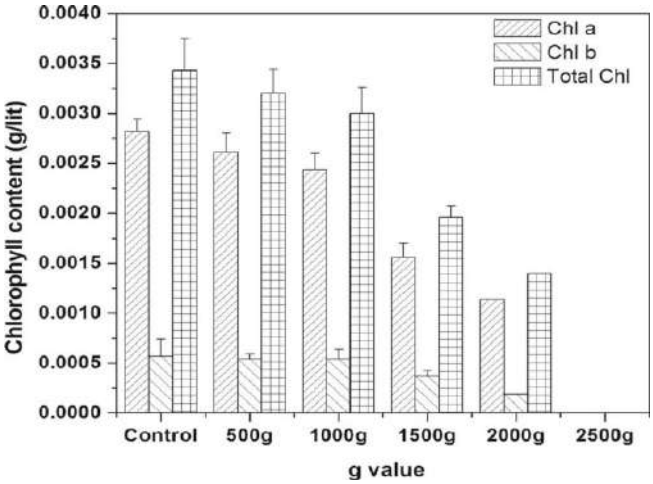

Fig. 4 Chlorophyll contents (Chl **a**, Chl **b** and total Chl, g/ltr) in shoots of 5 days old seedlings raised from control and short-term magnetic field exposed seeds.

Therefore, inhibition at the stage of germination can have adverse effect on the greening process of plants. Moreover, oxidative stress is responsible for the inhibition of chlorophyll biosynthesis.

We therefore investigated the chlorophyll concentration in short-term magnetic field treated seedlings with control. Major photosynthetic pigments, chl-a and chl-b, were significantly decreased in seedlings raised from short-term magnetic field exposed. Decrease in chlorophyll content was 7 %, 14 %, 45 % and 60 % in 500 *gauss*, 1000 *gauss*, 1500 *gauss* and 2000 *gauss*, respectively as compared to the control.

CONCLUSION

Present study has shown for the first time that imbibed seeds could sense and respond to magnetic field exposure given for a very short period of 10 min, without any physical damage. Further, they can retain this memory even while growing less than 1 *gauss* conditions post short-term hyper-gravity treatment. In conclusion, short-term magnetic exposure of 10 min might disrupt the *a*-amylase activity of germinating peas, which probably restricts the supply of sugars necessary for the embryo growth and development. Further, short-term magnetic field exposure reduced chlorophyll content and thus, the photosynthetic activity of growing peas seedlings. This can be related to the enhanced antioxidative enzyme activity in short-term magnetic field exposed seeds. Though such high *gauss* values used in the experiments do not exist in nature, situations may occur where hydrostatic forces of this order may exist. Moreover, without any special modification in the instrument design of centrifuge, it is possible to study the effect of short-term magnetic field on plants. This method in itself provides a simple and novel approach to study magnetic field effects on plants. As per our knowledge, this kind of study has not been reported previously.

Conflicts of interest: The authors stated that no conflicts of interest.

REFERENCES

1. Belyavskaya NA. Biological effects due to weak magnetic field on plants. *Adv Space Res*.,2004; 34: 1566-74.
2. Dattilo AM, Bracchini L, Loiselle SA, Ovidi E, Tiezzi A, Rossi C. Morphological anomalies in pollen tubes of Actinidia deliciosa (kiwi) exposed to 50 Hz magnetic field. *Bioelectromagnetics*. 2005; 26: 153-6.
3. De Souza A, Sueiro L, González L.M, Licea L, Porras EP, Gilart F. Improvement of the growth and yield of lettuce plants by non-uniform magnetic fields. *Electromagn Biol Med*.,2008; 27:173-84.
4. Fischer G, Tausz M, Kock M, Grill D. Effects of weak 16 3/2 Hz magnetic fields on growth parameters of young sunflower and wheat seedlings. *Bioelectromagnetic*s, 2004; 25:638-41.
5. Huang HH, Wang SR. The effects of inverter magnetic fields on early seed germination of mung beans. *Bioelectromagnetics*. 2008; 29:649-57.
6. Vashisth A, Nagarajan S. Exposure of seeds to static magnetic field enhances germination and early growth characteristics in chickpea (Cicer arietinum L.). *Bioelectromagnetics* 2008; 29: 571-8.
7. Aarti, D., Tanaka, R., Ito, H., Tanaka, A.: High light inhibits chloro-phyll biosynthesis at the level of 5-aminolevulinate synthesis during de-etiolation in cucumber (*Cucumis sativus*) cotyledons. Photochem. Photobiol. 2007; **83**, 171–176.
8. Arnon, D.I.: Copper enzymes in isolated chloroplasts Polyphenoloxi-dase in Beta vulgaris. *Plant Physiol*. 1989; **24**(1), 1–15.
9. Barjaktarovi´c Z, Nordheim A, Lamkemeyer T. Fladerer C, Madlung J, Hampp R. Time-course of changes in protein amounts of specific proteins upon exposure to hyper-*g*, 2-D clinorotation and random positioning of Arabidopsis cell cultures. *J. Exp. Bot*. 2007; **58**(15–16), 4357–4363.
10. Beck E, Ziegler P. Biosynthesis and degradation of starch in higher plants. *Annu. Rev. Plant Physiol. Plant Mol. Biol*.1989; **40**, 95–117.
11. Jagtap SS, Vidyasagar PB. Effects of high gravity (g) values on growth and chlorophyll content in wheat. *Int. J. Int. Biol.* BBB10 special issue, 2010; **9**(3), 127–129.

IRJSE *Int. Res. J. of Science & Engineering,* 2018; Special Issue A2 : 89-93 SJIF Impact Factor 4.11
ISSN: 2322-0015 UGC Approved Journal No. 63628
RESEARCH ARTICLE **OPEN ACCESS**

Optimization of Preparative Parameters for the Electrode position of Cdse Films for Photo electrochemical Solar Cell Applications

Dhanwate SV[1*], Kokate AV[2], Kulkarni HR[3]

[1]Swami Muktanand College of Science Yeola (Nashik) India
[2]Bhujbal Knowledge City, MET's Institute of Technology, Nashik India
[3]K. J. College of Engineering and Management Research, Pune, India.
Email: dhanwatesv67@rediffmail.com

Manuscript Details
Available online on http://www.irjse.in
ISSN: 2322-0015

Editor: Dr. Arvind Chavhan

Cite this article as:
Dhanwate SV, Kokate AV, Kulkarni HR. Optimization of Preparative Parameters for the Electrode position of Cdse Films for Photo electrochemical Solar Cell Applications, *Int. Res. Journal of Science & Engineering,* January 2018; Special Issue A2 : 89-93.

ABSTRACT

The experimental results on the optimization of reaction parameters such as bath temperature, deposition time and pH dependence of structural, optical and morphological properties CdSe nanocrystals in the electro-deposited films. The depositions were carried out on two different substrates viz. stainless steel strips and fluorine doped tin oxide (F.T.O.). The growth process and characterization of CdSe crystals are determined by UV–Vis spectroscopy, X-ray powder diffraction (XRD) and scanning electron microscopy (SEM). Also, the influence of reaction conditions on the photoelectrochemical (PEC) of CdSe nanocrystals photoanodes in combination with graphite as a counter electrode and polysulphide as a redox couple was studied systematically. This demonstrates that low reaction temperature and acidic bath are favourable for the formation of high quality CdSe films to explore them in PEC cells.

Keywords: XRD, SEM, PEC, Thin Films, CdSe

INTRODUCTION

Thin film science is a reasonably early and ever rising concept in the field of nanotechnology [1]. Since last decade thin film technology have been widely studied for the deposition of films of various chalcogenides due to their direct applications in various fields such as photovoltaic [2], surface engineering [3], metallurgical coating[4], magnetic science[5], telecommunications [6], optoelectronic devices [7], radiation detectors [8], laser materials[9], thermoelectric devices, solar energy converters for energy harvesting purposes. Be it in the past or the present, energy has played very vital role in the social and economic progress of the man. Besides, the rising population, intense industrialization and rapidly changing life styles have increased energy demands extremely. Off late, about 80 % of energy consumed is belongs to the natural sources and any major changes in this energy consumption scenario is not foreseen in the near future. Instead, the global energy demand is expected to increase by up to 60 % and CO_2 emission by 70 % by 2020 [9] which, put pressure on an already stressed energy system. Therefore, it is of great importance to develop new alternative sources like bio-fuels, wind, hydroelectric and solar energy. As the energy influx of Sun on the planet earth is about $4.3x10^{20}$ J per hour energy from the Sun dwarfs all other sources, whether they are conventional or non-conventional ones. In addition, it does not have any kind of environmental hazards, since there is no concern of release of hazardous waste and toxic gases associated with access of solar energy. Thus, among all above discussed applications of semiconductor thin films, now days; more emphasis is given to photovoltaic or solar energy conversion technology foe energy harvesting purposes.

Nonetheless, effect of post annealing of optimized electrodeposited CdSe photoanodes have been not studied widely. In view of this, CdSe, a binary chalcogenide semiconductor, is having energy band gap around 1.04 eV with high absorption coefficient, which makes it a suitable candidate as a sensitizer in PEC cells is studied systematically.

METHODOLOGY

To prepare CdSe thin films all of A. R. Grade chemicals (supplied by Sharad Chemicals, Pune) such as $(CH_3COO)_2$ $Cd.2H_2O$, SeO_2, EDTA, $(CH_2(OH)CH_2(OH))$ and Ethylene glycol. All the solutions with optimized concentration and volume were prepared in Ethylene glycol (CH_2 (OH) CH_2(OH). For the electrodeposition of CdSe firstly the 10 ml of 0.01 M $(CH_3COO)_2$ $Cd2H_2O$ was peprepared in ethylene glycol. Secondly, the 1 ml 0.01 M solution of EDTA is prepared under constant stirring and then added to the first bath. Further, 10 ml of 0.005 M SeO_2 prepared and then added to the reaction bath for the final deposition.

As Electrodeposition technique uses electrically conducting stainless steel strips of a size 1x 4=4cm^2 and fluorine doped tin oxide (F.T.O.) coated glass substrates for the deposition of thin films. It requires smooth and clean substrate to have uniform and adhesive electrodeposition of films [32-35]. The metallic and glass substrates were washed using Labolene solution and tap water. Also the substrates were etched subsequently by 25% dilute Hydrochloric acid for 20 to 30 seconds and cleaned with the help of ultrasonication. Finally the substrates were dried in the vapors of alcohol for the final deposition.

RESULTS AND DISCUSSION

Optimization of deposition potential:

Initially, the elementary depositions of Cd and Se were separately carried out with their optimized concentrations, volumes and deposition potentials, respectively. The current versus voltage (w.r.t SCE) curves (polarization curves) were plotted for examining the deposition potentials. Similarly, electrodeposition of CdSe thin film was carried out with suitable bath compositions and different polarization curves were obtained for CdSe thin films at various bath temperatures. The so obtained polarization curves for Cd and Se and CdSe are shown in figure 1 and the respective deposition potentials for various bath temperature are tabulated.

Table 1: Deposition Potentials for various bath compositions

Sr. no.	Bath Composition	Bath temperature (℃)	Deposition potential for SS (min)	Deposition potential for FTO (min)
1	$(CH_3COO)_2Cd2H_2O$ (0.01M)	30	-0.93	-1.77
2	SeO_2 (0.005M)	30	-2.56	-2.80
3	$(CH_3COO)_2Cd2H_2O$ (0.01M, 10ml) + EDTA (0.1M, 1 ml) + SeO_2 (0.005M, 10 ml)	30	-1.78	-1.80
4	$(CH_3COO)_2Cd2H_2O$ (0.01M, 10ml) + EDTA (0.1M, 1 ml) + SeO_2 (0.005M, 10 ml)	40	-1.86	-1.42
5	$(CH_3COO)_2Cd2H_2O$ (0.01M, 10ml) + EDTA (0.1M, 1 ml) + SeO_2 (0.005M, 10 ml)	50	-1.20	-1.41
6	$(CH_3COO)_2Cd2H_2O$ (0.01M, 10ml) + EDTA (0.1M, 1 ml) + SeO_2 (0.005M, 10 ml)	60	-1.17	-1.40
7	$(CH_3COO)_2Cd2H_2O$ (0.01M, 10ml) + EDTA (0.1M, 1 ml) + SeO_2 (0.005M, 10 ml)	70	-1.15	-1.42
8	$(CH_3COO)_2Cd2H_2O$ (0.01M, 10ml) + EDTA (0.1M, 1 ml) + SeO_2 (0.005M, 10 ml)	80	-1.10	-1.33

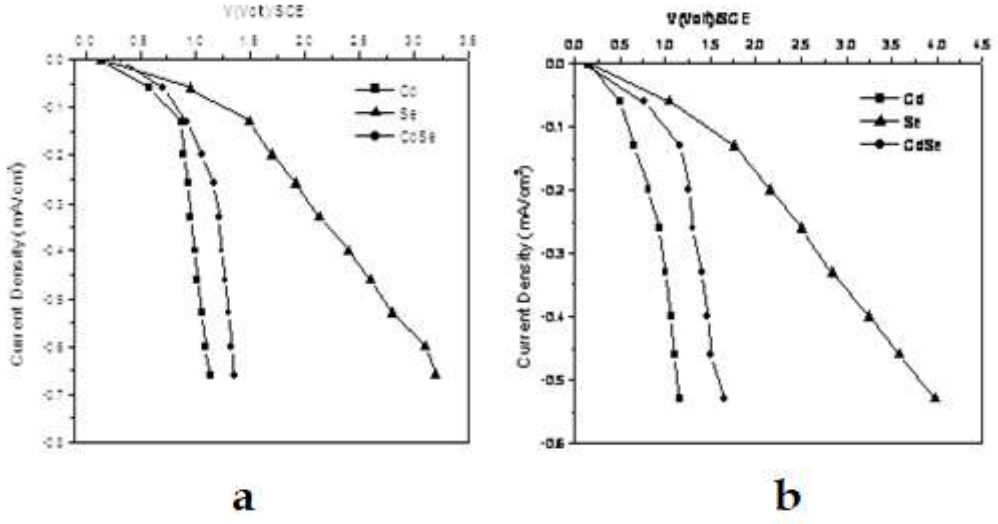

Fig. 1: Cathodic polarization curves for Cd and Se and CdSe on a) SS b) FTO

It is observed from Table.1 that, as the bath temperature increases, the potential required for deposition of films increases which further leads towards the increase in the grain size during deposition. The rise in the temperature beyond 40℃ causes the dissociation of the complex and causes the rise in concentration of simple ions [36]. It leads to the discharge of ions at a low potential. Thus, increase in temperature of the bath enhances the rate of diffusion and raises the motilities of ions and along with the conductivity of the bath [37]. As a result of this, in the present case, temperature of 40℃ is considered to be the optimized temperature.

Optimization of deposition time though thickness measurement:

To optimize the deposition time for the deposition of films, depositions were carried out for various time intervals. The plot of thickness Vs time is shown in the figure 2 (a and b) and the corresponding data is shown in Table 2.

Table 2: Thickness measurement

Sr. No.	Deposition time (min.)	Thickness (SS) µm	Thickness (FTO) µm
1	20	1.31	1.01
2	25	2.63	1.54
3	30	4.41	1.99
4	35	5.09	3.32
5	40	4.69	3.15

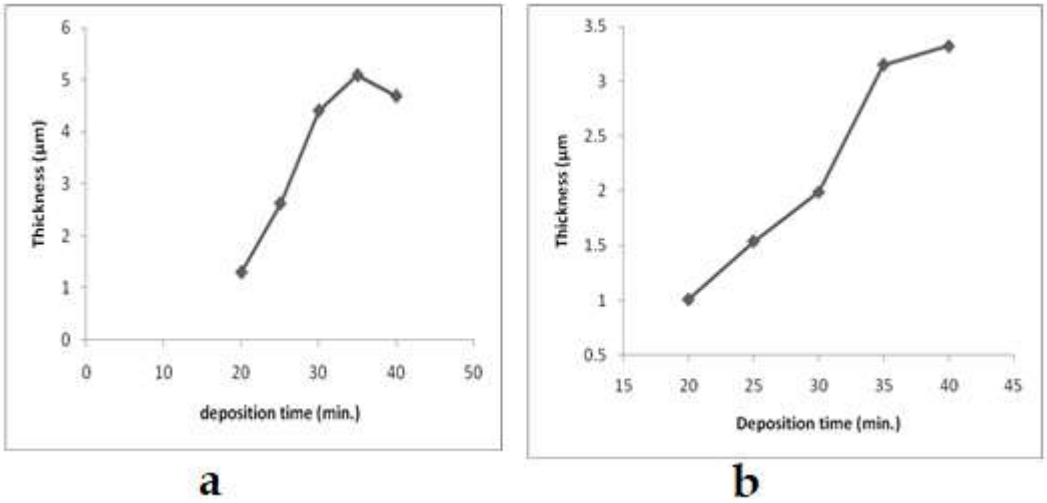

Figure 2(a): Change of Thickness with different deposition time on SS substrates
(b): Variation of Thickness with deposition time on FTO coated glass substrates

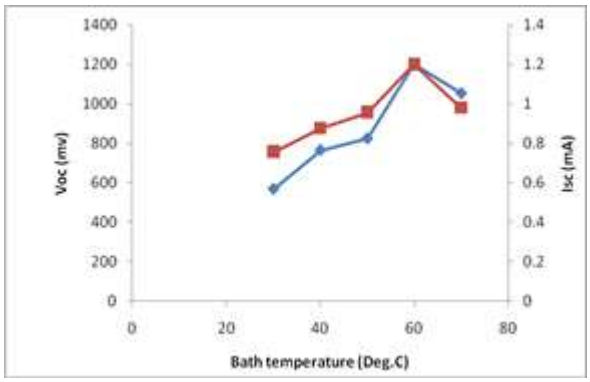

Figure 3: Variation of Isc and Voc with temperature of bath taken on SS substrates

Thus, as discussed earlier, the further electrodeposition of CdSe films were carried out for the deposition time of 35 min and deposition potential obtained for the bath temperature of 40℃ is used to obtain good adherence and appearance.

The X ray diffraction analysis for CdSe films on to SS and FTO glass substrates were recorded within the span of angle b etween 10° to 100° using Philips, PW 1710 diffractometer. Optical absorption studies were carried out by using UV- VIS- NIR spectrometer. (Hitachi, Japan, Model no. 330). JEOL, JXA – 840 reflection scanning electron microscope with EDAX arrangement model was to study the surface morphology and elemental composition for the annealed and as-deposited CdSe films. The Photovoltaic properties of the CdSe / 0.1 M polysuphide/graphite (2 x 4 x 0.3=2.4 cm^3.) PEC cells were studied systematically. The photovoltaic parameters such as current density, I_{sc} and open circuit voltage V_{oc} were recorded at different load resistance R_L. Fill factor and power conversion efficiency (η) of the electrodeposited CdSe material were also measured for the fabricated PEC cells.

Effect observed of Bath Temperature onto Photoelectrochemical Properties

The variation in Isc and Voc is studied for photo electrodes deposited at different bath temperatures and the variations are depicted in figure 3. From the curves, it is observed that, Isc increases initially with bath temperature. However, it attains its maximum value at particular temperature and then starts to decreases with further rise in temperature. This is in agreement with the earlier reports in the literature. The relatively observed higher value of Isc can be attributed to shifting of the materials towards stoichiometry. However, the observed decrease in the Isc may be attributed to the increase in the deposition rate as a result of more thermal energy supplied to the ions of electrolyte due to large temperature of bath. Thus, in present case, at a particular value of the temperature, the composition of the material formed is stoichiometric giving good results of the CdSe based PEC performance. In addition, From the fig.3 similar trend is observed for Voc for the CdSe based PEC cells.

Similarly, the effect of temperature of bath on the PEC properties of photoelectrode CdSe by using different substrates is studied by using the photoelectrodes prepared from the electrolytic bath of different temperatures.

CONCLUSION

In the present study, for the electrodeposition of the CdSe films various preparative parameters such as bath temperatures, pH, deposition time and deposition potential were optimized to obtain good quality films. In addition, the as-deposited films were annealed at three different temperatures to study their structural and optical properties to decide their suitability for photoelectrochemical cell applications. The results presented in the work illustrate the influence of reaction time, pH and bath temperature including the effect of annealing on the photovoltaic performance of CdSe based PEC cells.

Conflicts of interest: The authors stated that no conflicts of interest.

REFERENCES

1. Cherie Kagan, Paul Andry, Kagan R.Kagan, "Thin Film Transistors" Marcel Dekker Inc., New York (2003) 428.
2. Yoshihiro Hamakawa, Thin-Film Solar Cells: Next Generation Photovoltaics and Its Applications, Springer (2004) 244.
3. Ch.-H. Fischer, M. Bär, Th. Glatzel, I. Lauermann and M.C. Lux-Steiner, Solar Energy Materials and Solar Cells, 90 (2006) 1471.
4. Maury F, L. Gueroudji and C. Vahlas, Surface and Coatings Technology, 86 (1996) 316.
5. Terentiev AN, Moffat SH, Hughes RA, Preston JS, van Lierop J and HarrisonJP, *Cryogenics*, 37(1997) 113.
6. Ziyad Elalamy, Emmanuel Drouard, Theresa Mc. Govern, Ludovic Escoubas, Jean- Jacques Simon and François Flory, Optics Communications 235 (2004) 365.
7. Miguel A. Contreras, Manuel J. Romero and R. Noufi, Thin Solid Films 511(2006) 51.
8. Lakew B, S. Aslam, H. Jones, B. Moeckly, J. Brasunas and D. Franz, Physica C: Superconductivity, 440(2006) 1.
9. Monica Sorescu, L. Diamandescu and A.Grabias, Intermetallics, 14 (2006) 780.

IRJSE *Int. Res. J. of Science & Engineering,* 2018; Special Issue A2 : 94-97 SJIF Impact Factor 4.11
ISSN: 2322-0015 UGC Approved Journal No. 63628
RESEARCH ARTICLE **OPEN ACCESS**

Impacts of Meteorology on Surface Ozone Variability at Shevgaon

Kakade AD

New Arts, Commerce and Science College, Shevgaon Dist:Ahmednagar (MS) India-414502
Email: adk.kakade@rediffmail.com

Manuscript Details
Available online on http://www.irjse.in
ISSN: 2322-0015

Editor: Dr. Arvind Chavhan

Cite this article as:
Kakade AD. Impacts of Meteorology on Surface Ozone Variability at Shevgaon , *Int. Res. Journal of Science & Engineering,* January 2018; Special Issue A2 : 94-97.

ABSTRACT

Measurement of surface ozone (O_3) mixing ratio was made from January 2016 to December 2016 in Shevgaon (19.35◦N, 75.22◦E,1669 feet above sea level), India. The monthly average of daytime maximum of O_3 mixing ratio ranged from 17 to 68 parts per billion by volume (ppbv) with an annual average of about 23.5 ppbv. The diurnal variations of O_3 is characterized by maximum of 38.8 ppbv in the afternoon and minimum of 8.4 ppbv early in the morning. Monthly average maximum air temperature and relative humidity (RH) are 33.2 0C and 73% respectively.

Keywords: ozone surface, diurnal variation, meteorological parameters.

INTRODUCTION

Surface ozone O_3 is one of the key trace gases in the atmosphere. Air pollution and climate change have been shown to represent major threats to global food security. Air pollutants like surface ozone that negatively affects human health and agriculture crops yield[1]. In India, a few O_3 measurements studies have been reported [2-4]. They have reported that high O_3 mixing ratio between 34 and 151 ppbv in urban sites. Many studies around the globe have shown that the O_3 in rural locations near the industrial areas have increased significantly[5-6]. The human activites are responsible to increase the O_3 concentrations near the earth surface. In this present

study, we report the diurnal variation of O_3 measured at Shevgaon in the light of meteorological parameters, such as air temperature, RH, cloud cover etc.

Location and Measurements

Fig. 1 represents a map of India with the measuring site-Shevgaon and other major cities. The measuring site is surrounded by four sugar industries namely Gangamai sugar factory, Kedareshwar sahakari sugar factory, Dnyaneshwar sahakari sugar factory, and Shri Vrudheshwar sahakri sugar factory, each is at a distance of 25 km from measurement site and Jayakwadi dam is located on north side .

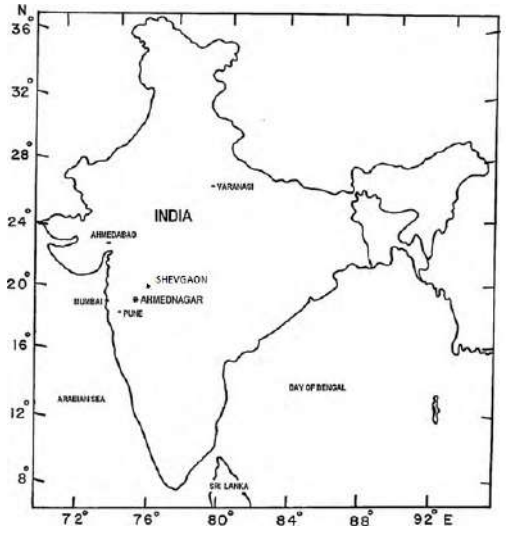

Fig. 1 Location map of the measurement site at Shevgaon.

The sampling site of O_3 is surrounded by cultivated field and some small and big trees. The present population of Shevgaon is about 0.2 millions as per 2011India census and vehicular p opulation nearly 0.02 millions. Aurangabad and Ahmednagar are the nearest metropolitan urban city located at about 80 and 70km in the northeast and south direction.

METHODOLOGY

The Aeroqual Series 500 Monitor have been designed to accurate measurement of ambient gas. Different sensor heads are for specific gases and interchangeable on the same unit. The monitors are modular in design and composed of two main components, a series 500 monitor, and a sensor head. The sensor head is calibrated prior to delivery and does not normally need to calibrated. The concentration can be displayed either in ppm or mg/m^3. The monitor is able to log up to 8000 data points. The data logging interval can be set in one minute increments. In this study, all O_3 analyses are based upon the hourly average data, Indian Standard Time (IST), which is 5:30 h plus Greenwich Mean Time.

RESULTS AND DISCUSSION

Diurnal variations:

It is seen from fig.2 that the O_3 mixing ratio starts increasing after sunrise in the morning, attains maximum during daytime due to photochemical production and again decreases until the next morning. The O_3 reaches to maximum value at noon due to large photochemical production. The corresponding minimum of O_3 mixing ratio 8.4 ppbv was observed at about 07:00 h in the morning. During nighttime, production of O_3 ceases and hence due to lack of sunlight, O_3 decreases throughout the nighttime by chemical loss of O_3, to a lesser extent with nitrate radical (NO_3), and dry deposition at the surface. Therefore, high O_3during summer is only due to both local photochemical production of O_3 and transport of O_3 from upwind northeast and northwest cities.

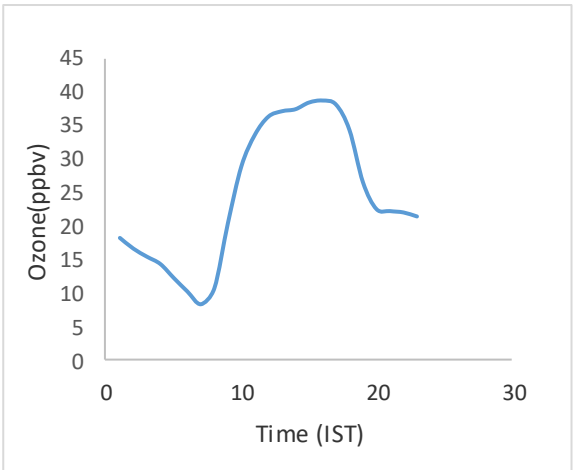

Fig.2 Annual average diurnal variations of O_3 mixing ratio (ppbv) at Shevgaon.

Table1. Monthly average ozone, maximum air temperature, maximum relative humidity (RH), and cloud cover (cc) observed at Shevgaon.

Month	O_3 (ppbv)	Max. air temperature (^{0}C)	Max. RH (%)	Cloud cover (%)
January	21.4	29.8	75	30
February	22.6	32.6	65	25
March	25.7	37.4	44	23
April	30.8	40.9	39	37
May	24.5	40.3	54	43
June	16.6	31.5	69	80
July	11.5	30.2	76	82
August	10.8	28.6	83	87
September	16.3	32.4	80	66
October	19.7	32.8	73	65
November	20.5	31.5	74	41
December	21.3	30.8	75	40
Average	23.5	33.2	73	51.6

Hence, stratospheric ozone intrusion in the troposphere at the ground-level is also ruled out. Therefore, high O_3during afternoon is only due to both local photochemical production of O_3 and transport of O_3 from upwind northeast and northwest cities. In other study [7], similar diurnal variation of O_3 is observed at rural site.

Monthly average ozone along with meteorological parameters:

Table 1 shows the monthly average O_3 mixing ratio along with the meteorological parameters, such as maximum air temperature, maximum relative humidity (RH), and cloud cover (CC) observed at Shevgaon. The highest O_3 mixing ratio (30.8 ppbv) is observed in April. due to maximum air temperature (40.9 0C) and minimum relative humidity (39 %); while lowest O_3 mixing ratio (10.8 ppbv) is observed in August due to minimum air temperature (28.6 0C) and maximum relative humidity(83%); maximum cloud cover (87%). It is clear that meteorological parameters are having important role in the O_3 formation.

CONCLUSION

The monthly average of O_3 mixing ratio ranged from 10.8 ppbv to 30.8 ppbv with an annual average of about 23.5 ppbv. The magnitude of diurnal variation of O_3 mixing ratio was highest in April due to intense solar radiation and high temperature. The RH and cloud cover have shown negative impact on O_3 mixing ratio.

Acknowledgement

The author gratefully acknowledge the University Grant Commission, Western Regional Office, Pune-7, for providing financial assistance for this research work.

Conflicts of interest: The authors stated that no conflicts of interest.

REFERENCES

1. WHO, Guidelines for Air Quality, World Health Organization, Geneva, 2000, pp.190.
2. Jain S.L., Arya B.C., Kumar A., Ghule S.D., Kulkarni P.S. (2005) Observational study of

surface ozone at New Delhi, India, Int. J. Remote Sens. 21 (16) 3515-3526.
3. Debaje S.B., and Kakade A.D. (2009) Surface ozone variability over western Maharashtra, India, J. Hazard. Mater 161, 686-700.
4. Beig B., Gunthe S., Jadhav D.B. (2007) Simultaneous measurements of ozone and its precursors on a diurnal scale at a semi-urban site in India, J. Atmos. Chem. 57, 239-253.
5. Khemani L.T., Momin G.A., Rao PSP, Vijaykumar R., Safai P.D. (1995) Study of ozone behavior at urban and forested sites in India, Atmos. Environ., 29,2021-2024.
6. Londhe A.L., Jadhav D.B., Buchunde P.S., Kartha M.J. (2008) Surface zone variability in the urban and nearby rural locations of tropical India, Curr. Sci., 95 1724-1729.
7. Reddy R.R., K. Rama Gopal, L., Siva Sankara Reddy, K. Narasimhulu, K. Raghavendra Kumar, Y. Nazeer Ahammed, C.V. Krishna Reddy, (2008) Measurements of surface ozone at semm-arid site Anantpur (14.620N 77.650E, 331 masl) in India, J. Atmos. Chem., 47-59, doi: 10.1007/s10874-008r-r9094-1.

IRJSE *Int. Res. J. of Science & Engineering,* 2018; Special Issue A2 : 98-101 SJIF Impact Factor 4.11
ISSN: 2322-0015 UGC Approved Journal No. 63628
RESEARCH ARTICLE OPEN ACCESS

Effect of Solar and Sun Drying on Vitamin A, and Vitamin C Content of Fenugreek Leaves

Navale SR[1], Thorat SK[2] and Mohite KC[3]

[1]Department of Physics, S.N. Arts, D.J.M. Commerce and B.N.S. Science College Sangamner, M.S.,
[2]Department of Physics, Adv. M. N. Deshmukh College, Rajur, Akole, M.S., India,
[3]School of energy studies, S. P. Pune University, Pune, M.S., India
Email: sainathnavale09@gmail.com

Manuscript Details
Available online on http://www.irjse.in
ISSN: 2322-0015

Editor: Dr. Arvind Chavhan

Cite this article as:
Navale SR, Thorat SK and Mohite KC. Effect of Solar and Sun Drying on Vitamin A, and Vitamin C Content of Fenugreek Leaves, *Int. Res. Journal of Science & Engineering,* January 2018; Special Issue A2: 98-101.

ABSTRACT

The use of conventional energy sources for the dehydration of vegetables is not feasible now days since there is scarcity of conventional energy sources. Therefore suitable technology should be adapted for the drying of vegetables. In present research, a cabinet solar dryer has been fabricated. The comparative study of solar dryer and open sun was studied for the drying of fenugreek leaves. The sample of 1kg fenugreek leaves was dried in cabinet solar dryer and open sun. After complete drying, powdered samples were prepared and vitamin A and vitamin C content was determined. The result obtained revealed that, the vitamin A was increased 134 % in cabinet solar dried sample compared to open sun dried sample where as vitamin C shows 12.67 % reduction in cabinet solar dried sample in comparison with open sun.

Keywords: Cabinet solar drying, Open sun drying, Fenugreek, Nutrient.

INTRODUCTION

Dehydration is a straightforward course of removing surplus water from leafy vegetables or fruity vegetables. It is the traditional method of food preservation. Generally many agricultural products contain higher moisture i.e. in the range of 25 % to 85 % [1]. But for long preservation, the value of moisture content is much higher than required one [2].

The higher moisture content resulted into fungal and bacterial growth rapidly. The bacteria and enzymes sometimes spoil the foodstuffs and responsible for the reduction in nutrient content. The reduction of moisture content in the vegetables to a certain level slows down the bacterial, enzymes and yeasts effects [3, 4]. Hence it is very important to reduce the moisture content in the vegetables for its long preservation.

The application of solar drying technologies are very much useful than using fossil fuels and other energy sources. The advantages of solar dryings are, it is pollution free, faster drying nutrients retains properly and reduces the emission of carbon particles in atmosphere [2, 4, 5 and 6]. Solar drying technologies are basically classified as direct solar drying, indirect solar drying and mixed mode solar drying. In present work a low cost direct solar dryer was fabricated and comparative study of fenugreek leaves for vitamin A and vitamin C was carried out.

METHODOLOGY

The sample of 1kg fenugreek leaves sample was collected from the one farm only to ensure the uniformity and to avoid the effect of soil variation on the nutrient content of the sample. The fresh and green fenugreek leaves were selected and discoloured, as well as wilted leaves removed to avoid bad odour and loss of nutrients after dehydration. The fenugreek leaves were cut from the stem in order to make them free of soil and dirt. The leaves were washed with ample of fresh and clean water number of times. After washing, the leaves were air dried at room temperature to eliminate the residual moisture in the sample. Any non leafy part present in the sample was then removed to get a homogenous collection of fenugreek leaves which was then separated in two equi-weighted quanta for open sun drying (OSD) and cabinet solar drying (CSD). The sample weight was recorded before the actual experimental drying was started. Both the drying systems i.e. CSD & OSD have the same surface area of the mesh used to spread the sample [4, 6]. The fenugreek leaves dried by OSD & CSD, were powdered using a grinder and were sifted by a fine mesh. Powdered samples were then analysed by nutritive tests (Vitamin A and Vitamin C). The tests were carried out at National Food and Agricultural Research Institute, Tilak Road, Pune (Certified by the Government of India).

Vitamin 'A' Content: The retinal acetate of 4 gm (Purity 98.50%) was taken and the volume was made 10 ml with ethanol. About 20 ml ethanol, 1 ml 50% KOH, 5ml ascorbic acid was then added to 1.3 ml of the above solution and was refluxed for 1 hr on boiling water bath. The content was then transferred in to separating funnel. The flask was washed with 10 ml each ethanol and water. 150 ml pet ether was then extracted in three portions and pet ether layer was then collected, washed till it is alkali free. The pet ether layer was passed through sodium sulphate and was kept on water bath to dry and reconstituted in IPA to10 ml. About 20 micro liters solution were injected on HPLC.The 50.0 gm of homogenized sample in a 500 ml flask was taken and adding it 200 ml ethanol, 2 ml ascorbic acid, 50 ml 50% KOH and well mixed the content. The solution was reflux on water bath for one hour with frequent swirling. The content was then transferred in to separating funnel. 180 ml pet ether was extracted in three portions and pet ether layer was then collected, washed till it is alkali free. The pet ether layer was passed through sodium sulphate and was kept on water bath to dry and reconstituted in IPA to10 ml. About 20 micro liters solution was injected on HPLC.

Vitamin A content (%) = A × C × E × F × G × 100 / B × D ×100

Where, A = Area of sample, B = Area of Vitamin A Acetate Standard

C = Concentration of retinal acetate standard in gram,
D = Weight of sample taken.
E = Sample diluted volume, F = Purity of Vitamin A Acetate Standard.

G = 1000 mg of retinol Acetate corresponds to 2906976.7 IU of Vitamin A.

Vitamin 'C' Content: About 5 gm to 10 gm of the sample was ground in a mortar using meta phosphoric acid and was transferred it into a 100 ml-graduated flask. The 100 ml volume was made up using meta phosphoric acid. It was then filtered

through a fluted filter paper No. 1. 10 ml of the filtrate was titrated rapidly with the indophenol solution. The end point was faint pink colour. Readings were noted and the vitamin content was calculated using following formula

Vitamin C = A × B × 1000 / W
Where, A = Volume in ml of the indophenol solution used for titration,
B = Weight in mg of the ascorbic equivalent to one millilitre of the indophenol solution,
W = Weight in gm of the sample taken for the test.

RESULTS AND DISCUSSION

The vitamin A (β carotene) and vitamin C measurements were carried out on the powder of fenugreek leaves dried in open sun and in cabinet solar dryer. The vitamin contents are as shown in following Table 1.

The dried fenugreek leaves showed higher vitamin A content as compared to the fresh leaves [7, 8]. The leaves dried in cabinet solar dryer exhibited maximum retention of β carotene (31265.70 µg/100gm) than in open sun (13565.41µg/100gm) and the fresh leaves (2340 µg/100gm). In comparison with other researchers [7, 8, 9] the retention of β carotene dried in cabinet solar dryer shows higher retention. Vitamin 'C' contained in the dried samples is observed to be much reduced than that in the fresh sample since it is highly water soluble. Furthermore, the vitamin C content in cabinet solar dryer shows more reduction compared to open sun drying as temperature in cabinet solar dryer is higher than the open sun. The level of vitamin C in vegetables is temperature dependent [8, 9].

The details of HPLC analysis for fenugreek leaves dried in open sun are as:
Column: Zorbaxr ODS
Mobile phase: Actronitrile, Dichloromethane and Methanol (70:20:10)
Detector variable wavelength: U. V-453 nm
Flow rate: 1.0 ml/min
Retention time: about 3.094 min
Area under the pick = 3872.99

The area under above blue pick of HPLC pattern shows the content of β carotene in the fenugreek leaves dried in open sun. The brown small picks in above HPLC pattern show the other ingredients (showing negligible percentage).

Table 1: Vitamin composition of dehydrated fenugreek leaves.

Nutrient	Fresh leaves	Open sun drying	Cabinet Solar dryer	Unit
Vitamin A(β Carotene)	2340	13565.41	31265.70	µg / 100gm
Vitamin C	52	13.97	12.2	mg / 100gm

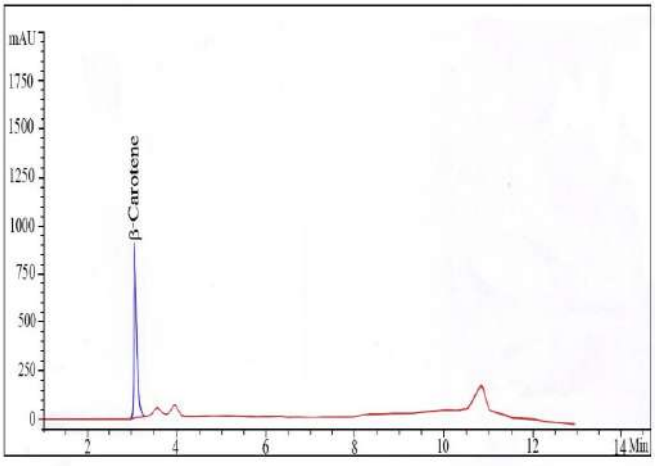

Fig.1: HPLC curve for fenugreek leaves dried in open

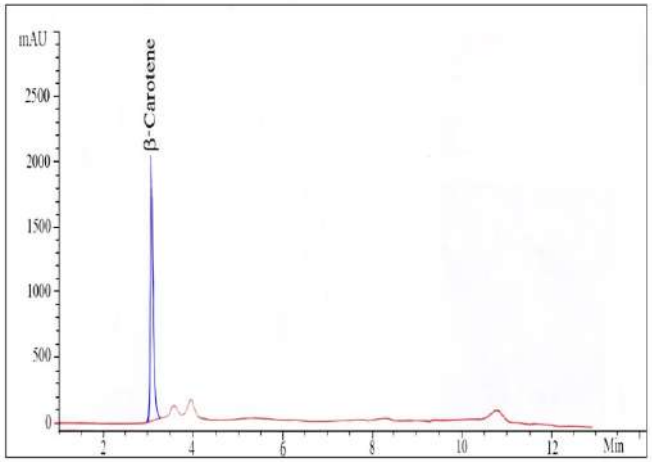

Fig. 2: HPLC curve for fenugreek leaves dried in

sun

The details of HPLC analysis for fenugreek leaves dried in cabinet solar dryer are as:

Column: Zorbaxr ODS

Mobile phase: Actronitrile, Dichloromethane and Methanol (70:20:10)

Detector variable wavelength: U. V-453 nm

Flow rate: 1.0 ml/min

Retention time: about 3.099 min

Area under the pick = 8936.64

The area under above blue pick of HPLC pattern shows the content of β carotene in the fenugreek leaves dried in cabinet solar dryer. The brown small picks in above HPLC pattern show the other ingredients (showing inferior percentage).

CONCLUSION

Dried Fenugreek leaves shows higher retention of vitamin A content. The retention of vitamin A content is higher in solar dried sample as compared to open sun. Dehydration reduces the vitamin C content as it is temperature dependent.

Conflicts of interest: The authors stated that no conflicts of interest.

REFERENCES

1. El-esbaii AA, and Shalaby SM. Solar drying of agricultural products: A review, Renewable and Sustainable energy Reviews, 2012, Vol.16, pp. 37-43.
2. Chaudhari AD and Salve SD. A review of solar dryer technologies. International journal of research in advent technology, 2014, Vol. 2, no.2, pp. 218-231
3. Mohanraj, M., Chandrasekar, P. Drying of copra in a forced convection solar drier. Bio systems Engineering, 2008, Vol.99, pp. 604-607.
4. Navale SR, Upasni Supriya, Harpale, VM and Mohite KC. Effect of solar drying on the nutritive value of fenugreek leaves. International journal of Engineering and advanced technology, 2014, Vol.4, pp. 133-136

cabined solar dryer

5. Rajkotia SD, Modi VH, Chauhan RJ. Performance improvement of solar dryer. International journal of scientific research, 2013, no.2, pp. 142-144.
6. Navale SR, Thorat SK, Harpale VM and Mohite KC. Dehydration of leafy vegetables using cabinet solar dryer. Indian stream research journal, 2013, Vol.3, pp. 1-6.
7. Babagana Gutti, Silas Kiman, Ahmed MM. Solar dryer – An effective tool for agriculture products preservation, Journal of applied technology in environmental sanitation, 2012, Vol.2, no.1, pp. 31-38
8. Babalola OO, Tugbobo OS, Darmola AS. Effect of processing on the vitamin C content of seven Nigerian green leafy vegetables. Advance journal of food science and technology, 2010, pp. 303-305.
9. Kiremire BT, Musinguzi E. Effects of vegetables drying techniques on nutrient content. African journal of food agriculture nutrition and development, 2010, no.10, pp. 2588-2599.

IRJSE *Int. Res. J. of Science & Engineering*, 2018; Special Issue A2 :102-106 SJIF Impact Factor 4.11
ISSN: 2322-0015 UGC Approved Journal No. 63628
RESEARCH ARTICLE **OPEN ACCESS**

Study of Wear & Corrosion Resistance of Cr Based Nitride and Carbide Thin Films

Goswami Vishal[1], Mundotia R[2], Thorat N[2], Mhatre U [2] Nadkarni MS[1]

[1] S.S & L.S Patkar-Varde College of Arts & science and V.P Varde College of Commerce & Economics, S.V Road, Goregaon (W), Mumbai-400062,
[2]Surface Modification Technologies Pvt. Ltd – Vasai Palghar.
Email: vishalgiri.h.goswami@gmail.com

Manuscript Details
Available online on http://www.irjse.in
ISSN: 2322-0015

Editor: Dr. Arvind Chavhan

Cite this article as:
Goswami Vishal, Mundotia R, Thorat N, Mhatre U Nadkarni MS. Study of Wear & Corrosion Resistance of Cr Based Nitride and Carbide Thin Films, *Int. Res. Journal of Science & Engineering*, January 2018; Special Issue A2 : 102-106.

ABSTRACT

Present work focus on developing various combinations of Chromium based nitride and Carbide thin films. These films deposited in the form of monolayer and nano-structured Bilayers thin film using advance cathodic arc process to produce coatings that have flexibility to modify the surface properties as per the need of application. Coatings produced exhibit a smooth surface suitable for most industrial applications such as Protective, cutting tools, Antireflective or decorative coating. Coatings on industrial equipment such as drills bits, fasteners, stampings and other parts and pieces that would go into heavy-duty applications. The monolayer/nano-structured Bilayer coatings of CrN, CrC and CrN/CrC is deposited. Coatings were deposited by varying coating parameters to obtain specific mechanical properties such as very high corrosion resistance, wear coefficient, toughness & hardness etc. this coating is use to coat on milling tools, round shank tools, trim tooling, plastic molds, punches and brazed carbide tooling. The Detailed investigation of this coating is by Adhesion Test, Wear Measurement and corrosion resistance measurement by potentiostat.

Keywords: cathodic arc process, monolayer, nano-structured Bilayer coatings.

INTRODUCTION

In metals, there is actual material loss either by dissolution (corrosion) or by the formation of nonmetallic scale or film (oxidation). Corrosion problem play a vital role in global economic, a huge percentage of an industrialized nation's income is spent on corrosion prevention and the maintenance or replacement of products lost or contaminated.

Stainless steels are highly resistant to corrosion it contain atleast 11% of chromium, which minimizes the formation of rust. Stainless steel are also susceptible to corrosion in some aggressive & corrosive environments and therefore type of environment may strongly reduce their mechanical and tribological properties. To prevent corrosion, a protective layer is coated on the surface of the metal that constantly comes in contact with moisture and oxygen in the atmosphere.

Few study shows hard coating–substrate systems also suffer a severe corrosion attack due to the defects in the coating structure (pores, pinholes) resulting from the PVD-typical film morphology [1,2] while our earlier study shows Hard and Hard layer combination shows improved tribological and morphology properties as compare to Hard and Soft layer combination.[3] C Liu,A Leyland et.al. were investigated in comparison with the columnar structure of TiN coatings, the dense structure with fine equiaxed crystallites made CrN coatings less permeable to the corrosive medium. Corrosion resistance improvement is not only attributed to the increase in thickness, but also to the internal microstructure and phase composition. [4] Douglas E. Wolfe, Brian M. Gabriel et.al. were investigated the erosion resistance of the (Ti,Cr)N coating the higher Cr content, lowest number of nanolayers and interfacial size had the best erosion performance.[5] In several industrial applications such as milling and forming processes coatings are required to have high hardness and elasticity, high oxidation resistance, which enables such coatings to be employed even under higher temperatures [6]. Meng-Tsun Lin et.al. results showed that the TiN/ZrN coating with a nano-composite structure improved the corrosion resistance about 243 and six times, respectively, as compared with uncoated Ti and SS304 in the O2-rich environment with F-ions and acid. [7] Hermann A. Jehn and Manfred E. Baumgartner studied Corrosion behavior hard coating with substrate systems. Their experimental result reflect the electrochemical properties of the coating and the influence of the underlying substrate when micropores, pinholes and other defects are present. [8].

Only limited studies exist on the corrosion behaviour of hard coating substrate systems. Therefore our main aim is to investigate the tribological behaviours of coatings with focus on their corrosion and wear mechanism. This paper attempts to improve the corrosion resistance by interlayers and multilayered coating structures.

METHODOLOGY

Coatings were deposited on mirror polished HSS or soft SS 304 coupons with diameter 22 mm and thickness 6 mm. Several samples of CrN, CrC, CrN/CrC coatings were prepared by first cleaning chemically by organic solvents and then heated to high temperature for removal of any impurity. These films will be subjected for different instrumentation methods such as coating thickness is measured using Ball crater, Roughness Measurements by Roughness tester, Mercedes test using Rockwell C Hardness instrument, Coating Wear Measurement is done by Calotest, and corrosion resistance measurement by potentiostat.

RESULTS AND DISCUSSION

Coating thickness is measured using Ball crater shows 1.30 µm, 2.06 µm and 3.49 µm for CrN, CrC and CrN/CrC coatings respectively [Fig.1]. Calo-wear test has been carried out to evaluate Wear coefficient of the CrN, CrC & CrN/CrC coating was 8.30 X 10^{-14} m^2/N, 1.51 X 10^{-13} m^2/N and 1.38 X 10^{-13} m^2/N respectively. Coating structures like CrN/CrC having duplex surface layer is essential in extending the wear life. Such a multicomponenent coating permit additional functionality in practical applications. example, some layers may provide superior friction and wear properties, while other layer may provide high resistance to corrosion.

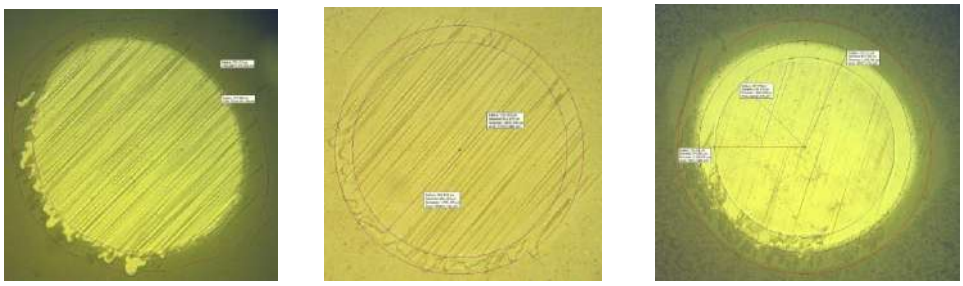

(a) (b) (c)

FIGURE 1. Ball crater images for (a) CrC (b) CrN and (c) CrN/CrC

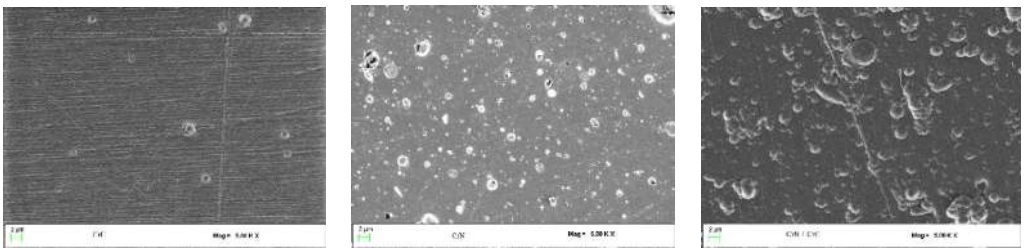

(a) (b) (c)

FIGURE 2. SEM images at magnification 5 KX for (a) CrC (b) CrN and (c) CrN/CrC

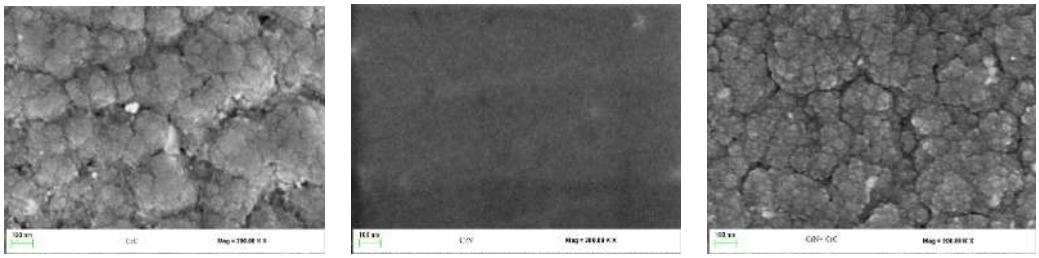

(a) (b) (c)

FIGURE 3. SEM images at magnification 200 KX for (a) CrC (b) CrN and (c) CrN/CrC

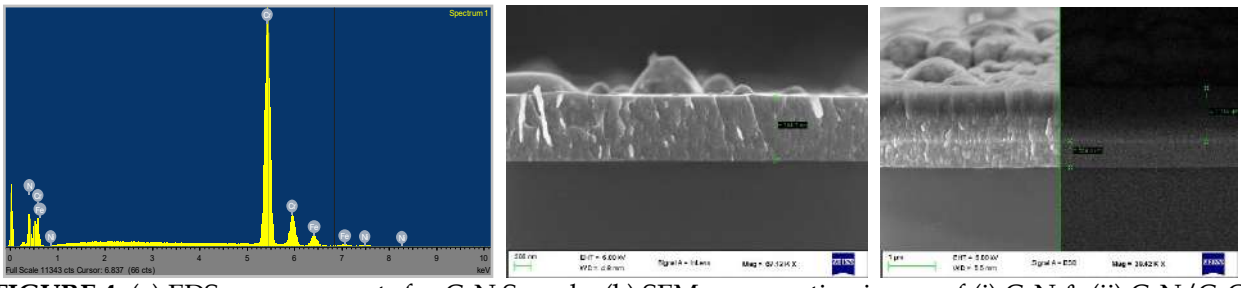

FIGURE 4. (a) EDS measurements for CrN Sample, (b) SEM cross-section image of (i) CrN & (ii) CrN/CrC

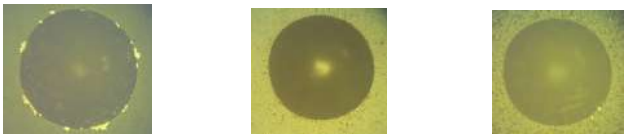

(a) (b) (c)

FIGURE 5. Rockwell C indentation of (a) CrC (b) CrN and (c) CrN/CrC

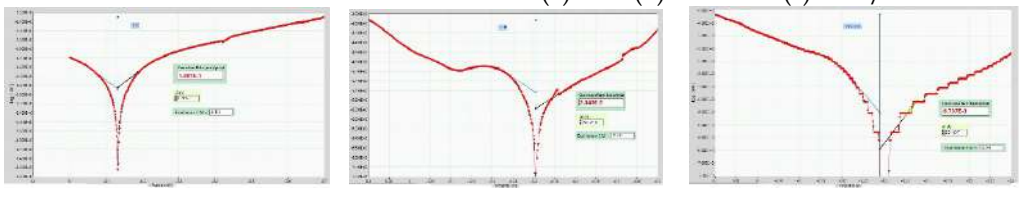

(a) (b) (c)

FIGURE 6. Corrosion resistance by potentiostat of (a) CrC (b) CrN and (c) CrN/CrC

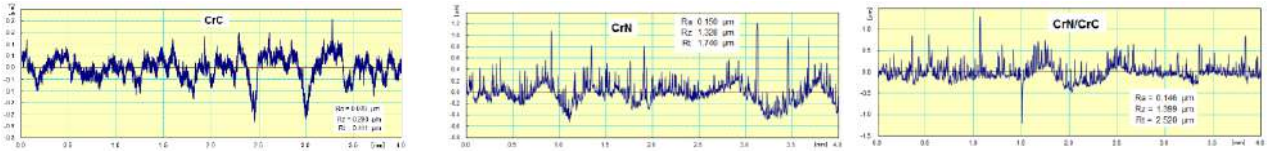

(a) (b) (c)

FIGURE 7. Surface roughness by Mitutoya profilometer of (a) CrC (b) CrN and (c) CrN/CrC

SEM images at magnification 5KX Fig.2 shows the SEM surface morphologies of CrN, CrC and CrN/CrC coatings, the CrC coating exhibited a very smooth surface while the surface of the CrN and CrN/CrC coating was rough with much micro-drops with granular deposition and pitting defects. chromium-depleted zone adjacent to the grain boundary, is highly susceptible to corrosion and it is called as Intergranular corrosion.

However, SEM images in fig.3 at magnification 200 KX shows small islands start coalescing with each other. The tendency is to form bigger islands is termed agglomeration. The structure of the films at this stage changes from discontinuous island type completely continuous film.

From these SEM images in fig.3 clearly shows that coating structure of CrC and CrN/CrC is island type which is also called as Volmer-Weber (VW) type and CrN coating structure is of layer type which is also called as called Frank-Van der Merwe (FV) type. The EDS measurements for CrN Sample in Fig.4 (a) confirm the composition of under-layer with a ratio of chromium & nitrogen is 51.45 & 44.98 respectively. The main contaminant was Fe and Ni with a content 3.35 & 0.25 atomic% which is because of SS 304 substrate. From the cross-section SEM image in Fig.4 (b) thickness of the CrN & CrN/CrC coating was estimated as 784.7 nm & 559.8/1134 nm respectively. The under-layer of CrN & CrN/CrC is clearly visible on the Si substrate.

Adhesion and coating toughness was evaluated by the Rockwell C indentation method as shown in Fig.5, CrC & CrN/CrC coating shows peel-off but incase of CrC the adhesion failures is more. In CrN coating there is no sign of spalling or adhesion failure.

Corrosion resistance is measured using potentiostat instrument of CrN, CrC & CrN/CrC coating was 2.349 X 10^{-2} mm/yr, 1.497 X 10^{-1} mm/yr and 6.737 X 10^{-3} mm/yr respectively. Standard 1 Molar HCl solution is used to calculate corrosion rate. Corrosion penetration rate is the thickness loss of material per unit of time. Corrosion rate is proportional to the current density associated with the electrochemical reaction. The corrosion rate of a reaction is limited by polarization, Polarization data are plotted as potential versus the logarithm of current density.

Coating surface roughness was measured by Mitutoya profilometer for CrC, CrN & CrN/CrC coating was having roughness (Ra) of 0.039 µm, 0.150 µm and 0.146 µm respectively.

CONCLUSION

Our studies also shows a clear evidences of improvement of the corrosion resistance of Chromium based nitride and Carbide thin films to oxidizing acids over a wide range of concentrations and temperatures. Common acids in this category are nitric acid, hydrochloric acid, perchloric, and hypochlorous acids.

Acknowledgement:
The authors would like to thank S.S. & L.S. Patkar-Varde College (Goregaon), Mumbai University, UGC, DST for financial support and Surface Modification Technology Pvt. LTD – Vasai Thane, for having rendered the experimental facilities for the present work.

Conflicts of interest: The authors stated that no conflicts of interest.

REFERENCES

1. Jehn HA. Improvement of the corrosion resistance of PVD hard coating–substrate systems. Surface and Coatings Technology, Volume 125, Issues 1–3, March 2000, pp 212-217
2. Hitoshi Uchida et.al. Electrochemical evaluation of pinhole defects in TiN films prepared by r.f. reactive sputtering. Materials Science and Engineering: AVolumes 234–236, 30 August 1997, Pages 649-652
3. Goswami VH, Nadkarni MS, Mahtre U et. al. A Study of Tribological Behavior of Titanium and Chromium based Nitride Monolayer and Nano-structured Multilayer Thin Films Prepared Using Advanced Cathodic Arc Deposition for Improving Performance of Industrial Tooling and Components. Research & Reviews: Journal of Pure and Applied Physics 2016 ISSN: 2320-2459
4. Liu C, Leyland A et.al. Corrosion resistance of multi-layered plasma-assisted physical vapour deposition TiN and CrN coatings. Surface and Coatings Technology, Volume 141, Issues 2–3, 18 June 2001, Pages 164-173
5. Douglas E. Wolfe, Brian M. Gabriel et.al. Nanolayer (Ti,Cr)N coatings for hard particle erosion resistance. Surface & Coatings Technology 205 (2011) 4569–4576
6. Wolfgang T, Siavash Mo, Fabian H. A study of mechanical and tribological properties of self-lubricating TiAlVN coatings at elevated temperatures. Tribology International; 2013. P.324–329.
7. Meng-Tsun Lin et.al. "Enhanced Corrosion Resistance of SS304 Stainless Steel and Titanium Coated with Alternate Layers of TiN and ZrN in a Simulated O^{2}-rich Environment of a Unitized Regenerative Fuel Cell" Int. J. Electrochem. Sci., 9 (2014) 7832 – 7845
8. Hermann A. Jehn and Manfred E. Baumgartner, Corrosion studies with hard coating-substrate systems. Surface and Coatings Technology, 54/55 (1992), pp 108-114.

IRJSE *Int. Res. J. of Science & Engineering,* 2018; Special Issue A2 : 107-111 SJIF Impact Factor 4.11
ISSN: 2322-0015 UGC Approved Journal No. 63628
RESEARCH ARTICLE **OPEN ACCESS**

Synthesis and Characterization of Electrochemically Deposited Copper Nanoparticles and their application for nano-fluids

Arote SA* and Palve BM

Department of Physics, S. N. Arts, D. J. M. Commerce, B. N. S. Science Sangamner, Dist: Ahmednagar 422 605
Email: sandeeparote@gmail.com

Manuscript Details
Available online on http://www.irjse.in
ISSN: 2322-0015

Editor: Dr. Arvind Chavhan

Cite this article as:
Arote SA* and Palve BM. Synthesis and Characterization of Electrochemically Deposited Copper Nanoparticles and their application for nano-fluids, *Int. Res. Journal of Science & Engineering,* January 2018 | Special Issue A2 |: 107-111.

ABSTRACT

Nanotechnology deals with the various structures of matter having dimensions of the order of a billionth of a meter. In the present work, we have prepared copper nanoparticles by using electro-deposition method. The structural, optical and morphological properties of the prepared Cu nanoparticles were characterized by using XRD, UV-Visible Spectroscopy and scanning electron microscopy, respectively. The XRD spectra reveal that the prepared Cu particle shows crystalline and cubic structure. In present investigation, we also studied the effect of the different parameters such as temperature, applied potential, time, stirring rate on properties of the Cu nanoparticles. Here it was observed that the freshness of an electrolyte also matters which is simply prepared from the ethanol, anhydrous $CuSO_4$ and HCl having specific quantity. The present work also investigated the effect of Cu nanoparticles on electrical conductivity of base fluid (DDW). The electrical properties of the base fluid get altered on the dispersion of nanoparticles. The effect of illumination under different source on electrical conductivity of the Cu nanoparticle with base fluid was also discussed.

Keywords: Nanotechnology, Nanoparticles, electro-deposition, electrical conductivity, copper etc.

INTRODUCTION

The nanoparticles are the particles which having the dimensions from 1nm to 100nm. Materials with structure at the nanoscale often have unique optical, electronic, or mechanical properties. Furthermore, the optical and electronic properties of nanomaterials which depend on their size and shape can be tuned via synthetic techniques [1-2]. Nanoparticles are of great scientific interest as they are effectively a bridge between bulk materials and atomic or molecular structures. A bulk material should have constant physical properties regardless of its size, but at the nano-scale this is often not the case. Nanoparticles exhibit a number of special properties relative to bulk material [3-4]. For example, the bending of bulk copper (wire, ribbon, etc.) occurs with movement of copper atoms/clusters at about the 50 nm scale. Copper nanoparticles smaller than 50 nm are considered super hard materials that do not exhibit the same malleability and ductility as bulk copper. Nanoparticles can be used in different fields like in agricultural, industrial, biological, medical, defence, [5-8]. The synthesized Cu nanoparticles are acts as an anti-biotic, anti-microbial, and anti-fungal agent when added to plastics, coatings, and textiles. Cu nanoparticles also for heat sinks and in highly thermal conductive materials. It also an efficient catalyst used in chemical reactions and for the synthesis of methanol and glycol. Sometime it is used as a in sintering additives and capacitor materials. There are several chemical methods for preparation of nanoparticles like Sol –gel method, Colloidal method, Co-precipitation method, Electro deposition methods etc. [9-12]. Among these electrodeposition method which is cheap and easy. Here we have synthesized copper nanoparticles from this method by applying certain potential difference with constant current supply and at the room temperature. This method of synthesis of nanoparticles is cheaper & easier. Multideposition of nanoparticles can be take place and easily portable method. The preparation of the nanoparticle can possible at room temperature in the laboratory by using electrodeposition method. The structural and morphological characterization of film has been carried out by X- ray diffraction (XRD) and Scanning electron microscopy (SEM) respectively and their optical and compositional properties have been studied by UV-vis-NIR spectrophotometer and Energy dispersive spectroscopy (EDS) technique respectively.

In the present work we successfully synthesized the Cu nanoparticles by using electrodeposition method and study its conducting as well other characteristics by using characterization technique.

METHODOLOGY

1. Electrodeposition technique:
It is very useful technique to deposit the metal layer on a conducting substance. The various parameters of the this technique which effect on the properties of the synthesized nanoparticles such as size and shape of electrodes, distance between the electrodes, concentration of the sample, applied voltage, electrolyte etc. In the present synthesis of Cu nanoparticles, 0.1 M $CuSO_4$ (0.80 gm) solution used as a cationic precursor.

Fig 1. Electro-deposition Setup in the laboratory

This solution added in the 50 ml ethanol in beaker. Stir the solution (180 rpm) properly on magnetic stirrer and add 20 drops of 50 % diluted HCl. The voltage given to the electrodes should be 3 V and 4.5 V. The pH of the electrolyte is one. The deposition time is 10 minute. The formation of Cu-NPs follows a series of color changes due to change in applied potential, which may result in variation of particle size. The copper nanoparticles dispersed in ethanol by ultrasonication and then kept at room temperature (27 °C) for 3 months to determine their stability. The X-ray diffraction studies of Cu nanoparticles was carried out using X ray diffractometer (Bruker D8), Scanning electron microscope (JEOL JSM-6360) was used for the surface morphological study. The optical absorption

spectra were recorded in the range 300-1200 nm at room temperature by JASCO spectrophotometer. The electrical conductivity of Cu nanoparticles in aqueous solution also measured.

2. Measurement of electrical conductivity:

The electrical conductivity of any fluid is a measure of its ability to carry an electric current. The electrical conductivity can be expressed as mhos (Reciprocal of ohms) or as siemens. In most fluids, the conductivity is very low, so millisiemens or microsiemens are used as units for conductivity. Chemical composition of fluid determines its conductivity. Since the charge on ions in solution facilitates the conductance of electrical current, the conductivity of a solution is proportional to its ion concentration and their mobility [13]. The ions in water act as electrolytes and conduct the electricity. Most conductivity measurements are made in aqueous solutions, and the ions responsible for the conductivity come from electrolytes dissolved in the water. Although water itself is not an electrolyte, it does have a very small conductivity, implying that at least some ions are present. The ions are hydrogen and hydroxide, and they originate from the dissociation of molecular water. The nano-fluids used in experiment were prepared using a two-step method. First, an appropriate amount of Cu nanoparticles has been weighed with the analytical balance and then mixed with water make conducting aqueous solution. . Then, samples were stirred for 30 min using magnetic stirrer. The electrical conductivity found to be a significant dependence on the dispersed particles and its concen-tration. Thus, the second step of preparation of samples was sonication in ultrasonic bath in order to break up the agglomerates remaining after the mechanical stirring. The time for sonication was 20 min. An ultrasound that we used has a power of about 350 W, and is equipped in ultra-wave generators with frequency about 34 kHz.

RESULTS AND DISCUSSION

1. Structural Analysis:

The crystallographic analysis was done by utilizing XRD. XRD analysis of the prepared sample of copper nanoparticles was taken for the range of 10 to 80 degrees as shown in Fig.2. The FCC Cu phase structure (JCPDS Card No. 04- 0836) is evidenced by the peaks appearing at 2θ =44, 49.89, 75.60, corresponds to (111), (200) and (220) respectively. The XRD spectra reveal that the sample demonstrated a high crystallinity level and the resultant particles are (FCC) Copper nanoparticles. The XRD peak of CuO and Cu_2O are not present in the XRD spectra. This result indicates that the pure nanoparticles were formed. The peak broadening suggested that a high surface area, and surface area to volume ratio of the nano-crystals.

X (2Θ)	hkl	d (Å)
44	(111)	0.2055
49.8969072	(200)	0.1825

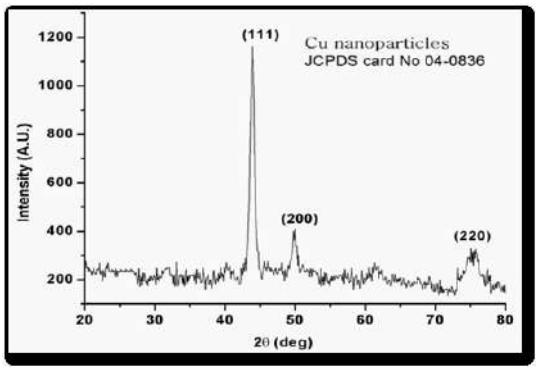

Fig 2. XRD spectra of synthesized Cu nanoparticles

2. Optical Analysis:

The optical analysis of the synthesized nanoparticle was carried out by using UV-Visible spectroscopy in the range of wavelength 300-800 nm. The NPs as observed in Figure 3 which showed a single absorption peak at 577 nm, which indicates formation of Cu-NPs . Since the 577nm wavelength lies between 400nm to 780nm that is in visible region, Cu nanoparticles absorbs visible light.

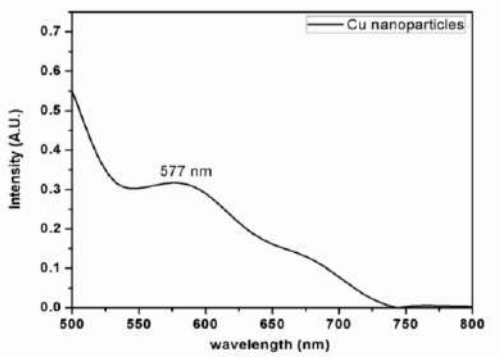

Fig 3: The UV visible spectrogram of synthesized Cu nanoparticles

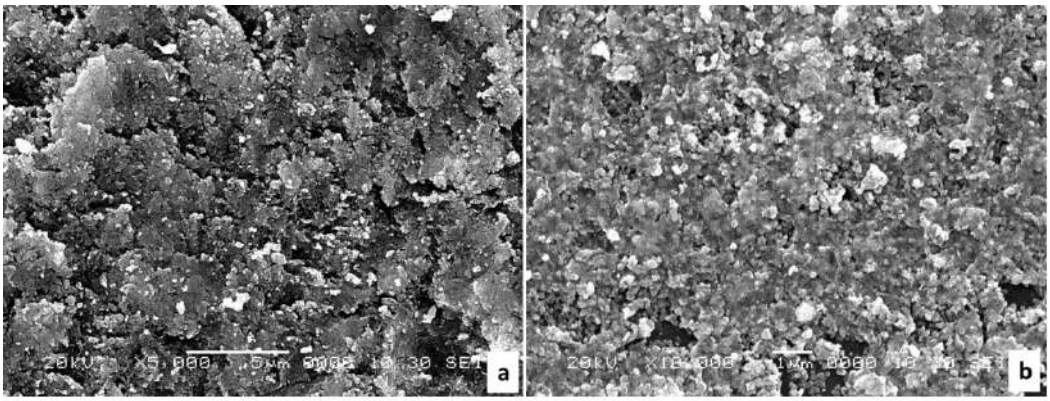

Fig 3: SEM images of electro-deposited Cu nanoparticles prepared at 3V potential

3. Microstructural Properties:

Surface morphology of Cu nanoparticles was characterized using scanning electron microscope. Fig. shows SEM micrographs of Cu nanoparticles. It is observed that the image showed micrometer-sized randomly distributed crystal aggregates, in the range of 2–20 μm. The higher magnification imaging (Fig. 3 b) revealed that the observed crystal aggregates consist of many smaller sized Cu nanoparticles. It happens because nanoparticles have a tendency to agglomerate into bigger aggregates, during continuous electro-deposition.

4. Electrical conductivity:

In the present study the electrical conductivity was measured using electrical conductivity meter. The fluid is subjected to illumination under different illuminating source in order to observe the effect of electromagnetic radiations on the electrical conductivity of prepared sample. The results are shown below as a effect of change in distance between illuminating source and sample.

Above tables shows the electrical conductivity values of water-based nano-fluids with Cu nanoparticles and various source of illumination compared with sun light. From the results, it is observed that the electrical conductivity for Cu nanoparticles prepared at 3V potential is more as compare to that prepared at 4.5V. This may be due to different particle size. It is also observed that the electrical conductivity gradually decreases as the distance between illuminating source and sample increases. It also increases in a nonlinear fashion for different illuminating sources. From all over study of above data we observed that we can obtain maximum electric conductivity in presence of sunlight. The main cause for the enhancement in electrical conductivity of base fluid is the formation of surface charges by polarisation of Cu nanoparticles when dispersed in the base fluid of water which is polar [14]. Thus from the above discussion, it is clear that polarisation is responsible for the current flux across the interface of the particles surface.

Distance(cm)	**Electrical conductivity (μS)**	
Tungsten lamp:		
	Cu(3V)	Cu(4.5V)
10	191.4	158.9
20	184.6	156.5
30	186.5	157.3
40	184.1	156.7
50	182.2	157.0
Sodium vapour lamp:		
10	185.9	168.4
20	183.2	163.3
30	181.7	162.7
40	180.5	162.0
50	179.3	161.1
IR lamp		
10	188.8	166.5
20	185.8	167.8
30	186.3	166.1
40	184.3	164.7
50	184.7	165. 5
Sunlight		
10	0.998	0.999
20	0.998	0.999
30	0.999	0.999
40	0.999	0.999
50	0.999	0.999

CONCLUSION

This study reports the synthesis of Cu nanoparticles by using electro deposition method. The preparation method used is quite cheaper & beneficial. From the XRD result, the synthesized Cu nanoparticle shows well defined peaks and nanocrystalline structure. The UV spectra reveal that the Cu nanoparticles shows maximum absorption in the visible region of the spectra. Copper nanoparticles can be used as conductive inks for flexible electronics. The main purpose of this study is to show that the copper nanoparticles can be use in solar cell because in sunlight absorbs more light. These Cu nanoparticles can be used in different devices such as photovoltaic devices, bio-sensing materials, and in antibiotic activity.

Acknowledgement:
Special thank from the authors to Ms. Kaveri Kanawade and Ms. Rutuja Naikwadi for their help in synthesis of Cu nanoparticles. Authors are also thankful to Department of Physics, SPPU, Department of Chemistry, Sangamner College, for characterization facility.

Conflicts of interest: The authors stated that no conflicts of interest.

REFERENCES

1. Bandyopadhyay AK. Nanomaterials (2nd Edition),
2. Kulkarni Sulabha K.Nanotechnology Principles and Practices (2nd Edition),
3. Charles P., Jr., Poole, J. Owens Frank. Introduction To Nanotechnology (Wiley-India Edition, 2012)
4. Kulkarni SK. Nanotechnology Principles and Practices 2nd Edn, (Capital Publisher, new Delshi, 2011,
5. Cullity BD and Stock SR, Suryanarayana C and Norton M. Elements of X-Ray Diffraction (3rd Edition). Prentice Hall, 2001, p. 664.
6. Sanpo N, Wang J, Berndt CC. *J. Nano Res*., 2013; 15: 110-121.
7. Kumar RV, Diamant Y, Gedanken A. Chem. Mater. 2000;12: 2301-2305.
8. Zhang X., Wang, G. Liu X., Wu, H. Fang, B., Cryst. Growth Des. 8 (2008) 1430- 1434.
9. Jana NR, Wang ZL, Sau TK, Pal T. Nanoparticles, *Curr. Sci.,* 2000; 79: 1367-1370.
10. Zhu H, Zhang C, Yin Y. Nanotech. 2005; 16 : 3079-3083.
11. Enders F, Schweizer A. *Phys. Chem. Chem. Phys*., 2000; 2:5455-5462.
12. Fotouhi L., Rezaei M., *Acta*, 2009; 167 :247-251.
13. McCleskey B. R., , *J. Chem. Eng. Data*, 2011; 56: 317–327.
14. Vajjha RS, Das DK, Mahagoankar BM. *Pet.Sci.Technol*., 2009;27(6):612.

IRJSE *Int. Res. J. of Science & Engineering,* 2018; Special Issue A2 : 112-115 SJIF Impact Factor 4.11
ISSN: 2322-0015 UGC Approved Journal No. 63628
RESEARCH ARTICLE **OPEN ACCESS**

Synthesis and XRD Study of Strontium Chalcogenide Thin Films Deposited on FTO Covered Glass Substrate

Gaikwad SV

Department of Physics, Abasaheb Garware College, Pune-4, Maharashtra (India)
Email: svg10@yahoo.com

Manuscript Details

Available online on http://www.irjse.in
ISSN: 2322-0015

Editor: Dr. Arvind Chavhan

Cite this article as:
Gaikwad SV. Synthesis and XRD Study of Strontium Chalcogenide Thin Films Deposited on FTO Covered Glass Substrate, *Int. Res. Journal of Science & Engineering,* January 2018; Special Issue A2 : 112-115.

ABSTRACT

Strontium Sulfide thin film was deposited on FTO coated glass surface. These films were characterized by polarization study, XRD study and SEM.

Keywords: SrS, Electrodeposition, SEM, XRD.

INTRODUCTION

The Electrodeposition technique has become very popular in recent decades, especially for thin film deposition, due to its low cost since no expensive and sophisticated vacuum equipments are required, ease of handling and ease of application to many compounds such as sulphides [1,2] and selenides which include SrS, ZnS, CdS, PbS, CdSe, CuS2, ZnSe, Sb2S3, TlS and HgS [3-12]. Strontium sulphide (SrS) is the alkaline earth metals, may be regarded as the divalent counter parts of the alkali halides, the IA-VIIB compounds. Most of the compounds of both of these groups have the same cubic crystal structure [13] and all are made up of ions having closed-shell electronic configurations similar to those of rare gases.

Among the numerous IIA-VIA compounds, strontium sulfide (SrS) is often chosen due to their high luminescent yields. In thin film form, these materials offer great potential for applications such as infrared sensors and X-ray radiation imaging plates [14],

optical storage media [15], and electroluminescent (EL) displays [16,17]. The strontium sulfide (SrS) is often chosen due to its large bandgap (Eg > 4ev), which indicates self-absorption. In the present work, SrS films were deposited using d.c. eletrodeposition technique was used to study different parameters of ($SrCl_2$+$Na_2S_2O_3$) thin films.

METHODOLOGY

Here we have used the F : SnO_2 (F.T.O.) covered glass substrates of size 5 x 1.5 x 0.1 cm^3. The F: SnO_2 (FTO) covered glass substrate was prepared in the following manner:

Solution Preparation:

The initial ingredients used to prepare SrS thin films were as follows –

(i) A.R. grade strontium chloride ($SrCl_2$. 6 H_2O)
(ii) A.R. grade ethylenediamine tetra-acetic acid (disodium salt)
(iii) A.R. grade hydrochloric acid (HCl)
(iv) A.R. grade HNO_3
(v) A.R. grade Sodium Thiosulphate ($Na_2S_2O_3$)

A appropriate weight of strontium chloride ($SrCl_2.6H_2O$) powder was taken using digital micro balance so as to get the required concentration of the solution (0.1M). The weighed strontium chloride powder was dissolved in an appropriate quantity of double distilled water to obtain desired concentration of the solution (0.1M). This solution was taken as a starting solution in electrolyte bath. The complexant Na_2-EDTA was prepared in double distilled water to obtain 0.1M concentration.

The strontium sulphide solution was prepared in following way. The strontium has higher reduction potential –3.122 V vs SCE [18]. This potential was reduced by complexing the strontium ion by varying the concentration of Na_2-EDTA with strontium chloride solution so as to form good, adherent thin films. [19, 20]. The pH = 4 was measured of the strontium chloride solution. The pH of solution was maintained constant by just simple adding dilute HCl to the strontium chloride solution. Now this solution was mixed with 0.1M $Na_2S_2O_3$ solution with appropriate ratio so as to form good quality of strontium sulphide thin films.

Formation of SrS Thin Film:

A general reaction in cathodic electrodeposition involving M^Z ions in aqueous solution takes the form,

$$M^Z.nH_2O + Ze^- \longrightarrow M + nH_2O \quad \text{------- (1)}$$

It proceeds in following successive steps:

We have prepared firstly strontium hydroxide thin film cathodically on to the cleaned FTO glass substrate using (0.1 M $SrCl_2.6H_2O$+0.1M EDTA) solution in aqueous medium. The dilute HCl is mixed to these solutions to reduce the electrodeposition potential.

The chemical reduction reaction at the cathode in an aqueous solution (pH, 4) is as follows –

$$SrCl_2 \longrightarrow Sr^{++}_{aq} + 2Cl^{-}_{aq} \quad \text{------- (2)}$$

The decomposition of water in hydrogen and oxygen occurs according to following reaction,

$$2H_2O + 2e^- \longrightarrow 2H^+ + 2OH \quad \text{- 1.0697 Vs SCE --- (3)}$$

Formation of OH^- ions results into changing the local pH at the cathode and there is large probability of hydroxide formation. **[21]**, as in present case the $Sr(OH)_2$ according to –

$$Sr^{2+} + 2OH^- \longrightarrow Sr(OH)_2,\ pH > 5 \quad \text{-------- (4)}$$

Measured pH before and after reaction was pH = 4. Thus from this mechanism it is concluded that electrodeposition from $SrCl_2$ precursor solutions onto stainless steel leads to the formation of $Sr(OH)_2$ film. Similarly sulphur film is electrodeposited from 0.1M $Na_2S_2O_3$ solution in aqueous medium (pH = 6) is as follows.

$$S_2O_3^{2-}\ (aq.) \rightleftharpoons S + SO_3^{2-}\ (aq.) \quad \text{----0.75V vs SCE ---(5)}$$

For the formation of SrS thin film, these two solutions of 0.1M normality are mixed with appropriate ratio to form a coherent, adhesive thin film. The chemical reactions for these are,

i) $Sr^{2+} + 2e^- \rightleftharpoons Sr$ ------ (6)

ii) $S_2O_3^{2-}\ (aq.) \rightleftharpoons S + SO_3^{2-}\ (aq.)$ ------ (7)

iii) $S + 2e^- \rightleftharpoons S^{2-}$ ------(8)

iv) $Sr^{2+} + S^{2-} \longrightarrow SrS$ - - 1.0 V vs SCE ------(9)

The pH value remains same before and after reaction (pH, 4). Thus we get SrS thin film, which is uniform, dense and adherent to the substrate.

RESULTS AND DISCUSSION

1) Polarization studies:

The polarization curves were drawn for the variation in current density with the potential. The deposition potentials are determined for strontium, sulphur, strontium sulphide, strontium hydroxide thin films for 0.1M concentration on FTO covered glass substrate. For strontium sulphide thin films, a whitish colour film is observed. For the potential (-1.5 V vs SCE), a strontium hydroxide thin film is formed. This potential is achieved by adding complexing agent (Na_2-EDTA) and nature of the substrates. The deposition potentials were estimated by extrapolating straight line curve portions to x-axis.

2) X-ray diffraction (XRD):

The structural identification and determination of lattice parameters are based on the interpretation of X-ray diffraction patterns. The phenomenon of X-ray diffraction can be considered as a reflection of X-rays from the crystallographic planes of the material and it is governed by Bragg's Law,

$$2dSin\theta = n\lambda \quad \text{------ (1)}$$

Where 'd' is the lattice spacing, λ is the wavelength of monochromatic X-rays, n is the order of diffraction (n = 1), and θ is the diffraction angle. For thin films, the powder technique (Debye-Scherrer method) [22, 23] in conjunction with diffractometer is most commonly used. The 'd' values are calculated using relation (1) for known values of θ, λ and n. For this purpose a catalogue of d-spacing of many thousands of crystals has been prepared. Joint Committee Powder Diffraction Standards (JCPDS) data of 'd' spacing is compared with the data obtained from diffractometer to identify the unknown material. This data can also be used to determine the dimensions of the unit cell.

Table 1: Electro-Deposition potentials for $Sr(OH)_2$, S & SrS thin films on FTO Glass Substrate.

Sr. No.	Bath Composition	Estimated Deposition Potential V vs SCE	Standard Deposition Potential V vs SCE
1	0.1 M $SrCl_2$ – EDTA	- 1.5	- 3.122
2	0.1 M $Na_2S_2O_3$	- 0.74	- 0.7182
3	0.1 M $SrCl_2$ – 0.1 M $Na_2S_2O_3$– 0.1 M EDTA – dil. HCl	- 1.2	--

Table 2 : Comparison of interplaner distance 'd' of strontium sulphide deposited on FTO coated glass substrate.

Sr. No.	Angle $2\theta^0$	Observed 'd' values A^0	Standard 'd' values A^0	Plane h k l	Composition	Structure
1	27.432	3.0153	3.0039	(2 0 0)	SrS	Face-centered cubic
2	50.211	1.8089	1.81142	(3 1 1)	SrS	Face-centered cubic
3	67.648	1.3438	1.34338	(4 2 0)	SrS	Face-centered cubic

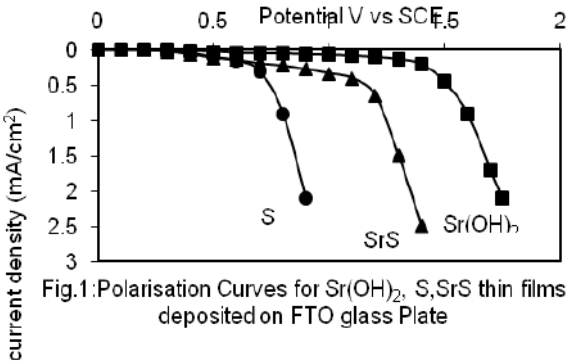

Fig.1:Polarisation Curves for $Sr(OH)_2$, S,SrS thin films deposited on FTO glass Plate

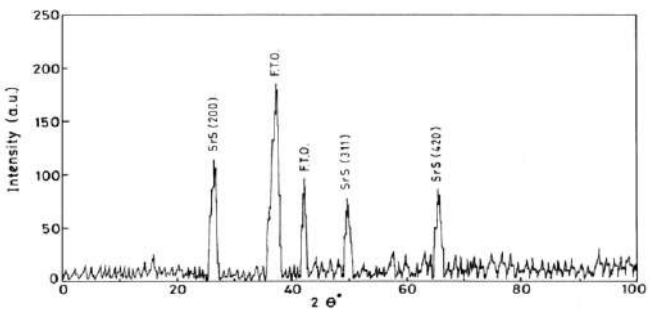

Fig. 2 : XRD Pattern of SrS Thin Film deposited on FTO Glass Substrate

From the data obtained from analyzing the sample by X-ray diffractometer, the crystallinity of the sample can be probed. From the position of reflections, the lattice parameter is calculated and using Debey-Scherrer formula the size of the crystallites (mean crystalline diameter, D) is calculated using the following relation.

$$D = 0.9\lambda / \beta \cos\theta \qquad \text{------ (2)}$$

Where λ is wavelength of X-rays, β is the full width at half maximum (FWHM) (in radians) of the peak intensity and θ is the Bragg's angle of X-ray diffraction. The X-ray diffractometer (Philips Pw - 1710) with Cukα radiation (λ = 1.5418A^0) was used for structural studies. The structural properties of strontium sulphide, films deposited on FTO coated glass substrate are studied by X-ray diffraction technique in the range of 2θ between 0^0 to 100^0. The XRD patterns of the strontium sulphide film at room temperature deposited from aqueous bath are shown in Fig. 2. The X-ray diffraction pattern of the deposited strontium sulphide film shows formation of SrS phase.

The films were polycrystalline orientation along (2 0 0). (3 1 1) and (4 2 0) plane. This plane corresponds to face centered cubic strontium sulphide. The d-values (inter planers spacing) of XRD reflection are compared with standard d-values taken from Joint Committee on Powder Diffraction Standards (JCPDS) data file for SrS, (No – 75-895), are shown in Table No. 2.

3) SEM:

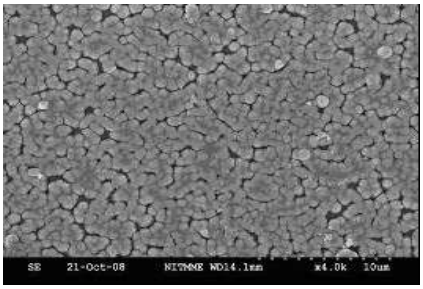

Fig.3: SEM Image

Scanning electron microscopy (SEM) is a convenient method for studying the microstructure of thin films. Figure.3 show the surface morphology of SrS nanoparticle thin films deposited at room temperature and annealed at 100°C. From the micrographs, it is observed that the films were formed from uniformly deposited nanoparticles and covered the substrate well. SEM image also reveals the grain boundaries around the crystallites.

Conflicts of interest: The authors stated that no conflicts of interest.

REFERENCES

1. Pandey RK, Sahu SN and Chandra S. Handbook of Semiconductor Electrodeposition',Marcel Dekker, Inc. New York (1996) 37.
2. John O'M Bockris and A.K.N. Reddy, Modern Electro-Chemistry, Vol. 2, Macdonald and Co. London, (1970), 936.
3. Oladeji IO, Chow L. *Thin Solid Films,*1999; 333, 148
4. Oladeji IO, Chow L. *J. Electrochem. Soc*., 1997; 144, 2342.
5. Ezugwu SC, Ezema FI, Osuji RU Asogwa PU, Ezekoye BA, Ekwealor ABC. Chigbo C, Anusuya M, Mahaboob M Beevi, Optoelectron. Adv. Mater. – Rapid Comm. **3,** 528 (2009)
6. Gaiduk P, P.I. Gaiduk, A.N. Larsen, Thin Solid Films, 2008; **516,** 3791.
7. Ezema FI, M.N. Nnabuichi, R. U. Osuji, Trends in Applied Sciences Research **1,** 467 (2006)
8. Asogwa PU, S.C. Ezugwu, F.I. Ezema, R.U. Osuji, Chalcogenide Letters **6,** 287 (2009)
9. Ezema FI, A.B.C. Ekwealor, R.U. Osuji, Turk J. Phys, 2006; **30,** 157.
10. Estrella VB, Nair MTS, Nair PK, *Thin Solid Films, 2002;* **414,** 289.
11. Patil RS, Gujar TP, Lokhande CD, Mane RS, Han S, *Solar Energy, 2007;* **81,** 648 (2007)
12. Seitz F, *Revs. Modern Phys*., 1946; **18,** 384;
13. Seitz F, *Revs. Modern Phys*., 1954;**26:** 7.
14. Jutamulid S, Storti G, Lindmayer J, Seiderman W, *Proc. Soc. Photo Opt. Instrum. Eng*.1990; 1151; 83.
15. Lindmayer J. *Solid State Technol*., 1988; **8:** 135.
16. King CN. *J Vac. Sci. Technol. A*.,1996; 14 (3) 1729.
17. Rack PD, Naman A,. Holloway PH, Sun SS, Tuenge RT, MRS Bull, 1996; **21(3)**

IRJSE *Int. Res. J. of Science & Engineering*, 2018; Special Issue A2 : 116-121 SJIF Impact Factor 4.11
ISSN: 2322-0015 UGC Approved Journal No. 63628
RESEARCH ARTICLE **OPEN ACCESS**

Effect of temperature on structural, optical and electrical properties of spray deposited TiO_2 thin films

Gapale DL[1*] and Borse RY[2]

[1]S.N. Arts, D.J.M. Commerce and B.N.S. Science College Sangamner, Dist- Ahmednagar 422 605
[2]Thin and Thick film Laboratory, Dept. of Electronics M.S.G. College, Malegaon Camp (Pin 423105), Dist. Nashik, Maharashtra, India
*Correpsonding author: Email: gapaledeepak@gmail.com

Manuscript Details
Available online on http://www.irjse.in
ISSN: 2322-0015

Editor: Dr. Arvind Chavhan

Cite this article as:
Gapale DL and Borse RY. Effect of temperature on structural, optical and electrical properties of spray deposited TiO_2 thin films, *Int. Res. Journal of Science & Engineering*, 2018; Special Issue A2: 116-121.

ABSTRACT

In present paper, the effect of the deposition temperature on structural, Optical and Electrical properties of pure TiO_2 thin films was investigated. The pure TiO_2 thin films were successfully deposited by spraying 0.1M titanium trichloride solution onto the glass substrate. The X ray diffractometric studies revealed that the deposited TiO_2 thin films have polycrystalline anatase phase with dominant (101) plane. The crystallite size was found to increase with increased substrate deposition temperature. The micro-strain and dislocation density in the film was observed to decrease as the crystallite size increased. The band gap energy of TiO_2 films with different deposition temperatures was measured using absorption spectra of UV-Vis spectrophotometer. The optical band gap of the TiO_2 films decreased from 3.30 eV to 3.54 eV as the substrate temperature was varied from 350^0C to 500^0C. The electrical resistances, temperature coefficient of resistance and activation energy of the films were calculated by measuring DC sheet resistance of the films at different temperatures.

Keywords: TiO_2 thin films, Spray pyrolysis technique, Structural, optical properties etc.

INTRODUCTION

The development of modern society considerably depends on the research in basic sciences which underline advancement in technology. During last several decades, nanotechnology has been developed dynamically; wherein nanomaterials different geometrical shapes like nano rod, flowers, belts, web like etc [1-5] were obtained to enhance their properties, such as structural, electrical, optical, photocatalytic activity, gas sensing etc. Thin film technology studies have directly or indirectly advanced many more new areas of research in solid-state Physics and Chemistry. The application areas of nanotechnology are based on the phenomena that are the unique characteristics of the thickness, geometry, surface to volume ratio, porosity and structural morphology of the films. Many new technologies have been emerged from the nanotechnology; a few to name include, etching, lithography, coating technology etc. The coating technologies have given considerable attention, mainly due to their functional advantages over bulk materials, processing flexibility, and cost considerations [6]. There are several physical and chemical methods used for film coatings. Spray pyrolysis is one of the chemical methods in which liquid precursor solution is sprayed over a substrate for a film deposition. The spray pyrolysis technique was first introduced by Chamberlin and Skarman [7] in 1966; with successful deposition of CdS thin films for solar cell applications. In general the spray pyrolysis is a simple technique with numerous advantages over the other techniques. Advantages of the method include lower cost, coating on different substrates with complex geometries, uniform and high quality coatings, ambient operations, mass production, reproducibility of films and rapid film growth rates (up to 100 nm/s) [8–12]. Titanium dioxide is one of the best candidates for solar cell application which in turn has attracted immense interest in synthesis to modify the TiO_2 nanomaterials using different techniques. Titanium dioxide exists in nature in either anatase (tetragonal, a = 3.7842 Å, c = 9.5146 Å), rutile (tetragonal, a = 4.5845, c = 2.9533 Å) or brookite (orthorhombic, a = 9.184 Å, b = 5.447 Å, c = 5.145 Å) forms[13]. Out of these, rutile is the thermodynamically stable form of titanium dioxide whereas the anatase phase rapidly transforms to rutile above 700^{o}C.In this article, influence of deposition temperature on the structural, electrical and optical properties of the titanium dioxide thin films, deposited by modified spray pyrolysis technique is reported.

METHODOLOGY

A modified spray pyrolysis setup has been developed, designed and assembled in our laboratory to overcome limitations of conventionally designed setup; such as number of optimized parameters, reliability and homogeneity of the deposited films etc. The titanium dioxide (TiO_2) thin films were deposited onto glass substrates using spray pyrolysis technique. A 0.1M precursor solution was prepared by dissolving 1m of titanium trichloride ($TiCl_3$) in to 77.3m of double distilled water. The prepared precursor solution was sprayed onto the substrate at 350^{0}C, 400^{0}C, 450 ^{0}C and 500^{0}C temperatures. The other optimized spray parameters include; Solution Flow rate= 1m /minute, Carrier air flow rate = 7.5 pm, Gun to substrate distance = 30cm, Solution spread = 20m and Spray time =20min. The deposited films were annealed in air atmosphere at 500^{0}C for 4 hr for further oxidization and crystallization. The surface properties such as the phase and crystallinity of the films were analyzed by X ray diffractmetry (XRD) using a BRUKER D8 ADVANCE diffractometer and surface morphology was studied using scanning electron microscopy (SEM) with a JEOL-540LV microscope. The electrical properties like DC sheet resistance, temperature coefficient of resistance (TCR), activation energy were characterized by static gas sensing system. The optical absorption, transmittance of deposited films was investigated using a Perkin Elmer Lambda 950 spectrophotometer (Waltham, Massachusetts, USA) in the range of 200–800 nm UV–Vis spectrometer.

RESULTS AND DISCUSSION

X Ray Diffractometry

The effect of the deposition temperature on the crystallite plane orientation of the films was investigated by calculating the texture coefficient. The

texture coefficient for all the crystallite planes was calculated using the following expression. [14]

$$T_c(hkl) = \frac{I(hkl)/I_0(hkl)}{(1/N)\sum I(hkl)/I_0(hkl)} \quad \text{----------(1)}$$

Where $T_c(hkl)$is texture coefficient of the (hkl) plane, I(*hkl*) is the measured intensity from the (hkl) plane, $I_0(hkl)$ is JCPDS standard intensity of the (*hkl*) plane, and N is the number of diffraction peaks.

The crystallite size is evaluated using the Scherrer's formula from the average crystallite size of the all matched planes. [15].

$$D = \frac{K\lambda}{\beta \cos\theta}$$

Where K = 0.9 is the shape factor, λ is the X-ray wavelength of CuKα radiation (1.5406 Å), θ is the Bragg's angle and β is full width at half maximum of the peak.

The micro strain (ε) developed in the TiO_2 thin films can be calculated using the relation [16].

$$\varepsilon = \frac{1}{2}(\beta - \lambda/D\cos\theta)\frac{1}{\tan\theta}$$

The value of dislocation density (δ) is calculated using the following relation [17]

$$\delta = n/D^2$$

Where, n is a factor, which when equal unity giving minimum dislocation density and D is the crystallite size.

X ray diffractograms of the films are given in figure 1. Films deposited at lower temperature, that is, below 300^{0}C, show amorphous nature of [18,19]. As the deposition temperature is increased from 350^{0}C to 500^{0}C, the deposited films showed were polycrystalline nature with anatase TiO_2 crystalline phase. With the increase in deposition temperature, the films showed increased crystallinity, which is manifested by corresponding increase in intensity of the peaks in diffractograms. The films annealed at a temperature of 500^{0}C were polycrystalline in nature and oriented along anatase TiO_2 (101), (112), (200), (105), (211), (204) (220), and (216) planes with the anatase plane A (101) being the predominant peak. The *as deposited* and annealed films exhibited tetragonal crystal structure with space group I41/amd, unit cell parameters a = 3.7852 Å, c = 9.5139 Å. The peak intensities showed a good agreement with the JCPDS data (#21-1272). Intensity and full-width half maximum of the diffraction peaks was observed to increase proportionally with the deposition temperature, which is in agreement with the literature. [5].

The structural parameters such as crystalline size, dislocation density and micro strain were determined from the appropriate equations and are reported in Table 1. With increasing substrate temperature, the size of the crystallites also showed an increase from 32.93 nm to 55.34 nm and is consistent with earlier reports [20]. From the table 1, it can be perceived that the strain and dislocation density in the film decreases as the crystallite size increases; which is a well-known phenomenon [21].

Scanning Electron Microscopy

The surface micrographs of TiO_2 thin films prepared at different deposition temperature and annealed at 500 ^{0}C are presented in figure 2. It is a observed from fig. that all films prepared at low temperatures i.e up to 400^{0}C are free from the pinholes and shows formation of uniform and dense interconnected web-like structure. With increase in deposition temperature the surface roughness increases and some pinholes are appeared. Similar web-like morphology has been reported for TiO_2 thin film prepared by spray pyrolysis method [5]. The interconnected webs are of variable diameter, which may be due to the sequential growth of webs; one above another during the growth process.

Optical Properties

The optical absorption spectra of pure TiO_2 thin films deposited on glass substrate using modified spray pyrolysis technique were obtained using UV-Vis spectrophotometer. Figure 4shows the optical absorption spectra of pure TiO_2 thin films deposited at 350°C and 500°C. The absorption edge was found to be sharp and showed a shift towards lower wavelength region with increase in the deposition temperature. This may be due to the change in crystal orientation in the film. The optical absorption spectra of TiO_2 films were investigated in the wavelength range 200-900 nm, at ambient temperature. The energy band gap of the films was evaluated from the relation [22] $(\alpha h\nu)^2 = A(h\nu - E_g)$

Where A is a proportionality constant and E_g is the direct transition band gap, α is optical absorption coefficient as a function of the wavelength; estimated using the relation from the $(\alpha h\nu)^2$ Vs h plot, as shown in figure 3. The band gap values decreased from 3.54 eV to 3.30 eV with increase in substrate temperature as shown in table 1. This may be due to the increase in grain size corresponding increase in deposition temperature and is consistent with quantum confinement effect [23].

Electrical Properties

The electrical properties, namely, electrical resistance, temperature coefficient of resistance (TCR), and activation energy were determined using static gas sensing system. The electric resistance of the films was measured at different temperatures with the help of half bridge method. The measured electric resistance was found to decrease with increase in temperature of the films. The thermal activation energy of the films was measured from the slope of the Arrhenius plot. The temperature coefficient of resistance was estimated using the relation.

$$\alpha = \frac{1}{R_t}\left(\frac{R_2 - R_1}{T_2 - T_1}\right)$$

where R_t is resistance of the film at room temperature and $\frac{R_2 - R_1}{T_2 - T_1}$ is slope of the resistance versus temperature plot. The measured values of film resistance at room temperature, TCR and activation energy for heating and cooling cycle are presented in table 1.

Table 1: Influence of deposition temperature on structural Optical and electrical properties of TiO_2 thin film deposited using spray pyrolysis technique.

Sample	Crystallite Size (nm)	Texture coefficient of (101) plane	Micro strain	Dislocation density	Optical Band gap	TCR ($^0C^{-1}$)	Activation energy (eV)
S_{350}	32.93	1.3781	0.1068	0.03036	3.54	0.0014068	0.339566
S_{400}	40.09	1.5239	0.08769	0.02494	3.48	0.0010697	0.326715
S_{450}	53.08	1.4791	0.06644	0.01883	3.39	0.0010115	0.313691
S_{500}	55.34	1.3821	0.06346	0.01807	3.30	0.001004	0.299029

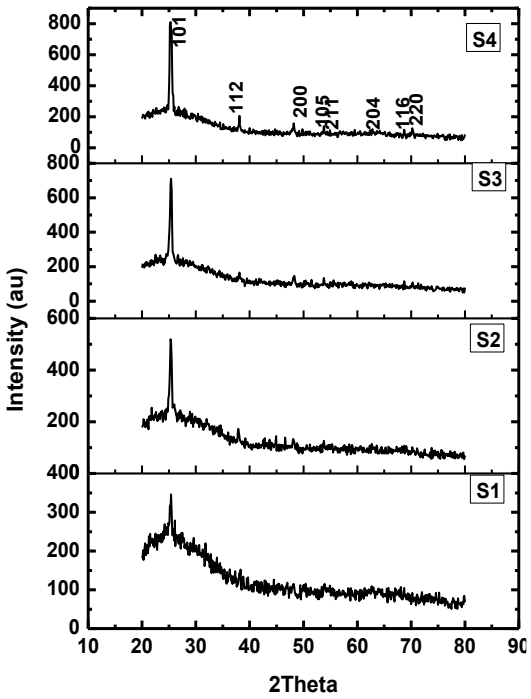

Figure 1: XRD spectra of TiO_2 thin films deposited at different substrate temperature.

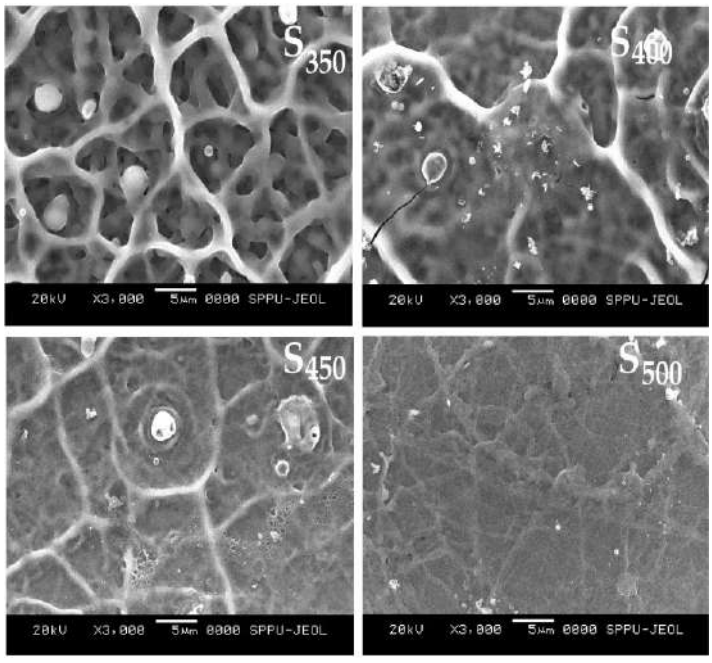

Figure 2: SEM images of spray pyrolysis deposited TiO_2 thin films for different deposition temperature from 350 ^{0}C to 500 ^{0}C.

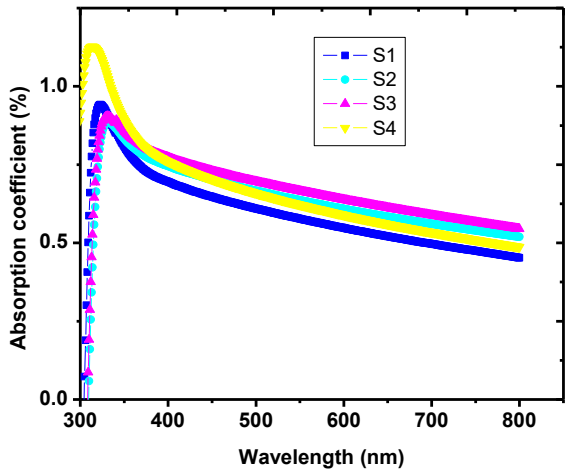

Figure 3: Optical absorption spectra of TiO_2 thin films for different deposition temperature.

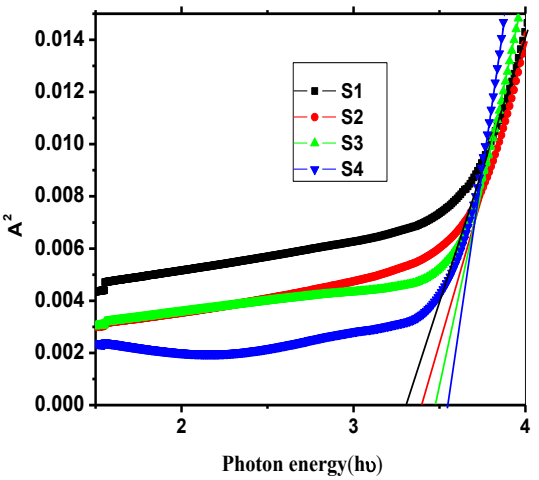

Figure 4: optical band gap calculations.

The temperature coefficient of resistance and activation energy of the films was found to decrease with increase in film deposition temperature [24]. As the deposition temperature increases the thickness of the film decreases therefore, the activation energy of the film also showed a declining nature.

CONCLUSION

The pure TiO_2 thin films were successfully deposited by spraying 0.1M titanium trichloride solution onto the glass substrate. The XRD study revealed that the deposited TiO_2 thin films have polycrystalline anatase phase with dominant (101) plane. The crystallite size of the film material was found to increase with increased deposition (substrate) temperature. The micro-strain and dislocation density of the films were decreased with increase in crystallite size. The optical band gap of the TiO_2 films was observed to decrease from 3.54 eV to 3.30 eV as the deposition temperature was increased from 350^0C to 500^0C. The temperature coefficient of resistance and activation energy of the films showed inverse variation with deposition temperature. The electrical resistance of the films decreased with temperature of film, which reveals semiconducting nature of the film material.

Acknowledgement:
We thanks to all faculty members of department of Physics Sangamner College, Sangamner for synthesis of the material also thankful to Thin and Thick film Laboratory, Dept. of Electronics M.S.G.College, Malegaon Camp. We also appreciate technical support and characterization facility provided by Department of Physics S.P. Pune University.

Conflicts of interest: The authors stated that no conflicts of interest.

REFERENCES

1. Mogilevsky G, Chen Qiang, Kleinhammes Alfred Wu. The structure of multilayered titania nanotubes based on delaminated anatase, *Chemical Physics Letters*. 460 (4–6): 517–520 (2008).
2. Fakharuddin A, Giacomo FD, Palma AL et al., Vertical TiO_2 Nanorods as a Medium for Stable and High-Efficiency Perovskite Solar Modules, *ACS Nano*, 2015, 9 (8), pp 8420–8429.
3. Li M, Jiang Y, Ding R et al. *Journal of Elec Materi* (2013) 42: 1290. doi:10.1007/s11664-013-2593-0
4. Zhao Z, Tian J, Sang Y, Cabot A, Liu H, Structure, synthesis, and applications of TiO_2 nanobelts, *Adv Mater.* 2015 Apr 24;27(16):2557-82. doi: 10.1002/adma.201405589. Epub 2015 Mar 19.
5. More AM, Gunjakar JL, Lokhande CD. Liquefied petroleum gas (LPG) sensor properties of interconnected web-like structured sprayed TiO_2 films, *Sensors and Actuators B* 129 (2008) 671–677
6. Nakaruk A and Sorrell C. Conceptual model for spray pyrolysis mechanism: fabrication and annealing of titania thin films, *Journal of Coatings Technology and Research*, vol. 7, no. 5, pp. 665–676, 2010.
7. Chamberlin RR and Skarman JS. Chemical spray deposition process for inorganic films, *Journal of the Electrochemical Society*, vol. 113, no. 1, pp. 86–89, 1966.

8. Filipovic L, Selberherr S, Mutinati GC., et al, Modeling Spray Pyrolysis Deposition, *Proceedings of the World Congress on Engineering* 2013 Vol II, WCE 2013, July 3 - 5, 2013, London, U.K.
9. Okuya M, Prokudina NA, Mushika K, Kaneko S. TiO_2 Thin Films Synthesized by the Spray Pyrolysis Deposition (SPD) Technique, *J. Eur. Ceram. Soc.*, 19 903–906 (1999).
10. Kavitha, R, Meghani, S, Jayaram, V, Synthesis of Titania Films by Combustion Flame Spray Pyrolysis Technique and its Characterization for Photocatalysis, *Mater. Sci. Eng. B*, 139 134–140 (2007)
11. Chakraborty A, Mondal T, Bera SK, Sen SK, Ghosh R, Paul GK. Effects of Aluminum and Indium Incorporation on the Structural and Optical Properties of ZnO Thin Films Synthesized by Spray Pyrolysis Technique, *Mater. Chem. Phys*., 112 162–166 (2008).
12. Nakaruk, A, Ragazzon, D, Sorrell, C C, Anatase–Rutile Transformation Through High-Temperature Annealing of Titania Films Produced by Ultrasonic Spray Pyrolysis, *Thin Solid Films* 518 3735–3742 (2010)
13. U. Diebold, *Surface science reports* **2003**, *48*, 53.
14. Nasser SA, Afify HH., E-Hakim SA., Zayed MK. *Thin Solid Films* 315 , 327 (1998).
15. Cullity BD., Elements of X-ray diffraction, 2nd Edition Addition Wesley, Reading M.A, 1978.
16. Chung F H, Smith D K. Industrial applications of X-ray diffraction. New York: Marcel Dekker; 1999. p. 798.
17. Sing P., Kumar A., Kaushal A., Kaur D., Pandey A., Goyal N. In situ high temperature XRD studies of ZnO nanopowder prepared via cost effective ultrasonic mist chemical vapour deposition, *Bull. Mater. Sci.* 31(3) (2008) 573-577.
18. Hitchman ML and Zhao J. The LPCVD of rutile at low temperature, *Journal de Physique IV France*, 9, 357 – 364 (1999).
19. Leinen D, Espinas JP. Fernandez A. and Gonzalez-Elipe AR. Friction and Energy Dissipation at the Atomic Scale: A Review, *Journal of Vacuum Science and Technology A*, 12, 5 (1994).
20. Wollschlager J., Suendorf M., Neumann M., Jayachandran M. and Sanjeeviraja C., Low temperature TiO_2 rutile phase thin film synthesis by chemical spray pyrolysis(CSP) of titanyl acetylacetonate *Thin Solid Films*, 519, 129 – 135 (2010).
21. Edelestein AS. and Camarata R.C., Nanomaterials Synthesis Properties and Applications, Nanomaterials Synthesis Properties and Applications, Institute of Physics Publishing, (1998).
22. Mardare, D, M. Tasca, M. Delibas, G.I. Rusu,On the structural properties and optical transmittance of r.f sputtered films, *Applied Surface Science* 156, 200-206, (2000).
23. Guang-Lei T., Hong-Bo, H., & Jian-Da, S. (2005). Effect of microstructure of TiO_2 thin films on optical band gap energy, *Chinese physics letters*, 22(7), 1787.
24. Rajesh KR & Menon CS. Electrical and optical properties of vacuum deposited ZnPc and CoPc thin films and application of variable range hopping model, *Indian Journal of Pure & Applied Physics* Vol. 43, December 2005, pp. 964-971.

IRJSE *Int. Res. J. of Science & Engineering,* 2018; Special Issue A2 : 122-127
ISSN: 2322-0015
SJIF Impact Factor 4.11
UGC Approved Journal No. 63628
RESEARCH ARTICLE **OPEN ACCESS**

Exciton Captura rate in GaN / AlGaN Quantum Hetero-structures by Computer Simulation

Patil Jyoti and Chaudhari Sharmila

Baburaoji Gholap Research Center, New Sangvi, Pune, India
Email: Jyot.physics@gmail.com , shar_chaudhari@yahoo.co.in

Manuscript Details
Available online on http://www.irjse.in
ISSN: 2322-0015

Editor: Dr. Arvind Chavhan

Cite this article as:
Patil Jyoti and Chaudhari Sharmila. Exciton Captura rate in GaN/AlGaN Quantum Hetero-structures by Computer Simulation, *Int. Res. Journal of Science & Engineering,* 2018; Special Issue A2 : 122-127.

ABSTRACT

Research of the optical properties of III- nitrides quantum well is use to improve the efficiency of optical properties of for light-emitting diodes (LEDs) and laser diodes (LDs). Also III- nitride semiconductors are used in applications like water sterilization, skin treatment and security. Twodimension multiple quantum well (MQW) & Modified Symmectric Quantum Well (MSQW) carrier confinement are neccessary to increase the efficiency of AlGaN/lGaN. Therefore AlGaN-based materials are suitable for development of ultraviolet light source. Study of optical properties of the specific structure of AlGaN/GaN has been done in this research. Examination of carrier confinement mechanism and the carrier life time by exciting the material in quantum barrier energy under continuous wave operation in the visible spectrum region ranging from green to blue colors is reported in this research. The theoretical analysis for energy band gap, Refractive indices, Dielectric function and model parameters has been carried out and results of simulation along with temperature drift of various parameters are presented. The paper concludes with the possible application of these results in the design of GaN waveguides, which are to be used at the elevated temperatures and for GaN/AlGaN hetero-structure lasers.

Keywords: quantum well, AlGaN/GaN, Optics, laser diodes

INTRODUCTION

Quantum Well (QW) lasers are estimated to show superior lasing properties such as lower threshold current density, higher differential gain as compared to heterostructure laser diodes. The variation of the quantum well width, the thickness of the top barrier layer and the potential depth controls the relations between carriers confined within the well region and surface states. Using MATLAB we have theoretically calculated the carrier capture time by the quantum well involves the computation of the probability per unit time that a carrier in some initial state in quantum well heterostructure emits a longitudinal optical (LO) phonon, and ends up in some final state within the quantum well as dictated by energy and momentum conservation conditions. Further the capture time of the electron and the hole in the quantum well shows huge implication in the lasing action and needs the concentration for the expansion of the laser diode efficiency and to lower the threshold current[1]. Emission of optical phonons or carrier-carrier scattering in a layered system. The wide band-gap III–V nitrides has very largr capacity optoelectronic devices emitting in the spectral range from visible to ultraviolet. the refractive indices of GaN and AlGaN and their relative change with temperature is the important part of this research. Another factor is diaelectric function of GaN and AlGaN layers grown under different conditions for a wide spectral range at room temperature by means of spectroscopic ellipsometry [3].

METHODOLOGY

Phonon modes and their potentials

We use a macroscopic dielectric continuum model to describe the optical phonons in these systems.2 It has been shown, based on lattice dynamical calculations, that the dielectric continuum model gives a good representation of electron-phonon scattering rates in quantum-well systems. Here we use electromagnetic boundary conditions for the phonons that have been shown to give a good representation of electron-phonon scattering rates [5,8] Within each semiconductor material the displacement field satisfies ∇.D and the electric field is given by D=ε(ω)E. The dielectric function is taken to be ε(ω)= ε∞,n(ω2- ω2n,LO)/ (ω2- ω2n,TO),where n=1 for GaN n=2 for AlGaN, and ωn,LO ωn,TO O are the longitudinal- and transverse-optical mode frequencies. Within this approach the frequencies of the confined LO modes are ωn,LO . The interface modes satisfy the condition ∇.E=0 that the conditions that E and D' are continuous at the interfaces. The parameters used here for GaN are Eg=3.28 ev, me=0.20 mo, mhh = 1.4 mo,ε=8.9, mv=1.5 m0 [4].

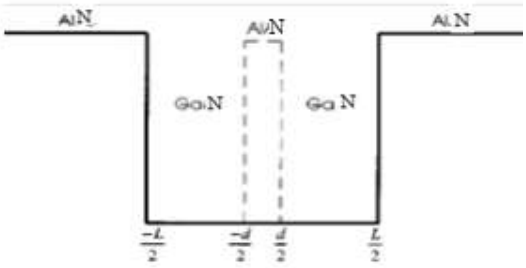

Fig. 1 Sketch of a simple quantum well (SQW) and a structurally modified quantum well (SMQW). The quantum-well material is GaN. The barriers and the thin layer in the quantum well are AlGaN All calculations have been done with d=8 Å. [4]

For a simple GaN/AlGaN quantum well of width L, the frequencies of the symmetric interface modes satisfy the condition

$$\varepsilon GaN(\omega)\tanh\left(\frac{qL}{2}\right) = -\varepsilon AlGaN(\omega) \quad (1)$$

and the antisymmetric modes satisfy

$$\varepsilon GaN(\omega)\coth\left(\frac{qL}{2}\right) = -\varepsilon AlGaN(\omega) \quad (2) \quad [1]$$

Applying the same conditions to the quantum well of width L with an additional AlAs layer of width d in the center

yields, for the frequencies for the symmetric interface modes of a SMQW,

$$\varepsilon GaN(\omega)\{\varepsilon GaN(\omega)(1+e^{-qd})\tanh\left(\frac{q(L-d)}{2}\right)+\varepsilon AlGaN(\omega)\}+\varepsilon AlGaN(\omega)\{\varepsilon AlGaN(\omega)(1-e^{-qd})\tanh\left(\frac{q(L-d)}{2}\right)+\varepsilon GaN(\omega)\} = 0 \quad (3)$$

The antisymmetric interface modes in the SMQW satisfy

εGaN(ω) { $\varepsilon_{GaN}(\omega)(1-e^{-qd})+\varepsilon_{AlGaN}(\omega)\coth\left(\frac{q(L-d)}{2}\right)$ }+ εAlGaN(ω)

{ $\varepsilon_{AlGaN}(\omega)(1+e^{-qd})+\varepsilon_{AlGaN}(\omega)$ } $\coth\left(\frac{q(L-d)}{2}\right)$ = 0 (4) [1]

which gives Semi-classical analysis of hole capture in Gallium Nitride quantum wells In the following we develop a semiclassical model of the heavy hole capture time. Under the collision-free hole transport conditions, the thermionic emission current fills the QW. Then one can estimate the thermionic capture time for a hole using the relation

$$\tau_{\text{therm}} = \frac{b}{2}\left(\frac{\pi m_h^B}{2E_h^B}\right)^{1/2}\exp\left(\frac{e\Phi}{k_B T}\right), \quad (3.6)$$

Where m_h^B is the heavy hole effective mass and E_h^B is the hole energy, both in the AlGaN barrier. $e\Phi$ in Eq. (3.6) represents the potential wall for the hole in the AlGaN, created by the space charge. This potential can be estimated from the Poisson equation assuming the spatially independent densities for electrons and holes on the AlGaN barriers. One gets

$$\Phi = \frac{e}{2\kappa^B}(n_e - n_h)\left(\frac{b}{2}\right)^2, \quad (3.7)$$

Where κ^B is the static permittivity of the AlGaN barrier.

Now we wish to argue that in the experiments of interest the barrier e was negligibly small. Experimental measurements show that there is no dependence of the capture time on an excitation density in the range from 3×10^{15} to $2\times10^{17}\text{cm}^{-3}$. These results were obtained for undoped semiconductor QW structures as well as for the semiconductor QW structures with n-doped and p-doped QWs. The absence of density dependence of the carrier capture time in such a broad range of carrier densities strongly suggests that $\exp[e\Phi/(k_B T)] \approx 1$. We can then estimate from that the space charge density in the AlGaN barrier, $n_e - n_h$, is smaller than $2.5\times10^{14}\text{cm}^{-3}$.

Certain number of holes remains in the barrier because they are electrostatically repulsed by holes captured in the QW. In the same time, the electron density decreases owing to the electron attraction by the holes captured in the QW. As a consequence of this ambipolar process, the electron and hole densities in the barrier tend to remain the same. Thus Eq. (3.6) can be reduced to a simple relation, [3]

$$\tau_{\text{therm}} = \frac{b}{2}\left(\frac{\pi m_h^B}{2E_h^B}\right)^{1/2}. \quad (3.8)$$

If the hole mean free path due to the polar optical phonon emission, ℓ, is greater than the GaN QW width w, the hole capture rate should be reduced by the probability $[1-\exp(-w/\ell)]$ that the hole emits optical phonon when crossing the QW:

$$\frac{1}{\tau_h} = \frac{1}{\tau_{\text{therm}}}\left(1-e^{-\frac{w}{\ell}}\right). \quad (3.9)$$

If we assume that the hole is moving in the barrier as a classical particle, then the phonon emission probability in the QW is

$$1-e^{-\frac{w}{\ell}} = 1-\exp\left(-\frac{w}{\tau_{h-p}(E_h)\,v_h^W}\right) \quad (3.10)$$

Where v_h^W is the z-component of the hole velocity above the QW.The hole scattering time due to the optical phonon (h-p) emission reads

$$\frac{1}{\tau_{h-p}(E_h)} = \frac{1}{\tau_{h-pop}(E_h)} + \frac{1}{\tau_{h-nop}(E_h)}, \quad (3.11)$$

$$E_h = E_{\text{excess}}\frac{m_e}{m_e+m_h} + V_w^h, \quad (3.12)$$

is the kinetic energy of the hole crossing the QW, Excess is the laser excess energy, V_w^h is the depth of the QW in the valence band, and me and mh are the electron and heavy hole effective masses in the QW, respectively.

The first term on the right-hand side of Eq. (3.11) is the emission rate via the heavy hole-polar optical phonon

(h-pop) interaction which has the form

$$\frac{1}{\tau_{h-pop}(E_h)} = \sqrt{m_h/2}\,\frac{e^2\omega_{LO}}{4\pi\hbar}\left(\frac{1}{\kappa_\infty}-\frac{1}{\kappa}\right)\frac{1}{\sqrt{E_h}}\ln\left|\frac{\sqrt{E_h}+\sqrt{E_h-\hbar\omega_{LO}}}{\sqrt{E_h}-\sqrt{E_h-\hbar\omega_{LO}}}\right|,$$

(3.13)

Where ω_{LO} is the frequency of longitudinal optical phonons, κ and κ_∞ are the static and high frequency permittivities, respectively, in the QW. The second term represents the heavy hole non polar optical phonon (h-nop) emission rate in the form

$$\frac{1}{\tau_{h-nop}(E_h)} = \frac{(2m_h)^{3/2}D_0^2}{4\pi\hbar^3\rho\,\omega_0}\sqrt{E_h-\hbar\omega_0},$$

(3.14)

Where D0 is the non polar optic deformation potential, ρ is the mass density, vL is the velocity of sound, and ω_0 is the non polar optic phonon frequency In Eq. (3.10) the z-component of the hole velocity can be found from the laser excess energy as

$$v_h^W = \sqrt{\frac{2}{m_h}\left(\frac{1}{3}E_{\text{excess}}\frac{m_e}{m_e+m_h}+V_w^h\right)}.$$

The model (3.8)-(3.10) can be further improved if we take into account that the carrier can be quantum-mechanically reflected at the edges of the QW (at points $-w/2$ _ and $w/2$;).Then

$$\frac{1}{\tau_h} = \frac{2}{b}\left[\frac{2E_{\text{excess}}}{3\pi(m_e^B+m_h^B)}\frac{m_e^B}{m_h^B}\right]^{1/2}T_{B\to W}\left[1-\exp\left(-\frac{w}{\tau_{h-p}(E_h)\,v_h^W\,T_{W\to B}}\right)\right],$$

(3.15)

where the transmission coefficient from the AlGaN barrier into the QW is defined as

$$T_{B\to W}(E_h-V_w^h) = \frac{4\sqrt{m_h^B m_h(E_h-V_w^h)E_h}}{\left(\sqrt{m_h^B(E_h-V_w^h)}+\sqrt{m_hE_h}\right)^2},$$

the transmission coefficient from the QW into the AlGaN barrier as

$$T_{W\to B}(E_h) = T_{B\to W}(E_h-V_w^h),$$

(3.16)

and m_e^B e is the electron effective mass in the barrier.

RESULTS AND DISCUSSION

The carrier capture process is of great significance in the quantum well region. The population inversion occurs due to capturing of electrons and holes in the quantum well region and a short capture time of these carriers reduces the threshold current.

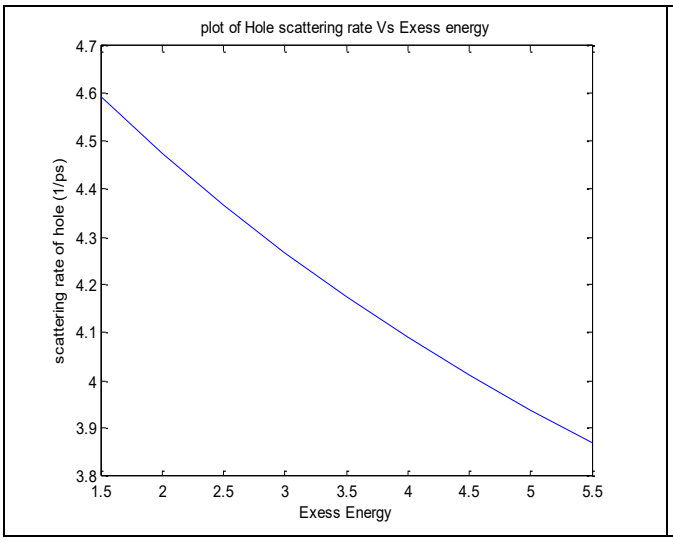

Fig. 1: variation of Scattering Rate of hole With Excesses Energy of hole

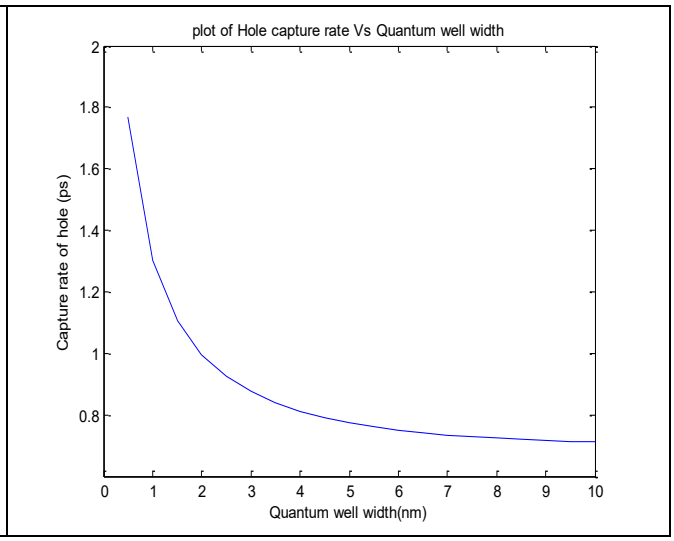

Fig2: Variation of capture rate of hole(ps) with Quantum well width(nm)

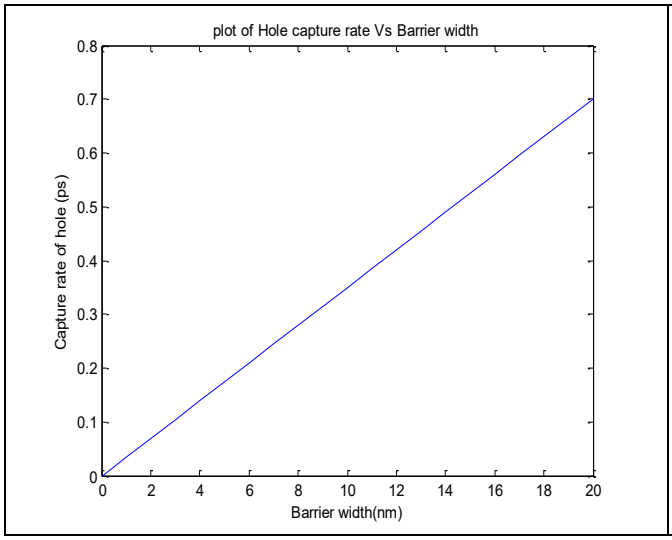

Fig. 3: Variation of capture rate of hole(ps) with Barrier width(nm)

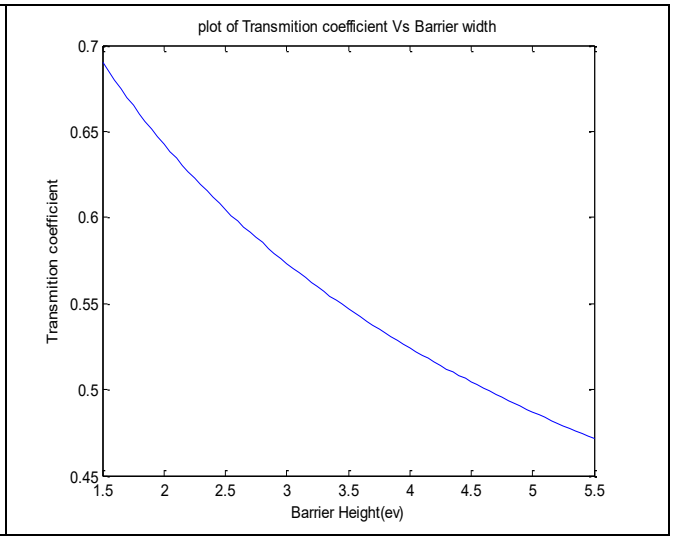

Fig. 4. Variation of Transmission Coefficient with Barrier height.

Fig. 2 shows the holes capture time dependence on the barrier width and Aluminum mole fraction of AlGaN. The minor variation in hole capture time has been observed due to variations in barrier width and with the increase in barrier width the hole capture time increases linearly as expected. The simultaneous study of the mole fraction dependence has been carried out and Fig. 2 reveals that increase in mole fraction enhances strongly the hole capture time. The hole capture time was found increase from 12 ps to 65 ps for the values of Aluminum mole fraction changing from 0 to 100% respectively. The barrier width was considered to change from 10 nm to 20 nm. The higher capture time is obtained for larger values of the Aluminum mole fraction due to the increase in the band offset between the quantum well and barrier regions.

CONCLUSION

Detail analysis of hole capture in a Gallium Nitride quantum wells has been carried out with hole-optical phonon scattering mechanism using semi-classical model to enhance the performance of quantum well lasers operating with fast switching speeds. The hole capture time was deduced as a function of the excess energy, quantum well width, barrier width and aluminum (Al) mole fraction in the barrier layer. Our analysis reveals strong dependence of hole capture time and scattering rate on the geometry and material composition of the well and the barrier. The hole capture time was found to change from 0.3 ps to 65 ps with variation of structural parameters of the quantum well and Al mole fraction in the barrier. Our analysis provides useful physical insight to improve the performance of the quantum well lasers by proper optimization of structural and material parameters of GaN and AlGaN.

Conflicts of interest: The authors stated that no conflicts of interest.

REFERENCES

1. AlAs layers, Cynthia R. McIntyre Electron-phonon scattering rates in semiconductor quantum wells with thin Department of Physics, *Physical Review* 1997 ;56(20)-II.
2. Dependence of the refractive index of AlxGa1−xN on temperature and composition at elevated temperatures, *Journal Of Applied Physics*, 2001
3. Samuel EP, Bhole MP, Patil DS, Semiconductor *Science and Technology*.2006; 21, 993).
4. Vurgaftman I., Meyer JR., Ram-Mohan LR. *Journal of Applied Physics*,2001; 89, 5815
5. Darakchieva V, Valcheva E, Paskov PP et. al. *Physical Review*, 2005; B 71, 115329.

6. Lu W, Li DB, Li CR, Shen F, Zhang Z, *J. of Appl. Phys*., 2004; 95, 4362.
7. Cho KS, Huang Tsai-Yu, Huang Chao-Ping, Chiu Yi-Hsing, CT. Liang, Y. F. Chen, *J. of Appl. Phys*., 2004; 96, 7370.
8. Capasso F et. al. IEEE J.on Selected Topics in Quantum Electronics, 2000; 6, 931.
9. Abdi-Ben S.Nasrallah, N. Sfina, N. Bouarissa, M. Said. *J. Phys.:Condens. Matter*. 2006; 18, 3005.
10. Liu YX, Ting DZY, T. C. McGill Physical Review B 54, 5675 (1996).
11. M. Baro, H. Chr. Kaiser, H. Neidhardt, J. Rehberg, J. of Mathematical Physics. 45, 21 (2004).
12. Gmachl C, Sivco DL, R., F. Colombelli, F.Capasso, Cho AY. *Letters to Nature*, 2002; 415, 883,
13. Baraff GA, *Physical Review*, 1998; B 58, 13799000.
14. Marchi A, Bertoni A, Reggiani S, Rudan M. Semiconductor Science and Technology, 2004; 19, S415-S417.
15. Fischetti MV. *J. Applied Physics*, 1998; 83,270.
16. Boykin TB, Klimeck G. *Eur. J. Phys*.2004; 25, 503.
17. Mamishev AV, Rajan KS, Yang F, Du Y, Zahn M. Proceedings of the IEEE, 2004; 92, 808.
18. Suski T et. al. *Applied Physics Letters,* 2004; 84, 1236.

IRJSE *Int. Res. J. of Science & Engineering,* 2018; Special Issue A2 : 128-131 SJIF Impact Factor 4.11
ISSN: 2322-0015 UGC Approved Journal No. 63628
RESEARCH ARTICLE **OPEN ACCESS**

Study of linear absorption and mass attenuation coefficient of various materials using G. M. Counter

Kadhum Saad Jundee, Yande Jyoti and Aghav SD

Baburaoji Gholap College, Sangvi, Pune 41127 (SPPU), India
E-mail: sdaghav@gmail.com

Manuscript Details
Available online on http://www.irjse.in
ISSN: 2322-0015

Editor: Dr. Arvind Chavhan

Cite this article as:
Kadhum Saad Jundee, Yande Jyoti and Aghav SD. Study of linear absorption and mass attenuation coefficient of various materials using G. M Counter, *Int. Res. Journal of Science & Engineering,* January 2018; Special Issue A2: 128-131

ABSTRACT

In the areas where the people have to encounter ionizing radiation daily, it is necessary to provide shielding materials for radiation safety. Present study is intended to investigate the attenuation coefficient for the various materials of different thickness as absorbers for radioactive source and establish the relations among linear attenuation coefficient, mass attenuation coefficient and density of materials. Radioactive sources Co^{60} was used as sources of the gamma rays. Geiger Muller counter is used as detector. Lead, aluminum, iron, stainless steel, glass, plastic and wood materials are used as absorber.

It had been observed that attenuation can be achieved using a wide range of materials. Once basic principles involved in gamma ray interaction with matter is understood, it will be easier to select shielding material for given application. Though lead had found to have a higher attenuation coefficient and have a better radiation shielding rather than others but it is not environment free. Linear attenuation coefficient, mass attenuation coefficients, half value layer HVL($X_{1/2}$) of absorber materials is calculated and study will be useful in selecting shielding material.

Key words: G. M. Counter, mass absorption coefficient, nuclear safety, cobalt Co60, shielding material.

INTRODUCTION

The provision of enough protection against nuclear radiation remains an important problem in the countries which are exposed to nuclear radiation. Radiation protection is serious concern in nuclear power plants, industrial or medical x ray system, particle accelerator and radiology. In such areas people are exposed to ionizing radiation continuously. The provision of adequate protection from undue exposure of radiation to individual is necessary as harmful effects of ionizing radiation can cause significant health hazards [1]. Radiation shielding depends on principle of attenuation, stopping power of radiation particles and the shielding material used [2]. Most common structure of defending materials include rigid materials such as high density concrete, lead bricks, steel plates and cooling pools filled with water. They have insufficient portability. The gamma attenuation of these materials has been usually studied [3].

In addition to these well distinguished shielding materials, complex materials are becoming increasingly available. Even lead free composite material from tungsten can be used against electron beam in radiotherapy [4].The attenuation of gamma radiation is dependent upon the energy of the incident gamma radiation, the atomic number, density of the elements in the shielding material, and the thickness of the shielding. Composite materials may offer additional benefits in chemical resistance, physical durability and portability [5, 6]. Present study deals with comparative study of linear attenuation coefficient, mass attenuation coefficients, half value layer of six materials.

METHODOLOGY

Equipment/Accessories used consist of G.M Counting System with detector. Radioactive sources Co-60 is used as gamma ray source. Aluminum ,Iron ,Steel ,Glass, Plastic and wood absorber set with 1 mm thickness each one also lead absorber two slab 0.5 cm each one.

Procedure adopted is as follows.

Set GM voltage at the operating voltage of the GM tube (Fig1a). Without source, make a few (about 5 readings) background measurements and take an average for a preset time of say 60 sec. Compute Average background counts in 60 sec (Ba = $(b_1+b_2+b_3+b_4+b_5)$ / 5).Compute Background rate = Ba/t (t = 60sec). Place a Gamma source in the source tray at about 7 cm from the end window of the GM tube and take reading of zero absorber thickness. Take the Aluminum absorber set. Place an aluminum absorber of 1mm thickness in the absorber holder at about 2 cm from the end window of the GM tube and record the counts for three times and take mean. The absorber thickness is increased in steps of 1mm up to 1cm and every time counts are recorded [7].

Fig 1 (a) G M Counter **(b) Absorbers**

This process is repeated with all absorbers that used in this study (Fig1b). Data is to be collected for Co-60

source. (35 KBq, Mar-2015);Half-life for Co-60 is $T_{1/2}$=5.2714 y) having present activity (A) =31.367 KBq.

Subtract the background count rate from each measured count rate. Plot a graph of corrected counts(I) VS absorber thickness (Fig.2). Find I_0 for x=0 by extrapolation of the curve for I/I0=0.5 and obtain X1/2.From the plotted graph extrapolate and obtain X1/2. Half value layer (HVL) of absorbing medium is defined as thickness X1/2 which will cut the initial intensity to half. Substitute X1/2 in the equation μ= 0.693/x1/2 to calculate linear absorption coefficient. Once linear absorber /attenuation coefficient is known, we can find out mass attenuation coefficient μm = μ/ρ where ρ is density of material of the absorber.

RESULTS AND DISCUSSION

Table 1 indicates comparison of half value layer, linear absorption and mass absorption coefficients.

Measuring count rate as a function of Gamma energy:1-Isotope: Co 60

Distance between source and detector: 5(cm), Time: 60 (sec), Operation voltage: 450 volt count with source without Absorber=1756

Background count (NB) = 15.3 Background count rate (IB) = 0.255, count rate=29.2.

These measurements are shown in Table 2.

Energy calculated by formula = (R+160)/543 MeV,

Where R is taken from the Graph of Log Nc Vs mx , i.e. intersecting point of line with X axis. Count rate depends on density and thickness of material

Table 1: comparison of half value layer, linear absorption and mass absorption coefficients.

Material	Density(g/cm^3)	X1/2(cm)	μL (cm^{-1})	μm(cm^2/gm)
Stainless steel	7.9	0.1	6.93	0.87
Iron	7.874	0.11	6.93	0.88
Al	2.7	0.12	5.775	2.13
Glass	2.58	0.11	6.3	2.44
Plastic	1.05	0.085	8.15	7.7
Wood	0.7	0.09	7.7	11

Table. 2: Measuring count rate as a function of Gamma energy:1-Isotope: Co 60

Material	Thickness (cm)	Absorber Mass thickness (gm/cm2) = thickness X-density	Count (1)	Count (2)	Count (3)	Mean	Count rate	Corrected Count rate (I)	Ln(I)	Emax MeV
Lead (Pb)	0.5	5.67	502	499	461	487.3	8.12	7.86	2.06	0.298895
	1	11.34	365	386	383	378	6.3	6.045	1.799	
S.steel	0.5	3.95	479	539	508	508.6	8.47	8.22	2.106	0.297422
	1	7.9	480	500	494	491.3	8.188	7.933	2.07	
Iron(Fe)	0.5	3.937	538	586	527	550	9.166	8.911	2.187	0.297238
	1	7.874	496	516	515	509	8.48	8.228	2.107	
Aluminum (Al)	0.5	1.32	609	584	554	582.3	9.705	9.45	2.14	0.299263
	1	2.64	552	508	531	530	8.83	8.57	2.149	
Glass	0.5	1.29	620	570	588	592.6	9.87	9.62	2.264	0.299171
	1	2.58	570	534	544	549.3	9.155	8.9	2.186	
Plastic (polystyrene)	0.5	0.525	570	610	605	595	9.916	9.661	2.26	0.292818
	1	1.05	572	603	631	568.6	9.476	9.221	2.221	
7-Wood (MDF)	0.5	0.35	617	584	568	568.6	9.826	9.5716	2.258	0.293278
	1	0.7	581	572	590	581	9.683	9.428	2.243	

CONCLUSION

The present study provides the values of the gamma-ray mass attenuation coefficients, linear absorption coefficient and half value layer of materials (stainless steels, Iron, aluminum, Plastic, glass, Plastic and wood). Our results show that attenuation can be achieved using a wide range of materials. Once basic principles involved in gamma ray interaction with matter is understood, it will be easier to select shielding material for given application. Interaction of gamma radiation with matter obeys the exponential attenuation law. There is decrease of the attenuation coefficient with increasing energy of gamma quanta and increase of the attenuation coefficient with increasing atomic number of the absorber.

Acknowledgement:
Authors are grateful to Principal Dr. M.G. Chaskar of Baburaoji Gholap College and office beares of P.D.E.A .Pune for allowing us to use the facility in labortory. Saad Jundee Kadhum acknowledge Republic of Iraq for felloship offered by government for his P.G.study.

Conflicts of interest: The authors stated that no conflicts of interest.

REFERENCES

1. SB Grover, J Kumar, A Gupta, L Khanna. Protection against radiation hazards: Regulatory bodies, safety norms, dose limits and protection devices . *Nursing Practices*, 2002;12(2):157-167.
2. Price BT et al. Radiation shielding. Peragoman press.1957, pp 267-277.
3. Knoll GF. Radiation Detection and Measurement. 3rd Edition. New York: John Wiley & Sons, (2000): 48 – 55.
4. Aleksander Samarin. Concrete as a Biological Shield from Ionizing Radiation. Energy and Environmental Engineering,2013; 1(2):90-97
5. Yue K. A new lead free radiation shielding material for radiotherapy. Radiation Protection Dosimetry, 2009; 133(4) :256-260.
6. Limkitjaroenporn P, J. Kaewkhao, W. Chewpraditkul and P. Limsuwan, Mass Attenuation Coefficient and Effective Atomic Number of Ag/Cu/Zn Alloy at Different Photon Energy by Compton Scattering Technique, Procedia Engineering, 2012; 32: 847 –854.
7. Narender Reddy J, M.S.R.Murty. Experiments with G.M. Counter. Manual by Nucleonics System Pvt Ltd.Hyderabad :1-49

IRJSE *Int. Res. J. of Science & Engineering,* 2018; Special Issue A2 : 132-134 SJIF Impact Factor 4.11
ISSN: 2322-0015 UGC Approved Journal No. 63628
RESEARCH ARTICLE **OPEN ACCESS**

Comparative Study of Rate Constant of Metallophthalocyanines as Nitrogen Dioxide Sensor

Datir AM

Agasti Arts, Commerce and Dadasaheb Rupwate Science College, Akole, Ahmednagar, Maharashtra, India 422601.
Email: ashokdatir526@gmail.com

Manuscript Details
Available online on http://www.irjse.in
ISSN: 2322-0015

Editor: Dr. Arvind Chavhan

Cite this article as:
Datir AM. Comparative Study of Rate Constant of Metallophthalocyanines as Nitrogen Dioxide Sensor, *Int. Res. Journal of Science & Engineering,* January 2018; Special Issue A2 : 132-134.

ABSTRACT

Cobalt Phthalocyanine (CoPc), Copper Phthalocyanine (CuPc), Zinc Phthalocyanine (ZnPc) and Iron Phthalocyanines (FePc) are synthesized by chemical reaction from phthalic anhydride and urea. After characterization of materials by XRD, UV Visible and FTIR, sensor samples are prepared in the form of pellets. The change in electrical resistance due to exposure of samples to different concentrations of nitrogen dioxide (NO_2) of the samples is studied. All samples are studied at room temperature. Response curves of the samples are plotted and best fitted with the chemisorptions kinetics to determine rate constant. The rate constants for different NO_2 concentrations and different materials are compared. ZnPc showed highest response rate than CuPc and CoPc and FePc.

Key words: Metal Phthalocyanine, Gas Sensor, Nitrogen Dioxide, Rate constant.

INTRODUCTION

The main issue of public health is the degradation of the air quality in industrial and highly dense fuel vehicle areas. It is due to unavoidable emission of toxic air pollutants [1]. The combustion of diesel generates suspended particulate matter (SPM), nitrogen oxides (NO_x), sulphur dioxide, polycyclic aromatic hydrocarbon (PAH) and also carbon monoxide (CO). Highly pollutant and toxic gas like NO_2 in an environment has become important as a result of increased automobile fuel

vehicles and production in the chemical industries [2]. Phthalocyanines (Pcs) and structurally related compounds are of interest in gas sensor applications. In earlier paper Chakane et el. studied NO_2 sensor using metallophthalocyanine (MPc) coated on porous silicon [3]. The family of MPc has been found to be highly reactive with strong oxidizing gases such as NO_2 [4]. CuPc, CoPc, ZnPc, FePc are belongs to this family of organic molecular solids. Their composition consists of hydrogen, carbon, nitrogen and substituted metal atom arranged into a macrocycle. Their semiconducting properties are exploited for gas sensing applications. The gas sensing principle is based on the change of conductivity upon the adsorption of gas species at the surface. The conductivity of p-type MPcs increases on the adsorption of oxidizing molecules, because of the increase of the hole carriers induced by the formation of charge transfer complexes at the surface of phthalocyanines [5]. The response characteristics study in this work shows that the rate of change of sensitivity is different for different concentrations of NO_2 gas. The response rate increases with increase in NO_2 gas concentration in the air surrounding the sample. The rate of change of sensitivity is expressed in form of the equation in terms of rate constant. The response characteristics are best fitted with the equation to determine rate constant. The comparative study of the determined rate constants respective to various NO_2 concentrations and different sensor materials is discussed in this paper.

METHODOLOGY

Synthesis procedure of MPcs involves mixing of phthalic anhydride, urea and metal salt taken in the weight proportion of 4:4:1 along with the catalyst ammonium molybdate. These precursors are crushed together and mixed properly. The mixture is then heated with constant stirring. Reaction took place at about 200°C– 250°C. The residue is crushed to a fine powder. Un-reacted precursors are removed by several times washings with methyl alcohol and distilled water. The powder is then air-dried under IR lamp and uniformly crushed to make fine and uniform granules. Synthesized MPcs were characterized by bulk XRD, UV-Visible absorption spectra and FTIR spectroscopy. Samples in the form of pellets were prepared for studying the gas response. The synthesized MPc material was compacted into the pellets of 13 mm diameter using press technique. Three parameters viz. pressure, time weight of MPc material were optimized. Electric contacts were made by coating silver paste on either surface of the pellet.

Gas exposure tests of prepared sensor samples were performed in a controlled environment at room temperature using specially designed glass chamber to obtain data toward the detection of NO_2 mixed with atmospheric air. Electrodes from sample were connected to keithley-2000 electrometer in order to measure sample resistance. Electrometer is interfaced to computer through RS-232 port provided at the back panel of electrometer. Software provided by keithley is used to monitor the resistance in the domain of time.

RESULTS AND DISCUSSION

CuPc, CoPc, ZnPc and FePc sensor samples were exposed to 0.5 volume % concentration of NO_2. The resistance is monitored with 30 seconds interval and the response is plotted. The response of CuPc samples with different NO_2 concentration is shown in Figure 1 in terms of instantaneous sensitivity S(t) given by equation 1.

$$S(t) = \frac{\left(R_a - R_g\right)}{R_a} \times 100\% \qquad (1)$$

Where, R_a and R_g are initial resistance and resistance in the presence of gas of the sample respectively.

It is seen from the response graph shown in figure 1 that the response rate is different phthalocyamines for same NO_2 gas concentrations. The variation of electric current or resistance during the doping stage of the sensing period is given by kinetic model based on gas adsorption/desorption theory. The derived general form of it is expressed as equation 2 [6].

$$S(t) = S(1 - e^{-b\,t}) \qquad (2)$$

Where, S (t) is instantaneous value of sensitivity, S is steady state value of sensitivity, b is rate constant in the doping stage and t is time. In order to determine the rate constant b, equation 2 can be modified as,

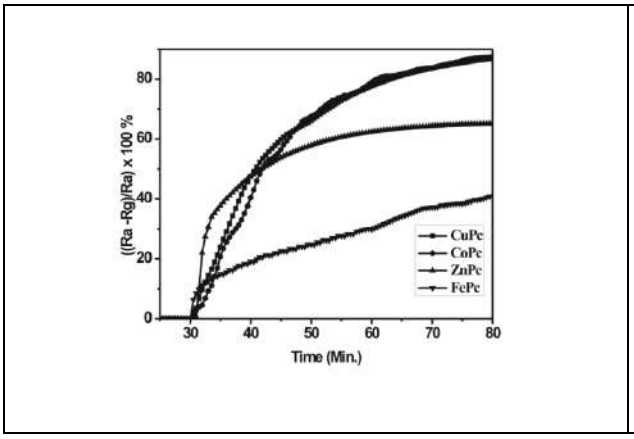

Figure 1: Response of CuPc, CoPc, ZnPc and FePc pellets to 5000 ppm NO_2.

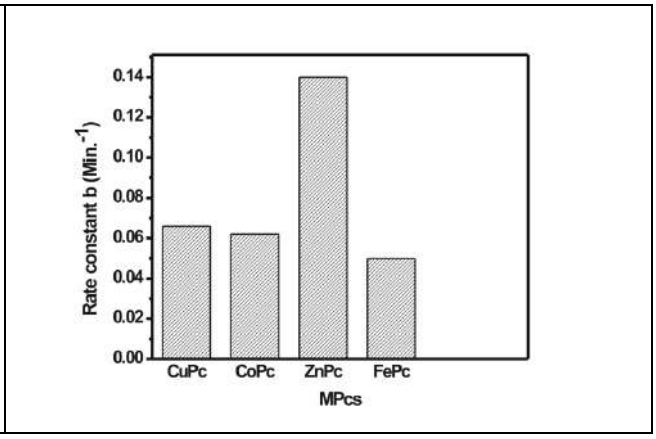

Figure 2: Rate constant for CuPc, CoPc, ZnPc and FePc pellets to 5000 ppm NO_2.

$$\ln\left(\frac{S}{S-S(t)}\right) = b\,t \qquad (3)$$

The slope of graph of $\ln\left(\frac{S}{S - S(t)}\right)$ versus t will give the value of rate constant b. The rate constant b is related to the rate constant of adsorption (K_a) and desorption (K_d) as $b = K_a C_0 + K_d$. C_0 represents the bulk concentration of NO_2 present in the test chamber. The comparative values of rate constant b are plotted in the following graph.

It is seen from figure 2 that the value of rate constant of ZnPc pellet is highest and that of FePc is smallest. Hence ZnPc shows highest response rate. Further studies are needed to study the adsorption and desorption process which is responsible for response rate.

CONCLUSION

The time dependence of the response of MPc sensors to NO_2 changes with MPc material. ZnPc showed highest response rate, the sensitivity of which is smaller than CuPc and CoPc. Hence the materials having small sensitivity can be used as gas sensors if initial short time exposure to the gas is taken into account.

Conflicts of interest: The authors stated that no conflicts of interest.

REFERENCES

1. Pummakarnchana O., Tripathi N., Dutta J., Air pollution monitoring and GIS modeling: a new use of nanotechnology based solid state gas sensors, *Science and Technology of Advanced Materials,* **6,** 251 **(2005)**.
2. El-Bosaty A. B., El-Brolossy T.A., Abdalla S., Negm S., Abdella R.A., and Talaat H., Surface Plasmon-Cobalt Phthalocyanine Sensor for NO_2 gas, *Egypt. J. Solids*, **29**(1), 121, (**2006**).
3. Chakane Sanjay, Gokarna Anisha, Bhoraskar S.V., Metallophthalocyanine coated porous silicon gas sensor selective to NO_2, *Sensors and Actuators B*, **92**, 1-5 , (**2003**).
4. Jones T. and Bott B., Gas-induced electrical conductivity changes in metal phthalocyanines, *Sens. Actuators*, **9**, 27, **(1986)**.
5. Kuo-Chaun Ho and Yi-Ham Tsou, Chemiresistor-type NO gas sensor based on nickel phthalocyanine thin films. Sensors and Actuators B **77**, 253-259 **(2001)**
6. Yuh-Lang Lee, Chuan-Yi Hsiao, Rung-Hwa Hsiao; Annealing effects on the gas sensing properties of copper phthalocyanine films, Thin Solid Films, **468**, 280–284 **(2004)**.

IRJSE *Int. Res. J. of Science & Engineering*, 2018; Special Issue A2 : 135-139 SJIF Impact Factor 4.11
ISSN: 2322-0015 UGC Approved Journal No. 63628
RESEARCH ARTICLE **OPEN ACCESS**

Studies on nano-fluids based on Electrochemically Deposited Tin Nanoparticles

Arote SA*[1], Palve BM[1], Gapale DL[1] and Pande VR[2]

[1]Department of Physics, S. N. Arts, D. J. M. Commerce, B. N. S. Science Sangamner, Dist:Ahmednagar 422 605
[2]Department of Physics, B.S. Thorat College Sangamner, Dist: Ahmednagar 422 605 India.
Email: sandeeparote@gmail.com

Manuscript Details
Available online on http://www.irjse.in
ISSN: 2322-0015

Editor: Dr. Arvind Chavhan

Cite this article as:
Arote SA, Palve BM , Gapale DL and Pande VR. Studies on nano-fluids based on Electrochemically Deposited Tin Nanoparticles, *Int. Res. Journal of Science & Engineering*, January 2018; Special Issue A2 : 135-139.

ABSTRACT

In the present work, we have prepared Tin nanoparticles by using electro-deposition method. The structural, optical and morphological properties of the prepared Tin (Sn) nanoparticles were characterized by using XRD, UV-Visible Spectroscopy and scanning electron microscopy, respectively. The XRD spectra reveal that the prepared Sn nanoparticle shows crystalline and cubic structure. In present investigation, we also studied the effect of the different parameters such as temperature, applied potential, time, stirring rate on electrical properties of the Sn nanoparticles. The present work also investigated the effect of Sn nanoparticles on electrical conductivity of base fluid (DDW) by using different sources. The electrical properties of the base fluid get altered on the dispersion of nanoparticles. The effect of illumination under different source on electrical conductivity of the Sn nanoparticle with base fluid was also discussed.

Keywords: Nanotechnology, Nanoparticles, electro-deposition, electrical conductivity, Tin etc.

INTRODUCTION

Nanoparticles are of great scientific interest as they are effectively a bridge between bulk materials and atomic or molecular structures. The properties of many conventional materials change when formed from nanoparticles. This is typically because nanoparticles have a greater surface area per weight than larger particles which causes them to be more reactive to some other molecules. There are many advantages of nanoparticles in medical field, in cosmetics, in industries, in biomedical, textiles, electronics, health care, food agriculture, etc.[1-4]. There are so many methods for preparation of metal nanoparticles such as spry pyrolysis method, CVD, PVD, ball milling method, colloidal method, electrodeposition method, etc [5].In the experiment we have prepared metal nanoparticles. So, a solid material which is typically hard, shiny, malleable, fusible, and ductile, with good electrical and thermal conductivity (e.g. iron, gold, silver, and aluminum) is the metal & nanoparticles of such material is the metal nanoparticle [6]. Nanoparticles often possess unexpected optical properties as they are small enough to confine their electrons and produce quantum effects. Absorption of solar radiation is much higher in materials composed of nanoparticles than it is in thin films of continuous sheets of material. Tin has significantly higher electrical conductivity compared to silicon (10^{-7} Ω·m versus 2×10^{3} Ω·m). It has high volumetric density and a maximum theoretical capacity upon lithiation (994 mAh/g) that also exceeds that of graphite [7]. There are several methods for preparation of metal nanoparticles such as are, spry pyrolysis method, CVD, PVD, ball milling method, colloidal method, electrodeposition method, etc. [8-9]. From these methods we have used electrodeposition method which is cheap and easy. Here we have synthesized copper nanoparticles from this method by applying certain potential difference with constant current supply and at the room temperature. The preparation of the nanoparticle can possible at room temperature in the laboratory by using electrodeposition method. The structural and morphological characterization of film has been carried out by X- ray diffraction (XRD) and Scanning electron microscopy (SEM) respectively and their optical and compositional properties have been studied by UV-vis-NIR spectrophotometer.

In the present work we successfully synthesized the Sn nanoparticles by using electrodeposition method and study its conducting as well other characteristics by using characterization technique. The prepared tin nano particles shows various properties. Tin nanoparticles shows maximum absorbance of UV light. Therefore it is applicable in sunscreen lotions, cosmetics, sunglasses, etc. to protect the human organs from harmful UV rays [10-11].

METHODOLOGY

1. Electrodeposition technique: In the present synthesis of Sn nanoparticles, 0.1 M $SnCl_2$ (1.13 gm) solution used as a cationic precursor. This solution added in the 50 ml ethanol in beaker. Stir the solution (180 rpm) properly on magnetic stirrer and add 20 drops of 50 % diluted HCl. The voltage given to the electrodes should be 3 V and 4.5 V. The pH of the electrolyte is one. The deposition time is 10 minute. The synthesized Sn nanoparticles dispersed in ethanol by ultrasonication and then kept at room temperature (27 °C) for 3 months to determine their stability. The X-ray diffraction studies of Sn nanoparticles was carried out using X ray diffractometer (Bruker D8), Scanning electron microscope (JEOL JSM-6360) was used for the surface morphological study. The optical absorption spectra were recorded in the range 300-1200 nm at room temperature by JASCO spectrophotometer. The electrical conductivity of Sn nanoparticles in aqueous solution also measured.

Fig 1. Electro-deposition Setup in the laboratory

2. Measurement of electrical conductivity:

The electrical conductivity of any fluid is a measure of its ability to carry an electric current. The electrical conductivity can be expressed as mhos (Reciprocal of ohms) or as siemens. In most fluids, the conductivity is very low, so millisiemens or microsiemens are used as units for conductivity. Chemical composition of fluid determines its conductivity. Since the charge on ions in solution facilitates the conductance of electrical current, the conductivity of a solution is proportional to its ion concentration and their mobility [12-13]. The ions in water act as electrolytes and conduct the electricity.

Most conductivity measurements are made in aqueous solutions, and the ions responsible for the conductivity come from electrolytes dissolved in the water. Although water itself is not an electrolyte, it does have a very small conductivity, implying that at least some ions are present. The ions are hydrogen and hydroxide, and they originate from the dissociation of molecular water. The nano-fluids used in experiment were prepared using a two-step method. First, an appropriate amount of Sn nanoparticles has been weighed with the analytical balance and then mixed with water make conducting aqueous solution. . Then, samples were stirred for 30 min using magnetic stirrer. The electrical conductivity found to be a significant dependence on the dispersed particles and its concentration. Thus, the second step of preparation of samples was sonication in ultrasonic bath in order to break up the agglomerates remaining after the mechanical stirring. The time for sonication was 20 min. An ultrasound that we used has a power of about 350 W, and is equipped in ultra-wave generators with frequency about 34 kHz.

RESULTS AND DISCUSSION

1. Structural Analysis:

The crystallographic analysis was done by utilizing XRD. XRD analysis of the prepared sample of Tin nanoparticles was taken for the range of 10 to 80 degrees as shown in Fig.2 The XRD study reveal that the synthesized sample shows high crystallinity level and tetragonal structure. The tetragonal Sn phase structure (JCPDS Card No. 04- 0673, space group: I41/amd, 141) is evidenced by the peaks appearing at 2θ = 30.07°, 31.58°, 43.96°, 45.06°, 54.97°, 62.19°, 63.84° and 73.40°, corresponds to (200), (101), (220), (211), (301), (112), (321) and (411) respectively. The peak broadening suggested that a synthesized Sn particle shows nanocrystalline nature.

X (2Θ)	Y (Intensity)	hkl (miller indices)	D
30.0744559	307.023031	(200)	0.2968
31.5819015	144.697185	(101)	0.2829
43.9721993	119.050327	(220)	0.2056
45.0687285	178.163207	(211)	0.2009
54.9793814	93.5598521	(301)	0.1668
62.1958763	135.157805	(112)	0.1490
63.8476518	96.3745512	(321)	0.1456
73.4054983	133.906739	(411)	0.1288

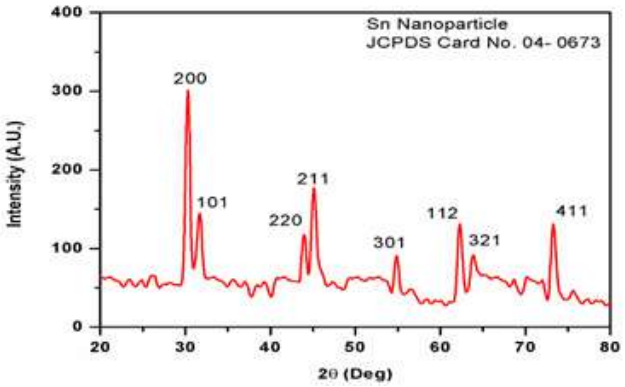

Fig 2. XRD spectra of synthesized Sn nanoparticles.

2. Optical Analysis: The optical analysis of the synthesized nanoparticle was carried out by using UV-Visible spectroscopy in the range of wavelength 300-800 nm. In the optical spectra, the prominent peak is appeared at 250nm, so we can conclude that Sn nanoparticles absorb light of wavelength of 250 nm.

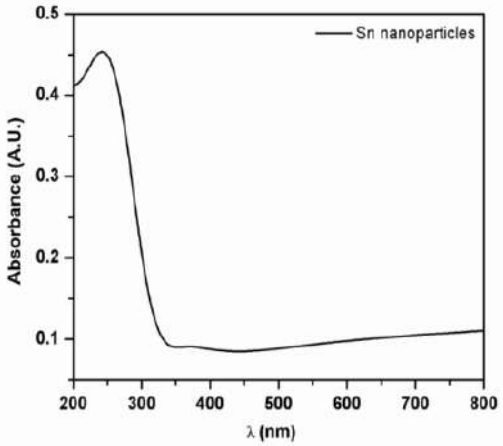

Fig 3: The UV visible spectrogram of synthesized Sn nanoparticles

Since the 250nm wavelength lies between 100 nm to 400 nm that is in ultra-violet region, Sn nanoparticles absorbs UV light. The position and shape of the absorption peaks are dependent on the particle morphology, dielectric functions of the metal and the surrounding medium as well as surface-absorbed species.

3. Microstructural Properties:

Surface morphology of Sn nanoparticles was characterized using scanning electron microscope. Fig. 3 shows SEM micrographs of Sn nanoparticles. It is observed that the image showed micrometer-sized randomly distributed crystal aggregates, in the range of 0.2–2 µm. The higher magnification imaging (Fig. 3 b) revealed that the irregular shaped nanocrystal are agglomerated and formed big size crystal.

4. **Electrical conductivity:** In the present study the electrical conductivity was measured using electrical conductivity meter. The fluid is subjected to illumination under different illuminating source in order to observe the effect of electromagnetic radiations on the electrical conductivity of prepared sample. The results are shown below as a effect of change in distance between illuminating source and sample.

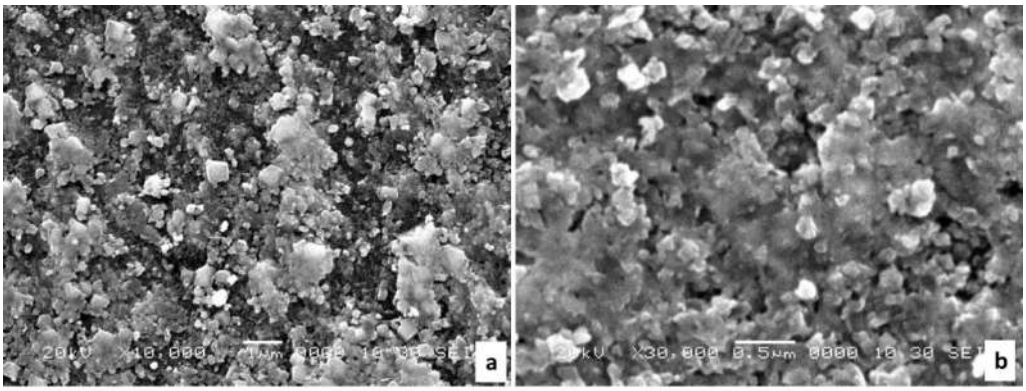

Fig 4: SEM images of electro-deposited Sn nanoparticles prepared at 3V potential

1) In tungsten lamp:

Distance (cm)	Sn(3V)	Sn(4.5)
10	119.3	123.0
20	119.0	122.2
30	118.3	121.7
40	118.8	121.5
50	118.1	121.9

2) In sodium lamp

Distance (cm)	Electrical conductivity(µS) Sn(3V)	Sn(4.5)
10	191.2	0.712×10^{-3}
20	197.1	0.728×10^{-3}
30	196.6	0.734×10^{-3}
40	197.3	0.737×10^{-3}
50	196.6	$0.742 \quad 10^{-3}$

3) In IR lamp

Distance (cm)	Sn(3V)	Sn(4.5)
10	194.2	0.709×10^{-3}
20	196.8	0.727×10^{-3}
30	196.4	0.741×10^{-3}
40	196.6	0.789×10^{-3}
50	196.9	0.801×10^{-3}

4) In Sunlight

Distance (cm)	Electrical conductivity(µS) Sn(3V)	Sn(4.5)
10	0.998	0.999
20	0.998	0.999
30	0.999	0.999
40	0.998	0.999
50	0.999	0.999

From the results, it is observed that the electrical conductivity for Sn nanoparticles prepared at 3V potential is more as compare to that prepared at 4.5V. This may be due to smaller and uniform particle size of Sn nanoparticles. It is also observed that the electrical conductivity gradually decreases as the distance between illuminating source and sample increases, due to decrease in intensity of

electromagnetic radiations. Under illumination with sunlight the sample shows more electrical conductivity. Electrical conductivity measured with illumination under monochromatic source is less as compare to white light source. The huge enhancement in electrical conductivity was observed for Sn nanoparticles suspended in double distill water as a fluid. The significant electrical conductivity enhancement is caused, among others, by creating a double electrical layer around nanoparticles and creating conduction paths in higher concentrations of nanoparticles in base fluid. The polarisation current density is found and applied electric field being known, the electrical conductivity of polarised particles in the aqueous medium. The polarisation process is quantified by the effective dielectric constants.

CONCLUSION

This study reports the synthesis of Sn nanoparticles by using electro deposition method. The preparation method used is quite cheaper & beneficial. From the XRD result, the synthesized Sn nanoparticle shows tetragonal and nanocrystalline structure. The UV spectra reveal that the Sn nanoparticles shows maximum absorption in the ultraviolet region of the spectra. Sn nanoparticles can be used in cosmetics (sunscreen lotion), sunglasses, etc to protect human skin from the harmful UV rays. The synthesized Sn NPs has more electrical conductivity in sunlight. Therefore these NPs has future application in solar cells which will be very beneficial. Nano tin dispersed in lubricating oil can be obtained specific performance of multi-purpose oil additives. That means can be used in lubricants. Also can be used in metal electric padding, conductive slurry. The huge enhancement in electrical conductivity was observed for Sn nanoparticles suspended in double distill water as a fluid.

Acknowledgement: Special thank from the authors to Ms. Kaveri Kanawade and Ms. Rutuja Naikwadi for their help in synthesis of Sn nanoparticles. Authors are also thankful to Department of Physics, SPPU, Department of Chemistry, Sangamner College, for characterization facility.

Conflicts of interest: The authors stated that no conflicts of interest.

REFERENCES

1. Pradeep T., Nano the essential, Mc graw hill , vol.(2007).
2. Subbian Balaji , Nanobiotechnology , mjppublishers , vol.(2010).
3. Edelstein A.S. & R.C. Cammarata , Nanomaterials:Synthesis, Properties, applications , Taylor & Francis Group LLC , vol.(1996).
4. Vishwanathan B. , Nanomaterials, Narosa , VOL.(2009).
5. Kulkarni Sulbha K., Nanotechnology Principles and Practices, Capital Publishing Company , 2nd edition , vol.(2011).
6. Charles P. Poole Jr, frank J. Owens , Introduction Nanotechnology, Wiley- India edition , vol.(2006)
7. Winter, M. & Besenhard, J. O. Electrochim. Acta 45, 31–50, doi: 10.1016/S0013-4686(99)00191-7 (1999).
8. Guozhong Cao. Ying Wang,Nanostructure & Nanomaterial, World Scientific , 2nd edition.
9. Edelstein A.S. & R.C. Cammarata , Nanomaterials:Synthesis, Properties, applications , Taylor & Francis Group LLC , vol.(1996).
10. Rathi Er Rakesh , Nanotechnology , S. Chand , vol.(2009).
11. Baliyan Sidharth , Basics of Nanoresearch , Anmol publication , vol(2011).
12. Sarojini K., K, Manoj S. V, Singh P. K, Pradeep T, Das S. K. Colloids Surfaces A: Physicochem Eng Aspects. 2013; 417:39–46
13. Wong K. F, Bhshkar T. ASME 2006. Transport properties of alumina nanofluids; 251–260.

Int. Res. J. of Science & Engineering, 2018; Special Issue A2 :140-143 SJIF Impact Factor 4.11
ISSN: 2322-0015 UGC Approved Journal No. 63628
RESEARCH ARTICLE **OPEN ACCESS**

Synthesis and characterization of Nanocrystalline HfO_2

Taur SM

Department of Physics, Bharatiya Jain Sanghatana's Arts, Science and Commerce Collage, Wagholi.
Tal- Haveli, Dist- Pune, Maharashtra, India
E mail: shaileshtaur@gmail.com

Manuscript Details
Available online on http://www.irjse.in
ISSN: 2322-0015

Editor: Dr. Arvind Chavhan

Cite this article as:
Taur SM. Synthesis and characterization of Nanocrystalline HfO_2 , *Int. Res. Journal of Science & Engineering,* January 2018; Special Issue A2 : 140-143.

ABSTRACT

Nanostructured materials are materials consisting of nanoparticles building blocks on the scale of nanometers (i.e. 10^{-9} m). Composition, crystallinity and morphology can enhance or even induce new properties of the materials, which are desirable for todays and future technological applications. In this work, we have shown new strategies to synthesis metal oxide and metal nitride nanomaterials. The first part of the work deals with the study of synthesis of metal oxide nanoparticles. The optical properties of nanocrystalline HfO2 synthesized using a Sol-gel method. Nanocrystalline hafnium oxide having particle size of the order 10–15 nm were obtained in the present method. The nanopowder was characterized using UV-Spectroscopy X-ray diffraction studies. All these studies confirm that the phase formation is complete in the combustion synthesis and monoclinic phase [P21/a(14)] of HfO2 is obtained without the presence of any impurities or additional phases. The optical constants such as refractive index ,extinction coefficient, optical conductivity and the band gap were estimated from UV–vis spectroscopic techniques. The band gap of nanocrystalline $HfO_2$was found to be 5.1 eV.

Keywords: Band Gap, Nanocrystalline HfO_2, UV–vis, etc.

INTRODUCTION

Hafnium oxide (HfO_2) is an important ceramic material due to It's high dielectric constant (εr~ 30), high melting point (2758^{O}C) and greater chemical stability [1]. HfO_2 and its solid solutions with SiO_2 are promising replacements for SiO_2 for their potential applications as gate dielectrics [2]. Recently the optical applications of HfO_2 are gaining wide spread interest. Due to its transparency over a wide range from ultraviolet to mid-infrared, it is used as materials for heat resistant, reflective and protective optical coating [3–5]. HfO2found promising optical coating applications such as filters, beam splitters, anti-reflection coating, high reflectivity mirrors, etc. [6,7].

METHODOLOGY

Firstly, 1 mol of citric acid (CA) was dissolved in distilled water, followed by the addition of the corresponding amount of $HfCl_4$. After complete dissolution 4 mol of ethylene glycol (EG) was added. This process is carried out at room temperature. Next, the solution was heated at ~90 °C under stirring conditions to remove excess water and to accelerate polyesterification reactions. This treatment produced a viscous material that became a semi-transparent glassy resin upon cooling. In order to obtain the HfO_2 nanocrystals, the resin prepared with these methods were heat-treated in a furnace at 500 and 800 °C in air for 2 h.

Table 1 : For variation of parameters in experimental procedure

Citric Acid Concentartion	$HfCl_4$	Ethylene Glycol Concentration	Annealing Temperature
1 mol	0.1 mol	4 mol	500^{o} C
1 mol	0.1 mol	4 mol	800^{o} C

RESULTS AND DISCUSSION

X-ray diffraction Analysis :

Structural characterization was carried out with help of XRD (D8 ADVANCED Bruker). Figure shows the XRD pattern of sample annealed at 500° C and 800° C synthesized by sol-gel method. The crystal structure, size and orientation of the nanocrystalline HfO_2 were investigated with XRD diffraction pattern. All the diffraction peaks are exactly matches to standard JCPDS (***34-0104)*** data. So it is confirmed that formation of HfO_2 takes place . It is observed that the crystalline nature was obtained for HfO_2 and complete monoclinic phase transformation (reference JCPDS card number: 34-0104). The intensity of the two strong diffraction peaks located at 2θ = 28.47 and 31.84 (Fig. 4) are assigned to the (−111) and (111) planes which reveals that the crystallinity of HfO2 increases with increase in annealing temperature.

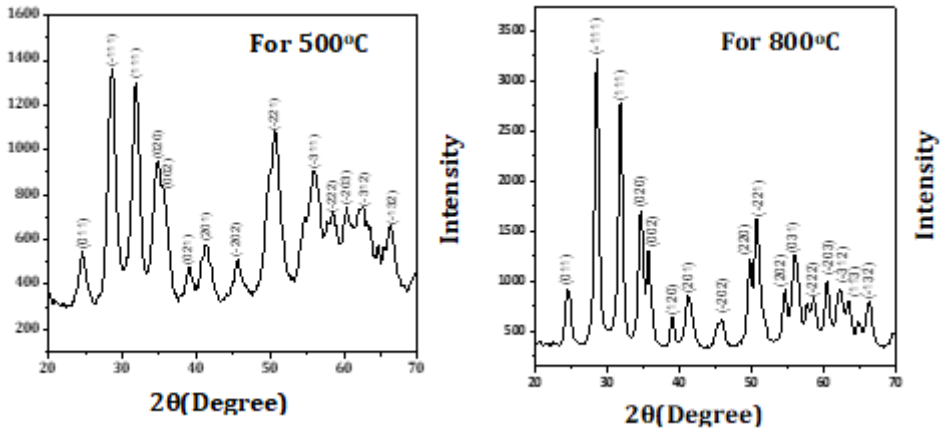

Fig.1 : XRD Pattern of HfO_2 nanocrystals annealed at at 500^{O}C and 800^{O}C

Table 2 : Data for particle size of nanocrystals annealed at 500°C and 800°

θ	*FWHM*	*Size (nm)*	*θ*	*FWHM*	*Size (nm)*
12.28	0.01645	**8.62**	12.28	0.01645	**8.6**
14.25	0.01872	**7.64**	14.27	0.00927	**15.4**
15.91	0.01872	**7.69**	15.91	0.01155	**12**
17.41	0.03027	**4.79**	17.31	0.00715	**15.65**
19.55	0.01715	**8.57**	19.48	0.00702	**20.80**
20.68	0.02331	**6.35**	20.63	0.01645	**21.00**

Optical Analysis :

Optical characterization was carried out with help of UV-VIS absorption spectrometer (JASCO-UV-VIS-NIR spectrometer ; model V-670) . Optical absorption measurements are essential for the understanding of the band gap of material. Figure shows optical absorption spectra of Hafnium Oxide nanocrystals annealed at 500°C and 800°C. Maximum absorption occurred within the UV region from where the absorbance decreased with increase in wavelength. The sudden rise in absorption is observed in UV-region. The absorption spectra shows that for 800°C it is shifted towards the higher wavelength it is due to increase in crystalline size after annealing.

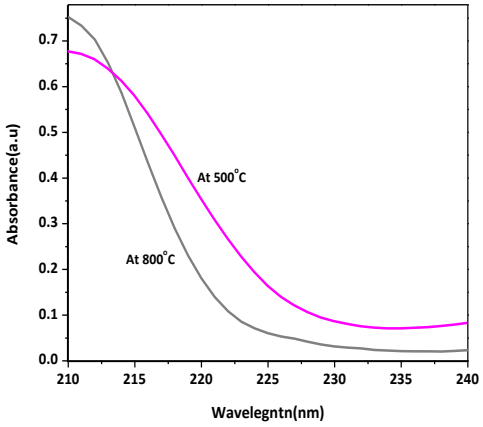

Fig 2: Tauc's plot for HfO_2 nanocrystals annealed at at 500°C and 800°C

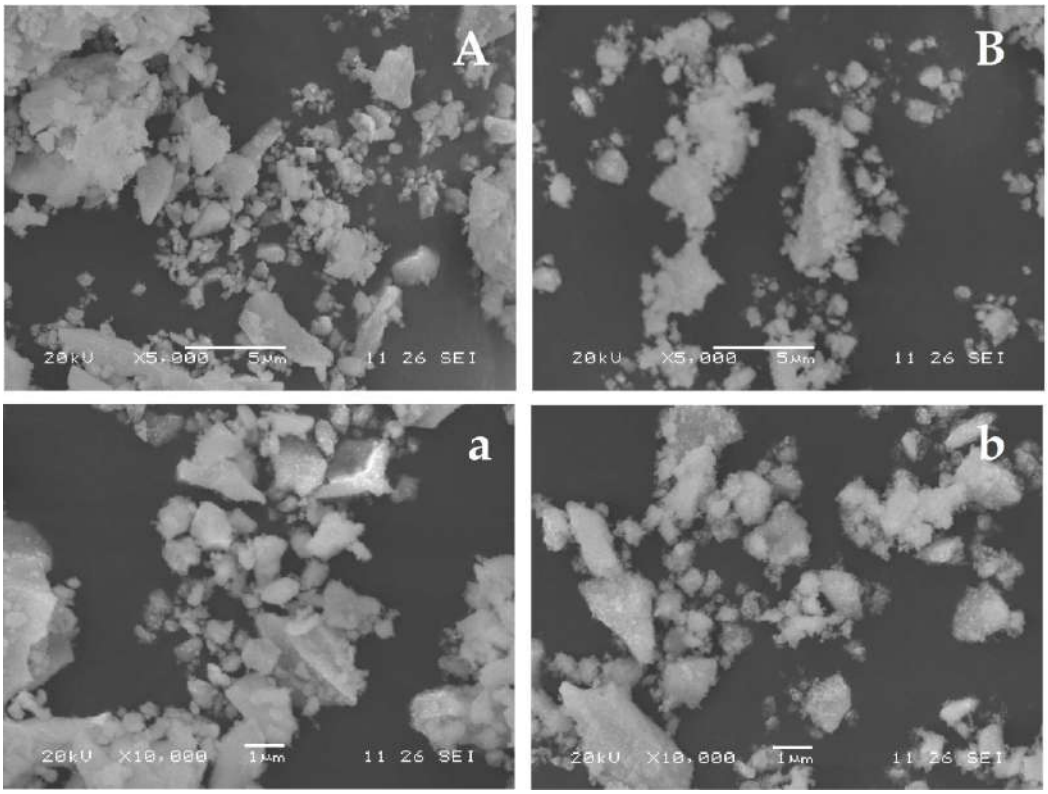

Fig 3 : A & B SEM images of HfO_2 nanocrystals annealed at 500°C and 800°C . **a &** b are corresponding magnified images

The monoclinic HfO_2 structure is reported as an indirect band gap material (9,10,11).The band gap can be obtained from the extrapolation of the straight-line portion of $(\alpha h\nu)^{1/n}$ vs. hv plot . The band gap energy E_g of nanocrystalline HfO_2 was calculated using n=2 and extrapolating the linear portion of curve or tail as shown in fig. The band gap value calculated from Tauc's plot are 5.48 eV and 5 eV for sample annealed at 500°C and 800°C. The obtained result indicating an E_g lower than the reported in the literature (12,13). Comparing the band gap of both samples, it is seen that increase in annealing temperature which predicts a decrease in the width of band hence a decrease in the value of band gap energy Eg. This is due to increase in particle size with increase in annealing temperature .In our study, the band gap value of HfO_2 decreases with increase in the crystalline size . The value of the band gap for our sample is in good agreement with the literature values for HfO_2 nanoparticles obtained by many techniques.

CONCLUSION

- Nanocrystalline HfO_2 can be successfully synthesized by sol-gel method
- XRD confirms the formation of monoclinic structure of Hafnium Oxide (HfO_2).
- After increase in annealing temperature crystallinity of particles increases.
- The average crystalline size was estimated around 7.27 nm and 15.57 nm for nanocrystals annealed at 500°C and 800°C respectively.

- Optical spectra for Hafnium Oxide material shows the Maximum absorption occurred within the UV region.
- The band gap value calculated from Tauc's plot are 5.48eV and 5 eV for both annealed at 500^{o}C and 800^{o}C.
- From band gap of both samples it is observed that band gap energy decreases with increase in annealing temperature. This is due to increase in particle size with increase in annealing temperature.

Conflicts of interest: The authors stated that no conflicts of interest.

REFERENCES

1. Tang J., J. Fabbri, R.D. Robinson, Y. Zhu, I.P. Herman, M.L. Steigerwald and L.L.E.Brus, Chem. Mater., 16, 1336–1342 (2004).
2. Wilk GD, R.M. Wallace and J.M. Antony, J. Appl. Phys., 89, 5243–5275 (2001).
3. Giuri C, M.R. Perrone and V. Piccinno, Appl. Opt., 36, 1143–1148 (1997).
4. Al-Kuhali MF, Opt. Mater., 27, 383–387 (2004).
5. Magunov I.R., R.L. Magunov and G.P. Kornitskiy, Funct. Mater., 8, 563–565(2001).
6. Edlou S.M., A. Smajkiewicz and G.A. Al-Jumaily, Appl. Opt., 32, 5601–5605(1993).
7. Gilo M.and N. Croitoru, Thin Solid Films, 350, 203–208 (1999).
8. Tauc J., Amorphous and Liquid Semiconductors, Plenum, New York (1974).
9. Park J.W., D.K. Lee, D. Lim, H. Lee and S.H. Choi, J. Appl. Phys., 104, 033521(2008)
10. Ramo D.M., J.L. Gavartin and A.L. Shluger, Phys. Rev. B, 75, 205336 (2007).
11. Park J. W., D. K. Lee, D. Lim, H. Lee, and S. H. Choi; Optical properties of thermally annealed hafnium oxide and their correlation with structural change; *J. Appl. Phys.* 104, 033521 (2008).
12. Cheynet M.C., S. Pokrant, F.D. Tichelaar and J.L. Rouvière, J. Appl. Phys., 101,054101 (2007).
13. Nguyen N.V, A.V. Davydov, D.C. Horowitz and M.M. Frank, Appl. Phys. Lett., 87,192903 (2005).

IRJSE *Int. Res. J. of Science & Engineering,* 2018; Special Issue A2 : 144-146 SJIF Impact Factor 4.11
ISSN: 2322-0015 UGC Approved Journal No. 63628
RESEARCH ARTICLE **OPEN ACCESS**

Synthesis and characterization of Co Doped in Lead Ferrite Nanopowder Using Sol-Gel Method

Bhong VA[1], Dhongade AG [2], Rathod SM[3*]

[1]Asistant Professor, P.K technical Campus, Chakan 410501,

[2]PG and Research Center, [3]Associate Professor Departmrnt of Physics, Abasaheb Garware College, Pune 411 004

Manuscript Details
Available online on http://www.irjse.in
ISSN: 2322-0015

Editor: Dr. Arvind Chavhan

Cite this article as:
Bhong VA, Dhongade AG, Rathod SM. Synthesis and characterization of Co Doped in Lead Ferrite Nanopowder Using Sol-Gel Method, *Int. Res. Journal of Science & Engineering,* January 2018; Special Issue A2 : 144-146.

ABSTRACT

Co_x Pb_{1-x} Fe2O4 (where x=0.2, 0.4, 0.6) Nano ferrite powders were synthesized by sol-gel method at cost effective low temperatures. The synthesized powders were sintered at740^{0}C.The prepared samples were characterized by X-ray diffraction and VSM. From XRD characterization the structure of the material is found to be spinel ferrite. The lattice constants and average particle size were studied by X-ray diffraction. The substitution of Co in Pb Ferrite shows the remarkable changes in particle size and magnetic property. The average particle size is in range of 17 to 30 nm. The magnetic properties were studied by VSM.

Keywords: Pb-Co Nano ferrite, sol-gel, XRD, VSM etc

INTRODUCTION

Recent studies have shown that the physical properties of nanoparticles are enhanced significantly by various processing technique and with different composition.This method is used to obtain improved properties, more homogeneity and narrow particle distribution, thereby influencing structural, electrical and magnetic properties of ferrite. It is interesting and important to develop techniques by which the size and structure of the particles can be well controlled. In the present work we have successfully synthesized and studied the effect of Co on the structural properties of $PbFe_2O_4$ samples. $PbCoFe_2O_4$ Nano-particles were successfully prepared by Sol-gel auto-combustion method.

METHODOLOGY

The high purity AR grade ferric nitrate ($Fe_2(NO_3)_2.9H_2O$), Lead nitrate ($Pb(NO_3)_2.6H_2O$), Cobalt nitrate ($Co(NO_3)_2.6H_2O$), citric acid ($C_6H_8O_7$), ammonium hydroxide solution (NH_4OH) were used to prepare Pb_{1-x} Co_x Fe_2O_4(x=0.2,0.4,0.6) nanoparticles by sol-gel auto combustion synthesis technique. In this chemical process Citric acid was used as a Fuel. These nitrates and citric acid were weighed accurately to have proper stoichiometric proportion required in the final product. The mixed solutions of all the chemicals were stirred until the homogeneous solution is obtained. During the stirring process ammonium hydroxide solution was added drop by drop to obtain pH of 7. The mixed solution was simultaneously stirred at 100˚C for 3 to 4 hours to form a gel after that it takes auto-combustion. The prepared powder was sintered at 740˚C for 6hours.

RESULTS AND DISCUSSION

XRD Analysis:

From figure 1 the XRD pattern is used to estimate the average size of very small crystallites, from the measured width of the peaks in the different pattern.

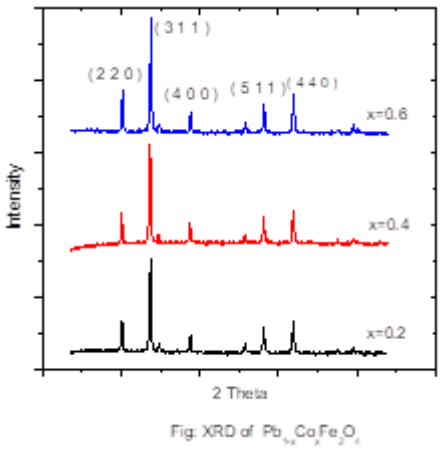

Fig: XRD of $Pb_{1-x}Co_xFe_2O_4$

Figure 1: shows the XRD pattern of $Pb_{1-x}Co_xFe_2O_4$

Composition	Average particle size "t" (nm)	Interplanar distance "d" (nm)	Lattice constant "a" (A^0)
$Pb_{1.8}Co_{0.2}Fe_2O_4$	17.3360	2.5311	8.5841
$Pb_{1.6}Co_{0.4}Fe_2O_4$	23.3625	2.5277	8.4712
$Pb_{1.4}Co_{0.6}Fe_2O_4$	30.1255	2.1423	8.3715

Composition	Hc in Oe	Mr emu/gm	Ms emu/gm
$Pb_{1.8}Co_{0.2}Fe_2O_4$	1657.5926	5.6996	5.8912
$Pb_{1.6}Co_{0.4}Fe_2O_4$	1090.7407	7.94	9.0851
$Pb_{1.4}Co_{0.6}Fe_2O_4$	833.5802	12.6901	27.4317

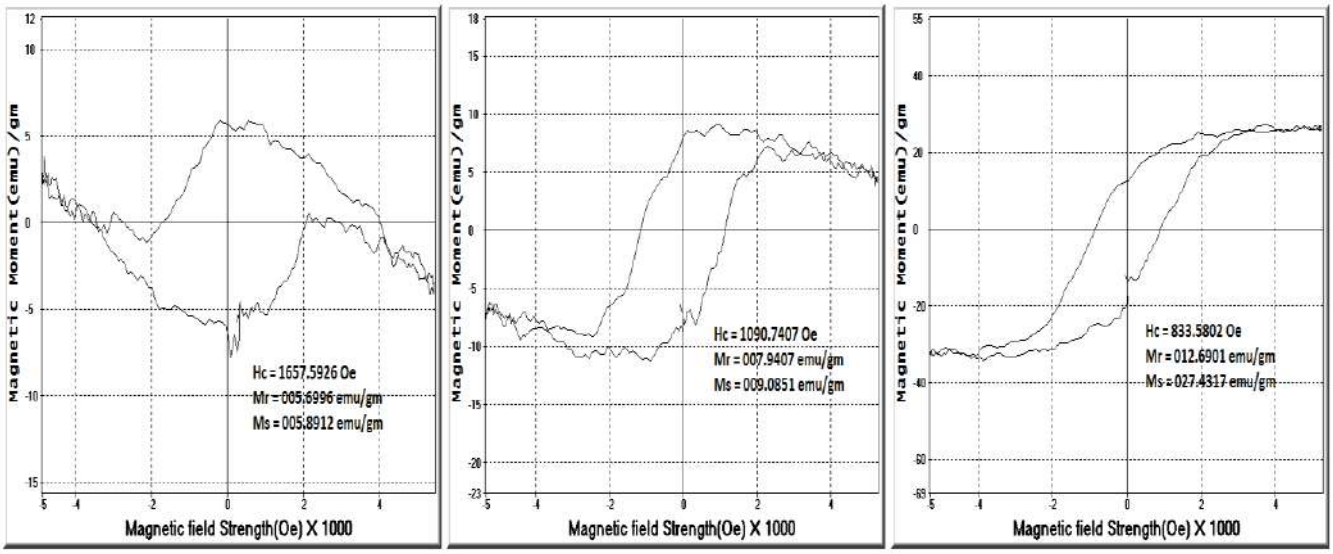

Figure 2: (a) VSM of $Pb_{1.8}Co_{0.2}Fe_2O_4$Fig3: (b) VSM of $Pb_{1.6}Co_{0.4}Fe_2O_4$ (c) : VSM of $Pb_{1.4}Co_{0.6}Fe_2O_4$

The particle size were calculated using Scherer's formula:

$$t = \frac{0.9\lambda}{\beta\cos\theta}$$

Where,
λ =wavelength of X-ray used,
β = Full Width Half Maxima (FWHM) in radians,
θ = peak position.

Lattice parameter (a) of the sample was calculated by using the formula

$$a = d \times \sqrt{h^2 + k^2 + l^2}$$

Where,
a = Lattice Constant,
(hkl) are the Miller Indices

VSM Characteristics (Hysteresis Loop):
The Figure 2 shows that the magnetic properties of the synthesized material from the hysteresis loop it clear that the figure 2 (a) to Figure 2 (c) it increasing the Pb concentration in Cobalt the property of the material changes from hard to soft ferrite.

CONCLUSION

$Pb_{(1-x)}Co_{(x)}Fe_2O_4$ Nano sized ferrite powder were synthesized successfully by sol gel- auto combustion method. From XRD calculation it is conclude that average grain size goes on increasing as concentration of cobalt increases this influence is occur due to ionic radii and exchangeability of ions and it is in the nanostructure range and spinel ferrite. Form, the magnetic properties were studied by hysteresis loop and it is found that the magnetic saturation goes on decreasing as percentage of Co goes on increasing also it convert hard ferrite to soft ferrite.

Conflicts of interest: The authors stated that no conflicts of interest.

REFERENCES

1. P. RAVINDERNATHAN, K.C. PATIL, JOURNAL OF MATERIALS SCIENCE 22 (1987) 3261.
2. D. STOPPELS, JOURNAL OF MAGNETISM AND MAGNETIC MATERIALS 160 (1996) 323.
3. H. Gul, F. Amin, A.Z. Abbasi, M. Anis-Ur-Rehmanb, A. Maqsood,"Physical and Magnetic Charecterization of Co-Precipitednanosize Co-Ni Ferrite" Scriptamaterialia 56 (2007) 497.
4. Erumpervaiz, I. H. Cul, „ Low Temperature Synthesis and Enhanced Electrical Properties by Substitution of Al^{3+} and Cr^{3+} In Co-Ni Nanoferrites"; Journal of Magnetism and Magnetic Materials, Vol 343 (2013), Pp 194-202.

IRJSE *Int. Res. J. of Science & Engineering,* 2018; Special Issue A2 : 147-149 SJIF Impact Factor 4.11
ISSN: 2322-0015 UGC Approved Journal No. 63628
RESEARCH ARTICLE **OPEN ACCESS**

Purification of water *via* nano oxide-charcoal composite

Diggikar Rahul S

Department of Chemistry, New Arts, Commerce and Science College, PARNER, Ahmednagar
E-mail: diggikarrs@gmail.com

Manuscript Details
Available online on http://www.irjse.in
ISSN: 2322-0015

Editor: Dr. Arvind Chavhan

Cite this article as:
Diggikar Rahul S. Purification of water *via* nano oxide-charcoal composite, *Int. Res. Journal of Science & Engineering,* January 2018; Special Issue A2: 147-149.

ABSTRACT

Herewith, presented the application of nano metal oxides for the purification of water. Metal oxides in the different nanoforms made composite with activated charcoal, the surface area increases ultimately adsorption increases. Metal oxides like V_2O_5 in the nano level found excellent ecofriendly reagent useful for purification of water through selective adsorption.

Keywords: Adsorption, oxalic acid, Nanophase, V_2O_5, charcoal.

INTRODUCTION

One of the fundamental requirements for life on earth is water. World is suffering from growing health and hygienic problems and a high percentage of diseases in developing countries is caused by polluted water supply.

In this contest, contaminants from industrial waste streams, that seriously threaten human health and the environment has assumed growing importance in recent years [1]. Reduction, if not elimination, of such pollutants can be achieved through a combination of resource management, product reformulation, process modification and some form of end-of-pipe treatment [2]. The established technologies are based on incineration, biological treatment, condensation and absorption and adsorption processes.

In the field of nanotechnology, the special particles which are known as nanoparticles require minimum space for accommodation and gives more efficiency, as a rule

activated carbon is more effective in adsorbing nonelectrolytes from a solution than electrolytes, and the extent of adsorption is usually greater of the adsorbate [3]. Conversely, inorganic solids tend to adsorb electrolytes more readily than nonelectrolytes [5]. This tendency of adsorbents to attract certain substances in preference to other occasionally leads to the phenomenon of negative adsorption i.e. the concentration of a solute is actually increased after the treatment with the adsorbing agent. The explanation suggested for negative adsorption is that the solvent, in this case the water is adsorbed in preference to the electrolyte, and as a consequence the concentration of solute is raised [5].

The adsorption decreases as the temperature increases and increases when the surface area increases, by taking this advantage we are in touch to increase the surface of charcoal by making nanocomposite with nanomaterial because nanomaterial like V_2O_5 can act as catalyst as well as a good adsorbing agent by which the rate of adsorption increases because activation energy increases[6-8]. These characteristic features have tuned us to find feasibility of using nanomaterials for enhancing the charcoal adsorption in purification of water.

In this manuscript, we present the preparation of V_2O_5 in nano oxide powder ultimately used for water purification [9-10].

METHODOLOGY

All the chemicals were used of AR grade. Ammonium metavanadate, hydrogen peroxide, oxalic acid, activated charcoal etc. are the precursors.

The implemented method is divided into three parts. The first part consists of synthesis and characterization of V_2O_5 nano oxides. In the second part the preparation of composite of charcoal and nano oxides was done. In the third part we verified the validity of Frudndlich- Langmuir adsorption isotherm principle by which water purification is possible.

RESULTS AND DISCUSSION

Fig. 1 presented the XRD of V_2O_5 and charcoal composite. The sharp peaks indicated the microcrystalline state of composites.

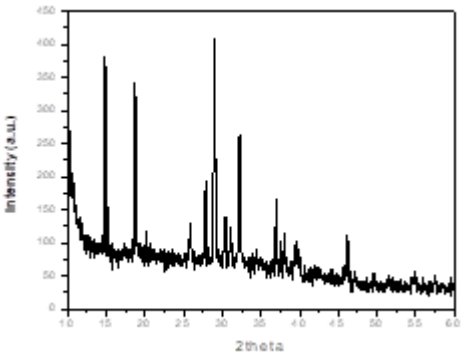

Fig. 1 XRD of V_2O_5 – charcoal composite

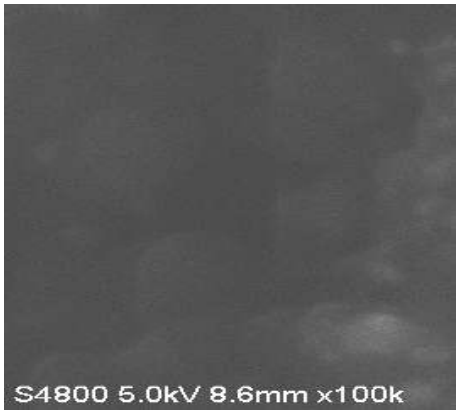

Fig. 2 SEM image of V_2O_5 – charcoal composite

Fig. 2 pertains the SEM image of V_2O_5 – charcoal composite. In the figure it is clearly observed that the V_2O_5 nanoparticles are clearly embedded in the layer of charcoal.

Experimental

The obtained nanophase oxide powders were sonicated in water and incorporated in the matrix of activated charcoal through adsorption. The oxide incorporated charcoal materials have been used as the adsorbing bed for the removal of trace amounts of pollutants from water.

The charcoal embedded fine powders of the inorganic oxides have been able to remove pollutants from water an efficient adsorption of charcoal using nanophase V_2O_5 powder [8]

Solid surfaces can adsorb dissolved substances from solutions of oxalic acid in water is shaken with activated carbon, part of the acid is removed by the carbon and the concentration of the solution decreases.

Observation No.1	Weight of Charcoal = 100 mg Oxalic acid concentration in water =0.05N Sodium hydroxide concentration = 0.01N Total quantity of solution consisting of charcoal and oxalic acid is 25 ml From 25 ml of total solution 5 ml is pipette out and titrated it with standard solution sodium hydroxide we found that 1.97 gm of oxalic acid is adsorbed with charcoal calculated by some tedious calculations of Frudndlich- Langmuir adsorption isotherm principle equation.
Observation No.2	Weight of Charcoal = 50 mg Weight of (V_2O_5) Nano oxide = 50 mg Oxalic acid concentration in water =0.05N Sodium hydroxide concentration = 0.01N Total quantity of solution consisting of charcoal and oxalic acid with (V_2O_5) Nanomaterials is 25 ml. From 25 ml of total solution 5 ml is pipette out and titrated it with standard solution sodium hydroxide we found that 2.08 gm of oxalic acid is adsorbed with charcoal calculated by of Frudndlich- Langmuir adsorption isotherm principle
Observation No.3	By changing the concentrations of charcoal and nanomaterials we found that the 1:1 ratio is more suitable for adsorption of oxalic acid on charcoal as well as on nanomaterials.
Observation No.4	Above observations are obeyed the important Frudndlich-Langmuir adsorption isotherm principle

CONCLUSION

Use of nanomaterials is feasible for enhancing the charcoal adsorption in purification of water; it is proved by the verification of Frudndlich-Langmuir adsorption isotherm principle.

Acknowledgement: This work was financed by the University Grants Commission, New Delhi, India (File No MRP-MAJOR- MATE-2013-39299).

Conflicts of interest: The authors stated that no conflicts of interest.

REFERENCES

1. Diggikar R M.Phil. DissertationYCMOU, Nasik 2009
2. Poole C and Oweoos F 2008 *Ind. Pub.* **11** 281
3. Diggikar R Kulkarni M Kale G and Kale 2013 *J. Mater. Chem. A* **1** 3992
4. Diggikar R Dhavale V Shinde D Kanbargi N K Kulkarni M and Kale B 2012 *RSC Adv.* **2** 3231
5. Diggikar R Ambekar J Kulkarni M Kale B *New J. Chem*. **37** 3236
6. Zhang, X. Liu Y Sun C Ji H. Zhao W Sun S, Zhao C 2015 *RSC Adv*. **5** 100651.
7. Pore D Desai U Thopate T Wadgaonkar P *Russian Journal of Organic Chemistry* **43 (7)** 1088
8. Desai U Thopate T Pore D Wadgaonkar P*Catalysis Communications* **7 (7)** 508
9. Diggikar R Late D and Kale B 2014 *RSC Adv.* **4** 22551
10. Diggikar R Patil R Kale S Thombre D Gade WKulkarni M 2013 *Applied Microbio. And Biotech.* **97 (18)** 8283

IRJSE *Int. Res. J. of Science & Engineering,* 2018; Special Issue A2 :150-155 SJIF Impact Factor 4.11
ISSN: 2322-0015 UGC Approved Journal No. 63628
RESEARCH ARTICLE **OPEN ACCESS**

Study of Influence for Various Parameters to Electro-chemical Synthesis of Polyaniline Thin Film by Galvanostatic Method

Deshmukh VB[1], Paithankar KS[1], Shelke UN[1], More ST[2], Iyyer SB[1] and Gade VK[3]*

[1]Department of Physics, Ahmednagar College Ahmednagar, (M.S.) India,
[2]Institute of Technology, Kuran, Pune (M.S.) India,
[3]Department of Physics, Shri Anand College, Pathardi (M.S.) India
Email: vbdeshmukhsir@gmailcom

Manuscript Details
Available online on http://www.irjse.in
ISSN: 2322-0015

Editor: Dr. Arvind Chavhan

Cite this article as:
Deshmukh VB, Paithankar KS, Shelke UN, More ST , Iyyer SB and Gade VK. Study of Influence for Various Parameters to Electro-chemical Synthesis of Polyaniline Thin Film by Galvanostatic Method, *Int. Res. Journal of Science & Engineering,* January 2018; Special Issue A2 : 150-155.

ABSTRACT

Electrochemical synthesis of Polyaniline films will be prepared by galvanostatic method for various supporting electrolytes which provides a constant oxidative current at the anode. The electrochemical deposition of aniline monomer and their copolymer films were carried out by using a galvanostatic technique at temperature 27 °C, after synthesis of the polymer coated film it will rinse thoroughly in deionized water and then dried in cold air then used for consequent characterization. The synthesized composite films will subjected to various characterizations such as FTIR, UV-Visible spectroscopy and SEM etc. and effect of influence of pH, current, monomer concentration and potential etc. these parameters are studied for optimization of the film formation.

Keywords: Electrochemical, Galvanostatic, Polymer. Aniline.

INTRODUCTION

Polymers have literally take charge as conductors by discarding their traditional role as electric insulator. Now a day polymers are being used for wide range of novel applications. Researchers from various subjects i. e. Physical science, Electronics, Chemistry, Biology etc are now coming together to study this organic materials, which show significant conducting properties.

A new class of polymers known as intrinsically conducting polymers or electro-active conjugated polymers has recently emerged. These materials exhibit excellent electrical and optical properties. Conducting polymers have attracted a lot of interest as a suitable matrix for the setup of enzymes. Conducting polymers are used to enhance the speed, sensitivity and versatility of biosensors. Electrically conducting polymers have excellent flexibility in its chemical structure, which can be modified as per the requirement of specific application. Therefore, conducting polymer film is being used for various biosensor applications viz. Pesticides, Insecticides, Glucose, Cholesterol, Lactate, Urea etc. Pesticide is a term used in broad sense for organic toxic compounds used to control insects, bacteria, weeds, nematodes and other pests. The pesticide residues may enter into the food chain through air, water and soil. They have an effect on ecosystems and cause several health problems to animals and humans. Pesticides can be carcinogenic and cytotoxic. They can produce bone marrow and nerve disorders, infertility, and immunological and respiratory diseases [1]. The present research work deals with the optimization of process parameters i.e. concentration of monomer, various supporting electrolytes, pH of the electrolyte and current density etc. for the synthesis of conducting polymers. We have optimized process parameters of aniline there are various active research groups worldwide working in the field of conducting polymer-based biosensor since several years. Electrochemical polymerization is recognized as an effective technique for the synthesis of conducting polymers. It is widely reported, because it is simple and can be used as a one step method [2-12]. Polypyrrole family is suitable for various applications, such as solar cells, electrodes for rechargeable batteries, biosensors etc. [13-18]. It has been reported that the N-substituted polymers of pyrrole have low conductivity but large mechanical strength and relatively low production cost. The large mechanical strength of N-substituted polymers of pyrrole is very useful for biosensor applications [19-21]. It is well known that the dopant (i.e. anion or cation) used during synthesis causes the changes in the electrochemical, structural, morphological, optical, electrical and mechanical properties of the film [22-24]. The lifetime and stability of the enzymes determines the sensitivity and reliability of the biosensors signals. The good operational stability of the enzymes in the polymer matrix can be achieved by synthesizing the conducting polymers with polyelectrolyte [25-26]. The charge neutrality is an important factor for the immobilization of bio-components. It is reported that, the polymer film synthesized with polyelectrolyte gives good operational stability in the polymer matrix with increased growth rate and higher compactness. It is also useful for improving the conductivity [27]. The influence of dopants/supporting electrolytes on the synthesis of conducting polymers is being studied [28-30]. However, still it is essential to study the effect of process parameters and dopants/supporting electrolytes on the synthesis of conducting polymers, so that we will be possible to develop the biosensor with enhanced response, long lifetime and stability. In modern material science, the synthesis of conducting polymer has been the point of research activity. This is an interdisciplinary and emerging research field. The specific objective of the work were optimization of process parameters viz. concentration of monomer and various supporting electrolytes such as HCl, NaCl, KCl (dopant), pH of the electrolyte, current density etc. for the synthesis of conducting polymer.

METHODOLOGY

The aniline monomer was double distilled before use. Hydrochloric acid (HCl) used as supporting electrolyte. All above reagents were obtained from Avra Chemical, Pune (India). An aqueous solution of aniline (99%) and various electrolyte concentrations were prepared in distilled water. The reference electrode was kept in close proximity to the working electrode to minimize the electrolytic ohmic drop. The pH was adjusted by adding nitric acid or sodium hydroxide. The polymerization of polyaniline was carried out by galvanostatic technique in electrochemical cell. Platinum foil was used as a counter electrode, Indium tin oxide ITO (20 mm × 0.5mm) was used as a working electrode and Ag/AgCl was used as a reference electrode. All three electrodes were placed vertically in cell. An 80 ml solution was used for each reaction. The pH of the electrolyte was measured by calibrated ELICO LI120

pH meter. We have varied the monomer concentrations (0.05M, 0.1M, 0.2M,), supporting electrolyte concentrations (0.1M, 0.3M, 0.5M), pH of the solution (1, 1.5. 3), and current density (0.5, 1, 2) mA/2cm^2 during synthesis of aniline. The electrochemical characterization was carried out by galvanostatic technique, which maintains a constant current throughout reaction. The optical absorption study was carried out in Analytic Jena specord 210 plus (Wavelength 200nm-800nm) UV-visible spectrophotometer. The conductivity was measured by using four-probe technique (S.E.S. Instrument Pvt. Ltd. Rookies).

RESULTS AND DISCUSSION

3.1 Influence of supporting electrolytes:

The study of different supporting electrolyte viz. type of electrolyte, electrolyte concentration and current density have been studied during polymerization of poly (aniline). The aqueous solution (80 ml) containing 0.1M aniline, 0.5M supporting electrolytes/dopants and deionized water with 2pH was prepared. It was subjected to electrochemical polymerization by galvanostatic method at 27 ^{0}C; with 2mA/2cm^2 applied current density. The chronopotentiogram recorded during electrochemical polymerization of PANI at various concentrations of supporting electrolyte solution viz KCl, NaCl and HCl with monomer of aniline at 2mA/2cm^2 current density at 3.0 pH are shown in Figure 3.1.The matrix with higher conductivity will be more useful for electron transfer process. Above fig: 3.1 indicate that HCl shows lower polymerization potential than KCl and NaCl. Dotted line indicates polymerization of KCl and NaCl, compound type line shows polymerization of aniline with HCl supporting electrolyte.

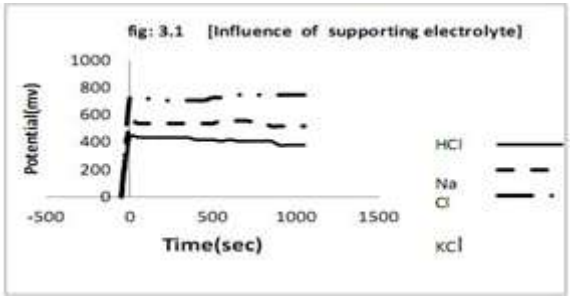

Fig 3.1: Influence of various supporting electrolyte on polymerization potential

3.2 Influence of concentration ratio of monomer and supporting electrolyte.

Fig 3.2 shows the concentration ratio viz. 0.1:0.1, 0.1:0.2 and 0.1:0.5 for the monomer and the supporting electrolyte (2 AP and HCl) respectively has been successfully studied. The matrix with higher conductivity will be more useful for electron transfer process. We have synthesized polyaniline films with 0.1N, 0.2N, 0.5N concentration of supporting electrolyte HCl. The chronopotentiogram recorded during electrochemical polymerization of polyaniline with various concentrations of HCl. 0.1N concentration of monomer, 2mA/2cm^2 is current density and pH 3.0 is as shown in Figure (3.2) for HCl. This indicates that the synthesized polyaniline film shows highest conductivity for 0.5N concentration of HCl as compared with other concentrations 0.1N and 0.2N. This concentration is stable, porous and adherent to the surface.

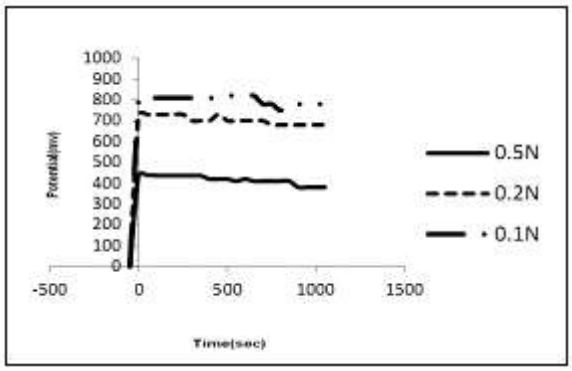

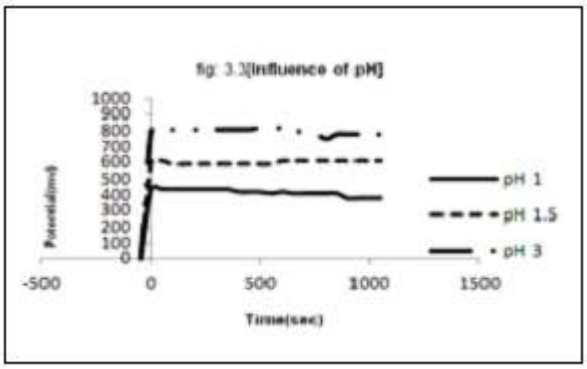

Fig 3.2: Concentration ratio

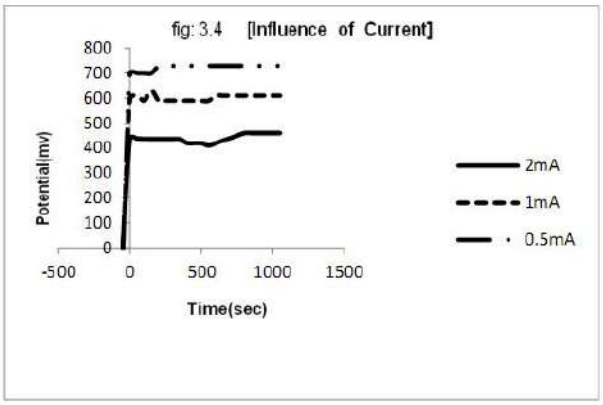

Fig. 3.3 Influence of pH

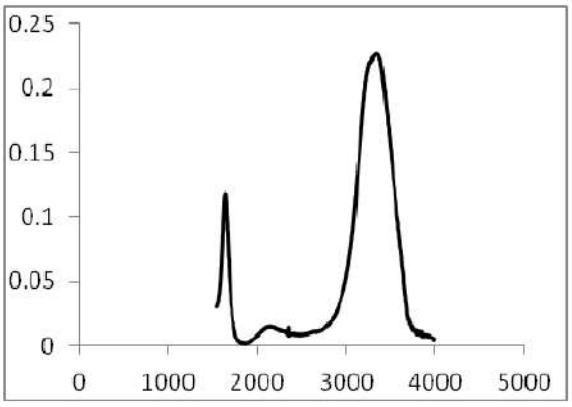

Fig.3.4: Influence of Current

Fig 3.5: UV of Polyaniline

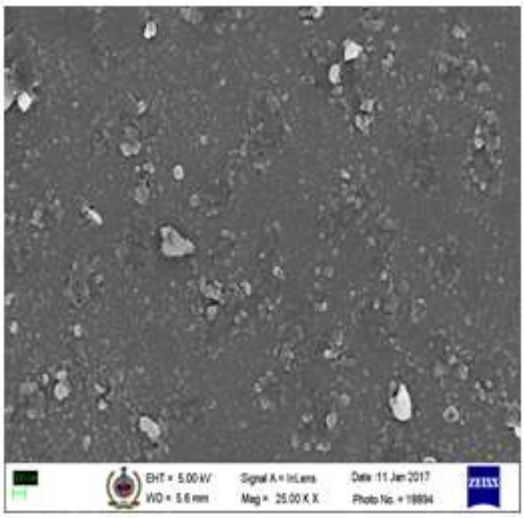

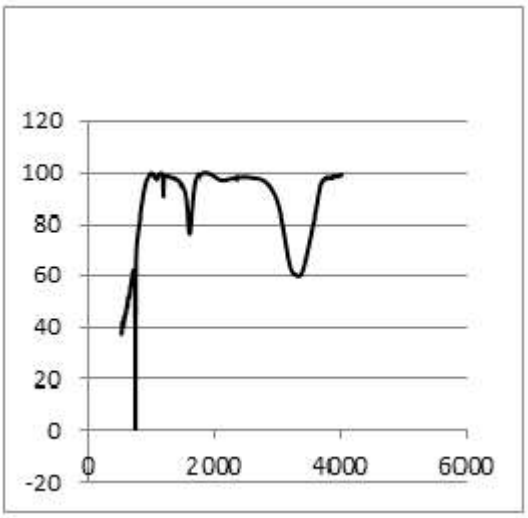

Fig 3.5 shows SEM images

Fig 3.6: FT-IR of polyaniline

However, the polymerization potential recorded during synthesis of aniline with 0.1N concentration of HCl was lower as compared with 0.2N concentration of HCl.

3.3 Influence of pH:

Below fig 3.3 shows the influence of pH (viz. 1, 1.5 and 3) has been studied on the galvanostatic deposition of Polyaniline film. We have recorded lowest polymerization potential for the synthesis of polyaniline films at 2mA/2cm² current density at3.0 pH is compared to pH 1.5 and 1, which indicate higher conductivity. The synthesized films is uniform and adhesive at current density 2mA/2cm² and pH 3.0

3.4 Influence of current density:

Fig 3.4 show the influence of current density (viz. 0.5, 1, 2 mA/2cm²) has been successfully studied on the galvanostatic deposition of Polyaniline film. The chronopotentiogram shows lowest potential for the current 2mA/2cm² than the current 0.5 mA and 1mA. Current 2.0 mA/2cm² gives porous and uniform film.

3.5 UV-Visible spectroscopy (UV):

UV–Vis spectrum of synthesized PANI film is shown in Fig. 3.5 recorded using UV Visible 160 spectrophotometer, Shimadzu in the range of 400–1100 nm. This shows very good closeness with the polymerization potential. The absorption spectra observed for synthesized composite films gives good agreement with the earlier reported work. Fig 3 5 UV–Vis spectra of PANI film in aqueous solution at current density 2 mA/cm²and pH 3.0.

3.6 FTIR Studies of PANI- composite Film:

Transmittance verses Wavelength

The FT-IR spectrum of synthesized composite PANI is shown in Fig.3.6 The FT-IR spectrum was verified using Shimadzu FT-IR-8400 series, using KB rpellets in the region 350–4000 cm^{-1}. Spectrum show broad peak at 3623 cm^{-1}corresponds to O–H stretching.. Further evidence of the existence of this anion in the polymer film is revealed by peaks at 1382 and 1635 cm^{-1} which may be assigned to SO_2 stretch in sulphonates. The trembling bands are observed at 1730 cm^{-1}(C=O), These bands correspond to the characteristic bands for Aniline; it shows very good agreement.

3.7 Scanning Electron Microscopy (SEM):

Fig 3.5 shows SEM images, at 5 micron. It clearly shows porous morphology of PANI Film. This nature of the thin film helps for the biosensor applications. This facility provided by Dept of Physics, University of Pune, India. The **JEOL JSM-7500F** is an ultra high resolution field emission scanning electron microscope (FE-SEM) equipped with a high brightness conical FE gun and a low aberration conical objective.

CONCLUSION

The influence of electrochemical process parameter on the surface morphology and the conductivity of polyaniline films were successfully studied. Process has been developed for the aqueous electro-polymerization of PANI coating on ITO substrates. The 0.1:0.5 concentration ratios of Aniline and HCl for the synthesis of PANI film on ITO electrode are good combination for the deposition. The film shows good conductivity for current density 2 $mA/2cm^2$ at pH 3.

1. HCl is the best supporting electrolyte for synthesis of polyaniline film.
2. The concentration ratio 0.1N: 0.5N of aniline and hydrochloric acid is good combination on ITO electrode.
3. The pH 3 gives good conductivity and surface morphology for the film.
4. The aniline HCl film shows good conductivity for applied current density $2mA/2cm^2$ at 27 ^{0}C.

The process parameters viz. type of supporting electrolytes/dopants, concentrations of monomer and supporting electrolytes/dopants, current density, pH of electrolyte solution etc for the synthesis of conducting polymers were optimized. It was found that the galvanostatically deposited conducting polymers viz. (Polyaniline)/HCl are very good matrices with excellent uniformity, porosity and stability for the immobilization of biocomponent.

Conflicts of interest: The authors stated that no conflicts of interest.

REFERENCES

1. Audrey Sassolas, Beatriz Prieto-Simón, Jean-Louis Marty,American Journal of Analytical Chemistry, 3,{ 2012}. 210-232
2. Gade V.K., D.J. Shirale, P.D. Gaikwad, P.A. Savale, K.P. Kakde, H.J. Kharat, M.D. Shirsat Reactive Functional Polymers 66 (2006) 1420–1426
3. Lawal A.T., S.B. AdelojuJournal of Molecular Catalysis B: Enzymatic 63 (2010) 45–49
4. Skotheim TA, R.L. Elsenbaumer and J.R. Reynolds (Ed.) Handbook of Conducting Polymers Vol 2. Marcel Dekker, New York, 1998.
5. Rahman M. M., Muhammad J.A. Shiddiky , Md. Aminur Rahman, Yoon-Bo Shim , Analytical Biochemistry 384 (2009) 159–165
6. Arunas Ramana vicius, Asta Kau sait, Almira Ramana viciene, Sensors and Actuators, B, 111–112 (2005) 532-539
7. Ntlatseng G.R. Mathebe, Aoife Morrin, Emmanuel I. Iwuoha Talanta 64 (2004) 115–120
8. Suman Singh, Pratima R. Solanki, M.K. Pandey, B.D. Malhotra Sensors and Actuators B 115 (2006) 534–541
9. Hasoon Salah Abdulla and Abdullah Ibrahim Abbo, Int. J. Electrochem. Sci., 7 (2012) 1066–10678
10. [E. Garfias-García, M. Romero-Romo, M. T. Ramírez-Silva, J. Morales, M. Palomar-Pardavé Int. J Electrochem. Sci., 5 (2010) 763 – 773
11. Tarushee Ahujaa, Irfan Ahmad Mira, Devendra Kumara, Rajesh Biomaterials 28 (2007) 805
12. Gade V.K., D.J. Shirale, P.D. Gaikwad, K.P. Kakde, P.A. Savale, H.J. Kharat, B.H. Pawar and M.D.Shirsat Int. J. Electrochem. Sci., 2 (2007) 270 - 277
13. Bard A.J. and L .R.Faulker, Electrochemical

Methods, Fundamentals and Applications, Willey, New York, 1980
14. Diaz A.F., K.K. Kanazawa and G.P. Gardini, J. Chem. Soc.Chem. Commun (1979) 635.
15. Asavapiriyanont S., G.K. Chandler, G.A. Gunawardena and D. Pletcher, J. Electroanal. Chem .177 (1984) 229
16. Milella E., M. Penza, Thin Solid Films 327–329 (1998) 694
17. Granholm P., J. Paloheima, H. Stubb, Synth. Met 84 (1997) 783.
18. Agbor N.E. , J. P. Cresswell, M.C. Petty, A .P. Monkman, Sens. Actuators B. 41 (1997), 137
19. Ram M.K., S. Carrara, S. Paddeu, C. Nicolini, Thin Solid Films 302 (1997) 89.
20. Bartlett P.N. , R. G. Whitaker, J. Electroanal. Chem 224 (1987) 37
21. Matsue T. et al, J. Electroanal. Chem 300 (1991) 111
22. Bartlett P .N., J.M. Cooper, J. Electroanal. Chem. 363 (1993) 1
23. Geetha S. and D. C.Trivedi,Materials Chemistry and Physics 88 (2004) 388.
24. Narula A .K., R. Singh and S. Chandra, Bull. Mater, Sci. 23, 3 (2000) 227
25. Masuda H. and D.K. Asano, Synth. Met.135-136 (2003) 43
26. Wang L.X., X.G. Li and Y.L. Yang, Reactive and Functional Polymers 47 (2001) 125.
27. Gerard M., A. Chaubey and B.D. Malhotra, Biosensors and Bioelectronics 17 (2002) 345.
28. Khalkhali R.A. , W.E. Price, G.G. Wallace, React. Funct. Polym. 56 (2003) 141
29. Partridge A .C., C.B. Milestone, C.O. Too, G.G. Wallace, J Membrane Sci. 152 (1999)61
30. Hallik A., A. Alumaa, V. Sammelselg, J. Tamm, J. Solid State Electrochem. 5 (2001) 265

IRJSE *Int. Res. J. of Science & Engineering,* 2018; Special Issue A2:156-160 SJIF Impact Factor 4.11
ISSN: 2322-0015 UGC Approved Journal No. 63628
RESEARCH ARTICLE **OPEN ACCESS**

Cation Distribution and Stress Sensitivity of Cobalt Ferrite

Kakade SG[1*], kambale RC[2], Mathe VL[3] and Kolekar YD[4]

[1]Department of Physics, Sir Parashurambhau College, Pune, Maharashtra, India-411 030,
[2]Department of Physics, Savitribai Phule Pune University, Pune, Maharashtra, India-411 007
Email: sundipkakade@gmail.com

Manuscript Details
Available online on http://www.irjse.in
ISSN: 2322-0015

Editor: Dr. Arvind Chavhan

Cite this article as:
Kakade SG, kambale RC, Mathe VL and Kolekar YD. Cation Distribution and Stress Sensitivity of Cobalt Ferrite, *Int. Res. Journal of Science & Engineering,* January 2018; Special Issue A2 :156-160.

ABSTRACT

Cobalt ferrite **(**$CoFe_2O_4$) nanoparticles were synthesized by sol-gel auto combustion method. The pure spinel phase formation of face centered cubic lattice was confirmed using X-ray diffraction technique. We have investigated the structural, cation distribution using Mössbauer spectroscopy and magnetostrictive properties of synthesized cobalt ferrite nanoparticles. FE-SEM image show the almost spherical nanoparticles of cobalt ferrite (CFO) with the particle size of 42 nm. The presence of two vibrational bands in IR spectrum around 694 cm^{-1} (υ_1) and 458 cm^{-1} (υ_2) are associated with the tetrahedral and octahedral group complexes of the spinel lattice. The synthesized cobalt ferrite at nanoscale shows the maximum values of the magnetostrictive coefficient (λ_{11} = **-**240 ppm and λ_{12} = 122 ppm) at the lower value of applied magnetic field (6 kOe). Mössbauer spectroscopy shows that the cobalt ferrite at nanodimension is not perfectly spinel. The cobalt ferrites nanoparticles should be the promising candidates for automotive stress sensing.

Keywords: Cobalt ferrite, I-R Spectroscopy, FE-SEM, Cation Distribution, Stress Sensitivity

INTRODUCTION

Magnetic oxide nanoparticles attract increasing interest in fundamental sciences as well as in technological applications. Ferrite is a generic term for a class of magnetic iron oxide compounds. Cobalt ferrite ($CoFe_2O_4$) exhibits unique properties like strong spin-orbit coupling, high coercivity, high magneto-crystalline anisotropy, high Curie temperature and spontaneous magnetization [1−3]. $CoFe_2O_4$ (CFO) is utilized in the development of microwave devices, solar cells, spintronics, transducers and actuators [1−3]. Various ferrites and natural magnetite were used for actinide and heavy metal removal from wastewater [4]. Also, the most chemotherapeutic approaches to cancer treatments are non-specific in nature. Moreover, the targeted delivery of anti-tumor agents adsorbed on the surface of MNPs is a promising alternative to the conventional chemotherapy [5]. In consideration of the different applications of cobalt ferrite in magnetostrictive sensing, we have synthesized cobalt ferrite particles in nanometer regime. The application of synthesized CFO nanoparticles depends upon the site occupancy of metal cation among spinel structure, therefore, it important to obtain the distribution of cations among spinel structure [2-3, 6]. Mössbauer spectroscopy is mostly utilized and most accurate technique to determines site occupancy [3,6].

METHODOLOGY

Synthesis:

The nano particles of Cobalt ferrite ($CoFe_2O_4$) has been synthesized by sol gel autocombustion method. The analytical grade raw materials, $Co(NO_3)_2 \cdot 6H_2O$, $Fe(NO_3)_3 \cdot 9H_2O$, $C_6H_8O_7 \cdot H_2O$ and $NH_3 \cdot H_2O$ were utilized for the synthesis of CFO. Intially, $Co(NO_3)_2 \cdot 6H_2O$ and $Fe(NO_3)_3 \cdot 9H_2O$ were dissolved in the $C_6H_8O_7 \cdot H_2O$ as per the stoichiometric proportion of Co and Fe in CFO. The citric acid and metal nitrates were dissolved in deionized water according to their molar proportion. The pH of the solution was maintained to neutral value using liquid ammonia [7]. The solution was continuously stirred on magnetic stirrer at constant temperature of 80°C for uniform mixing and to obtain clear sol. The obtained sol was then converted into the xerogel at 120^{0}C. The contionous heating on magnetic strrier leads to a self propagating combustion reaction and after complete cobustion the obtained CFO nanopowder was annealed at 700^{0}C for 5 hours.

RESULTS AND DISCUSSION

1. X ray Diffraction:

Crystal structure of the cobalt ferrite was examined using the X-ray diffraction (XRD) with Bruker D8 advanced diffractometer (Cu Kα radiation, λ=1.54178Å). The XRD patterns obtained for $CoFe_{2-x}O_4$ are shown in Figure 1. XRD pattern of CFO exhibit all the characteristic reflections with the most intense (311) peak. The XRD data confirms the formation of CFO matrix (JCPDS cards:22-1086) with single phase cubic spinel structure (space group Fd3m (227)) without any trace of impurity. The lattice constant obtained from XRD is 8.39 Å. The crystallite size (D) of CFO samples was calculated using the well- known Scherrer formula [8]:

$$D = \frac{K\lambda}{\beta \cos\theta}$$

where K is a related to crystallite shape, normally taken as 0.9, λ is the wavelength of X-ray in nanometer(nm), β is the full width at half maximum (in radians) of the diffraction peak. The result shows the decrease in crystallite size , 40 nm for the synthesized CFO nanoparticles.

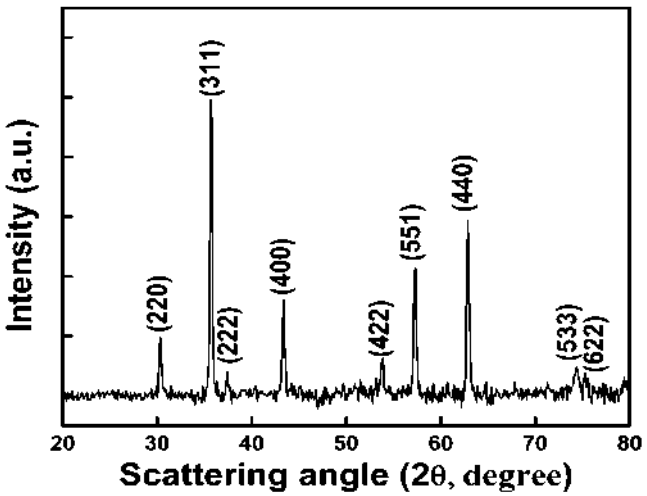

Figure 1. XRD pattern of Cobalt ferrite nanoparticles

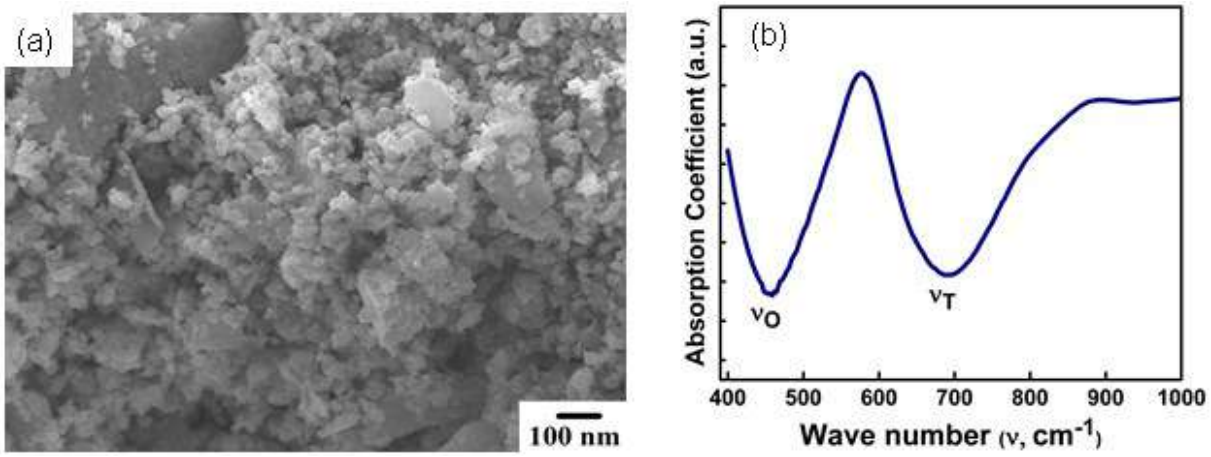

Figure 2 (a) FE-SEM image and **(b)** FT-IR Spectrum of Cobalt Ferrite nanoparticles

2. Surface Morphology:

The morphology and particle size of the synthesized cobalt ferrite nanoparticles by the sol gel auto combustion methods are studied using field emission scanning electron microscopy (FESEM). The instrument utilized to observe the microstructure was JEOL-JSM-6360. The FE-SEM image as shown in Figure 2(a), authenticates the spherical surface morphology for CFO nanoparticles. The average particle size obtained from FESEM image is of 42 nm. The agglomeration of magnetic nanoparticles may leads to the some large lumps as seen in FESEM photograph.

3. IR analysis:

The information on the chemical changes taking place during the synthesis can be obtained by infrared absorption spectra analysis. The IR spectra of annealed CFO nanoparticles at 700 °C are shown in Figure 2(b). The broadning of absorption peaks in IR spectrum authenticate the nanosized grains [9]. In ferrites, the metal ions are situated in two different sub lattices designated as tetrahedral (A-site) and octahedral (B-site) according to the geometrical configuration of the oxygen nearest neighbors. Waldron have attributed the absorption band around 700 cm^{-1} to stretching vibrations of tetrahedral groups (ν_A) and around 400 cm^{-1} to the octahedral group (ν_B) [10]. In the present study, the IR spectra shows two main absorption bands (ν_1) and (ν_2) that were observed at nearly 694 cm^{-1} and 458 cm^{-1} which corresponds to the stretching vibration of the tetrahedral and octahedral sites of spinel lattice, respectively [10]. The position and intensities of ν_1 and ν_2 vary slightly due to the difference in the (Fe^{3+} - O^{2-}) distances for the tetrahedral and octahedral sites. In the present case, it is observed that due to Co^{2+} content, ν_1 shifts to lower frequency side while ν_2 shifts to the higher frequency side, and this may be due to changes that occurred in the cation distribution of the spinel lattice. Here an incre-ase of the population of Co^{2+} (0.78 A˚) cations and decrease of Fe^{3+} (0.64 A˚) cations at the A site contri-butes to the increase of ionic radii of the A site while an decrease of the population of Co^{2+} cations at the B site contributes to the decrease of ionic radii of the B site. Furthermore, the change in the spectral position is expected because of the difference in the (Fe^{3+}- O^{2-}) distances for the octahedral and tetrahedral complexes. It was found that the (Fe^{3+}- O^{2-}) distance of the A site (0.189 nm) is smaller than that of B site (0.199 nm) [11]. As the vibrational frequency is proportional to force constant (K), the band shift of ν_1 and ν_2 to lower and higher frequency with Co^{2+} occopancy indicates that the change in force constant. The calculated values of the force constant are 352 dyne/ cm (K_T) and 153 dyne/ cm(K_o) for A and B sites respectively. The following relation are utilized to calculate force constant [12].

$K = 4\pi^2c^2\nu^2m$;

where K is the force constant, c is Speed of light ~ 2.99 x 10^8 m/sec, ν is the vibration frequency of the A and B sites, m is reduced mass for the Fe^{3+} ions and the O^{2-} ions (~2:065×10^{23}gm/mol).

4. Magnetostrictive Properties:

Magnetostriction is measured at room temperature up to a maximum magnetic field strength of 6 kOe in

both parallel as well as the perpendicular directions to the applied magnetic field. The magnetostriction

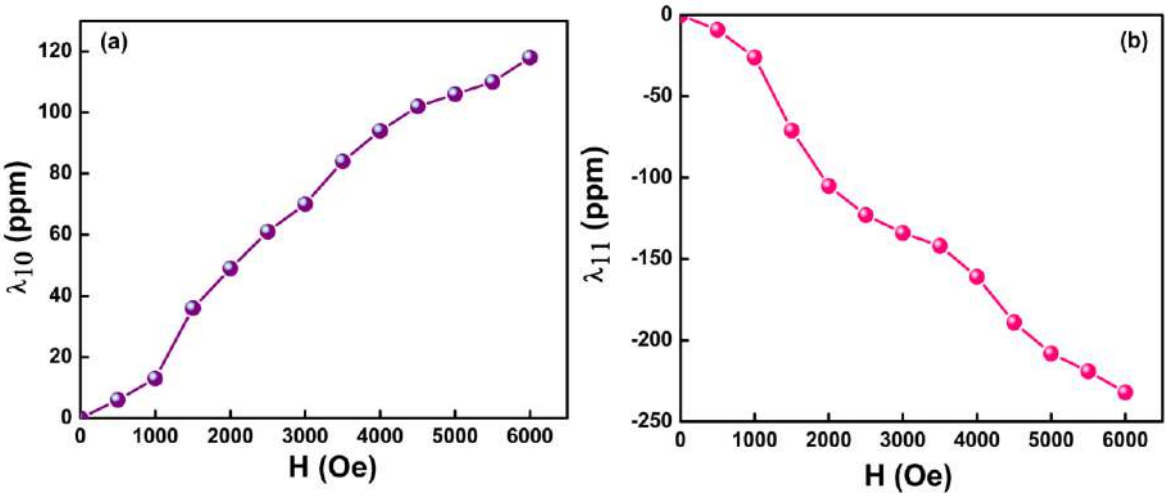

Figure 3. Magnetostriction as a function of magnetic field recorded in the **(a)** perpendicular direction (λ_{10}) and **(b)** parallel direction (λ_{11}) to the applied magnetic field.

curves recorded for cobalt ferrite prepared via modified sol gel auto combustion method are shown in Figure 3 (a) and 4(b), respectively. The highest magnetostriction is obtained for the sample synthesized by the auto combustion method and the lowest value is obtained for the sample synthesized by the ceramic method [13-14]. This may be due to the lower grain size [9, 13]. cobalt ferrite prepared by the combustion method shows an enhanced magnetostriction of 197 ppm at the lower value of applied magnetic field (6 kOe). The magnetostriction curves recorded in the perpendicular direction ($\lambda_{\perp}$) for synthesized CFO also shows higher values than the reported values [14]. Thus, the presence of smaller and uniform sized grains seen in microstructure plays an important role in enhancing the magnetostrictive properties of cobalt ferrite for stress sensitivity.

5. Cation Distribution:

The cation distribution of the synthesized cobalt ferrite was obtained by using Mössbauer spectroscopy technique. The cation distribution is represented using the formula $[Co_{1-x}Fe_x]_A[Co_xFe_{2-x}]_BO_4$, where x is the inversion parameter. Mössbauer spectra of the synthesized CFO nanoparticles shown in Figure 4.

The ratio of area under the absorption curve was considered for the determination of cation distribution of Fe^{3+} ions among the tetrahedral (*A*) and octahedral (*B*) interstitial sites. In ideal inverse spinel structure Fe^{3+} ions are equally distributed at A and B site of face centre cubic oxygen lattice are filled by Fe^{3+} and Co^{2+} ions. However in real practice the degree of inversion is not complete in cobalt ferrite matrix [14-16]. This may be due to the heat treatment provided to the sample during synthesis affects the degree of inversion [13-16]. The obtained cation distribution is: $[Co_{0.21}Fe_{0.79}]_{tet}$ $[Co_{0.79}Fe_{1.21}]_{oct}$ O_4, shows that Co^{2+} ions are migrated towards tetrahedral site from the octahe-dral site. This may be due to the strong A-B super exchange lattice interaction [13-16].

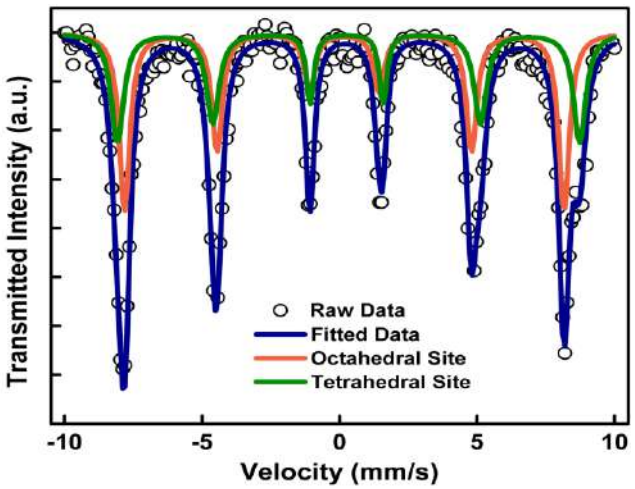

Figure 4 Mössbauer spectrum of cobalt ferrite nanoparticles.

CONCLUSION

Nanoparticles of $CoFe_2O_4$ were successfully synthesized using sol-gel auto combustion method.

XRD analysis confirms the formation of cubic spinel structure without any impurity phases. XRD and FESEM results authenticate the nanometer regime of synthesized CFO. Magnetostrictive properties signify the use of sample in automotive sensing. IR spectroscopy and Mössbauer spectroscopy confirms the cation distribution of Co^{2+} ions among A and B site, hence authenticate the physical properties of the synthesized cobalt ferrite for possible spintronic applications.

Conflicts of interest: The authors stated that no conflicts of interest.

REFERENCES

1. Limaye MV, Singh SB, Date SK, Kothari D, Reddy VR, Gupta A, Sathe V, Choudhary R and Kulkarni SK, *J. Phys. Chem. B*, 2009; 113, 9070-9076 (2009)
2. Prathapani S, Monaji VR, Jayaraman TV and Das D. *J. Appl. Phys*., 2014; 116, 023908.
3. Kakade SG, Ma Y, Kolekar YD and Ramana CV, *J. Phys. Chem. C*, 2016; 120, 5682-5693.
4. Tiwari Dhermendra K, Behari J, Sen P, *World App.Sci. J*. 2008; 417.
5. Mazario E, Menéndez N, Herrasti P, Cañete M, Connord V and Carrey J, *J. Phys. Chem. C*, 2013; 117, 11405-11411.
6. Shinde SS, S Singh Meena, S. M. Yusuf, and K. Y. Rajpure, *J. Phys. Chem. C*, 2011; 115, 3731–3736.
7. Kakade SG, Kambale RC and Kolekar YD, AIP Conf. Proc., 2015; 1665, 130057.
8. Kulkarni SK. Nanotechnology: Principles and Practices, Springer Publication (2014).
9. Naik SR and Salker AV. *J. Mater. Chem.*, 2012; 22, 2740-2750.
10. Waldron RD. *Phys. Rev*.,1955; 99, 1727.
11. Zaki HM, Dawoud HA. *Physica B*, 2010; 405, 4476.
12. Zhoua B, Zhanga Y, Liaoa C, Yana CH and Wangb SY. *J. Magn. Magn. Mater.*, 2004; 280:327.
13. Kakade SG, Kambale RC, Ramanna CV and Kolekar YD. *RSC Adv*.,2016; 6, 33308–33317.
14. Bharati Kamala K, Ph. D. Thesis, I. I. T, Chennai, (2010).
15. Krieble K. *J. Appl.Phys*., 2008; 103, 07E508.
16. Kharat SP, Darvade TC, Gaikwad SK, Baraskar BG, Kakade SG, Kambale RCand Kolekar YD. AIP Conference Pro., 1731, 130056, (2016)

IRJSE *Int. Res. J. of Science & Engineering,* 2018; Special Issue A2 :161-164 SJIF Impact Factor 4.11
ISSN: 2322-0015 UGC Approved Journal No. 63628
RESEARCH ARTICLE **OPEN ACCESS**

Synthesis and Dosimetry Characterization of $CaF_2:Ce^{3+}$ Phosphor Material

Punse VS and Arsad SS

Department of Physics, Shri Shivaji Science College, Amravati. 444603 (INDIA)
Email: punse.vikas2@gmail.com arsadswapnil@yahoo.co.in

Manuscript Details

Available online on http://www.irjse.in
ISSN: 2322-0015

Editor: Dr. Arvind Chavhan

Cite this article as:
Punse VS and Arsad SS. Synthesis and Dosimetry Characterization of $CaF_2:Ce^{3+}$ Phosphor Material, *Int. Res. Journal of Science & Engineering,* January 2018; Special Issue A2 : 161-164.

ABSTRACT

With the help of simple, fast as well as cost effective process of wet chemical method followed by reactive atmospheric process, $CaF_2:Ce^{3+}$ can be successfully synthesized. The XRD analysis shows the desired phase of CaF_2 and the photoluminescence spectra shows excitation and emission spectra satisfactorily.

Keywords: Dosimetry, PL (photoluminescence), wet chemical method, OSL (optically stimulated Luminescence), RAP (reactive atmospheric process).

INTRODUCTION

Luminescence is the process of emission of optical radiation from a material except incandescence. The material absorbs energy, store fraction of it, convert and emit it in the optical radiation. When an organic and inorganic material absorb some form of energy by any means, it tries to attain equilibrium by disposing part of extra energy absorbed by way of heat, chemical or structural changes and luminescence. Phosphor materials convert UV radiation into visible radiation. Lamp Phosphor is mostly white in colour and they should not absorb the visible radiation. Optically Stimulated Luminescence (OSL) is a related phenomenon in which the luminescence is stimulated by the absorption of optical energy, rather than thermal energy. In the history, the Optically Stimulated Luminescence (OSL) is used for radiation dosimetry.

METHODOLOGY

CaF_2: Ce^{3+} phosphor was synthesized by Wet Chemical method followed by Reactive Atmospheric Process. In this method we used $CaCO_3$ [1.00 gm. (as $1mole = \frac{1 * molewt.}{100} \cong 1.00\ gm.$)] as a precursor. The calcium carbonate ($CaCO_3$) was taken in Teflon beaker. We added of $Ce(SO_4)_3$ (stock solution) + HNO_3 + HCl. A little amount of double distilled water then HCl was added in beaker. Then heat was given to become transparent solution. Then 2-3 ml hydro-fluoric acid (HF) was added in it to get precipitation. Then solution was kept to evaporate and to get dry powder for 24 hrs. We crushed the dried powder sample and transferred to a glass tube and about 1% of wt. RAP agent (i.e. ammonium fluoride NH_4F) was added. The tube was closed by a tight stopper and kept the glass tube in the pre-heated muffle furnace at 500°C for 1 hr. The stopper was removed and the powder was transferred to a pre-heated graphite crucible. After heating in the graphite crucible for 1hr. the resulting melt phosphor was rapidly quenched to room temperature. This is known as Melt and Quench process. The complete process discussed above was represented as a flow chart in fig. 1.

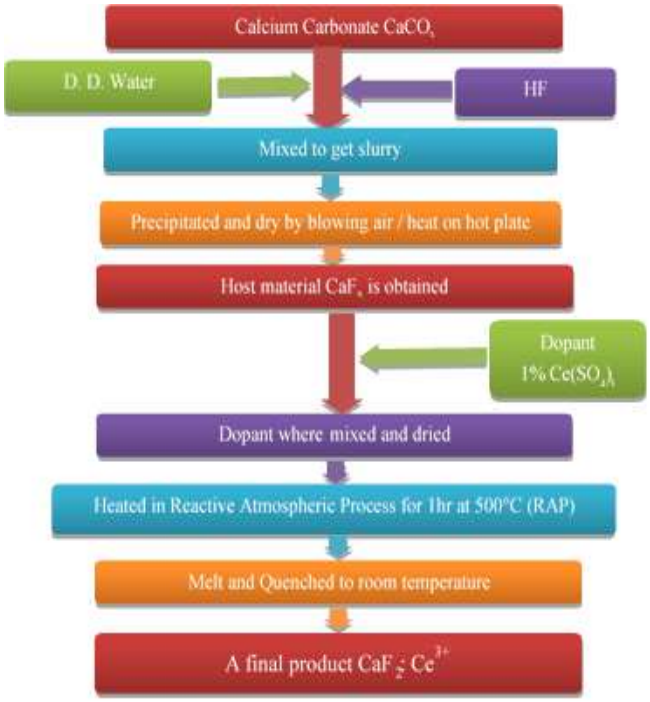

Fig.1. Flow chart of CaF_2: Ce^{3+} prepared via RAP.

RESULTS AND DISCUSSION

PL Analysis

The figure shows ground state configuration of Ce^{3+} ion, one 4f electron and exited state configuration one 5d electron with empty 4f shell. The $4f^1$ yields two levels viz. $^2F_{5/2}$ and $^2F_{7/2}$ due to spin orbit coupling and the $5d^1$ exited state configuration is split by crystal field in 2 and 5 components. The Ce^{3+} emission occurs from the lowest crystal field component of $5d^1$ configuration to the 4f ground state levels. Since 4f → 5d transition is parity allowed and spin selection is not appropriate, the emission transition is fully allowed one. We got the Excitation of CaF_2: Ce^{3+} at 258 nm and 303 nm for 336 nm Emission. Figure 2 and shows the excitation and emission spectrum of CaF_2: Ce^{3+}.

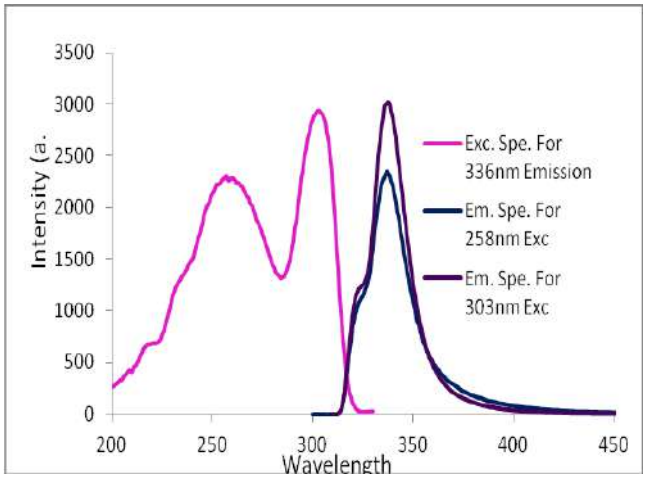

Fig.2. Comparison of excitation spectrum for 336 nm emission and emission spectrum for 258 nm 303 nm excitation.

OSL Analysis

By studying optically stimulated luminescence (OSL) responses of different time interval for radiation doses, we observe that as the time period for radiation dose increases the area covered by the peak/graph increases. And if we increased the time period dosimetry the intensity will also increases. The OSL response is linear as shown in following figures.

The figure 3 shows OSL response for the doses of time period of 10 sec, 15 sec, 20 sec, and 25 sec respectively.

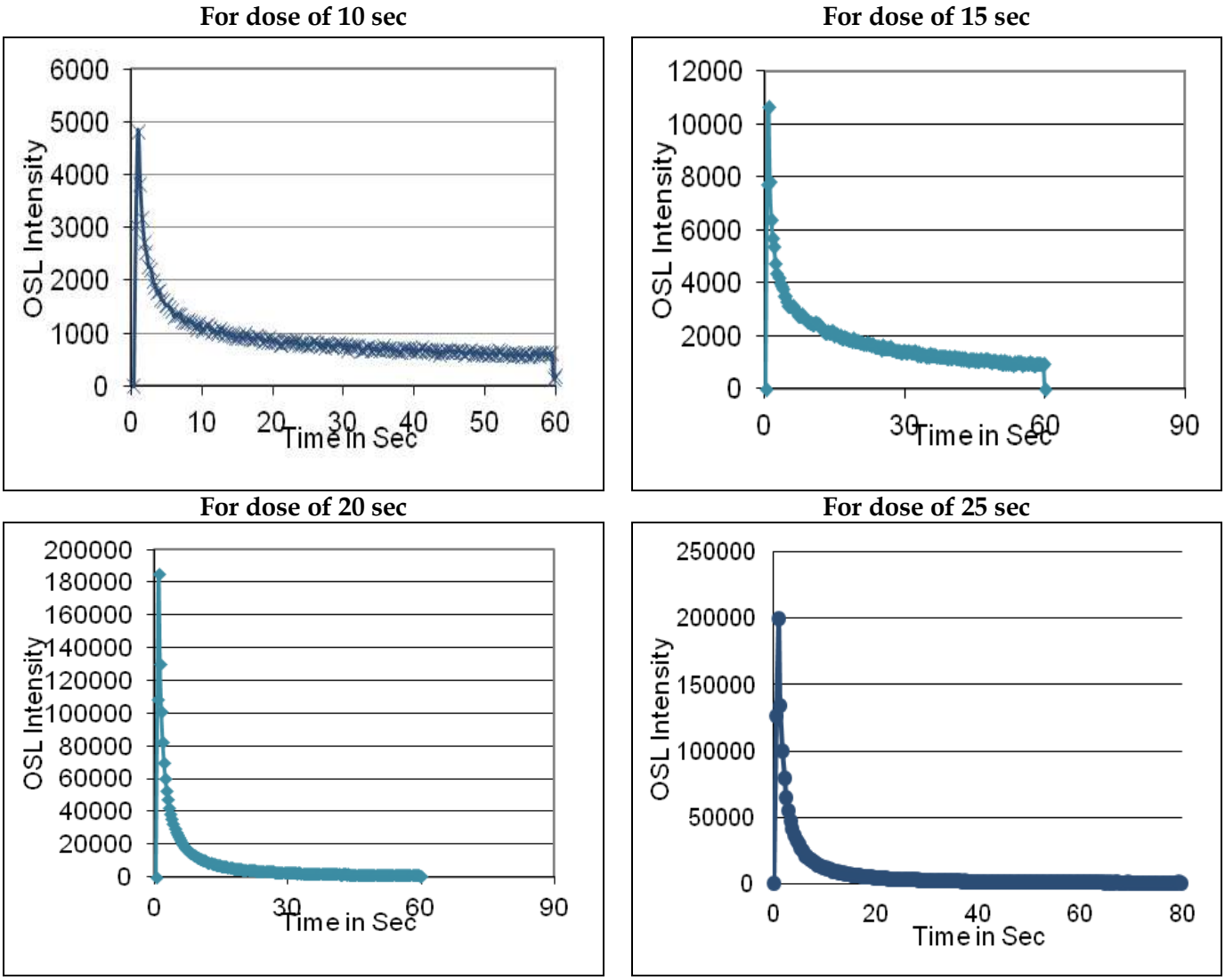

Fig.3. OSL Response of doses for different time periods.

CONCLUSION

The CaF_2: Ce^{3+} phosphor was successfully synthesized by Wet Chemical Method followed by Reactive Atmospheric Process. The process of synthesis was simple, fast and cost effective. We have analysed that the XRD pattern which indicates the presence of a cubic phase for CaF_2. The Photoluminescence Spectra shows excitations at 258 nm and 303 nm for 336 nm Emission. The best luminescent material obtained though the above process, as we got very good Optically Stimulated Luminescence (OSL) response, which is linear with time.

Acknowledgement:
We are thankful to radiation therapy unit, government super speciality hospital, Amravati dist. Amravati (Maharashtra) for radiation doses. One of the authors V. S. Punse is thankful to Head, Department of Physics, Shri Shivaji Science College, Amravati and Head, Department of Physics, Sant Gadge Baba Amravati University, Amravati for providing necessary facilities.

Conflicts of interest: The authors stated that no conflicts of interest.

REFERENCES

1. Jaiswal SR, Nagpure PA, Bhatkar VB, Omanwar SK, Energy transfer and visible Quantum Cutting in BaF_2 co-doped with Gd^{3+}, Eu^{3+} Phosphor synthesis via wet chemical method followed by Reactive Atmosphere Process. International journal of Luminescence and applications, 2016; 6(2): 131-134.
2. Yukihara EG, McKeever SWS, Optically stimulated luminescence (OSL) Dosimetry in medicine, IOP Publishing- Phys. Med. Biol., 2008; 53: R351-R379.
3. Bhatkar VB, Thakare DS, Omanwar SK, Synthesis and Luminescence Properties of $Sr_5(PO_4)_3Cl:Eu^{2+}$. (IJAEST) International Journal of Advanced Engineering Sciences and Technologies, 2011; 5: 209-211.
4. Bhatkar VB, Thakare DS, Omanwar SK, Synthesis of Tricolour Lamp Phosphor: $CeMgAl_{11}O_{19}:Tb^{3+}$. International Review of Applied Engineering Research, 2011; 1; 67-70.
5. Nagpure PA, Omanwar SK, UV emitting borate phosphors for phototherapy lamps. Indian Journal of Pure & Applied Physics, 2015; 53: 77-81.
6. Nagpure PA, Sonekar RP, Omanwar SK, Pande AC, Photoluminescence Study Of Green PDP Phosphor $LaBaB_9O_{16}$:Tb/CeTb. (IJAEST) International Journal of Advanced Engineering Sciences and Technologies, 2011; 8: 311-315.
7. Nagpure PA, Omanwar SK, Synthesis and Characterization of Blue Emitting Phosphor $CaAl_2B_2O_7:Eu^{2+}$. Inernational Journal of Basic and Applied Research, 2012; 191-194.
8. Ingale JT, Sonekar RP, Nagpure PA, Omanwar SK, Synthesis and UV Photoluminescence of Red Emitting Borate Host PDP Phosphors $YCaBO_4:Eu^{3+}$ and$YBO_3:Eu^{3+}$. International Journal of Current Research, 2013; 5: 529-531.

IRJSE *Int. Res. J. of Science & Engineering,* 2018; Special Issue A2 : 165-167
ISSN: 2322-0015
SJIF Impact Factor 4.11
UGC Approved Journal No. 63628
RESEARCH ARTICLE **OPEN ACCESS**

Opto-electronic properties of nanostructured CdS thin film grown by chemical route

Taur Vidya S and Sharma Ramphal

Thin Film and Nanotechnology Laboratory, Department of Physics, Dr. Babasaheb Ambedkar Marathwada University, Aurangabad 431004,
E-mail: rps.phy@gmail.com

Manuscript Details

Available online on http://www.irjse.in
ISSN: 2322-0015

Editor: Dr. Arvind Chavhan

Cite this article as:
Taur Vidya S and Sharma Ramphal. Opto-electronic properties of nanostructured CdS thin film grown by chemical route, *Int. Res. Journal of Science & Engineering,* January 2018; Special Issue A2 : 165-167.

ABSTRACT

In present study, we report on the nanostructured CdS thin films synthesized at an optimum low temperature on glass substrates using cost effective chemical method for photosensor applications. The as-deposited nanostructured thin films were characterized for optical and electrical properties. The optical transmittance spectrum indicates high transmission (~ 60 %) with direct energy band gap of 2.42 eV. The thermoelectric power (TEP) measurements confirms the n-type conductivity of the nanostructured CdS thin film. The I-V studies show significant increase in photo response (~ 96 %) of the nanostructured thin film on illumination with light source of 100 mW/cm^2.

Keywords: Nanostructured; thin films; electrical conductivity; photoresponse.

INTRODUCTION

Cadmium sulphide is one of the members of II-VI group which has maintained its identity as photosensor device, particularly in solar cell. CdS is n-type semiconductor with direct band gap of 2.42 eV [1]. In general, the high energy band gap material is used as window material associated with p-type radiation absorber layer whose band gap ranges between 1.1 eV to 1.5 eV to form hetero-junction configuration. These two opposite conductivity (n and p) semiconductor materials in heterojunction are referred as absorber layer and window layer respectively

having band gap difference of $Eg_2 > Eg_1$ [2]. The higher band gap of CdS thin film enhances the performance of solar cell by omitting the absorbance loss [3,4].

METHODOLOGY

The CdS thin films have been synthesized by simple, cost effective chemical route on glass substrate. The growth parameters such as pH, molarities of the reactants, temperature of the bath and the reaction time were optimized to obtain large area uniform deposition over the entire substrate. The as–deposited CdS thin films are characterized for optical and electrical properties. The optical characterization (absorbance and transmittance as a function of wavelength) were performed using UV–Vis spectrophotometer (Perkin Elmer, Lambda 25). Thermo electric power (TEP) measurements were perform to know the type of conductivity. The Current–Voltage (I–V) characteristics were measured using Lab equipment (model no. 2004) interfaced with computer. Silver (Ag) contacts were prepared on thin film by vacuum evaporation technique to ensure good ohmic contacts.

RESULTS AND DISCUSSION

Optical analysis:

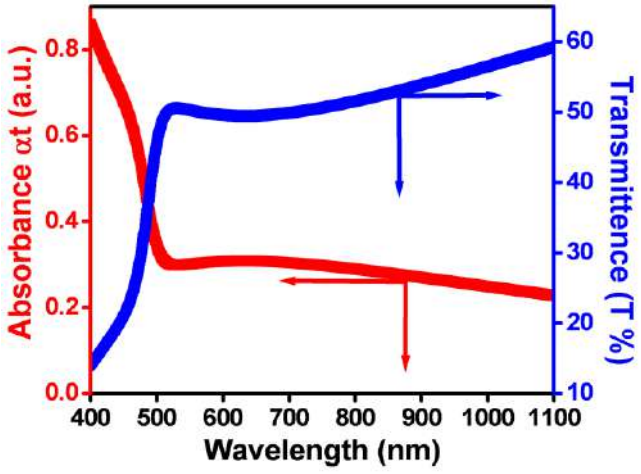

Fig. 1 Energy band gap of nanostructured CdS thin film.

Fig. 1 shows the plot of optical transmittance and absorbance against the wavelength of light for CdS thin film deposited on glass substrate. Optical transmittance of 60% is observed for higher wavelength of light, which is one of the prerequisite for optoelectronic devices particularly as solar cell window layer [5, 6].

Where, '*hν*' is the photon energy, '*A*' is constant. E_g is energy band gap. The exponent n is 0.5 for direct allowed and 1.5 for direct forbidden, 2.0 for indirect allowed and 3.0 for indirect forbidden transition. Fig. 6 shows plot of $(ahv)^2$ versus hν for calculation of energy band gap. The presence of only one slope in the curve indicates single phase with direct allowed transition. The band gap energy of the thin film is determined by extrapolating the linear portion of plot of $(ahv)^2$ versus *hν*. The calculated band gap of the film Eg = 2.42eV is in good agreement with that reported in literature [5].

Electrical analysis:

TEP measurements: The nature of conductivity of the CdS thin film is decided by performing the thermoelectric power measurement. The Fig. 2 shows the plot of thermo emf against the temperature.

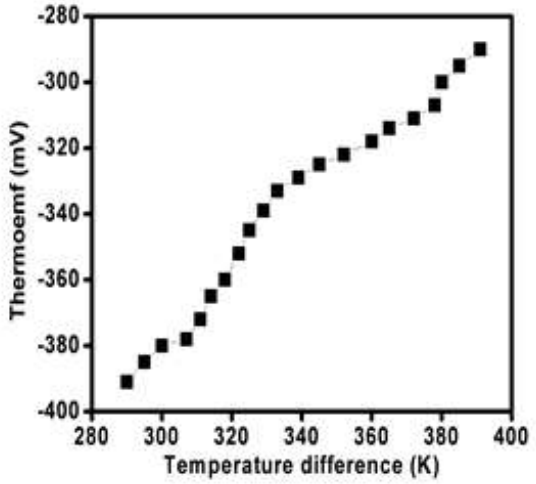

Fig. 2. Graph of thermo emf versus temperature of nanostructured CdS thin film.

From the plot it is observed that the emf of the thin film increases as the temperature is increased. Thermo electric power (TEP) is found to be 13.96 mV/°C calculated from the slope of the graph. In addition to this the polarity of the thermoelectric voltage of CdS film is positive towards the hot end, which indicates that the CdS exhibits n-type conductivity.

I-V measurements: I-V graph of nanostructured glass substrate CdS thin film is shown in Fig. 3 under dark and illumination condition.

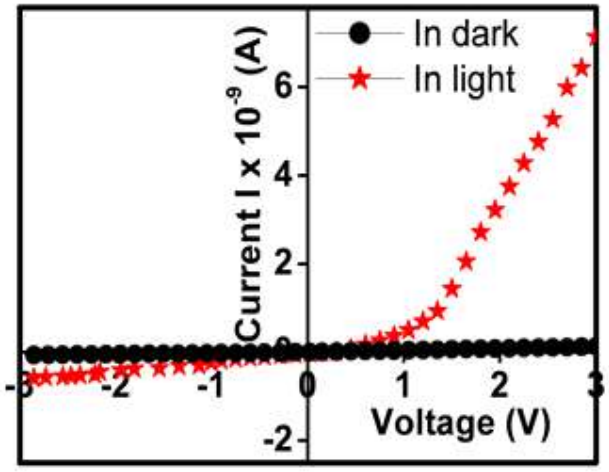

Fig. 3: I-V plot of nanostructured CdS thin film under dark and illumination.

The I-V curve shows that the current increases nonlinearly with the applied bias, Furthermore, the conductance of the CdS thin film in dark is noted to be poor, however when the thin film is exposed to light the conductivity is enhanced. Here the resistance of the thin film under dark and illumination condition is measured this change in the resistance is proposed as the photoresponse calculated using the following relations, the photoresponse is observed to be ~ 96 % where, S is the photoresponse, R_d and R_L is the resistance under dark and illumination condition.

CONCLUSION

Nanostructured CdS thin films were successfully grown on glass substrate with good crystalline quality by using soft chemical route at lower temperature. These CdS thin films were characterized for optoelectronic properties. From the optical study, the transmittance was observed to be 60% and the energy band gap derived was 2.42eV. The morphological analysis revealed leaf-like rough structure which might be useful for harvesting the light. The photoresponse calculated from the I-V plot is found to be 96%. The above discussed characteristics of nanostructured CdS thin film confirm its utility as a window material for solar cell applications.

Acknowledgement:
The authors are thankful to the Head, department of Physics, Dr. B.A.M. University, Aurangabad for providing the laboratory facility to carry out the work.

Conflicts of interest: The authors stated that no conflicts of interest.

REFERENCES

1. Km P, Wang CR, Li Q and Hark SK. *Appl. Phys. Lett.*,2004; 84: 795.
2. Ting LC and Shirley SC. *Solid State Electron*, 1995; 38: 533-549.
3. Bhattacharya RN and Ramanathan K. *Solar Ener.*, 2004; 77: 679-683.
4. Sadigov MS, Ozakan M, Bacaksiz E, Altunbas M and Kopya AI. *J. Mater. Sci.*,1999; 34: 4579-4584.
5. Archbold MD, Halliday DP, Durose K, Hase TPA, Boyle DS, Mazzamuto S, Romeo N and Bosio A. *Thin Solid Films*, 2007; 515: 2954-2957.
6. Hiie J, Dedova T, Valdna V and Muska K. *Thin Solid Films*, 2006; 443 (2006) 511-512.

Int. Res. J. of Science & Engineering, 2018; Special Issue A2 : 168-171 SJIF Impact Factor 4.11
ISSN: 2322-0015 UGC Approved Journal No. 63628
RESEARCH ARTICLE **OPEN ACCESS**

Study of Electrical and Dielectric properties of Zn doped Ni-Cu Ferrite

Padampalle AS [1]*, Suryawanshi AD[2], Suryawanshi DD[3], Patil SS[4] and Gurav SK[5]

[1]Department of Physics, S. C. S. College, Omerga, 413606 (M. S.) India,[2]Department of Physics, B. J. College, Ale (Pune) 412411 (MS) India.3Department of Chemistry, B. S. S. College, Makani, 413606(MS) India.,[4]Department of Physics, S C College Junnar (Pune) 412411 (MS) India.,[5]Department of Physics, S. M. P. College Murum, 413606 (M.S.) India
Email: aspadampalle@yahoo.com

Manuscript Details

Available online on http://www.irjse.in
ISSN: 2322-0015

Editor: Dr. Arvind Chavhan

Cite this article as:
Padampalle AS, Suryawanshi AD, Suryawanshi DD, Patil SS and Gurav SK. Study of Electrical and Dielectric properties of Zn doped Ni-Cu Ferrite, *Int. Res. Journal of Science & Engineering*, January 2018; Special Issue A2 : 168-171.

ABSTRACT

Ni-Cu-Zn ferrite is prepared by sol-gel autocombustion method using metal nitrates and citric acid. The information of single phase formation was confirmed by X-ray diffraction and lattice constant and particle size is evaluated. The electrical resistivity has been studied as a function of temperature. Dielectric constant; Dielectric loss and loss tangent were studied at fixed frequency 1KHz and varying temperature.

Keywords: Nanocrystalline; DC resistivity; dielectric constant; ferrite;

INTRODUCTION

Ferrites which have many applications at microwave frequencies are very good dielectric material. Ferrites have high electrical resistivity, low dielectric loss and chemical stability. Nanocrystalline material ferrites have many applications in making cores of audio frequency and high frequency transformers, chokes, permanent magnets, microwave absorbers, wave guides and chlorine gas sensors, high density information storage, color imaging, bioprocess, medical diagnosis, electromagnetic wave absorption, etc. Multi layer chip indicator (MLCI) has recently been developed as one of the key surface mounting devices [1].

Due to their reduced sizes, the nanocrystalline materials passes novel and improved properties in comparison to bulk materials, which have been extensively used in electronic devices for high frequency telecommunications [2]. Very fine ferrite particles can be produced by the chemical co-precipitation and sol–gel methods [3–5]. Several researchers have reported the synthesis of Ni-Zn ferrites using different techniques like, ceramic [6], hydrothermal [7], combustion [8], co-precipitation [9], spark plasma sintering [10], micro emulsion [11] and ball milling etc. The size and shape of the ferrite particles are dependent on the synthesis process. Sol-gel autocombustion method is a simple process, which offers a significant saving in time and energy consumption over the traditional methods.

In this paper, we prepare Cu doped Ni-Zn ferrite and studied electrical and dielectric properties. The study of dielectric properties gives valuable information on the behavior of localized electronic charge carriers leading to greater understanding of mechanism of dielectric polarization in ferrites.

METHODOLOGY

Nanocrystalline spinel ferrite $Ni_{0.7-x}Cu_xZn_{0.3}Fe_2O_4$ where x= 0.0 to 0.5 were prepared by sol-gel autocombustion method using metal nitrates and citric acid. Citric acid $C_6H_8O_7$, ferric nitrate $Fe(NO_3)_3.9H_2O$, nickel nitrate $Ni(NO_3)_2.6H_2O$, zinc nitrate $Zn(NO_3)_2.6H_2O$ and copper nitrate $Cu(NO_3)_2.3H_2O$ were used as raw materials with molar ratio of metal nitrates to citric acid 1:3. All nitrates and citric acid were dissolved in distilled water and stirred continuously. During the constant stirring ammonia solution was added drop wise to adjust PH 7; the solution was heated at 100°C to transform into gel. The gel burnt in a self propagating combustion manner until all gels were completely burnt to form ashes. The as-prepared powder was ground using a mortar and pestle, and then calcined in muffle furnace at 500^0Cfor 5h and cooled slowly to room temperature. The X-ray diffraction patterns of the ferrite samples were taken in our laborites using Regaku Miniflex II diffractometer with Cu Kα radiation (λ= 1.54056 Å) in the range of 2θ from 20^o to 80^o. Dc electrical resistivity was measured by using two probe methods. Dielectric properties as a function of temperature were studied with fixed frequency I KHz using LCRQ meter.

RESULTS AND DISCUSSION

3.1. XRD:

The X-ray diffraction pattern of $Ni_{0.7-x}Cu_xZn_{0.3}Fe_2O_4$ ferrite for x= 0.0 and 0.1 is as shown in Fig.1. All the peaks could be indexed with cubic spinel ferrite structure showing that all the samples were formed in single phase and were well crystalline in nature. By knowing the values of interlplanar distance (d) and Miller indices (hkl) lattice parameter *a* calculated by using formula, $[a=d(h^2+k^2+l^2)^{1/2}]$. The value of lattice parameter increases by increasing Cu^{2+} ions. This increase in lattice parameter is due to increase in ionic radii of Cu^{2+} (0.72A°) as compared to ionic radii of Ni^{+2} (0.69A°). The value of lattice parameter is as shown in table 1. The FWHM of the most intense peak is used to get average particle size using scherrer's equation,

$$t = 0.9\lambda / \beta \cos\theta$$

Where, λ the wavelength of x-ray radiation (Cu Kα, 1.54056 Å), β is full width at half of the intensity maximum of plane in radian and t is diameter of crystal particle. The crystallite size of the as-burnt powder estimated from the X-ray. Peak broadening of the diffraction peak is 40 nm to 80 nm. This shows that the synthesized powder has nano-sized crystallites.

3.2 D. C. electrical resistivity:

The variation of logρ with 1/T the sample is shown in Fig.2. Form figure, it can be noted that the resistivity decreases with increasing temperature. The ferrites show semiconducting behavior. The decrease in resistivity may be attributed to facts that existence of Fe^{3+} in B-site. It is well known that the conductivity of ferrite depends upon the ratio of Fe^{3+} to Fe^{2+}, since this ratio decreases with increasing composition, then resistivity should exhibits a continuous decrease with increasing composition. The breaks in resistivity plots denote two regions of conductivity and temperature corresponding to the break is Curie temperature of the samples confirmed. The lower temperature region

below Curie temperature corresponds to the ordered ferromagnetic region with low activation energy while the higher temperature region above Curie temperature corresponds to a paramagnetic region with comparatively high activation energy [12]. The value of Curie temperature is shown in table1. It represents that as composition increases Curie temperature decreases.

Table 1: Variation of Lattice parameter and particle size for $Ni_{0.7-x}Cu_xZn_{0.3}Fe_2O_4$ ferrite for (x= 0.0 to 0.5).

Compositions *X*	Lattice Constant *a in*(A°)	Particle size *t* (nm)	Curie temp. (T_c) in (°K)
0.0	8.3654	40.23	735
0.1	8.3979	47.28	702
0.2	8.4012	55.13	684
0.3	8.4067	67.34	664
0.4	8.4108	72.51	700
0.5	8.4154	79.31	665

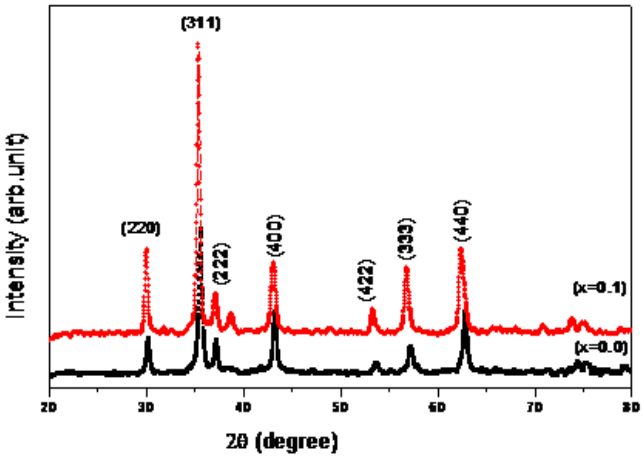

Figure 1 : X-ray diffraction pattern

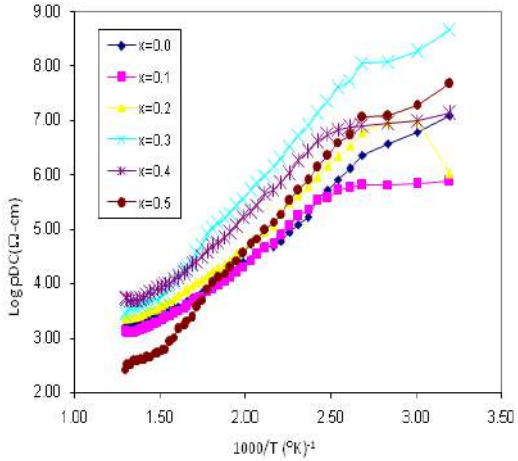

Figure2: Variation of resistivity with temperature of $Ni_{0.7-x}Cu_xZn_{0.3}Fe_2O_4$ ferrite for x= 0.0 and 0.1

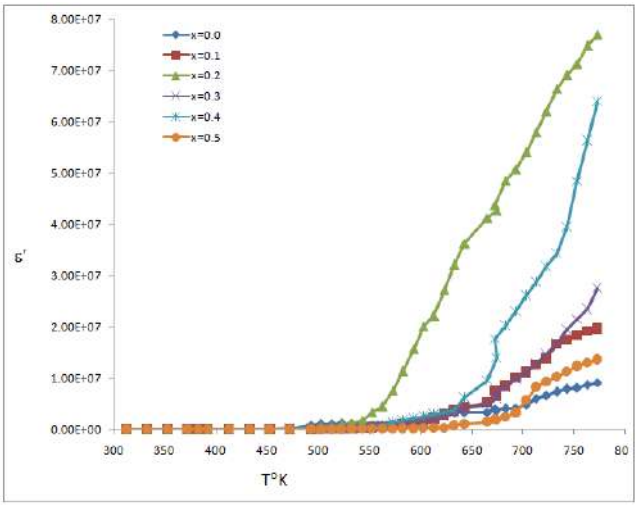

Figure 3: Variation of dielectric constant with temp of Ni0.7-xCuxZn0.3Fe2O4 ferrite for (x= 0.0 to 0.5)

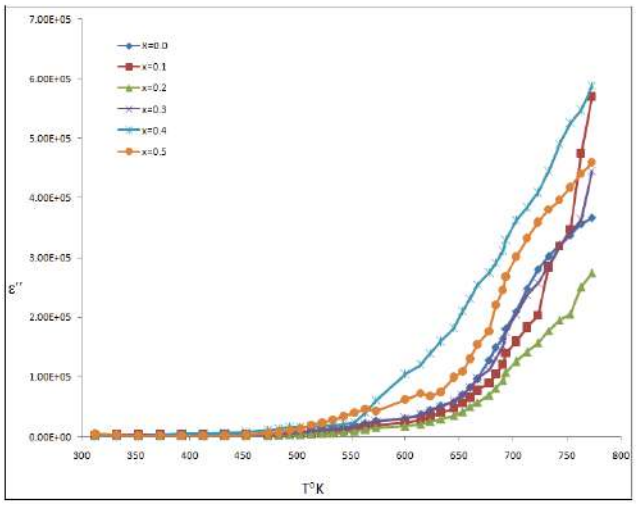

Figure 4 Variation of dielectric constant with temp of $Ni_{0.7-x}Cu_xZn_{0.3}Fe_2O_4$ ferrite for (x= 0 to 0.5)

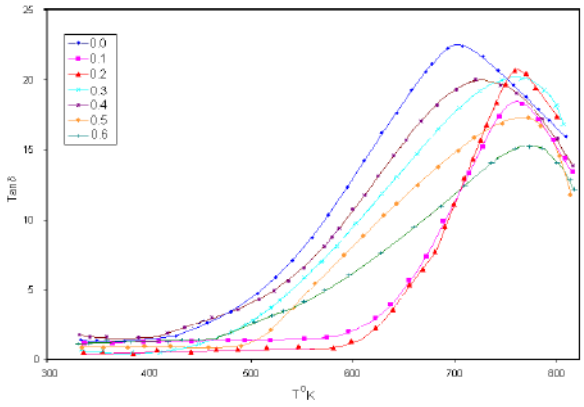

Figure 5: Variation of loss tangent with temperature of $Ni_{0.7-x}Cu_xZn_{0.3}Fe_2O_4$ ferrite for (x= 0.0 to 0.5).

3.3 Dielectric Properties:

The variation of dielectric constant (ε'), dielectric loss (ε'') and loss tangent (tanδ) as a function of temperature at a fixed frequency 1 KHz is as shown in Fig. 3, 4 and 5 respectively. From figures, it is observed that dielectric constant (ε'), dielectric loss (ε'') and loss tangent increases gradually with an increasing temperature. This increase is due to polarization in ferrites has largely attributed to the presence of Fe^{2+} ions which give rise to heterogeneous spinel structure. Since Fe^{2+} ions are easily polarisable, the larger the number of Fe^{2+} ions the higher would be dielectric constant [13]. The electric hopping between Fe^{2+} and Fe^{3+} ions and hole hopping between Ni^{2+} and Cu^{2+} on B-sites are responsible for electric conduction and dielectric polarization. As Cu ion substation increases replacing Ni ions some Fe ions will be forced to migrate from B to A sites [14-15].

CONCLUSION

In Cu-doped Ni-Zn ferrite, the resistivity is found to be decrease with increasing temperature for all samples. The ferrites show semiconducting behavior. The dielectric constant, dielectric loss and loss tangent are increases with increasing temperature. This increase in dielectric constant with increasing temperature is due to local displacement of electrons in the direction of electric field which determine the polarization process.

Conflicts of interest: The authors stated that no conflicts of interest.

REFERENCES

1. Murthy YLN, Kasi Viswanath IV, T Kondala Rao, and Rjendra Singh, *International Journal of Chem. Tech. Research*, 2009;1(4): 1308-1311.
2. John Zhang Z, Zhong L, Wang Bryan, Chakoumakos C and Jin SY. *J. Am. Chem. Soc*., 1998; 120 (8): 1800.
3. Chen CJ, Bridger K, Winzer SR, Paiverneker V, *J. Appl. Phys*., 1988; 63: 3786.
4. Lin CH, Chen SQ, *Chin. J. Mater. Sci*., 1983; 15, 31.
5. Yue Z, Li L, Zhou J, Zhang H, Gui Z, *Mater. Sci. Eng*., 1999; B64: 68.
6. Jacobo SE, Duhalde S and Bertorello HR, *Journal of Magnetism and Magnetic Ma-terials*, 2004; Vol. 272-276, No. 3: 2253-2254.
7. Shenoy SD, Joy PA and Anantharaman MR, *Journal of Magnetism and Magnetic Materials*, 2004; 269(2):217-226.
8. Morrison SA, Cahill CL, Carpenter EE, Calvin S, Swaminathan R, McHenry ME and Harris VG, *Journal of Applied Physics*, Vol. 95, No, 11, (2004) 6392- 6395.
9. Sun J, Li J, Sun G and Qu W, *Ceramics International*, 2002; 28(8): 855-858.
10. Lopez GP, Silvetti SP, Urreta SE and Cabanillas, ED. *Physica B*, 2007; 398 (2): 241-244.
11. Upadhyay C, Mishra D, Verma HC, Anand S and Das RP. *Journal of Magnetism and Magnetic Materi-als*, 2003; 260,(1-2):188-194.
12. Bhosale AG and Chougule BK, *Materials letters*, 2006; 60: 3912-3915.
13. Verma A, Thakur OP, Prakash C, Goel TC and Mendiratta RG. *Material Science and Engineering B*, 2015; 116: 1-6.
14. Shabasy MEI., *Journal of magnetism and magnetic material*, 1997; 172 : 188-192.
15. Khan M, Al. Dallab S, Memon A, Ahmad A and Khan S. *Journal of material Science*, 1993; 28: 60-70.

Int. Res. J. of Science & Engineering, 2018; Special Issue A2 : 172-175 SJIF Impact Factor 4.11
ISSN: 2322-0015 UGC Approved Journal No. 63628
RESEARCH ARTICLE **OPEN ACCESS**

Synchronous luminescence spectroscopy for determination of possibility of medicinal and food values of plants

Suryawanshi AD[1], Padampalle AS[2], Sanap VB[3], Suryawanshi DD[4], Pawar BH[5]

[1]Dept of Physics, B.J. College, Ale (Pune),[2]Dept. of Physics, S.C.S. College, Omerga (Osmanabad),[3]Dept. of Physics, Y. C. College, Sillod (Aurangabad),[4]Dept of Chemistry, B.A.M. University, Aurangabad'[5] Ex. Head, Dept. of Physics, S.G.B. Amravati University, Amravati.
Email: *ajitdsuryawanshi@rediffmail.com*

Manuscript Details

Available online on http://www.irjse.in
ISSN: 2322-0015

Editor: Dr. Arvind Chavhan

Cite this article as:
Suryawanshi AD, Padampalle AS, Sanap VB, Suryawanshi DD, Pawar BH. Synchronous luminescence spectroscopy for determination of possibility of medicinal and food values of plants, *Int. Res. Journal of Science & Engineering,* January 2018; Special Issue A2: 172-175.

ABSTRACT

The study of the effect of various stresses like light stress, temperature stress, pollutant stress etc. may be performed using various spectroscopic techniques like absorption spectroscopy, fluorescence spectroscopy, fluorescence kinetics, Fourier Transform Infrared spectroscopy etc. In addition to these techniques the synchronous luminescence technique may be successfully employed to study the effect of stresses on the plant health. In this technique the fluorescence signal is recorded by simultaneously scanning both the excitation and emission wavelengths at same speed with a fixed wavelength interval between the excitation and emission wavelengths.

Key words: Photosynthesis, Deuterium/Halogen source, SL spectra.

INTRODUCTION

In this technique the fluorescence signal is recorded by simultaneously scanning both the excitation and emission wavelengths at same speed with a fixed wavelength interval between the excitation and emission wavelengths. Since it takes the advantage of the absorption as well as emission properties of the molecules, it leads to considerable amount of simplification in the measured fluorescence spectral profile. In the present attempt we are going to use the

synchronous luminescence spectroscopy for the study of plant health and classification. As per our information the type of measurements made by us is the first report of this kind. It is seen that more information can be obtained from the analysis of synchronous luminescence spectra of the plant leaves.

METHODOLOGY

Sample preparation:
The plants that are selected for the experiment have been grown in the campus of the nursery at Amravati. The plants are developed in the natural condition of light and temperature. Plants are well watered and regularly nourished and developed in the good environmental conditions. Typical and healthy leaf from a plant has been chosen for the study of the synchronous luminescence spectra.

Experimental Method:
A block diagram for recording synchronous luminescence spectrum is shown in fig 1.

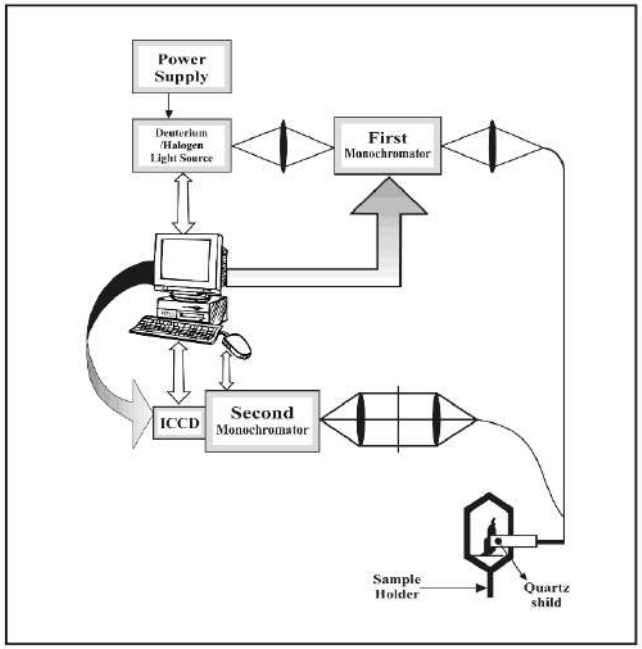

Figure 1 Experimental arrangement for recording synchronous luminescence spectra of plants leaves. Commercial spectra physics fluorometer (SPEX, USA, Fluorolog –II) was used to record the synchronous luminescence spectra.

The spectra were recorded by scanning both the excitation and emission monochromator simultaneously at the same speed of 5 nm/s with a fixed wavelength separation between them. For these studies wavelength difference between excitation and fluorescence emission was chosen to be 20 nm since it lead to the most resolved spectra. The band pass of both the excitation and emission monochromator was kept 2 nm wide. A xenon lamp of 45 W is used as the excitation source. The light from xenon lamp was incident perpendicular to the sample surface to a spot of size approximately 2mm X 4 mm and the emitted light was collected at approximately 20^0 angle with respect to the direction of the excitation light. Excitation intensity varied with wavelength but was always less than 40 W/mm^2.

A bundle of seven optical fibers is used as light transporting system. A single central fiber carries light from the source to the sample and six fibers surrounding the centro fiber collect the fluorescence signal given by sample.

RESULTS AND DISCUSSION

The synchronous luminescence spectra of many plants belonging to different family have been recorded using SPEX USA fluorolong–II spectrophotometer and results are displayed in figure 2 (a-c).

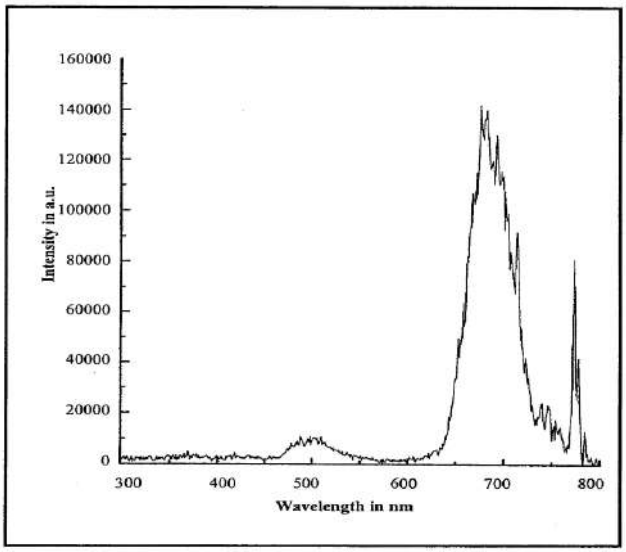

Figure 2 (a) Synchronous luminescence spectra of plants of Fiscus benghalensis [Family-Moraceae].

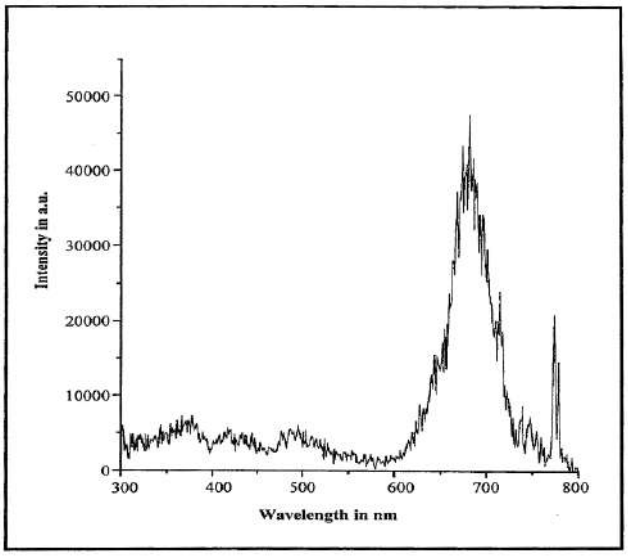

Figure 2 (b) Synchronous luminescence spectrum of leaf of Fiscus religiosa [family-Moraceae].

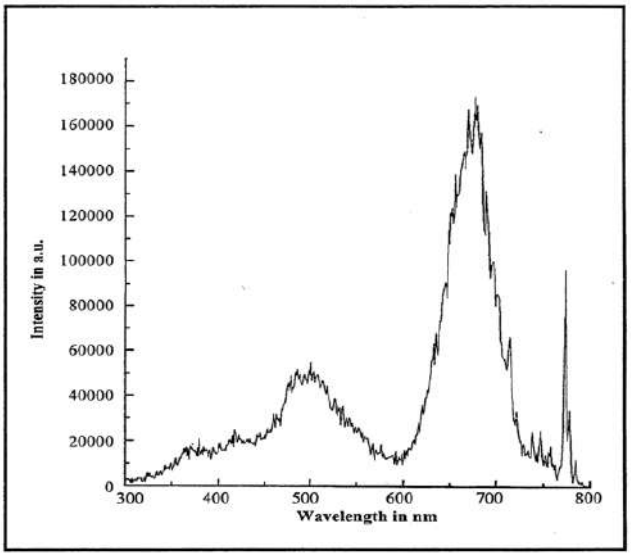

Figure 2 (c) Synchronous luminescence spectrum of leaf of Hibiscus rosasinensis [Family-Malvaceae].

All the spectra recorded by us exhibit novel structure difference. The number of peaks observed in the spectra and the intensity of peaks differ from plant to plant.

All the synchronous luminescence spectra of plant leaves were characterized by 2 to 5 narrow spectral bands with peak around 366, 416, 500, 677 and 772 nm. A prominent peak around 677 nm exhibits some extra structure of few plants. Significant differences can be seen in the intensities of different spectral band of different plants. The peak position of the different spectral bands characteristics of the different intrinsic fluorophores provide a rapid qualitative estimate of the relevant contains of the fluorophores present in the leaf cells. For example the peak at 500 nm spectral band is similar in case of all the plants. From the analysis of the peak structure one would expect no significant difference in the concentration of pigments in the plant cells. However, significant difference in the peak positions in the spectra would suggest that there is significant difference in the quantity of the different pigments present in the cells.

The synchronous luminescence spectra contains main peak and few side peaks. The main peak in the emission spectrum is wide and appears around 680 nm. However, there is a slight difference in the position of the other peaks depending upon the species selected for the studies. For getting better understanding about the structure and density of the pigments in the leaf heights of the peaks in the spectra are normalized to the height of the prominent peak near 680 nm.

It should be noticed that position of the main peak lies between 650 to 683 nm and the width of the main peak is between 40 to 70 nm FWHM (full width at half maximum) for all samples under investigation.
It should be noticed from the analysis of the spectra that all plants on the longer wavelength slope of the main peak exhibit peaklets. It is also clear that lot of information about the plant health may be extracted from the position and properties of peaklets with respect to main peak.

The synchronous luminescence spectra of all the plants exhibit a narrow peak near 680 nm. The relative height of this peak shows the considerable difference depending upon the families of the plant. The structure of peak carry a lot of physiological information about the plants as the related height of the peak changes from 0.2 to 0.3 with respect to the height of main peak.

Depending upon the plant type we get the different structure such as prominent peak of maximum height, double peak structure near the main peak or extra structure at main peak, widths of the different peaks,

exact position of the peak, number of peaks in the spectrum, position of peaklets near the main peak.
Thus several excitation and emission spectra are required to obtain the information on fluorophores concentration, the same information can be obtained more conveniently in the single step by recording synchronous luminescence spectra. Since synchronous luminescence spectrum provides more information compared to emission spectrum at single excitation wavelength. The study of synchronous luminescence spectra may lead to better discrimination in the plant physiology. The study of the synchronous luminescence spectra is helpful in the investigation of band structure of the pigments present in the plant leaves.

CONCLUSION

It is cleared that each sample of plant leaves from various families and plant types gives the different feature. An attempt can be made to record the synchronous luminescence spectra of all possible samples having some medicinal value or special characteristics such as oil producing plant, poisoning plant etc. and then by differentiating and classifying according to various parameters such as peaklets position, total number of peaks, position and intensity of various peaks in the spectra, full width at half maximum of each peak, the ratio of different peak heights. Some conclusion may be drawn about the position of the plant.

An unknown sample may be identified as a medicinal and nonmedicinal plant. The synchronous luminescence spectroscopy is very much useful in the identification of various plants, which belong to different families, species etc.

It is obvious that from the study of synchronous luminescence spectra large amount of information may be provided to the branch of bio-informatics.
Synchronous luminescence spectral study also gives good information about leaf structure, degree of stresses and leaf contents. Thus the synchronous luminescence spectroscopy is very powerful tool for investigation of plant physiology.

Conflicts of interest: The authors stated that no conflicts of interest.

REFERENCES

1. Gupta P.K. and Bhawalkar D. D. Current Sci., vol.,77, No 7, 1999.
2. Wolbarsht M. L., "Laser applicatipon in medicine and biology." Pelenum press NewYork, Vol.1-5, 1991.
3. Gupta P. K., Pradhan A. S., Bhatnagar P. K. Reddy A. R. 'Medical Physics for Human Health Care'.Scientific Publisher, Jodhapur.
4. Servik-Muraca E, and Benaron D. " Trends in optics and photonics on Biomedical optical spectroscopy and Diagnostics," Optical society of America, Washington DC, Vol. 3, 1996.
5. Majumdar S. K., Mohanty S. K., Ghosh N., Gupta P. K. and et al "A Pilot Study on the use of Autofluorescence Spectroscopy for Diagnosis of the cancer Of Human Oral Cavity," Current Science, Vol. 79, No. 8, pp 1089-1094, 2000.
6. Lang Michael, Lichtenthaler H. K., "Changes in the Blue –Green and Red Fluorescence Emission Spectra of Beech Leaves During the Autumnal Chlorophyll Breakdown," J. Plant Physiol, Vol. 138, pp. 550-553, 1991.
7. Krause G. H. and Wies E. 'Chlorophyll Fluorescence and Photosynthesis: The Basics', Annual Review Plant Physiology, Vol. 42, pp. 313-349, 1991.
8. Gitelson A. A. and Marzlyak M. N., "Signature Analysis of Leaf Reflectance Spectra: Algorithm Development for remote sensing of chlorophyll", J. Plant Physiol, 148, 494-500, 1996.
9. Gitelson A. A., Buschmann C., Lichtenthaler H. K., "Leaf chlorophyll Fluorescence Corrected for Re-absorption by Means of Absorption and reflectance Measurements", J. Plant physiology, Vol, 152, pp. 283-296,1998.

IRJSE *Int. Res. J. of Science & Engineering,* 2018; Special Issue A2 : 176-179 SJIF Impact Factor 4.11
ISSN: 2322-0015 UGC Approved Journal No. 63628
RESEARCH ARTICLE **OPEN ACCESS**

Deposition and Characterization of CdSe Thin Films by Spray Pyrolysis Technique

Akolkar L, Akolkar A, Bawaskar R, Kakade N

Dadapatil Rajale Arts & Science College, Adinathnagar, Pathardi, Dist. - Ahmednagar-414505
Email: akolkarlahu@gmail.com

Manuscript Details

Available online on http://www.irjse.in
ISSN: 2322-0015

Editor: Dr. Arvind Chavhan

Cite this article as:
Akolkar L, Akolkar A, Bawaskar R, Kakade N. Deposition and Characterization of CdSe Thin Films by Spray Pyrolysis Technique, *Int. Res. Journal of Science & Engineering,* January 2018; Special Issue A2 |: 176-179.

ABSTRACT

CdSe thin films have been deposited by spray pyrolysis technique. The glass substrate temperature was varied from 250°C to 340°C. Uniform growth of the thin film is observed at 300°C. CdSe thin films are characterized for Structural and optical properties. X-ray diffraction pattern shows that films are polycrystalline in nature with hexagonal crystal structure. Optical study of thin film shows energy gap similar to n type semiconductor and suitable for photovoltaic action.

Keywords: Spray pyrolysis, CdSe, thin films, X-ray diffraction, polycrystalline

INTRODUCTION

Now a day the research on nano scale has eventually exaggerated because of its anomalous behavior and different medical applications. In recent year's researchers having a closer look at nano-mechanisms, they are making significant improvements in different areas from delicate electronics to life-saving medical techniques [1]. Considerable attention has been given to the development of CdSe thin film compounds because of their important properties like optical, mechanical, thermal and electronic properties and their various important applications in industry and solar systems. Research on Thin film compounds is also an attractive and versatile field for their numerous applications in various electromagnetic devices. CdSe is an II-VI binary semiconductor compound.

Because of high absorption coefficient and nearly optimum band gap energy, CdSe is a promising photovoltaic material which is essential for efficient absorption of light and converting it into electrical power. A direct band gap range from 1.65 eV to 1.84 eV has been observed for the CdSe material in different studies of various researchers [2]. Because of intermediate energy band gap and reasonable conversion efficiency makes CdSe as one of the most widely useful materials for photovoltaic solar cells [3]. Semiconductor devices which are based on CdSe thin films strongly depends on the structural properties, optical properties and electrical properties of the films obtained from various experimental techniques. In recent years, CdSe nanoparticles have been synthesized by using spray pyrolysis method [4]. The grain size at the surface of the film is found to depend on thickness of the film [5]. Surface morphology of the CdSe film is strongly correlated with the amount of CdSe deposited on the surface [6]. In the present work spray pyrolysis deposition technique was successfully employed to prepare CdSe thin film by simple and low cost chemical spray pyrolysis technique (SP). The prepared film have been characterised by X-ray diffraction (XRD) and UV-VIS optical measurement techniques. The results have been discussed.

METHODOLOGY

$CdCl_2$ and Seleno-urea chemicals were used for synthesis of $CdCl_2$ & Se particles. Formula for molar solution

For seleno-urea:

$$W = N * M * \frac{V}{1000}$$

= 0.025*100*123.02/1000

=0.307 gm

For cadmium chloride:

$$W = N * M * \frac{V}{1000}$$

$$= 0.025 * 100 * 201.32/1000$$

=0.50 gm

First 0.307 ml of seleno-urea was mixed with the 20 ml double distilled water, stirred it for 5 minutes. Then in another beaker 20 ml of distilled water was mixed it with 0.50gm of $CdCl_2$ and stirred it. Both mixtures were taken in funnel on instrument. Air compressor was used to give pressure in spray pyrolysis unit (2 kg/m^3). Temperature was varied for different glass substrates by electronic controller. Different samples of glass substrates were characterized for UV-visible spectroscopy and X-ray diffraction (XRD) technique.

Characterization

UV–visible spectroscopy: Optical transmittance measurements of the films were used to estimate the band energy from the position of the absorption coefficient edge. The energy of light quanta near the fundamental edge for direct electron transition is given by $\alpha = (h\upsilon - E_g)^{1/2}$ or $\alpha^2 = h\upsilon - E_g$

Thus a plot of α^2 against $h\upsilon$ gives a straight line. A plot of α^2 versus $h\upsilon$ in the region deviates from being straight but extrapolation of the straight portion of the graph to $\alpha^2 = 0$ gives the band gap E_g of the CdSe thin films. Where α is the optical absorption coefficient of the material and $h\upsilon$ is the photon energy, gives the value of band gap energy (E_g). The optical band gap of energy of the CdSe films deposited at 300 ^oC with observed condition is 1.80 eV. This value is in good agreement with the nature of Semiconductor. The intercepts (extrapolations) of these plots (straight lines) on the energy axis give the energy band gaps. The direct band gaps for all the films were determined. With increasing selenium content energy band gap of CdSe thin films decreases.

X-ray diffraction:

The CdSe thin films fabricated at different substrate temperatures were characterized by analysis of X-ray diffraction (XRD) patterns. The (h k l) miller indices for each diffraction peak were calculated from corresponding observed and standard d-values. The XRD patterns revealed that films were polycrystalline in nature because these are having more than one peak. The high intense is observed for (002), (100) and for (110) peak while low intense (110) peak were identified for CdSe. X-ray diffraction patterns recorded for the spray deposited CdSe films on glass substrates at 300 ^oC temperature is shown in Fig. 2. The observed diffraction peaks of CdSe films are found at 2θ values of 23.5, 26, 27.5 and 42 corresponding to the hkl planes (100), (002), (101) and (110) respectively. CdSe thin films deposited at temperature 300^{o}c are smooth and uniform. The

height of (100), (002) and (110) peak in X-ray diffraction pattern for CdSe thin films deposited at temperature 300 °C has shown sharper peaks.XRD results shows that the deposited CdSe films are polycrystalline in nature having hexagonal structure with preferred orientation along (002) plane.

RESULTS AND DISCUSSION

Table 1 :

CdSe	Thickness=460nm				
λ(nm)	Absorption(αt)	α	hυ	αhυ	(αhυ)^2
500	0.7585	1.65E+04	2.48	4.08E+04	1.67E+09
520	0.7282	1.58E+04	2.39	3.78E+04	1.43E+09
540	0.6985	1.52E+04	2.30	3.49E+04	1.22E+09
560	0.6623	1.44E+04	2.22	3.19E+04	1.02E+09
580	0.6199	1.35E+04	2.14	2.89E+04	8.33E+08
600	0.5853	1.27E+04	2.07	2.63E+04	6.94E+08
620	0.5605	1.22E+04	2.00	2.44E+04	5.96E+08
640	0.5430	1.18E+04	1.94	2.29E+04	5.25E+08
660	0.5287	1.15E+04	1.88	2.16E+04	4.68E+08
680	0.5086	1.11E+04	1.83	2.02E+04	4.08E+08
700	0.4986	1.08E+04	1.77	1.92E+04	3.70E+08
720	0.4873	1.06E+04	1.73	1.83E+04	3.34E+08
740	0.4731	1.03E+04	1.68	1.73E+04	2.98E+08
760	0.4599	1.00E+04	1.63	1.63E+04	2.67E+08
780	0.4540	9.87E+03	1.59	1.57E+04	2.47E+08
800	0.4404	9.57E+03	1.55	1.49E+04	2.21E+08
820	0.4240	9.22E+03	1.51	1.40E+04	1.95E+08

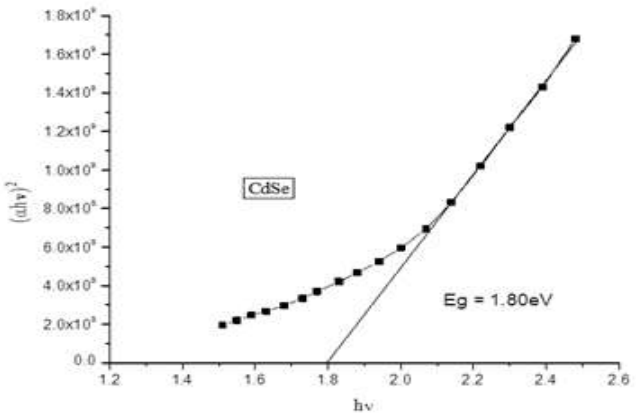

Fig. 1:

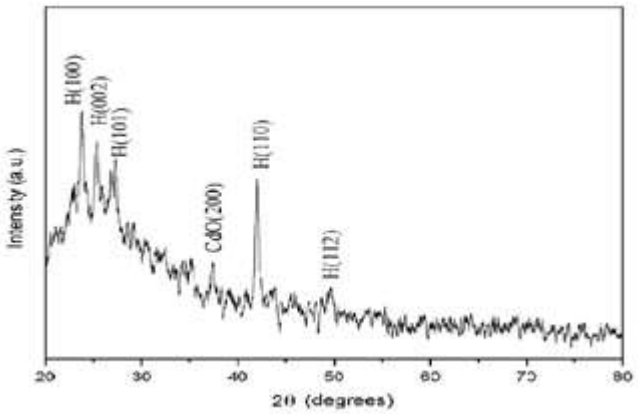

Fig. 2:

Fig. 1: Variation of $(\alpha h\nu)^2$ vs. Photon energy (hν) at temperature 300 °C

Fig: 2. XRD patterns of CdSe thin films deposited at substrate temperatures of 300°C

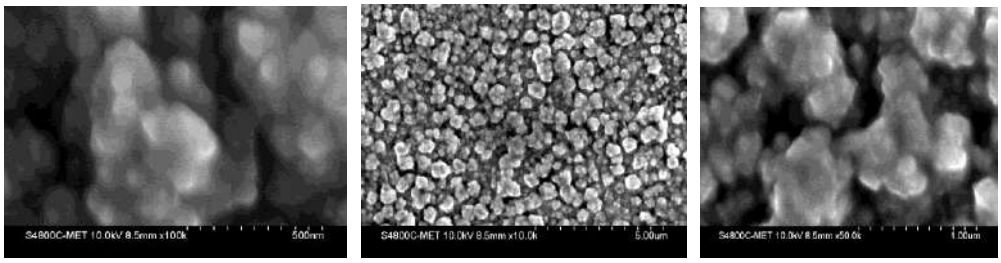

8.5mm×100k 500nm 8.5mm×10k 5 µm 8.5× 1µm 1 µm

Fig: 3. Scanning Electron Microscope images

CONCLUSION

Optical properties which were observed in this study depend on thicknesses of CdSe thin films and increase in band gap of the films corresponds to increase in thickness of films**.** The CdSe thin films deposited on glass substrates at temperatures 300 ^{o}C employing spray pyrolysis technique is uniform and smooth. X-ray diffraction pattern reveals that the CdSe films are of hexagonal in structure. Various structural parameters such as grain size of the films are found to be increased with increasing temperature. Optical transmittance measurements indicate that the deposited films have a direct band gap of 1.80 eV which means CdSe is n-type window layer suitable for photovoltaic action.

Conflicts of interest: The authors stated that no conflicts of interest.

REFERENCES

1. Hashim M, Meena S. S.,. Kotnala R. K, Shirsath S. E., Roy A. S., Parveen A., Bhatt P., Kumar S., Jotania R. B., Kumar R., Alimuddin, *Journal of Alloys and Compounds, Elsevier*, 2014, 602, 150-156.
2. Baban C., Rusu G. I., Prepelita P., *Journal of Optoelectronics and advanced materials*, 2005, 7, 817.
3. Chu T. L. and Chu S. S., *Solid-State Electronics*, 1995, 38, 533.
4. Yadav A. A., Barote M. A. and Masumdar E. U., *Solar Energy*, 2010, 8, 763.
5. Bakry A. M., *Egypt. J. Solids,* 2008, 31**,** 1.
6. Su B., Choy K. L., *Thin Solid Films,* 2000, 102, 361-362.

IRJSE *Int. Res. J. of Science & Engineering,* 2018; Special Issue A2 : 180-182 SJIF Impact Factor 4.11
ISSN: 2322-0015 UGC Approved Journal No. 63628
RESEARCH ARTICLE **OPEN ACCESS**

Electrical behaviour of some of the vegetables, fruits and food grains

Nagarbawadi Mehboob [1] and Bagwan Sohail[2]

[1]Department of Physics, AKI's Poona College, Camp, Pune-411001.INDIA,[2]Department of Physics, Abeda Inamdar Sr. College, Camp, Pune-411001.INDIA.
Email: dr_mehboobn@rediffmail.com

Manuscript Details
Available online on http://www.irjse.in
ISSN: 2322-0015

Editor: Dr. Arvind Chavhan

Cite this article as:
Nagarbawad Mehboob and Bagwan Sohail. Electrical behaviour of some of the vegetables, fruits and food grains, *Int. Res. Journal of Science & Engineering,* January 2018; Special Issue A2 : 180-182.

ABSTRACT

The electrical behaviour of some of the vegetables, fruits and food grains have been studied using the method of two probe resistance measurement at various levels of frequencies. The aim of the present study was to investigate the behaviour of its capacitance as a function of frequency. Electrical capacitance was found to decrease exponentially with increasing frequency, but the dielectric constant was a function of the moisture content thereby increasing its ability to store energy.

Key words: Dielectric constant, dielectric loss, conductivity, frequency.

INTRODUCTION

Agricultural products are highly perishable with short storage time. However, demand for agricultural products will never desist as long as human population growth continues to increase. This is a problem and hence there is an opportunity to increase the added value of the products. Achieving these objectives requires continuous assessment including in terms of technology in horticulture and in the field of basic science. Properties of these products are mostly affected by external factors such as weather, pests and post-harvest handling errors. Internal factors such as changes in chemical composition, metabolism, fibre conditions, moisture content, acidity etc. Also affect the quality of the agricultural produce. Measurements of the properties of agricultural products generally employ destructive methods.

The measurements of all parameters were done when the vegetables, fruits and food grains were still in fresh condition. Electrical parameters are measured using LCR meter. The samples were placed between two plate conductive electrodes as dielectric material. The conductive plates were of copper. The parameter values of electricity were measured within a frequency of 50 Hz to 1 kHz. Each sample was measured for several times and the average was calculated for tomato, sweet potato, apricot, wheat powder and rice powder.

1 Material permittivity ε:

The permittivity of tested samples was measured using

$$\varepsilon = C\, d / A$$

Where:

C: is the capacitance of the food material in farad.

d: is the distance between the two electrodes of the capacitance in m.

A: is the surface area of the electrode in m^2.

2 Relative permittivity ε':

The dielectric constant or relative permittivity of the food material was determined using the relation

$$\varepsilon' = \varepsilon / 8.85 \times 10^{-12}$$

3 Dielectric loss factor ε":

The dielectric loss factor was determined according to ASAE (1994) as follows:

$$\varepsilon'' = \sigma / (55.36(2450)10^{-12}$$

Where: σ: is the electrical conductivity of the food material

RESULTS AND DISCUSSION

The experimental result for the electrical conductance of sweet potato as a function of signal frequency is as shown in Fig.1. Electrical conductance value for sweet potato at low frequency is very small. Sweet potato shows resistive properties, so it is an insulator or a poor conductor. Thus, the ions and electrons in the skin and flesh are bound and are relatively stable. The low conductance indicates that ions are strongly bound to the constituent substances of sweet potato. Electrical conductance values express the ability of charge movement in the material and depend on the number of ions or free electrons in the material. Electrons of conductive material easily follow changes in the external alternating current. Thus, increasing of electrical conductance would easily occur if the frequency is increased, which is not easily possible in the resistive material. So, increasing the frequency only, slightly changes the conductance value of the resistive material.

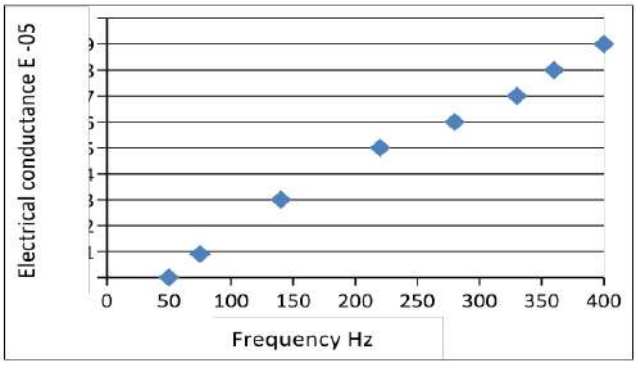

Fig1: Electrical conductance (10^{-5}) against Frequency of sweet potato

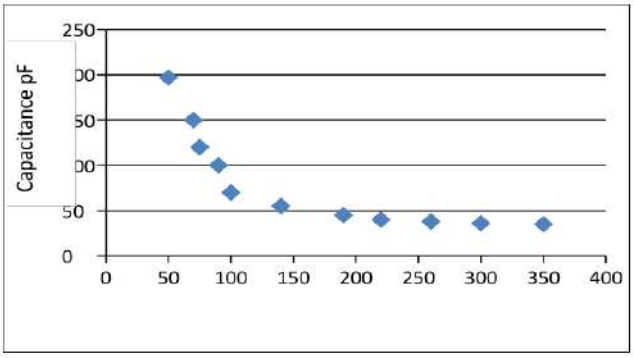

Fig 2: A graph of capacitance in pF against frequency for sweet potato.

Correlation between the frequencies and the conductance does not occur linearly but exponentially. Electrical conductance values of sweet potato increased slightly when the frequency is increased. The most significant improvement occurs when frequencies is above 100 Hz. Increased frequency of the signal will increase the rate of movement of electric charge, so the ions move in sweet potato more effectively. Capacitance describes the ability of capacitors to store energy in the form of electrical charge. The presence of a dielectric material in capacitors causes an increase in the capacitance value. The dependence of dielectric parameters have been examined by plotting curves of capacitance Vs frequency as shown in Fig2.Electrical permittivity is a dielectric property used to explain interactions of

foods with electric fields. It determines the interaction of electromagnetic waves with matter and defines the charge density under an electric field. In solids, liquid, and gases the permittivity depends on two values viz.
1. The dielectric constant, related to the capacitance of a substance and its ability to store electrical energy and
2. The dielectric loss factor, related to energy losses when the food is subjected to an alternating electrical field (i.e., dielectric relaxation and ionic conduction).

In foods, permittivity can be related to chemical composition, physical structure, frequency, and temperature, with moisture content being the dominant factor. Dielectric properties are primarily determined by their chemical composition (presence of mobile ions and permanent dipole moments associated with water and other molecules) and, to a much lesser extent, by their physical structure. The influence of water content largely depends on the manner in which they are bound or restricted in movement by other food components. Free water has a high dielectric activity, while bound water has low activity. Power dissipation is directly related to the dielectric loss factor and depends on the specific heat of the food, density of the material, and changes in moisture content (for example: Vaporization, soaking). Permittivity also depends on the frequency of the applied alternating electric field. Frequency contributes to the polarization of molecules such as water. In general, dielectric constant increases with temperature, whereas loss factor may either increase or decrease depending on the operating frequency. Both the dielectric constant and loss factor decrease significantly. Same results were observed for tomato though water content is more. We observed that capacitance value is more for apricot than wheat powder and rice powder. The moisture content of the food increases the loss factor (for tomato, sweet potato) and determines the dissipation of the energy out of the material or into the material. High values of capacitance at low frequency (50 Hz) could be attributed to high mobility of dipole due to free water state and electrode polarization. Frequency changes will affect the condition of the ions in the material. Ionic loss is inversely proportional to frequency and become critical as we go to the lower frequency. Dissipation of dipolar energy at higher frequencies is less dominant and ionic loss become almost absent. Decrease in the capacitance is not linear when the frequency increased. So it can be said, increasing the frequency of the signal cannot be linearly followed by changes in the internal dipole moment of sweet potato. The frequency of the signal source is a description of the speed of change in the direction of an external electric field. Changes in the external electric field will be followed by changes in the internal electric field of the sweet potato. Increased frequency will increase the speed of dipole changes. Thus, the frequency of the electrical signal will have consequences on the time for polarization. The value of high frequency gives a short time for polarization.

Conflicts of interest: The authors stated that no conflicts of interest.

REFERENCES

1. Incropera, F.P. & Dewitt, D.P. (2002), Fundamentals of heat and mass transfer, 5th ed., John Wiley & Sons, New York.
2. Mohsenin, N.N. (1980), Thermal properties of foods and agricultural materials, Gordon & Breach, New York.
3. Coskuner, Y.; Karababa, E. (2007), Some physical properties of flaxseed (Linum usitatissimum L.), Journal of Food Engineering, 78, 1067–1073.
4. Marzouk M. Bekhit and Saad A. Khalil, "Electrical Properties of Moist Limestone Samples In The Frequency Range 1Hz-10 Hz From Abu Rawash Area", Australian Journal of Basic and Applied Sciences, Vol. 1, No. 4, 2007, pp. 741-750.
5. Zeleny L. (1954): Methods for grain moisture measurements, Agricultural engineering, 35(4)252- 256.
6. Wittkopf J. J. and Macdonald M. D. (1949): Dielectric properties of Douglas fir at high frequencies, Bull. No. 28 Eng. Exp. Sta., Oregon State System of Higher Education, Oregon State Coll., Corvalis, Ore., p. 23.
7. Venkatesh M. S., Raghavan G. S. V. (2005): An overview of dielectric properties measuring techniques, Canadian Biosystem Engineering (47), p.7.15-7.29.
8. Sembery P., Géczi G. and Váczy G. (2001), Measurement Methods of Dielectric Properties of Mustard Seeds at Microwave Frequency Hungarian Agricultural Research, HU ISSN 1216- 4526, Vol. 10, No.3, p.16-18
9. ASAE.1994.Standared, Engineering Practice data, ISBN-929355-50. Lib. of Congress, by Am. Soci. of Ag. Eng, 459-466.
10. Theraja B.L.1993, A text book electrical technology, Pub. division of Nirja Constr. & Dev. Co. (p) Ltd. Ram Nagar, New Delhi-100055,118- 160.

Int. Res. J. of Science & Engineering, 2018; Special Issue A2 :183-186 SJIF Impact Factor 4.11
ISSN: 2322-0015 UGC Approved Journal No. 63628
RESEARCH ARTICLE **OPEN ACCESS**

Study of Laser Radiation Effects on Diabetic Human Blood Using FTIR Spectroscopic Techniques

Ghadage Vijay H and Lokare SA

Anantrao Pawar College, Pirangut, Tal – Mulshi, Dist – Pune, Pune-412115
Email: ghadagevh@gmail.com | lokaresmita@gmail.com

Manuscript Details

Available online on http://www.irjse.in
ISSN: 2322-0015

Editor: Dr. Arvind Chavhan

Cite this article as:
Ghadage Vijay H and Lokare SA. Study of Laser Radiation Effects on Diabetic Human Blood Using FTIR Spectroscopic Techniques, *Int. Res. Journal of Science & Engineering,* January 2018, Special Issue A2: 183-186.

ABSTRACT

Laser tissue interactions can be understood by using different spectroscopic techniques and Scanning electron microscope. In the present work blood samples were collected from diabetic human subjects under standard laboratory conditions. Diabetic blood samples were irradiated by HeNe (Helium-Neon) laser (wavelength λ=700 nm, Power =5 mW). The FTIR spectra of nonradiated diabetic blood samples are compared with the FTIR spectra of radiated diabetic blood samples. The significant changes are observed between the O-H(Free group),P-H(Phosphine) and C=O (amide group) due to laser radiation on diabetic blood samples for time 10 to 40 min. respectively. The decrease in percentage of transmittance for C=O (amide group) for 30 and 40 min. for diabetic blood samples shows the denaturation of proteins.

Keywords: He-Ne laser, Voltex Power supply (Model S-22), FTIR, Diabetic blood.

INTRODUCTION

Diabetes is serious disease that affects not only the patients internal organs,circulation system and eyesight but also their entire body[1]. Diabetic foot ulcers as one of the most common complications of diabetics for long lasting in diabetic patients [2].Diode lasers and free electron lasers have been important tools for advanced medical research, while pulsed lasers contributed more to laser surgery. In low power laser to have any effect on living biological system, the photons must be absorbed

by electronic absorption bands belonging to some molecular chromophores or photo acceptor [3]. Different advanced photonics methods & laser stimulation techniques are effectively used in biomedical science & clinical studies [4]. This wavelength effect is consistent with the absorption spectrum of hemoglobin, reflecting that hemoglobin may be one of the action targets under laser irradiation [5].

METHODOLOGY

Blood samples were collected from diabetic subjects from the Joshi Pathology, Pirangut-412115. Blood samples were also collected from age-matched persons. Fourier Transform Infra Red spectra were obtained using FTIR spectrophotometer (JASCO -6100) for control and He-Ne laser radiated whole (2ml) diabetic blood samples in vitro.

Experimental

The experimental set up consists of a He-Ne laser of wavelength λ=700nm, Power = 5 mW, sample holder, power supply and currents for whole blood sample. FTIR (Jasco-6100) system and scanning electron microscope (JEOI JSM -6360A) system were also part of the experimental setup. The Voltex "S" series of AC input power supplies has been given something new to this industry. They may now be plugged into any standard AC power from 115 to 240 VAC without setting any switches. It Operates most 2mW to 7mW HeNe lasers and has universal 115 to 240VAC input.

Specifications:

Input Volts: 115 to 240 VAC +/-10%.50/60 Hz

Input Current: .32 Amps at 115VAC, .16A at 230VAC*

Line filtering: Internal EMI line filter.

Remote plug: A low voltage removable plug on rear panel allows remote disconnected of AC power.

Output

Voltage: 1900-2600 VDC

Current: 4 to 7 mA . User adjustable

Start Voltage: >10KV

Output current Ripple: <5% P-P (<2% RMS.

Output Fault Protection: Open, Short, Arc

Conversion Efficiency: >85%

CDRH Delay: 3-5 seconds.

Output Connector: Alden style, high voltage

RESULTS AND DISCUSSION

FTIR spectra of normal diabetic blood without laser radiation shows the group O-H(Free group),P-H(Phosphine) and C=O (amide group) in the region between the wave number 4000 to 400cm^{-1} (Fig.1). The wave number 3319.54Cm^{-1}, 2360.93Cm^{-1} and 1643.93Cm^{-1}(table1) shows the O-H, P-H and C=O group. Fig. 2 to5 shows the HeNe laser radiation for 10, 20, 30and 40 min. respectively.

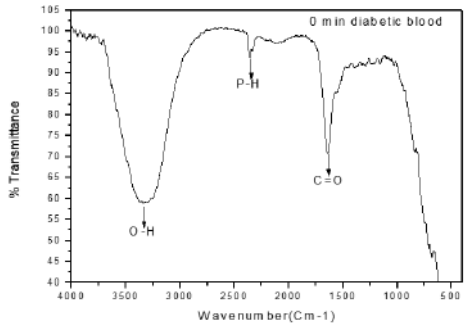

Fig 1: FTIR for diabetic Blood sample (Control)

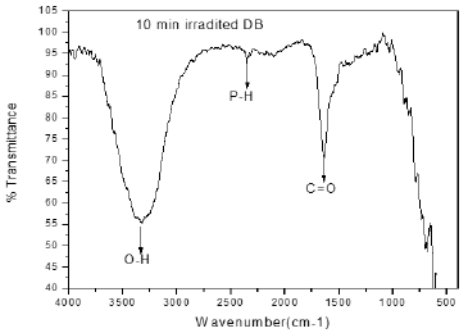

Fig 2: FTIR for radiated diabetic blood with He-Ne laser (10 min)

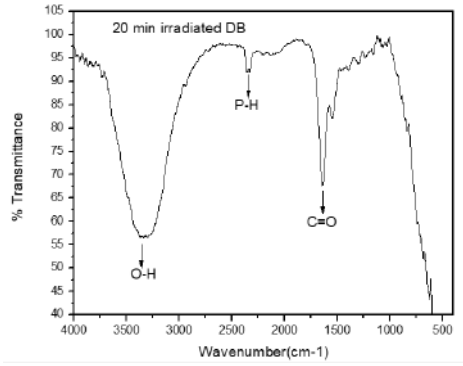

Fig. 3: FTIR for radiated diabetic blood with He-Ne laser (20 min)

Table 1: FTIR Spectra of diabetic blood (Control) & radiated with He-Ne laser for duration 10, 20, 30 & 40 minutes.

FTIR spectra Of diabetic blood				FTIR spectrum of diabetic blood radiated with He-Ne laser			
Sr. No.	Wavenumber cm^{-1}	Group	% T	Radiated Time (min)	Wavenumber cm^{-1}	Group	%T
1	3319.54	O- H (free group)	59.39	10	3330.25	O-H (free group)	56.65 ↓
2	2360.64	P-H (Phosphine)	94.04		2350.75	P-H (Phosphine)	93.38 ↓
3	1643.93	C=O (Amide)	71.47		1634.05	C=O (Amide)	70.80 ↓
4	3319.54	O-H (free group)	59.39	20	3340.13	O-H (free group)	56.43 ↓
5	2360.64	P-H (Phosphine)	94.04		2340.86	P-H (Phosphine)	92.47 ↓
6	1643.93	C=O (Amide)	71.47		1634.05	C=O (Amide)	67.60 ↓
7	3319.54	O-H (free group)	59.39	30	3299.77	O-H (free group)	58.94 ↓
8	2360.64	P-H (Phosphine)	94.04		2350.75	P-H (Phosphine)	89.73 ↓
9	1643.93	C=O (Amide)	71.47		1643.93	C=O (Amide)	65.55 ↓
10	3319.54	O-H (free group)	59.39	40	3330.25	O-H (free group)	55.74 ↓
11	2360.64	P-H (Phosphine)	94.04		2350.75	P-H (Phosphine)	91.78 ↓
12	1643.93	C=O (Amide)	71.47		1634.05	C=O (Amide)	67.82 ↓

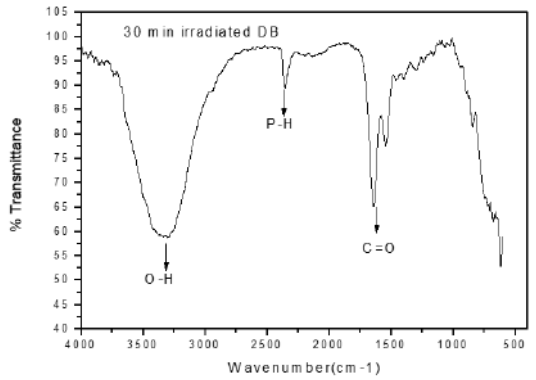

Fig.4: FTIR for radiated diabetic blood with He-Ne laser (30 min)

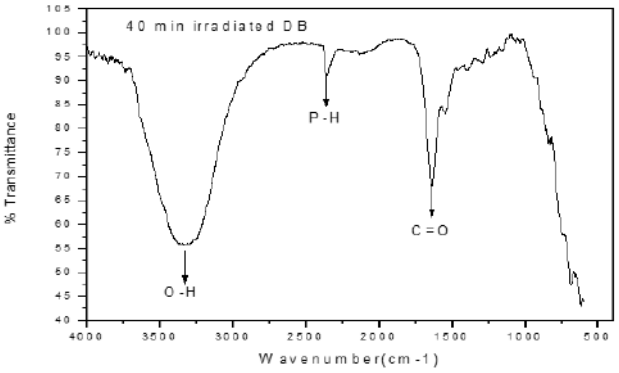

Fig.5 : FTIR for radiated diabetic blood with He-Ne laser (40 min)

The wave number 3319.54 cm^{-1} indicated O-H bonded peak. Amide I is mainly associated with C=O stretching vibrations and also related to the backbone conformation. Phosphine is mainly associated with P-H stretching vibrations. The wave numbers 2360.64 cm^{-1} & 1643.93 cm^{-1} are indicates that P-H & C=O peak. The spectral region 3400 – 2400 cm^{-1} comprises of O-H stretching vibrations of the proteins. The strong absorption band at 1643.93 cm-1 correspond to C=O stretching vibrations (amide I).

FTIR spectra of diabetic whole blood irradiated with He-Ne laser for10, 20, 30 & 40 min. duration respectively are shown in figure (2 to.5). FT-IR spectra of radiated diabetic whole blood with He-Ne laser shows transmittance decreases. The comparison of normal diabetic blood with radiated blood spectra shows the decrease in transmittance for group O-H,P-H , C=O and it shows the breaks of polypeptide bonds due to conformational changes of proteins[6,8] .

CONCLUSION

In present work we study the changes of diabetic blood before & after He-Ne laser radiation by using Fourier Transform Infrared Spectroscopy. The important groups O-H, P-H & C=O are observed in all FTIR spectra.FTIR analysis is good tool to study the molecular level changes in diabetic blood due to laser radiation.

Acknowledgement:
Financial assistance from BCUD, Savitribai Phule Pune University, Pune (O.S.D./BCUD/330 dated 11/10/2013) is duly acknowledged.

Conflicts of interest: The authors stated that no conflicts of interest.

REFERENCES

1. Mercy Adusei Boatemaa*[1] and Srinath Doss[2] (2017). Non invasive glucose estimation based on near infrared laser diode spectroscopy. Asian Journal of Biomedical and Pharmaceutical Sciences.Volume 7,issue 60.
2. Kathrin H.Beckmann,Gesa Meyer-Hamme and Sven Schroder (2014).Review Article:Low level laser therapy for the treatment of diabetic foot ulcers>Evidence based complementary and alternative medicine Volume 2014(2014),Article ID 626127.
3. Sutherland, J. C. (2002). Biological effects of polychromatic light. Photochem. Photobiol. 76, 164-170.
4. Tuchin, V.V. (2010).Handbook of Photonics for Biomedical Science. CRC Press Taylor and Francis Group, 717-737.
5. Mi,X.Q., Chen, J.Y., Liang, Z.J., and Zhou, L.W. (2004). A comparative study of 632.8 and 532 nm laser irradiation on some rheological factors in human blood in vitro. Journal of Photochemistry and Photobiology B: Biology, 74(1), 7-12.
6. V. H. Ghadage and G. R. Kulkarni, "Effects of Nd: YAG laser irradiation on human erythrocytes *in Vitro*," International Journal of Integrative Biology, vol. 9, pp. 149–151, 2010.
7. Kulkarni, G. R. (1988). Laser tissue interaction studies for medicine. Bull. Mater. Sci., vol. 11, Nos. 2 & 3,239-244.
8. Vijay H. Ghadage, Gauri R. Kulkarni (2011). Effects of HeNe laser irradiation on Red Blood Cells in vitro. Optical Interactions with Tissue and Cells XXII, Proceeding of SPIE, BIOS, San Francisco, California, USA, Vol. 7897, 789701-789710.
9. Vijay H. Ghadage, Gauri R. Kulkarni, Sudha V. Bhoraskar (2012). Study of Fourier transforms infrared spectra of cockroach nervous tissue and chitin. SPIE BIOS Conference 2012 San Francisco, California, USA, Paper no. 8221-38. *Proc. SPIE* 8221, Optical Interactions with Tissue and Cells XXIII, (February 9, 2012); doi:10.1117/12.907895.
10. Prasad, P.N. (2003).Introduction to Biophotonics. Wiley inter science Pub.
11. Wasik, M., Gorksha, Modzelewska, M. Nowicki, K., Jakubczak, B., and Demkow, U. (2007). The influence of low power Helium-Neon laser irradiation on function of selected Peripheral blood cells. Journal of Physiology and Pharmacology, 58 suppl 5, 729-737.
12. G. A. Zalesskaya and I. I. Kalosha, "Effect of *in vivo* irradiation of blood by low-intensity emission from a He-Ne laser on molecular components of blood," *Journal of Applied Spectroscopy*, vol. 76, no. 5, pp. 720–726, 2009.
13. Devi, T.S.R., Gunasekaran, S., Hudson, J.W., Joybell, S.A., "Analysis on renal failure patients blood samples: characterization and efficacy study"., Indian J. Of Science and Technology. *2009,2,46-50*.

IRJSE *Int. Res. J. of Science & Engineering*, 2018; Special Issue A2 : 187-191 SJIF Impact Factor 4.11
ISSN: 2322-0015 UGC Approved Journal No. 63628
RESEARCH ARTICLE **OPEN ACCESS**

Effect of Reaction Time on Some characterization of ZnO Nanoparticles

Shaikh RS[1] and Ravangave LS[2]

[1]Department of Physics SGBS College, Purna (Jn) Dist: Parbhani, MS (India)
[2]Department of Physics SSGM College, Loha, Dist: Nanded, MS (India)
E-mail: shaikhraju99@gmail.com, lsravangave@gmail.com

Manuscript Details
Available online on http://www.irjse.in
ISSN: 2322-0015

Editor: Dr. Arvind Chavhan

Cite this article as:
Shaikh RS and Ravangave LS. Effect of Reaction Time on Some characterization of ZnO Nanoparticles, *Int. Res. Journal of Science & Engineering*, January 2018, Special Issue A2 : 187-191.

ABSTRACT

ZnO nanoparticles were synthesized using chemical sol-gel precipitation method using solution of zinc acetate and sodium hydroxide distilled water as starting materials. The stock solutions of Zinc acetate (0.5M) and Sodium hydroxide (0.5M) were used for synthesis of ZnO nanoparticles at different reaction time via, 2hours, 4hours, 6hours and 8hours. The synthesized samples were calcined at 100^{o}C temperature for two hour. The four different samples were prepared by using reaction times 2h, 4h, 6h and 8h. Prepared ZnO particles were characterized by using XRD, FTIR, scanning electron microscopes (SEM), UV-visible spectrophotometer and Photoluminescence (PL). The XRD pattern exhibit wurtzite hexagonal crystal symmetry. The particle size estimated by using Debye-Scherrer formula was found varying with increasing reaction time. The characterizations, scanning electron microscopes (SEM) and FTIR show the significant structural and morphological changes of ZnO particles. The optical study carried out using UV-visible spectrophotometer and photoluminescence spectroscopy (PL) of the samples shows that absorption edge of UV-spectra are highly blue shifted. The Photoluminescence spectrum exhibits two emission peaks one at 389nm and excitation emission located at 524 nm. The green emission peak attributed to oxygen vacancy or interstitial related defects. The significant morphological changes of the ZnO nanoparticles were investigated from SEM images.

Keyword: ZnO Nanoparticles, XRD of ZnO, Uv-Visible spectra of ZnO.

INTRODUCTION

The objective of the present work is to synthesis of hexagonal wurtzite ZnO nanoparticle with different surface modification have a desirable properties and applications in biological physical chemical and medical fields. ZnO is an important compound semi-conductor material due to its direct energy band gap (3.37eV) and large excitation binding energy (60meV) at room temperature. It has the unique physical and optical properties which can be used in a variety of application such as oxide coatings for solar cell, gas sensors, UV photodiode, optoelectronics, and chemi-cal catalytic, photochemical and electric properties [1-3]. ZnO nanostructure has a great advantage to apply to a catalytic reaction process due to their large sur-face area and high catalytic activity [4]. ZnO semico-nductor nanowires and nanorodes are attractive compounds for nano-metre scale electronic and photonic device application because of their unique chemical and physical properties [1-2]. A wide variety of nano-devices including ultraviolet photodectectors, sensor, p-n junction diode, schottky diode LED device have been fabricated using ZnO nanorodes and nano-wires. ZnO has also been confirmed as a promising functional material for nanodevices such as field emitter and gas sensors [4-5]. Various methods have been described in earlier literature for the production of ZnO nanostructures such as. Hydrothermal, Che-mical precipitation, Chemical Vapor, Co-precipitation, Anodization, Thermal decomposition, Spray pyro-lysis, Electro-chemical deposition, Combusion method and Chemical Sol-gel precipitation method [6-16].

In the present paper ZnO nanoparticles have been prepared by using simple very economic chemical Sol-gel method. The growth of ZnO nanoparticles depends upon reaction time variation solution mixture. We study the effect of reaction time on structural, morphological, optical change of ZnO nanoparticles.

METHODOLOGY

Using chemical precipitation Sol-gel method, Zinc acetate and sodium hydroxide were used in the expe-riments. The entire chemical used were of analytical reagent grade obtained from Merck (Mumbai) India and distil water is used for the preparation of solution. A solution of Zinc acetate (0.5M) and Sodium hydroxide (0.5M) were prepared. The solutions were individually stirred vigorously for two hours. The solutions of Zinc acetate and Sodium-hydroxide was then added slowly drop wise in a molar ratio of 1:2 under vigorous stirring and the stirring was continuous for two hours. The precipitate obtained was filtered and washed thoroughly with distil water. The precipitate was dry in an oven at 100^{o}Cfor 2 hours. Other samples were prepared for reaction time 4h, 6h and 8hours and precipitates obtained were dried and ground to fine powder using agate mortar and pestle. The obtained powder was calcined at temperature 100°C, for 2 hours. The prepared samples were then characterized by various techniques such as XRD, SEM, FTIR, UV- Visible spectrophotometer and Photoluminescence spectrometer.

RESULTS AND DISCUSSION

XRD Study:

The XRD pattern of ZnO particles grown at different reaction time (2h, 4h, 6h and 8h) was shown in figure 1. The XRD pattern exhibit distinct peaks attributed to hexagonal structure of the ZnO particles. All the samples exhibit wurtize structure with hexagonal symmetry. The pattern is well matched with standard JCPDS card Number [36-1455], the various peaks at different diffracting angles (2θ) correspond to different reflections from the planes (100), (002), (101), (102), (110), (103) and (200). Similar structure of hexagonal ZnO nano particles was investigated in earlier literature [7]. The high intensity and narrow line width indicate the good crystallinity [5] of ZnO NPS. The XRD pattern reveals that crystallites vary with reaction time of solution mixture. The crystallities of ZnO structure was found increased on increasing from reaction time of solution mixture used in the preparation. The crystallity is found increased for time 2h to 8h. The particle size calculated form Debye-Scherer relation (1) varies from 33nm to 42 nm.

$$D=\frac{0.94\lambda}{\beta Cos\theta} \qquad (1)$$

Where D is the crystalline size (nm), λ is a wavelength of incident X – ray (nm) β is the full width at half maximum and θ is the diffraction angle. The XRD study concluded that ZnO nanoparticles are increased in size for time of reaction mixture 2h to 8h.

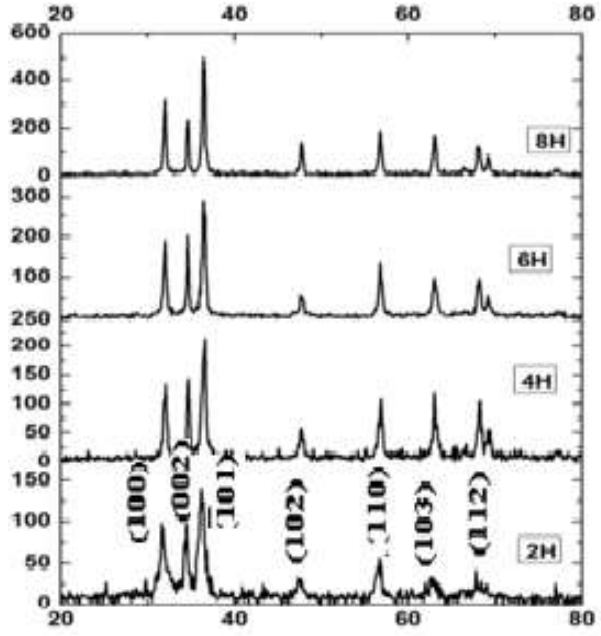

Fig. 1. XRD of ZnO Nanoparticles

ZnO sample with different reaction Time	ZnO crystalline size (D)nm
ZnO 2 H	33.32
ZnO 4H	35.57
ZnO 6H	38.40
ZnO 8H	42.63

FTIR Study:

Figure 2 shows the FTIR spectra of ZnO nanocrystals prepared at different time reaction of mixture. The FTIR is powerful tool for investigation of structure and functional groups. The FTIR spectra exhibit very low intense peak at 3482 cm^{-1} can be assigned to O-H stretching mode due to adsorption of atmospheric moisture. The peak at 1632 cm^{-1} is attributed to OH bending mode of water and at about 1410.14cm^{-1} the -COO mode arises from the absorption of atmospheric CO_2 on the surface of the nanoparticles [7]. A strong band at 666.30 cm^{-1} is assigned to the stretching mode of Zn-H. The main absorption band at 496cm^{-1} is due to Zn-O stretching vibrations. The O-H bending and –COO vibration bands decreasing in case of 2h to 8h ZnO NPs.

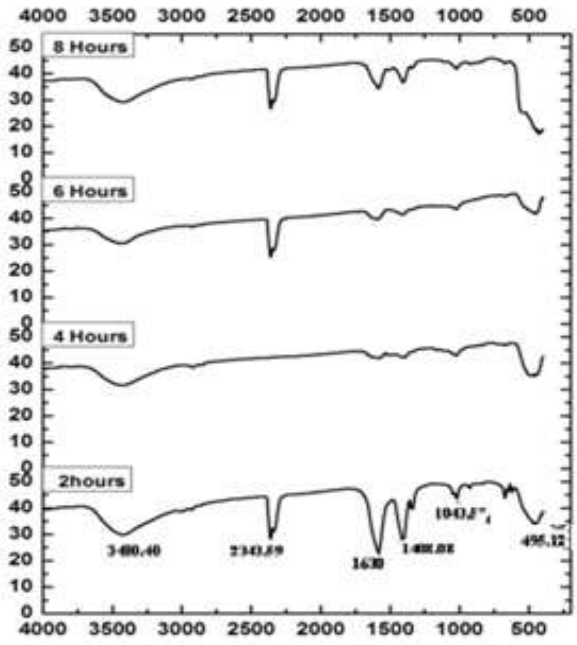

Fig. 2 FTIR Spectra of ZnO Nanoparticles

Frequency of Vibrational Band	Intensity	Vibrational Group
496.67	23.769	Zn-
1410.14	61.665	Zn-O
1632.25	51.237	ZnO-H
3482.83	47.281	OH

Surface Morphology:

The morphology of the nanostructures obtained for prepared ZNO NPS by using Scanning Electon Miscroscopy tool. The obtained SEM images are as shown in Figures 3. The SEM micrographs exhibit different morphology depending upon reaction time of solution mixture used in preparation of ZnO NPS. The ZnO nanoparticles prepared from reaction time 2h to 8h exhibit excellent nanorods. The different morphology of ZnO NPS leads to significant change in structural and optical properties.

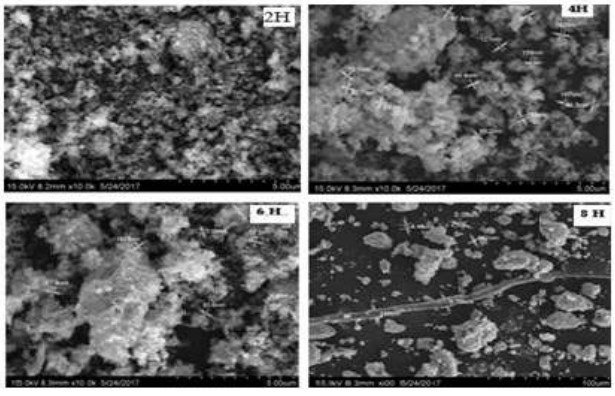

Fig. 3 SEM Images of of ZnO Samples

UV-Visible Absorption Study:

UV- visible absorption spectra of prepared ZnO nanoparticles is presented in figure 4. The optical absorption exhibits strong absorption peaks in UV region at 362 and 352 nm of the electromagnetic spectrum by the ZnO NPs prepared for reaction time 2h to 8h. The spectra show intense absorption at 192 to 216 nm wavelength. The samples 4H and 8H show higher blue shifting as compared to others. The band gap energies obtained from the spectra are tabulated in table 1 shows variation with reaction time. The ZnO particles Prepared form reaction mixture for reaction time 2h to 8h exhibit increasing trend of the band gap energy.

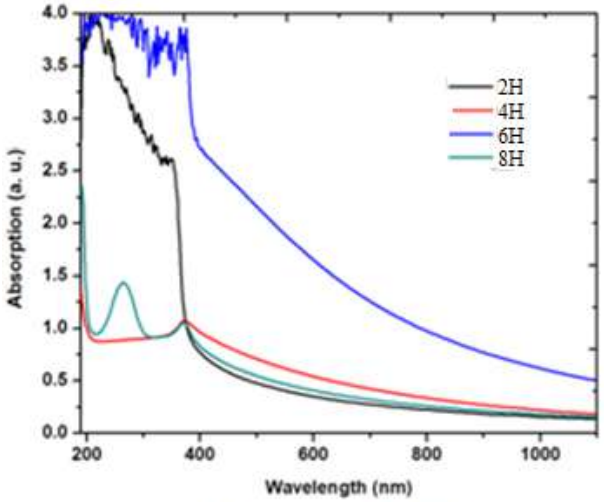

Fig. 4 UV- Visible Spectra of ZnO Particles

Table 3. Grain size and Band Gap

Reaction Time	Grain Size (nm)	Band Gap Eg (eV)
2 hours	33	3.31
4 hours	35	3.33
6 hours	38	3.36
8 hours	42	3.42

PL photo luminance:

In PL spectra of the 8 hours reaction time samples was shown in figure 5. The presence of the peak at 372nm is corresponding to the excitation emission or UV emission in ZnO Nanoparticles. The peak in the spectral range 472nm to 562nm corresponding to the visible emission of ZnO nanoparticles. The peak 420nm corresponds to the blue band and the peak at 460nm corresponds to weak blue-green band, the peak at 442nm to 566nm is due to various defects such as interstitial Zn and the presence of the acceptor and donor states in the region between the valance and conduction bands. The green band results due to the presence of slight oxygen vacancy defect in the ZnO nanoparticles.

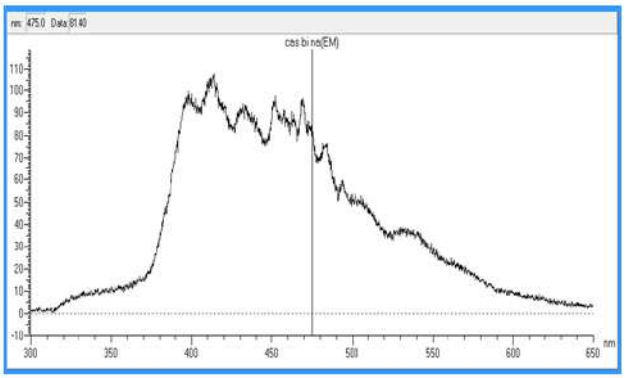

Fig. 5 PL spectra of Zno particles prepared for reaction time 8H

CONCLUSION

In this study, ZnO nanorods of significant morphology were successfully prepared by Sol-Gel chemical precipitation method. The XRD pattern confirms the excellent hexagonal crystallinity of ZnO nanorods prepared from reaction mixture of time variation 2hours to 8hours. XRD spectra confirms the ZnO samples constitute nano size particles. The FTIR spectra exhibits strong absorption band at 496 cm^{-1} attributed to Zn-O stretching mode for time variation reaction 2h to 8h. FTIR study concludes that samples prepared were of Zinc oxide material in spite of the surface absorption of H_2O and CO_2. The sharp optical absorption peak at 362 nm and 352 nm exhibited by ZnO (2h to 8h) nanoparticles in the UV region of electromagnetic spectrum with significant blue shifting. From the study of XRD, FTIR SEM and UV – Visible it is concluded that for presently employed Sol-gel preparation technique, good quality ZnO nanoparticles can be obtained from the reaction mixture at time variation reaction 2h to 8h.

Acknowledgement:

The authors are acknowledges to Director, Physics Research Centre, Shri Sant Gadge Maharaj College Loha. Maharashtra, India 431708 for providing research facilities.

Conflicts of interest: The authors stated that no conflicts of interest.

REFERENCES

1. Ho Jung Chang et. al., Journal of the Korean Physical Society, Vol. 45, No. 4, October 2004, pp. 959-962
2. Geon Joon Lee_ and YoungPak Lee et.al., Journal of the Korean Physical Society, Vol. 57, No. 6, December 2010, pp. 1624-1629
3. L. E. Greene, B. D. Yuhas, M. Law, D. Zitoun and P. Yang, "Inor-ganic Chemistry, 45(19), 7535-7543 (2006).
4. F. Li, W. Bi, L. Liu, Z. Li and X. Huang, Colloids and Surfaces A, 334 (1-3), 160-164 (2009).
5. T. Jin, D. Sun, J. Y. Su, H. Zhang and H. J. Sue, Journal of Food Science, 74 (1), M46-M52 (2009).
6. D. Zvekić, V. V. Srdić, M. A. Karaman and M. N. Mata-vulj, Processing and Ap-plication of Ceramics, 5(1), 41-45 (2011).
7. A. Ghosha, N.G., Deshpande,Y.G.,Gudagea, R.A. Joshi, A.A. Sagade , D.M. Phase , Ramphal Sharma, Journal of Alloys and Compounds , 469, 56-60, 2009.
8. M. L. Singla, M. Shafeeq and M. Kumar, Journal of Luminescence, 129 (12), 434-438 (2009).

.

IRJSE *Int. Res. J. of Science & Engineering,* 2018; Special Issue A2: 192-194 SJIF Impact Factor 4.11
ISSN: 2322-0015 UGC Approved Journal No. 63628
RESEARCH ARTICLE **OPEN ACCESS**

A Simple Hydrothermal Synthesis, and Characterization of SnO_2 micro sheets and micro flex like Structures

Bhise AB[1] and Bhise RB[2]

[1]Department of Physics, C.T. Bora College, Shirur, Dist. Pune (MS), Pin-412210, India,[2]Department of Physics, B. J. College, Ale (Junnar), Dist. Pune (MS), Pin-412411, India.
E-mail: ashok_bhise1959@yahoo.co.in

Manuscript Details

Available online on http://www.irjse.in
ISSN: 2322-0015

Editor: Dr. Arvind Chavhan

Cite this article as:
Bhise AB and Bhise RB. A Simple Hydrothermal Synthesis, and Characterization of SnO_2 micro sheets and micro flex like Structures, *Int. Res. Journal of Science & Engineering,* January 2018; Special Issue A2: 192-194.

ABSTRACT

Nanostructures of metal oxide have attracted a lot of attention because of their superior properties over their bulk counter parts. Tin oxide (SnO_2) in nanometric form is one of the most important semiconductor oxides because of its properties and potential applications. This is widely used for solar cells, gas sensors, and transparent electrodes. However, it should be noted that the size and morphology of the materials greatly affect their properties as well their further applications. Recently, solvothermal routes have been developed to fabricate SnO_2 nanostructures. The hydrothermal method is one of the most promising routes due to its low cost, environment friendly, mild conditions, and potential advantage for large scale production. Besides, hydrothermal treatments present a positive effect in enhancing thermal stability and gas response. Zinc oxide doped Tin oxide (Zn-doped SnO_2) microsheet and Tin oxide (SnO_2) microflex like two-dimensional crystalline structures have been synthesized via a simple solvothermal method. The microstructures showed orientation growth behavior and sheet & flex like morphology highly useful for gas sensing application.

Key words: SnO_2.microsheet, microflex, microstructures, morphology, hydrothermal.

INTRODUCTION

One–dimentional (1D) nanostructured metal oxides have attracted a lot of attention because of their superior properties over their bulk counter parts. SnO_2 in nanometric form is one of the most important semiconductor oxides because of its properties and potential applications. This is widely used for solar cells, gas sensors, and transparent electrodes. However, it should be noted that the size and morphology of the materials greatly affect their properties as well their further applications. Recently interest has been developed in tin oxide due its mechanical and chemical stability, environmental and good thermal properties. In the bulk form, SnO_2 has a tetragonal structure (a = b = 4.737A and c= 3.186 A) similar to the rutile with wide energy gap (Eg = 3.67 eV, at 300K), an insulator and becomes n-type semiconductor. SnO_2 plays an important role as transparent conducting oxide material with remarkable opto electrical properties. Up till nowSnO_2 with various nano and microstructures have been successfully prepared using various methods including thermal evaporation. Recently, solvothermal routes have been developed to fabricate SnO_2 nanostructures. The hydrothermal method is one of the most promising route s due to its low cost, environment friendly, mild conditions, and potential advantage for large scale production. Besides, hydrothermal treatments present a positive effect in enhancing thermal stability and gas response.

Here, we reported large scale growth of single crystalline SnO_2 nanoflowers using $SnCl_4{:}5H_2O$ as a precursor by a hydrothermal route. In the synthesis process, alcohol and water, which were friendly to the environments, were used as solvents.

METHODOLOGY

In a typical synthesis, the experimental procedure is described as follows: 0.45 gm $SnCl_4{:}5H_2O$ and 0.4 gm NaOH were dissolved completely into 40 ml basic mixture of ethanol and water (1/1V/V). Then 0.08 gm citric acid was dissolved into the mixture solution. A white precipitate formed was stirred using magnetic stirrer for few hours. Afterwards the as–obtained solution was transferred into a Teflon –lined stainless steel autoclave, sealed and maintained at 180^0C in an electric oven for 18 Hrs. After cooling to room temperature naturally, the product was collected by centrifugation, washed with distilled water and ethanol for several times, finally dried in an oven at 60^0C for 6 Hrs. To investigate the mechanism of crystal growth and morphology evolution of SnO_2 in the system, different hydrothermal reaction times and stirring times of precursor solution were tested.

Characterization:

The crystallinity and phase purity of the as synthesized products were characterized by X-ray diffraction (XRD) analysis using a Bruker Advance (JEOL JEM) diffractrometer (Cu Kα, λ =1.5418A) in the range of $10^0 \leq 2\theta \leq 80^0$. The XRD pattern figure- d showed the presence of the tetragonal structure. The morphologies of the as synthesized SnO_2 product were characterized using scanning electron microscopy (SEM) (JEOL). The SEM images **figure a, b, c** show sheet, flex and flower like morphology of the as-synthesized tin dioxide micro structures. The chemical composition was analyzed by energy dispersive X-ray analysis (EDAX), which is in the earlier reported composition ratio.

RESULTS AND DISCUSSION

The XRD spectrum of the prepared powder is shown in figure d in agreement with the standard for rutile bulk SnO_2.No other peaks were observed indicating pure crystallinity of the obtained SnO_2 powder. The sharp peaks suggest high crystallinity of the as synthesized SnO_2 sample. Figure a,b,c shows a typical SEM image of the as synthesized product.

The morphology of as synthesized SnO_2 product was characterized using scanning electron microscopy (SEM). The SEM image show sheet and flex like morphology of the as-synthesized tin dioxide microstructures. The structure of SnO_2 microstructures were characterized by X-ray diffraction (XRD), The XRD pattern showed the presence of the tetragonal structure. The chemical composition was analyzed by energy dispersive X-ray analysis (EDAX), which is in the earlier reported composition ratio. We report on the large-scale hydrothermal synthesis of SnO_2 microstructures.

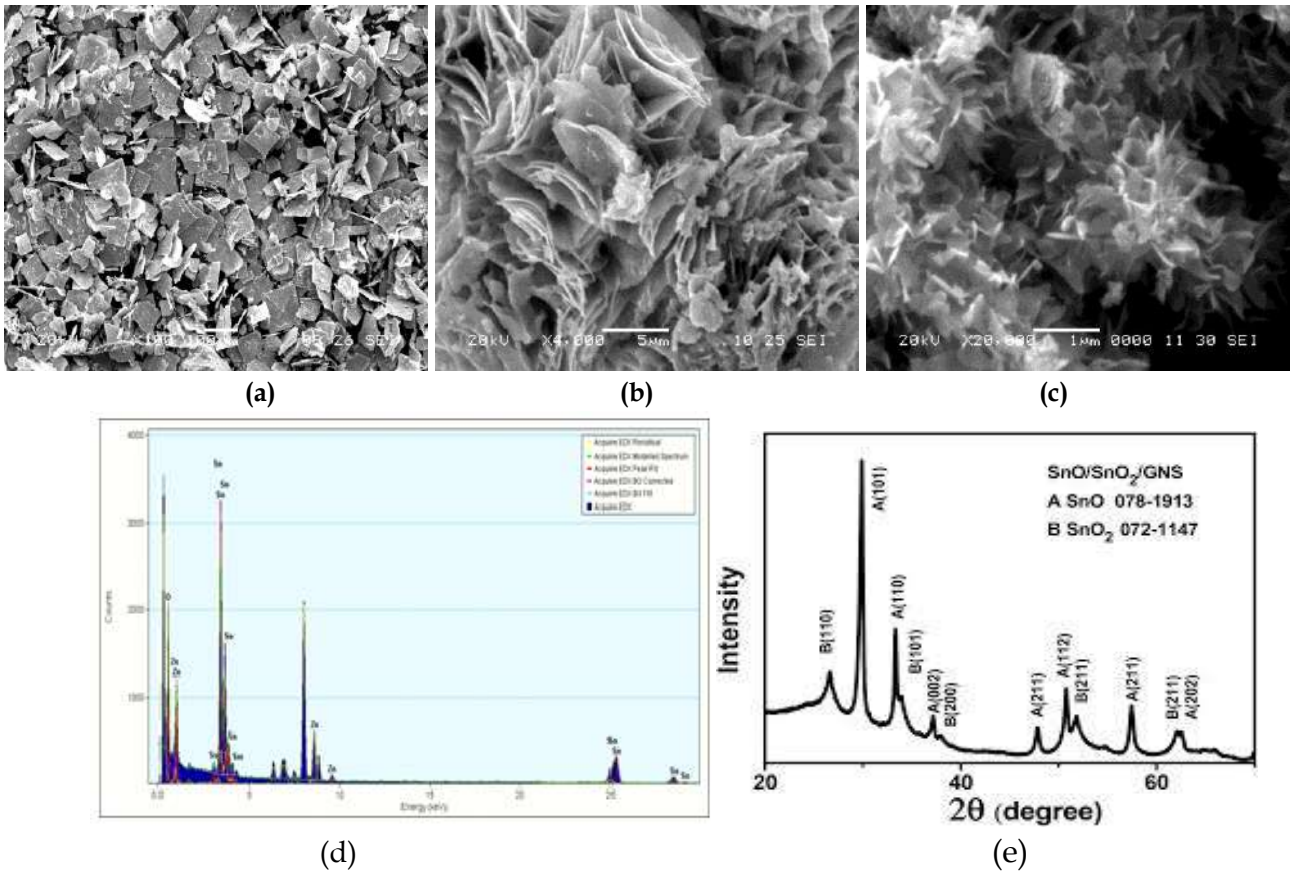

Fig.-1. SEM images of as grown product. **[a]** Micro sheets **[b]** Micro flex **[c]** Nano flower[d] EDS spectrum [e] XRD pattern

CONCLUSION

In summary, large scale SnO_2 nanostructures were successfully synthesized via a simple hydrothermal method. The as- synthesized products consists of micro sheet and flex like structures and nano flower like structures of uniform size. The as synthesized products have potential application in gas sensor, field emission display devices.

Conflicts of interest: The authors stated that no conflicts of interest.

REFERENCES

1. Pan ZW, Dai ZR, Wang ZL,*Science*,2001; 291, 1947.
2. Chen X, R. Fan, *Chem. Mater.* 13802 (2001).
3. Ying Z, Wan Q, Song ZT, Feng SL. *Nanotechnology*,1682 (2004).
4. Akoi A, Sasakura H, *Japan J.Appl.Phys*.582 (1970).
5. Paraguay Delgado F.et al Nanotechnology 688 (2005).
6. ChengB, J.M.Russell, W.Shi, L.Zhang and E.T.Samulski J. Am. Chem. Soc. 126 5972 (2004).
7. Lee EJH, Ribeiro C, Giraldi TR, Logo E, Leite ER and Varela JA, *Appl.Phys.Lett*. 2004; 84,1745.
8. Du F, Z Guo and G Li, *Mater. Lett*. 2005; 59 2563
9. Fujihara S, Maeda T, Ohgi H, Hosono E, Imai H and Kim S, Langmuir 20 6476(2004).

IRJSE *Int. Res. J. of Science & Engineering,* 2018; Special Issue A2 :195-201 SJIF Impact Factor 4.11
ISSN: 2322-0015 UGC Approved Journal No. 63628
RESEARCH ARTICLE **OPEN ACCESS**

Solar Photocatalytic Degradation of Rhodamine B using Co-Doped TiO_2 Nanoparticles

Bhosale RR[1], Pujari SR[1], Muley GG[2], Kande SR[3], Ghoshir UG[3], Kalokhe SB[3], Gambhire AB [3*]

[1]D.B.F. Dayanad College of Arts and Science, Solapur, 413002, Maharashtra, India,
[2]Dept of Physics, SGB Amravati Univeristy, Amravati, 444602, Maharashtra, India,
[3]Dept of Chemistry, Shri Anand College, Pathardi, Ahmednagar, 414102, MS, India
E–mail: abg_chem@ymail.com

Manuscript Details
Available online on http://www.irjse.in
ISSN: 2322-0015

Editor: Dr. Arvind Chavhan

Cite this article as:
Bhosale RR, Pujari SR, Muley GG, Kande SR, Ghoshir UG, Kalokhe SB, Gambhire AB. Solar Photocatalytic Degradation of Rhodamine B using Co-Doped TiO_2 Nanoparticles, , *Int. Res. Journal of Science & Engineering,* January 2018, Special Issue A2 : 195-201.

ABSTRACT

A series of co-doped TiO_2 nanocomposites were synthesized by doping Fe(III), Zn(II), Zr(IV) Sb(III), Ce(IV) with C and N, separately by sol-gel method, combined with surfactant incorporation method. The as prepared sample were characterized by X-ray diffraction (XRD), Transmission electron microscopy (TEM), X-ray photoelectron spectroscopy (XPS), Brunauer-Teller method (BET), UV–Vis diffuses reflectance spectroscopy (DRS) and Photoluminescence spectroscopy (PL). The results shows that phase composition, crystallite size, BET surface area and optical absorption of co-doped TiO_2 nanocomposites varied significantly with the nature dopants. The photocatalytic activities of these co-doped TiO_2 nanocomposites were investigated by degradation Rhodamine B (RhB) in aqueous solution under solar-light illumination. The results showed an appreciable enhancement in the photoactivity of the Fe, C co-doped TiO_2 (Fe-C/TiO_2) as compared to other co-doped TiO_2 because of smaller particle size, higher surface area and the synergistic effect created by higher solar-light absorption and the improved charge separation. The degradation rate of Rhodamine B (RhB) reached 99% in 30 min which is about 10 times higher than that of pure TiO_2 photocatalyst.

Keywords: Co-dopant, Sol-gel process, Nanomaterials, Photocatalytic activity.

INTRODUCTION

Heterogeneous photocatalysis has received a great deal of attention as an advanced oxidation process for the treatment of air and water streams [1-3]. Among the various semiconductors studied, TiO_2 is the most promising and extensively studied photocatalyst because of the biological and chemical inertness, high stability and strong oxidizing power [4, 5]. However, high photocatalytic activities of photocatalyst are primarily determined by its physicochemical properties such as crystallite structure, particles size, specific surface area and the use of renewable solar energy. Doping of TiO_2 with transition metals and non-metals was reported in the literature [6]. It came to light that C-doped TiO_2 showed an appreciable enhancement in the photocatalytic activity under solar-light illumination. In addition, composites, such as co-doped TiO_2 with *3d* transition metals (such as Mo, W and Os) and nonmetals (such as C, N, F) can reduce recombination of separated electron-hole pairs and enhance the photocatalytic activity [7, 8] as a result of a synergistic effect among co-dopants [9]. Gai et al., showed that co-doping of TiO_2 with Mo and C significantly enhance water splitting capability of composite material [10]. Further, Cu-N [11], N-F [12], Mo-N [13], W-N [14] and Fe-N, Ni-N, Ag-N, Pt-N) co-doped TiO_2 [15], were also investigated to improve the photocatalytic activity. The doping of two kinds of atoms into TiO_2 has gained much attention because it resulted in higher photocatalytic activity than single element doping. This effect could be due to the synergistic effect of the doped two kinds of atoms [16]. This synergistic effect of the combination of transition metals with carbon and nitrogen on TiO_2 has previously reported for the degradation of some organic molecules in the photocatalytic process [9, 11]. The enhanced photocatalytic activity obtained with co-doping of TiO_2 with metals and non-metals might be due to common contact interface between the different solid phases in TiO_2 and synergistic effect created by the higher visible light absorption and the improved charge separation capability.

Although, there are many merits for co-doped TiO_2 with metals and non-metals, few studies have been reporting the comparative study on photocatalytic degradation of organic compound using a series of transition metals and non-metals co-doped TiO_2. In the present study, a series of co-doped TiO_2 nanocomposites were synthesized by doping transition metals with carbon and nitrogen, separately towards photocatalytic decomposition of RhB. Furthermore, most of the research work has been carried out by irradiating catalyst suspension with artificial visible light [13-16], which is not feasible and economical. The present study focuses on the efficient use of sunlight and the ability of prepared photocatalyst to decompose RhB under solar light illumination using a series of co-doped TiO_2 nanocomposites synthesized by sol-gel method.

METHODOLOGY

2.1 Synthesis of co-doped TiO_2:

The dopants starting materials; metal nitrates of Fe(III), Zn(II), Zr(IV), Sb(III), Ce(IV)-loaded (3 wt.%) TiO_2 nanomaterials were synthesized by sol-gel process. Titanium butoxide (98%, Aldrich) was used as the precursor of TiO_2. An amount, 25 ml of titanium butoxide was hydrolyzed in 300 ml water containing 1.5 ml nitric acid. The cationic surfactant cetyltrimethylamonium bromide (CTAB), 20% (10 ml) in ethanol was dropped into the above solution. Gel formed was stirred continuously at room temperature to form a highly dispersed sol. To this, Fe, Zn, Zr, Sb, and Ce (3 wt.%) solutions were added, separately to synthesize metal ion containing TiO_2 sol. Then, a certain amounts of ethylene glycol and citric acid (source of carbon) in 50 ml of deionized water were added drop wise into this sol under vigorous stirring. The resulted alkoxide solution was left hydrolyzing to the TiO_2 sol. After keeping the sol for aging (5 days), it was concentrated and dried at 80°C. The samples, after overnight drying at 110°C, were calcined for 2 h at 500°C. Meanwhile, in the second set of samples, a certain amount of ammonia (source of nitrogen) in 50 ml deionized water were added drop-wise to the solution of above mentioned metal nitrate-TiO_2 sol, separately in order to synthesize metal-nitrogen co-doped TiO_2. The remaining process is similar as per the above used to synthesize metal-carbon co-doped TiO_2.

2.2 Characterization:

X-ray powder diffraction (XRD) patterns have been recorded on a model D8 Bruker AXS with monochromatic Cu radiation (40 kV and 30 mA), over the 2θ collection range of 20-80°. The particle size of anatase was calculated from XRD measurement. BET surface area measurements were carried out using a Quantachrome NOVA 1200 instrument. The microscopic nanostructures were observed by transmission electron microscopy (TEM; FEI, Tecnai F30, HRTEM, FEG operated at 300 kV). FT-IR spectra were recorded on a Shimadzu-8400 spectrometer in the range of 4000-500 cm^{-1}. X-ray photoelectron spectroscopy (XPS; ESCA-3000, VG Microtech, Uckfield, UK) was used to study the chemical composition of the samples. Non-chromatic X-ray beams of Al Kα (hν = 1486.6 eV) and Mg Kα (hν = 1253.6 eV) radiation were used as the excitation source. A hemispherical sector analyzer and multichannel detectors were used to detect the ejected photoelectrons as a function of their kinetic energies. XPS spectra were recorded at a pass-energy of 50 eV, 5-mm slit width and a take-off angle of 55°. The spectrometer was calibrated by determining the binding energy values of the $Au4f_{7/4}$ (84.0 eV), $Ag3d_{5/2}$ (368.4 eV) and $Cu2P_{3/2}$ (932.6 eV) levels using spectroscopically pure materials. The instrumental resolution under these conditions was 1.6 eV full-width at half-maximum (FWHM) for $Au4f_{7/4}$ level. The Cls (285 eV) and Au $4f_{7/4}$ (84.0 eV) were used as internal standards when needed. Photoluminescence (PL) spectra measured at room temperature on a fluorescence spectrophotometer (F-7000, Hitachi, Japan) with an excitation wavelength of 315 nm, scan rate of 1200 nm/min and PMT voltage of 700 V. The excitation and emission slits both had a width of 5.0 nm. . FT-IR spectra were recorded on a Shimadzu-8400 spectrometer in the range of 4000-500 cm^{-1}. UV-Vis diffuse reflectance spectra (UV–Vis–DRS) were recorded in an air at room temperature in the wavelength range of 200–800 nm using a PE LAMBDA35 spectrophotometer.

2.3 Photocatalytic activity:

All the solar photocatalytic experiments were carried out at the same conditions on March 2017 from 12.00 p.m. to 1.00 p.m. Solar light was used as the irradiation source, and the average insolation of the solar irradiation was 25.28 W/m^2 measured by an UV irradiance meter at range of 375-475 nm. Photocatalytic experiments were carried out by adding 10 mg of photocatalyst to 50 ml of aqueous RhB (50 ppm) solution. Prior to irradiation, the suspensions were magnetically stirred in the dark for 30 min to ensure establishment of an adsorption-desorption equilibrium among the photocatalyst, RhB and atmospheric oxygen. At a given irradiation time interval, 10 ml of the suspension was collected, and then filtered through a Millipore filter to separate the photocatalyst. The changes in RhB concentration were analyzed by a UV-Visible spectrophotometer and the absorption peak at 650 nm was recorded.

RESULTS AND DISCUSSION

3.1. XRD analysis:

To understand phase symmetry in the calcined samples, a systematic X-ray diffraction study was undertaken. Fig. 1 (a-k) shows the XRD patterns of the pure TiO_2, and co-doped TiO_2 with transition metal, N and S, separately.

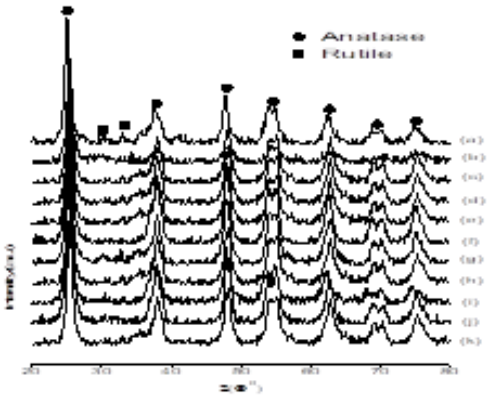

Fig. 1(a-k). XRD profiles of (a) Pure TiO_2, (b) Fe-C/TiO_2, (c) Fe-N/TiO_2, (d) Zn-C/TiO_2, (e) Zn-N/TiO_2, (f) Zr-C/TiO_2, (g) Zr-N/TiO_2, (h) Sb-C/TiO_2, (i) Sb-N/TiO_2, (j) Ce-C/TiO_2, (k) Ce-N/TiO_2.

Pure TiO_2 shows two main peaks at 2θ=25.4 and 27.5, corresponding to (101) phase of anatase and (110) phase of rutile, respectively. In the case of co-doped TiO_2, the rutile phase is < 1%, which means co-doping retards the transformation from anatase to rutile phase. Co-doping of the TiO_2 stabilizes a well-crystallized pure anatase upon calcination at 500°C, in

contrast with the simultaneous growth of the rutile phase observed for the pure TiO_2. Further, all peaks measured by XRD analysis could be assigned to those of TiO_2 crystal. No peaks corresponding to the metal and non-metal oxide is detected. The peaks of TiO_2 have been slightly shifted due to solid solution of metal and non-metal ion with TiO_2. The average particle sizes of the samples were calculated using Debye-Scherrer formula based on the XRD peak broadening analysis at 101 peaks, listed in Table 1. The particle size calculated from XRD data is as large as 15-20 nm for the Zr-C/TiO_2, Zr-N/TiO_2, Sb-C/TiO_2, Sb-N/TiO_2, Ce-C/TiO_2, Ce-N/TiO_2 and as small as 7-10 nm for the Fe-C/TiO_2, Fe-N/TiO_2, Zn-C/TiO_2, Zn-N/TiO_2. This apparent fall in the particle size (higher specific surface area) will ensure higher photocatalytic activity for the Fe-C/TiO_2, Fe-N/TiO_2, Zn-C/TiO_2, and Zn-N/TiO_2, when it is used for photocatalytic applications.

3.2. TEM analysis:

In order to confirm the effect co-doping on particle size of TiO_2 and hence higher specific surface area, the particle size of Fe-C/TiO_2, Fe-N/TiO_2, Zn-C/TiO_2, and Zn-N/TiO_2 samples were observed using TEM. Fig. 2(a-d) shows TEM images of (a) Fe-C/TiO_2, (b) Fe-N/TiO_2, (c) Zn-C/TiO_2, and (d) Zn-N/TiO_2 samples and its corresponding Fourier transfer patterns (FTT) are also presented in the inset of figures. It can be seen that the particle size of Fe-C/TiO_2, and other co-doped samples (Fe-N/TiO_2, Zn-C/TiO_2, Zn-N/TiO_2) are about 7 and 10 nm, respectively.

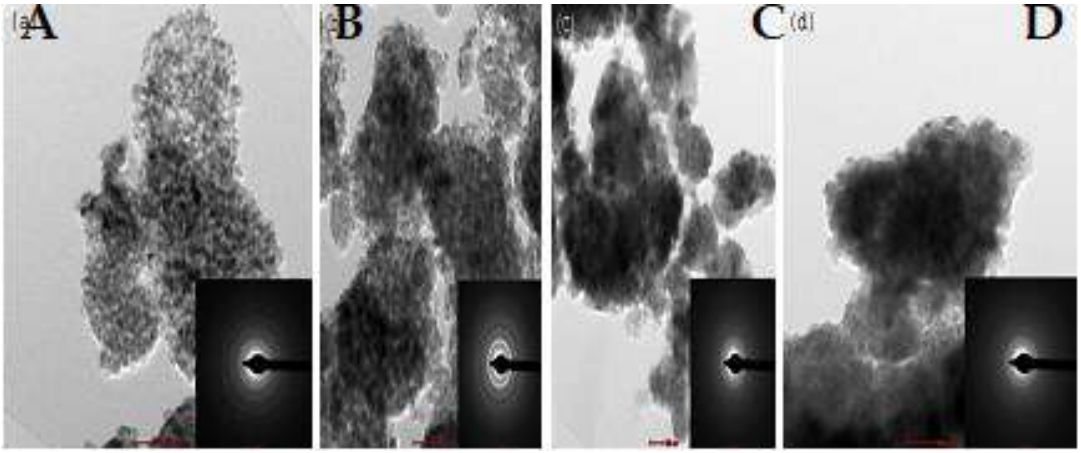

Fig. 2(a-d). Typical TEM images of (a) Fe-C/TiO_2, (b) Fe-N/TiO_2, (c) Zn-C/TiO_2, and (d) Zn-N/TiO_2; and the inset of Fig. 2(a-d) are its corresponding FFT.

Table 1: Characteristics of co-doped TiO_2 composites after heat treatment for 2 h at 500°C.

Samples	Average crystalline size (nm)		BET [m^2/g]	Energy of the band gap (eV)
Pure TiO_2	22.50	30	3.2	30.40
Fe-C/TiO_2	7.00	146	2.25	99.00
Fe-N/TiO_2	10.37	133	2.63	90.00
Zn-C/TiO_2	10.00	140	2.75	86.56
Zn-N/TiO_2	10.65	104	2.77	84.00
Zr-C/TiO_2	16.32	82	2.72	57.80
Zr-N/TiO_2	18.00	65	2.82	53.48
Sb-C/TiO_2	20.22	60	2.30	64.00
Sb-N/TiO_2	19.00	65	2.30	62.20
Ce-C/TiO_2	15.21	100	2.90	65.00
Ce-N/TiO_2	15.01	103	2.77	65.00

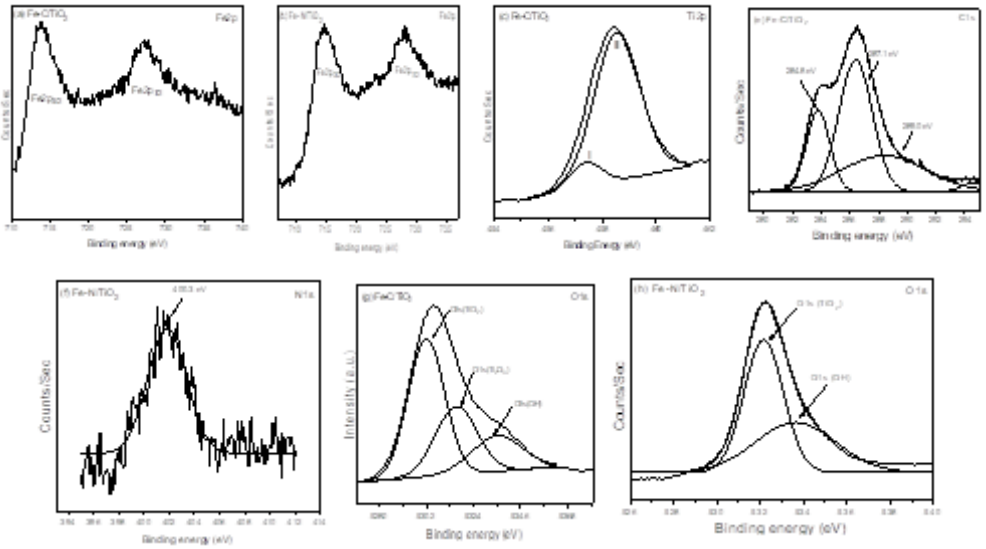

Fig. 3(a-h). High resolution XPS spectra of the Fe2p, Ti2p, C1s, N1s, O1s taken on Fe-C/TiO_2 and Fe-N/TiO_2.

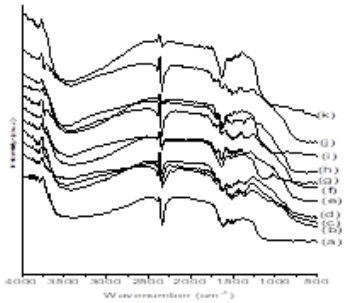

Fig. 4(a-k). F-IR spectra of (a) pure TiO_2 , (b) Fe-C/TiO_2, (c) Fe-N/TiO_2, (d) Zn-C/TiO_2, (e) Zn-N/TiO_2, (f) Zr-C/TiO_2, (g) Zr-N/TiO_2, (h) Sb-C/TiO_2, (i) Sb-N/TiO_2, (j) Ce-C/TiO_2, (k) Ce-N/TiO_2.

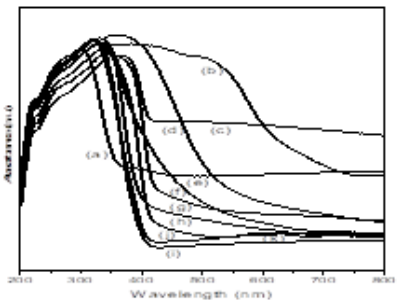

Fig. 5(a-k). UV-Vis-DR spectra of (a) (a) pure TiO_2 , (b) Fe-C/TiO_2, (c) Fe-N/TiO_2, (d) Zn-C/TiO_2, (e) Zn-N/TiO_2, (f) Zr-C/TiO_2, (g) Zr-N/TiO_2, (h) Sb-C/TiO_2, (i) Sb-N/TiO_2, (j) Ce-C/TiO_2, (k) Ce-N/TiO_2.

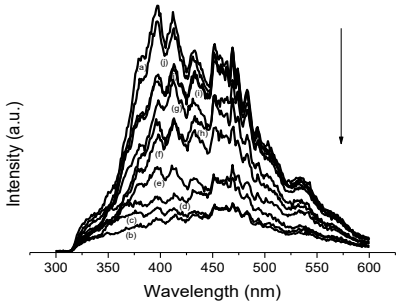

Fig. 6(a-k). PL spectra of (a) (a) pure TiO_2 , (b) Fe-C/TiO_2, (c) Fe-N/TiO_2, (d) Zn-C/TiO_2, (e) Zn-N/TiO_2, (f) Zr-C/TiO_2, (g) Zr-N/TiO_2, (h) Sb-C/TiO_2, (i) Sb-N/TiO_2, (j) Ce-C/TiO_2, (k) Ce-N/TiO_2.

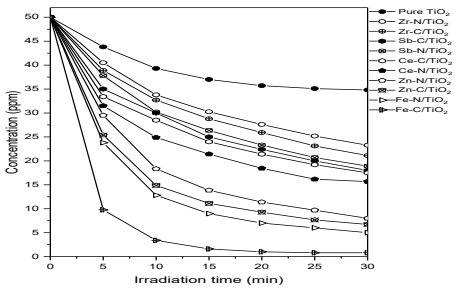

Fig. 7(a-k). Rate of decomposition of RhB by using (a) (a) pure TiO_2 , (b) Fe-C/TiO_2, (c) Fe-N/TiO_2, (d) Zn-C/TiO_2, (e) Zn-N/TiO_2, (f) Zr-C/TiO_2, (g) Zr-N/TiO_2, (h) Sb-C/TiO_2, (i) Sb-N/TiO_2, (j) Ce-C/TiO_2, (k) Ce-N/TiO_2.

3.3. BET surface area:

All co-doped samples exhibit relatively high specific surface areas with respect to pure TiO_2 (Table 1). Co-doping reduces the extent of surface area loss during high temperature calcinations. This is based on higher resistance to sintering as well as the delayed transformation from amorphous to crystalline state acquired by co-doping with metal and non-metal. The metal oxide species, along with the non-metal ions, prevent the agglomeration of TiO_2 particles, resulting in a higher specific surface area. The surface area of Fe-C/TiO_2, Fe-N/TiO_2, Zn-C/TiO_2, and Zn-N/TiO_2 samples are 146, 133, 140, and 121 m^2g^{-1}, respectively.

3.4. XPS studies:

The spectra of Fe2p, Ti2p, C1s, N1s and O1s level were recorded under the same conditions of vacuum and pass energy. Fig. 3(a-b) shows high resolution XPS spectra of Fe2p region of Fe-C/TiO_2 and Fe-N/TiO_2, respectively. The Fe2p spectra of both samples shows peak positions at binding energies of 710.8 eV which correspond to elements in the oxidation states Fe^{3+}. The $Ti2p_{3/2}$ level of Fe-C/TiO_2 (Fig.3(c)) shows asymmetry towards the lower binding energy side. The peaks resolved into two components, with binding energy values of 457.5 and 458.6 eV for the first and second components, respectively. These binding energies are well matching with the binding energy value of Ti_2O_3 and TiO_2 [17].

On the contrary Fe-N/TiO_2 sample (Fig. 3(d)) shows two peaks centered at 458.4 eV and 464.1 eV assigned to $Ti2p_{3/2}$ and $Ti2p_{1/2}$ states of Ti^{4+}. The formation of Ti_2O_3 (Ti^{3+}) in Fe-C/TiO_2 sample might be due to the reduction carbon in the layer at 500°C draws oxygen from the surrounding atmosphere, which causes a reduction of some Ti(IV) to Ti(III) species. The C1s spectra of Fe-C/TiO_2 sample (Fig. 3(e)) shows C-C and C-H at 284.8 eV, residual oxygenated moieties at 287.1 eV and C-O bonds at 289.0 eV. The N1s XPS spectra of Fe-N/TiO_2 sample (Fig. 3(f)) shows peak at around 400.3 eV indicating the presence of N-containing species [13]. The O1s level of Fe-C/TiO_2 (Fig. 3(g)) shows broadening and asymmetry towards the higher binding energy side. These peaks are also resolved into three components with binding energies values of 530.5, 531.7, 533.4 eV for the first, second and third peak, respectively. The binding energy of the first, second and third peak is well matching with the binding energy of TiO_2 and Ti_2O_3 lattice oxygen, respectively, while the third peak is either adsorbed oxygen or hydroxyl species on the surface. The O1s spectra of Fe-N/TiO_2 (Fig. 3 (h)) shows two peaks centered at 530.4 eV and 533.5 eV, assigned to TiO_2 lattice oxygen, while the second peak is either adsorbed oxygen or hydroxyl species on the surface.

3.5. FT-IR analysis:

Fig. 4(a-k) shows FT-IR spectra of samples in the range of 4000 to 500 cm^{-1}. Within this it shows up the band corresponding to surface hydroxyl groups. Two clear bands can be seen Fig. 4(a-k), one around 3400 cm^{-1} and a second one located around 3185 cm^{-1}. These bands can be attributed to the different OH groups at the surface, in which one is ascribed to adsorbed water and the other is surface hydroxyl group of TiO_2 [18]. The bands in the low-wave number region (400-600 cm^{-1}) can be assigned to Ti-O bond vibrations [19]. The FT-IR spectra of the modified samples do not show any band corresponding to the transition metal oxide, which confirms the XRD results.

3.6. UV-vis DR spectral analysis:

UV-vis diffuse reflectance spectroscopy Fig. 5(a-k) permits the detection of frame work of Ti in the samples. In all the samples, characteristic band for tetrahedrally coordinated titanium appears at about 350 nm. A progressive red-shift in the band gap absorption is noticed with co-doping than that pure TiO_2. The edges of the absorption of the metal incorporated samples were shifted to approximately 500 nm, corresponding to band gap energy of 2.25 eV. The absorption is associated to the $O^{2-} \rightarrow Ti^{4+}$ charge-transfer, corresponding to electronic excitation from the valence band to the conduction band. The absorption onsets were determined by linear extrapolation from the inflection point of the curve to the baseline.

3.7. Photoluminescence study:

In PL process, an electron is excited from valence to conduction band by monochromatic light having photon energy equal to greater than band gap. The radiative recombination of an excited electron either takes place at the edge of valence band or through traps within the band gap. The lower PL intensity may indicate the lower radiative recombination rate of electrons and holes. As shown in Fig. 6(a-k) their PL intensities decreases in the order of TiO_2>Ce-C/TiO_2>Sb-N/TiO_2>Zr-N/TiO_2>Sb-C/TiO_2>Zr-C/ Ti O_2>Zn-N/TiO_2>Zn-C/TiO_2>Fe-N/TiO_2>Fe-C/TiO_2. C and N-doping suppresses the photogenerated charge separation, which should be due to the mid-gap states introduced by C and N-doping as recombination centers [20]. Conventionally, the higher the recombination rate is, the stronger the PL peak intensity is [21].

3.8. Photocatalytic activity:

The photocatalytic activities of pure TiO_2 and co-doped TiO_2 are shown in Fig. 7(a-k). In the presence of pure TiO_2 decomposition of RhB was not observed. However, in the presence of co-doped TiO_2, the decomposition of RhB obviously increased. Among the different co-doped samples, Fe-C/TiO_2 exhibited the highest photocatalytic activity under solar light irradiation, only 1% of RhB remained, and in the case of Fe-N/TiO_2, Zn-C/TiO_2, Zn-N/TiO_2 10-15% of RhB remained after exposure to solar light for 30 min. While as high as 40-50% remained in the case of Zr-C/TiO_2, Zr-N/TiO_2, Sb-C/TiO_2, Sb-N/TiO_2, Ce-C/TiO_2, and Ce-N/TiO_2. These results are in good agreement with previously reported work, excluding the time needed for the decomposition of organic dye was double using C-TiO_2 [6], in comparison with the present work. From the observed results it was found that the Fe-C/TiO_2 is found to be composite photocatalyst, once optical excitation occurs, the photogenerated electrons can transferred to the lower-lying conduction bands of Fe-C, while the holes will accumulate in the valence band of TiO_2, and effectively scavenged by the photo-oxidation of RhB, whereas the photogenerated electrons can be transferred into the surface of Fe-C, rather than undergoing bulk recombination. The PL spectra of Fe-C/TiO_2 show weaker peak intensity indicates enhancement in the efficiency of photo-excited charges separation. The enhancement may be explained in terms of the synergistic effect on the specific adsorption property and efficient photo-excited charges separation at the Fe-C/TiO_2 nanocomposite photocatalyst. Further, the high surface area of Fe-C/TiO_2 effectively concentrates RhB around it and produces high concentrations of organic compounds for the TiO_2 photocatalyst. Furthermore, the carbon in Fe-C/TiO_2 reduces TiO_2 to form T^{3+} ions. Ti^{3+} can trap photogenerated electron in the conduction band and prevent the recombination of photo-excited charges under solar-light irradiation. Thus, increase in Ti^{3+} content enhances photocatalytic activity [22], which is evident from XPS spectra showing the formation of Ti^{3+} species. Moreover, co-doped samples shows red-shift in the absorption range compared with pure TiO_2. The existence of oxygen deficiencies, leads to localized electronic states between the valence and conduction band, shows certain absorption in the visible range.

CONCLUSION

Co-doped TiO_2 nanoparticles were successfully prepared by sol-gel method. The prepared samples were characterized by XRD, TEM, FT-IR, XPS, PL and UV-Vis-DRS techniques. It was found that the prepared photocatalyst exhibited smaller shape particles and higher specific surface area. In addition to oxides of Ti^{4+}, there was a certain amount of Ti^{3+} oxides existed in Fe-C/TiO_2 photocatalyst. The Fe-C/TiO_2 photocatalyst shows superior photocatalytic activity than other co-doped samples. The highest photocatalytic activity of the composite catalyst could be attributed to the synergistic effects of enhanced solar-light absorption, efficient charge separation.

Acknowledgement: This work was financed by Science & Engineering Research Board (SERB), New Delhi, India, Grant No. SB/EMEQ-029/2014.

Conflicts of interest: The authors stated that no conflicts of interest.

REFERENCES

1. Molinari A, Sarti E, Marchetti N, Pasti L, *Appl. Catal. B: Environ*. 2017; 203, 9-17.
2. Garza-Campos BR, Guzmán-Mar JL, Reyes LH, Brillas E, Hernández-Ramírez A, Ruiz-Ruiz EJ, *Chemosphere*, 2014; 97, 26-33.
3. Parent Y, Blake D, Magrini-Bair K, Lyons C, Turchi C, Watt A, Wolfrum E, Prairie M, *Solar Energy*, 1996; 56, 429-437.
4. Gambhire AB, Lande MK, Arbad BR, Rathod SB, Gholap RS, Patil KR, *Mater. Chem. Phys*.,2011; 125: 807-812.
5. Momeni M, Saghafian H, Golestani-Fard F, Barati N, Khanahmadi A. *Appl. Surf. Science*, 2017; 392 : 80-87.
6. Bhosale RR, Pujari SR, Muley GG, Patil SH, Patil KR, Shaikh MF, Gambhire AB. *Solar Energy*; 2014; 103: 473-479.
7. Gai YQ, Li JB, Li SS, Xia JB, Wei SH. *Phys. Rev. Lett.,* 102 (2009) 036402.

IRJSE *Int. Res. J. of Science & Engineering,* 2018; Special Issue A2 :202-206 SJIF Impact Factor 4.11
ISSN: 2322-0015 UGC Approved Journal No. 63628
RESEARCH ARTICLE **OPEN ACCESS**

Silver nanoparticles as a new generation of antimicrobials –a review

Suryawanshi AD[1], SanapVB[2] Padampalle AS[3], Suryawanshi DD[4]

[1]Dept of Physics, B.J. College, Ale (Pune), [2]Dept. of Physics, Y.C. College, Sillod (Aurangabad),[3]Dept. of Physics, S.C.S. College, Omerga (Osmanabad),[4]Dept. of Chemistry, B.A.M. University, Aurangabad
Email: ajitdsuryawanshi@rediffmail.com

Manuscript Details

Available online on http://www.irjse.in
ISSN: 2322-0015

Editor: Dr. Arvind Chavhan

Cite this article as:
Suryawanshi AD, SanapVB Padampalle AS, Suryawanshi DD. Silver nanoparticles as a new generation of antimicrobials –a review, *Int. Res. Journal of Science & Engineering,* January 2018 ; Special Issue A2: 202-206.

ABSTRACT

The major challenge the world is facing today is the mode of treatment of pathogenic bacteria which have become resistant to the existing antibiotics. Day by day, the resistance to existing antibiotics or drugs is increasing for one or other reasons. This increasing incidence of antibiotic resistance among the microbial organisms necessitates an alternate therapy to curb the resistant infections microorganisms. A new approach to prevent or combact microbial pathogens is by the use of silver nanoparticles especially synthesized with the help of natural medicinal plants. The synthesized silver nanoparticles are generally characterized by UV-vis spectroscopy, scanning electron microscopy (SEM), Transmission electron microscopy (TEM), Fourier transform infrared spectroscopy (FTIR), Zeta potential, X-ray diffraction (XRD), etc.

Keywords: Silver nanoparticles, medicinal plants, nanotechnology, structural characterization

INTRODUCTION

Nanotechnology is now creating a growing sense of excitement in the life sciences especially biomedical devices and Biotechnology [1]. Nanoparticles exhibit completely new or improved properties based on specific characteristics such as size, distribution and morphology. The silver nanoparticles have various and important applications. Historically, silver has been known to have a

disinfecting effect and has been found in applications ranging from traditional medicines to culinary items. It has been reported that silver nanoparticles (SNPs) are non-toxic to humans and most effective against bacteria, virus and other eukaryotic micro-organism at low concentrations and without any side effects [2]. Moreover, several salts of silver and their derivatives are commercially manufactured as antimicrobial agents3. In small concentrations, silver is safe for human cells, but lethal for microorganisms [4]. Antimicrobial capability of SNPs allows them to be suitably employed in numerous household products such as textiles, food storage containers, home appliances and in medical devices [5]. The most important application of silver and SNPs is in medical industry such as tropical ointments to prevent infection against burn and open wounds [6]. Biological synthesis of nanoparticles by plant extracts is at present under exploitation as some researchers worked on it [7,8] and testing for antimicrobial activities [9, 10, 11]. For the last two decades extensive work has been done to develop new drugs from natural products because of the resistance of micro-organisms to the existing drugs. Nature has been an important source of a products currently being used in medical practice [12]. The present study is a review of silver nanoparticles (medicinal plant mediated) a new generation of antimibrocials to combact microbial pathogens.

Medicinal plants: an alternative source as antimicrobics:

A new hope of treating such multidrug resistant infections came from medicinal plants since nature is the only source to provide a variety of chemical compounds that can be used for new drug discovery. A number of secondary metabolites like phenols, flavonoids, glycosides, alkaloids, saponins, triterpenes, etc. produced by plants are pharmacologically active. The added advantages of using natural products therapeutically is they are safe, economical, and with lesser side effects. The plant extract can be used singly or in combination with antibiotics or other plant extracts or some chemicals i.e. combination therapy. This was the next approach to combact the multidrug resistant bacteria. However, the development of drug resistant strains is rising alarmingly and the search for new and novel ways of fighting the drug resistsnce mechanism and win-win or re-emerging microbes goes on.

Need for novel approach:

Increasing resistance against antibiotics is a burning health problem. So there is an urgent and dire need to improve the existing drugs or find new, novel strategies to overcome this problem. Reducing the particle size is an efficient and reliable tool to endeavor. The therapeutic applicability of silver and medicinal plants in treating bacterial infections is already well known. Recently, synthesis of silver nano particles (SNPs) with the help of medicinal plants is attempted; the reduction of silver to nano size is accomplished by the secondary metabolites present in the medicinal plants. Nano particles, generally considered as particles with a size of up to 100 nm, exhibit completely new or improved properties as compared to the larger particles of the bulk material that they are made up of.

There are various methods of synthesizing silver nano particles such as ultraviolet irradiation, aerosol technologies, lithography, laser ablation, ultrasonic fields, heating and electrochemical reduction, photochemical reduction and application of reducing chemicals like hydrazine hydrate and sodium citrate, sodium borohydride, formaldehyde, polyethylene glycol, glucose, etc. but these techniques are expensive and sometimes hazardous chemicals are involved in their synthesis which is harmul to the environment also. To circumvent this many biological systems like bacteria, fungi, yeast, cyanobacteria, actinomycetes and plants have been used. But the best one appears to be the use of plants. Any part of the plant can be utilized for the synthesis of silver nanoparticles. The use of various parts of plants for the synthesis of nanoparticles is considered as a green technology as it does not involve any harmful chemicals. The synthesis of silver nanoparticles by means of using aqueous extracts of medicinal plants is simple, efficient, eco friendly, inexpensive, safe and it does not require any sophisticated instrumentation.

Synthesis of silver nanoparticles – medicinal plants mediated:

The first step is to make aqueous plant extract, which is usually done by boiling the plant material in distilled water. The time generally varies from 2 to 15 minutes. This plant extract is added to $AgNO_3$ and the moment the two solutions are mixed the formation of

silver nano particles begins. As soon as the plant extract is added to $AgNO_3$, the colour of $AgNO_3$ changes from colourless to yellow, brown, orange indicating the synthesis of silver nano particles in the aqueous solution. However, this time duration changes from plant to plant. The initiation of formation of silver nano particles varies from few minutes to few hours after which, there is slight variation in its formation but normally the procedure is continued for 24 h. There are many factors which affect the formation of silver nano particles. The concentration of the aqueous plant extract plays an important role in the formation of silver nano particles. The higher concentration of the plant extract will lead to the formation of more silver nano particles; The concentration of $AgNO_3$ also influences the formation of silver nano particles but higher concentration of $AgNO_3$ will produce larger silver particles and vice versa. The other factors that influence the shape and size of silver nano particles are pH and temperature. Large particles are formed at lower pH whereas at higher pH, highly dispersed and smaller nano particles are formed.

Mechanism of antibacterial activity of silver nanoparticles:

The antibacterial activity exhibited by silver nano particles depends on $AgNO_3$ concentration. It is inversely proportional i.e. less metal concentration more is the activity and vice versa. This is because smaller particles have larger surface area available for interaction and will give more bactericidal effect than the larger particles. Nano particles exhibit completely new or improved properties based on specific characteristics such as size, distribution and morphology. The cell membrane of microorganisms is negatively charged and silver nano particles are positively charged and when these positively charged silver nano particles accumulate on negatively charged cell membrane, it brings about a substantial conformational change in the membrane and it ultimately loses permeability control which leads to cell death.

Mubarak Ali et al. stated that once silver nano particles enter the bacterial cell, they would interfere with the bacterial growth signaling pathway by modulating tyrosine phosphorylation of putative peptides substrates critical for cell viability and cell division. The nanoparticles release silver ions in the bacterial cells, which enhance their bactericidal activity [13,14]. Mahendra et al[15] stated that silver nano particles preferable attack the respiratory chain, cell division finally leading to cell death.

According to Amro et al.[16] metal depletion may cause the formation of irregularly shaped pits in the outer membrane and change membrane permeability, which is caused by progressive release of lipopolysaccharides and membrane proteins. Or perhaps DNA loses its replication ability and expression of ribosomal subunits proteins as well as some other cellular proteins and enzymes essential to ATP production becomes inactivated[17]. The other mechanism proposed by Danilczuk et al. [18] and Kim et al.[19] is the formation of free radicals which subsequently induces membrane damage leading to efficient antimicrobial property of silver nano particles. The other mechanism proposed is involvement of interaction of silver nano particles with biological macromolecules such as enzymes and DNA through an electro-release mechanism. The nanoparticles get attached to the cell membrane and penetrate inside the bacteria. The bacterial membrane contains sulfur containing proteins and the silver nanoparticles interact with these proteins in the cell as well as with the phosphorus containing compounds like DNA. Their interaction may cause damage to DNA and proteins resulting in cell death. Ag+ binds to functional groups of proteins, resulting in protein denaturation. The silver nano particles show efficient antimicrobial property due to their extremely large surface area, which provides better contact with microorganisms. It is reasonable to state that the binding of the nano particles to the bacteria depends on the interaction of the surface area available. Smaller particles having a larger surface area available for interaction will have a stronger bactericidal effect than will larger particles

Application of silver nanoparticles:

Antimicrobial capability of SNPs allows them to be suitably employed in numerous household products such as textiles, food storage containers, home appliances and in medical devices. The most important application of silver and SNPs is in medical

industry such as tropical ointments to prevent infection against burn and open wounds. Silver nano particles are reported to have many therapeutic uses. There are reported to possess anti-viral, antibacterial, antifungal, anti-parasitic, larvicidal activity, and anticancer properties. Due to strong antibacterial property silver nano particles are used in clothing, food industry, sunscreens, cosmetics and many household appliances. Few studies have showed that silver nanoparticles kill fungal spores by destructing the membrane integrity.

Characterization of silver nanoparticles:
The synthesized silver nanoparticles are generally characterized by UV-vis spectroscopy, Scanning electron microscopy (SEM), Transmission electron microscopy (TEM), Fourier transform infrared spectroscopy (FTIR), Zeta potential, X-ray diffraction (XRD), etc.

A] Ultraviolet – Visible (UV-VIS) spectroscopy:
UV-vis spectroscopy is a valuable tool for structural characterization of SNPs. It is a fundamental technique to ascertain the formation of stable metal nanoparticles in aqueous medium. It is well known that the optical absorption spectra of metal nanoparticles are dominated by surface plasmon resonances (SPRs) that shift to longer wavelengths with increasing particle size. Also, it is well recognized that the absorbance of Ag NPs depends mainly upon size and shape. In general, the number of SPR peaks decreases as the symmetry of the nanoparticle increases. The position and shape of the plasmon absorption depends on the particles' size and shape, and the dielectric constant of the surrounding medium. The appearance of SPR peaks at 446 nm provides a convenient spectroscopic signature for the formation of silver nano particles.

B] Scanning electron microscopy (SEM) studies:
The SEM analysis is employed to characterize the size, shape, morphology and distribution of synthesized silver nano particles.

C] Transmission electron microscopy (TEM) studies:
TEM measurements are conducted in order to estimate the particle size and size distribution of the synthesized silver nano particles. The plant extract should be sufficient enough to be coated on the synthesized silver nano particles, otherwise aggregation of particles is accelerated and the particles are not sufficiently stabilized.

D] Fourier transform infrared spectroscopy (FTIR) studies:
FTIR measurements are carried out to identify the possible biomolecules responsible for reduction, capping and efficient stabilization of silver nano particles and the local molecular environment of the capping agents on the nanoparticles.

E] Zeta potential:
Zeta potential is an essential parameter for the characterization of stability in aqueous nano suspension. A minimum of + 30 mV zeta potential values is required for indication of stable nano suspension Higher zeta potential indicates greater stability of the synthesized silver nano particles.

F] X- ray diffraction (XRD) studies:
The XRD has proven to be a valuable research tool to prove the formation of silver nano particles, and to determine the crystal structure of the prepared silver nano particles and to calculate the crystalline particle size. Mounting evidences suggest that silver nanoparticles act as promising antimicrobial agents and may emerge as an alternative to conventional antibiotics. They could be of immense use in the medical field for their efficient antimicrobial function.

CONCLUSION

The present review describes silver Nanoparticles synthesized by medicinal plants can be used as a new novel source of antimicrobics to combat multiple drug resistant tough microorganisms and also can be therapeutically utilized to combat other diseases and disorders. Silver nanoparticles have good antimicrobial activity against different microorganisms. It is confirmed that silver nanoparticles are capable of rendering high antifungal efficacy and hence has a great potential in the preparation of drugs used against fungal diseases.

Conflicts of interest: The authors stated that no conflicts of interest.

REFERENCES

1. Prabhu N, Divya TR, Yamuna G. Synthesis of silver nanoparticles and their antibacterial efficacy. *Digest. J. Nanomater. Biostruct*, 2010, 5, 185-189.
2. Jeong SH, Yeo SY, Yi SC. The effect of filler particle size on the antibacterial properties of compounded polymer/ silver fibers. *J. Mat. Sci*, 2005, 40, 5407-5411.
3. Krutyakov Y.A., Kudrynskiy A, Olenin A.Y, Lisichkin G.V., Extracellur biosynthesis and antimicrobial activity of silver nanoparticles. Russ. Chem. Rev, 2008, 77, 233.
4. Sharma V.K, Yngard R.A, Lin Y., Silver nanoparticles: Green synthesis and antimicrobial activities. Adv. Coll. Int. Sci, 2009, 145, 83-96.
5. Marambio-Jones C, Hoek E.M.V., A review of the antibacterial effects of silver nano materials and potential implications for human health and the environment J. Nanopart. Res, 2010, 12, 1531-1551.
6. Ip M, Lui S.L, Poon V.K.M, Lung I, Burd A., Antimicrobial activities of silver dressings: An in vitro comparison. J. Medical. Microbial, 2006, 55, 59-63.
7. Bhyan SB, Alam MM, Ali MS. Effect of plant extracts on Okra mosaic virus incidence and yield related parameters of Okra. Asian. J. Agric. Res, 2007, 1, 112-118.
8. Calvo MA, Angulo E, Costa-Batllori P, Shiva C, Adelantado C, Vicente A., Natural plant extracts and organic acids: synergism and implication on piglet's intestinal microbiota. *Biotechnology*, 2006, 5, 137-142.
9. Saxena A, Tripathi R.M., Singh R.P., Biological Synthesis of silver nanoparticles by using Onion (Allium cepa) extract and their antibacterial activity. *Digest. J. Nanomater. Biostruct*, 2010, 5, 427-432.
10. Khandelwal N, Singh A, Jain D, Upadhyay M.K., Verma H.N., Green synthesis of silver nanoparticles using Argimone mexicana leaf extract and Evaluation of their antimicrobial activities. *Digest. J. Nanomater. Biostruct*.,2010, 5, 483-489
11. Thirumurgan A, Tomy N.A, Jai Ganesh. R, Gobikrishnan S., Biological reduction of silver nanoparticles using plant leaf extracts and its effect an increased antimicrobial activity against clinically isolated organism. De. Phar. Chem, 2010 , 2, 279-284.
12. Thirumurguan G, Shaheedha S.M., Dhanaraju M.D., In vitro evaluation of antibacterial activity of silver nanoparticles synthesized by using phytothora infestans. Int. J. Chem Tech Res, 2009, 1, 714-716.
13. Sondi I, Salopek-Sondi B. Silver nanoparticles as antimicrobial agent: a case study on *E. coli* as a model for Gram-negative bacteria. *Journal of Colloids Interface Science*. 2004; 275: 177–182.

IRJSE *Int. Res. J. of Science & Engineering*, 2018; Special Issue A2 : 207-209 SJIF Impact Factor 4.11
ISSN: 2322-0015 UGC Approved Journal No. 63628
RESEARCH ARTICLE **OPEN ACCESS**

Structural, Thermal and Optical Characterization of an Organic NLO Material – BTSCCdS

Kalokhe SB[1*], Dhumane NR[2] and Muley GG[3]

[1,2]Shri Anand College of Science, Pathardi 414102, Ahmednagar, Maharashtra, India, [3]Department of Physics, Sant Gadge Baba Amravati University, Amravati-444602,
Email: suryakantkalokhe@gmail.com

Manuscript Details
Available online on http://www.irjse.in
ISSN: 2322-0015

Editor: Dr. Arvind Chavhan

Cite this article as:
Kalokhe SB, Dhumane NR and Muley GG. Structural, Thermal and Optical Characterization of an Organic NLO Material – BTSCCdS, *Int. Res. Journal of Science & Engineering*, January 2018; Special Issue A2 : 207-209.

ABSTRACT

The growth of Benzene Thiosemicarbazide Cadmium Sulphate. BTSCCdS Single crystals grown by slow evaporation growth technique, BTSCCdS crystals were grown by partial substitution of Cadmium sulphate. The incorporation of sulphate in the grown crystals was qualitatively analyzed from FTIR studies. Absoption spectra taken for the BTSCCdS crystals reveal the better Nonlinear Optical (NLO) crystal. NLO have potential uses in many devices utilizing their ability of frequency conversion, frequency mixing, electro-optic modulation etc. UV-VIS spectroscopy shows the improvement in the optical transparency. Crystal structure has been studied by powder X-Ray diffraction. Thermal analysis has also been performed on the grown crystals to study thermal stability.

Keywords: Crystal growth, BTSCCdS, FTIR, UV-VIS, EDS, Optical properties.

INTRODUCTION

In the growth of nonlinear optical (NLO) Materials there are wide applications in optoelectronic and photonic applications most of the organic crystals usually have poor mechanical and thermal properties and are susceptible for damage during processing moreover growth of bulk large size. Single crystal is difficult to grow for device application.

Inorganic materials have excellent, mechanical and thermal properties, but possess relatively modest optical nonlinearity because of the lack of extended π-electron delocalization. Due to above reasons interests have been made on semi organic crystals like higher mechanical strength, chemical stability, high damage threshold, wide transparency range which make them suitable for device fabrication. Hence it is necessary to synthesize and grow novel semi organic crystals which have positive aspects of both organic and semi organic materials.

METHODOLOGY

Benzene Thiosemicarbazide Cadmium Sulphate were taken in beaker containing doubly deionized water of 2:1 molarity. BTSCCdS crystals were grown at room temperature by slow evaporation technique by dissolving 20.84 gm of Cadmium sulphate and 0.7 thiourea in 100ml of deionized water under magnetic stirring. The temperature was maintained around 35°c to avoid decomposition of element from the compound, A colorless, transparent crystal was obtained. The crystals of BTSCCdS were required up to two to three weeks for crystal formation.

Fourier transform infrared (FTIR) spectrum of BTSCCdS crystal was recorded at a resolution 2 cm-1 in the range 500 – 3500 cm-1 Employing BRUKER IFS – 66V spectrometer using KBr-pellet technique. The optical absorption and transmittance spectra of BTSCCdS crystals were recorded in the range of 200 – 1200 nm using VARIAN CARY 5E spectrometer. Energy Dispersive analysis spectra of BTSCCdS were recorded with JEOL JEO2300 Analysis Star ion of counting rate 3133cps and Energy range 0-20kev. (ZAF method Standard less Qualitative Analysis)

RESULTS AND DISCUSSION

1. FT-IR

Fourier transform infrared (FTIR) spectrum of BTSCCdS crystal shown in the Fig. 1. In the high energy region between 3470 and 2323 $cm^{-1}$the appearance of broad absorption band is attributed to hydrogen bond symmetric and asymmetric vibrations. The C=O group gives rise to a strong absorption in the region 1820 – 1660 cm^{-1}. The peak is often the strongest in the spectrum and of medium width. 3085 =C-H stretch for sp2. C-H occurs at values greater than 3000cm-1 (3095-3010cm^{-1}). Stretch occurs in the range 730 – 550 cm^{-1}. C-Cl stretching vibrations – These bands which appear in the range from 730 – 550 cm-1 are best observed if KBr plates or cells are used. [2] One strong C-Cl appearance in the spectrum of acetyl chloride in other aliphatic and chlorides one may observe as many as four bands due to the many confirmation that are possible. The absorption band at 1733, 1614, and 1580 cm^{-1} can be assign to C=O. the last 1580 cm^{-1} corresponds to bending of primary and secondary amides. 1505 cm^{-1} corresponds to N-O. 3085 cm^{-1}[3] Corresponds to stretch of carboxylic acid O-OH. Stretch for sp2 C-H 0ccures at values greater than 3000 cm^{-1} (3095 - 3010 cm^{-1}).

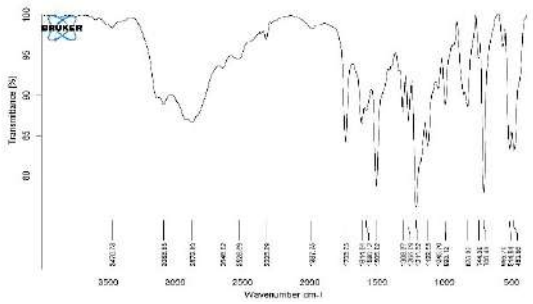

Fig. 1 FTIR Spectra

2. UV-VISIBLE SPECTRA

The optical transmission spectrum of BTSCCdS crystal was recorded in the region 200–1200 nm, using a LAMBDA 35 spectrophotometer. The recorded optical transmission spec-trum of BTSCCdS are shown in Fig. The lower cutoff wavelength of grown crystal is 190 nm. The lower cutoff wavelength of pure LSTH is 200 nm. It was observed that the CDS doped BTSC crystal had good transmittance window than pure BTSC in the region of 400–600 nm. In general the crystals had good transmittance for entire visible and IR region.[1].

3. ENERGY DISPERSIVE ANALYSIS SPECTRUM

Energy Dispersive analysis spectra of BTSCCdS were recorded with counting rate 3133cps and Energy range 0-20kev. (ZAF method Standerdless Qualitative

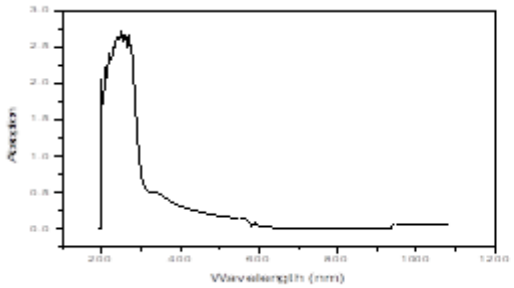

Fig. 2a. UV-visible Spectra

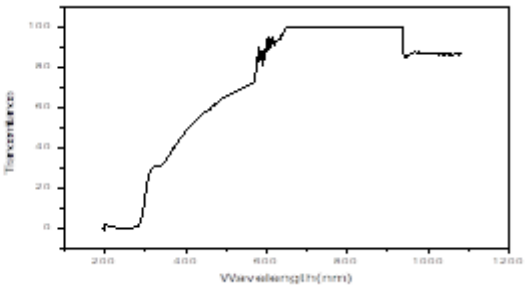

Fig. 2b UV-visible Spectra

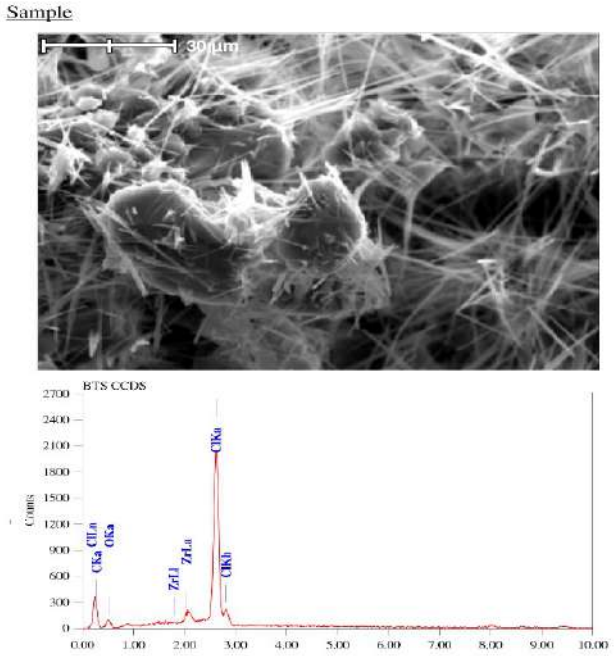

Fig. 3 EDAX Spectra

Analysis). Fig. shows the energy dispersive X-ray analysis (EDAX) of BTSCCdS. From EDAX spectrum, the presence of carbon, oxygen, zirconium and chlorine is confirmed. The incorporations of zirconium and chlorine in BTSCCdS are clearly understood from the EDAX spectral analysis[4]. The incorporation of metal ions in the sublattices may increase the number of charge carriers for the material to be dipolar.

CONCLUSION

Single crystals of CdS doped BTSC crystals have been grown by slow evaporation solution growth method. FTIR spectra confirm the presence of all functional groups present in the crystals. UV–Vis spectra show that the grown crystals of this work have good optical transmittance in the visible and IR region. The above results show CdS doped BTSC crystal is a potential material for optoelectronic applications. Microstructure and compositional analyses were discussed using EDAX studies.

Conflicts of interest: The authors stated that no conflicts of interest.

REFERENCES

1. Ushashri PM, Jayavel R, Ramaswamy P. Growth and characterization of phosphate mixed ZTS single crystals" *Material science and Engineering*. B65 (1999) 153-158
2. Maadeswaran P, Chandrasekaran J, Trirumal-airajan S. Synthesis growth, spectral, thermal, and photoluminescence properties of a new semi-organic NLO crystal-Thaiosemicarbazide lithium chloride (TSLC)" *Optik*, 2011; 122: 259
3. Selvam A, Pandi S, Selvakumar S, Srinivasan S, Growth and characterization of Urea citic acid (UCA) single crystals by slow evaporation process" *Scholar Research library*, 4 (2012) 2474-2478.
4. Anbuselvi D, Jayaraman D, Arul J. Martin Mani, Joseph V. Growth and optical, thermal, mechanical and surface morphology studies semiorganic nonlinear optical material: Diclorobis (L-Proline) zinc (II) crystal"*Molecular and Biomolecular Spectroscopy*; 114 (2014) 405-414

IRJSE International Research Journal of Science & Engineering
Int. Res. J. of Science & Engineering, 2018; Special Issue A2 : 210-213
ISSN: 2322-0015
SJIF Impact Factor 4.11
UGC Approved Journal No. 63628
RESEARCH ARTICLE **OPEN ACCESS**

Preparation and Characterization of Rare Earth Doped Nanoparticles for Biological Application

Tarannum Vahid Attar[1*] and Khandpekar Mahendra M[2]

[1]Department of Physics, G.M.Momin Womens College, Bhiwandi (Affiliated to University of Mumbai),
[1]Material Research Laboratory, Department of Physics, Birla College, Kalyan (University of Mumbai)
Email: azra23oct2005@gmail.com

Manuscript Details
Available online on http://www.irjse.in
ISSN: 2322-0015

Editor: Dr. Arvind Chavhan

Cite this article as:
Tarannum Vahid Attar and Khandpekar Mahendra M. Preparation and Characterization of Rare Earth Doped Nanoparticles for Biological Application, *Int. Res. Journal of Science & Engineering,* January 2018; Special Issue A2: 210-213.

ABSTRACT

We report the synthesis, antibacterial and antioxidant studies of hexagonal shaped lanthanum fluoride nanoparticles doped with Praseodymium (Pr^{3+}) and Holmium(Ho^{3+}) ions prepared with co-precipitation method using deionised water as solvent. The X-ray diffraction, SEM, TEM and selected area electron diffraction SAED pattern have been used for identification of crystal structure. Cell parameters are a = b = 7.0800AU and c = 7.2380AU and confirms with the JCPDS standard card (32-0483) of pure LaF_3 crystals. Antibacterial activity was assessed for both gram positive and gram negative bacterial strains. At 500µg/disc and 1mg/disc concentration the test substance showed very good activity against Pseudomonas aeroginosa and Salmonella typhi. Antioxidant activity was measured by DPPH free radical scavenging method. Synthesised nanoparticles showed very less antioxidant activity as compared to standard Ascorbic acid.

Keywords: Antioxidant activity, X-ray diffraction, SEM, TEM, etc.

INTRODUCTION

Rare earth elements are commonly used industrially in lasers, glasses, magnets and in many other applications. Lanthanum based fluorides are important materials for their optical properties. In the form of thin films or as nanoparticles, rare earth doped lanthanum fluorides show interesting up-conversion effect from near IR to visible light. Also X-ray luminescence has been observed on doped lanthanum fluorides. Luminescent properties of these materials can be used in many applications such as biological applications and for light emitting applications such as their use in diodes [1,2].

Lanthanum fluoride nanoparticles can be prepared by variety of ways. Hydrothermal synthesis has been widely employed for preparation of these materials [3-5]. Co-precipitation method [6, 7], micellar emulsion method [8] or using ionic liquid based synthesis [9] are been used. Among various host materials, lanthanum fluoride (LaF_3) possesses advantageous properties over the oxygen-based systems, as the former results from lower vibration energy and minimization for the quenching of the excited state of RE ions [10–15].

METHODOLOGY

LaF_3: Pr^{3+}, Ho^{3+} nanocrystals were synthesized by an aqueous route using microwave assisted technique operated at low power range. The method is simple and cost effective. Water soluble $LaCl_3$+ $PrCl_3$ + $HoCl_3$ (1 unit) and NH_4Cl (3units) are mixed to obtain a solution in 1:3 molar proportion [16]. A 10 ml homogeneous mixture is prepared in deionized water in a 100ml beaker using 0.192 mol of $LaCl_3$+ $PrCl_3$ + $HoCl_3$. To this 10ml solution of 0.576 mol NH_4F is added through separate syringe to avoid contamination. The complete setup was placed inside a conventional microwave oven set at low power range (in on-off mode set at 30sec) for around 30 minutes time. The low power range setting largely helped us avoiding spill off of the solution. A white ultrafine crystalline precipitate identified as doped LaF_3 (LFPH) nanocrystals appears almost instantly having settled down at the bottom of the beaker (Figure1). The precipitate was washed several times with de-ionized water and then dried in the microwave oven for about 15 minutes. The dried sample was then stored in sealed tubes for further characterization.

RESULTS AND DISCUSSION

1.**Structural Characterization:**
Well dispersed hexagonal geometry nanocrystals of LaF_3:Pr^{3+},Ho^{3+} have been synthesized in deionized water using precipitation method.XRD analysis shows hexagonal crystal structure with a = b = 7.080(A^0), c = 7.238(A^0), $\alpha = \beta = 90^0$ and $\gamma = 120^0$. The strongest peak is found to lie on (111) plane.

Traces of broad, hexagonal and spherical like nanocrystals have been observed. The average crystallite size is found to be 15nm by TEM measurements. TEM results are found to be in close agreement with the XRD studies with Debye Scherrer particle size of 11.17nm. The selected area electron diffraction (SAED) pattern shows four diffraction rings corresponding to the (110), (111), (300) and (221) reflections, which is in agreement with the hexagonal LaF_3 structure. The c/a ratio is found to approach unity in synthesized nanocrystals. SEM pattern shows dispersed particles with traces of aggregates. EDAX spectra confirmed the elemental components in the nanocrystals with certain trace elements. The FTIR spectrum has been used for identification of fundamental vibrational groups present in the material.

FIG 1. Synthesis of LFPH

2. Antimicrobial activity of the Lanthnum based nanoparticles LaF_3:Pr^{3+},Ho^{3+}

Preparation of sample: Lanthanum based nanoparticles were dissolved in water and used for antimicrobial activity. For antibacterial assay both

gram positive and gram negative bacterial strains were used. A total of five standard human pathogenic bacteria were procured from Government hospital. The organisms were maintained on nutrient agar slants and stored at 4 ° C with periodic sub-culturing.

Antibacterial activity was tested in triplicate using the standard paper disk diffusion method [17,18]. Stock solution of synthesized nanoparticles was prepared by dissolving in 50 mg/ml of methanol. The test concentrations of lanthanum nanoparticles 50µg, 100µg, 500µg and 1 mg per disk were applied to sterile paper disks (6 mm in diameter). The discs were dried before they were placed onto agar plates that had been seeded with reference bacterial strains. The diameters of the inhibition zones (diameter of inhibition zone minus diameter of disk) were measured in millimeters after incubation at 30^0C for 24 hours. Solvent (sterile distilled water) control disks without lanthanum nanoparticles prepared in the same manner were never observed to inhibit bacterial growth.

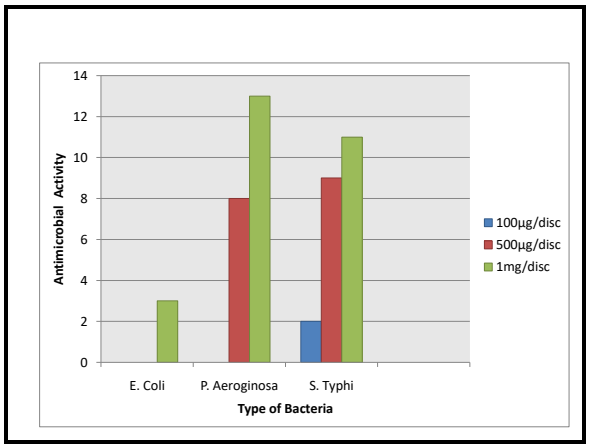

Fig.2:Antimicrobial activity of $LaF_3:Pr^{3+},Ho^{3+}$

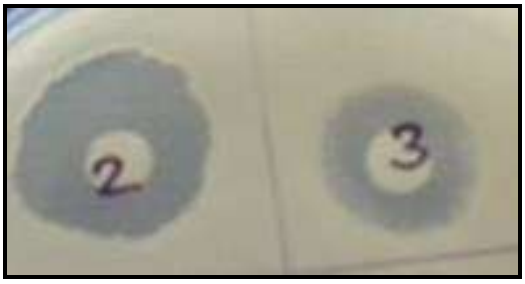

Fig.3:Antimicrobial activity of $LaF_3:Pr^{3+},Ho^{3+}$ nanoparticles against *Pseudomonas aeroginosa* at 1mg/disc (2) and 500µg/disc(3) concentrations.

3. Antioxidant activity of the Lanthnum based $LaF_3:Pr^{3+},Ho^{3+}$nanoparticles

The antioxidant activity of lanthanum nanoparticles was checked on the basis of scavenging effect of the stable 2,2-diphenyl-1-picrylhydrazyl (DPPH) free radical activity[19].The standard antioxidant ascorbic acid was taken for comparison. Here standard ascorbic acid solution (1ml) and different concentrations (50, 100, 200, 400, 500 µg/ml in methanol) of 1ml of lanthanum nanoparticles were mixed with 3 ml of 0.4M DPPH solution. These mixtures were kept in dark for 30 minutes and after that the absorbance was measured at 517 nm using UV-Visible Spectrophotometer. In this assay ascorbic acid was used as a positive control. Lower absorbance of the reaction mixture indicated higher free radical-scavengingactivity.

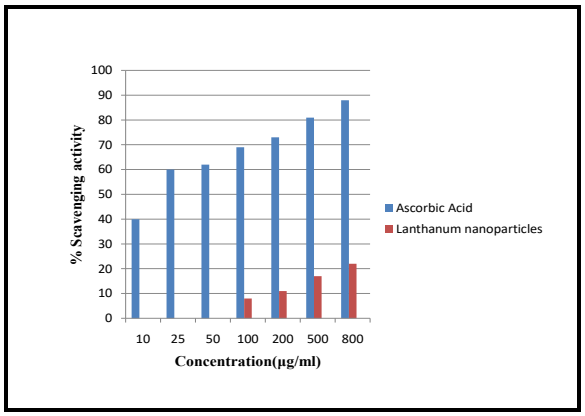

Fig.4:Antioxidant activity of $LaF_3:Pr^{3+},Ho^{3+}$

CONCLUSION

New rare earth doped lanthanum fluoride nanoparticles (LFPH) with enhanced properties have been grown. Attempt has been made to study biological application of the synthesized material.The results of antimicrobial activity of synthesized nanoparticles LaF_3: Pr^{3+}, Ho^{3+} were promising. At 500µg/disc and 1mg/disc concentration the test substance showed very good activity against *Pseudomonas aeroginosa* and *Salmonella typhi*. The slight inhibition of *E. coli* bacterial strain was observed at very high concentration but this activity was negligible. In Antioxidant activity test of LaF_3: Pr^{3+}, Ho^{3+} nanopartoicles both ascorbic acid and

$LaF_3:Pr^{3+},Ho^{3+}$ nanoparticles showed dose dependent activity. Lanthanum nanoparticles showed less significant amount of DPPH free radical scavenging effect compared to ascorbic acid. These biological analysis indicates that $LaF_3:Pr^{3+}$, Ho^{3+}nanoparticles are potential candidates for biomedical applications like biolabeling or biotagging.

Acknowledgement: The authors thank the staff of SAIF (IIT Mumbai) and ISFAL Punjab for providing experimental facilities. The authors wish to thank Material Research Laboratory, Birla College for providing research facilities and K.M.E Society's G.M.Momin Womens College, Bhiwandi for institutional support.

Conflicts of interest: The authors stated that no conflicts of interest.

REFERENCES

1. Sivakumar R, van Veggel F, Raudsepp M, *J. Am. Chem. Soc*. **2005;** 127: 12464–12465.
2. Fujihara S, Tokumo K, *J. Fluorine Chem*.2009; 130**:** 1106–1110.
3. Li C, Liu X, Yang P, Zhang C, Lian H, Lin J, *J. Phys. Chem*. C., 2008; **112**: 2904.
4. Meng JX, Zhang MF, Liu YL, Man SQ, *Spectrochim. Acta Part A* **66** (2007) 81.
5. Zhang T, Guo H, Qiao YM, *J. Lumin*.2009; **129:** 861.
6. Shen HX, Wang F, X. P. Fan, M. Q. Wang, *J. Exp. Nanosci*. 2007; **2:** 303.
7. Kumar DA, Selvasekarapandian S, Nithya H, Sakunthala A, Hema M. *PhysicaB: Cond. Mater*. 2010; **405** 3803.
8. Ma XH, Zhao YB, Wu ZS, *Acta Phys.-Chim*. Sin. 2008; **24:** 2037.
9. Zhang C. Chen J, Zhou YC, Li DQ, *J. Phys. Chem*. C, 2008; **112;** 10083.
10. Yu RB, Yu KH, Wei W, Xu XX, Qiu XM, Liu SY, Huang W, Gordon T, Harold F, B. Peng, 2007; **19** 838.
11. Yu YY, Chien WC, Chen SY, *Mater. Des.* 2010; **31** 2061.
12. Stouwdam JW, van Veggel FC, *Langmuir*, 2004; **20:** 11763.
13. Yi GS, Chow GM, *J. Mater. Chem*. 2005; **15 :** 4460.
14. Wang LY, Li P, Li YD, *Adv. Mater*. 2007; **19:**3304.
15. Cui XX, She JB, Gao C, Cui K, CQ Hou, W. Wei, B. Peng, *Chem. Phys. Lett. 2010;* **494:** 60.
16. Meng J, Zhang M, Liu Y, Spect. *Acta. A*, **66** (2007) 81.
17. Balouiri M, Sadiki M, Ibnsouda SK, *J. of Pharmaceutical Analysis*, 2016; **6:** 71.
18. Valgas C, deSouza SM, Smania EFA, Jr.,Brazalian AS. *J. of Microbiology, 2007;* **38:** 369.
19. Rahman MA, Rana MS, Zaman MM, Uddin SA, Akter R, *J. Sci. Res*. 2010; **2** (1): 169.

IRJSE *Int. Res. J. of Science & Engineering*, 2018; Special Issue A2 : 214-216 SJIF Impact Factor 4.11
ISSN: 2322-0015 UGC Approved Journal No. 63628
RESEARCH ARTICLE **OPEN ACCESS**

Low Frequency Dielectric Response of Modified Fly Ash Zeolite

Kalyankar_AN[1] and Choudhari AL[2]

[1]Bahirji Smarak Mahavidyalaya Basmath, Maharashtra, India-431512,[2]Ex-Professor, School of Physical Sciences, S.R.T.M.U. Nanded, Maharashtra, India-431602
Email: kalyankaranil@gmail.com

Manuscript Details

Available online on http://www.irjse.in
ISSN: 2322-0015

Editor: Dr. Arvind Chavhan

Cite this article as:
Kalyankar AN and Choudhari AL. Low Frequency Dielectric Response of Modified Fly Ash Zeolite, *Int. Res. Journal of Science & Engineering*, January 2018; Special Issue A2: 214-216.

ABSTRACT

In Thermal power stations for generation of electricity, coal is burnt on large scale so that the coal fly ash is produced on large scale in India. In this paper, the modified zeolite A synthesized using fly ash is used for studying the dielectric properties. The zeolite is modified by ion exchanging so as to form Co-A type zeolite. The samples were tested for dielectric constant (ε′), dielectric loss (ε′′), electrical conductivity (ε_{ac}). The dielectric properties depend upon the percentage of encapsulated metal cations. This cost effective zeolite reported in this work provides a new path to fabricate highly sensitive materials for dielectric applications from hazardous solid waste fly ash.

Keywords: Fly ash, Zeolite Co-A, dielectric properties.

INTRODUCTION

Zeolites are alumino silicates and their applications in many disciplines are well known. Synthesis of zeolites using coal fly ash is a best alternative to utilize this hazardous solid waste. Since coal fly ash includes a large amount of silica and alumina, they are easily converted into zeolite by hydrothermal treatment in an alkaline solution [1, 2]. Fly ash is a fine grained powder, which is mainly composed of spherical glassy particles, produced during the combustion of pulverized coal. Many researchers have been synthesized zeolite A from fly ash [3]. Nowadays, a novel application of zeolite in electronics

is necessary [4]. This paper reports the dielectric effects on zeolite Co-A synthesized from coal fly ash.

METHODOLOGY

The starting material was fly ash obtained from thermal power station, Parali Vaijnath, Maharashtra (India). The fly ash zeolite A synthesized using fly ash based on previous study [5] is used. The zeolite A thus formed is ion exchanged with 1 M solution of NH_4NO_3 at 80^0C for 12 h. This process was repeated thrice so as to get proper ion exchange. The product was filtered, air dried at 60^0C for 24 hr and then calcined at 450^0C so that the NH_4-A is decomposed into H- A i.e.protonic form then the zeolite which when ion exchanged with 0.1M, 0.2M and 0.3M solution of cobalt nitrate [$Co(NO_3)_2.nH_2O$], so as to obtain the **$Na_{(1-x)}Co_xA$** zeolite where x = 0.1, 0.2, 0.3M.

Characterization:

The physical properties of coal fly ash and synthesized products were measured as follows. The chemical composition fly ash was determined by using a X-ray Fluorescence Spectroscopy. The chemical composition was analyzed using X-ray fluorescence analysis equipment (Phillips PW -2404). The sample phases were characterized by X-ray diffraction (XRD) using a (Philips PW 3710) diffractometer with Cu- K radiation (1.5496Å).

Dielectric Measurement:

The samples of Na-A and Co- A zeolite were compressed to form pellet of 10 mm diameter and 1 mm thickness. The pellets were heated to 300^0C to obtain a hard solid sintered material. The pellets were polished with silver paste for good electrical contact. The electrical conductivity was measured in the frequency range 20Hz–1MHz at room temperature 25^0C using LCR-meter (HP-4284A).

RESULTS AND DISCUSSION

1. XRF:

The elemental composition analysis by XRF in Table 1 indicated that coal fly ash contained large quantities of silica and alumina which are the two main components in zeolite. The chemical analysis of the fly ash used as the starting material in this work showed it to be a high-silica ash with the mole ratio of SiO_2: Al_2O_3 = 5.127: 1.

Table1. Chemical composition of fly ash

Oxides	% wt	Mol/100 g of fly ash
SiO_2	70.23%	1.169
Al_2O_3	23.27%	0.228
Fe_2O_3	4.38%	0.027
MgO	1.26%	0.031
Na_2O	0.42	0.0067
LOI	0.44%	-

2. XRD:

The X-ray diffraction pattern of fly ash based zeolite H–A and its exchanged form Co-A is shown in fig.1. The d values are compared with the standard [6]. The peaks located in the region of $7° < 2\theta < 34.1°$ are representative peaks of a typical H-A zeolite. The peaks at $2\theta = 36.8°$ is representative peak of a cobalt [7]. As can be seen in Figure 1, the intensity of peaks corresponding to H-A zeolite decreased, whereas, the intensity of peaks corresponding to cobalt increased on increasing the cobalt loading on H-A zeolite.

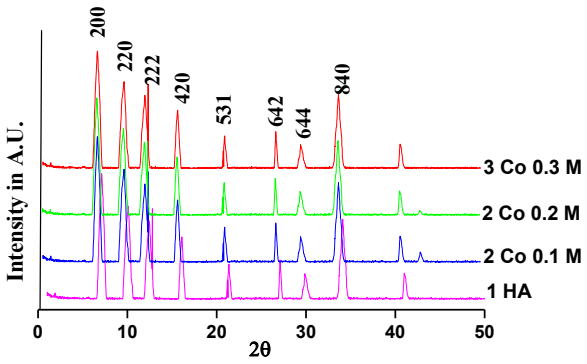

Figure 1. X-ray diffraction patterns of H-A/Co-A zeolite.

The intensity ratios (I/I_m) were calculated by considering peak intensities (I) at $2\theta = 7.1^0$ for A zeolite. The XRD for Co-A were found to be similar to that of original H-A sample, indicating that there is no structural changes occur after ion exchange with Cobalt nitrate [8].

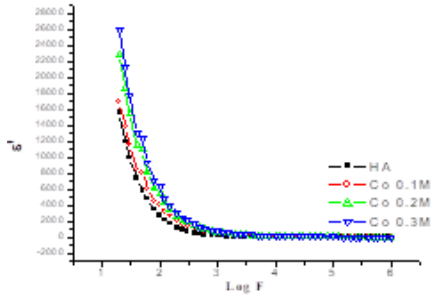

Figure 2.Variation of dielectric constant (ε') with log f

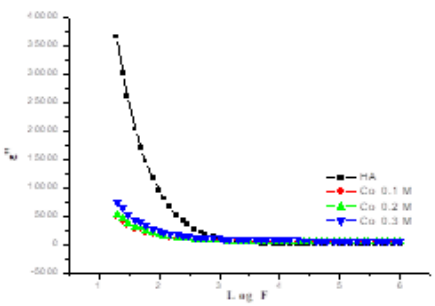

Fig.3 Variation of dielectric loss (ε'') with Log F

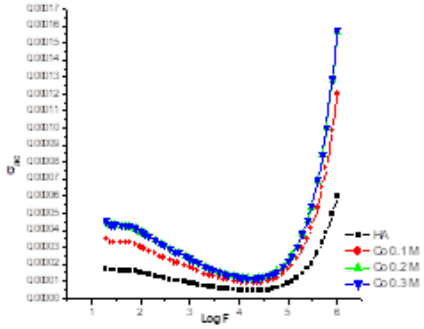

Fig4 Variation of ac conductivity (σ_{ac}) with Log F

3. Dielectric Measurement:

The variation of dielectric constant (ε′), dielectric loss (ε′′), ac conductivity (σ) with log f for H -A and Co-A zeolites are shown in figure 2, 3, and 4. In Figure 2, the permittivity (ε′) of zeolite HA was found to decrease with an increase in frequency. This characteristic gives the increase of the permittivity at low frequency. The low dielectric constant of zeolites (ε′) suggests, however, that such processes in the zeolite channels should involve concerted action rather than strong charge separation.

In fig.3 the variation of dielectric loss (ε′′) with frequency at room temperature is shown. This dielectric loss is frequency dependent and also influenced by water content of the zeolite [9]. The loss is in lowest frequency region and has been frequently observed in zeolites is supposed to be due to a dc ionic conductivity loss and grain boundary effect [10]. In fig. 4 the variation of ac conductivity (σ) with frequency at room temperature is shown. The conductivity increases with increase in frequency. The conductivity of zeolite HA is less than Co -A, as the conductivity depends on the cation size and the channels within the zeolites structure.

CONCLUSION

Zeolite A is successfully synthesized from solid waste material fly ash and it shows no structural change after modification with cobalt. The zeolite A and Co-A shows good response for dielectric applications.

Acknowledgement:

One of the authors, Kalyankar A.N. is thankful to University Grants Commission, New Delhi, India, for financial assistance under minor research project XI Plan.

Conflicts of interest: The authors stated that no conflicts of interest.

REFERENCES

1. Yaping YE, Xiaoqiang Z and Weilan Q, Mingwen W, *Fuel*. (2008); 87:1880-1886.
2. Pena Penilla R, Guerrero Bustos A, Goni Elizalde S, *Journal of the American Ceramic Society*, 2003; 86, : 1527–1533
3. Querol X, Moreno N, Umaña JC, Alastuey A, Hernández E, Lopez-Soler A and Plana F, *Int. J. Coal geology*,2002; 50: 413-423.
4. Normann Herron, Journal of inclusion phenomena and molecular recognition in chemistry, (1995), 21, 283-298.
5. Kalyankar AN, Joshi AA, Choudhari AL. *Int. J. Basic & App. Res*. 2011; 01: 59-63.
6. Breck DW, Zeolites Molecular Sieves, Wiley,New York, 1971
7. Yuelun Wang, Yuan Jiang, Jun Huang, Hui Wang, Zhuo Li ,Jinhu Wu, RSC Adv., 2016,**6**, 107498-107506.
8. Hsiao-Lan Chang ,Wei-Heng Shih, Ind. Eng. *Chem. Res.*, 2000, 39 (11), 4185–4191.
9. Tatsuo Ohgushi, Kazushi Ishimaru, *Chem. Commun*.2002;1714.
10. Barrer RM, Coen PJ, *Nature*, 1963; 199, (1963) 587.

IRJSE International Research Journal of Science & Engineering
Int. Res. J. of Science & Engineering, 2018; Special Issue A2 : 217-220
ISSN: 2322-0015
SJIF Impact Factor 4.11
UGC Approved Journal No. 63628
RESEARCH ARTICLE **OPEN ACCESS**

Study of Temperature Dependence for Iron oxide Nanoparticles

Gawali Swati R[1], Zagade Bhau S[2] and Jayashree Pant[3*]

[1]CESS Dr. A. B. Telang Sr. College, Nigdi, Pune,[2]S. N. R. H. and Jr. College, Indapur,
[3]Abasaheb Garware College, Karve road, Pune
Email: swati.r.gawali@gmail.com, jpant.agc@gmail.com

Manuscript Details
Available online on http://www.irjse.in
ISSN: 2322-0015

Editor: Dr. Arvind Chavhan

Cite this article as:
Gawali Swati R, Zagade Bhau S and Jayashree Pant. Study of Temperature Dependence for Iron oxide Nanoparticles, *Int. Res. Journal of Science & Engineering*, January 2018, Special Issue A2 : 217-220.

ABSTRACT

Iron oxide exhibits different phases such as hematite (α-Fe_2O_3), maghemite (γ-Fe_2O_3) and magnetite (Fe_3O_4). Of these, hematite is the most stable phase. Nanoparticles of hematite have versatile applications and are used as pigments, adsorbents, photo-catalysts, solar energy conversion, lithium- ion batteries and sensors. Hematite nanoparticles were synthesized by Sol- Gel method using ferric nitrate and oxalic acid as precursors. The as-prepared samples were subjected to calcination at different temperatures from 400 °C to 800 °C. These samples were characterized by X-ray Diffraction (XRD) and Scanning Electron Microscopy (SEM). The size of the particles was calculated from the XRD spectra with the help of Scherrer formula. It was found to increase from 52 nm at 400 °C to 67 nm at 800 °C. The phase of the synthesized nanoparticles was found to be α-Fe2O3 (hematite) with hexagonal rhomb-centered structure. SEM results show hexagonal morphology of the particles and confirm the increase in size with temperature. The local lattice distortion (strain) of these nanoparticles was calculated using Williamson-Hall plot and was found to be about 0.06%. These results are discussed in this paper.

Keywords: Hematite, Sol-Gel method, Williamson-Hall plot.

INTRODUCTION

In the past decade magnetic nanoparticles have been under observations of scientific and technological interests due to their strong influence on chemical and physical properties. Among them iron oxide nanostructures have gained remarkable attention due to its wide range of applications in the various fields like gas sensor, catalysis, lithium-ion batteries, magnetic recording media, pigments and water treatment [1-4]. This transition metal oxide is considered as an ideal candidate for many technological applications due to its low cost, biodegradability, high resistance to corrosion and high stability [5-7]. Iron oxide is found in different polymorphs such as α-Fe_2O_3, γ- Fe_2O_3 and Fe_3O_4. Among all α-Fe_2O_3 (hematite) is the most stable and extensively studied structure. Bulk hematite has wide band-gap energy of 2.2 eV which gets enhanced in the nanoscale [8] regime. This property is used in many applications like solar energy conversion and photo catalysis.

A variety of methods like high energy ball milling method [9], hydrothermal approach [10] and auto-combustion method [11] had been reported to synthesize α-Fe_2O_3 nanoparticles. However it is still a challenge to yield mono-size nanoparticles. In the present work we report synthesis of iron oxide nanoparticles by sol-gel technique.

METHODOLOGY

Iron oxide nanoparticles were synthesized by sol-gel method. All the AR-grade chemicals in the present work were obtained from Merck and used as received. Homogeneous solution of ferric nitrate was prepared in organic solvent under continuous stirring and used as a precursor. Small amount of oxalic acid was added drop by drop with stirring in this precursor solution as a thickening agent. This colloidal solution is heated up to 80 ^oC with continuous stirring for 15 minutes. The stirring was then stopped and heating continued till brownish thick gel was formed. It was then dried overnight in air. The dried gel was calcined from 400°C to 800°C for 2 hours each.

The as-synthesized iron oxide nanoparticles were investigated in terms of their morphological, structural and compositional properties by using various analytical techniques. The analysis of crystalline properties like crystalline nature, phase and the size of the as-prepared nanoparticles were determined by X-Ray Diffraction (XRD) using D8 Advance Diffractometer. The morphology of these particles was carried out by Scanning Electron Microscopy (SEM) using JEOL JSM 5600. The Energy Dispersive Spectroscopy (EDS) was used to estimate the atomic percentages of iron and oxygen in the samples. All these measurements were carried out at the Department of Physics, University of Pune.

RESULTS AND DISCUSSION

Structural and morphological Analysis:

The crystal phase was examined by X-ray diffraction with Cu-Kα radiation (λ = 1.54 Å) in the range of 10-80° with a scanning rate of 2°/min. Fig. 1 shows comparative XRD patterns of all the iron oxide samples calcined at various temperatures from 400 °C to 800 °C. The finite width of the diffraction peaks clearly indicates the formation of nanoparticles. All diffraction patterns match well with that of JCPDS data no. 860550 indicating the formation of α- Fe_2O_3 phase of iron oxide nanoparticles. Hexagonal – rhombo centric lattice structure is seen in these crystals of α- Fe_2O_3 nanoparticles. Moreover no extraneous peaks appear in the spectra which clearly indicate the formation of pure samples. The particle size is determined by using Debye Scherrer formula [12] and increases from 52 nm to 67 nm as the calcination temperature increases from 400 °C to 800 °C. It is usually seen that when a particle enters into a nano regime, a common phenomenon observed is lattice strain. This lattice strain can influence the properties of the nanostructures. X-ray diffraction analysis is widely used to determine the lattice strain. The average grain size of the synthesized nanoparticles could be due to finite size effect or due to a combined effect of size and strain. The Williamson- Hall plot is plotted to determine the particle size and the lattice strain. Fig. 2 presents a plot of $(\beta \cos \theta)/0.94\lambda$ versus $(4 \sin \theta)/0.94\lambda$ for all

samples. The crystalline size (d) and the local lattice distortion η can be estimated by fitting and extrapolating the linear curve. The reciprocal of the y intercept gives the particle size while the slope of the linear curve gives the value of the local lattice distortion η [13]. It is observed that the local lattice strain remains constant (0.06 %) for the α- Fe_2O_3 nanoparticles calcined at different temperatures from 400 °C to 700 °C. But for the α- Fe_2O_3 nanoparticles calcined at 800 °C the strain increases up to 0.09 %. We are finding the possible reasons behind this sudden increase. The variation of particle size and local lattice strain as a function of calcinations temperature is listed in the following table1.

Table 1: Variation of particle size and lattice strain with temperature

Temperature (°C)	Particle Size (nm)	Lattice Strain (ηin %)
400	52.55	0.062
500	58.09	0.061
600	61.69	0.060
700	63.72	0.062
800	67.03	0.090

The morphology evolution of the α- Fe_2O_3 nanoparticles is studied by SEM. The SEM image of the as-prepared α- Fe_2O_3 nanoparticles calcined at 800 °C is shown in Fig. 3.

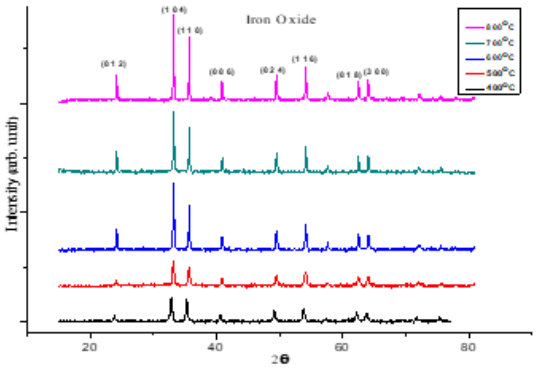

Fig. 1: XRD Spectra of Iron oxide Nanoparticles

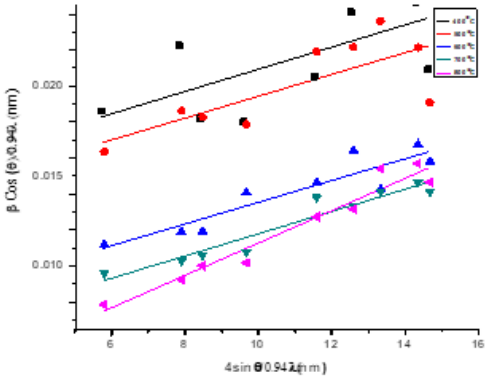

Fig. 2: W-H Plot for Iron oxide Nanoparticles

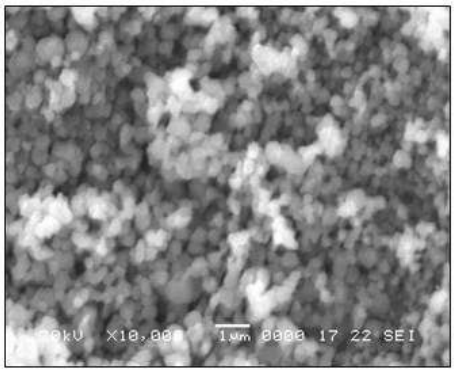

Fig. 3: SEM Image of Iron oxide Nanoparticle

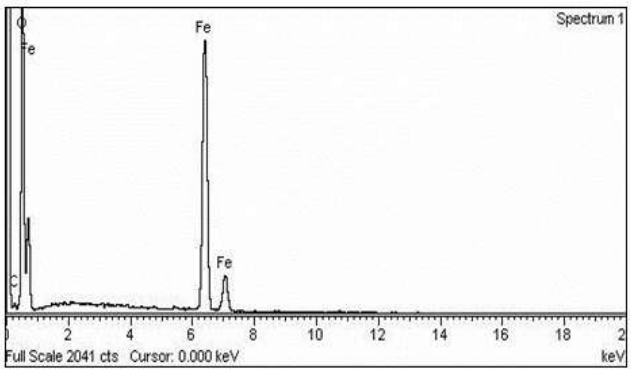

Fig. 4: EDS Spectra for Iron oxide Nanoparticles

The SEM image shows formation of well separated and uniformly distributed nano-particles of α- Fe_2O_3. These nanoparticles exhibit hexagonal symmetry. The Energy-dispersive spectroscopy (EDS) is a useful tool for confirming the atomic percentages of the constituent elements in the prepared sample. Fig. 4 presents the EDS results of the as-prepared α- Fe_2O_3 nanoparticles calcined at 800 °C. It contains the peaks corresponding to only iron and oxygen thereby confirming the purity of the sample.

CONCLUSION

In the present work α-Fe2O3 nanoparticles of various sizes have been successfully synthesized by simple Sol-Gel method. The as-prepared iron oxide nanoparticles show α-Fe2O3 phase and exhibit hexagonal symmetry. The dependence of size on temperature and the corresponding local lattice distortions have been determined.

Conflicts of interest: The authors stated that no conflicts of interest.

REFERENCES

1. Zhan SH, Chen DR, Jiao XL and Liu S. Facile Fabrication of long α-Fe_2O_3, α-Fe and γ-Fe_2O_3 hollow fibers using sol-gel combined co-electro spinning technology. *J. Colliodal Interface Sci*. 308, 2007, 265.
2. Chen J, Xu L, Li W and Gou X. α-Fe_2O_3 Nanotubes in Gas Sensor and Lithium-ion Battery applications. *Adv. Mater*. 17, 2005, 582.
3. Cao SW and Zhu YJ. Hierarchically nanostuctured α-Fe_2O_3 hollow spheres : Preparation, growth mechanism, photocatalytic properties and application in water treatment. *J. Phys. Chem. C* 112 (16), 2008, 6253-6257.
4. Zhang XL, Sui CH, Gong J, Su ZM and Qu LY. Preparation and formation mechanism of different α-Fe_2O_3 morphologies from snowflake to pair Microplates, dumbbell and Spindle microstructures. *J. Phys. Chem.* C 111 (26), 2007, 9049-9054.
5. Gubin SP, Koksharov YA, Khomutov GB and Yurkov GY. Magnetic Nanoparticles: Preparation, Structure and Properties. *Russ. Chem. Rev*. 74, 2005, 489-520.
6. Zhu W, Cui X, Wang L, Liu T and Zang Q. Monodisperse porous pod-like hematite: Hydrothermal Formation, Optical Absorbance and Magnetic Properties. *Mater. Lett*. 65, 2011, 1003-1006.
7. Jacob J and Khadar MA. VSM and Mossabauer study of nanostructured hematite. *J. Magn. Magn. Mater*. 322, 2010, 614-621.
8. Al-Kuhaili MF, Saleem M and Durrani SMA. Optical properties of iron oxide (α-Fe_2O_3) thin films deposited by the reactive evaporation of iron. *J. Alloys and Comp*. 521, 2012, 178-182.
9. Wang LL and Jiang JS. Preparation of α-Fe_2O_3 nanoparticles by high energy ball milling. *Physica B* 390, 2007, 23–27.
10. Jia CJ, Sun LD, Yan ZG, You LP, Han XD, Pang YC, Zhang Z and Yan CH. Single crystalline iron oxide nanotubes. Angew. Chem. Int. Ed. 44 (28), 2005, 4328-4333.
11. Wang X, Zhang L, Ni Y, Hong J and Cao X. Fast Preparation, Characterization, and Property Study of r-Fe2O3 Nanoparticles via a Simple Solution-Combusting Method. J. Phys. Chem. C 113, 2009, 7003–7008.
12. Patterson AL. The Scherrer formula for x-ray particle size determination. Phys. Rev. 1939, 56 (10), 978-982.
13. Bi H, Li S, Zhang Y and Du Y. Ferromagnetic-like Behavior of Ultrafine NiO Nanocrystallites. J. Magn. Magn. Mater. 2004, 277, 363-367.

IRJSE International Research Journal of Science & Engineering
Int. Res. J. of Science & Engineering, 2018; Special Issue A2 : 221-224
ISSN: 2322-0015
SJIF Impact Factor 4.11
UGC Approved Journal No. 63628
RESEARCH ARTICLE **OPEN ACCESS**

Characterization of CdS Thin Film Grown by Chemical Bath Deposition

Sonawane Shivaji M

Head, Department of Physics, Bharatiya Jain Sanghatana's Arts, Science and Commerce Collage, Wagholi, Dist-Pune, Maharashtra, India
Email: sonawaneshivaji77@gmail.com

Manuscript Details
Available online on http://www.irjse.in
ISSN: 2322-0015

Editor: Dr. Arvind Chavhan

Cite this article as:
Shivaji M. Sonawane. Characterization of CdS Thin Film Grown by Chemical Bath Deposition, *Int. Res. Journal of Science & Engineering,* January 2018; Special Issue A2: 221-224.

ABSTRACT

Cadmium sulphide (CdS) thin films were deposited by chemical bath deposition method on glass substrates from aqueous solution. The influence of the solution temperature and pH is investigated in this work. Cadmium sulphate , ammonia and thiourea were used as the source materials for the preparation of the thin films sources. These films were then characterized using UV spectroscopy for studying the optical properties. XRD were used for structural studies. SEM and EDAX revealed the morphological characteristics. The X-ray diffraction (XRD) analysis showed that the prepared CdS films were polycrystalline with hexagonal structure. CdS thin films were obtained with (002) preferred orientation and having crystallite size 50 nm. It was determined from the broadenings of corresponding X-ray diffraction peaks by using Debye Scherrer's formula. Band gap of CdS thin film by UV spectroscopy was 2.42 eV.

Keywords: CdS thin films, UV spectroscopy, SEM and EDAX, Etc..

INTRODUCTION

Cadmium Sulphide is II–VI group binary semiconductor material, widely used as an efficient window layer in thin films based solar cell structures due to its high absorption coefficient, stability, and low resistivity [1].They are used as a window layer in CIGS and CdTe heterojunction based solar cells [5], field effect transistors [10–12], gas sensors [12], photo detectors [10], information storing devices [9] and light emitting diodes. CdS is an n-type of semiconducting material with direct optical bandgap 2.42 eV at room temperature .CdS thin films are prepared bydifferent methods such as spray pyrolysis [2],vacuum evaporation [3], electro deposition [4], sputtering [5] and chemical bath deposition (CBD) [6]. Chemical bath deposition is suitable method for preparing high efficient thin film due to its advantages such as simple, large area films, low temperature and low cost method.Bonding in this compound is a mixture of covalent and ionic types. We have prepared the CdS thin films by chemical bath deposition method on the glass substrate at 70 °C temperature.

CdS has two types of crystal structures- cubic zinc blende and hexagonal wurtzite. The type of structure obtained is depends on deposition parameter such as substrate temperature, pH, concentration of precursor, etc. The investigation of the fundamental properties of CdS thin films is of paramount importance in the understanding and development of modern CdS solar cells. Many researchers have been studying these properties to see how the quality of this layer can be improved for better performance with good optoelectronic properties suitable for photovoltaic applications. The best efficiency recently reported is 22.1% for CdS/CdTe solar cell prepared by vacuum deposition techniques.

METHODOLOGY

The deposition of thin film was carried out by using glass substrate which was initially cleaned by soap solution, double distilled water and ultrasonication. The CdS thin films were deposited in aqueous solution containing 0.1 M cadmium sulphate, 0.1 M Thiourea and ammonia as complexing agent. Add this weighed CdSO4 and ammonia in 50 ml distilled water in the glass beaker and stir this solution continuously for several minutes to become homogeneous solution at moderate rate. Ammonia was added drop by drop in solution to maintain the pH value of the solution is 10 at temperature 70 oC. When the temperature of solution reaches 70oC then adds the thiourea. The cleaned glass substrate was immersed in bath and solution was no stirred during the deposition process. CdS thin film was deposited for 15 minutes then samples were washing under distilled water and dry in air. The CdS thin films obtained were compact, hard, and good adhesion to the glass substrate.
Reaction Mechanism for deposition of CdS thin film

RESULTS AND DISCUSSION

$$CdSO_4 + 4\ NH_4Cl \rightarrow Cd(NH_3)_4^{2+} + Cl^- + 4H_2O$$

$$H_2O \rightarrow H^+ + (OH)^-$$

$$CS(NH_2)_2 + (OH)^- \rightarrow H_2N(COH)NH + SH^-$$

$$Cd(NH_3)_4^{2+} + SH^- \rightarrow \mathbf{CdS} + NH_4^+ + 3NH_3$$

X-ray diffraction Analysis:

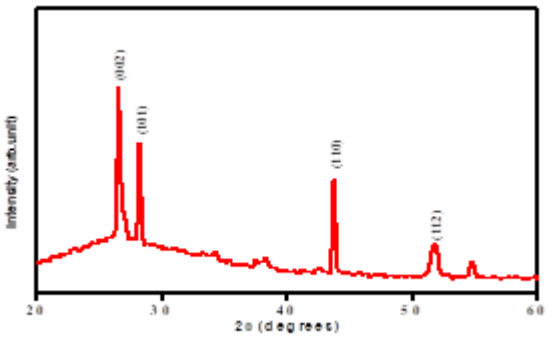

Fig . 1 : XRD Pattern of of CdS thin film

The XRD analysis for as-deposited film has been recorded by X ray diffractometer with scanning angle 20-80 degree using CuKα radiation of wavelength 1.5406Ao. In XRD analysis reveals that a prominent broad peak appear at an angle 2θ = 26.6°, 28.2, 43.7 and 51.8 which correspond to the (002), (101), (110) and (112) planes (JCPDS- 89-2944). The XRD results confirmed that the deposited CdS thin films were polycrystalline in nature with hexagonal structure having (002) plane as the preferred oriented. The

samples deposited at 70 °C have higher peak intensities, indicating better crystallinity. The average crystalline size (t) was calculated using the Debye-Scherrer formula,

$$t = 0.9\lambda/\beta\cos\theta$$

Where λ=1.5409Ao is the X-ray wavelength (CuKα), θ is the Bragg diffraction angle, and β is the full width at half maxima (FWHM) of the XRD peak appearing at the diffraction angle θ=26.6. The average crystallite size was calculated from X-ray broadening peak and Scherer equation was found to be about 50 nm.

Scanning Electron Microscopy (SEM):

Figures show the SEM images of the CdS thin films deposited on glass substrate. Scanning electron microscope (SEM) was used for the morphological study of CdS thin films. Spherical and relatively uniform surface morphology can be clearly seen in as-deposited samples. All the films were compact, uniform and very well adhesive to the glass substrates. The average particle size of CdS thin films was 0.5µm. The bigger grain with less grain boundaries can be obtained by choosing the approximate annealing temperature, ambient condition and annealing time. The as-grown CdS films colour changes with the concentration from greenish yellow to bright yellow.

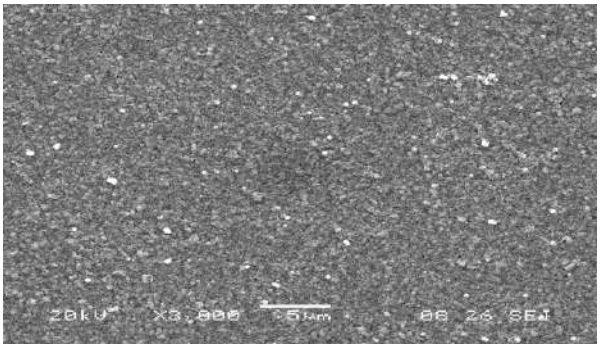

Fig : SEM image of CdS thin film

Energy Dispersive Spectroscopy (EDS):

The elemental analysis of the films was carried out by EDS. The EDS spectra of the CdS thin films confirmed the presence of Cd and S in the thin films. The atomic percentage ratios of Cd: S for samples deposited at 70 °C are 49.74:50.26, which show that the films had a good stoichiometry.

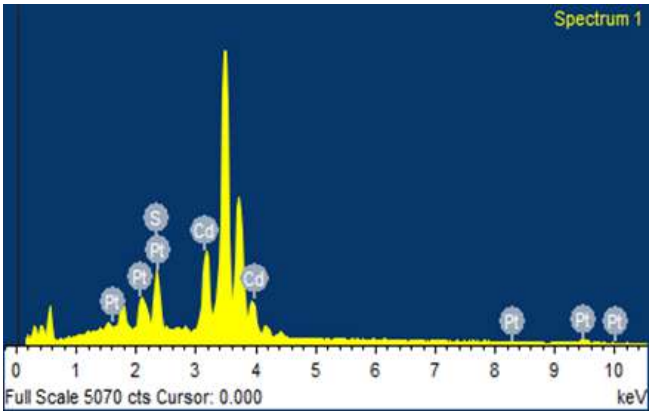

Fig 3. EDS of CdS thin film

Optical Analysis

The optical band gap energy of the semiconductor is an important parameter that plays a major role in the construction of photovoltaic cells. Optical properties of the CdS films were studied in the wavelength ranging from 300 to 800 nm. Figure shows the plots of $(\alpha h\upsilon)2$ versus energy $(h\upsilon)$ for CdS thin films deposited at 70oC. The optical band gap was found to be 2.42 eV (± 0.05) for as-deposited samples.

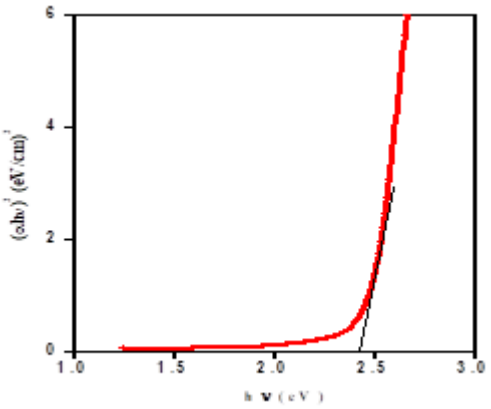

Fig 4. Optical absorption spectra of CdS thin film

CONCLUSION

CdS thin films have been successfully deposited on glass substrates using chemical bath deposition method. XRD results revealed that the films deposited at 70oC were nanocrystalline with hexagonal structure. SEM shows the spherical morphology of films deposited at various concentrations. Uuniform and compact film deposited over the entire substrate. CdS films deposited in presence of ammonia as complexing agent were close to the stoichiometry. The

films have very good stoichiometry with nearly 1:1 cadmium to sulphur ratio. The band gap was estimated is 2.42eV. The band gap of the films was found to be increased upon increasing the concentration of thiourea in the bath.

Conflicts of interest: The authors stated that no conflicts of interest.

REFERENCES

1. Green MA et.al. Prog.Photovoltaic. Res. Appl. 24, 905-913 (2016).
2. Lisco F, Kaminski PM, Abbas A, Bass K, Bowers JW, Claudio G, Losurdo M, WallsJM. Thin Solid Films 582 ,323–327(2015).
3. Bath A. Beggasa,b, B. Benhaouaa, A. Attafb, M.S. Aida c, Optik 127, 8423–843 (2016).
4. Hani Khallaf a, Isaiah O. Oladeji b, Guangyu Chai c, Lee Chow, Thin Solid Films 516, 7306–7312 (2008).
5. Chang YJ, Munsee CL, Herman GS, Wager JF, Mugdur P, Lee DH and Chang CH . *Surf. Interface Anal*. 37,398–405 (2005).
6. Moualkia H, Hariech S, Aida MS, *Thin Solid Films* 518 1259–1262 (2009).
7. Prabhu RR, Abdul Khadar M, *Bull. Mater. Sci*. 31 ,511(2008).

IRJSE International Research Journal of Science & Engineering
Int. Res. J. of Science & Engineering, 2018; Special Issue A2: 225-229
ISSN: 2322-0015
SJIF Impact Factor 4.11
UGC Approved Journal No. 63628
RESEARCH ARTICLE **OPEN ACCESS**

Novel Synthesis of Antimicrobial Cotton Fibers Embedded with Enriched Zinc Chloride Nanoparticles

Sali Nitin and Patil Tushar

Padmashri Vikhe Patil College of Arts, Science and Commerce, Pravaranagar, MS, India
Email: snitind7@gmail.com

Manuscript Details
Available online on http://www.irjse.in
ISSN: 2322-0015

Editor: Dr. Arvind Chavhan

Cite this article as:
Sali Nitin and Patil Tushar. Novel Synthesis of Antimicrobial Cotton Fibers Embedded with Enriched Zinc Chloride Nanoparticles, *Int. Res. Journal of Science & Engineering,* January 2018, Special Issue A2 : 225-229.

ABSTRACT
An attempt is made to synthesisze the cotton fibers embedded with enriched zinc chloride nanoparticles. The Zinc chloride solution was treated with green reducing agent d-glucose in autoclave. Autoclave treatment time was optimized based on single type of particle presence which is followed by microwave radiation cycles for selected time intervals. Synthesized nanoparticles were analysed using UV spectroscopy, IR spectroscopy and Scanning electron microscopy SEM. Purified particles were analyzed for presence of antibacterial and antifungal activity. Cotton fibers were treated in presence of obtained nanoparticles and starch as capping agent. Treated fibers also retained antibacterial activity.

Keywords: zinc chloride nanoparticle, autoclave, microwave treatment, infrared spectroscopy,scanning electron microscopy, antibacterial cotton fibers.

INTRODUCTION

It is wel known fact that the Nanotechnology deals with small structure and small size material of dimension in the range of few nanometers to less than 100 nm (1, 2, 3). Properties like particle size,shape and interparticle interaction of synthesized metal nanoparticles are determined by change in absorbance**.** In synthesis and assembly strategies of nanoparticles precursors from liquids, solids or gas phase are used applying physical and chemical deposition approach (4,5,6). Over the last few decades, the applications of nanotechnology in

medicine have been extensively explored as antibacterial and antifungal agents. The green synthesis of zinc chloride nanoparticles involves three main steps selection of solvent medium, selection of environmentally benign reducing agent, and selection of nontoxic substances (7, 8, 9). Among the many possible natural products, Polysaccharides and biologically active plant products having hydroxyl groups, a hemiacetal reducing end can play important roles in reduction and the stabilisation of metallic nanoparticles (Y. Park Et al Polysaccharides and phytochemicals: a natural reservoir for the green synthesis of gold and silver nanoparticles, IET Nanobiotechnol., 2011). Microwave based synthesis was recent approach for green synthesis (10, 11). In present work d-glucose is used as the reducing agent and starch as the capping agent for zinc chloride nanoparticle synthesis. Cotton fibers are used as the source for embedment. Medicinal application of this present work is tested against the most commonly isolated serotypes of bacteria and fungi.

METHODOLOGY

The synthesis method and optimization of autoclave treatment time for ZnCl nanoparticles:
50 ml 2% starch (Merck Pvt.ltd) solution was prepared. 1mM D-glucose (Merck Pvt.ltd) and 1 mM zinc chloride (Merck Pvt.ltd.) was added in it. This solution was autoclaved at 15 lb/inch^2 pressure for 10, 15 and 20 minutes and analyzed by UV spectroscope (Elico ltd.) followed by addition of 1mM NaOH (Merck Pvt.ltd) to make pH alkaline.

The optimization of Microwave treatment cycles:
Microwave radiation treatment for autoclaved solution was given at 2.45 GHz frequency in domestic microwave oven (LG make). Each cycle consist of 15 second exposure to microwave irradiation followed by cooling time interval of 15 second. Maximum 12 cycles had given. Resulting solution was centrifuged at 14000 rpm for 20 minute followed by washing with 70% ethanol.

Characterization of zinc chloride nanoparticles:
Harvested particles were made into fine powder. This powder was dissolved in double distilled water and analyzed on UV spectrophotometer (Elico make) from 190 nm to 600 nm wavelength ranges followed by FTIR spectroscopy. Powder was also analyzed by using scanning electron microscopy (SEM).

The specific antibacterial and antifungal activity of zinc chloride nanoparticles:
Zinc chloride nanoparticle powder was further analyzed for antibacterial and antifungal activity by disc diffusion test against *Salmonella typhi*, *Klebsiella pneumoniae*, *Staphylococcus aureus* and *Pseudomonas aeruginosa* bacteria and *Rhizopus*, *Candida albicans* and *Aspergillus niger* fungi. Sterile 6mm filter paper disc were aseptically placed on Luria Bertani (LB) agar surface for antibacterial activity and potato dextrose agar for antifungal activity. Sterile disc was soaked in zinc nanoparticle solution for 30 min. After 30 min ,disc were placed on medium .The plates were left at ambient temperature for 15 min to allow excess prediffusion of solution prior to incubation at 37^0 C for 24 hrs for antibacterial activity and 30^{o}C for 48 hrs for antifungal activity. After incubation Inhibition zones were measured.

The preparation of Zinc chloride nanoparticle (ZnClNP) embedded cotton fibers:
The Cotton fibers were cut in small pieces and deeped in solution containing 10mM zinc chloride 1mM glucose, 2 % starch. This solution was autoclaved at 15 lbs/ inch^2 for 15 minutes. After autoclaving solution was cooled to normal temperature. pH of solution was made alkaline followed by 9 cycles of Microwave treatment. Antibacterial activity of cotton fibers was analyzed by incubating the bacteria in presence of treated cotton fibers.

The antibacterial and antifungal activity of ZnClNP embedded cotton fibers:
In this, Liquid culture medium dilution method was used to measure the minimum inhibitory concentration (MIC) for each bacterial and fungal strain using Luria Bertani medium and potato dextrose agar respectively. 900 µL of medium was placed in a sterilized test tube. 1 gm nanoparticle embedded cotton fibers and 10 µl of the cultured bacterial solution (final bacterial count of 1 × 10^6 cfu/ml) were added. The tube was incubated for 48 hrs at 37^{0}C for bacterial growth and 30^{0}C for fungal

growth. No bacterial and fungal growth were observed confirming antibacterial and antifungal action of nanoparticle embedded cotton fibers.

RESULTS AND DISCUSSION

Optimization of autoclave treatment time for zinc chloride nanoparticle synthesis: Present investigation utilizes autoclave assisted microwave mediated synthesis approach with d-glucose as reducing agent. In alkaline condition, Glucose oxidizes itself by reducing zinc chloride solution in water. Comparative zinc chloride nanoparticle synthesis was analyzed by observing the absorbance at 350 nm. Increase in autoclave treatment time showed increase in absorbance at 350 nm. This reaction was performed in autoclave at 15 lb/inch^2 pressure for 15 minute at 121^{0}C.

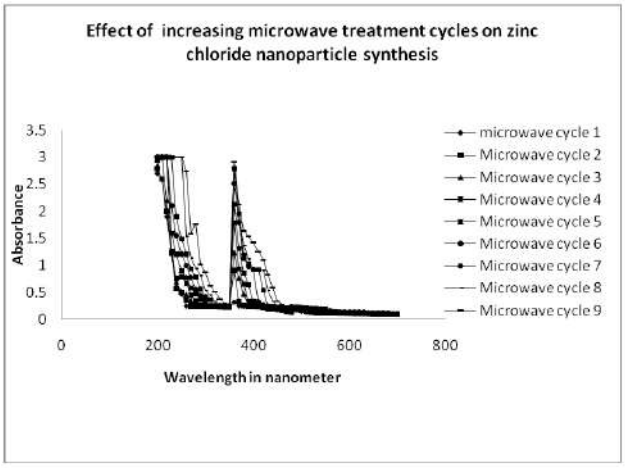

Fig.1

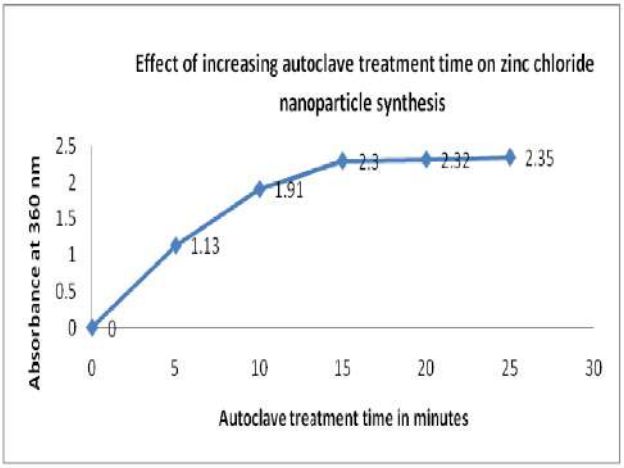

Fig. 2

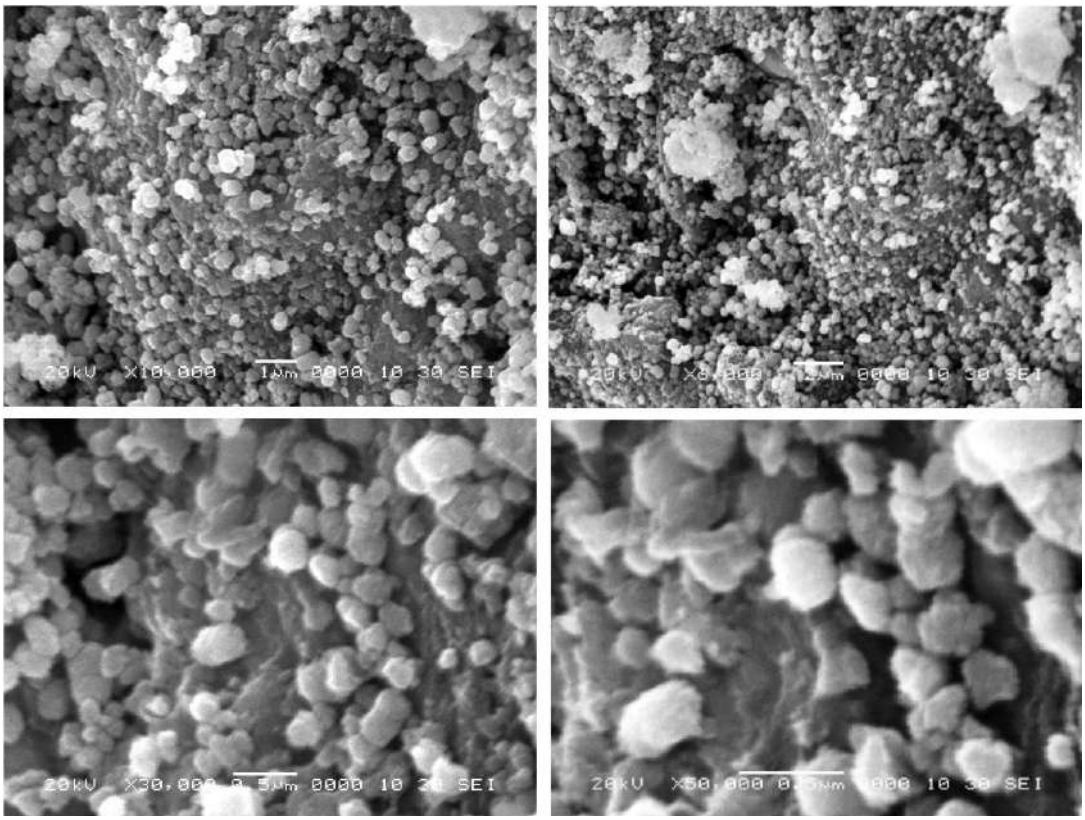

Fig.2 SEM image of synthesized zinc chloride nanoparticles

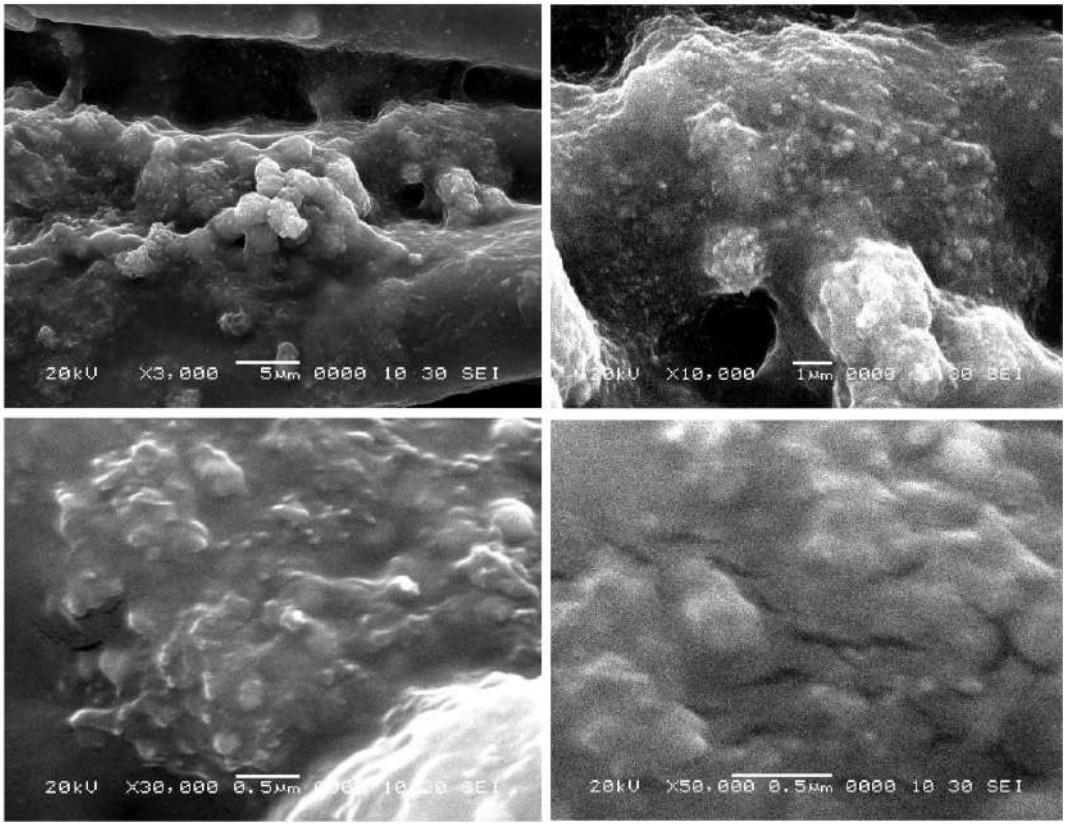

Fig. 3 : SEM image of treated fiber

	5ppm*	10 ppm	15ppm
Name of bacteria	Zone of inhibition (diameter in mm)		
Salmonela typhi	11mm	15mm	22mm
Staphyloccus aureus	03mm	04mm	07mm
Psudomonas aurogenosa	12mm	23mm	28mm
Klebsiella	4mm	9mm	16mm
Name of fungus			
Rhizopus	12mm	19mm	24mm
Candida albicans	14mm	17mm	25mm
Aspergillus niger	7mm	9mm	16mm

*1ppm zinc chloride nanoparticle solution was prepared by dissolving 1miligram of zinc chloride nanoparticle powder in 1000ml of double distilled deionized water.

Optimization of Microwave treatment cycles for zinc chloride nanoparticle synthesis:

Microwave treatment cycle was optimized at 9 cycles each comprising of 15 second duration. Treated samples showed maximum absorbance at 350 nm Each Microwave treatment cycle showed significant absorbance of autoclaved zinc chloride solution at 350 nm. Figure 1 shows the zinc chloride nanoparticle synthesis as increase inmicrowave treatment cycle confirming presence of zinc chloride nanoparticles.

FTIR Characterization

The spectrum in the range 300-4000 cm^{-1} was showing IR absorption due to the various vibrations involved. The FT-IR report of the synthesized zinc nanoparticles showed the fingerprint region peaks at 441.71, 497.86, 515.01 cm^{-1} was attributed to the ZnCl stretching mode frequency, 705.97, 731.05, 859.42 cm^{-1} due to 3, 6-anhydro - β- galactose skeletal bending in starch, 1014.59, 1134.18 cm^{-1} corresponds to the ester-sulfate link vibration, 1228.7 cm^{-1} due to C-O stretching,

1319.35 cm^{-1} due to C-H stretching, 1425.44 cm^{-1} due to C=O ring stretching and significant peaks at 1626.05 cm^{-1} corresponds to O-H bending of absorbed water, 2430.39, 2895.25 cm^{-1} due to carboxylic acid O-H stretch, 3255.95 and 3540.14 cm^{-1} corresponds to alcohol phenol O-H stretch associated with starch. All the obtained peaks indicate that the ZnCl nano particles are embedded in the starch matrix.

SEM analysis

Scanning Electron Microscopy (SEM) is used for the morphological studies of the ZnCl nano particles and starch embedded ZnCl nano particles . This characterization was done at the medium energy electrons in the range 5-50Kv in a fine beam scanning the specimen. Both X-rays and secondary electrons are emitted by the sample. SEM image of synthesized zinc chloride nanoparticles is shown in figure 2. SEM images confirmed synthesis of nanoparticles with size ranging from 50 nm to 100 nm.Figure 3 show the SEM images of ZnCl – starch nanocomposite at different magnifications. The SEM observation clearly illustrates that the Zinc chloride nanoparticles are formed in agar matrix varying in size from 50 nm – 100 nm. The low-magnification images demonstrate that the ZnCl nanoparticles are dispersed in the starch matrix (Figure 3)

The antimicrobial activity of zinc chloride nanoparticles

Antimicrobial activity of zinc chloride nanoparticles was observed as zone of inhibition. Table 1showed antibacterial and antifungal activity of Zinc chloride nanoparticles at varying concentration. ZnClNP inhibited growth of all selected bacteria and fungi. In bacteria, *Psudomonas aurogenosa* showed maximum zone of inhibition and *Staphyloccus aureus* showed minimum zone of inhibition while in fungi, *Candida albicans* showed maximum zone of inhibition and *Aspergillus niger* showed minimum zone of inhibition. Stability in inhibition activity further remained for more than 6 months.

Antimicrobial activity of zinc chloride nanoparticle embedded cotton fibre

SEM image of treated fiber (Fig. 4) further confirmed embedment of synthesized zinc chloride nanoparticles Treated cotton fibers showed significant inhibition activity against all selected bacterial and fungal pathogens.

Conflicts of interest: The authors stated that no conflicts of interest.

REFERENCES

1. Karch J, Birringer R and Gleiter H, *Nature*, 330 (1987) 556.
2. Gotoch A, Ikasaki F, *J Mat. Sci. let*, 1996; 15:881-882.
3. Madhukumar P, Balsubramanian C, Sali ND, Bhoraskar SV, Rohatgi VK, Badrinayanan S. Mat. Sci. Eng B63 (1999) 215-227.
4. Special Ceramic Proceeding Issue J AICHE 43.
5. Andrievski RA, *J. Matt. Sci*.29(1994) 614;
6. Gleiter H, Prog. Mat. Sci.33(1989)223.
7. Jing Chen, Jing Wang, Xin Zhang, Yeling Jin, Microwave-assisted green synthesis of silver nanoparticles by carboxymethyl cellulose sodium and silver nitrate, Materials Chemistry and Physics, 2008; 108, 421–424.
8. Jongnam Park, Jin Joo, Soon Gu Kwon, Youngjin Jang, and Taeghwan Hyeon, Synthesis of Monodisperse Spherical Nanocrystals, DOI : 10.1002/anie.200603148.
9. An-Hui Lu, E. L. Salabas, and Ferdi Schth, Magnetic Nanoparticles: Synthesis, Protection, Functionalization, and Application, DOI: 10.1002/anie.200602866.
10. Mikhail Soloviev, Nanobiotechnology today: focus on nanoparticles, Journal of Nanobiotechnology 2007, 5:11 doi: 10.1186/1477-3155-5-11.
11. Xueqing Zhang, Qin Guo and Daxiang Cui, Recent Advances in Nanotechnology Applied to Biosensors, Sensors 2009, 9, 1033-1053; doi:10.3390/s 90201033.
12. Virender K. Sharma, Ria A. Yngard, Yekaterina Lin, Silver nanoparticles: Green synthesis and their antimicrobial activities, Advances in Colloid and Interface Science 145 (2009) 83–96)

IRJSE International Research Journal of Science & Engineering
Int. Res. J. of Science & Engineering, 2018; Special Issue A2 : 230-236
ISSN: 2322-0015
SJIF Impact Factor 4.11
UGC Approved Journal No. 63628
RESEARCH ARTICLE **OPEN ACCESS**

Synthesis, Characterization and Gas sensing properties of Cu surface modified BaTiO3 thick films

Nahire SB[1], Patil GE[2], Jain GH[2], Gaikwad VB[3], Deshmukh Sushant B[4]

[1]Department of Physics, Arts, Science and Commerce College, Ozar (Mig) Nashik 422103, India 422 206,[2]Dept of Physics, SNJB's KKHAArts, SMGL Commerce & SPHJ Science College, Chandwad 423101, India,[3] Prin. Dept. of Chem. KTHM College , Nashik 422 005,[4]Department of Physics, JES College, Jalna 431203, India
Email: nahiresandip@gmail.com

Manuscript Details
Available online on http://www.irjse.in
ISSN: 2322-0015

Editor: Dr. Arvind Chavhan

Cite this article as:
Nahire SB, Patil GE, Jain GH , Gaikwad VB, Deshmukh Sushant B. Synthesis, Characterization and Gas sensing properties of Cu surface modified BaTiO3 thick films, *Int. Res. Journal of Science & Engineering*, January 2018; Special Issue A2: 230-236.

ABSTRACT

Barium titrate oxide ($BaTiO_3$) is synthesized by co-precipitation method with surface modification by Cu to improve the sensitivity and tailoring the operating temperature, when the surface modified thick films are exposed to H_2S. The thick film sensor is prepared by screen printing technique. Then $BaTiO_3$ thick films are surface-modified by Cu, using cupric acid. Influence of Cu on the film phase composition, microstructure and sensing characteristics is discussed. Dynamic response properties show that the operating temperature of the surface modified $BaTiO_3$ thick film is at 100 ^oC, which is about 250 ^oC for pure $BaTiO_3$. Response time of the sensor is about 10 s while recovery time is 30 s. The selectivity of the sensor elements for H_2S against different gases was also discussed.

Key words: Cu, BaTiO3 thick films, XRD

INTRODUCTION

Semiconductor metal oxides as gas sensing materials have been extensively studied for a long time due to their advantageous features, such as good sensitivity to the ambient conditions and simplicity in fabrication [1–3]. Nevertheless, there are still some critical limitations to be overcome for the commercial sensors based on particulate or thin-film semiconductor metal oxides, such as limited maximum sensitivity, high working

temperatures and lack of long-term stability. Recently, several groups reported the sensors based on semiconductor nanowires and nanoribbons. Barium titanate (BaTiO3) is a perovskite ferroelectric oxide, barium titanate (BaTiO3) have been extensively investigated, affording wide applications in devices such as thermistors [4], multilayer ceramic capacitors (MLCCs) [2], electro-optic devices [3], and dynamic random access memories (DRAM) [4]. Doped barium titanate has found wide application in semiconductors, positive temperature coefficient resistors, ultrasonic transducers, piezoelectric devices, and has become one of the most important ferroelectric ceramics. Large number of different dopants can be accommodated in the BaTiO3 lattice, therefore, doping of BaTiO3 ceramics is very important to obtain required characteristics for its applications in Hydrogen sulphide gas is harmful to human body and environment. The threshold limit value (TLV) defined for H2S is 10 ppm. Human exposure to H2S gas at level higher than 250 ppm are likely to result in neurobehavioral toxicity and may even cause death[6]. Metal oxide semiconductor gas sensors have advantageous features such as high response under ambient conditions, low cost and simplicity in fabrication [7, 8]. The sensor performance can be improved by increasing the porosity. The fundamental sensing mechanism of metal oxide based gas sensors relies on change in electrical conductivity due to the interaction process between the surface complex such as O-, O2- , H+ , OH+, reactive chemical species and the gas molecules to be detected [9]. Semiconductor BT is sensitive to many sets of gases and has high satisfactory stability, but it has some disadvantages, such as high working temperature of 400^{o}C–500 ^{0}C; poor gas selectivity and comparatively low response. Furthermore, it has also been reported that the gas response and selectivity of semi-conductive complex oxides can be influenced by dipping or doping. Some workers discovered that complex oxides exhibit good response to reducing gases [8,9]. Metal oxide gas sensors are stable at high temperature [8]. Sensing principle is based on the change in the electrical resistance of semiconductor oxide films when specific gas interacts with its surface [9]. Gas sensitivity, selectivity and durability are the most important sensor properties [10-11]. High gas sensitivity is the key factor in detecting gases at very low concentrations; for example, leakage of a harmful gas in a work environment should be detected as early as possible. It has been suggested that gas sensitivity can be enhanced by controlling the microstructure of thin films of the sensing material, e.g., dispersing small pores at the grain boundaries or decreasing the grain size [12,13]. Gas selectivity is another very important indicator that measures the ability of a sensor to precisely identify a specific gas in a mixture of a several gases [14]. To improve the gas selectivity, microstructure control and doping of hetero component are known to be effective, because active sites for particular gas species can be produced. $BaTiO_3$ has been mainly studied in bulk or thick film form as a material for gas sensing. Following this consideration, the aim of the present work is to study the gas sensing properties of $BaTiO_3$ materials surface modified in the solution $CuCl_2$.

METHODOLOGY

Synthesis of BT and preparation of BT thick films: BaTiO3 fine submicron powders were prepared from $Ba(OH)_2$ and $TiCl_4$ using a co-precipitation process. The titanium precursor was slowly introduced in a strong basic $Ba(OH)_2$- NaOH aqueous solution (pH>13) kept at 100 ^{o}C. After 6 h ageing at 100 ^{o}C, the powder was washed with distilled water until Cl ions were completely removed from the supernatant. The powder was further annealed at 600 ^{o}C for 2 h. The details of preparation are described elsewhere [11]. The as-prepared powder, characterized by XRD, scanning electron microscopy, UV-visible spectroscopy. The XRD spectrum of as prepared powder confirmed the sub-microcrystalline perovskite phase. The thixotropic paste was formulated by mixing the fine powder of BT with a solution of ethyl cellulose (a temporary binder) in a mixture of organic solvents. The ratio of the inorganic to organic part was kept at 75:25 in formulating the paste. This paste was screen printed [12-13] on a glass substrate in a desired pattern. The films were fired at 550 ^{o}C for 30 min.

Preparation of Cu surface modified BT thick films: The screen is held at about a few mm above the substrate on a printing set up. The required paste is poured on the top surface of the stencil and squeegee

pushed the paste through the opening while it is passed from one end to the other. Any paste for electronic thick film passive component or sensing element contains at least two ingredients: an organic vehicle and functional material or active ingredient. The thick films of BT from as-prepared powders were surface modified with Cu by dipping of BT thick films in an aqueous solution of the copper chloride. In order to compare gas sensing performances, thick films were dipped for different interval timing as 5 min, 10 min, 15 min. 20 min and 30 min and referred respectively as CuBT1, CuBT2, CuBT3, CuBT4 and CuBT5. These films were dried at 100 °C, followed by firing at 550 °C for 30 min and then used for further characterization such as UV-visible spectroscopy, scanning electron microscopy, XRD and tested their gas sensing properties. After annealing, the concentration of Cu (mass %) on the surface of the films was determined by EDX. These surface modified films are termed as 'Cu-modified BT' (CuBT) films

RESULTS AND DISCUSSION

1. X-ray diffraction (XRD) analysis

Figures 1 and 2 shows the x-ray diffraction pattern of the samples modified with different Cu content of CuBT1, CuBT2, CuBT3, CuBT4 and CuBT5. It can be found that the positions and intensities of the diffraction peaks are similar and no secondary phases were observed. All the above patterns of XRD show the single phase tetragonal system and similar to that of standard pattern of JCPDS of pure $BaTiO_3$ [14]. It indicates that influence of CuO did not affect the structural properties.

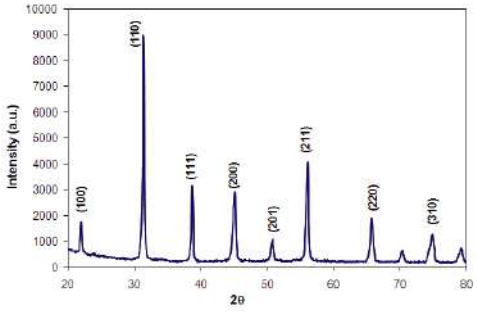

Fig. 1: X-ray diffraction pattern of pure BT

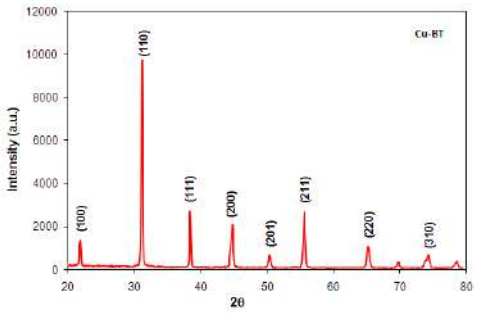

Fig. 2: X-ray diffraction pattern of CuBT4 sample

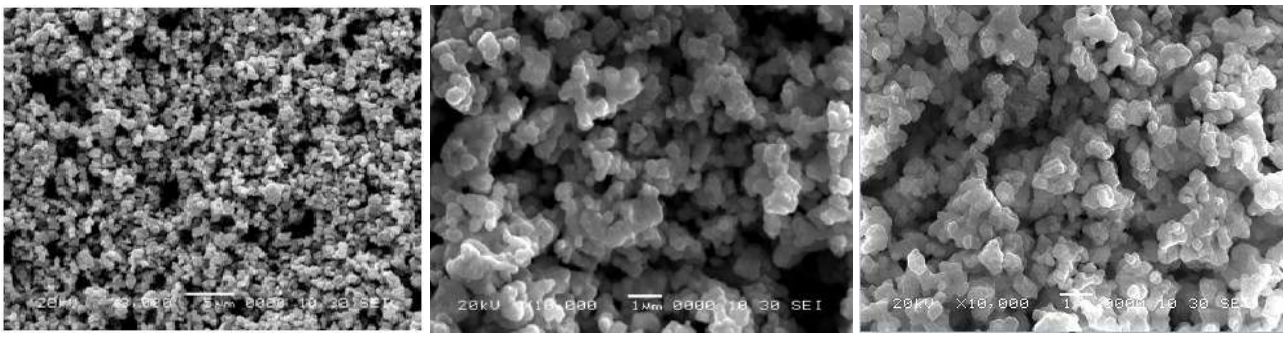

(a) Pure BT (b) CuBT 5 min (c) (c) CuBT 10 min

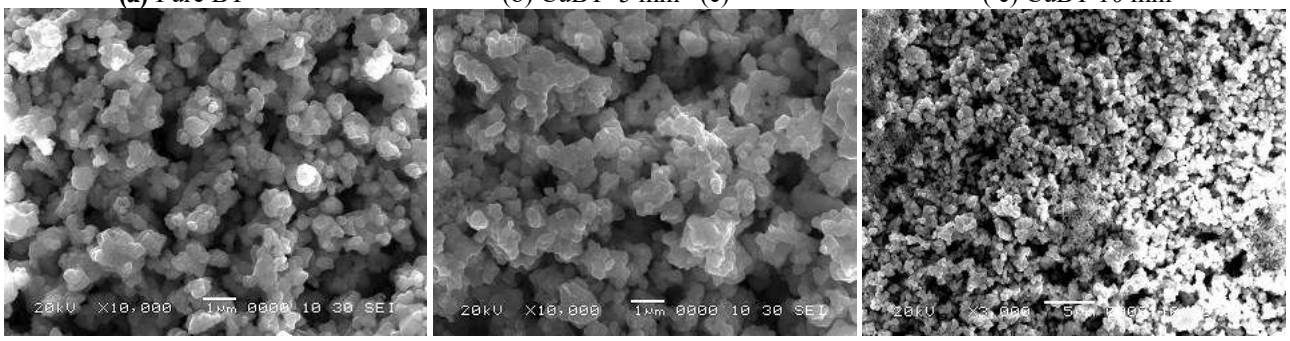

(d) CuBT 15 min (e) CuBT 20 min (f) CuBT 30 min

Table 1: Quantitative elemental composition of pure BT and surface modified Cu-BT thick films.

Element	Pure BT mass %	CuBT1 mass %	CuBT 2 mass %	CuBT3 mass %	CuBT4 mass %	CuBT5 mass %
O	16.38	15.89	15.35	15.81	15.66	14.34
Ti	12.04	10.74	9.31	10.10	9.75	6.90
Ba	71.58	72.09	72.72	70.87	70.17	74.61
Cu	-	1.28	2.62	3.21	3.41	4.64
Total	100	100	100	100	100	100

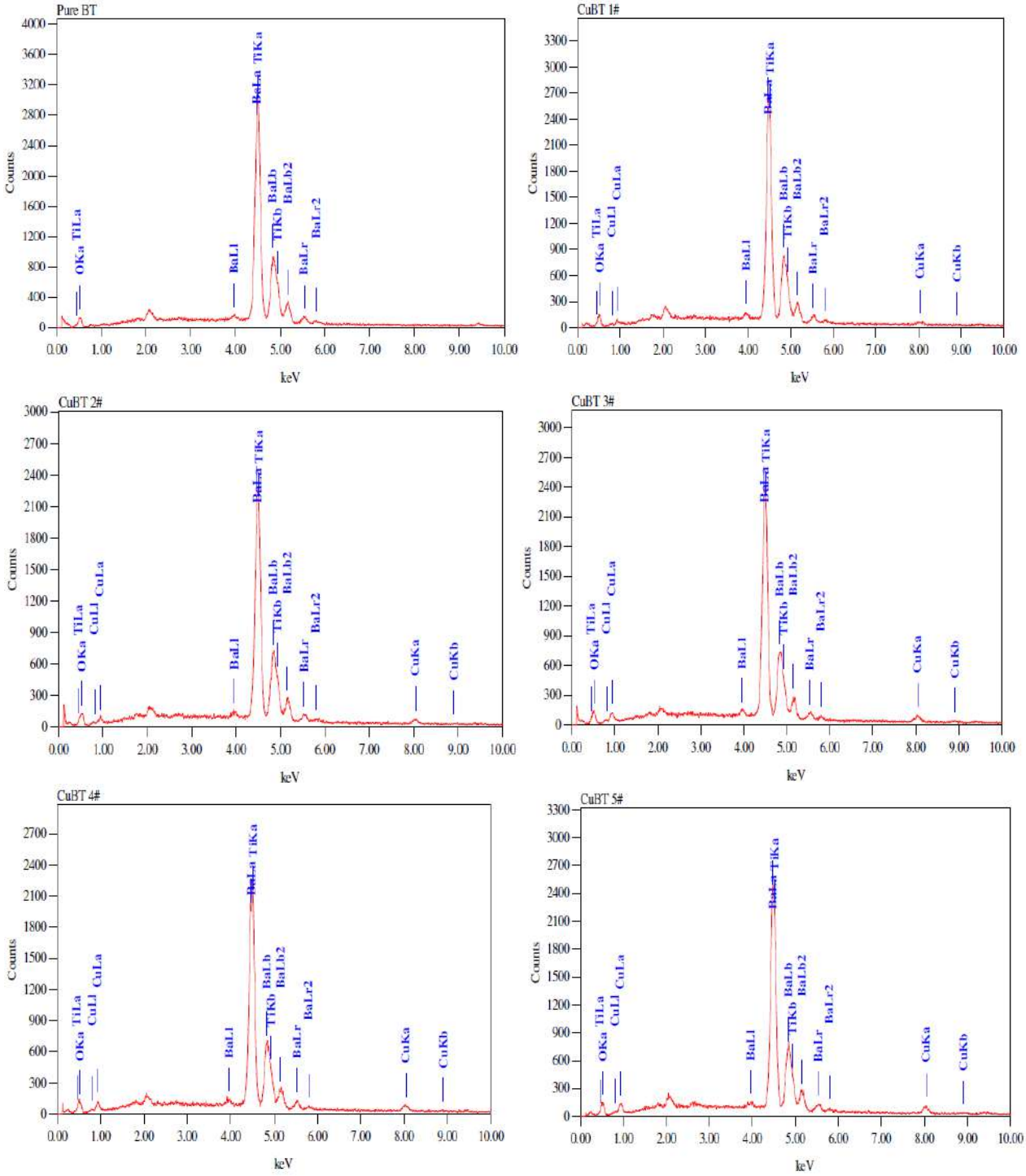

Fig.4 (a-f): EDX spectra of pure BT and surface modified by Cu BT thick films

3.2 Surface morphology by SEM and elemental composition by EDX analysis

The microstructure with surface morphology and the composition analysis were investigated using scanning electron microscope (SEM) with energy dispersion X-ray spectroscope attached. The compositional analysis was carried out at different spots on the samples. The SEM images of pure BT and surface modified BT thick films are shown in Fig. 3. From the SEM micrographs it is clear that grain distribution was uniform with porosity throughout the samples surface. The surface modified porous films which can be advantageous for gas sensing (Fig. 3(b-f)). The top surface of the sensors modified from Cu Fig. 3 (b-f) looks more porous compared to that pure BT.

The quantitative elemental composition of the pure and Cu modified BT films was analysed using an energy dispersive spectrometer and atomic percentage (mass %) of Ba, Ti, O and Cu are represented in Table 1. All samples were observed to be oxygen deficient. Also, the films dipped in Cu were observed to be most oxygen deficient than the pure BT film. It is clear from Table 1 that the mass % of Cu goes on increasing and mass % of oxygen goes on decreasing with the dipping time.

3.2.2 Optical properties by UV-visible spectroscopy

UV-visible absorption spectra were used to estimate the band gap of BT and surface modified BT thick films. The spectra were obtained using a UV-VIS spectrometer (UV-2500PC, SHIMADZU). Fig. 4 shows variation of absorbance with wavelength for samples pure BT, CuBT1, CuBT2, CuBT3, CuBT4 and CuBT5. The absorption at higher wavelengths in the visible region is low and at wavelength 350-410 nm an intense absorption can be seen for modified samples.

The value of absorption coefficient (α) is of the order of 10^3 cm^{-1}. The band gap of the films corresponding to samples pure BT, CuBT1, CuBT2, CuBT3, CuBT4 and CuBT5. were calculated by plotting the graph of $(\alpha h\nu)^2$ verses hν using the relation,

$$\alpha h\nu = A\,(h\nu - Eg)^{n}, \qquad (2)$$

where α is absorption coefficient, A is constant, Eg is band gap energy, hν is photon energy and n is constant.

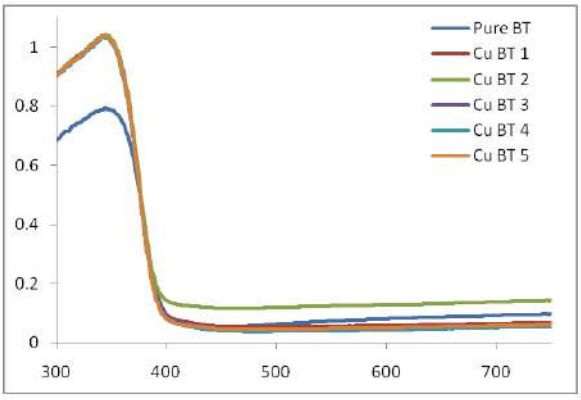

Fig. 5: Variation of absorbance with the wavelength for pure BT, CuBT1, CuBT2, CuBT3, CuBT4 and CuBT5.

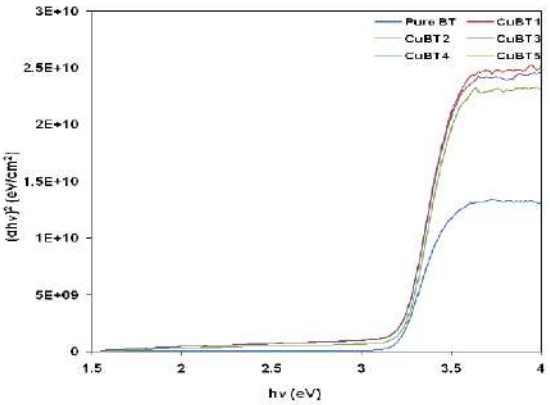

Fig. 6: Plot of the $(\alpha h\nu)^2$ verses photon energy (hν)

The value of n is 1/2 or 2 depending on presence of the allowed direct and indirect transitions. The variation of $(\alpha h\nu)^2$ with hν, shown in Fig. 5, has a straight line portion indicating that the transition involved is direct [15]. The direct band gap, determined by extrapolating the straight line portion to the energy axis to $(\alpha h\nu)^2 = 0$, is found to be 3.20 eV for pure BT. The intercepts on energy axis gives the value of band gap energy for all the modified samples and found to be 3.2210 to 3.2434 as given in Table 4. Notably, the band gaps of all CuBT films were larger than that of the pure BT thick film. There is only slight change observed in band gap energy for samples with increasing dipping time of BT thick films in Cu.

Table 2: Band gap energy pure and modified BT thick films.

Sample	Band gap (eV)
Pure BT	3.20
NBT1	3.2210
NBT2	3.2215
NBT3	3.2321
NBT4	3.2445
NBT5	3.2434

3.2. Electrical conductivity

Fig. 7 represents the variation of conductivity with temperature for the pure $BaTiO_3$ and CUBT films. The legends suffixed 5, and 15' are the graphs for the conductivities of the films in the air ambient, while legends suffixed '10, 30 and 20 are the graphs for conductivities of the films in the H_2S gas ambient. It is clear from the graphs that the conductivity is varying approximately linearly with temperature for all films. The conductivity of CuBT films was observed to be increased.

3.3. Temperature dependence of sensitivity of pure and modified BT thick films to H_2S Gas sensing properties of pure and modified BT thick films

The sensor was placed in a gas test chamber, exposed to gases. The properties of the investigated sensor were determined by the measurements of sensitivity S. This parameter was defined as the ratio of sensor electrical conductance in air (Ia) to that containing detected gas (Ig) [15]. The sensitivity depends on factors, such as morphology, dopants and their concentrations, thickness of film and operating temperatures. We tested sensitivity of pure BT and Cu surface modified BT thick films towards various reducing and oxidizing gases, such as H_2S, H_2, CO_2, CO, liquid petroleum gas, Cl_2, NH_3 and ethanol vapors. All the samples showed maximum sensitivity to H_2S gas. Fig. 8 shows the sensitivity of the pure BT, CuBT1, CuBT2, CuBT3, CuBT4 and CuBT5 sensor element as a function of operating temperature to H_2S gas for 100 ppm. It is seen that the sensitivity changes significantly with the operating temperature. It increases with increasing temperature and reaches a maximum at around 250 °C for pure BT. It has been observed in the present investigation that increasing the dipping time of the BT thick films in $CuCl_2$ solution and thereby increasing the Cu coating on surface improves the sensor sensitivity quite significantly. For modified thick film (CuBT3) a remarkable sensitivity towards H_2S gas is observed at 150 °C operating temperature. It is found that in comparison to CuBT1, CuBT2, CuBT3, CuBT4 and CuBT5shows highest sensitivity towards H_2S gas. Selectivity or specificity is defined as the ability of a sensor respond to a certain (target) gas in the presence of other gases [15]. Fig. 9 the shows a histogram of pur BT and CuBT3 selectivity towards 100 ppm of H_2S and 1000 ppm of other test gases such as H_2, CO_2, CO, liquid petroleum gas, Cl_2, NH_3 and ethanol vapors at 150 °C.

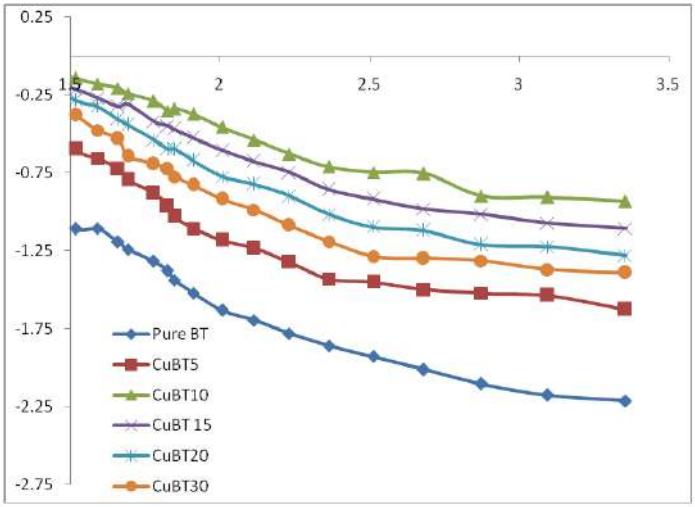

Fig 7 : Variation of electrical conductivity with temperature

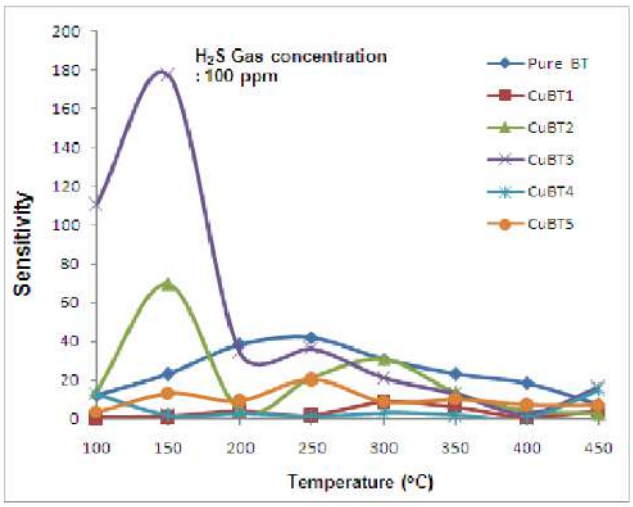

Fig. 8: Variation of sensitivity of pure and modified BT thick films with operating temperature

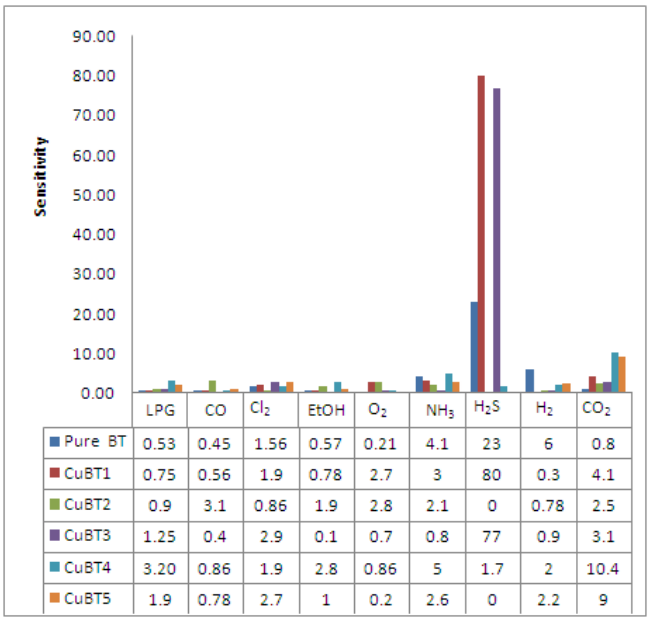

	LPG	CO	Cl_2	EtOH	O_2	NH_3	H_2S	H_2	CO_2
Pure BT	0.53	0.45	1.56	0.57	0.21	4.1	23	6	0.8
CuBT1	0.75	0.56	1.9	0.78	2.7	3	80	0.3	4.1
CuBT2	0.9	3.1	0.86	1.9	2.8	2.1	0	0.78	2.5
CuBT3	1.25	0.4	2.9	0.1	0.7	0.8	77	0.9	3.1
CuBT4	3.20	0.86	1.9	2.8	0.86	5	1.7	2	10.4
CuBT5	1.9	0.78	2.7	1	0.2	2.6	0	2.2	9

Fig. 9: Selectivity pure and modified BT thick films.

CONCLUSION

1. Pure BT. thick films were prepared by screen printing technique
2. Pure BT thick film showed maximum sensitivity to H_2S at 250°C for 100 ppm concentration.
3. Cu surface modified BT thick films were prepared by dipping pure Fe2O3 thick films in a 0.1M aqueous solution of cupric chloride for different intervals of dipping time of 5, 10, 20, 30 and 45 min.
4. SEM images of the films reveal surface morphology of the film. The grains found loosely connected with narrow size distribution which may be because of the final thermal treatment performed at 550 °C.
5. Elemental analysis shows that the film with dipping time 30 min is more oxygen (21.17) deficient and at the same time it is the one having highest wt% of Cr (8.34).
6. The surface-modified BT sensor showed larger sensitivity to H_2S gas (100 ppm) at 150°C.
7. Cu on the surface of the film shifts the reactivity of film from higher operating temperature to lower operating temperature.
8. Cu modified BT thick film with dipping time 20 minutes showed notable gas response (26.3458) to ethanol (300 ppm) at 350 oC as well as to H2S (gas response = 7.86) at same temperature.
9. The sensor showed good selectivity to H_2S against LPG, NH_3, H_2, CO, CO_2 and Cl_2.

Conflicts of interest: The authors stated that no conflicts of interest.

REFERENCES

1. Hennings D, Klee M, Waser R. Adv Mater 1991;3:334–40.
2. Mori M, Kineri T, Kadono K, Sakaguchi T, Miya M,Wakabayashi H, Tsuchiya T. J Am Ceram Soc 1995;78:2391–4.
3. Kingon AI, Streiffer SK, Basceri C, Summerfelt SR. MRS Bull 1996;21:46–52.
4. Nowotny J, Rekas M. Solid State Ionics 1991;49:135–54.
5. Buscaglia MT, V. Buscaglia, M. Viviani, P. Nanni, M. Hanuskova, "Influence of Foreign Ions on the Crystal Structure of BaTiO3", J. Eur. Ceram. Soc., 20 (2000) 1997–2007.
6. Kasap S, Capper P. Thick Films, Springer Handbook of Electronic and Photonic Materials, 2006.
7. Toan NN, Saukko S, Lantto V. Physica B 2003;327:279.
8. Wang, Yee SS, Carey WP. Sens Actuat B 1995; 24:454.
9. Dayan NJ, Karekar RN, Aiyer RC, Sainkar SR. J Mater Sci 1997;8:277.
10. Reddy MHM, Chandarkar AN. Thin Solid Films 1999;349: 260.
11. Jain GH, Patil, L.A. Gas sensing properties of Cu and Cr activated BST thick films 2006 Bulletin of Materials Science 29(4) 403-411
12. Shinde SD, Patil GE, Kajale DD, Gaikwad VB and Jain GH. International Journal on Smart Sensing and Intelligent System Vol. 5, No. 1, March 2012, pp. 57-70.
13. Chavan DN, Gaikwad VB, Kajale DD, Patil Ganesh E, Jain GH, Journal of Sensors, Volume 2011, Article ID 824215, 8 pages doi:10.1155/2011/824215.

IRJSE *Int. Res. J. of Science & Engineering,* 2018; Special Issue A2 : 237-240 SJIF Impact Factor 4.11
ISSN: 2322-0015 UGC Approved Journal No. 63628
RESEARCH ARTICLE **OPEN ACCESS**

Synthesis and Characterization of Cds on Glass by Chemical Bath Deposition Method

Shinde Priyanka and Bhise RB

Department of Physics, B. J. College, Ale, Tal: Junnar, Dist: Pune 412411, MS, India
Email: priyanka20591shinde@gmail.com , bhiseramesh@gmail.com

Manuscript Details
Available online on http://www.irjse.in
ISSN: 2322-0015

Editor: Dr. Arvind Chavhan

Cite this article as:
Shinde Priyanka and Bhise RB. Synthesis and Characterization of Cds on Glass by Chemical Bath Deposition Method, *Int. Res. Journal of Science & Engineering,* January 2018; Special Issue A2: 237-240.

ABSTRACT
Synthesis of CdS was monitored by scanning the spectrum of material from 200 to 800nm by using glass as blank. The fundamental properties of CdS thin film, prepared using CBD method were investigated. UV-Visible spectroscopy analysis was performed at room temperature with last cuvette of 1 cm path length as a sample holder. The maximum absorbance was observed at 620nm which indicated the synthesis of CdS. The band gap energy is calculated and it is found to be 2.39eV. Which is in good agreement with theoretical band gap values of CdS is 2.4eV. XRD pattern clearly illustrated that, the CdS synthesized by the present method were slightly crystalline in nature. The crystalline size is found to be approximately 30nm. The morphology and the size of the synthesized CdS were determined by SEM image. The smaller grains are distributed all over the structure in uniform size distribution. The properties studied include thickness, bandgap, crystal structure and morphology energy of CdS thin film were determined.

Keywords: CdS synthesis,CBD Method,SEM image.

INTRODUCTION

Thin film technology has drawn a considerable amount of interest after its application in different electronic, optoelectronic and photovoltaic device application. Research has been going on this field for quite some decades now but it's slowly picked up the place in the last quarter especially in photovoltaic and optoelectronic sector due to the demand and need of renewable energy

resources uses in recent years. Initially, with respect to the photovoltaics research, it all began when Einstein discovered the photoelectric effect during the 1900. But device fabrication applications started to emerge during the sixties with the CdS/Cu2S binary structures being a possible candidate for optoelectronics and thin film applications, subsequently followed by the heterojunction ternary structures of CdS/CZT & CdS/CuInSe2 era. However, currently in the twenty first century a whole new gamut of organic and inorganic materials has come up for PV & other branches of electronics related research. It is proving to be an exciting and challenging time for researchers ushering a newera for electronics as experimentations are going on presently all over the world with different methods of fabrication methodologies to produce a cheap, sustainable, environment friendly, high efficiency solar cell and other Nano electronic devices. In recent years, there has been growing interest in II-VI semiconductor materials for their potential applications in optoelectronic and photovoltaic industries. One of the most promising alternative materials is a cadmium sulphide (CdS) thin film, which is a chalcogenide n-type semiconductor having a direct energy band gap between 2.28 eV and 2.45eV. Owing to its interesting structural, optical and electrical properties that are much different compared to bulk materials, these films can be applied to many technologies such as window layer in solar cells, optical sensors, transistors, diodes, etc. Various methods such as electro-deposition, spray pyrolysis, successive ionic layer adsorption and reaction (SILAR), pulsed laser deposition, vacuum evaporation and chemical bath deposition (CBD), etc. are used to obtain CdS thin films. Among these fabrication methods, CBD is known as the simplest and most economical method for the large-area productions in obtaining semiconductor thin films. It is well known that CdS thin films may be exist in either cubic or hexagonal phase or as a mixture of bath phases depending on many factors including deposition technique. The difficulty in the formation of monocrystalline CdS thin films stems from a strong self-compensation effect due to sulfur cacncies and the depth of the acceptor level in CdS. Therefore, it is very important to var morphological, optical and electrical properties of CdS thin films by adjusting the grain size for technological applications using low cost and an easy method. Hence, nanocrystal line CdS thin films are deposited on glass substrates using CBD method.

METHODOLOGY

a) Cleaning of substrates:

Glass slides of dimension 75 mm x 5 mm x 1.1mm were used as substrate. The substrates were cleaned in the freshly prepared piranha solution (3:1 mixture of conc. (H_2SO_4 and H_2O_2)). The substrate was kept in the solution for 20 to 30 minutes. It removed all the dust and organic substances. After removing the glass substrates from the mixture, they were washed thoroughly in running tap water and then in distilled water. Finally, they were dried and stored for future uses.

b) Preparation of the bath solution:

Two washed beakers (say b1 and b2) were taken, each were filled with 100ml of deionized water. In bl, 0.48 gm of cadmium chloride (NH_4Cl_2) were taken. In b2, 2.24gm of thiourea ($(NH_2)_2CS$) was taken. Both the solutions were heated separately to about 40^0 C and then mixed together with constant stirring. To the resultant solution, liquid ammonia solution (NH_4OH) was added dropwise to raise the Ph between 10.5 and 11.

c) Chemical reactions involved:

The preparation of cadmium sulfide involves the reaction of cadmium ions (Cd^{2+}) with sulfide ions (S^+). The reactions involved in the process can be presented as follows:

The decomposition of thiourea is given by

$$(NH_2)_2CS + OH^- \longrightarrow SH\text{-}CH_2N_2 + H_2O$$

$$SH^- + 2OH^- \longrightarrow S^{2-} + H_2O$$

$$Cd^{2+} + 2OH^- \longrightarrow Cd(OH)_2$$

$Cd(OH)_2$ then reacts with the ammonia buffer to form a cadmium tetra mine complex which then reacts with the sulphide ions to give cadmium sulfide. NH_3 is involved as a byproduct of the reaction.

$$Cd(OH)_2 + NH_4OH \longrightarrow [Cd(NH_3)_2]^{2+}$$

$$[Cd(NH_3)_2]^{2+} + S^{2-} \longrightarrow CdS + 4NH_3$$

The CdS thus formed sticks to the surface of the substrate mounted vertically the solution.

d) The chemical bath deposition process on glass substrate:

The glass substrates were mounted vertically in the solution and the solution was heated rapidly up to 50°C with the help of heater and then places on a hot tray plate where the temperature was maintained at 70°C. The deposition took place for 30 minutes. Colors of the solution could be observed while temperature was rising. At first the solution was transparent, then successively changed as yellowish transparent (at around 50°C), greenish yellow (at around 60°C), light orange (at around 65°C) and reddish orange (at and above 70°C). In the slow process of deposition this color change could be observed clearly. Deposition was carried out for 30 minutes in each step. Slides were then removed from the bath solution and washed in the flow of tap water and finally washed with deionizes water to remove the loosely adhered CdS particles and subsequently dried at room temperature. The deposition occurred on both sides of the glass substrates and it is to be mentioned here that the thin film deposited on the one side of the glass substrate was removed before thickness determina-tion. For multiple deposition the process was repeated several times until the desired thickness was achieved. After the deposition the back sides of the substrates were removed using dilute HCl.

RESULTS AND DISCUSSION

Result from X-ray diffraction:

Using shimadzu maxima 7000 X-ray diffractometer with CuK $\propto$ radiation with the scanning range in Between 0 to 80 showed the XRD pattern of CdS. The XRD has proven to be a valuable research tool to prove the formation of CdS, determining the crystal structure and calculating the theoretical particle size of prepared CdS. XRD pattern thus clearly illustrated that, the CdS synthesized by the present method were slightly crystalline in nature. The crystalline size is calculated using Debye-Scherrer method. It is found to be approximately 30nm.

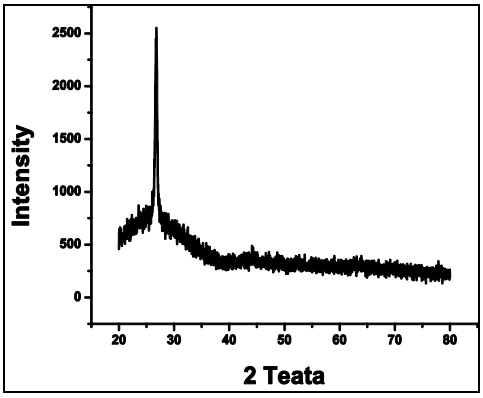

Figure-1: XRD pattern of CdS thin film

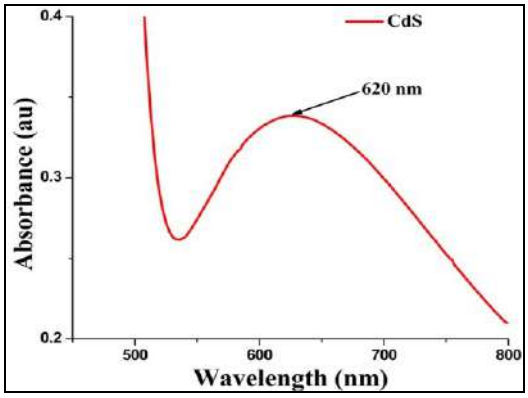

Figure-2: UV visible pattern of CdS thin film

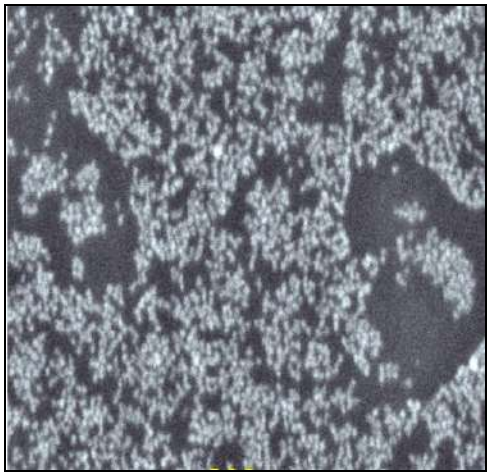

Figure-3: SEM pattern of CdS thin film

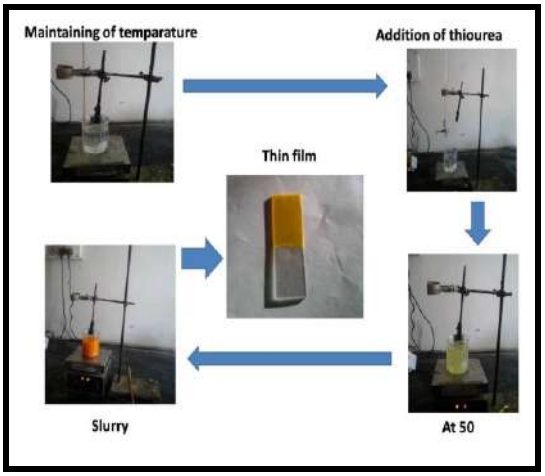

Figure-4: Experimental of CdS thin film

Morphology from SEM analysis:
SEM image were carried out by using [QUANTA-200, FEI Ltd. Netherland]. Thin film of carbon coated copper grid a sample was placed, where excess of sample was removed by using the cone of a blotting paper and sequentially arrange in a grid box. The morphology and the size of the synthesized CdS were determined by SEM image. The smaller grains are distributed all over the structure in uniform size distribution.

Band gap calculation from UV-spectrophotometry:
UV-Visible spectroscopy analysis was performed using LAB UV 3000 at room temperature with glass cuvette of 1 cm path length as a sample holder. The formation of CdS was monitored by scanning the spectrum of material from 200 to 800nm by using glass as blank. No of experimental trails confirmed that reduction and synthesis of CdS was better in starring condition as compared to open other parameters. The maximum absorbance was observed at 620nm which indicated/supported the formation of CdS.The band gap energy is calculated and it is found to be 2.39eV. Which is in good agreement with theoretical band gap values of CdS is 2.4e

CONCLUSION

UV-Visible spectroscopy analysis was performed using LAB UV 3000 at room temperature with last cuvette of 1 cm path length as a sample holder. The formation of CdS was monitored by scanning the spectrum of material from 200 to 800nm by using glass as blank. No of experimental trails confirmed that reduction and synthesis of CdS was better in starring condition as compared to open other parameters. The maximum absorbance was observed at 620nm which indicated/supported the formation of CdS. The band gap energy is calculated and it is found to be 2.39eV. Which is in good agreement with theoretical band gap values of CdS is 2.4eV. Using shimadzu maxima 7000 X-ray diffractometer with CuK $\propto$ radiation with the scanning range in between 0 to 80 showed the XRD pattern of CdS. The XRD has proven to be a valuable research tool to prove the formation of CdS, determining the crystal structure and calculating the theoretical particle size of prepared CdS. XRD pattern thus clearly illustrated that, the CdS synthesized by the present method were slightly crystalline in nature. The crystalline size is calculated using Debye-Scherrer method. It is found to be approximately 30nm. SEM image were carried out by using [QUANTA-200, FEI Ltd. Netherland]. Thin film of carbon coated copper grid a sample was placed, where excess of sample was removed by using the cone of a blotting paper and sequentially arrange in a grid box. The morphology and the size of the synthesized CdS were determined by SEM image. The smaller grains are distributed all over the structure in uniform size distribution. The fundamental properties of CdS thin film, prepared using CBD method were investigated. The properties studied include thickness, bandgap, crystal structure and morphology energy of CdS thin film were determined.

Conflicts of interest: The authors stated that no conflicts of interest.

REFERENCES

1. Kasturi LC and Inderjeet K. Thin film device applications: Plenum press New York, 1983.
2. Khomane S. Crystallographic, Morphological, Optical and electrical properties of CBD deposited, 2011.
3. Kathirvel D, Sariyanaraya N, Prabaher S. and Srikanth. Electrical properties of chemical bath deposited cadmium sulphide thin film, 2011.

IRJSE International Research Journal of Science & Engineering
Int. Res. J. of Science & Engineering, 2018; Special Issue A2 : 241-244
ISSN: 2322-0015
SJIF Impact Factor 4.11
UGC Approved Journal No. 63628
RESEARCH ARTICLE **OPEN ACCESS**

Synthesis of Nano-Bioceramic Material using Chemical Precipitation Method

Jadhav Madhuri S and Bhise RB

Department of Physics, B. J. College, Ale, Tal: Junnar, Dist: Pune 412411, MS, India
Email: mjadhav277@gmail.com bhiseramesh@gmail.com

Manuscript Details
Available online on http://www.irjse.in
ISSN: 2322-0015

Editor: Dr. Arvind Chavhan

Cite this article as:
Jadhav Madhuri S and Bhise RB Synthesis of Nano-Bioceramic Material using Chemical Precipitation Method, *Int. Res. Journal of Science & Engineering,* January 2018; Special Issue A2 : 241-244.

ABSTRACT

In the present work, we have synthesized nano-bioceramic material by using simple cost effective chemical precipitation method. Calcium Nitrate and Di-ammonium hydrogen orthrophosphate are used as a source of calcium and phosphrous to maintain the Ca:P ratio 1.66 which is similar to our natural bone .The pH was maintained at 12 by using liquid Ammonia and synthesis is carried out at constant temperature 100^{o}C for continuously stirred for 3 hrs. Afterwords synthesized material is dried at 100degree celcius for 2 hrs. Structural investigation is carried out by using XRD and morphological evaluation is examined by Scanning Electron Microscope. It is observed that the synthesized material is found in the range of 30-60 nm as investigated by XRD and SEM. Hence it is remarkable to note that the one-pot chemical precipitation method is successfully used to synthesize nano-bioceramic.

Keywords: Calcium Nitrate, Diammonium Hydrogen Orthrophosphate, XRD, SEM.

INTRODUCTION

A biocompatible ceramic (inorganic solid held by ionic or covalent bond) consisting of calcium and phosphates. Eg. Hydroxyapetite. Nanopowder is a solid powder of artificial origin that contains nano objects, aggregates of nano objects and dimension ranging from 1-100nm. Nano powder is characterized by Mean size of particle,

Size distribution of particles and Rate of agglomeration of particle. Calcium phosphate based bioceramic are nontoxic having biological effects is widely used in biomedical, tissue engineering. It is denoted as $[M_{10}(XO_4)_6Z_2]$ where M is a metal divalent cations, such as Ca^{2+} , Sr^{2+} etc., X is a trivalent species such as phosphate and is anion such as OH^- , F^- or a halogen. If OH^- anion is present in given structure it I named as hydroxya-patite, if F^- then it is known as fluorapatite, and if Cl^- then named as chloroapetite. The chemical composi-tion of pure calcium phosphate is $Ca_5(PO_4)_3(OH)$ (pentacalcium- hydroxyl-triphosphate) , but it is usually written as $Ca_{10}(PO_4)_6(OH)_2$. The crystal unit cell consist of two molecules and its Ca:P atomic ratio is 10:6 (i.e. 1.67). Hydroxyapatite, having chemical formula $Ca_{10}(PO_4)_6(OH)_2$ shows that it contains 39.85 wt % of Calcium, 18.51 wt % of Phosphorus, 41.41 wt % of Oxygen, and 0.20 wt % of Hydrogen. If Ca/P ratio is low, the acidity and solubility of mixture is high. But for mixture having Ca/P ratio close o 1.67, it has low acidity and solubility. Hydroxyapetite exist in two phases as monoclinic and hexagonal. But chemi-cally pure Hap exist in monoclinic phase. There is phase transition of monoclinic to hexagonal above 250^0C. Hydroxyapetite crystal is basically composed of Ca ions, PO_4 tetrahedra, and OH groups. Inside the crystal, each hydroxyl cation is completely surround-ded by calcium anions, while each calcium anion is surrounded by phosphate cations. Th difference of monoclinic and hexagonal structure is due to the arrangement of hydroxyl ions. Hexagonal hydroxy-apatite has a disordered hydroxyl arrangement, while monoclinic hydroxyapatite has an ordered hydroxyl arrangement. The hexagonal structure of calcium hydroxyapatite is a more common one for biomedical applications.

Nanocrystalline hydroxyapatite is synthesized by various techniques such as sol-gel, hydrothermal, wet chemical precipitation, microwave irradiation, etc. A stoichiometric and well crystalline product is obtained with solid state method but it requires high tempera-ture- pressure and long heat treatment time. Nano-cryastal can be formed at temperature below 100^0C with the help of wet chemical precipitation method. Crystallinity and stoichiometry obtained by these method is relatively close to well crystallized stoichio-metric hydroxyapatite. So we synthesized Hap by wet chemical precipitation due to easy preparation, low cost of instrumentation, low temperature synthesis.

METHODOLOGY

Synthesis for Hydroxyapatite

1) For 0.6 M of di-ammonium hydrogen orthrophosphate-

   Molecular weight of $(NH_4)_2HPO_4$= 132.06gm

   For 0.66 M of $(NH_4)_2HPO_4$ x=8.7159 gm in 100ml

   For 6.6 M of $(NH_4)_2HPO_4$ x=87.159 gm in 1000ml

   For 50ml x= 4.357gm

   Dissolve 4.357 gm of di-ammonium hydrogen orthrophosphate in 50ml of distilled water and stir to form clear solution.

2) For 1M of calcium nitrate tetra hydrate-

   Molecular weight of $Ca(NO_3)_4H_2O$ = 236.15gm

   For 1M of solution in 100ml y= 23.615gm

   For 1M of solution in 50ml y= 11.08 gm

   Dissolve 11.08 gm of calcium nitrate tetra hydrate in 50ml of distilled water and stir to form clear solution.

3) Now dropwise 0.6 M of di-ammonium hydrogen orthrophosphate is added into 1M of calcium nitrate tetra hydrate solution.

4) Liquid ammonia is added to maintain pH of solution upto 12.

5) Process is carried out by stirring continuously at 100^0 C for 3 hrs.

6) Solution is kept in steady state for a night to settle ppt at bottom.

7) Formed white ppt is washed 3-4 times with double distilled water and dried in air oven for a two nights.

8) Now it is grinded with the help of mortar and hydroxyapetite is formed.

9) Further it is used for characterization.

The reaction is as follows

$$6(NH_4)2HPO_4 + 10Ca(NO_3)_2 + 8NH_4OH$$

$$\downarrow$$

$$6H_2O + 20NH_4NO_3 + Ca_{10}(PO_4)_6(OH)_2$$

[Hydroxyapetite]

Table 1: Table showing properties of Hap

Paremeters	Values
Chemical composition	$Ca_{10}(PO_4)_6(OH)_2$
Ca/P ratio	10:6 (1.67)
Crystal	Hexagonal
Biocompatibility	High
Bioactivity	High
Biodegradation	Low
Osteoconduction	High

Characterization Techniques-

X-ray Powder Diffraction (XRD):

X-ray diffraction (XRD) is used for the characterization of crystalline solids and determination of their structure. When X-ray is incident on given structure, it interact with atoms and constructive interference is obtained which gives detailed information.

By Braggs law, $n\lambda=2d\sin\theta$

Where, n= an integer, λ= the wavelength of the X-rays, d= the spacing between atomic layers, θ=the angle between the incoming X-ray and the atom layer.

Mean dimension D is given as

$$D = \frac{K\lambda}{\beta\cos\theta}$$

Where, K is constant approximately equal to unity and related to thecrystalline shape, β is FWHM of the diffraction peak.

The wavelength of the X-ray source empoloyed is 1.54056 A^0 with photon energy of 8 KeV. The XRD peaks are recorded in the 2θ range of 20^0-60^0. We saw peaks at 2θ value 25.6^0, 25.4^0 , 28.5^0 , 30.1^0 , 31.7^0 ,32.7^0, 35.1^0, 36.1^0, 40.1^0, 43.3^0, 49.3^0, 52.5^0, 57.5^0, which confirm the crystalline hexagonal phase. The average crystalline size calculated is 27 nm.

FTIR Analysis:

Fourier Transform Infrared Spectroscpy(FTIR) is a technique used to obtain an infrared spectrum of absorption or emission of solid, liquid, gas. FTIR spectrometer simultaneously collects high spectrum resolution data over a wide spectral range. FTIR spectra of Hap film is recorded at room temperature in the wave number range 4000 and 400 cm^- . The spectra confirm the presence of water, hydroxyl and phosphate species. The FTIR spectrum of the pure Hap shows the presence of hydroxyl stretching modes in the apatite structure at 3572 cm^- .The absorption peaks for hydroxyl liberation mode are found at 727 cm^- and 1603 cm^-. The bands appearing at 963 cm^- and 901 cm^- correspond to anti symmetric bending motion to v_3 stretching mode in $PO4^{3-}$ group. The study of FTIR spectra showed all bands corresponding to pure Hap structure.

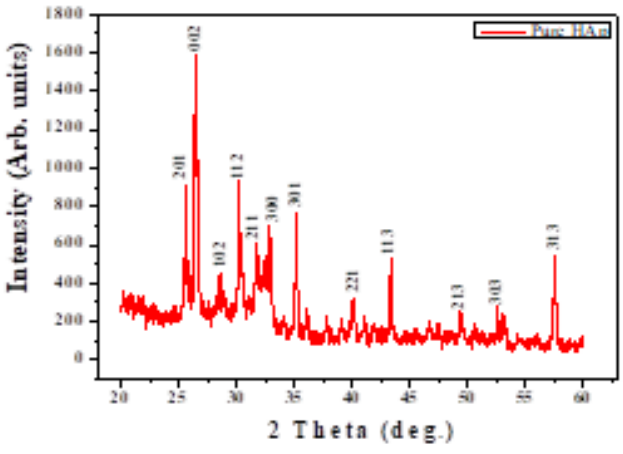

Fig.1: XRD pattern of pure HAp thick films

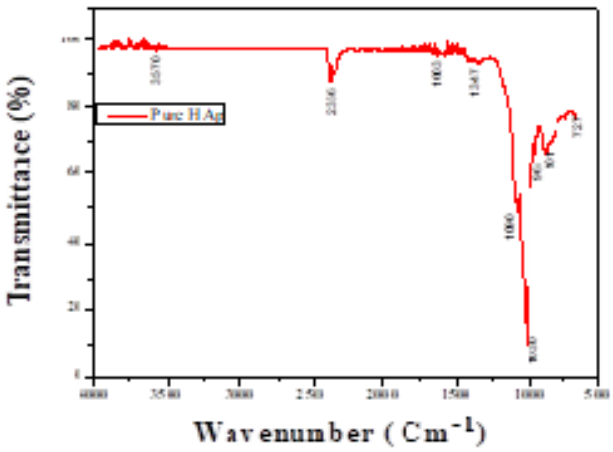

Fig.2: FTIR spectrum of HAp thick films

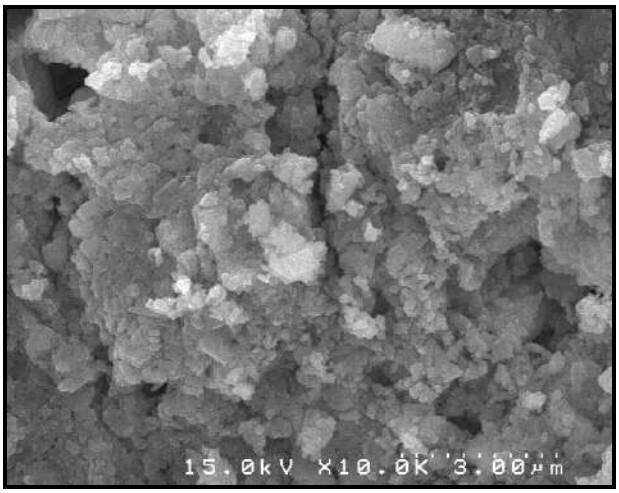

Fig.3: SEM pattern of pure HAp thick films

Scanning Electron Microscopy (SEM):

SEM is a type of electron microscope that produces images of a sample by scanning it with a focused beam of electrons. Electrons interact with atoms in the sample, producing various signals that can be detected and contain information about sample surface composition. The principle is based on the interaction of an incident electron beam and the solid specimen. The study of SEM shows presence of smaller grains with a uniform size and shape covering whose surface along with microporous structure.

CONCLUSION

Nano-crystalline hydroxyapatite is synthesized by using wet chemical process. The synthesized Hap powder shows hexagonal phase with nano-sized grains. The surface morphology of Hap film showed separated grains with of micro porous structure. The elemental composition of Hap film is confirm by EDS.

Conflicts of interest: The authors stated that no conflicts of interest.

REFERENCES

1. Dorozhkin SV, *Materials*, 2009, 399.
2. Posner AS, Betts F,Blumenthal NC, Progr. Cryst. Growth Char., 1980, 49.
3. Elliott JC, Young RA, *Natur*e,1967, 904.
4. Heness G, and Ben-Nissan, *Material forum*, 2004, 104.
5. Levitt SR, Crayton PH, Condrate RA, J.Biomed Mater. Res.,1969,683.
6. Blakeslee KC, Condrate RA, J. Am. Ceram. Soc., 1971,559.
7. Garrington GE, Lightbody PM, J. Biomed. Mater. Res.,1972,333.
8. Cini L, Sandrolini S, Paltrinieri M, Trentani C, Chir. Organi Mov., 1972,423.
9. Rivault MA, Rev. Fr. Odontostomatol,1966, 1367.
10. Dumont A, Appel M, Favard E, Ann. Odontostomatol,1968,231.
11. Hulbert SF, Hench LL, Forbers D,Bowman LS, Ceram. Int. ,1982,131.
12. Hulbert SF, Hench LL, Forbers D,Bowman LS, History of bioceramics. In Ceramics in Surgery; Ed.; Elsevier: Amsterdam, The Netherlands, 1983, 3.

IRJSE International Research Journal of Science & Engineering
Int. Res. J. of Science & Engineering, 2018; Special Issue A2 : 245-250
ISSN: 2322-0015
SJIF Impact Factor 4.11
UGC Approved Journal No. 63628
RESEARCH ARTICLE **OPEN ACCESS**

Design & Development of Tube in Tube Helical Coil Heat Exchanger

Patil Sateesha, Sanket Patel, Prashant Vavhal, Harshal Rahate

Mechanical Engineering Department, Savitribai Phule Pune University, Pune, MS, India,
Department of Engineering, P.K. Techanical Campus, Chakan (Pune), MS, India
Email: prashantvavhal44@gmail.com

Manuscript Details

Available online on http://www.irjse.in
ISSN: 2322-0015

Editor: Dr. Arvind Chavhan

Cite this article as:
Patil Sateesha, Sanket Patel, Prashant Vavhal, Harshal Rahate.Design & Development of Tube in Tube Helical Coil Heat Exchanger , *Int. Res. Journal of Science & Engineering,* January 2018; Special Issue A2 : 245-250.

ABSTRACT

Conventional heat exchangers are large in size and heat transfer rate is also less. In conventional heat exchanger dead zone is produce which reduces the heat transfer rate. To create turbulence in conventional heat exchanger some external means is required. The fluid in conventional heat exchanger is not in continuous motion with each other. Tube in tube helical coil heat exchanger provides a compact shape with its geometry offering more fluid contact and eliminating the dead zone, increasing the turbulence and hence the heat transfer rate. An experimental setup is fabricated for the estimation of the heat transfer characteristics. A wire is wounded in the core to increase the turbulence in turn increases the heat transfer rate. The paper deals with the pitch variation of the internal wounded wire and its result on the heat transfer rate. The Reynolds number and Dean Number in the annulus compared to the numerical data. The experimental result compared with the analytical result which confirmed the validation. This heat exchanger finds its application mostly in food industries and waste heat recovery.

Keywords: Tube-in-tube, Nusselt number, wire wound, Reynolds number, Dean Number, dead zone

INTRODUCTION

Heat Exchanger is a device in which the exchange of energy takes place between two fluids at different temperature.

A heat exchanger utilizes the fact that, where ever there is a temperature difference, flow of energy occurs. So, That Heat will Flow from higher Temperature heat reservoir to the Lower Temperature heat Reservoir. The flowing fluids provide the necessary temperature difference and thus force the energy to flow between them. The energy flowing in a heat exchanger may be either sensible energy or latent heat of flowing fluids. The fluid which gives its energy is known as hot fluid. The fluid which receives energy is known as cold fluid. It is but obvious that, Temperature of hot fluid will decrease while the temperature of cold fluid will increase in heat exchanger.

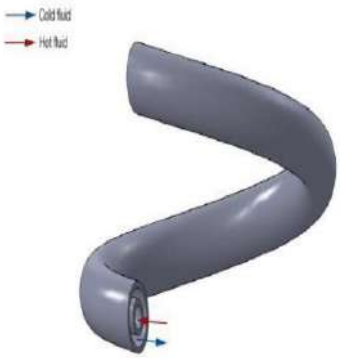

Fig. 1.1 Concept of Tube

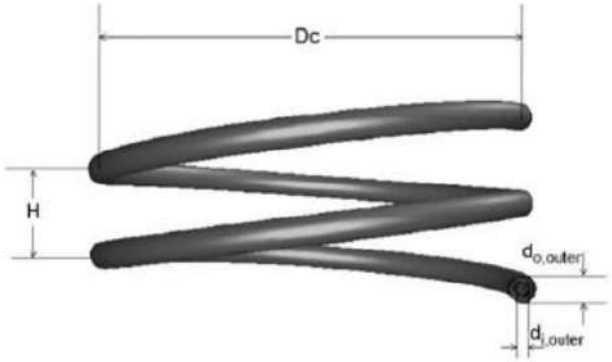

Fig. 1.2. Dimensional Representation of Tubein tube Helical Coil Hear exchanger

These types of heat exchanger are known as condensers or evaporators. Heat exchangers with the convective heat transfer of fluid inside the tubes are frequently used in many engineering application. The techniques of heat transfer enhancement to accommodate high heat flux i.e. to reduce size and cost of heat Exchangers have received serious attention passed years. Enhancement of heat transfer Rate in all types of thermo technical apparatus is of great significance for industry. Beside the savings of primary energy, it also leads to a reduction in size and weight. Up to the present, several heat transfer enhancement techniques have been developed.

The heat exchangers have an important role in the energy storage and recovery. Due to the development of modern technology, the heat exchangers required in various industries for high heat-flux cooling to the level of megawatt per meter square. At this level, cooling with conventional fluids such as water and ethylene glycol and so forth, are challenging. Hence, it is necessary to increase the heat transfer performance of working fluids in the heat transfer devices. Heat transfer augmentation techniques (passive, active and compound) are commonly used in areas such as process industries, heating and cooling in evaporators, thermal power plants, air-conditioning equipment, refrigerators, radiators for space vehicles, automobiles, etc. The rate of heat transfer can be increased passively by increasing the surface area, roughness, and by changing the boundary conditions. The active method involves addition of nano sized, high thermal conductivity and metallic powder to the base fluid, to increase the heat transfer rate. Such a fluid is termed as nano fluid. Where inserts are used in the flow passage to augment the heat transfer rate, are best suited compared to active techniques. Because the insert manufacturing process is simple and these techniques can be easily applied in an existing application. Shell-and-tube heat exchangers are the most common type of thermal equipment employed in chemical process industries. This widespread use can be justified by its versatility, robustness and reliability. Despite the technological advances of other exchanger types (e.g., plate-and-frame, spiral, lamella, etc.), shell-and-tube heat exchangers will maintain a central position in industrial.

Several studies have indicated that helically coiled tubes are superior to straight tubes when employed in heat transfer applications. The centrifugal force due to the curvature of the tube results in the development of secondary flows (flows perpendicular to the axial direction) which assist in mixing the fluid and

enhance the heat transfer. In straight tube heat exchangers there is little mixing in the laminar flow regime, thus the application of curved tubes in laminar flow heat exchange processes can be highly beneficial. These situations can arise in the food processing industry for the heating and cooling of either highly viscous liquid food, such as pastes or purees, or for products that are sensitive to high shear stresses. Another advantage to using helical coils over straight. tubes is that the residence time spread is reduced, allowing helical coils to be used to reduce axial dispersion in tubular reactors. The first attempt has been made by Dean to describe mathematically the flow in a coiled tube. A first approximation of the steady motion of incompressible fluid flowing through a coiled pipe with a circular cross-section is considered in his analysis. It was observed that the reduction in the rate of flow due to curvature depends on a single variable, K, which is for low velocities and small It was then continued for the study of Dean for the laminar flow of fluids with different viscosities through curved pipes with different curvature ratios.The result shows that the on set of turbulence did not depend on the value of the Re or the De. It was concluded that the flow in curved pipes is more stable than flow in straight pipes. It was also studied the resistance to flow as a function of De and Re. There was no difference in flow resistance compared to a straight pipe for values of Deless than 14.6.

Rough estimates can be made using either constant heat flux or constant wall temperature from the literature. The study of fluid-to-fluid heat transfer for this arrangement needs further investigation. The second difficulty is in estimating the area of the coil surface available to heat transfer. As can be seen in Figure, a solid baffle is placed at the core of the heat exchanger. In this configuration the baffle is needed so that the fluid will not flow straight through the shell with minimal interaction with the coil. This baffle changes the flow velocity around the coil and it is expected that there would be possible dead-zones in the area between the coils where the fluid would not be flowing. The heat would then have to conduct through the fluid in these zones, reducing the heat transfer effectiveness on the outside of the coil. Additionally, the recommendation for the calculation of the outside heat transfer coefficient is based on the flow over a bank of no staggered circular tubes, which is another approximation to account for the complex geometry. Thus, the major drawbacks to this type of heat exchanger are the difficulty in predicting the heat transfer coefficients and the surface area available for heat transfer. These problems are brought on because of the lack of information in fluid-to-fluid helical heat exchangers and the poor predictability of the flow around the outside of the coil.

METHODOLOGY

PROBLEM STATEMENT

The objective of this work is to determine the heat transfer characteristics for a helical double-pipe heat exchanger by varying the flow rates of a single fluid in both the inner and outer tubes for counter flow and to compare the same with the double-pipe straight tube heat exchanger. Correlations between Nusselt number and Dean Number for the helical coiled heat exchanger are also developed. The problem is defined the flow and temperature contours of both the heat exchangers.

OBJECTIVE

Our prime objective is to study the performance of Helical Coil Tube in Tube heat exchanger compared to traditional heat exchanger, using an experimental setup. Further our project aim is studying the temperature drops in Helical coil Tube in Tube Heat Exchanger.

1. Design a helical double-pipe tube in tube helical coil heat exchanger.
2. Experimental analysis of a helical double-pipe tube in tube helical coil heat exchanger and Find out heat transfer rates, LMTD, overall heat transfer coefficient and Reynolds number, Nusselt number ,Dean number for counter flow arrangement.
3. Comparison of Experimental results of heliacal tube in tube heat exchanger to the traditional heat exchanger.

SCOPE

1. Heat transfer rate can be achieved at high amount in row spacing.

2. To reduce labor cost and labor time.
3. Reduce size of heat exchanger and increase the heat transfer rate.
4. Perform the various simultaneous operations and hence save the labor requirements.

Problem Identification

Heat exchanger is the process equipment designed for effective transfer of heat energy between two fluids; a hot fluid and coolant .Heat exchangers serve a straight forward purpose controlling a system's or substance's temperature by adding or removing thermal energy.

The main objective of this research is to determine the heat transfer characteristics of a helical heat exchanger, both numerically and experimentally, and to determine the effects of heat exchanger geometry and fluid properties on the heat transfer characteristics. To accomplish this goal, the following problems were encountered:

- Various parameters changing due to coil shape, temperature gradient and various Thermodynamic properties.
- Problems in determining overall heat transfer coefficient due to fouling, and other
- Parameters, Design and Construction of a physical model of the heat exchanger.
- Testing of the physical model under different flow rates and flow configurations.(Parallel flow and counter flow).
- Comparison of the results from both theoretical and experimental work.

CONSTRUCTION AND WORKING

Construction

This project, we study considering the double tube helical coil heat Exchanger or tube in tube helical coil heat exchanger with six (6) numbers of turns. For simplification in numerical analysis we consider only six turns but in practical problems it may be large number of turns depending on the requirements. The coil diameter (D) was varying from 80 mm to 240 mm in an interval of 40 mm that is 120 mm, 160 mm and 200 mm respectively. As the coil diameter increases the length of the exchanger (L) also increases. The inner tube diameter (d1) was 8mm.thethickness (t) of the tube was taken 0.5 mm. The outer tube diameter (d2) was taken 17mm.In this project we studying fixed the tube diameter (both inner and outer diameter) of the heat exchanger and vary the coil diameter of the tube to see the effect of curvature ratio (d/D) on heat transfer characteristics of a helical coil heat exchanger. The pitch of the coil was taken 30mm that is the total height of the tube was 315 mm.

The heat exchanger was made of STAINLESS STEEL. The fluid property was assumed to be constant for analysis. In this study we considered the counter flow heat exchanger as it has better heat transfer rate compared to parallel heat exchanger. The cold fluid and the hot fluid flow in opposite directions in their respective tube. In this study for analysis, turbulent fluid flow was considered. Both the hot fluid and cold fluid flow with a velocity, for which Reynolds number is greater than critical Reynolds number as per the correlation calculated by Schmidt. The flow velocity of cold fluid is remained constant and the hot fluid flow rate varied to find the heat transfer rate, friction factor and optimize the heat exchanger to have minimum pressure loss and maximum heat transfer. After creating the geometry on CATIA V5R18 and doing the drafting in AUTO CAD 2007 the 2D model was drown on AUTO CAD (2007) for different manufacturing process as above mention method.

Working

A test run was completed on the apparatus. Once all of the components were in place, the system was checked thoroughly for leaks. After fixing the leaks, the apparatus was prepared for testing. The test run commenced with the apparatus being tested under laboratory conditions. Data was recorded every five minutes until the apparatus reached steady state. The hot temperatures fell as expected; the cold temperatures seemed to be more unpredictable in one instance rising six degrees in five minutes and then on the next reading falling three degrees. The apparatus took 120 minutes to reach steady state, which can vary based on operating conditions. Readings were taken until the three-hour mark;

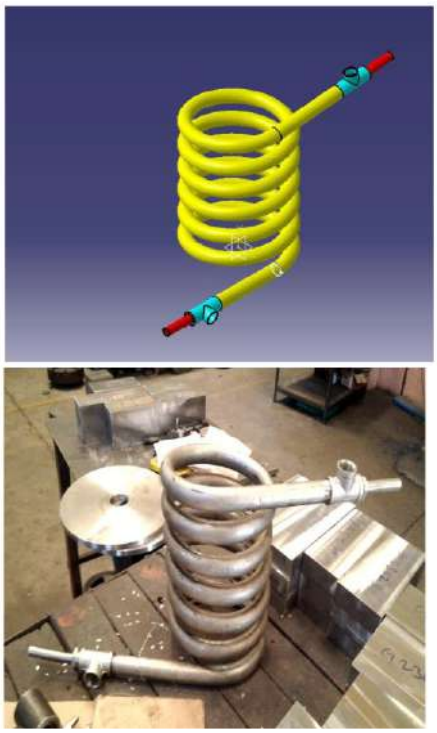

Fig.2 Assembly of TTHC Heat Exchanger

however, the data became inconsistent, so a steady state set was determined based on proximity of the readings. Flow rates in the annulus and in the inner tube varied. The following five levels were used: 100, 200,300, 400, and 500 LPH. All possible combinations of these flow rates in both the annulus and the inner tube were tested. These were done for all the coils in counter flow configurations. Furthermore, three replicates were carried out every combination of flow rate, coil size and configuration. This resulted in a total of 50 trials. Temperature data was recorded every ten seconds. The data used in the calculations was synthesized only after the system had stabilized. Temperature measurements from the 120 s of the stable system were used, with temperature reading fluctuations within ±1.10C. All the thermocouples were constructed from the same roll of thermocouple wire thus carried out for the repeatability of temperature readings being high.

ADVANTAGES AND APPLICATION

Advantage

1. Compact size provides a distinct benefit. Higher film coefficients the rate at which heat is transferred through a wall from one fluid to another and more effective use of available pressure drop result in efficient and less-expensive designs.
2. True counter-current flow fully utilizes available LMTD (logarithmic mean temperature difference). Helical geometry permits handling of high temperatures and extreme temperature differentials without high induced stresses or costly expansion joints.
3. High-pressure capability and the ability to fully clean the service-fluid flow are added to the exchanger's advantages.
4. Coils give better heat transfer performance, since they have lower wall resistance& higher process side coefficient.
5. A coil can provide a large surface area in a relatively small reactor volume.
6. High heat transfer rates.
7. Very close approach temperature - up to 2 °C
8. More compact due to increased overall heat transfer coefficient.
9. Suitable for high heat duty application.
10. Minimum cooling water requirement.
11. Suitable for low flow rates at high pressure / high temperature applications.
12. Maximum counters current efficiency.
13. Eliminates the tendency of dead spot formations.
14. Low pressure drop on outer tube side.
15. Rugged design, highly resistant to thermal and hydraulic shocks.
16. Easy to install.

APPLICATION

1. To cool process streams

- Gasoline product going to storage is cooled to reduce loosed because of its vapor pressure.
- General unit intercoolers remove the heat of reaction between reactors
- Absorber intercoolers on gas concentration units remove the heat of absorption and thereby increase the efficiency of the absorber.
- Fractionators condensers condense the overhead, part of which may be the product and the other part of which may be reflux that is returned to the column to help effect a separation.

2. To heat process streams
- Fractionator's re-boilers are used to add heat to fractionation column that effects a separation.
- Reactor charge heaters are used to heat the charge up to their action temperature.

3. To exchange heat between hot and cold process streams.
- Feed exchangers that are used to heat the reactor charge by exchanging heat with the reactor effluent.
- Fractionator's feed-bottoms exchanger that is used to heat the feed by exchanging heat with the bottoms.

4. Food industry
5. Textile industry
6. Pharmacy industry
7. Paper industry
8. Mostly used in give feed to the boiler

CONCLUSION

Various research works has been carried out in the past regarding to effectiveness of helical coiled heat exchanger and also form this experiment it is found that the helical coil heat exchanger may be a great option for effective heat transfer between two fluids in the modern industries where it may incorporated in the place of straight tube heat exchanger**.** Heat transfer is going to be very well along the heat exchanger. Fluid flow will become completely turbulent. Especial shape of the heat exchanger and secondary flows lead to random movement of the fluid particles in all directions so that axial, radial, and swirly movements exist together that mix the fluid very well and force the flow to be turbulent. Nusselt number magnitude is higher in the entrances because of the more temperature difference but it decreases as fluids go forward through the heat exchanger toward the exit points and as the temperature difference decreases.

Conflicts of interest: The authors stated that no conflicts of interest.

REFERENCES

1. Gavade Pravin P, Kulkarni P.R 'Experimental Evaluation of Helical Coil Tube in Tube Heat Exchanger" International Journal of Emerging Engineering Research and Technology Volume 3, Issue 2, PP 12-17.
2. Desai1 Vijay P, Borse Sachin L (2013),"Experimental Study on Enhancement Of Thermal Performance of Wire Wound Tube In Tube Helical Coil Heat Exchanger" International Journal of Engineering Research and Applications (IJERA) Vol. 3, Issue 4,,2013, 340-346.
3. Kshirsagar Mrunal P, Kansara Trupti J,Aher Swapnil M "Fabrication and Analysis of Tube-In-Tube Helical Coil Heat Exchanger" International Journal of Engineering Research and General Science Volume 2, Issue 3
4. Kumar Vimal, Faizee Burhanuddin, Mridha Monisha, Nigam KDP "Numerical studies of a tube-in-tube helically coiled heat exchanger" Sciencedirect Department of Chemical Engineering, Indian Institute of Technology, Delhi, HauzKhas, New Delhi-110016.
5. Hingane Pariksheet, KanasePatil AB "Design-Fabrication and Testing of Helical Tube in Tube Heat Exchanger" International Engineering Research Journal (IERJ) Special Issue Page 1245-1248, ISSN 2395-1621.
6. Gavade PP, Malgave SS, Patil DD, Bhore HS, Wadkar VV "Analysis of tube in tube helical coil & straight tube heat exchanger" Journal of Mechanical Engineering and Technology (JMET) Volume 3, Issue 2

IRJSE International Research Journal of Science & Engineering
Int. Res. J. of Science & Engineering, 2018; Special Issue A2 : 251-255
ISSN: 2322-0015
SJIF Impact Factor 4.11
UGC Approved Journal No. 63628
RESEARCH ARTICLE **OPEN ACCESS**

Application of Optimization Techniques in Water Jet Cutting of Granite

Vavhal Prashant[1], Katale Chetan[2] Beloshe, Tejas[2], Patil Navnatha[2], Durge Mayur[2]

[1]Mechanical Engineering Department, Savitribai Phule Pune University, Pune (MS), India,[2]*Departemnt of Engineering, P. K. Techanical Campus, Chakan (Pune) India*
Email: prashantvavhal44@gmail.com

Manuscript Details
Available online on http://www.irjse.in
ISSN: 2322-0015

Editor: Dr. Arvind Chavhan

Cite this article as:
Vavhal Prashant, Katale Chetan, Beloshe, Tejas, Patil Navnatha, Durge Mayur. Application of Optimization Techniques in Water Jet Cutting of Granite, *Int. Res. Journal of Science & Engineering,* January 2018; Special Issue A2: 251-255.

ABSTRACT

This paper attempts to select the significant process parameters by Taguchi methodology while machining of STAINLESS STEEL 410 by AWJM. Different process parameters like pressure, feed rate, and standoff distance in three different levels are selected for optimization with three contravene responses, higher MRR and low machining timing by a single parametric combination. For Design of experiment L9 orthogonal array is prepared to set the input significant parameters for final product is calculated for better optimization purpose also different combinations of the factors are ranked on basis of grey relational grade.

Keywords: Teaching-learning-based optimization (TLBO), Taguchi method, Stand-off distance, nozzle transfer speed, Abrasive flow rate

INTRODUCTION

"Gabbro", commonly known as black granite refers to a large group of dark, often phaneritic (coarse-grained), mafic intrusive igneous rocks chemically equivalent to basalt. It forms when molten magma is trapped beneath the Earth's surface and slowly cools into a holocrystalline mass. Much of the Earth's oceanic crust is made of granite, formed at mid-ocean ridges. Gabbro is also found as plutons associated with continental volcanism. applied loosely to a wide range of intrusive rocks, many

of which are merely "gabbroic". Black granite Due to its variant nature, the term "gabbro" may be applied loosely to a wide range of intrusive rocks, many of which are merely "gabbroic". Black granite has numerous applications for structural and decorative purposes. It is utilized for outdoor sculpture, external walls, floor covering, decoration, stairs, and pavements, table tops, and novelties. Traditionally granite is cut using diamond tools .To obtain complex shapes of the stone, it is necessary to know how the type of diamond grains, hardness of matrix, water cooling and machining process influence the quality and productivity of machining. Because of the present problems encountered in conventional cutting of granite, attempts can be made for cutting of granite using non-traditional machining process such as Ultrasonic machining , Water jet machining (WJM), Abrasive Water Jet machining (AWJM), Laser beam machining (LBM) etc. Ultrasonic machining can be applied to non-conductive as well as brittle materials, but it is a slow and time consuming process, tool wear rate is very high even greater than the metal removal rates expected from the process. Machining is an important manufacturing process because, it is almost always involved if precision is required and is the most effective process for small volume production. In production/manufacturing context, optimization of machining processes is one of the most important areas of research to find out the best process environment for any machining operation. Using various techniques, this optimization problem is solved for various kinds of metals. It has been seen that these methods are not efficient enough due to so many assumptions and limitations imposed upon it as compared to the actual environmental working conditions. Therefore, researchers are emphasizing on hybridizing various methods to empower advantageous aspects which ultimately results into elimination of inherent limitations of the proposed methodology. The present study aimed to develop such a hybrid method which could efficiently be applied for continuous quality improvement for a process/product and to facilitate in off-line quality control of any manufacturing process. The modern machining processes are now replacing the conventional machining processes rapidly for many applications due to their significant advantages which are proving beneficial to a greater extent to the present industrial scenario The various modern machining processes getting widely used in the industries are: electric discharge machining (EDM), abrasive jet machining (AJM), ultrasonic machining (USM), electrochemical machining (ECM) and laser beam machining (LBM) including various modified versions of these processes. .These processes work on a particular principle by making use of certain properties of materials which makes them most suitable for some applications and at the same time put some limitations on their use. These processes involve large number of respective process variables (also called as process parameters) and selection of exact parameters setting is very crucial for these highly advanced machining processes which may affect the performance of any process considerably. Due to involvement of large number of process parameters, random selection of these process parameters within the range will not serve the purpose. The situation becomes more severe in case if more number of objectives are involved in the process. Such situations can be tackled conveniently by making use of optimization techniques for the parameters optimization of these processes.

During the past two decades, few researchers had developed some good quality advanced optimization techniques such as genetic algorithm (GA), simulated annealing (SA), artificial bee colony (ABC), ant colony optimization (ACO), particle swarm optimization (PSO), teaching-learning-based optimization (TLBO), etc. which had already proved their significance in the field of parameters optimization of various manufacturing processes. Modelling and optimization of parameters of a modern machining process through advanced optimization techniques is now proving as a milestone for the future in manufacturing field.

METHODOLOGY

In this investigation, the work piece material stainless steel was used with the following main properties: Tensile Strength 90 MPa, Modulus of elasticity 69 GPa, and Density 2.71 g/cm3. The abrasive used was garnet with mesh size of 80 and hardness of 7.5 Mohs.

PROBLEM STATEMENT:

GRANITE is usually cut by using conventional diamond cutting tool machine. Kerf is observed while the cutting operation. Also design of diamond tool for complex structures is a difficult process. In this, we are using water jet machine to cut the granite with standoff distance, Nozzle traverse speed and Abrasive flow rate as work parameters and optimize the cutting process. Taguchi method is applied to find optimum process parameter for Abrasive water jet machining (AWJM). Abrasive water jet machining is a non–traditional process of removal of material by impact erosion of high pressure, high velocity of water and entrained high velocity of grit abrasives on a work piece. Experimental investigation were conducted to assess the influence of abrasive water jet machining (AWJM) process parameters on MRR of STAINLESS STEEL The approach was based on Taguchi's method and analysis of variance (ANOVA) to optimize the AWJM process parameter for effective machining and to predict the optimal choice for each AWJM parameter such as pressure, standoff distance, Abrasive flow rate and Traverse rate. For each combination of orthogonal array we have conducted three experiments and with the help of ANOVA it is found that these parameters have a significant influence on machining characteristics such as metal removal rate (MRR). The analysis of the Taguchi method reveals that, in general the standoff distance significantly affects the MRR while, Abrasive flow rate affects the surface Roughness. Experiments are carried out using orthogonal array by varying pressure, standoff distance, Abrasive flow rate and Traverse rate respectively. Experimental results are provided to verify this approach.

OBJECTIVE:

To optimize the process parameter (Standoff Distance, nozzle traverse speed, abrasive flow rate) of water jet cutting of granite material.

To apply regression model coupled with TLBO in water jet cutting of granite material.

To minimize the kerf obtained during water jet cutting of granite.

SCOPE:

The water jet cutting of granite are published by many researchers but optimization of water jet cutting using combination TLBO and ANN are not yet reported in literature.

PROBLEM IDENTIFICATION:

Experimental investigation were conducted to assess the influence of abrasive water jet machining (AWJM) process parameters on MRR of STAINLESS STEEL The approach was based on Taguchi's method and analysis of variance (ANOVA) to optimize the AWJM process parameter for effective machining and to predict the optimal choice for each AWJM parameter such as pressure, standoff distance, Abrasive flow rate and Traverse rate. For each combination of orthogonal array we have conducted three experiments and with the help of ANOVA it is found that these parameters have a significant influence on machining characteristics such as metal removal rate (MRR). The analysis of the Taguchi method reveals that, in general the standoff distance significantly affects the MRR while, Abrasive flow rate affects the surface Roughness. Experiments are carried out using orthogonal array by varying pressure, standoff distance, Abrasive flow rate and Traverse rate respectively. Experimental results are provided to verify this approach.

CONSTRUCTION AND WORKING

CONSTRUCTION

There are five main process characteristics to water jet cutting

1. Uses high velocity stream of Ultra High Pressure Water 30000-90000 psi (210-620 MPa) which is produced by an intensifier pump with possible abrasive particles suspended in the stream.
2. Is used for machining a large array of materials, including heat-sensitive, delicate or very hard materials.
3. Nozzles are typically made of sintered boride or composite tungsten carbide.
4. Produces a taper of less than 1 degree on most cuts.

5. Distance of nozzle from workpiece affects the size of the kerf and the removal rate of material. Typical distance is .125 in(3.2 mm).

The equipment used for machining the samples is STREAMLINE SL-V 50S Plus jet machining centre as shown in Figure 4.1. A plate of Black granite having size 304.8mm x 304.8mm x 35mm is chosen as the work piece. Table 4.2 indicates the important properties of Black granite (material chosen for experimentation). As discussed in the literature review, a large number of variables are involved in the AWJM and virtually all these variables affect the cutting results. Therefore only those parameters are selected which shows a considerable influence on objectives of the study i.e. kerf taper angle. These parameters are nozzle traverse speed, stand-off distance and abrasive mass flow rate. The rest of the parameters are kept constant which are given in

Fig1: Experimental setup

Fig2: Water jet Machine

WORKING

To achieve a thorough cut it was required that the combinations of the process variables give the jet enough energy to penetrate through the specimens. Screening experiments are performed to limit the range of process parameters at which cutting through the full thickness of the work piece can be performed. The minimum value of stand-off distance as well as abrasive flow rate at which through cutting can take place come out to be 1mm and 150 g/min respectively. Experiments were also conducted to find out maximum value of nozzle traverse speed for the through cut. It comes out to be 100 mm/min at threshold levels of other two input variables for through cutting. The higher levels of stand-off distance and abrasive flow rate and lower level of nozzle traverse speed are selected at the threshold levels permitted by the machine tool as input. Table 4.3 indicates variable process parameters and their levels selected.

parameters	level 1	level 2	level 3	level 4
Stand-off Distance (mm)	1	2	3	4
Nozzle Traverse Speed (mm/min)	25	50	75.5	100
Abrasive Flow Rate (g/min)	150	300	450	600

For experimentation, a full factor experimental design is done by first dividing the range of each parameter in 4 levels and obtaining 64 experimental combinations. In order to quantitatively evaluate experimental results, a measurement of the kerf characteristics such as top kerf width and kerf taper angle was made. The measurement of kerf taper, top kerf width and depth of cut was carried out from the end of the kerf prior to separating the specimens to measure the smooth depth of cut. It was anticipated that in AWJ contouring the two kerf wall might not be symmetrical due to the jet tail back effect. Thus the kerf taper and smooth depth of cut was obtained on each of the kerf walls. The kerf taper was obtained by measuring the kerf wall inclination (Wt – Wb) from the top kerf edge as shown in Figure 3.The taper angle is calculated by the following relation. Table 4 presents the design matrix as well as data about the observations.

$\Theta = \tan^{-1}\{(Wt-Wb)/2t\}$

Where Wt is the top kerf width, Wb is the bottom kerf width and 't' is the thickness of the work piece.

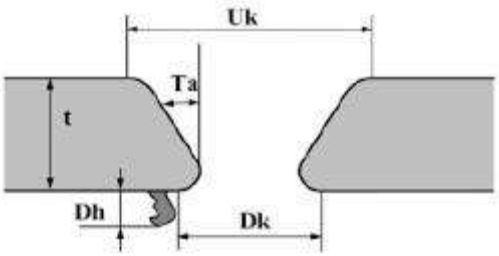

Fig.3. Kerf geometry of an AWJ cut

ADVANTAGES

1. Extremely fast step and programing
2. No. start hole required
3. There is only one tool
4. Low capital cost
5. Less vibration
6. No heat generate in work piece
7. Environmental friendly

CONCLUSION

Present work explored the abrasive water jet machining of Granite using TLBO and subsequent analysis. From the work, following inferences can be drawn:

- Optimal settings of process parameters for minimum top kerf width are Stand-off distance, nozzle transfer speed and Abrasive flow rate are 4 mm, 27.305 mm/min and 589.5 g/min.
- Average error was with
- Regression model and TLBO was applied accurately.
- Confirmation test was in proper limit.

Conflicts of interest: The authors stated that no conflicts of interest.

REFERENCES

1. Aultrin KS, Jai Anand Dev M. Optimization of Machining Parameters in AWJM Process for an Copper Iron Alloy Using RSM and Regression Analysis, *International Journal of Emerging Engineering Research and Technology*, 2014, Volume 2, Issue 5, 19-34
2. Dixit Abhishek, "Water Jet Machining: An Advance Manufacturing Process" International Journal of Engineering Research and General Science ,2014Volume 3, Issue 2, Part 2.
3. Xu Jiazhong, You Bo, Xiangbing Kong Xiangbing " Design and Experiment Research on Abrasive Water-jet Cutting Machine Based on Phased Intensifier" Proceedings of the 17th World Congress The International Federation of Automatic Control Seoul, Korea,2011, 2008
4. Ali1 Md. Irfath, Kalpana K, Sastri A.Pathanjali, Lakshmi B" A Holistic Approach to Risk Assessment and Decision Analysis to Improve Project Performance " International Journal of Emerging Engineering Research and Technology,2014,Volume 2, Issue 5, 99-103
5. Senthilkumar N, "Optimization of Process Parameters in Abrasive Water Jet Machining" International Journal of Innovative Research in Science, Engineering and Technology (An ISO 3297: 2007 Certified Organization), 2016,Vol. 5, Special Issue 8.

IRJSE International Research Journal of Science & Engineering
Int. Res. J. of Science & Engineering, 2018; Special Issue A2 : 256-259 SJIF Impact Factor 4.11
ISSN: 2322-0015 UGC Approved Journal No. 63628
RESEARCH ARTICLE **OPEN ACCESS**

Effect of Pb^{2+} Doped in Co Nanoferrite on Magnetic Properties Synthesized by Sol-gel Technique

Altaf Isuf Fakir[1], Magare GK[2], Mundhe BS[3], Rathod SM[2*]

[1]PG and Research Center, Dept. of Physics, Abasaheb Garware College, Pune 411 004
[2]Department of Physics, Laxamrao Apte College, Apte Road, Pune 411004,[2]Department of Physics, KKM College, Manwat, Parbhani 431505
Email: smragc@rediffmail.com

Manuscript Details
Available online on http://www.irjse.in
ISSN: 2322-0015

Editor: Dr. Arvind Chavhan

Cite this article as:
Altaf Isuf Fakir, Magare GK, Mundhe BS, Rathod SM. Effect of Pb^{2+} Doped in Co Nanoferrite on Magnetic Properties Synthesized by Sol-gel Technique, *Int. Res. Journal of Science & Engineering,* January 2018; Special Issue A2: 256-259.

ABSTRACT

Lead doped (Pb^{2+}) – cobalt (Co) nanoferrite as Co1-xPbxFe2O4 (were x = 0.1, 0.2, 0.3, 0.4, 0.5) were synthesized by a simple cost effective method involving sol-gel auto combustion method. Synthesized samples were sintered at 600 ^{0}C temperature. The Magnetic properties are studied using hysteresis loop terser field of 10 kOe. The magnetization of the prepared nanoparticles was investigated, and the saturation magnetization (M_s), remanence (M_r), and coercivity (H_c) were derived from the hysteresis loops. The results revealed that as the (Pb^{2+}) Lead substitution in (Co) cobalt nano ferrite increases the magnetic properties remanence (M_r), and coercivity (H_c) goes on decreasing, the saturation magnetization (M_s), first it is increases upto x = 0.3 and then decreases for higher Pb^{2+} substitution such changes in magnetic properties may be due to the exchange interaction between the tetrahedral and the octahedral sites. From the magnetic properties it is clear that the synthesized materials shifted from hard to soft ferrit.

Key words: sol-gel, Cobalt nanoferrite, magnetization (M_s), remanence (M_r), and coercivity (H_c)

INTRODUCTION

Nanocrystalline ferrites are currently the subject of interest because of its wide application in industrial as well as research areas. They are attractive because of their importance in ferrofluids , magnetic drug delivery, hyperthermia for cancer treatment, etc. [1].An interesting ex-ample is that of CoFe2O4 which is a familiar hard magnetic material with high saturation magnetization (Ms), high coercivity (Hc) among all the ferrite family[2].These properties along with its great physical and chemical stabilities make Co-ferrite nano-particles be suitable for many technical applications[3]. Their applications include high frequency devices, memory cores, high density information storage and also in biomedical field [4]. It is well known that several chemical techniques, such as hydrothermal, co-precipitation and sol-gel synthesis have been used to prepare ultrafine ferrite powders. Among these techniques, sol-gel method offers high degree of compositional homogeneity content in a relatively short processing time at a very low temperature. An understanding of the magnetic properties is essential in order to design new magnetic materials .The present work deals with the synthesis of nano particles of lead substituted cobalt ferrite (Co1-xPbxFe2O4 where x = 0.1, 0.2, 0.3, 0.4, and 0.5) via sol-gel method. Magnetic measurements are done with the help of VSM. This work is an attempt to investigate the magnetic properties of lead substituted cobalt ferrites.

METHODOLOGY

Pb substituted in Co-ferrite powders were synthesized by sol-gel auto combustion method at low temperature for different compositions Co1-xPbxFe2O4 (where x = 0.1, 0.2, 0.3, 0.4, and 0.5) raw material are used in experiments are AR grade nitrate (Co(No3)2.6H2o, Pb(No3)2, Fe2(No3)2 and C6H8O7) is used as fuel in the ratio 1:3, all from Merck co. using stoichiometric ratio and dissolved in distilled water. the mixture of the raw material was stirred at low temperature on hot plate magneto –stirrer .after maintaining the PH at 7 solution temperature raise up to 800^{0}C, it was continuously stirred to obtain uniform gel. After 3-4 hours it converts from gel to ash form,

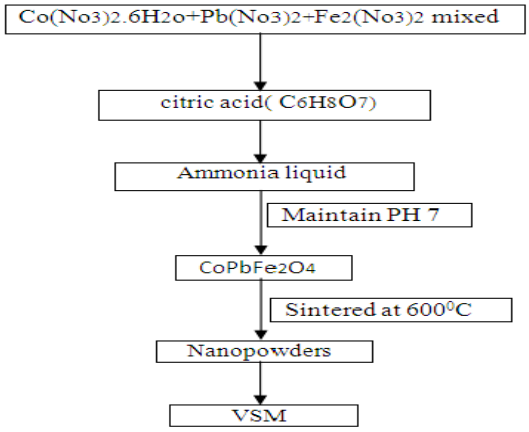

Figure 1. Sol-gel method for the preparation of ferrites

which was sintered at 600^{0}C.from VSM the magnetic properties of the samples show remarkable changes with change of Pb percentage.

RESULTS AND DISCUSSION

Typical hysteresis loops of CoPbFe2O4 as obtained and after sintering of sample at 600^{0}c.Typical hysteresis loops for the samples Co0.9Pb0.1 Fe2O4, Co0.8Pb0.2Fe2O4, Co0.7Pb0.3Fe2O4, Co0.6Pb0 .4Fe2O4, Co0.5Pb0.5Fe2O4 are shown in **Figure 2**

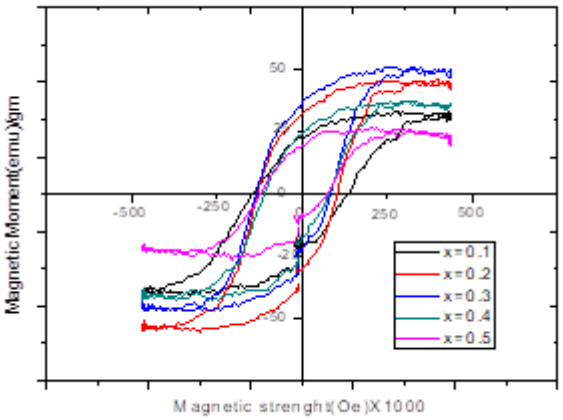

Figure 2. Hysterisis loop of Co1-xPbxFe2O4 where x = 0.1, 0.2, 0.3, 0.4, and 0.5after sintering at 600°C

In a cubic system of ferromagnetic spinels, the magnetic order is mainly due to a super exchange interaction mechanism occurring between the metal ion in the A and B sub lattices. The substitution of

nonmagnetic ion such as lead, which has a preferentially A site occupancy results in the reduction of the exchange interaction between A and B sites. Hence, by varying the amount of lead substitution, it should possible to vary magnetic properties of the samples.

The saturation magnetization for all the ferrites after sintering is listed in **Table 1** it is clear that for the samples Co0.9Pb0.1 Fe2O4, Co0.8Pb0.2Fe2O4, Co0.7 Pb0.3Fe2O4 the saturation magnetization increases from 33.15-50.96 emu/gm. This could be due to Pb^{2+} (with zero magnetic moment) replace ion on the tetrahedral A–sites, causing the decrease of magnetic moment in the sub lattice M_A, resulting in the increase magnetic moment which increases saturation magnetization. On further increase of lead substitution in Co0.6Pb0.4Fe2O4 and Co0.5Pb0. 5Fe2O4 the saturation magnetization decreases from 37.48-22.41 emu/gm. This could be due to further increase in the concentration of Pb2+ (more than 0.4), the exchange interaction between A and B sites gets lowered resulting in strengthening of B-B interaction and weakening of A-B interaction, which leads to decrease of saturation magnetization.

Table 1:

Sr No.	composition	Hc (Oe)	Mr (emu/gm)	Ms (emu/gm)
1	Co0.9Pb0.1 Fe2O4	134.610	22.67	33.15
2	Co0.8Pb0.2Fe2O4	110.801	30.09	46.09
3	Co0.7Pb0.3Fe2O4	106.249	32.4	50.96
4	Co0.6Pb0.4Fe2O4	91.15	22.2	37.48
5	Co0.5Pb0.5Fe2O4	90.53	15.53	22.41

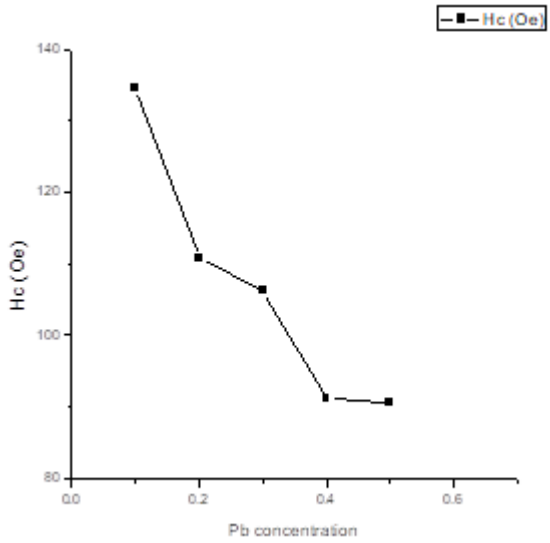

Fig. 3(a) Variation of coercivity (*Hc*) with Pb concentration (*x*).

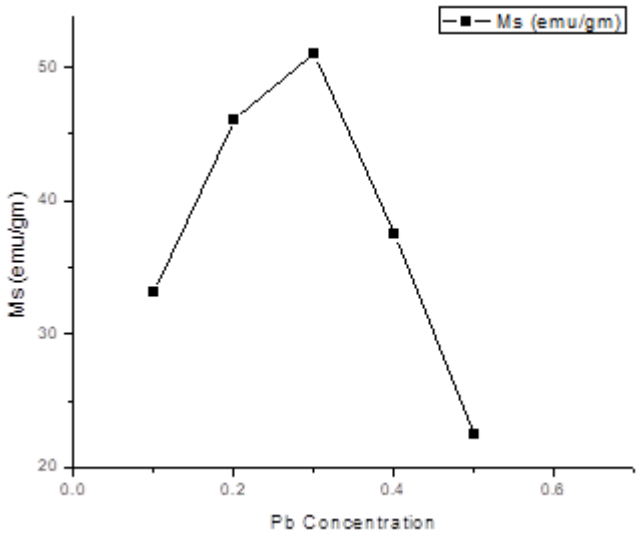

Fig. 3(b) Variation of saturation magnetization (*Ms*) with Pb concentration (*x*);

From the hysteresis loop taken of different sample of CoPbFe2O4 it is found that with increasing concentration of $Pb^{2+,}$ coercivity (H_c) goes on decreasing these can be utilized to change magnetic properties of cobalt ferrite and hard magnetic material can be converted to soft magnetic material.

CONCLUSION

Lead substituted cobalt ferrite nanoparticles ($Co_{1-x}Pb_xFe_2O_4$ with x = 0.1, 0.2, 0.3, 0.4, and 0.5) were prepared via sol-gel auto combustion route. From VSM it is clear that for the samples $Co_{0.9}Pb_{0.1}$ Fe_2O_4, $Co_{0.8}Pb_{0.2}Fe_2O_4$, $Co_{0.7}Pb_{0.3}Fe_2O_4$ the saturation magne-

tization increases from 33.15-50.96 emu/gm. On further increase of lead substitution in $Co_{0.6}Pb_{0.4}Fe_2O_4$ and $Co_{0.5}Pb_{0.5}Fe_2O_4$ the saturation magnetization decreases from 37.48-22.41 emu/gm. It was found that with increasing concentration of Pb^{2+}, coercivity (H_c) goes on decreasing these can be utilized hard magnetic cobalt ferrite can be converted to soft magnetic material. DC electrical resistivity study of the samples was found to be increases with increasing $Pb^{2+}$from $x = 0.1$ to $x = 0.5$. That means the conductivity decreases with increasing concentration of lead but it increases with increasing voltage.

REFERENCES

1. Raj K, Moskowitz R and Casciari R.Advances in Ferrofluid Technology," *Journal of Magnetism and Mag-netic Materials*, Vol. 149, No. 1-2, 1995, pp. 174-180.
2. Sharma RK *et al.* Synthesis of Chromium Substituted Nano Particles of Cobalt Zinc Ferrites by Coprecipitation. *Materials Letters*, 2005; **59**, 3402-3405. http://dx.doi.org/10.1016/j.matlet.2005.06.004
3. Mathew DS and Juang RS. An Overview of the Structure and Magnetism of Spinel Ferrite Nanoparticles and Their Synthesis in Microemulsions. *Chemical Engineering Journal*, 2007; **129**, 51-65. http://dx.doi.org/10.1016/j.cej.2006.11.001
4. Moya C. del Puerto Morales, M., Batlle, X. and Labarta, A. Tuning the Magnetic Properties of Co-Ferrite Nanoparticles through the 1,2-Hexadecanediol Concentration in the Reaction Mixture. *Physical Chemistry*, 2015; 17, 13143-13149. http://dx.doi.org/10.1039/C5CP01052G

IRJSE International Research Journal of Science & Engineering
Int. Res. J. of Science & Engineering, 2018; Special Issue A2 : 260-266 SJIF Impact Factor 4.11
ISSN: 2322-0015 UGC Approved Journal No. 63628
RESEARCH ARTICLE **OPEN ACCESS**

Inorganic $CuBiS_2$ NPs-based Photosensitized ZnO NRs for Solar cell application: Effect of volumetric ratio

Pasupula Ganga Shekar, Ekar SU and Mane RS

[1]PG and Research Center, Dept. of Physics, Abasaheb Garware College, Pune 411 004
[2]Department of Physics, Laxamrao Apte College, Apte Road, Pune 411004,[2]Department of Physics, KKM College, Manwat, Parbhani 431505
Email: smragc@rediffmail.com

Manuscript Details
Available online on http://www.irjse.in
ISSN: 2322-0015

Editor: Dr. Arvind Chavhan

Cite this article as:
Pasupula Ganga Shekar, Ekar SU and Mane RS Inorganic $CuBiS_2$ NPs-based Photosensitized ZnO NRs for Solar cell application: Effect of volumetric ratio, *Int. Res. Journal of Science & Engineering*, January 2018; Special Issue A2: 260-266.

ABSTRACT

In the present report; we have discussed inorganic $CuBiS_2$ NPs-based photosensitized ZnO NRs on ITO substrate. ZnO nanorods (NRs) have been grown by using simple seeding layer and chemical bath deposition (CBD) methods. Inorganic $CuBiS_2$ NPs with varying volumes of copper, bismuth at the rate of 2.5 mL and keeping the volume of sulphur constant equal to the sum volumes of copper and bismuth have been deposited on seeding layer and CBD deposited ZnO NRs at lower temperatures. The structural elucidation of as prepared $CuBiS_2$ NP_S-ZnO films have been determined by XRD (X-ray diffraction) and energy dispersive X-ray analysis (EDAX).The films were characterized by UV and Energy band gap analysis and observed that when the Bi-volume was greater than the Cu-volume, then increase in band gap was observed. The $CuBiS_2$ NP_S-ZnO electrodes have been examined for solar cell application and the maximum conversion efficiency (η) of the film has been determined as 0.278 % for Cu-volume 7.5 mL and Bi-volume 5 mL than the remaining cases of $CuBiS_2$ and bare ZnO. The electrochemical impedance spectroscopy (EIS) studies of solar cell have been discussed to study the charge transportation. The present work is novel.

Keywords - Seeding layer, CBD, ZnO NRs, Inorganic $CuBiS_2$ NP_S, Photo-sensitized solar cell.

INTRODUCTION

Presently researchers are attracting towards the development of heterostructured solar cells using wide band gap metal oxides combined with narrow band gap inorganic metal chalcogenide semiconductors. In the visible and infra-red regions of the solar spectrum, many photons are available with the energy lesser than 3 eV. The narrow band gap materials such as CdX, Cu_2X, Bi_2X_3 (X=S or Se) are able to absorb both UV and visible light. But the wide band gap materials such as and Zinc oxide (ZnO) can absorb only UV light. Utilizing both UV and visible lights by combining the narrow band gap inorganic semiconductors with wide band gap ZnO or TiO_2 many researches have been done so far to develop the efficient heterostructure solar cells. Among many metal oxides, like SnO_2, CdO, TiO_2, MgO which have been tested for dye-sensitizing properties, ZnO has received much attention owing to its band gap energy (3.4 eV), which is similar to TiO_2 (3.2 eV) [1].With wurtzite structure, high photosensitivity,high electron mobility at room temperature, ZnO finds many applications in various fields such as, gas sensor [2], opto-electronics and nanosensor [3], photo detectors [4], piezoelectrics [5],light-emitting diode [6], solar cells [1] and so on. ZnO a II-VI semiconductor with a direct and wide band gap nature exhibits various types of surface morphologies like nano-spikes and nanopillars [7], nano-seeds [8],nano-plates [9], nano-tubes [10], nano-rods [3,10] and so on. The ZnO can be prepared by many types of synthesis techniques that have been developed so far such as, electrodeposition [7],hydrothermal [8], chemical bath deposition (CBD) [2,9], spray pyrolysis [11], sol–gel process [12], SILAR (successive ionic layer adsorption and reaction) [13], and so on. Narrow band gap inorganic NPs sensitised solar cells are being studied due to their certain properties like easy fabrication, possibility to realize more light absorption in the solar spectrum. So far many researchers have reported with the combination of wide band gap semiconductor as photo-anode and narrow band gap inorganic NPs such as ZnO/Bi_2S_3 [14,15], ZnO/Cu_2S [14,16], PbS/ZnO [17], ZnO/GaAs [18], ZnO/CdTe [19], ZnO/CdS [20], and ZnO/CdSe [21], and so on by using various methods. The inorganic narrow band gap NPs like copper based ternary compounds such as $CuSbS_2$, $CuSbSe_2$, $CuBiS_2$, and $CuBiSe_2$ have been realized to be possible alternative solar absorbing materials. It was reported that the energy band gaps to be 1.3 eV for $CuBiSe_2$, 1.4 eV for $CuBiS_2$,1.5 eV for $CuSbSe_2$, and 1.7 eV for $CuSbS_2$ respectively [22-24].Of these ternary compounds, $CuBiS_2$ (Copper bismuth disulphide) finds many applications in thin film lithography, PECs (Photo-electrochemical cells), solar absorber coatings, and so on. To the best of our knowledge very few methods have been developed so far such as CBD [25], spray pyrolysis [26] for the deposition of $CuBiS_2$. There are many reports available with the combination of wide band gap ZnO and binary metal chalcogenides. But as per our knowledge there are no reports available with the combination of ternary $CuBiS_2$ NP_S with ZnO where an attempt is made in this report.

MATERIALS AND METHODS

2.1: Synthesis of ZnO NRs on bare ITO: The ZnO NRs were grown on ITO by using seeding layer and CBD methods. Initially seeding layer was used to deposit the ZnO on bare ITO and then CBD method was followed.To prepare ZnO solution, Zinc nitrate hexahydrate ($Zn(NO_3)_2.6H_2O$) was taken in a beaker to which DDW (Double distilled water) and small amount of aqueous ammonia (NH_4OH) were added. By adding NH_4OH drop wise, the solution becomes clear at pH~10.5.Using seeding layer method, the ZnO NRs were gown on ITO by immersing it in ammonia complexed zinc nitrate hexahydrate ($[Zn(NH_3)_4]^{2+}$) precursor kept at room temperature, and in hot DDW (H_2O) maintained at ~88 ^{O}C (±2) periodically for few cycles. To grow the ZnO NRs on pre-seeded ZnO substrate by CBD method, Zn precursor solution was prepared as described in the above case. The pre-seeded ZnO substrate was introduced in zinc precursor solution and the beaker was placed in the water bath which was maintained at ~88 ^{O}C (±2) for 90 min [13, 15, 27]. After 90 min the substrate with whitish film was removed and rinsed with DDW to remove the loosely bond hydroxide ions and dried in air. CBD second deposition was repeated to get the appropriate thickness of the film.

Table 1: Volumetric ratios of $Cu(NO_3)_2.3H_2O$; $Bi(NO_3)_3.5H_2O$ and $(NH_2)_2SC$ reaction process.

Beaker No	Volume of the Solution (mL)			Volumetric ratio	Total Volume (mL)
	Copper Nitrate Tri–Hydrate	Bismuth Nitrate Penta–Hydrate	Thiourea		
1	10	2.5	12.5		
2	7.5	5	12.5	$Cu_{(7.5)}Bi_{(5)}S_{2(12.5)}$	25
3	5	7.5	12.5	$Cu_{(5)}Bi_{(7.5)}S_{2(12.5)}$	25
4	2.5	10	12.5	$Cu_{(2.5)}Bi_{(10)}S_{2(12.5)}$	25

2.2.: Preparation of Cu-Bi-S Stock Solutions: The deposition of $CuBiS_2$ NP_S with volumetric ratio of Cu, Bi, and S by CBD on ZnO deposited ITO (Indium tin oxide) was discussed below. For this $Cu(NO_3)_2.3H_2O$ (Copper nitrate tri hydrate), $Bi(NO_3)_3.5H_2O$ (Bismuth nitrate penta hydrate) and $(NH_2)_2SC$ (Thiourea) were used as the sources for Cu, Bi and S and $Cu(NO_3)_2.3H_2O$; $Bi(NO_3)_3.5H_2O$,and $(NH_2)_2SC$ stock solutions in the molar ratio of 0.1:0.05:0.1M were prepared at room temperature as discussed below. Initially in a beaker $Cu(NO_3)_2.3H_2O$ solution was prepared by using 48 mL DDW and 2 mL TEA (Tri-Ethanalo-Amine) was added while the solution was under stirring at 600 rpm stirring at room temperature. To optimize the pH, few sodium hydroxide (NaOH) pellets were added slowly under constant stirring. Further in a separate beaker $Bi(NO_3)_3.5H_2O$ chemical was dissolved using concentrated HNO_3 (Nitric acid) (~1.5 mL) followed by 12 mL DDW and kept the beaker on the magnetic stirrer at 500 rpm stirring at room temperature. After 15-25 min, 2.5 mL TEA was added as a complexing agent followed by the addition of DDW to make 50 mL solution, while the solution was under stirring. The reaction takes place slowly. After 55 min, when the solution was stirring, 1 M basic solution of NaOH was added slowly to prepare alkaline solution and the solution becomes clear at alkaline pH. In another beaker $(NH_2)_2SC$ solution was prepared by using $(NH_2)_2SC$ chemical and DDW in a beaker. The solution turned to clear in a short interval of time.

2.3: Deposition of $CuBiS_2$ NP_S by CBD on ZnO deposited ITO: $Cu(NO_3)_2.3H_2O$,$Bi(NO_3)_3.5H_2O$ and $(NH_2)_2SC$ solutions were taken in 4 separate beakers in the volumetric ratio to prepare 25 mL of Cu-Bi-S mixed solution in each beaker as shown in Table (1). Now, previously deposited ZnO-ITOs were dipped in these mixed solution beakers. Beakers labelled as No.1 $[Cu_{(10)}Bi_{(2.5)}S_{2(12.5)}]$, 2 $[Cu_{(7.5)}Bi_{(5)}S_{2(12.5)}]$, 3 $[Cu_{(5)}Bi_{(7.5)}S_{2(12.5)}]$, and 4 $[Cu_{(2.5)}Bi_{(10)}S_{2(12.5)}]$, (Where, the subscripts in the brackets indicate the volumes of Cu, Bi and S respectively) were kept in the water bath at 62 ^oC temperature for about 65 min. After the deposition, the films with dark black colour were removed and washed with DDW and dried in air. The as-deposited films were annealed at 200 ^oC for 60 min and used for the characterization.

RESULTS AND DISCUSSION

3.1: Structural Elucidation:

The structural properties of the $CuBiS_2$ NP_S sensitised ZnO-ITO films were studied from the X-ray diffraction (XRD) patterns recorded by using an X-ray diffractometer with $CuK\alpha_1$ radiations (λ= 1.5406 Å) in 2θ range from 20-80 degree. Fig.1 shows the XRD pattern of $CuBiS_2$ NPs sensitised ZnO-ITO.The XRD peaks of ITO substrate were indicated by asterisk (*). The XRD peaks of ZnO electrodes on ITO were indicated by ZnO revealing the nanostructure well-aligned growth wurtzite (hexagonal) ZnO NRs [JCPDS No: 36-1451]. All the peaks give the hexagonal ZnO NRs structure. Fig.1 (a) characterises the diffraction peaks centred at 2θ=24.89^o, 56.30^o, 67.61^o and at 68.94^o be indexed to the (004), (314), (322) and (317) crystal planes, correspond to $Cu_{(10)}Bi_{(2.5)}S_{2(12.5)}$ NPs [JCPDS NO: 43-1473] respectively. Fig. 1(b) characterises the diffraction peaks centred at 2θ=24.87^o, 32.78^o, 56.45^o, and at 67.88^o be indexed to the (004), (113), (314) and (322) crystal planes, correspond to $Cu_{(7.5)}Bi_{(5)}S_{2(12.5)}$ NPs [JCPDS NO: 43-1473] respectively. Fig.1(c) characterises the diffraction peaks centred at 2θ = 25.16^o, 53.09^o, 56.38^o, 67.85^o, and

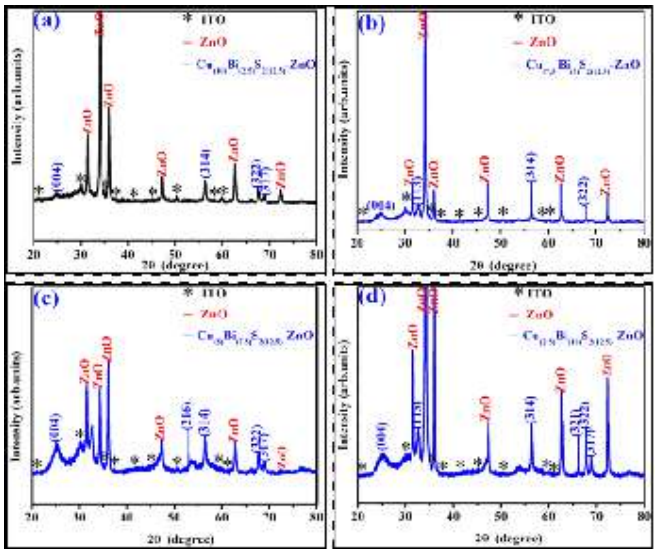

Fig. 1: XRD images of $CuBiS_2$ NPs sensitised ZnO electrodes

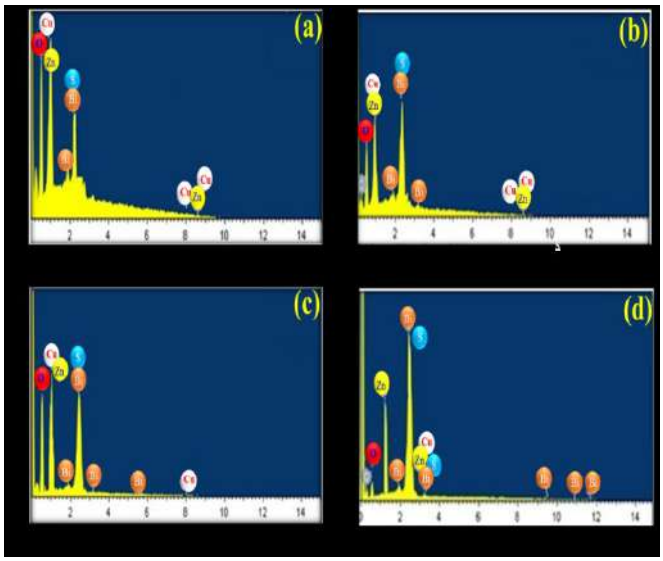

Fig. 2: EDAX images of $CuBiS_2$ NPs sensitised ZnO electrodes

at 68.98° be indexed to the (004), (216), (314), (322) and (317) crystal planes correspond to $Cu_{(5)}Bi_{(7.5)}S_{2(12.5)}$ NPs [JCPDS NO: 43-1473] respectively. Fig.1 (d) characterises the diffraction peaks centred at 2θ=25.28°, 32.54°, 56.27°, 66.25°,67.81°, and at 68.83° be indexed to the (004), (113), (314), (321),(322), and (317) crystal planes correspond to $Cu_{(2.5)}Bi_{(10)}S_{2(12.5)}$ NPs respectively [JCPDS NO: 43-1473].All the peaks of $CuBiS_2$ NPs in $CuBiS_2$ NPs sensitised ZnO electrodes give the orthorhombic crystal structure.

The presence of elements was identified by using energy dispersive X-ray (EDAX) spectroscopy joined with FE-SEM unit in the $CuBiS_2$ NPs sensitised ZnO electrodes heterostructre. Fig. (2) shows the EDAX spectra of the $Cu_{(10)}Bi_{(2.5)}S_{2(12.5)}$-ZnO,$Cu_{(7.5)}Bi_{(5)}S_{2(12.5)}$-ZnO,$Cu_{(5)}Bi_{(7.5)}S_{2(12.5)}$-ZnO,and $Cu_{(2.5)}Bi_{(10)}S_{2(12.5)}$–ZnO films. The spectrum shows solid evidence for the existence of Zn, O, Bi, Cu and S elements in Zn-O and Cu-Bi-S respectively.

3.2: UV analysis and Energy Band gap Study:

Fig. 3 describes the absorption spectra and energy band gaps of ZnO and $CuBiS_2$ NPs sensitised ZnO samples studied by using a UV-vis spectrophotometer (WantechWPG-100 Potentiostat /Galvanostatic) in the wavelength range between 350-650 nm for varying volumes of Cu, Bi and keeping the volume of the S constant. The absorption spectra of ZnO and $CuBiS_2$ NPs sensitised ZnO electrodes were studied and the absorption data were analysed to estimate the energy band gap by using the Tuac's relationship. Fig. 3(a) shows the absorbance peaks of ZnO and $CuBiS_2$ NPs sensitised ZnO electrodes. As prepared ZnO nano rod film shows good absorbance for 350<λ<400 nm [Fig 3: {a(A)}]. In visible region, $CuBiS_2$ NPs sensitised ZnO electrode heterojunction shows good absorbance for 400<λ<475 nm and low absorbance above 450 nm [Fig 3: {a (B-E)}]. Thus $CuBiS_2$ NPs sensitised ZnO heterostructure absorbs both visible and UV light indicating the wide range of absorption of light.

The relationship between "α" and" hv" is given by,

$$\alpha = \frac{\alpha_0 (h\nu - E_g)^n}{h\nu} \qquad (1)$$

Where α = absorption coefficient, E_g = optical band gap, v=frequency of light, h = plank's constant, hv = photon energy, n = constant.

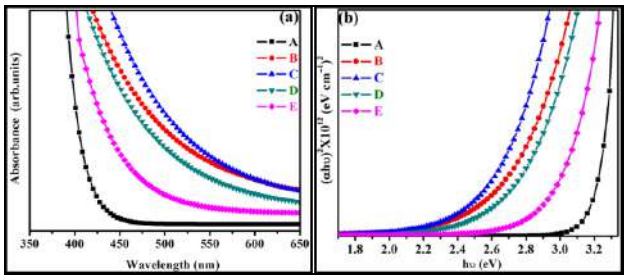

Fig 3: (a) UV and (b) Energy band gap images of ZnO and $CuBiS_2$ NPs sensitised ZnO electrodes

[Fig. 3 (b)] depicts the Tuac's plot for ZnO [Fig 3: {b(A)}] and $CuBiS_2$ NP_S sensitised ZnO electrodes [Fig 3: {b(B-E)}]. The Tauc's plot of $(\alpha h\nu)^2$ versus hv is linear and x-intercepts of the plot $(\alpha h\nu)^2$ versus hv (photon energy) illustrates the optical band gaps for ZnO and $CuBiS_2$ NP_S sensitised ZnO. The energy band gap values have been given in Table (2).From Fig. 3 (b) it can be understood that the band gap of $Cu_{(7.5)}Bi_{(5)}S_{2(12.5)}$-ITO was observed to be lower than the remaining cases of $CuBiS_2$ NP_S sensitised ZnO electrodes and ZnO. Thus it can be concluded that when Bi volume was higher than Cu volume and sum volumes of copper and bismuth equal to S volume constantly, the increased energy band gap can be observed.

Table 2: Energy band gap values of ZnO and $CuBiS_2$-ZnO electrodes.

S.NO.	Compound	Band gap (eV)
A	ZnO-ITO	3.19
B	$Cu_{(10)}Bi_{(2.5)}S_{2(12.5)}$-ITO	2.49
C	$Cu_{(7.5)}Bi_{(5)}S_{2(12.5)}$-ITO	2.45
D	$Cu_{(5)}Bi_{(7.5)}S_{2(12.5)}$-ITO	2.56
E	$Cu_{(2.5)}Bi_{(10)}S_{2(12.5)}$-ITO	2.89

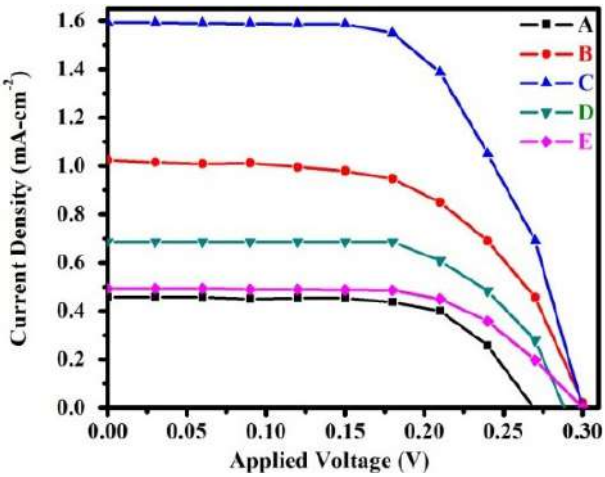

Fig. 4: JV analysis images of ZnO and $CuBiS_2$ NP_S sensitised ZnO electrodes.

3.3: Photo-Electrochemical Measurement :

The J-V characteristics for the devices under dark and illumination conditions of light were performed using Solar Simulator (with IGOR program and Keithley-2400 power sources meter) [Fig.4]. Under dark, the non-changing behaviour of curve upto 0.30 V indicates the formation of the good heterojunction of the formed device. Under illumination, the output photovoltaic performance i.e. the short circuit photocurrent density (J_{sc}), open-circuit photo voltage (V_{oc}), fill factor (FF) and power conversion efficiency (η) of the device were calculated. It was observed that the obtained solar cell efficiency of 0.278% [Fig.4 (C)] was observed to be higher than ZnO and the remaining cases of $CuBiS_2$ sensitized ZnO electrodes [Fig.4.(A, B, D, and E)]. Due to lower band gap, $CuBiS_2$-ZnO electrodes could absorb more number of photons than bare ZnO which led to the generation of higher number of electron-hole pairs and hence, improved solar cell power efficiency was obtained. Hence, $CuBiS_2$-ZnO heterostructure electrode showed improved solar cell performance than bare ZnO. Moreover when Cu volume is smaller than Bi volume, more efficiency was observed. Solar cell parameter values for all the electrodes are listed in Table 3.

Table 3: Photovoltaic parameters of photo electrochemical cells composed of $CuBiS_2$-ZnO electrodes.

Working electrode	V_{OC} (V)	J_{SC} (mA-cm^{-2})	FF (%)	Efficiency (%)
A	0.27	0.46	0.67	0.083
B	0.30	1.03	0.55	0.171
C	0.30	1.60	0.58	0.278
D	0.29	0.70	0.65	0.131
E	0.30	0.50	0.63	0.095

3.4: Electrochemical Impedance Spectroscopy Measurement:

The most important electronic and ionic phenomena in the solar cell can be investigated by using electrochemical impedance spectroscopy or EIS technique. In general EIS technique is a principal technique to describe the relation between the capacitance and resistances of the photo-anode materials and to study the charge transportation.Fig.5 represents the Nyquist plots for ZnO and $CuBiS_2$ NP_S-ZnO electrodes. The Nyquist plot is a graph plotted by taking the real part of the impedance on X-axis (Z') and imaginary part on Y-axis (Z''). The Nyquist plots of ZnO [Fig.5(A)] and $Cu_{(10)}Bi_{(2.5)}S_{2(12.5)}$-ZnO [Fig.5(B)], $Cu_{(7.5)}Bi_{(5)}S_{2(12.5)}$-ZnO [Fig.5(C)],$Cu_{(5)}Bi_{(7.5)}S_{2(12.5)}$–ZnO

[Fig.5(D)],and $Cu_{(2.5)}Bi_{(10)}S_{2(12.5)}$–ZnO [Fig.5 (E)] electrodes consisting of two arcs in the high and low frequency regions corresponding to charge transfer at counter electrode-electrolyte and electrolyte-photo-anodes, respectively. The series resistance values of $CuBiS_2$-ZnO electrodes are given in Table 4.

Table 4: Series resistance values of ZnO and $CuBiS_2$-ZnO electrodes.

Working electrode	R_S (Ω-cm)
A	41
B	50
C	57
D	61
E	52

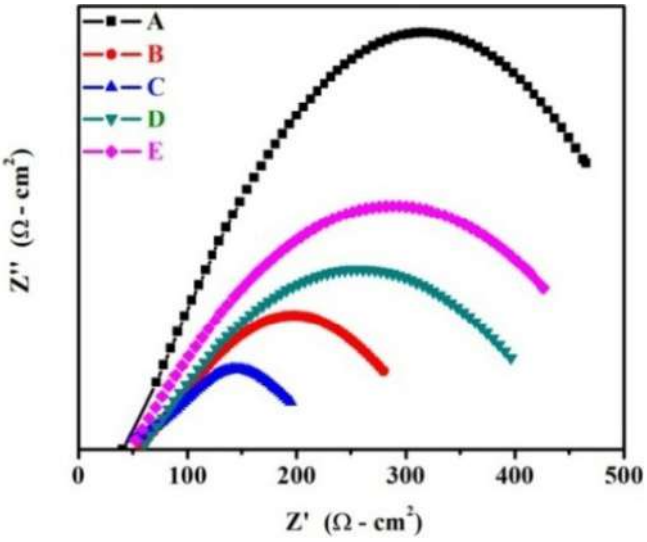

Fig. 5: EIS analysis images of ZnO and $CuBiS_2$ NPs sensitised ZnO electrodes

CONCLUSION

In summary, we demonstrate the use of simple and inexpensive seeding layer and CBD methods for the ZnO NRs synthesis. Inorganic $CuBiS_2$ NPs have been sensitised on ZnO electrodes and $CuBiS_2$ NPs sensitised ZnO electrodes solar cell heterostructre was achieved using CBD method. The present heterostructure of $CuBiS_2$ NPs-ZnO electrode solar cell has been successfully demonstrated for the solar cell application and observed power conversion efficiency for $CuBiS_2$ NPs sensitised ZnO electrodes as 0.278 % (for Cu-7.5 mL and Bi-5 mL volumes) which is greater than the remaining cases of Cu-Bi-S-ZnO and ZnO.

REFERENCES

1. R. S. Mane, W. J. Lee, H. M. Pathan, and S. H. Han, Nanocrystalline TiO_2/ZnO Thin Films: Fabrication and Application to Dye-Sensitized Solar Cells, J. Phys. Chem. B, 109 (2005) 24254-24259.
2. C.D. Lokhande, P.M. Gondkar, R.S. Mane, V.R. Shinde, S.H. Han, CBD grown ZnO based gas sensors and dye-sensitized solar cells, Current Applied Physics, 475 (2009) 304–311.
3. X. D. Wang, C. J. Summers, Z. L. Wang, Large-Scale Hexagonal-Patterned Growth of Aligned ZnO Nanorods for Nano-Optoelectronics and Nanosensor Arrays, Nano Lett., 4 (2004) 423–426.
4. S. Liang, H.Sheng, Y.Liu, Z.Huo,Y.Lu, H.Shen, "ZnO Schottky ultraviolet photodetectors",J Cryst Growth, 225 (2001) 110–113.
5. A. Janotti, C.G. Van de Walle, Fundamentals of zinc oxide as a semiconductor, Reports on Progress in Physics, 72 (2009) 12650–12658.
6. Jong H. Na, M. Kitamura, M. Arita, and Y. Arakawa, Hybrid p-n junction light-emitting diodes based on sputtered ZnO and organic semiconductors, Applied physics letters, 95 (2009) 253303.
7. D. Pradhan, M. Kumar, Y. Ando, K.T. Leung, Fabrication of ZnO nanospikes and nanopillars on ITO glass by template less seed-layer-free electrodeposition and their field-emission properties, ACS Appl. Mater. Interfaces, 1 (2009) 789–796.
8. W. B. Wu, G. D. Hu, S. G.Cui, Y. Zhou, H. T. Wu, Epitaxy of Vertical ZnO Nanorod Arrays on Highly (001)-Oriented ZnO Seed Monolayer by a Hydrothermal Route, Cryst. Growth Des., 8 (2008) 4014.
9. B. Cao, W. Cai, From ZnO Nanorods to Nanoplates: Chemical Bath Deposition Growth and Surface-Related Emissions, The Journal of Physical Chemistry C, 112 (2008) 680–685.
10. C. S. Rout, S. H. Krishna, S. R. C.Vivekchand, A. Govindaraj, C. N. R.Rao, Hydrogen and ethanol sensors based on ZnO nanorods, nanowires and nanotubes, Chem. Phys. Lett., 418 (2006) 586–590.
11. P. Singh, A. Kaushal, D. Kaur, Mn-doped ZnO nanocrystalline thin films prepared by ultrasonic spray pyrolysis, Journal of Alloys and Compounds, 471 (2009) 11–15.
12. W.P. Tai, J.H. Oh, Humidity sensing behaviors of nanocrystalline ZnO thin films by sol–gel process,

Journal of Materials Science – Materials in Electronics, 13 (2002) 391–394.

13. P. Suresh Kumar, A. Dhayal Raj, D. Mangalaraj, D. Nataraj, Growth and characterization of ZnO nanostructured thin films by a two-step chemical method, Applied Surface Science, 255 (2008) 2382–2387.
14. P. Chen, L. Gu and X. Cao, From single ZnO multipods to heterostructured ZnO/ZnS, ZnO/ZnSe, ZnO/Bi_2S_3 and ZnO/Cu_2S multipods: controlled synthesis and tunable optical and photo electrochemical properties, Cryst Eng Comm., 12 (2010) 3950-3958.
15. P.R. Nikam, P.K. Baviskar, J.V. Sali, K.V. Gurav, J.H. Kim, B.R. Sankapal, SILAR coated Bi_2S_3 nanoparticles on vertically aligned ZnO nanorods: Synthesis and characterizations, Ceramics International, 41 (2015) 10394.
16. K.Guo,X.Chen,J.Han,Z.Liu,Synthesis of ZnO/Cu_2S core/shell nanorods and their enhanced photoelectric performance, Journal of sol-gel science and technology, 72 (2014) 92-99.
17. J.M. Luther, J. Gao, M.T. Lloyd, O.E. Semonin, M.C. Beard, A.J. Nozik, Stability assessment on a 3% bilayer PbS/ZnO quantum Dot heterojunction solar cell, Adv. Mater.22, (2010) 3704–3707.
18. P. F. Zhang, X. L. Liu, R. Q. Zhang, H. B. Fan, A. L. Yang, H. Y. Wei, P. Jin, S. Y. Yang, Q. S. Zhu, and Z. G. Wang, Valence band offset of ZnO/GaAs heterojunction measured by x-ray photoelectron spectroscopy, Applied Physics Letters, 92 (2008) 012104.
19. X. Wang, H. Zhu, Y. Xu, H. Wang, Y. Tao, S. Hark, X. Xiao, Q. Li, Aligned ZnO/CdTe core-shell nanocable arrays on indium tin oxide: Synthesis and photoelectrochemical properties, ACS Nano, 4 (2010) 3302-3308.
20. G. Murugadoss, ZnO/CdS nanocomposites: Synthesis, structure and morphology, Nanotechnology, 10 (2012) 722.
21. C. Zhu, X. Pan, C. Ye, L. Wang, Z. Ye, J. Huang, Effect of CdSe quantum dots on the performance of hybrid solar cells based on ZnO nanorod arrays, Ceram. Int., 39 (2013) 2975-2980.
22. M. Kumar, C. Persson, Cu(Sb,Bi)$(S,Se)_2$ as indium-free absorber material with high optical efficiency, Energy Proc., 44 (2014) 176-183.
23. J.T.R. Dufton, A. Walsh, P.M. Panchmatia, L.M. Peter, D. Colombara, M.S. Islam, Structural and electronic properties of $CuSbS_2$ and $CuBiS_2$: potential absorber materials for thin-film solar cells, Physical Chemistry Chemical Physics., 14 (2012) 7229-7233.
24. D.J. Temple, A.B. Kehoe, J.P. Allen, G.W. Watson, D.O. Scanlon, Geometry, electronic structure, and bonding in $CuMCh_2$ (M = Sb, Bi; Ch = S, Se): alternative solar cell absorber materials?, J Phys. Chem. C, 116 (2012) 7334-7340.
25. P.S. Sonawane, P.A. Wani, L.A. Patil, Tanay Seth, Growth of $CuBiS_2$ thin films by chemical bath deposition technique from an acidic bath, Materials Chemistry and Physics, 84 (2004) 221-227.
26. S. H Pawar, A. J Pawar, P. N. Bhosale, Spray pyrolytic deposition of $CuBiS_2$ thin films, Bull Mater Sci.,8 (1986) 423-426.

P. K. Baviskar, P.R. Nikam, S.S. Gargote, A. Ennaoui, B.R.Sankapal, Controlled synthesis of ZnO nanostructures with assorted morphologies via simple solution chemistry, Journal of Alloys and Compounds, 551 (2013) 233

IRJSE *Int. Res. J. of Science & Engineering,* 2018; Special Issue A2 : 267-271 SJIF Impact Factor 4.11
ISSN: 2322-0015 UGC Approved Journal No. 63628
RESEARCH ARTICLE **OPEN ACCESS**

Growth, SHG and Z-Scan Studies of the Pure and L-Cysteine Doped Zinc Thiourea Sulphate Crystal for Photonic Device Applications

Shejwal NN[1*] Hussaini SS [3] and Shirsat MD[2]

[1*]AISSMS, College of Engineering, Pune-411001, Maharashtra, India
[2]RUSA Center for Advanced Sensor Technology, Department of Physics, Dr. Babasaheb Ambedkar Marathwada University, Aurangabad-431005, Maharashtra, India.
[3]Crystal Growth Laboratory, Department of Physics, Milliya Arts, Science and Management Science College, Beed- 431122, Maharshtra, India
Email: *mnshejwal@gmail.com*

Manuscript Details
Available online on http://www.irjse.in
ISSN: 2322-0015

Editor: Dr. Arvind Chavhan

Cite this article as:
Shejwal NN Hussaini SS and Shirsat MD. Growth, SHG and Z-Scan Studies of the Pure and L-Cysteine Doped Zinc Thiourea Sulphate Crystal for Photonic Device Applications, *Int. Res. Journal of Science & Engineering,* January 2018; Special Issue A2: 267-271.

ABSTRACT

In the current investigation the pure and L-Cysteine (LC) doped Zinc Thiourea Sulphate (ZTS), an optically transparent single crystal has been grown by slow evaporation technique. The encouraging third-order non-linear response of grown crystals has been investigated at 632.8 nm using Z-scan technique, and vital third-order non-linear optical (NLO) constants like third order nonlinear refraction (η_2), nonlinear susceptibility (χ^3), nonlinear absorption (β) and FOM of grown crystal has been evaluated to explore the various optical applications. The χ^3 of magnitude 1.43×10^{-3}esu confirms the strong polarizing nature of doped ZTS crystal. In Kurtz–Perry powder test, the second harmonic generation (SHG) efficiency of doped ZTS crystal is found to be 1.16 times that of ZTS material.

Keywords: Slow evaporation technique, Optical studies, Z-Scan studies, SHG efficiency, NLO materials.

INTRODUCTION

The demands of the nonlinear optical (NLO) crystals have been expedited in the field of photonics technology. The progress of semi organic crystals with superior properties have been focused due to huge applications in photonics and electro-optic modulations devices. [1] Recently, large number of thiourea based organo-metallic crystals with excellent nonlinear optical, mechanical, thermal properties has been reported. The zinc thiourea chloride (ZTC), zinc thiourea sulphate (ZTS), bis-thiourea cadmium acetate (BTCA), bis-thiourea cadmium chloride (BTCC) etc are the well-known crystals reported in the literature [2,3] The ZTS crystal is technologically vital crystal with superior properties as evident in literature.[2-3] Profound research has revealed that the chiral nature of amino acids promote enrichment in properties of various organo-metallic NLO crystals. [4] The various parameters of ZTS crystal have been investigated by doping variety of amino acids namely; glycine, L-Lysine etc. [5-6] The rigorous literature survey noticed that, the effect of L-cysteine (LC) on linear and nonlinear optical properties of ZTS crystal is not investigated. The LC is predominantly chiral amino acid with a thiol group which acquires high affinity towards bonding with metal ions. [7] This bonding ability of LC might serve an advantage to enhance the optical properties of ZTS crystal. Hence, in the current research work pure and LC doped ZTS (LC-ZTS) crystals have been grown and linear and nonlinear optical (NLO) characterization studies have been performed to explore the potential utility of LC-ZTS crystal for photonic device applications.

METHODOLOGY

The analytical reagent (AR) grade zinc sulphate and thiourea in molar ratio 1:3 in deionized water has been dissolved to get the ZTS salt. The recrystallization technique has been used to enhance the purity of the ZTS salt. The LC with 0.5 wt. %, 1 wt. % and 1.5 wt. % was added into supersaturated solution of ZTS. The LC-ZTS mixture was stirred well for 4h and filtered by Whatman filter paper in large size beakers. The beakers were covered by the thin transparent film and kept in isolated vibration free space. The grown crystal obtained from slow solution evaporation technique in 25 days is shown in Fig. 1(a)

Fig.1(a) LC-ZTS Crystal

NLO Test:

The Kurtz-Perry powder technique [8] was used for evaluating the SHG efficiency of grown crystals. The Q-switched Nd: YAG laser operating at 1064 nm was allowed to incident on the fine powder sample with the repetition rate of 10 Hz. At the output window, the emergence of green output of pure ZTS and LC-ZTS was recorded with a second harmonic signal of 60 mV and 66mV respectively. Thus the SHG efficiency of LC-ZTS is found to be 1.16 times that of pure ZTS. Thus, the LC-ZTS crystal is a promising material than ZTS for laser frequency conversion devices.

Z-Scan Studies:

The determination of third-order non-linearity at single wavelength helps to explore the applications ultrafast lasers and photonic systems. A sensitive Z-scan technique has been developed by Bahae *et al.* It is a significant tool for finding the nature and magnitude of third-order non-linearity of pure and LC-ZTS crystal. [9] In order to confirm the path-dependent third-order non-linearity, the transparent crystal sample was tightly focused by the He–Ne laser beam (632.8 nm) using a convex lens, and the crystal was move along the Z-direction with reference to focus ($Z = 0$). The respective path-dependent transmittance was noticed by means of photo detector placed at far field. The details of Z-scan set-up are given in table 1. The close aperture Z-scan technique has been used to determined third-order non-linear refraction (NLR) (n_2) of the grown crystals. The fig.2 and 3 noticed the closed aperture Z-scan transmittance curve of pure and LC-ZTS crystal. In the crystals, the pre-focus valley and the post-focus peak evidences the signature

of positive NLR which is the characteristic property of material foreshowing self-focusing nature.[10] The focused repetitive optical energy of laser beam is a crucial factor which leads to the localized absorption and spatial distribution of energy throughout the crystal surface causing a phase shift in NLR of the crystal material.[11]

The peak-to-valley transmission (ΔTp-v) can be expressedin phase shift as,

$\Delta T_{p-v} = 0.406(1 - S)^{0.25} |\Delta\phi|$

Where S = 1 – exp ($-2r_a^2/\omega_a^2$) is the aperture linear transmittance, r_a is the aperture radius and ω_a is the beam radius at the aperture. The third order non linear refractive index (n_2) of crystals has been determined using the relation, [9]

$$\eta = \frac{\Delta\varphi}{kI_0L_{eff}}$$

Where K = 2π/λ, I_0 is the beam intensity at the focus Z = 0. The effective thickness of the sampleis determine by using the equation, $L_{eff} = [1 - \exp(-\alpha L)/\alpha$, which depends on linear.

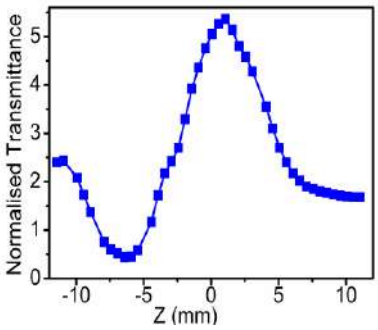

Fig.2. Closed apertures Z- scan transmittance curve of ZTS

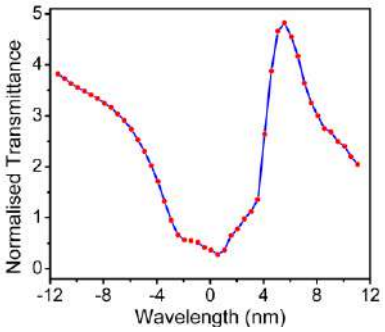

Fig.3. Closed aperture Z-scan transmittance curve of LC-ZTS

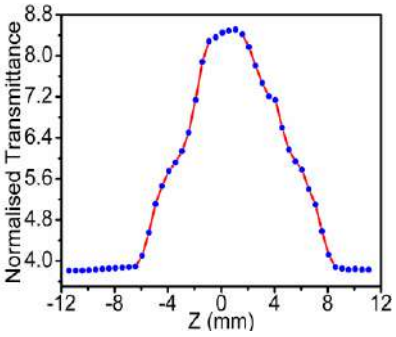

Fig.4. Open apertures Z- scan transmittance curve of ZTS

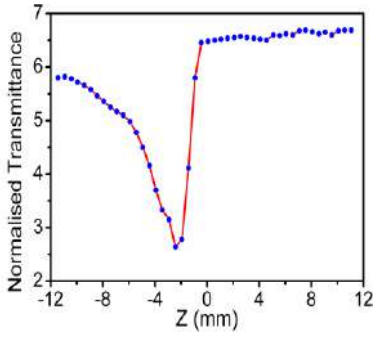

Fig.5. Closed apertures Z- scan transmittance curve of LC-ZTS

Table: 1. Optical details of Z- scan setup and measured parameters.

Laser beam wavelength (λ)	632.8nm	
Lens focal length (f)	8.5cm	
Optical path distance (Z)	115cm	
Aperture radius (r_a)	2mm	
Spot-size diameter in front of the aperture (ω_a)	1mm	
Incident intensity at the focus (Z = 0)	25MW/cm^2	
Sample thickness (L)	2mm	
Effective thickness (L_{eff})	1.81mm	
Nonlinear refractive Index (n_2)	LC-ZTS	ZTS
	3.21 x 10^{-7} cm^2/W	2.24 x 10^{-8} cm^2/W
Nonlinear absorption coefficient (β)	1.36x10^{-4} cm/W	3.91x10^{-3} cm/W
Third-order nonlinear susceptibility (χ^3)	1.42 x 10^{-3}esu	8.64 x 10^{-3}esu
Figure of Merit (FOM)	26.86	11.40

absorption coefficient (α) and thickness (L) of the sample.

The high magnitude of positive NLR relates directly to the prominent Kerr-lens mode locking (KLM) ability of the crystal. [12] The $n_2$value is found to be of the order of 10^{-7} cm²/W, such high magnitude of NLR suggests the strong Kerr-lensing effect which advocates the prominence of pure and LC-ZTS crystals for analyzing the stability limits of continuous wave mode locked laser systems and generating the shorter laser pulses. [13]

The open aperture Z-scan trace of LC-ZTS (fig.5) crystal identifies the fall in transmittance at focus, which indicates the prominence of multi-photon absorption (MPA) assisted by excited state absorption (ESA) phenomenon. [14] The MPA is a complex effect which is triggered due to contributions from two-photon absorption (TPA) along with the absorption governed by excited singlet and triplet states. [14,15] The nonlinear absorption coefficient (β) of both pure and doped ZTS can be evaluated using the open aperture transmittance data, according to the equation shown below, [9]

$$\beta = \frac{2\sqrt{2}\Delta T}{I_0 L_{eff}},$$

Where, ΔT is the one valley value obtained in open aperture Z-scan curve. The non-linear absorption coefficient (β) of LC-ZTS crystal is found to be 1.36× 10^{-4} cm/W which is superior to several reported materials.[16]The cubic susceptibly ($\chi 3$) of the crystals has been analyzed by solving the following equations,

$$Re\chi^3(esu) = \frac{10^{-4}(\varepsilon_0 C^2 n_0^2 n_2)}{\pi(cm^2/w)}$$

$$Re\chi^3(esu) = \frac{10^{-2}(\varepsilon_0 C^2 n_0^2 \lambda\beta)}{4\pi^2(cm/w)}$$

Where, ε_0 is the vacuum permittivity, n_0 is the linear refractive index of the sample and c is the velocity of light in vacuum. Thus, we can easily obtain the absolute value of χ^3 using equation,

$$\chi^3 = \sqrt{(Re\chi^3)^2 + (Im\chi^3)^2}\, esu$$

Where, ε_o, the vacuum permittivity, n_0 is the linear refractive index of the sample and c is the velocity of light in vacuum.

The LC-ZTS crystal has higher $\chi 3$ value than pure ZTS and other technologically vital crystals such as KDP, BTCF, BBO and $LiNbO_3$. [17] The observed enhancement in susceptibility of LC-ZTS crystal is an evidence of increased charge transfer through donor–acceptor channel which is the characteristic feature of strongly polarized material. The figure of merit (FOM = $\beta\lambda/n2$) is a decisive parameter to ascertain the worthiness of crystal for optical power limiting applications. [18] The pure and LC-ZTS crystals with attractive non-linear properties (see table 6.5) hold huge advantage for optical switching, calibrating optical distortions, optical logic gates and passive laser mode-locking systems. [19] The shifts observed in maximum valley transmittance of close (see figs. 6.15 and 6.16) and open (see fig.4 and5) aperture curves of LC-ZTS crystal confirm that LC is the potential dopant to tailor TONLO properties of ZTS crystal. It is interesting to note that LC has shifted the maximum valley transmittance of close and open aperture curves of ZTS crystal towards +Z direction which confirms L-cysteine as a potential dopant to tailor TONLO properties of ZTS crystal. Also, in regime of TMC crystals, the third-order non-linear susceptibility of pure and LC-ZTS crystals are remarkably greater than thiourea, BTZB, ZTS, BTZC and BTCF crystals. [8, 19].

CONCLUSION

Optically transparent pure and LC-ZTS crystals have been grown by slow evaporation solution growth technique. The enhanced SHG efficiency of LC-ZTS crystal is found to be 1.16 times that of pure ZTS crystals. The grown crystal showed potential third order nonlinear optical parameters ascertained from Z-scan technique at 632.8 nm. All above studies suggests the prominence of grown crystal for laser stabilization, microelectronics and integrated optical applications. The present studies concluded that the LC-ZTS possesses improved transparency, third order nonlinearity enhanced SHG efficiency which validates its applicability for NLO and photonic devices.

Acknowledgment
The authors thankful to Dr. P. K. Das, Department of Inorganic and Physical Chemistry, Indian Institute of Science, Bangalore for SHG measurement and

Department of Physics, S. P. Pune University for characterization facility.

.

REFERENCES

1. P M Ushasree, R Jayavel, C Subramanian, P M Ramasam,"Growth of zinc thiourea sulfate (ZTS) single crystals: A potential semiorganic NLO material", J.Cryst. Growth, 197 (1999) 216-220.
2. S Moitra, S Bhattacharya, T Kar and A Ghosh, "Dielectric properties and phase transition of zinc tris (thiourea) sulfate single crystal", Phys.ica B 403 (2008) 3244–3247.
3. M Anis, S S Hussaini, A Hakeem, M D Shirsat and G G Muley, "Synthesis, growth and optical studies of novel organometallic NLO crystal: Calcium bis-thiourea chloride", Optik127 (2016) 2137–2142.
4. M Anis, R N Shaikh, M D Shirsat and S S Hussaini, "Investigation of optical and electrical properties of L-Cystein doped zinc thiourea chloride (ZTC) crystal for nonlinear optical (NLO) applications", Opt. Laser Technol., 60 (2014) 124–129.
5. N R Dhumane, S S Hussaini, V G Dongre, M D Shirsat, "Influence of glycine on the nonlinear optical (NLO) properties of zinc (tris) thiourea sulfate (ZTS) single crystal", J. Optic. Mater. 31 (2008) 328-332.
6. J T J Prakash and M Lawrence, "Growth and characterization of pure and L-lysine doped Zinc (tris) thiourea sulphate crystals", Int. J. Comput. Appl., 8 (2010) 36–39.
7. D H Baker and G L Czarnecki-Maulden,"Pharmacologic role of cysteine in ameliorating or exacerbating mineral toxicities", J. Nutr. 117(1987) 1003-10.
8. S K Kurtz, T T Perry, "A powder technique for the evaluation of nonlinear optical materials", J. Appl. Phys. 39 (1968) 3798-3713.
9. M S Sheik-Bahae, A A Said, T H Wei, D J Hagan and E W Van Stryland, "Sensitive measurement of optical nonlinearities using a single beam", IEEE J. Quant. Electron., 26 (1990) 760–769.
10. X Q Wang, Q Ren, J Sun, H L Yang, T B Li, H L Fan, G H Zhang, D Xu and J H Zhao, "Preparation, physicochemical and third order nonlinear optical properties of bis (tetrabutylammonium) bis (2-thioxo- 1,3-dithiole-4,5-dithiolato) mercurate (II)", Cryst. Res. Technol., 44 (2009) 657–668.
11. B Gu, H T Wang and W Ji, "Z-scan technique for investigation of the non instantaneous optical Kerr nonlinearity", Opt. Lett., 34 (2009) 2769–2771.
12. F Helen and G Kanchana, "Investigation on the properties of L-Serine doped zinc tris (thiourea) sulphate crystal for NLO applications", Indian J. Pure Appl. Phys. 52, (2014) 821-828.
13. A Major, J S Aitchison, P W E Smith, F Druon, P Georges, B Viana and G P Aka,"Z-scan measurements of the nonlinear refractive indices of novel Yb-doped laser crystal hosts", Appl. Phys. B, 80 (2005) 199–201.
14. K Janardhana, V Ravindrachary, P C Rajesh Kumar, Yogisha and Ismayil, "Third order nonlinear optical studies of 1-(4-chloro phenyl)-3-(4-dimethylamino phenyl) prop-2-en-1-one", J. Cryst. Growth, 368 (2013) 11–20.
15. R Sai Santosh Kumar, S Venugopal Rao, L Giribabu and D Narayana Rao, "Femtosecond and nanosecond nonlinear optical properties of alkyl phthalocyanines studied using Z-scan technique", Chem. Phys. Lett., 447 (2007) 274–278.
16. N N Shejwal, M Anis, S S Hussaini and M D Shirsat, "Optical, thermal and electrical properties of pure and doped bis-thiourea cadmium formate (BTCF) crystal", Phys. Scr., 89 (2014) 125804–125811.
17. P Srinivasan, A Y Nooraldeen, T Kanagasekaran, A N Dhinaa, P K Palanisamy and R Gopalakrishnan, "Z-scan determination of the thirdorder optical nonlinearity of l-asparaginium picrate (LASP) crystal", Laser Phys., 18 (2008) 790–793.
18. T Kanagasekaran, P Mythili, P Srinivasan, A Y Nooraldeen, P K Palanisamy and R Gopalakrishnan, "Studies on the growth, optical, thermal, and mechanical properties of pure and o-nitroaniline doped benzyl crystals", Cryst. Growth Des. 8 (2008) 2335–2339.
19. B Thirumalaiselvam, R Kanagadurai, D Jayaraman and V Natarajan, "Growth and characterization of 4-methyl benzene sulfonamide single crystals", Opt. Mater., 37 (2014) 74–79.
20. T C Sabari Girisun, S Dhanuskodi, D Mangalaraj and J Phillip, "Synthesis, growth and characterization of bisthiourea zinc bromide for optical limiting applications", Curr. Appl. Phys., 11 (2011) 838–843.

IRJSE *Int. Res. J. of Science & Engineering,* 2018; Special Issue A2 : 272-275 SJIF Impact Factor 4.11
ISSN: 2322-0015 UGC Approved Journal No. 63628
RESEARCH ARTICLE **OPEN ACCESS**

Design and Development of Rack and Pinion for 180º Flipping Machine

Vavhal Prashant, Shivam Swami, Harshal Mahajan, Jueli Lad, Suraj Nanaware

Department of Mechanical Engineering, P. K. Techanical Campus, Chakan, Pune, MS, India
Email: prashantvavhal44@gmail.com

Manuscript Details
Available online on http://www.irjse.in
ISSN: 2322-0015

Editor: Dr. Arvind Chavhan

Cite this article as:
Vavhal Prashant, Swami Shivam, Mahajan Harshal, Jueli Lad, Nanaware Suraj. Design and Development of Rack and Pinion for 180º Flipping Machine, *Int. Res. Journal of Science & Engineering,* January 2018; Special Issue A2: 272-275.

ABSTRACT

This is 180 º Flipping Mechanism. In this mechanism the component is rotated at an angle of 180 º from its main position. In this mechanism the component is rotated with the help of rack and pinion mechanism. The Gears while transmitting the power develop stresses at the mating positions. A pair of teeth inaction is generally subjected to stresses like bending stresses inducing bending fatigue, Wear stresses inducing wear fatigue and Shear stresses inducing shear fatigue. It is required to explore some alternate materials to improve the performance of the spur gears and to sustain stresses. Composite materials provide adequate strength with weight reduction and they are emerging as a better alternative for replacing metallic gears. This work includes design and weight optimization of output pinion.

Keywords: 180º Flipping Machine, Rack and Pinion, etc.

INTRODUCTION

Gears are mechanical components used for transmitting motion and torque from one shaft to another. Ever since invention of rotating machines, gears existed. During early centuries gears made of either wood or stone teeth set in wood. Later during metal ages Iron, Bronze or tin were used instead of stone. A rack and pinion is a type of linear actuator that comprises a pair of gears which convert rotational motion into linear motion. A circular gear called "the pinion" engages teeth on a linear "gear" bar called "the rack"; rotational motion applied to the

Pinion causes the rack to move relative to the pinion, Thereby translating the rotational motion of the pinion into linear motion.The spur gear is simplest type of gear manufactured and is generally used for transmission of rotary motion between parallel shafts. The spur gear is the first choice option for gears except when high speeds, loads, and ratios direct towards other options. Other gear types may also be preferred to provide more silent low-vibration operation.

Figure 1.1 Rack and Pinion mechanisms

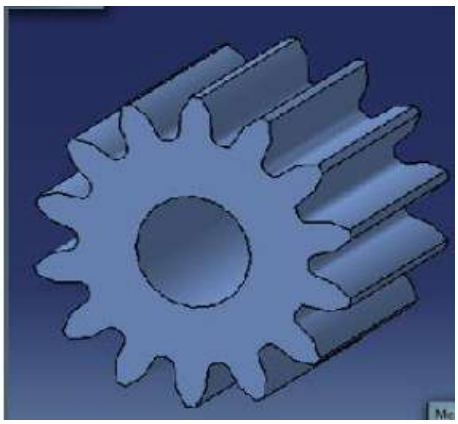

Figure 1.2: Rack and Pinion

A single spur gear is generally selected to have a ratio range of between 1:1 and 1:6 with a pitch line velocity up to 25 m/s. The spur gear has an operating efficiency of 98-99%. The pinion is made from a harder material than the wheel. A gear pair should be selected to have the highest number of teeth consistent with a suitable safety margin in strength and wear. The minimum number of teeth on a gear with a normal pressure angle of 20 degrees is 18. This is a cylindrical shaped gear in which the teeth are parallel to the axis. It has the largest applications and, also, it is the easiest to manufacture. They are simple in construction, easy to manufacture and cost less. They have highest efficiency and excellent precision rating. They are used in high speed and high load application in all types of trains and a wide range of velocity ratios. Hence, they find wide applications right from clocks, household gadgets, motor cycles, automobiles, and railways to aircrafts. During this phase, they encounter high stress at the point of contact. A pair of teeth in action is generally subjected to two types of cyclic stresses:

i) Bending stresses inducing bending fatigue
ii) Wear stress causing wear fatigue.

Both these types of stresses may not attain their maximum values at the same point of contact. However, combined action of both of them is the reason of failure of gear tooth leading to fracture at the root of a tooth under bending fatigue and surface failure, due to contact fatigue. When loads are applied to the bodies, their surfaces deform elastically near the point of contact. The highest stresses exist at regions where the lines are bunched closest together. The highest stress occurs at two locations:

a. At contact point where the force' F' acts
b. At the fillet region near the base of the tooth

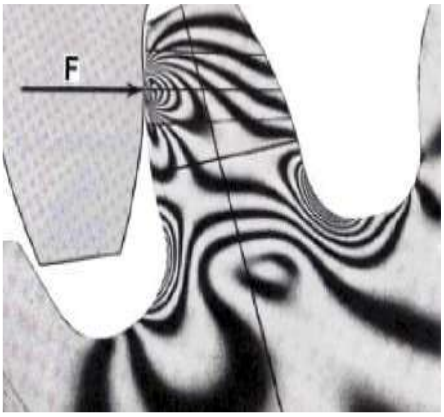

Figure 1.3: The highest stresses

PROBLEM STATEMENT

In this thesis spur pinion are widely used for 180^{o} Flipping mechanism. The failure is observed in pinion are due to various reasons like condition of loading, improper lubrication, corrosion etc. in the pinion failure generally start at root fillet radius and the cracks may have observed at fillets. This teeth failure may lead to failure in entire transmission system. this

problem can be minimizing by a selection of different material to a spur pinion. In the higher weight of part also lead problem in rotation of component in 180° to such the weight reduction can be achieved by changing the material of spur pinion.

OBJECTIVE

In spite of the number of investigations devoted to gear research and analysis there still remains to be developed, a general numerical approach capable of predicting the effects of variations in gear geometry, bending stresses and Von-Mises stresses. The objectives of this project are to use a numerical approach to develop theoretical models of the behavior of gears in mesh, to help to predict the effect of gear tooth stresses and transmission error. The main focus of the current research as developed here is to analyses the failure of spur pinion.

i) Model of baseline of spur pinion by solid edge ST7 software.
ii) Analyses the baseline spur pinion design by Ansys and evaluate deflection and stress for different material as steel and aluminum, composite material.
iii) Development of Spur Pinion with all Material.
iv) Compare Experimentally Material Testing and Loading Stress for all material

SCOPE

This work focuses on the use of less weight material like aluminum, composite material for spur pinion. It shows that the stresses are lower in the aluminum, composite material than in steel alloy. So it increases the life of gears used for180° Flipping Mechanism. Thus this work suggests replacing the metallic gears with less weight aluminum and composite gears which has better properties than metallic gears.

CONTRRUCTION AND WORKING

CONSTRUCTION

In this mechanism actuator and rack are assembles with the help of fasteners. That actuator moves rack linearly. There is rack and pinion assembly. There is also base plate and two support plate that is called holding device. Linear pneumatic actuator is used of size 45*45*344, Bore: 32mm, Stroke: 200mm; Port size: PT1/8 Action Type: Double Acting; Rod Type: Single Rod Net Weight: 820g

WORKING

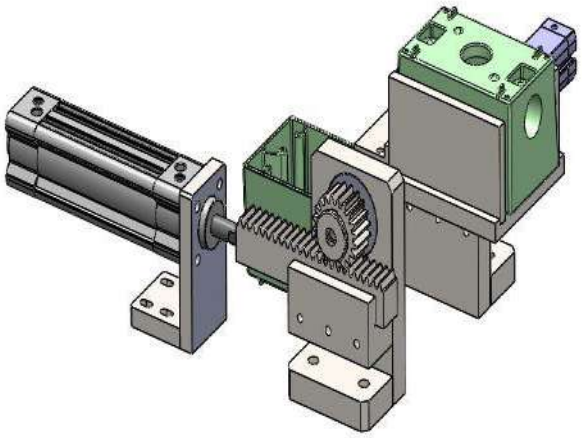

Figure 5.1 180° working model

This 180° Flipping mechanism is used to rotate the component in the 180° with less time and less human effort. In manufacturing work performed on top face of component or work piece, but sometimes it needs to work on its bottom side also for that we use 180° flipping mechanism. In this mechanism the power is supplied to run the linear pneumatic actuator. That is actuator moves forward and return stroke while power is transmitted.

The movement of actuator in forward direction that pushes the rack also in forward direction. Since there is rack and pinion assembly its rotates the pinion at the same time of rack moment. That pinion is attached to the shaft and when pinion rotates shaft also rotate. The holding device i.e. base plate and two support plate is welded to the shaft. The component is held in that holding device i.e. in between two support plate. When the pinion rotates the component is also rotating, which is held in that holding device. That component is rotated in 180° with this rack and pinion mechanism. This Flipping mechanism is like pick and place operation.

CONCLUSION

Various research works has been carried out in the past regarding to change of material of pinion. By changing the material of pinion increases the strength of rack and pinion. In various research by providing

the slots on the pinion weight can be reduced but strength will be reduced. This is simplest way to increase strength and reduce weight.

Conflicts of interest: The authors stated that no conflicts of interest.

REFERENCES

1. ABDUL MD, JUNAIDI RAHEEM, YAHIYA MD, AHMED MD NASER, AHMED MOHAMMED AQEEL, "DESIGN AND ANALYSIS OF HIGH SPEED HELICAL GEAR USING ANSYS" IJREAT INTERNATIONAL JOURNAL OF RESEARCH IN ENGINEERING & ADVANCED TECHNOLOGY,2016,VOLUME 4, ISSUE 1, ISSN: 2320 – 8791
2. RAJAPRABAKARAN V, AND ASHOKRAJ R "SPUR GEAR TOOTH STRESS ANALYSIS AND STRESS REDUCTION" E-ISSN: 2278-1684, P-ISSN: 2320-334X PP 38-48.
3. JABBOUR TONI, ASMAR GHAZI "TOOTH STRESS CALCULATION OF METAL SPUR AND HELICAL GEARS" JOURNAL OF MECHANISM AND MACHINE THEORY 92 ,2015, 375-390.
4. AMBADE VISHWJEET V, VANALKAR AV, GAJBHIYE PR "INVOLUTE GEAR TOOTH CONTACT AND BENDING STRESS ANALYSIS" INTERNATIONAL JOURNAL OF COMPUTATIONAL ENGINEERING RESEARCH, 2013,VOL. 03,30-36.
5. BADITHE MAHESH, SRIKANTH SRIMANTHULA, BODAPALLI JITHENDRA "STRESS AND REDUCTION ANALYSIS OF SPUR GEAR TOOTH" INTERNATIONAL JOURNAL ON EMERGING TECHNOLOGY AND ADVANCED ENGINEERING, 2014,VOL.4
6. SHINDE SP,NIKAM AA, MULLAH TS "STATIC ANALYSIS OF SPUR GEAR USING FINITE ELEMENT ANALYSIS." ISSN: 2278-1684, 26-31.
7. DOLAS DANANJAY ET AL. "STATIC ANALYSIS BENDING STRESS ON GEAR TOOTH PROFILE BY VARIATION OF GEAR PARAMETER WITH THE HELP OF FEA "IJERT,2014, VOL 3, 132-136

IRJSE *Int. Res. J. of Science & Engineering,* 2018; Special Issue A2 : 276-278 SJIF Impact Factor 4.11
ISSN: 2322-0015 UGC Approved Journal No. 63628
RESEARCH ARTICLE **OPEN ACCESS**

Study of Optical Properties of Doped Nonlinear Optical Materials

Bawaskar Ravi

Dept. of Physics, Dada Patil Rajale College, Adinathnagar, Tal: Pathardi, Dist. Ahmednagar (MS)
Email: bavaskarravi66@gmail.com

Manuscript Details
Available online on http://www.irjse.in
ISSN: 2322-0015

Editor: Dr. Arvind Chavhan

Cite this article as:
Bawaskar Ravi. Study of Optical Properties of Doped Nonlinear Optical Materials, *Int. Res. Journal of Science & Engineering,* January 2018; Special Issue A2: 276-278.

ABSTRACT

Single crystals of p-Toluidine p-Toluenesulfonate (PTPT), an organic nonlinear optical (NLO) material, have been grown by slow evaporation method at room temperature using ethanol as solvent. The crystal system was confirmed from the single crystal XRD analysis. UV-Vis-NIR spectrum showed that the UV cut-off wavelength of PTPT occurs at 200-400 nm and it has insignificant absorption in the wavelength region of 550–750 nm. The SHG efficiency of PTPT was measured.

Keywords: Nonlinear optics, XRD, Fourier transform infrared spectroscopy, etc.

INTRODUCTION

Single crystals form an indispensable part of the rapidly advancing technology which is dependent upon materials such as semiconductor, super conductors, super ionic conductors, polarizers, transducers, radiation detectors, ultra-sonic amplifiers, magnetic garnets, Solid-state lasers, Non-linear optics, piezoelectric, electro optic, photosensitive, refractories of different grades, crystalline film for micro-electronics and computer industry [1-3]. All these aspects of modern science and technology involve research in the field of crystal growth. The art of growing crystals has turned into a new direction of science with the discovery of wide spectrum of applications of single crystals and they have become one of the most the fundamental building blocks

for modern technology. A crystal is a three dimensional periodic array of atoms. Crystals are classified in two categories, single crystals and poly crystals. An ideal single crystal is constructed by infinite repetition of identical structural units in space [9]. Real crystals are finite and contain defects. The properties of material can be extensively studied when material is prepared in single crystal form. The uniformity of single crystal allows transmission of electromagnetic waves without scattering. Hence in the past few decades one could see that there is a lot of development in science and technology of crystals, especially in the field of electronics, fiber optics and lasers. The tunable lasers have been realized because of invention of nonlinear optical properties in some single crystal. Since solid state devices are being widely used in the field of computers, telecommunication etc, efforts are being made for producing larger single crystal. Nonlinear optical crystals are very important for laser frequency conversion. In recent years there has been considerable progress in the development of coherent UV sources based on nonlinear optical process in borate crystals. The success of these crystals can be attributed to the unique structural characteristics of boron-oxygen groups that confer these compounds with enhanced UV transparency, good nonlinearity and high resistance to laser damage. β-Barium Borate, Lithium Borate, Potassium beryllium boro-fluoride, Strontium beryllium borate, Cesium borate and Cesium lithium borate are promising for UV generation because of its wide band gap and adequate optical nonlinearity. YCa4O (BO3)3 (YCOB) and GdxY1-xCa4O (BO3)3 crystals are suitable for second and third harmonic generation of Nd:YAG laser radiation. Various kinds of NLO crystals have been developed because of possibility of extreme high optical nonlinearity [4,5]. The consistency of the characteristics of device fabricated from a crystal depends on the homogeneity and defect contents of the crystals. Hence, the process of producing single crystals which offer homogeneous media in the atomic level with directional properties, attract more attention than any other process involved. The procedure of growing crystals varies widely; it is mainly dictated by the characteristics of the material and its size. Day by day the demand for nonlinear optical crystals with superior properties is mounting due to quantum leap in the design of nonlinear optical devices with high performance. With progress in crystal growth technology, materials having attractive nonlinear properties are being discovered at rapid pace. To enable a material to be potentially useful for NLO applications, the material should be in bulk single crystal form. So the growth of new nonlinear optical material crystals and their investigation have become most indispensable and efficacious disciplines in the field of material science and engineering [11,12]

METHODOLOGY

Crystal Growth:

The resultant compound is obtained by the adding of p-toluenesulfonic acid (0.02 mol) with a solution of p-Toluidine (0.02 mol) in ethanol, in the stoichiometric ratio 1:1. Within 7 days, tiny crystals were formed due to the spontaneous nucleation. Optically transparent good quality crystals were used as seeds for further growth experiments. For growth, seed crystals were just immersed into the prepared solution. Good quality crystals with characteristic shape and size of mm^3 were obtained for 8 days. Figure 1 shows molecular structure of PTPT. Figure2 shows the growth of crystals.,

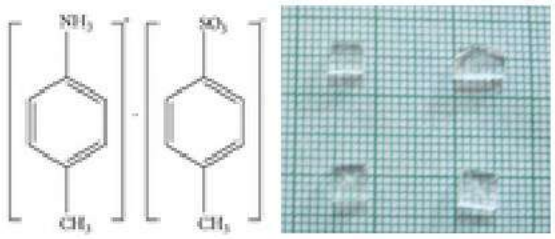

Figure 1: Figure 2:

Figure 1: Molecular Structure of PTPT

Figure 2: Grown Crystal of PTPT

which was sintered at 600^0C.from VSM the magnetic properties of the samples show remarkable changes with change of Pb percentage.

RESULTS AND DISCUSSION

XRD Studies:

The XRD pattern of PTPT is shown in Figure 3. Using the single crystal -ray diffraction analysis, the cell

parameters of PTPT were obtained from least-squares refinement of the setting angles of 25 reflections. The XRD study reveals that the crystal belongs to monoclinic system with lattice parameters of a = 5.8780 Å, b = 9.1152 Å and

c = 13.2312Å, Z = 2, and space group is $P2_1$.

UV-Vis-NIR Studies: The recorded UV-Vis-NIR spectrum of PTPT is shown in Figure 4. UV-Vis transmittance was recorded to analyze the optical properties of growth PTPT crystal. Therefore, well-polished sample of 1 mm thick from the grown crystal was used. The optical absorption study shows that the UV cut-off wavelength of PTPT occurs at 295 nm. It is well known that the efficient NLO crystal has an optical transparency at lower cut-off wavelength between 200 and 400 nm. There is no significant absorption in the entire visible region which reveals that it can find applications in the optoelectronic devices. The very low absorption around 550–750 nm signifies the resistance of the grown crystal to laser induced damage.

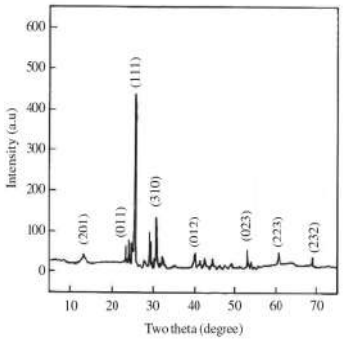

Fig. 3: XRD pattern of PTPT.

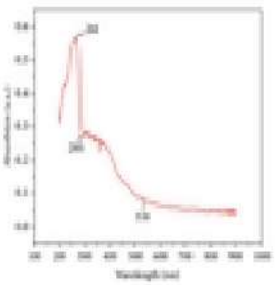

Fig. 4: UV-Vis-NIR spectrum of PTPT

CONCLUSION

Single crystals of p-Toluidine p-Toluenesulfonate (PTPT) were grown from ethanol solution by slow evaporation of the solvent at room temperature. The crystal system was confirmed from the single crystal XRD analysis. Optical absorption studies show that the sample has minimum absorption in the entire visible region. The SHG efficiency of PTPT was found to be 0.52 times than that of standard KDP.

.

REFERENCES

1. X.J. Liu, Z.Y. Wang, X.Q. Wang, G.H. Zhang, S.X. Xu, A.D. Duan, S.J. Zhang, Z.H. Sun, D. XuMorph ology and physical properties of L-arginine trifluoroacetate crystals Cryst. Growth Des., 8 (2008), pp. 2270-2274
2. J. Badan, R. Hierle, A. Perigaud, J. Zyss, D.J. Willia ms NLO properties of organic molecules and polymeric materials
3. American Chemical Symposium Series, vol. 233, American Chemical Society, Washington, DC(1993)
4. D.S. Chemla, J. ZyssNon-linear Optical Properties of Organic Molecules and Crystals Academic Press, Orlando, New York (1987)
5. D. Xue, S. Zhang Chemical bond analysis of the correlation between crystal structure and nonlinear optical properties of complex crystals Physica B, 262 (1999), pp. 78-83
6. M. Fleck, M. Aram Petrosyan, Salts of Amino Acids, Crystallization, Structure and Properties Springer International Publishing, Switzerland (2014)
7. R. Mohan Kumar, D. Rajan Babu D. Jayaraman R. Jayavel, K. Kitamura Studies on the growth aspects of semi-organic L-alanine acetate: a promising NLO crystal J. Cryst. Growth, 275 (2005), pp. e1935-e1939

International Research Journal of
Science & Engineering
An International Peer Reviewed Open Access Refereed Journal

Special Issue A 2 January, 2018
on
Advanced Methods for Material Characterization

ORIGINAL ARTICLES

ISSN 2322-0015